Modeling Long-Term Erosion at the West Valley Demonstration Project and Western New York Nuclear Services Center

Prepared by:
West Valley Erosion Working Group Modeling Team

Prepared for:
United States Department of Energy
and New York State Energy Research and Development Authority,
under contract to Enviro Compliance Solutions, Inc. (ECS).

Contract Number DE-EM0002446/0920/13/DE-DT0005364/001

April 25, 2018

Modeling Long-Term Erosion at the West Valley Demonstration Project and Western New York Nuclear Services Center

West Valley Erosion Working Group (EWG) Modeling Team:

TEAM LEADS:

Gregory E. Tucker, Ph.D.	University of Colorado, Boulder
Sandra G. Doty, M.S., P.E.	Consulting Geological Engineer

LEAD TECHNICAL SPECIALIST:

Katherine R. Barnhart, Ph.D.	University of Colorado, Boulder

UNCERTAINTY QUANTIFICATION SPECIALIST:

Mary C. Hill, Ph.D.	University of Kansas

CLIMATE DATA SPECIALIST:

Matthew W. Rossi, Ph.D.	University of Colorado, Boulder

GEOMORPHIC MODELING SPECIALISTS:

Charles M. Shobe	University of Colorado, Boulder
Rachel C. Glade	University of Colorado, Boulder

STUDY AREA MANAGER:

Michael Wolff, PG, CEG	Enviro Compliance Solutions, Inc.

Acknowledgments. This work utilized the RMACC Summit supercomputer, which is supported by the National Science Foundation (awards ACI-1532235 and ACI-1532236), the University of Colorado Boulder, and Colorado State University. The Summit supercomputer is a joint effort of the University of Colorado Boulder and Colorado State University. This work was supported in part by the Scalable Petascale Storage Infrastructure funded by NSF under grant OCI-1126839.

Storage Resources were provided by NSF-MRI Grant ACI-1126839, MRI: Acquisiton of a Scalable Petascale Storage Infrastructure for Data-Collections and Data-Intensive Discovery.

Contents

Part I

Executive Summary

Executive Summary

The Western New York Nuclear Services Center and West Valley Demonstration Project Site ("the Site") hosts radiological waste material that may be vulnerable to exhumation by erosional processes in the distant future. Because of the hazardous nature of these materials, release into the environment could pose a health hazard to communities in the site area, the Cattaraugus Creek corridor, and the Lake Erie basin. Management, monitoring, and performance assessment at the Site require estimates of potential future erosion rates and patterns. Although a number of model-based estimates have been made, none have quantified the associated uncertainties. In addition, newly available data on erosion processes and geologic history obtained by the Erosion Working Group (*Bennett*, 2017; *Wilson and Young*, 2018), as well as new high-resolution LiDAR topography, afford an opportunity to improve on past erosion studies. To address this need, the Erosion Working Group developed an improved framework for long-term erosion modeling at the Site, and used that framework to produce model-based ensemble projections of future erosion, with quantified uncertainties, up to 10,000 years into the future. The resulting database can be used to inform Site monitoring, management, and performance assessment. The framework can also be applied to future erosion-modeling needs as new data become available and new questions emerge.

The approach involved the use of 37 different models of long-term erosion. The application of multiple models was designed to provide a measure of the uncertainty in model structure, which reflects uncertainty in present scientific knowledge of the governing processes as well as uncertainty in nature of the particular processes and materials at the Site. For purposes of model sensitivity analysis and calibration, the topography of the Franks Creek watershed as it likely appeared at the time of last glacial recession, approximately 13,000 years ago, was reconstructed. The reconstructed topography was represented at a resolution of 24 feet per model grid cell, with a model domain consisting of approximately 100,000 grid cells. To represent the elevation history of the watershed's outlet from 13,000 years ago to the present day, two alternative reconstructions developed by the Erosion Working Group from geologic dating were used. By starting the models with the post-glacial topography and applying the reconstructed outlet-lowering histories, it was possible to run each model forward in time to the present day and compare the observed and simulated terrain. To determine the relative importance of different model inputs, a systematic sensitivity analysis was performed on each model and with each combination of initial topography and outlet-lowering history. The sensitivity analysis indicated that the comparison of observed and simulated topography is largely insensitive to details of reconstructed post-glacial topography or lowering history.

Each model was calibrated by systematically varying its parameters in order to identify an optimal match between observed and simulated modern topography. The calibration process

provided a test of the relative performance of different models, as well as identification of the optimal set of input parameters for each model. A validation test was then performed in which each calibrated model was initialized with post-glacial topography for a separate watershed, the size and geology of which were similar to the size and geology of the Franks Creek watershed, located on the northeast side of the Buttermilk Creek valley. The results of the test indicated that those models that performed better in calibration also performed better in validation, and vice versa. Based on calibration and validation results, nine models were selected for further use. The most important model element associated with good performance in calibration and validation testing was explicit representation of the two major lithologies (bedrock and glacial sediments). This feature was present in all nine selected models. Models also tended to perform better when they included an erosion threshold and/or a nonlinear representation of down-slope movement of soils and sediments. The one model that included all three of these elements ranked highest in calibration.

A key objective of the study was to quantify uncertainty in projected future erosion. Sources of uncertainty addressed included: future climate, future downcutting in the Buttermilk Creek valley, model structure, calibration of model parameters, human modification to contemporary topography, and the potential for stream capture. Uncertainty in climate was addressed by formulating three alternative future-climate scenarios, based on climate-model projections for the 21st century and assuming long-term persistence of changes. Uncertainty in downcutting was represented by using three alternative, geologically defensible projections for the future erosion rate in the Buttermilk Creek valley. Model structure uncertainty was addressed by using a suite of nine models. Uncertainty in calibration of parameter inputs was addressed by propagating the joint distribution of parameter values estimated though calibration into a distribution of the value for projected erosion at 25 selected points at the Site. The impact of minor (±5 feet) variations in Site and watershed topography was quantified through the use of ensembles of simulations with random perturbations on the starting digital elevation model. These random perturbations are intended to represent relatively minor human modification to the surface that may alter the surface drainage patters on the plateau. Finally, uncertainty arising from the potential for stream capture was addressed with an experiment that explored a set of potential capture scenarios that considered two different capture locations and several different time frames.

To incorporate these various sources of uncertainty in erosion projections, the projection model runs were organized into three experiments. The main experiment addressed uncertainty in future erosion arising from model structure, future climate, future downcutting, and human modification to contemporary topography. The experiment involved about 8,200 model evaluations. The second experiment addressed uncertainty arising from model parameter values. This experiment used a surrogate approach, in which 16,000 model evaluations were used to construct surrogates for future erosion at intervals of 100 years at each of 25 selected locations at the Site. A very large ensemble of evaluations on these surrogate models enabled the construction of probability distributions future erosion at each selected point in 100-year increments. The third experiment used 180 model evaluations to explore the likelihood and potential consequences of stream capture.

The results of these calculations are a series of maps and digital data files that depict projected erosion depth and the associated uncertainty at different locations across the watershed. An example of a composite expected-erosion map is shown in Figure 1. The map

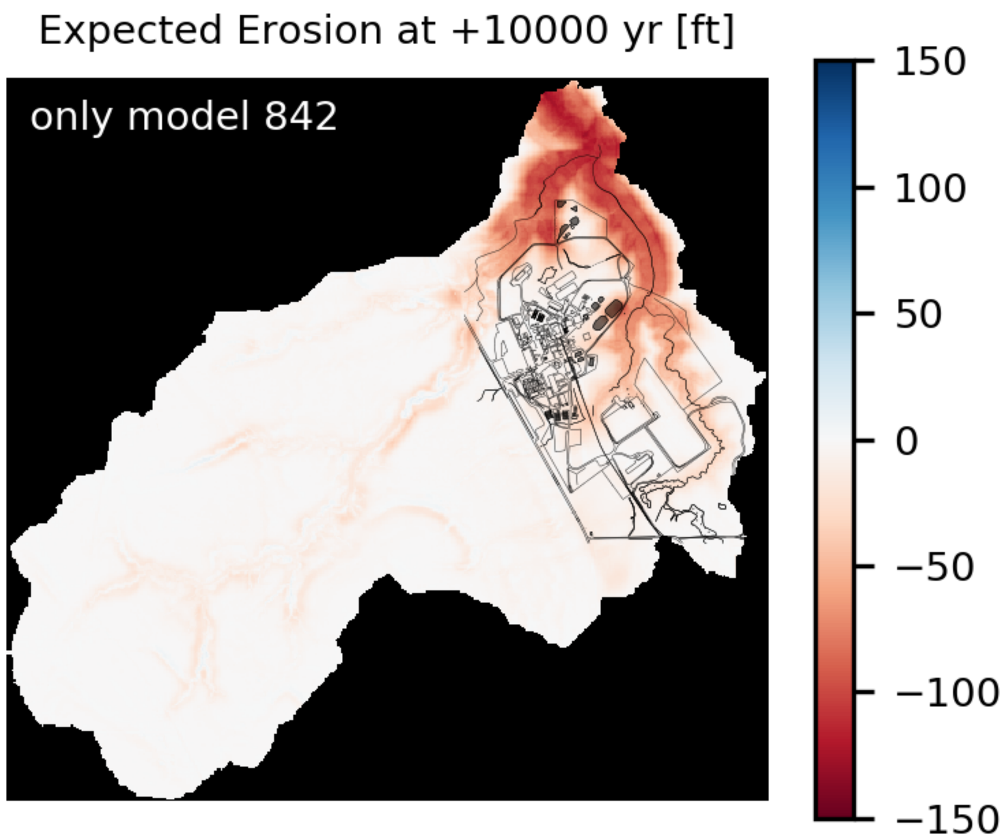

Figure 1: Composite map of expected erosion at 10,000 years in the future, from top-calibrated model.

depicts, in color shading, the total expected depth of cumulative erosion at each grid cell at 10,000 years into the future, based on the top-ranked model. The total 1-σ (one standard deviation) uncertainty associated with this map is shown in Figure 2. The uncertainty maps combine uncertainties from all sources except input-parameter uncertainty, which is addressed on a point-by-point basis (because of the prohibitive computational cost of calculating parameter uncertainty at each model grid cell). An alternative way to view expected erosion and the associated uncertainty is through maps that show projected erosion at a certain outer confidence interval. For example, maps of projected erosion from the leading model, plus and minus two standard deviations, are shown in Figures 3 and 4. Maps like the ones in Figures 1–4 are provided in this report for a range of different time intervals, and for both the leading model alone and a composite of all nine selected models. The 25 specific locations for which at-a-point erosion trajectories are plotted and discussed, and for which model-parameter uncertainty bounds are calculated, are shown in Figure 5. Table 1 lists projected erosion depths and their uncertainty bounds at 10,000 years into the future for these 25 selected points.

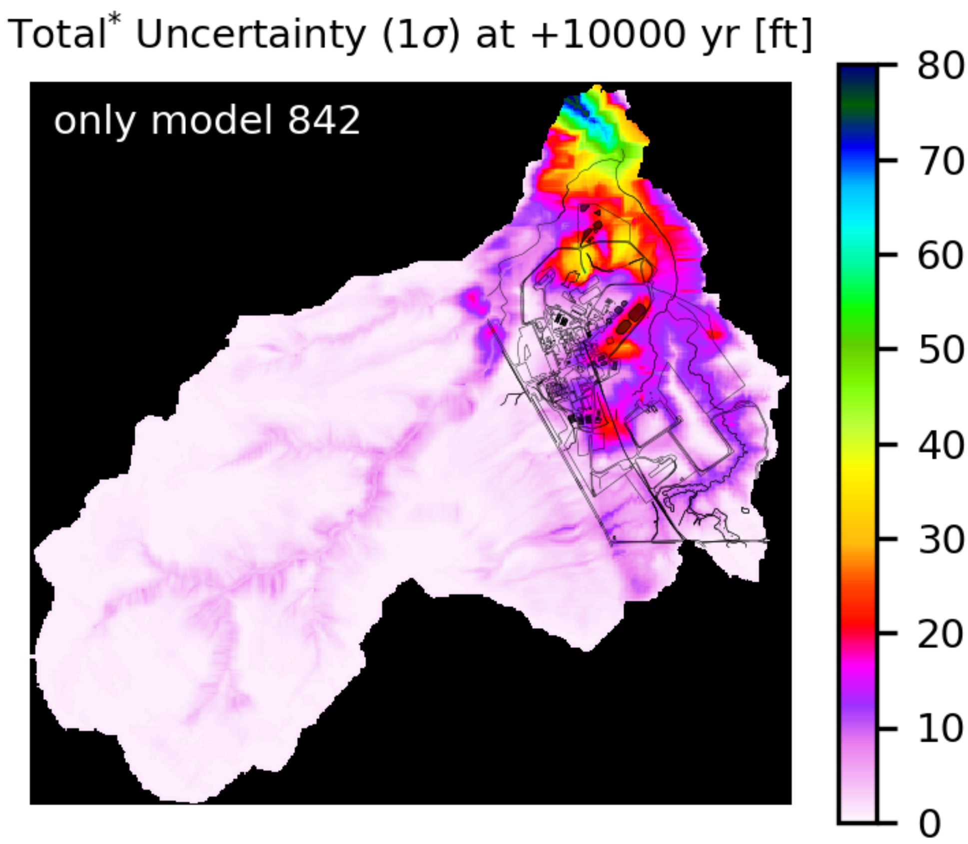

Figure 2: Map showing total uncertainty from all sources except calibration of model parameters, for 10,000 years in the future, from top-calibrated model.

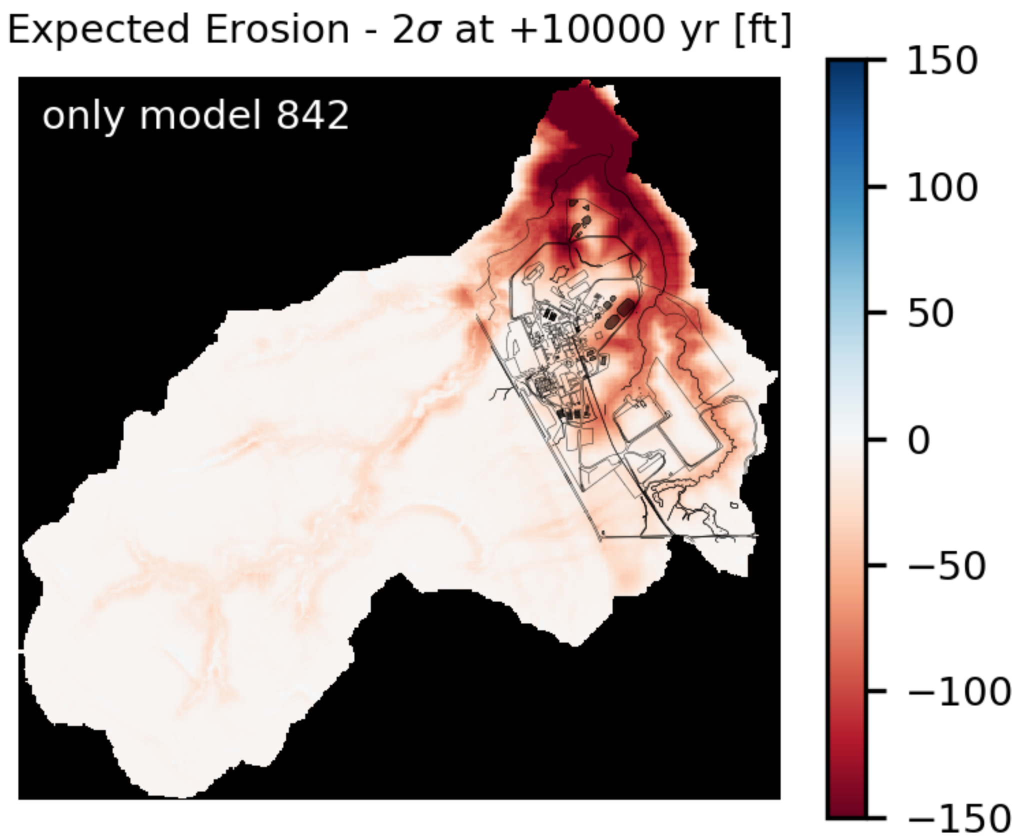

Figure 3: Composite maps of expected erosion minus 2σ (i.e., more erosion than the expected values) at 10,000 years in the future, for top-calibrated model.

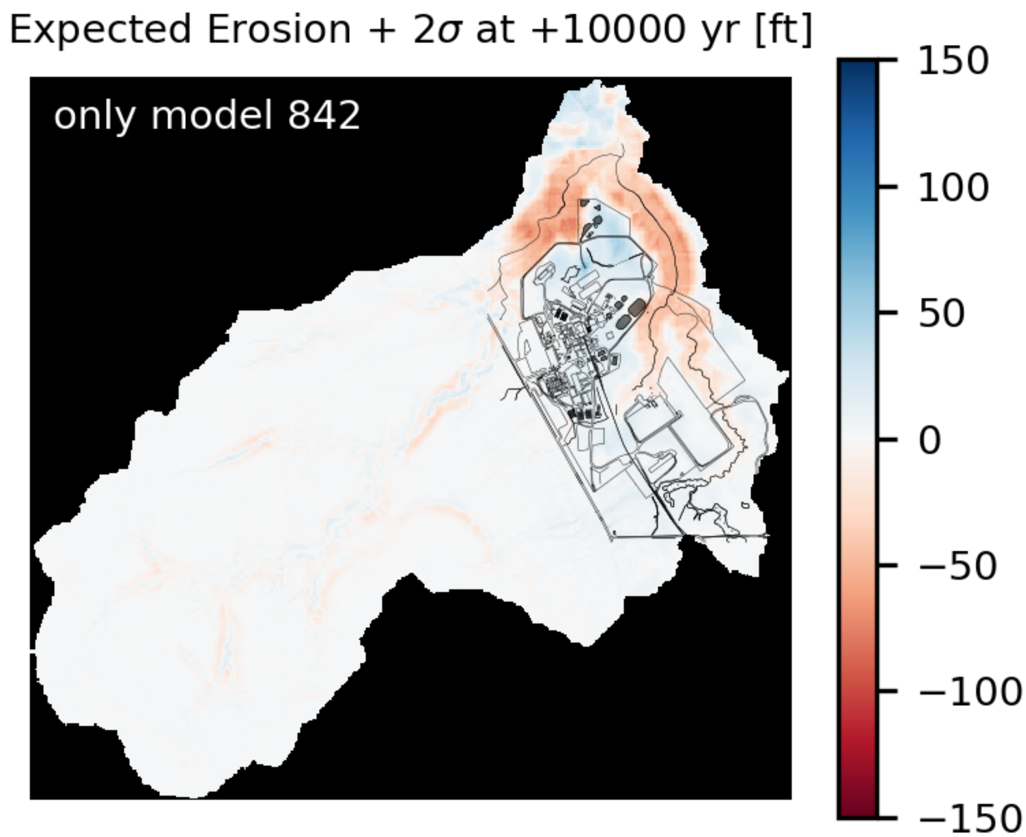

Figure 4: Composite maps of expected erosion plus 2σ (i.e., less erosion than the expected values) at 10,000 years in the future, for top-calibrated model.

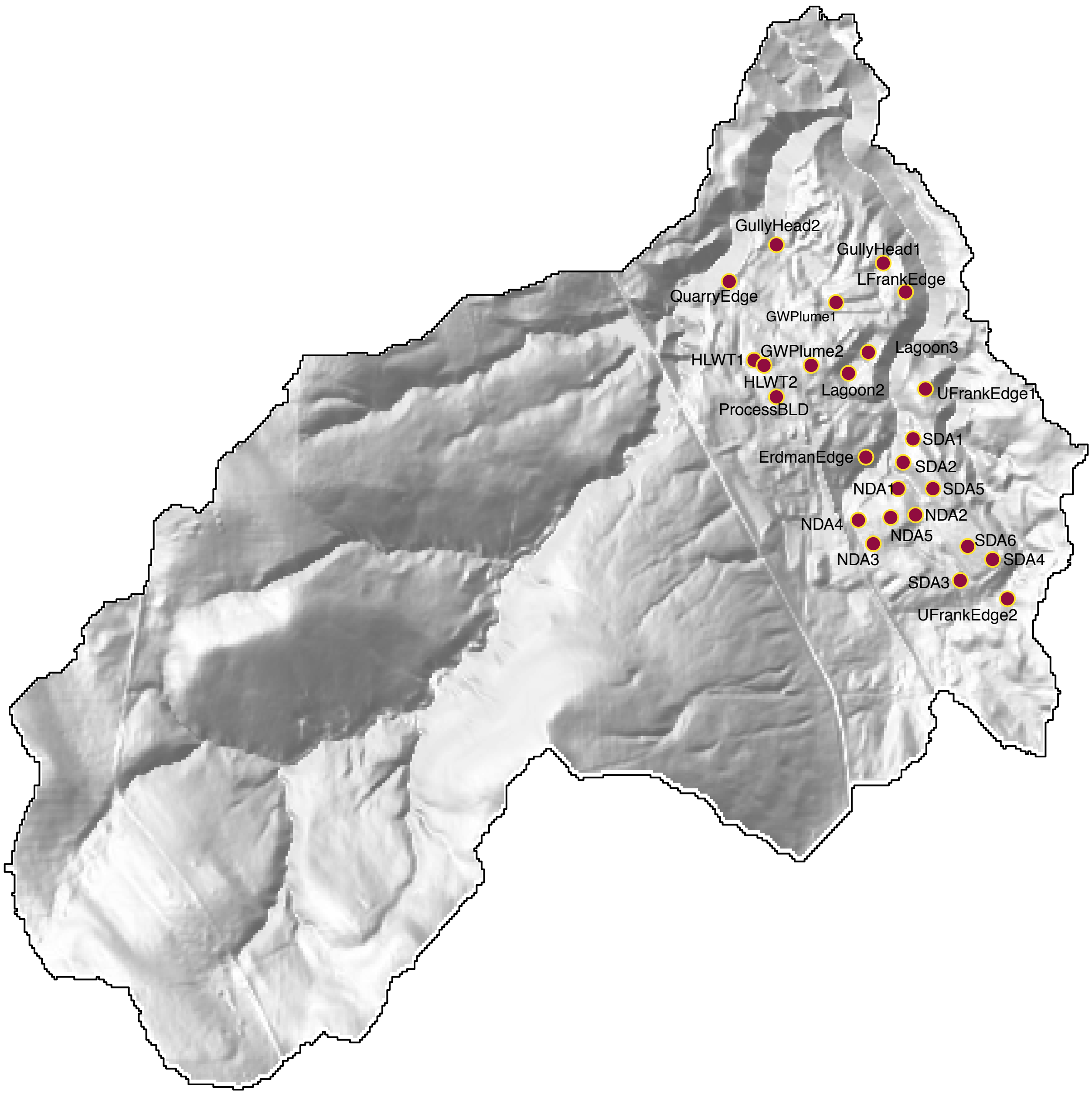

Figure 5: Map of Franks Creek watershed model domain with the locations of 25 analysis sites noted as red dots and text specifying the name used for each site.

Table 1: Mean and standard deviation for expected depth of erosion at the 25 detailed analysis points at 200, 500, 1000, and 10,000 years in the future. Positive values indicate erosion and negative values indicated deposition. Projections using both multi-model approaches (model 842 only and all nine 800 model variants) are presented. Presented standard deviation includes all considered sources of uncertainty.

		+200 years		+500 years		+1000 years		+10,000 years	
Location	Approach	μ [ft]	σ [ft]	μ [ft]	σ [ft]	μ [ft]	σ [ft]	μ [ft]	σ [ft]
ErdmanEdge	Model 842 Only	-0.16	3.03	0.15	2.72	0.85	2.86	30.57	17.07
	All nine 800s	0.05	2.92	0.43	2.26	1.59	2.40	35.49	15.52
GullyHead1	Model 842 Only	2.72	3.32	5.34	4.57	10.26	7.25	85.31	30.31
	All nine 800s	2.54	4.13	5.39	5.68	9.75	8.38	84.19	30.47
GullyHead2	Model 842 Only	1.14	5.03	6.14	6.75	13.18	9.36	101.62	28.25
	All nine 800s	3.74	9.30	8.84	12.98	16.41	15.97	105.52	23.52
GWPlume1	Model 842 Only	0.08	3.26	0.17	2.82	0.27	2.42	4.94	13.70
	All nine 800s	0.21	2.88	0.38	1.94	0.60	1.51	8.77	10.26
GWPlume2	Model 842 Only	-0.03	3.14	0.06	2.67	0.14	2.20	2.24	7.42
	All nine 800s	0.17	2.87	0.25	1.89	0.36	1.41	5.61	6.53
HLWT1	Model 842 Only	0.06	3.12	0.23	2.67	0.46	2.24	3.00	3.39
	All nine 800s	0.23	2.83	0.78	1.86	1.59	1.44	9.07	3.80
HLWT2	Model 842 Only	0.08	3.06	0.19	2.59	0.30	2.16	1.97	2.73
	All nine 800s	0.31	2.80	0.43	1.87	0.66	1.47	6.65	3.77
Lagoon2	Model 842 Only	0.11	3.01	0.22	2.57	0.42	2.43	32.00	28.50
	All nine 800s	0.21	2.86	0.43	1.95	0.71	2.18	33.44	30.02
Lagoon3	Model 842 Only	0.24	3.26	0.93	4.22	3.84	6.72	69.97	22.54
	All nine 800s	0.42	3.52	1.27	4.50	3.43	6.91	69.25	30.26
LFrankEdge	Model 842 Only	2.01	3.46	4.73	5.19	8.95	7.04	77.94	22.38
	All nine 800s	1.35	3.34	3.44	3.91	6.95	5.40	72.46	24.09
NDA1	Model 842 Only	0.05	3.34	0.24	2.87	0.62	2.80	23.23	15.62
	All nine 800s	0.17	2.96	0.41	2.15	1.02	2.16	27.72	13.32
NDA2	Model 842 Only	0.05	3.39	0.17	2.86	0.36	2.43	10.10	16.28
	All nine 800s	0.26	2.89	0.40	2.04	0.54	1.78	11.22	12.80
NDA3	Model 842 Only	0.64	3.35	0.86	2.82	1.10	2.31	4.05	8.54
	All nine 800s	0.82	2.86	1.31	1.88	1.63	1.40	6.25	6.70
NDA4	Model 842 Only	0.25	3.42	0.57	3.48	1.08	4.16	16.42	18.42
	All nine 800s	0.43	2.98	0.85	2.28	1.45	2.57	20.73	14.88
NDA5	Model 842 Only	-0.08	3.32	-0.05	2.78	-0.01	2.26	0.65	5.82
	All nine 800s	0.01	2.93	0.09	1.92	0.22	1.40	4.90	3.74
ProcessBLD	Model 842 Only	0.22	3.09	0.29	2.63	0.36	2.17	3.54	7.54
	All nine 800s	0.25	2.85	0.41	1.90	0.55	1.44	6.52	7.72
QuarryEdge	Model 842 Only	0.55	3.55	1.79	4.36	4.33	6.34	61.57	16.92
	All nine 800s	0.85	3.48	2.32	4.37	5.19	6.46	62.48	16.22

Table 1: (cont'd.)

Location	Approach	+200 years μ [ft]	σ [ft]	+500 years μ [ft]	σ [ft]	+1000 years μ [ft]	σ [ft]	+10,000 years μ [ft]	σ [ft]
SDA1	Model 842 Only	-1.18	3.29	-1.43	2.77	-1.67	2.28	11.23	12.20
	All nine 800s	-1.08	2.83	-1.62	1.88	-1.86	1.45	17.43	9.35
SDA2	Model 842 Only	1.07	3.08	1.51	2.62	2.15	2.26	26.38	13.65
	All nine 800s	1.10	2.85	2.28	1.97	3.87	1.72	33.64	10.82
SDA3	Model 842 Only	0.41	3.41	0.57	2.89	0.77	2.44	8.44	11.36
	All nine 800s	0.44	2.80	0.73	1.85	0.94	1.45	9.98	7.52
SDA4	Model 842 Only	0.11	3.00	0.23	2.50	0.37	2.04	1.60	4.64
	All nine 800s	0.40	2.86	0.72	1.84	1.12	1.33	10.25	4.80
SDA5	Model 842 Only	0.48	3.34	0.65	2.81	0.81	2.29	2.93	5.34
	All nine 800s	0.69	2.88	1.06	1.88	1.44	1.38	11.12	5.27
SDA6	Model 842 Only	0.09	3.13	0.18	2.59	0.28	2.05	0.61	2.00
	All nine 800s	0.39	2.84	0.56	1.84	0.69	1.32	3.07	1.87
UFrankEdge1	Model 842 Only	0.09	3.13	0.30	2.63	0.74	2.21	38.00	17.45
	All nine 800s	0.37	2.81	0.86	1.84	1.86	1.50	36.53	11.92
UFrankEdge2	Model 842 Only	0.05	3.35	0.30	3.02	0.68	2.88	20.53	13.79
	All nine 800s	0.00	2.93	0.08	2.16	0.44	2.06	19.49	12.13

As Figure 1 indicates, the greatest projected future erosion tends to be associated with the major valleys and their side-slopes, and with gullies that drain directly to these valleys. Among the main valleys, the areas of greatest erosion are projected to be the lower portion of Quarry Creek (downstream of Rock Springs Road) and the reach of Franks Creek downstream of its confluence with Erdman Brook. Though Erdman Brook and the upper portion of Franks Creek are not projected to experience as much erosion as lower Franks Creek, the projected cumulative depth along these streams is nonetheless considerable: on the order of 10s of feet after 10,000 years. Because of their proximity to the major valleys, the plateau side-slopes are also projected to be vulnerable to erosion. The projections show the interior of the north plateau to be susceptible to erosion from the headward propagation of gullies, either from the northwest rim, the northeast rim, or both. Particular "hot spots" on the north plateau include areas near and upslope of the present-day NP-1 Gully on the northwest rim, and NP-2 and NP-3 Gullies on the northeast rim. High uncertainty is associated with these locations (Figure 2) because small changes in plateau topography can alter the relative drainage area that contributes runoff to each of these gullies, and can in turn promote or dampen the erosion rates among the different rim gullies.

The portion of the north plateau rim around and down-valley from the EQ-1 Gully on the southeast edge also emerges as a susceptible area. Regarding the interior of the north plateau, propagation of gullies from the plateau edges constitutes the principle erosional threat. In general, the eastern portions of the plateau are projected to be more vulnerable than those farther west.

The margins of the south plateau are projected to be susceptible to erosion from valley widening along upper Franks Creek and Erdman Brook. The central portion of the south plateau is forecast to be less vulnerable to erosion, due to its relative isolation from the major valleys.

The modeled stream-capture scenarios suggest that successful capture is unlikely unless erosion in the potential capture locations (by gullies to the southeast of the watershed, or westward migration of the Buttermilk Valley rim) proceeds much faster than expected. The main consequence of capture from the southeast would be accelerated erosion along the southern edge of the south plateau. The models were unable to produce capture from the west, even when rapid erosion at the capture point was introduced unrealistically early (only 100 years into the future).

Regarding locations with hazardous material at the Site, the low-level wastewater treatment lagoons are projected to be among the most vulnerable. However, these lagoons and their radionuclide inventory and surrounding soils will be excavated, disposed offsite, and the excavations backfilled with clean soil during Phase 1 decommissioning of the WVDP. The north and east margins of the SDA are susceptible to valley-side erosion along Franks Creek and Erdman Brook, and from growth of the NDA Gully. The NDA itself is similarly vulnerable to the north (Erdman Brook valley widening) and east (NDA Gully).

The main process plant, which will be removed during Phase 1 decommissioning, is projected to be less vulnerable, reflecting its distance from the plateau edges. The high-level waste tanks are also in a relatively isolated location, but may be vulnerable to westward propagation of the present-day NP-1 Gully. The margins of the contaminated groundwater plume may be at risk from gully erosion and/or valley widening to the southeast, northeast, and northwest. However, the source area of the plume will be excavated, disposed offsite, and the excavation backfilled with clean soil during Phase 1 decommissioning of the WVDP. The remainder of the plume, which is principally Sr-90 with a half life of 28.8 years, will have decayed away before it can be impacted by gully or valley-wall migration from adjacent streams.

Overall, three of the primary sources of uncertainty in erosion projections are uncertainties in model structure, model parameters, and relatively subtle ($\pm$5-foot) modifications to contemporary topography, which can steer flow toward or away from particular gullies. The importance of uncertainty in future climate varies by location; at locations closer to the main streams, it can be the second or third most important contributor, whereas at more distant locations the contribution of climate-related uncertainty is less significant. The models are generally less sensitive to projected future downcutting rate in the Buttermilk Creek valley. The latter source of uncertainty primarily influences projected erosion in the lower reaches of Quarry Creek and Franks Creek.

The projections and uncertainty estimates developed in this study could be used to inform future performance assessments and decommissioning planning, including selective exhumation of buried waste, for the Site. The projections include quantitative estimates of uncertainty, both collectively and in terms of individual uncertainty sources. In addition, although the contribution of model-parameter uncertainty has only been estimated for 25 selected locations, the calculation tools and workflows developed for this project could be used to generate similar estimates at any desired grid location.

The methods and modeling framework developed for this study provide a more rigorous approach to erosion projection and uncertainty quantification at the Site than was previously possible. The overall methodology has been designed for flexibility, such that it can be adapted to address additional model concepts, data sources, and scenarios, should the need arise for further study in the future.

The development, testing, and model evaluation presented here required 1.36 million core-hours of computation. The erosion-modeling software used in this project is free and open-source. The erosion-model software was built on the Landlab Toolkit, which is freely available at `http://landlab.github.io`. The Sandia National Laboratories' *Dakota* package, which was used to implement ensemble model simulations, sensitivity analysis, calibration, and uncertainty quantification, is also freely available from Sandia; as of this writing, its documentation and distribution site is `https://dakota.sandia.gov/`.

Part II

Main Report

Chapter 1

Introduction

1.1 Phase 1 Erosion Studies

This report presents the results of Phase 1 Erosion Study 3—Model Refinement, Validation, and Improved Erosion Projections.

The Final Environmental Impact Statement (FEIS) presented predictions of future erosion at the facility (*DOE and NYSERDA*, 2010). The two responsible agencies, the United States Department of Energy (DOE), and New York State Energy Research and Development Authority (NYSERDA) differed in their views of the uncertainty associated with the conclusions of the FEIS erosion analysis. The Phase 1 erosion studies were conceived to enable improved forecasts of future erosion at the West Valley Demonstration Project (WVDP) and the Western New York Nuclear Service Center (WNYNSC) (together the "Site"), to reduce the associated uncertainty, and to assist the agencies in reaching consensus on the likely effects of future erosion. Figure 1.1 illustrates the relative locations of the WVDP and WNYNSC.

To address the study goals, DOE and NYSERDA convened the West Valley Erosion Working Group (EWG) to recommend specific erosion studies that would facilitate the agency goals. The EWG consists of a multidisciplinary panel of experts with prior experience with the Site issues and widely recognized expertise in the technical subject matter.

The EWG comprises the following members:

Sean J. Bennett, Ph.D.	Dept. of Geography, SUNY Buffalo
Sandra G. Doty, M.S., P.E.	Consulting Geological Engineer
Robert H. Fakundiny, Ph.D.	New York State Geologist, Emeritus
Gregory E. Tucker, Ph.D.	CIRES & Dept. of Geological Sciences, Univ. Colorado
Michael P. Wilson, Ph.D.	Dept. of Geosciences, SUNY Fredonia, Emeritus
Richard A. Young, Ph.D.	Dept. of Geological Sciences, SUNY Geneseo, Emeritus

Greg Tucker and Sandra Doty are the Study Co-Leaders for Study 3—Model Refinement, Validation, and Improved Erosion Projections. The Phase 1 Studies contractor, Enviro Compliance Solutions, Inc. (ECS) was tasked with managing the erosion studies.

DOE and NYSERDA initially tasked the EWG with formulating recommendations for erosion studies that could lead to improvements in erosion prediction. The EWG submitted

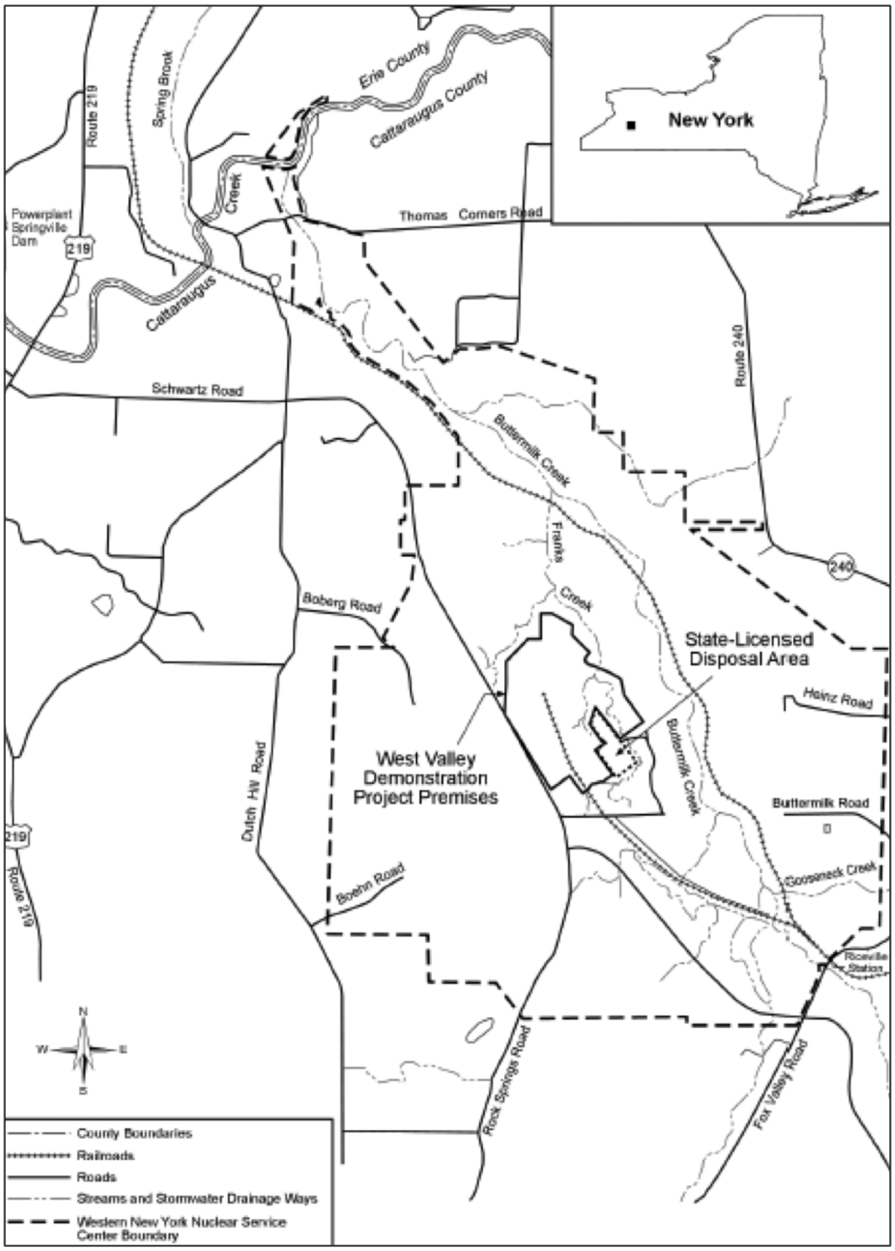

Figure 1.1: Location of the WVDP and WNYNSC

its recommendations in June 2012. In addition to DOE and NYSERDA, the recommendations were also reviewed by the Independent Scientific Panel (ISP) and other stakeholders, including the Nuclear Regulatory Commission (NRC), other regulatory agencies, interest groups, and the public.

On the basis of comments and feedback received on the EWG recommendations, the agencies tasked the EWG in June 2013 with addressing the specific sources of uncertainty in the previous FEIS erosion projections (and predictive erosion modeling in general), and with focusing the Phase 1 erosion study recommendations on tasks and activities having the greatest promise of uncertainty reduction. The EWG submitted its report on uncertainty and prioritization of the recommended erosion studies in October 2013.

The EWG concluded that six categories of uncertainty can be identified with regard to erosion prediction methodologies applied over a range of time- and space-scales. These categories are:

1. Experimental uncertainty, which refers to error in the measurement of a particular parameter, such as stream discharge;

2. Estimation uncertainty, which refers to the error in the prediction of a parameter by an equation or a model, such as the prediction of stream discharge;

3. Temporal estimation uncertainty, which refers to the error introduced in the prediction of a parameter because of unknown future conditions, such as predicting future stream discharge without knowing future rainfall rates, and would include all issues related to future climate change;

4. Theoretical uncertainty, which refers to error in the underlying theory of a model or how model complexity or simplicity might affect model predictions, such as aggregating all the complex processes of hillslope erosion into a single, simple equation;

5. Geologic uncertainty, which refers to the error in the interpretation of geomorphic features and surfaces, such as the uncertainty of the stratigraphic age or significance of a geologic landform (constrained by incomplete OSL analyses); and

6. Cognitive uncertainty, which refers to error in the quality of documentation and clarity in communication, such as the verbal description or identification of a geologic feature.

Some of the uncertainties listed above could be directly addressed and quantified (such as 1), while others would require additional discussion and research, potentially within the scope of the planned activities (such as 2, 3, and 4), and still others could be reduced by adopting multiple lines of evidence (such as 5 and 6). While categories of uncertainties and their sensitivities within the context of erosion prediction technology could be recognized and qualitatively gauged (see below), definitive statements regarding the magnitude of model estimate uncertainty reduction resulting from additional study could not be made *a priori*; rather, this could be assessed only after the current work was completed.

In the 2013 uncertainty report, the EWG critically examined the various sources and potential magnitudes of uncertainty with respect to erosion prediction technology and terrain analysis. A simple qualitative approach was adopted. For every model parameter or geomorphic attribute identified germane to erosion prediction, the EWG used professional judgment to assign an uncertainty and sensitivity measure to each (low, medium, or high), and then combined these measures into an uncertainty index. Sensitivity simply refers to the actual or perceived importance of a parameter or geomorphic feature in parameter estimation. Here, high uncertainty indices offer the greatest potential opportunity for reducing the uncertainty of erosion projections. Note that the present report significantly advances the identification and quantification of sensitivity and uncertainty in erosion forecasts, and apportions uncertainty among several different sources, as discussed in Chapters 7 and 11 and Appendix E.

Using this simplified but informed analysis, the EWG created a priority list of those specific studies and study components likely to reduce uncertainties in erosion prediction. The following parameters were identified as the most important for numerical modeling (ranked in order of relative importance as defined by EWG):

1. Bed sediment entrainment threshold;
2. Soil/till detachment threshold;
3. Storm depth, duration, and frequency parameters;
4. Soil/till detachability; and
5. Soil infiltration capacity.

The following parameters were identified for additional study for a gully erosion model (ranked in order of relative importance as defined by EWG):

1. Soil/till detachment threshold;
2. Soil particle size and bulk density;
3. Headcut height (if applicable);
4. Storm depth, duration, and frequency parameters;
5. Soil/till detachability; and
6. Soil infiltration capacity.

The following three tasks were identified for additional study for terrain analysis and age dating:

1. Construct a geologic and geomorphic history of the Site;
2. Relate postglacial climate events to stratigraphy or erosion and deposition, and
3. Estimate average rates of channel incision since the last glacial maximum.

On the basis of these findings, the EWG recommended fewer, more focused Phase 1 erosion studies to maximize the potential uncertainty reduction, focusing only on those having the greatest potential to reduce predictive uncertainty. The EWG submitted the Phase 1 Erosion Study Plan (the "Study Plan") in June 2015 (EWG, 2015). As described in the Study Plan, the individual studies were designed to produce converging lines of evidence toward predicting future landscape evolution at the Site, to improve the scientific defensibility of the results obtained, to supplement existing data, and to strengthen the confidence in short- and long-term forecasts of erosion processes. The collective studies comprised three principal study areas:

1. **Study 1:** Terrain Analysis, Age Dating, and Paleoclimate Evidence
2. **Study 2:** Recent Erosion and Deposition Processes
3. **Study 3:** Model Refinement, Validation, and Improved Erosion Projections

These studies were designed to be independent but complementary, and synergistically interactive to enhance reduction of erosion-prediction uncertainty.

1.2 Purpose of Study 3

The main purpose of this study was to improve model forecasts of future erosion at the Site, reduce the associated uncertainty, and assist the agencies in reaching consensus on the likely effects of future erosion. Although the Final Environmental Impact Statement (FEIS) presented a calibrated model with projections of future erosion at the facility, the model was not validated and uncertainty bounds were not calculated for the projections. Thus, the objectives of this study included validating erosion models at an appropriate analogue site and using formal analysis methods to determine the models' uncertainty, in addition to improving model forecasts. The term "model" or "models" is intended to mean any physical or numerical representation of the processes that occur in nature to modify topography at various scales from individual gullies to broad areas of the landscape, and over various time-frames from short (tens to hundreds of years) to long (thousands of years).

The goal of improving model forecasts of future erosion was achieved through evaluation of new data and formulation of modeling approaches at various time and space scales, together with uncertainty estimates. The formulation of modeling approaches, referred to as a multi-model analysis, was used to compare alternative formulations for the same processes at the site. Individual hydrologic and geomorphic process laws formed the basic ingredients for the multi-model analysis. The process laws were tested singly and in selected combinations in a modular modeling framework (Chapter 3 Appendix A), so that each contribution could be assessed individually and added (or deleted) on the basis of response. This multi-model analysis approach provided a means of quantifying model structure uncertainty and also helped reduce uncertainty by identifying and eliminating from further consideration those models that provided a poor fit to the available data.

Newly collected data also played a key role in meeting the objectives of this study. Age dates collected through Study 1 provided tighter constraints on the estimates of timing of past landscape evolution for use in model calibration and validation. Terrain analysis conducted in Study 1 supported this study both directly by providing additional insight into processes that should be represented in models, and defining an initial landscape surface for erosion-model testing and calibration, and indirectly by providing information needed to identify and interpret features for age dating, and thereby improve understanding of the geomorphic history for calibration and validation. Data collected in Study 2 supported this study by providing better constraints on model parameters to reduce uncertainty, as well as providing additional data for model testing.

1.3 Organization of Report

This report is organized as follows. Chapter 1 is an introduction. Chapter 2 provides an overview of the model analysis framework that guides the modeling efforts, starting with sensitivity analysis and calibration and ending with prediction under uncertainty. Chapter 3 presents an overview of the erosion modeling approach. Chapter 4 describes the initial and boundary conditions that were used in modeling for the postglacial to present day time period. Chapter 5 describes the input parameters that were used in the model analysis. Chapter 6 discusses the metrics that were used in the model-data comparison process. Chapter 7 presents the sensitivity analysis. Chapter 8 describes the techniques used to calibrate model parameters. Chapter 9 presents the model validation process. Chapter 10 presents an evaluation of the alternative models. Chapter 11 summarizes the erosion projection scenarios including uncertainty assessment. Chapter 12 presents an analysis of the modeling results that includes a discussion of limitations of the study and potential future improvements.

Figures and tables are interspersed within the text. Appendices provide supporting reports, data summaries, calculations, plots, and a bibliography. The appendices include a description of the erosion modeling framework (Appendix A), extensive figures and tables resulting from the sensitivity analysis and calibration efforts (Appendices B and C), approach used for stream capture simulation (Appendix D), the methods for uncertainty partitioning (Appendix E), and supporting information related to projection (Appendix F).

Chapter 2

Model Analysis Framework

2.1 Introduction

A model, with its defined parameters, quantitatively links system information used for model construction and the simulated equivalents of observations to the predictions of interest and measures of prediction uncertainty. This Chapter provides an overview of the model analysis used to quantitatively link the triad composed of observations, parameters, and predictions. A variety of methods and statistics can be used to take advantage of those links to answer important questions about simulated system performance, such as what parameters are informed by the observations in model calibration, and what parameters are not; what and how uncertain are the predictions and what causes this uncertainty. These analyses can lead to insights about actual system performance. In this work we largely follow the guidelines of *Hill and Tiedeman* (2007) in model development and application. The guidelines, modified for this application, are shown in Table 2.1. The idea of starting simple and building complexity slowly is often important when building models of complex environmental systems. While numerical models allow great complexity to be simulated, the data rarely support the complexity to be characterized. A problem with simple models is that individually they tend to underestimate prediction uncertainty. In this work that problem is addressed by evaluating multiple alternative models.

The workflow followed in this work is illustrated in Figure 2.1. Associated report chapters in which the methods and results are described are noted. Methods used for sensitivity analysis, calibration, validation, prediction, and uncertainty quantification are discussed by many authors. The most relevant to this work include, for example, *Hill and Tiedeman* (2007), *Saltelli et al.* (2008) and *Wilcock and Iverson* (2003). A brief description of the methods used in this work and the primary rationales and results is shown in Table 2.2.

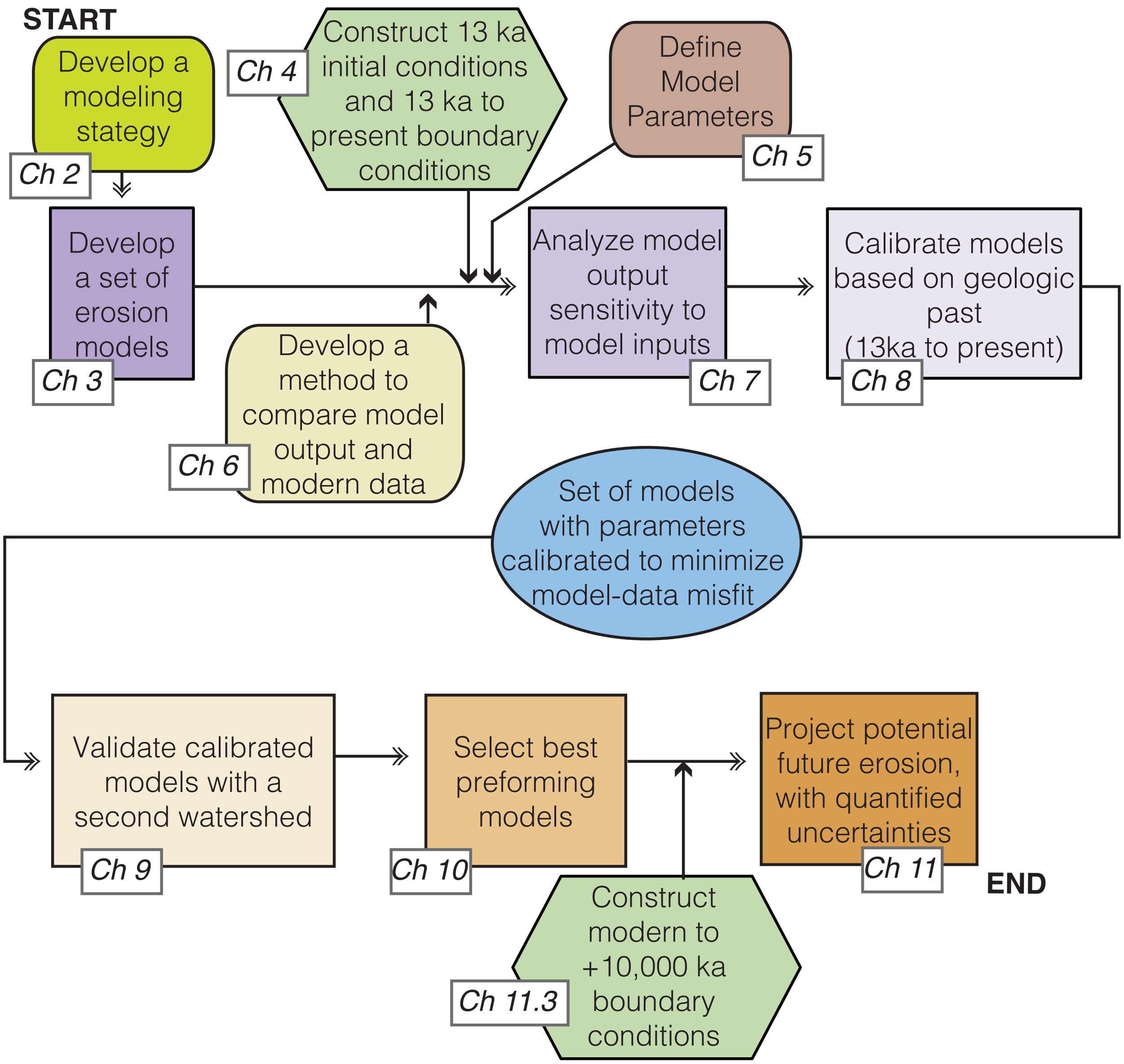

Figure 2.1: Steps taken for developing, calibrating, testing, and using the models developed in this work. The models are used to project future erosion and evaluate the uncertainty of those projections. Chapter numbers listed in the figure show where the methods and results related to each step are presented in this report.

Table 2.1: Guidelines for effective model calibration (modified from *Hill and Tiedeman* (2007); the potential new data evaluation steps 11 and 12 are omitted).

Model Development
1. Apply the principle of parsimony (start simple; build complexity slowly)
2. Use a broad range of information to constrain the problem
3. Include as many types of observations as possible
4. Use sensitivity analysis to identify parameters informed by the observations
5. Use prior information carefully
6. Account for data error by evaluating data collections and management procedures
7. Encourage optimal calibration by improving the model and evaluating the observations
8. Account for model error using alternative models
Test the Model
9. Evaluate model fit
10. Evaluate optimized parameters
Prediction Accuracy and Uncertainty
13. Evaluate prediction uncertainty and accuracy using model validation
14. Quantify prediction uncertainty using statistical methods

2.2 Software Used

In this report we used the Dakota software toolkit (*Adams et al.*, 2017a,b). We chose Dakota because of its flexible design, support of many model analysis algorithms for sensitivity analysis and calibration, and its support of surrogate-based methods.

Table 2.2: Brief description of methods and comments on rationale and results.

Chapter	Topic	Primary Methods	Comments on rationale and results
7	Sensitivity Analysis	Morris One-At-A-Time	Only a small number of parameters control the value of the objective function (e.g. the erodibility coefficient parameters).
8	Calibration	Gauss-Newton, NL2SOL, EGO, Bayesian Calibration with MCMC	A sequence of methods was needed to manage the execution time requirements. GN is computationally frugal but struggled with small local minima. It was followed by the other, more computationally demanding methods which met our criteria for calibration success.
9	Validation	Use calibrated parameters for each model in a neighboring site	Ability to reproduce current topography after 10,000 years of erosion was similar to results in the main study area.
10	Model Selection	Criteria reward close fit to data, penalize adding parameters. Synthesis of calibration and validation results	Consideration of only calibration results support use of only one model. Synthesis of calibration and validation provides support for a nine-model suite. Both options pursued. For the models considered, the same model selection was obtained using only criteria that rewarded model fit.
11	Projections	Multiple numerical experiments	Predictions range from little erosion at sites of concern to considerable erosion.
11	Projection Uncertainty Quantification	ANOVA	Prediction uncertainty varies substantially in space and time. When uncertainty is large, it primarily is attributable to model structure and uncertainty in rearrangement of surface hydrology due to human activity.

Chapter 3

Erosion Modeling

3.1 Introduction

The terrain in and around the West Valley site has changed considerably since the last retreat of glacial ice. Rapid downcutting along Cattaraugus Creek and its major tributaries, including Buttermilk Creek, has triggered incision on smaller tributary streams (such as Franks Creek) and gullies. Geomorphic analysis and age dating by the Erosion Working Group suggests that Buttermilk Creek and its tributaries cut their present-day valleys since the last glacial retreat, which appears to have occurred approximately 13,000 years ago (*Wilson and Young*, 2018). The average rate of postglacial downcutting on Buttermilk Creek, at roughly 13 feet (4 meters) per thousand years, was rapid by global standards (see, for example, review of landscape evolution studies by *Tucker* (2015)). If similarly rapid rates of stream and gully erosion continue into the future, then it is reasonable to conclude that landscape evolution in and around the site over the coming millennia may involve substantial changes in the terrain itself, possibly leading to the release of radiological and/or toxic materials.

Modeling erosion in a relatively rapidly evolving landscape, on time-scales of centuries to millennia, requires computational models that can account not just for the loss of soil material but also for the reshaping of the terrain itself by erosional processes. Because erosion and sediment transport rates depend strongly on the shape of the landscape and also alter that shape over time, there is a close feedback between erosion rates and changes in topography. Computational models that simulate this type of feedback are known as Landscape Evolution Models (LEMs) or Surface Process Models (SPMs). A typical landscape evolution model represents terrain as a grid of cells, and uses an algorithm to calculate the pathways that water would take across the terrain surface. The program will divide time into a series of discrete *time steps*. For each time step, the water-routing algorithm will normally calculate, for each grid cell, the total surface area upslope or upstream that contributes water to the cell in question. This quantity is known as the contributing drainage area, and is referred to here as "drainage area" for short. The erosion (or deposition) at each grid cell is then calculated on the basis of variables such as drainage area, local topographic slope, and any inputs of sediment from surrounding cells.

A variety of different landscape modeling approaches have been developed and explored by the research community, and a number of different computer codes have been written (see, for example, reviews by *Tucker and Hancock*, 2010; *Valters*, 2016). Many of these codes are publicly available through the Community Surface Dynamics Modeling System (CSDMS) Model Repository (`http://csdms.colorado.edu`).

This chapter briefly describes the Erosion Modeling Suite (EMS), which is a collection of erosion modeling programs written in the Python programming language using the Landlab Toolkit library (*Hobley et al.*, 2017) (`http://landlab.github.io`), together with common scientific libraries such as NumPy and SciPy. Details about EMS, its governing equations, and the scientific basis for its component models can be found in Appendix A.

3.2 Erosion Modeling Suite (EMS)

EMS was developed using Landlab to provide a range of alternative models that are potentially suitable for the particular processes and materials at the West Valley site, and for the space and time scales of concern. EMS consists of a series of alternative models, each of which combines a particular set of basic process ingredients to arrive at an integrated simulation of long-term landscape evolution.

The individual process laws identified in this chapter are intended to form the basic ingredients for a multi-model analysis. A multi-model analysis approach provides a means of quantifying model structure uncertainty by comparing alternative formulations for the same process (*Poeter and Hill*, 2007; *Burnham and Anderson*, 2003; *Foglia et al.*, 2013). Use of multiple models can also help reduce uncertainty by identifying and eliminating from further consideration (or assigning low probabilities to) those models that provide a poor fit to the available data.

For purposes of this study, the operative model ingredients were divided into five categories: hillslope processes, hydrologic processes, channel and gully erosion processes, site materials, and paleoclimate. The first three of these categories represent processes that contribute to erosion. The latter two categories are represented by parameters that describe initial and boundary conditions applied to the model (and in the case of paleoclimate, applied specifically to the model calibration process). For each of the five categories, we considered a range of options for how the process or property in question might be represented in a long-term erosion model for the West Valley site. Those treatments that were selected for inclusion in the multi-model study are summarized in Table 3.1. As the table indicates, the model elements selected were arranged as a set of binary options. For example, some landscape evolution models use an erosion law based on hydraulic power (commonly referred to as *stream power*), whereas others use a law based on hydraulic force per unit bed area (referred to as *boundary shear stress*). Because we had no *a priori* reason to prefer one over the other, we included the two formulations as one of the binary options.

For each of the categories shown in Table 3.1, we carefully considered a range of alternative methods of representation. Our choices were motivated by the following considerations:

- Does the process or property make sense in the context of the site, the time scale, and the spatial scale?

- Is there a basis for it in the scientific literature?

- Is it simple enough, with a sufficiently small number of free parameters, to be practical?

In the following subsections, we briefly present the rationale for our choices of model elements to include in the suite of models. The mathematics behind the various formulations discussed here are presented in detail in Appendix A.

3.2.1 Hillslope Processes

On the basis of prior work at the West Valley site, as well as our own observations, we infer that geologic material is transported downslope by two primary processes: landsliding and soil creep. Landsliding appears to be especially common in glacial materials, and becomes evident from morphology (as well as repeated on-site observations at certain locations) in areas where the slope angle is greater than about 20°. Based on our personal observations, we suggest that many of the slopes flanking Franks and Quarry Creeks could be classified as subject to shallow translational landsliding, where "shallow" implies a depth to the failure plane that is considerably smaller than the length of the slope, and "translational" implies down-slope translation of individual slabs or blocks of material that are bounded by slip surfaces. Deep-seated rotational landsliding, by which we mean rotation of blocks whose thickness may approach the height of the plateau above an adjoining stream, also appears to have occurred in the area. For example, in upper Heinz Creek, LiDAR imagery reveals a complex of valley-parallel ridges that we interpret to be rotated and down-thrown slide blocks.

Unfortunately, the geomorphology community presently lacks a universally agreed transport law for landsliding *sensu strictu*. (see, for example, *Dietrich et al.*, 2003). That said, linear diffusion theory has been used as a rough proxy for the long-term effects of landsliding (e.g., *Willgoose et al.*, 1991a), though it does not account well for the expected acceleration as a hillslope approaches an effective threshold angle for soil stability. Nonlinear diffusion theory has also been used as a proxy for the integrated effects of shallow landsliding, and has the advantage of capturing accelerated soil movement as the slope angle rises toward an effective angle of repose (*Andrews and Bucknam*, 1987; *Roering*, 2008). To our knowledge, no effective process law has been demonstrated for long-term erosion by deep-seated rotational failures. However, recent work by A.B̃ooth and colleagues (*Booth and Roering*, 2011; *Booth et al.*, 2013) suggests that earthflows—elongated and fairly deep forms of mass wasting that behave somewhat like "glaciers of mud"—may be effectively modeled using an approach that shares some important elements with nonlinear diffusion theory (in particular, the use of a transport law in which soil flux is proportional to a power of surface slope gradient).

By contrast, soil creep has a long history of study. Linear and nonlinear diffusion theory have both been successfully used to model slope forms in cases where soil creep—downslope motion of soil that often arises from repeated disturbance and displacement of material by processes such as bioturbation—is considered to be the primary source of transport.

Given the above considerations, we identify two alternative options for modeling downslope soil transport: linear creep theory, and nonlinear creep theory (Table 3.1). The linear model, which is simpler (having only one parameter), is used as the default option.

It is important to recognize that both the linear and nonlinear creep laws are designed to represent the long-term average effect of gravitational motion, rather than any single event.

Table 3.1: Binary options for process formulations and material properties.

Category	**Option A**	**Option B**
Hillslope processes	linear	nonlinear
Surface-water hydrology	deterministic	stochastic
	uniform runoff	variable source area runoff
Channel/gully erosion	fixed exponent	variable exponent
	no threshold	erosion threshold
	stream power	shear stress
	constant threshold[a]	depth-dependent threshold[a]
	detachment-limited	entrainment-deposition
	uniform sediment[b]	fine vs. coarse[b]
Material properties	no separate soil layer	tracks soil layer
	homogeneous lithology	two lithologies
Paleoclimate	constant erodibility	time-varying erodibility

[a] only applies to models that include a threshold
[b] only applies to entrainment-deposition models

In particular, we do not consider very large, rapid mass failure events (such as the tragic Oso landslide in Washington State that occurred in 2014), which we consider to be an issue that properly falls under the purview of a geotechnical panel or working group.

To summarize, there is one binary choice considered for soil transport by gravitational processes. The linear creep law is the default option, because it is so widely used and requires only a single parameter, the value of which has been estimated in a wide range of studies. The alternative is a nonlinear creep law, which we expect to provide a better representation of rapid downslope transport on steep valley side-slopes. The nonlinear law requires specification of one additional parameter: the critical slope gradient at which soil flow rate tends to accelerate substantially. Information about the mathematical form and parameters used in these rate laws is given in Appendix A, Section A.2.2.

3.2.2 Hydrologic Processes

One challenge in modeling erosion over thousands of years lies in the need to simplify the representation of climate and hydrology. With current computing technology, it is not practical to represent explicitly the minute-to-minute fluctuations in precipitation, runoff, and streamflow that can accompany weather events. A simple alternative, and one that has been applied in numerous erosion models, is to use drainage area as a surrogate for the erosionally effective flow of water over a period of years (e.g., *Willgoose et al.*, 1991a, their Appendix B). This is the default approach used in this study. With this method, the erodibility parameter in the water-erosion law (addressed below) embeds information about precipitation (the relation between erodibility and precipitation is discussed further in Chapter 11).

An alternative is to use a stochastic method in which precipitation rate is treated as a random variable, with the probability distribution based on an observed precipitation frequency distribution (*Tucker and Bras*, 2000; *Snyder et al.*, 2003; *Tucker*, 2004; *Lague et al.*, 2005; *DiBiase and Whipple*, 2011). Use of a stochastic approach has the advantage of capturing a spectrum of natural events, and further that it can be linked directly to precipitation statistics (though as shown in Chapter 11, a probabilistic approach can also be used to set the value of a deterministic erodibility coefficient). The primary disadvantage is complexity: the stochastic approach tested in this study requires specification of four additional parameters. This added complexity increases the computing time needed for model sensitivity analysis and calibration. Nonetheless, in order to test whether the added complexity produces a corresponding increase in explanatory power, the multi-model analysis includes several models that use a stochastic precipitation method.

The simplest forms of both deterministic and stochastic hydrology models described above use the assumption that the average runoff rate is proportional to drainage area. Yet as early as the 1970s, hydrologists discovered that certain areas of a drainage basin may sometimes contribute substantially more runoff than others, especially in vegetated, humid-temperate regions (*Dunne and Black*, 1970). This discovery led to what is sometimes referred to as the variable source-area concept: the notion that the majority of storm runoff tends to be generated in areas that are relatively flat and/or have relatively large upslope contributions of water (surface or subsurface). The variable source area concept has stimulated the development of fairly simple, topographically based mathematical models of runoff potential. In order to test the importance of variable source-area hydrology in long-term models of erosion at the West Valley site, several of our models include a simple representation in which the fractional area of a grid cell that produces runoff depends on its slope and contributing drainage area (Appendix A, Section A.2.3).

In summary, the hydrology components are built around two binary choices: use of a deterministic versus stochastic representation of precipitation and runoff, and assumption of uniform versus variable source-area runoff. The mathematical forms and parameters are presented in Appendix A, Section A.2.3.

3.2.3 Erosion by Channelized Flow

The geomorphology community has devoted considerable effort toward understanding the physics of channel incision into cohesive and/or rocky material (see, e.g., review by *Whipple*, 2004). Despite this effort, the community is still debating the core principles governing channel incision, and how those principles depend on considerations such as material properties and time scale of interest. With regard to modeling erosion at West Valley over decades to millennia, we have a wide range of possibilities to consider.

As a starting point, and for the sake of narrowing the range of options, it is useful to identify those elements of contemporary channel-incision theory that do *not* apply especially well to the West Valley site. Among these is the popular saltation-abrasion theory (*Sklar and Dietrich*, 2004; *Chatanantavet and Parker*, 2009), which considers wear of bedrock to occur primarily by abrasion by saltating grains. At West Valley, most geologic materials subject to erosion are either cohesive but mechanically weak sediment (such as the clay-rich Lavery Till), or possess a high density of fractures and/or bedding planes (as in the shale-rich sedimentary units). We consider abrasion to be a minimal contributor to the erosion of these materials, as compared with direct hydraulic detachment. On the other hand, the site's geologic materials clearly possess cohesive strength (sufficient, for example, to maintain near-vertical steps and waterfalls), which suggests that a conventional transport-limited model would also be inapplicable (for a general discussion and comparison of these types of model, see for example (*Whipple and Tucker*, 2002)).

Two general classes of channel-erosion model remain for consideration. The first is known as the *detachment limited* approach, because it assumes that the primary limitation on the rate of channel downcutting is the rate at which particles can be detached rather than the rate at which they can be transported (*Howard*, 1994). There exists in the literature a variety of different forms of detachment-limited model. In general, the rate of downcutting is assumed to depend on either hydraulic power (*stream power* per unit channel width) or friction force (*boundary shear stress*). Usually power or force are represented as a power function of channel slope, water discharge (or drainage area as a surrogate), and a factor that lumps together information about material properties, roughness, and channel dimensions. Sometimes an erosion threshold is included in the formulation: when power or force falls below this threshold, little or no incision occurs. In some cases, the exponents on discharge and/or slope are treated as calibration parameters.

The other major class of channel-erosion law generalizes detachment-limited theory by allowing for the possibility of sediment deposition as well as detachment and erosion. There is no generally agreed name for such models; here we will call this category *entrainment-deposition* models because they include terms for both entrainment of material from the channel bed into the flow, and deposition from the flow onto the bed. The essence of this approach is that the net rate of erosion is equal to the difference between the rate of particle detachment from the bed, and the rate of deposition from active transport. Entrainment-deposition models have been used both for large-scale landscape evolution (e.g., *Davy and Lague*, 2009) and for gully erosion (*Sidorchuk*, 1999; *Rengers and Tucker*, 2014). In tracking sediment detached from the bed, one has the option of distinguishing between coarser material that might be re-deposited, and fine (silt and clay) materials that are effectively removed from the channel network as soon as they are detached (an approach along these lines was suggested by *Kirkby and Bull*, 2000).

This brief review of channel incision theory suggests several options that might reasonably be considered as candidates for modeling erosion long-term erosion at the West Valley Site. Detachment-limited models have merit, given the cohesive but fine-grained nature of the Site's geologic materials. Such models have been used in prior studies of gully erosion (e.g., *Howard*, 1998) as well as numerous modeling studies of erosion in larger channel networks. On the other hand, entrainment-deposition models allow for the possibility of sedimentation in some locations; they too have been used to model both gully systems and larger-scale networks. Because we have no *a priori* reason to prefer one approach over the other, both are considered as alternatives in the models used for this study. Other binary choices include: whether to use a fixed or variable (calibrated) exponent on the discharge (or area) factor; whether to include an erosion threshold; and whether to distinguish between fine and coarse material (in the entrainment-deposition models only) (Table 3.1).

One additional option is worth considering. In a study of rapid post-glacial erosion in the Le Seuer River basin, Minnesota, *Gran et al.* (2013) tested several alternative models for channel downcutting. Having observed that the size of bed sediment increases downstream, they included among their models a formulation that allows the erosion threshold to increase with progressive incision. The model that included this depth-increasing threshold performed the best, and provided a good fit to the modern channel longitudinal profile. Given the similarity between the Le Seuer case and the West Valley Site, we included the option to allow the erosion threshold to increase with progressive incision depth. We note, however, a recent finding by the Erosion Working Group's Study 2 team that channels surveyed near the West Valley Site do not exhibit downstream coarsening, but instead have relatively uniform bed-material size (*Bennett*, 2017).

To summarize, the treatment of channel downcutting in the erosion models is built around six binary choices, as illustrated in Table 3.1. Note that "Option A" is always considered the default, which means that our basic default channel-erosion model is one that uses a detachment-limited stream-power formulation with a fixed drainage-area exponent and no erosion threshold. Details on the mathematical forms and computational implementation of these various options are provided in Appendix A, Section A.2.4.

3.2.4 Representation of Geological Materials

Lithology

Broadly speaking there are two primary geologic units within the Franks Creek watershed: late Quaternary glacial deposits, and bedrock. Within these two general categories many subdivisions could be made. For purposes of configuring erosion models, a balance must be struck between fidelity to the important differences in erosional susceptibility among different rock and sediment units, and the need to keep models simple enough that they can be effectively analyzed and calibrated.

An important consideration is that for many of the parameters that go into long-term erosion models, precise estimates can not be obtained directly from field measurements (though such measurements are very helpful in placing bounding constraints). Differences between the time and space scales of field measurement and the scales at which models are applied can lead to differences between a measured parameter and its true "effective" value. For this reason, erosion model parameters must generally be calibrated (as discussed further in Chapter 8). Calibration becomes exponentially more complicated and computationally intensive as the number of parameters increases. Each geologic unit included in an erosion model requires its own set of parameters. For practical purposes, then, the number of geological units must be kept as small as possible, while still retaining the most important material differences.

In light of these constraints, and given the geology of the site, we have developed models around two options regarding lithology. The first (default) option is to treat the site's geologic units as homogeneous. This option is based on the hypothesis that shale and clay-rich till are similar when it comes to erosion by running water or gravitational processes; both contain large fractions of clay-size material, both are mechanically rather weak, yet both possess enough cohesion to support vertical faces. The second option is to distinguish between glacial deposits (hereafter sometimes referred to as "till" for simplicity) and bedrock. This second approach represents the hypothesis that rock materials are significantly more resistant to erosion than the glacial sediment complex. Including both options in the modeling framework allows us to test the degree to which incorporating a distinction between rock and glacial sediments increases an erosion model's explanatory power.

Models that incorporate a distinction between rock and glacial sediments use, as an input, a digitized representation of the bedrock surface in the Buttermilk Creek valley (cropped to fit the area modeled). This digitized representation of the bedrock surface derives from *Randall* (1980), as discussed further in Chapter 4, Section 4.2.

Soils

Some long-term erosion models explicitly incorporate a layer of soil, as distinct from underlying parent material, while others effectively treat the soil-rock continuum as being effectively homogeneous. Incorporating a dynamic soil layer has the appeal of realism, but it requires a method to calculate the creation of new soil from the underlying parent material, as well as a rule to ensure that hillslope transport does not exceed the available soil supply. The West Valley Site's region is predominantly soil-mantled, but apart from that observation we have no *a priori* reason to prefer one approach over the other. We have therefore included, as one of the binary choices, the option to include or not include a dynamic soil layer. Comparing the performance of models with and without an explicit soil layer makes it possible to test how much explanatory power is added when this element of reality is honored.

3.2.5 Paleoclimate

One source of uncertainty in the model calibration process concerns paleoclimate: we do not know precisely how climate varied at the Site over the 13,000 year calibration period, or how such variations might have impacted erosion rates and processes during that time interval. We can gain some insight, however, from the TraCE-21ka model experiment and dataset, which derives from a continuous global simulation of past climate evolution over the last 21,000 years (*Liu et al.*, 2009) (`http://www.cgd.ucar.edu/ccr/TraCE/`). For the model grid cell that covers the western New York State, the modeled precipitation amounts stay roughly constant over the past 13,000 years but change in character (Figure 3.1). The biggest change is in convective precipitation, which rises from 13,000 to about 8,000 years ago then stays roughly constant. Large-scale stable snow is modeled as decreasing steadily over the last 13,000 years, with the trend flattening out by about 4,000 years ago.

To assess the degree to which uncertainty in paleoclimate during the calibration period translates into uncertainty in model behavior, we developed an additional model that incorporates the possibility of past variations in the effective erodibility coefficient for site materials (see Appendix A, Section A.2.1 for definition of the erodibility coefficient). In this model variant, the erodibility factor begins with a value that is higher or lower than its final (present day) value by a user-specified fraction. The value then linearly increases (if starting lower) or decreases (if starting higher) up to a specified model time, after which it becomes constant for the remainder of the run. The use of a linear increase or decrease followed by a constant value is based on the trends observed in precipitation type in the Trace-21ka simulations (Figure 3.1). Our supposition is that the trends in the paleoclimate model imply variations in precipitation intensity, which would in turn be reflected in variations in the effective erodibility coefficient. The translation from precipitation statistics to erodibility factor is discussed in Chapter 11. Sensitivity analysis with this and other models in the collection is presented in Chapter 7.

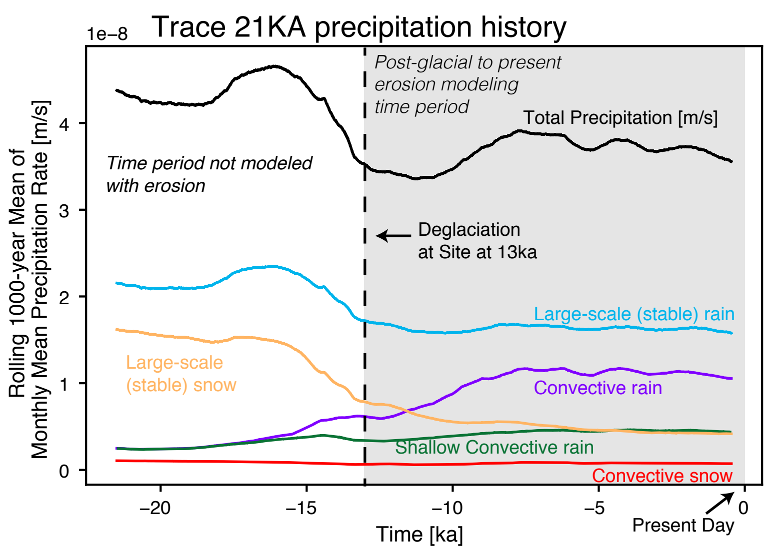

Figure 3.1: Modeled precipitation trends over time for the last 21,000 years, for the grid cell containing western New York, from the TraCE-21ka paleoclimate model simulation. Time on the x-axis is in thousands of years relative to the present day. Precipitation intensities on the y-axis are in meters per year. For reference 2×10^{-8} meters per second is equivalent to 0.63 meters per year.

Chapter 4

Postglacial to Present Initial and Boundary Conditions

4.1 Reconstructed Postglacial Topography

The starting condition for model sensitivity analysis and calibration is a Digital Elevation Model (DEM) that represents the pre-incision valley topography as it existed following the initial retreat of the ice sheet. The last glacial retreat from the area left behind thick accumulations of glacial deposits within the main valleys, including the valleys of the modern Cattaraugus Creek and its tributaries. In the Buttermilk Creek watershed, these glacial deposits, together with a thin mantle created by postglacial fan deposits, formed a low-relief surface sloping gently downward to the north-northwest.

After deglaciation, Cattaraugus Creek and its tributaries incised the glacial deposits (*Fakundiny*, 1985). Extensive remnants of the postglacial valley surface remain throughout the Buttermilk Creek basin, forming a dissected, semicontinuous, low-relief surface with an altitude that ranges roughly from 400 to 430 meters (1,300 to 1,400 feet) within the Buttermilk Creek basin. The remnants appear to be only thinly mantled by postglacial deposits (see, for example, Quaternary geologic map and generalized cross section in (*LaFleur*, 1979), so it is logical to assume that they provide a reasonably accurate representation of the valley topography shortly before stream incision began.

We constructed the pre-incision valley topography at three locations within the Buttermilk Creek basin (Figure 4.1). These locations are the Franks Creek watershed; a gully on the west bank of Buttermilk Creek just north of the Franks Creek watershed; and the watershed containing Area 6 as described in *Bennett* (2017). We selected the Franks Creek watershed because the majority of the WNYNSC facilities are located within it and data are available near its outlet for constraining its post-glacial downcutting history (*Wilson and Young*, 2018). We placed the watershed outlet at the junction of Franks Creek and Quarry Creek instead of the junction of Franks Creek and Buttermilk Creek. This reduction in watershed extent, to include only those parts that contain streams impinging on the Site, has the benefit of substantially decreasing model computation time.

We selected a gully location outside of the Franks Creek watershed in order to undertake the modeling efforts at a fine spatial resolution without the complication of human disturbance (i.e., the large amount of disturbance in or near gullies located within the WNYNSC facilities). For use in the model validation study, we selected the watershed containing Area 6 because the size of the drainage basin is comparable to that of the Franks Creek watershed, and the gullies identified within it have similar characteristics (*Bennett*, 2017). See Section 9.2 for a more comprehensive discussion of the validation site selection.

Using plateau remnants of the post-glacial valley surface for guidance, we constructed the pre-incision valley topography by revising the present-day topography in each of the three selected areas using GIS analysis. The starting point for the analysis was the most recently collected LiDAR elevation data of present-day topography (*Cortes*, 2016). We constructed DEMs from the LiDAR Log ASCII Standard (LAS) point files and contoured them. We inspected the DEMs and contour maps to identify remnant plateau areas. In these identified areas, we left the contours unchanged because they are assumed to provide a relatively accurate representation of the valley topography shortly before stream incision began. In other areas, such as where stream channels have dissected the post-glacial surface, we extrapolated the contour lines from the adjacent remnant plateau across the incised areas. These revised areas can be identified in Figures 4.2, 4.3, and 4.4, which show the present-day topography, pre-incision topography, and the pre-incision topography overlain on present-day topography for each of the modeled areas. The resulting pre-incision contours were smoothed and converted to DEMs using the 'topo-to-raster' interpolation technique (*ESRI*, 2014), which are also shown in Figures 4.2, 4.3, and 4.4. This technique yielded pre-incision surfaces with a gently sloping valley that preserved the slope of the remnant plateau and resulted in outlet elevations of approximately 1350 feet, which is consistent with the findings for the Study 1 downcutting history (*Wilson and Young*, 2018).

We used the pre-incision valley topography as the basis for constructing five additional initial condition DEMs. We constructed the additional initial condition DEMs using a procedure of lightly etching the present-day drainage network into the pre-incision valley topographic surface. The etching procedure, which has been used in other landscape modeling studies (such as *Anderson*, 1994), does not substantially alter the macroscopic erosion patterns (which are dictated by the generalized topography and the process parameters), but it does help reduce the number of "false negative" solutions in which the computed erosion depths and spatial patterns are comparable to the present day but the main streams are shifted to one side or the other in the main valley due to small discrepancies between the actual and modeled initial conditions.

We used an algorithm to etch the pre-incision valley topography surface. It took a small percentage of the difference between the present-day and pre-incision valley topographic elevations at each cell location and then subtracted it from the pre-incision valley topographic elevation. Hydrologic analysis of the Franks Creek watershed DEM drainage pattern with and without etching revealed that a value of seven percent in the algorithm was adequate to avoid shifting of the main stream. Thus, we used seven-percent etching into the pre-incision valley topography as one of the six initial condition DEMs. We created two additional initial condition DEMs using half and double the preferred seven-percent etching percentage (i.e., 3.5 percent and 14 percent) to provide reasonable bounds for assessing uncertainty in the modeling analyses. We also created an initial condition DEM using an algorithm that added random noise to the seven-percent etched DEM elevations based on the uncertainty of the LiDAR-generated elevations (i.e., the algorithm generated normally-distributed

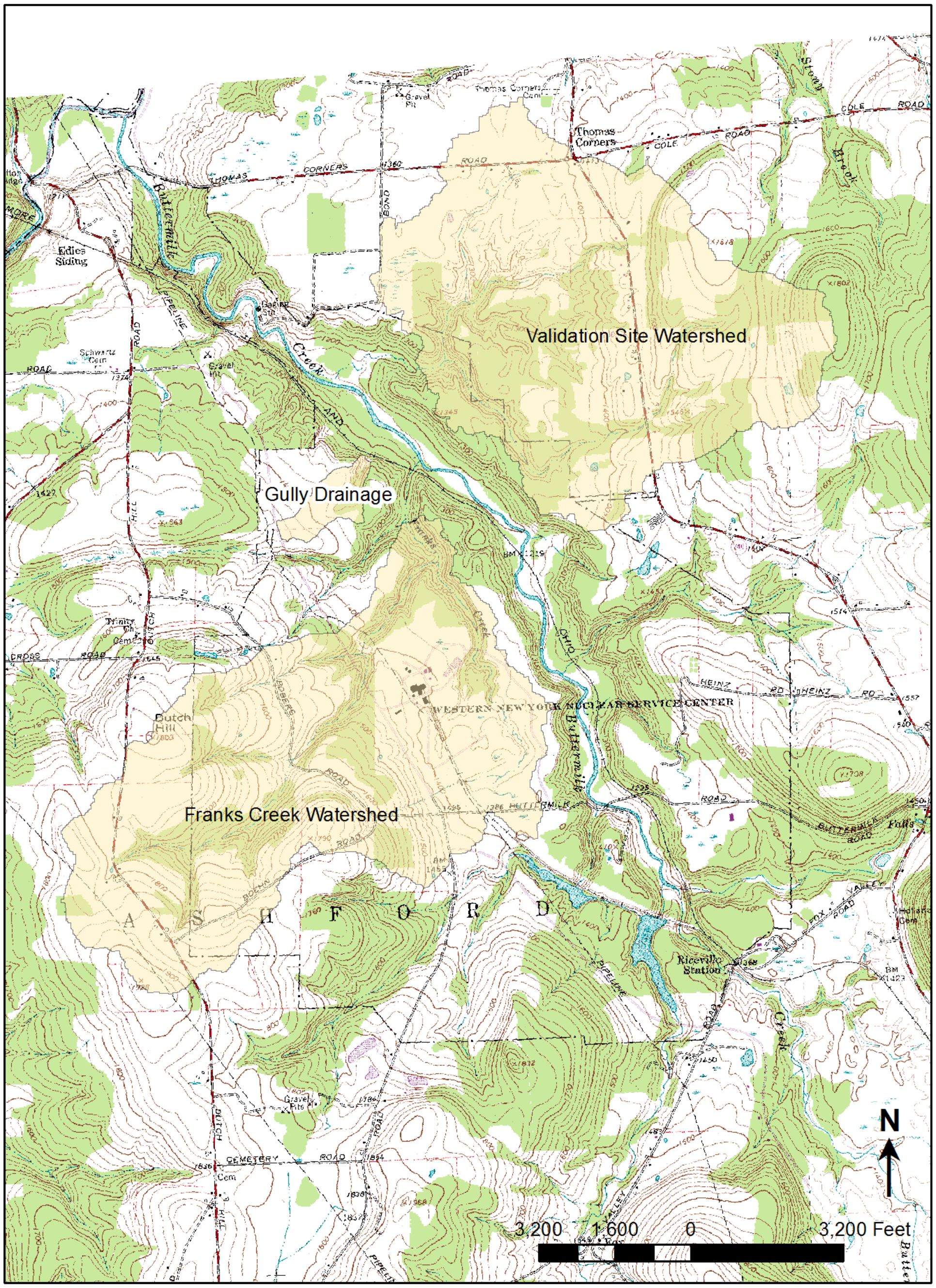

Figure 4.1: Location of the modeled areas. Scale is in feet.

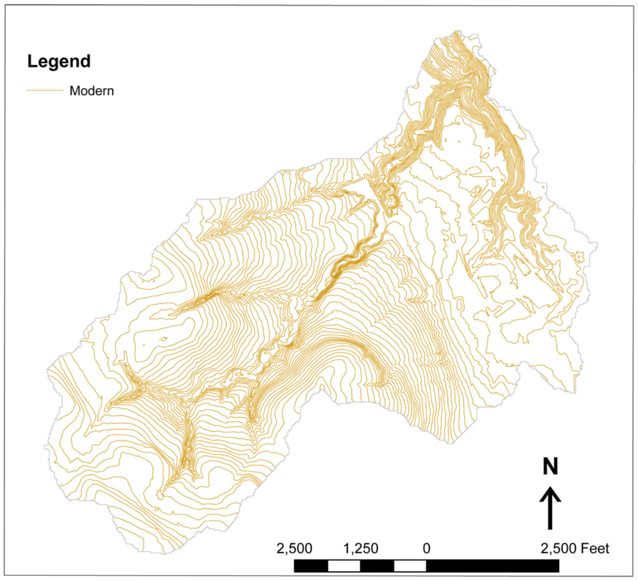

(a) Franks Creek: present-day topography

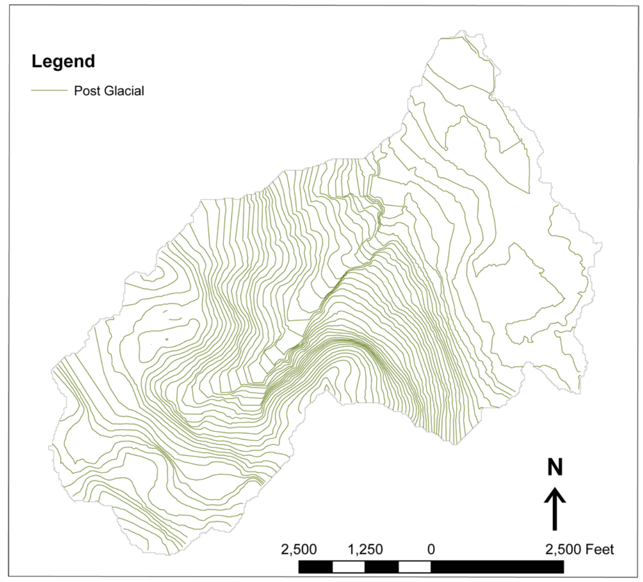

(b) Franks Creek: pre-incision topography

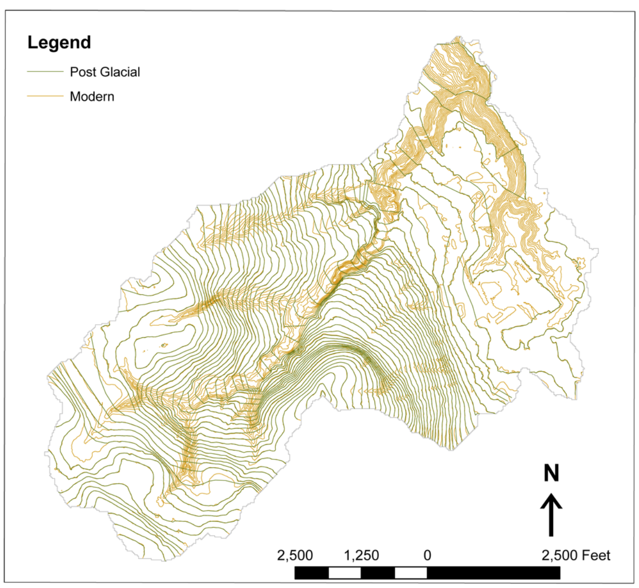

(c) Franks Creek: pre-incision topography overlain on present-day topography

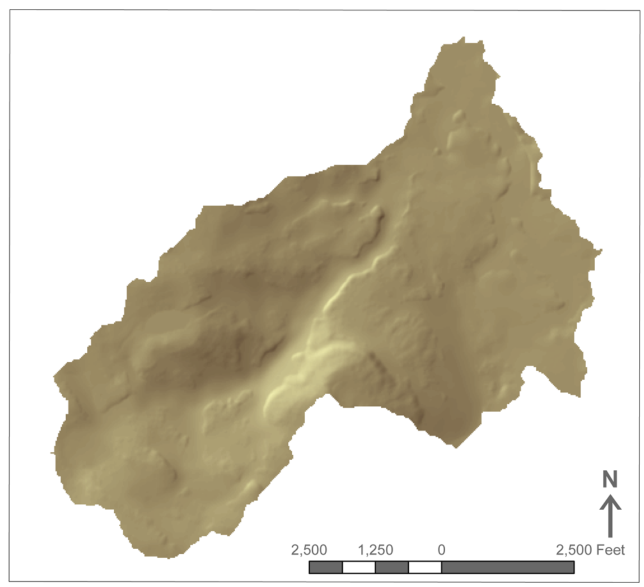

(d) Franks Creek: pre-incision DEM

Figure 4.2: Topography of the southeast Franks Creek watershed model domain following glacial retreat (pre-incision topography and present-day topography). All units in feet. Contour interval is 10 feet.

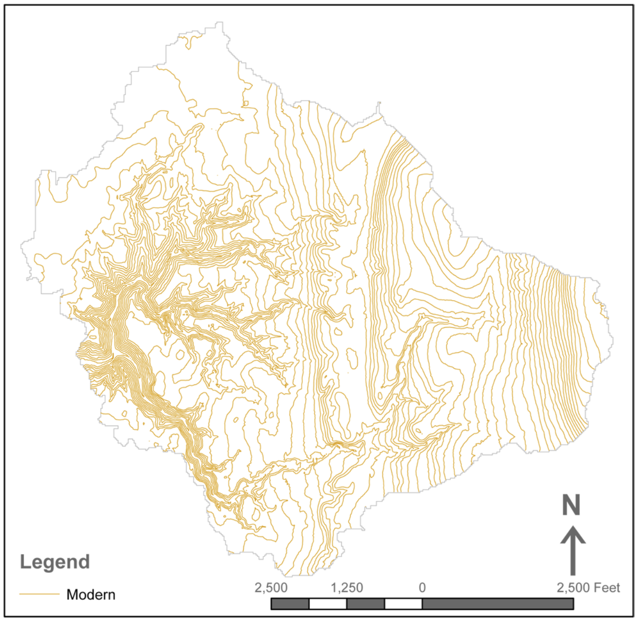

(a) Validation site: present-day topography

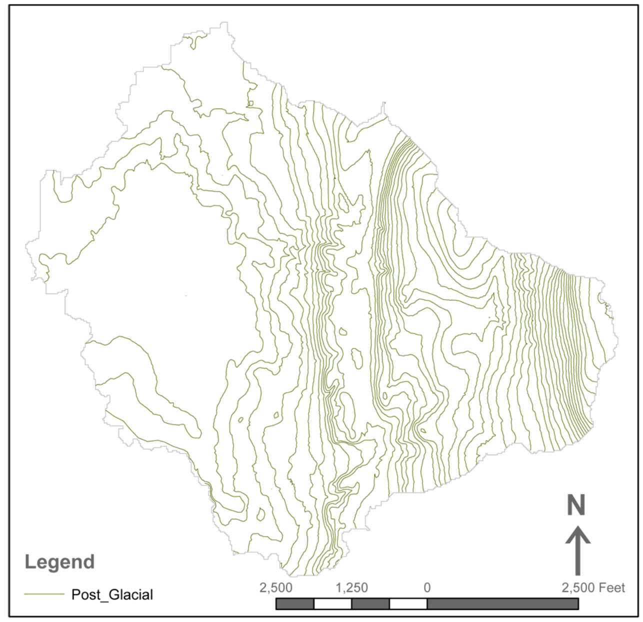

(b) Validation site: pre-incision topography

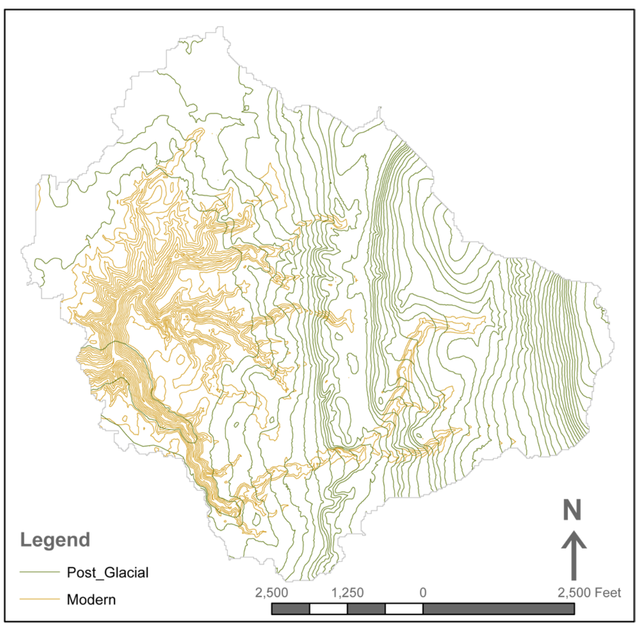

(c) Validation site: pre-incision topography overlain on present-day topography

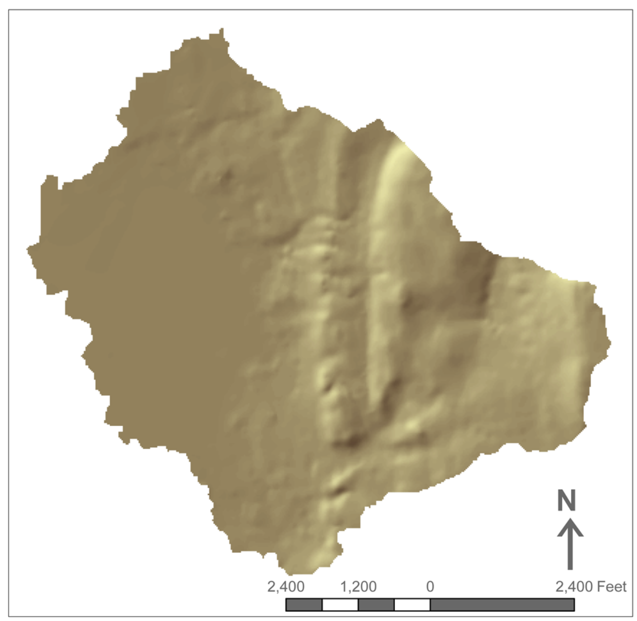

(d) Validation site: pre-incision DEM

Figure 4.3: Topography of the validation site model domain following glacial retreat (pre-incision topography and present-day topography). All units in feet. Contour interval is 10 feet.

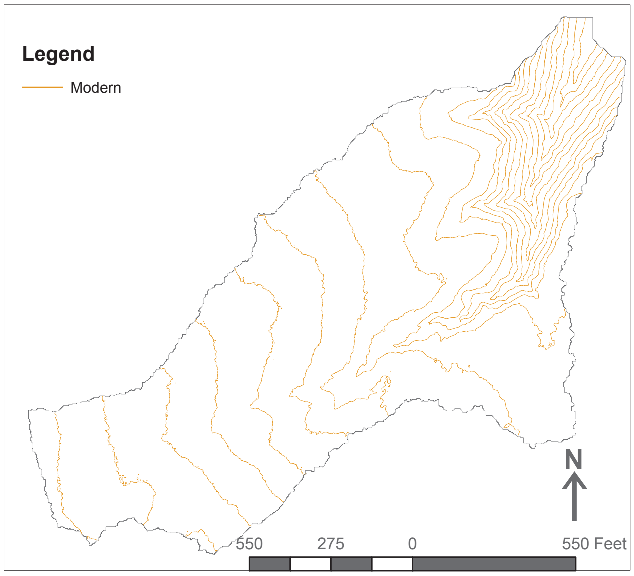

(a) Gully: present-day topography

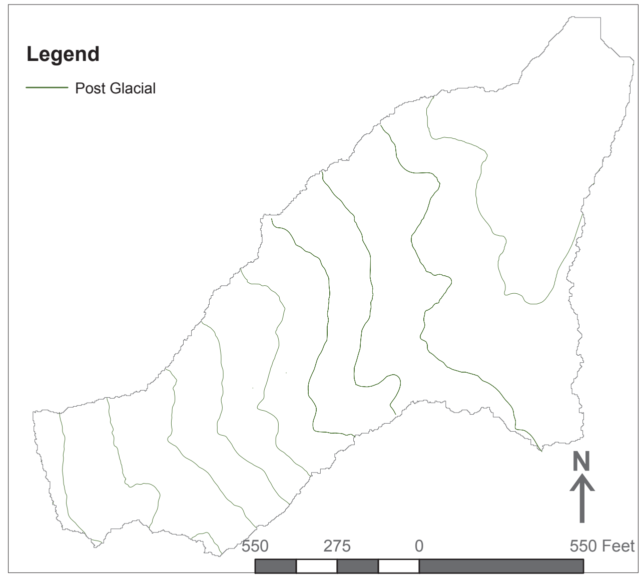

(b) Gully: pre-incision topography

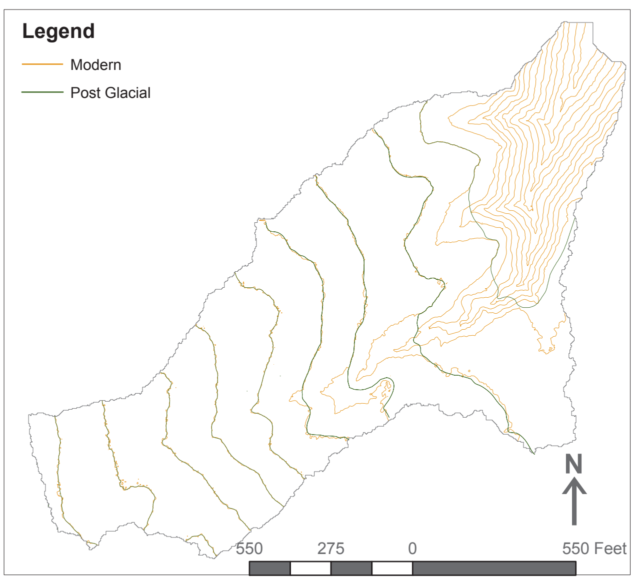

(c) Gully: pre-incision topography overlain on present-day topography

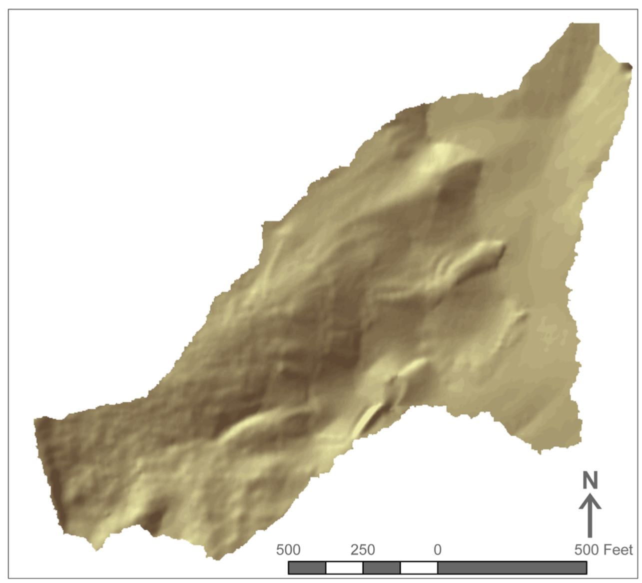

(d) Gully: pre-incision DEM

Figure 4.4: Topography of the gully model domain following glacial retreat (pre-incision topography and present-day topography). All units in feet. Contour interval is 10 feet.

Table 4.1: Modeling Initial Conditions at Franks Creek Watershed (FC), Gully (G), and Validation (V) Site

Initial Condition	Features	Use
1	Pre-incision DEM with no etching	FC,G,V
2	Pre-incision DEM with 3.5 pct	FC,G,V
3	Pre-incision DEM with 7 pct etching	FC,G,V
4	Pre-incision DEM with 14 pct etching	FC,G,V
5	Pre-incision DEM with 7 pct etching and random noise	FC,G,V
6	Revised Pre-incision DEM (no change to bedrock and 7 pct etching in glacial fill area)	FC

random numbers within one standard deviation of the LiDAR vertical accuracy of ±0.132 feet to apply at each grid cell). Lastly, we created one final initial condition DEM using the seven-percent etching on a pre-incision valley surface that was not modified within the bedrock portion of the Franks Creek watershed (i.e., not modified in the upper portion of the watershed west of Rock Springs Road at an elevation above where post-glacial deposition occurred). This initial condition DEM accounts for the uncertainty associated with the lack of a data set available at present on which to base such corrections. Table 4.1 and Figures 4.5, 4.6, and 4.7 show the initial condition DEMs that were created for each of the three modeling domains.

4.2 Subsurface Initial Conditions

The most strongly contrasting rock or sediment types observed at WNYNSC are represented as individual lithologic units in some of the models (see Chapter 3 and Appendix A). These units are: (1) Paleozoic bedrock, (2) thick but unlithified glacial till sediments, and in some of the modeling cases (3) shallow surface soils/sediments. We did not divide the landscape and its subsurface into additional individual lithologic units in the models to avoid several problems. First and most important, including additional lithologic categories increases the number of poorly constrained parameters that must be calibrated. Second, the more loosely constrained parameters that are included in a model, the harder it is for an analyst to understand and interpret the model's behavior. Third, information about the spatial distribution of lithologies, particularly in the subsurface, may be (and usually is) limited or incomplete. Thus, in keeping with our model development guideline of applying the principle of parsimony, we chose to err on the side of simplicity wherever possible, which included limiting the representation of lithologic variability in the sensitivity analysis and calibration runs to the primary and most strongly contrasting lithology classes observed at WNYNSC.

The starting point for generating the bedrock surface (the interface between the Paleozoic bedrock and the thick but unlithified glacial sediments) was a contour map prepared by

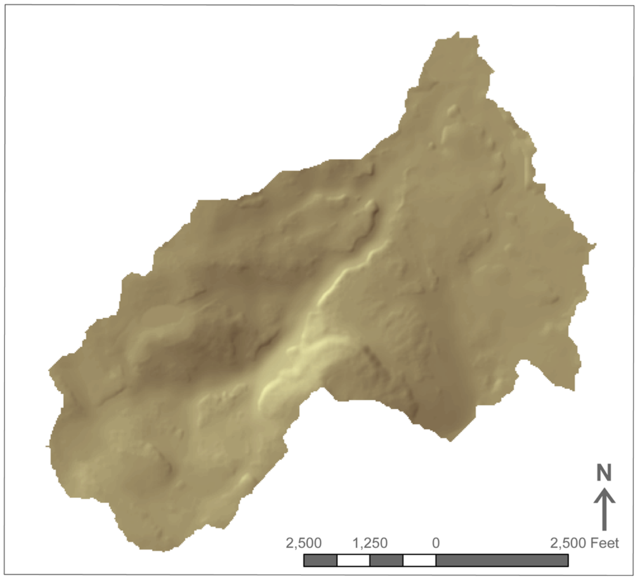

(a) Pre-incision DEM with 3.5 percent etching

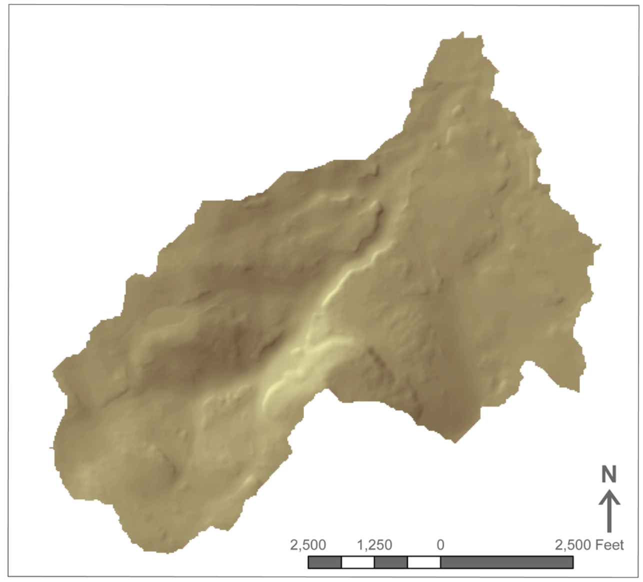

(b) Pre-incision DEM with 7 percent etching

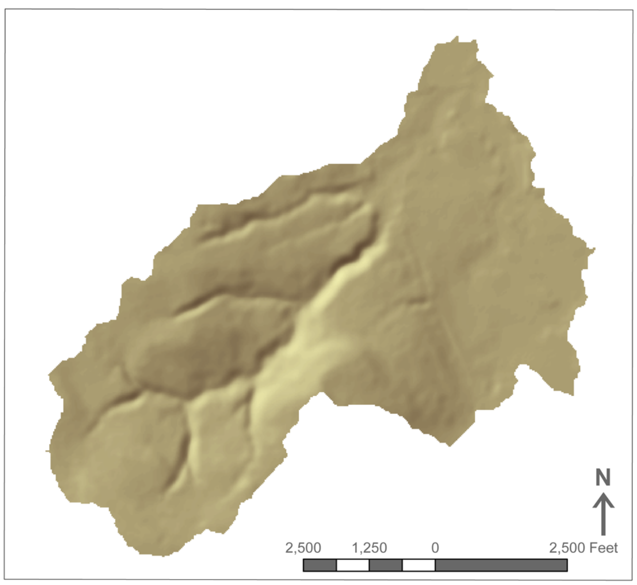

(c) Pre-incision DEM with 7 percent etching and no fill in upper watershed

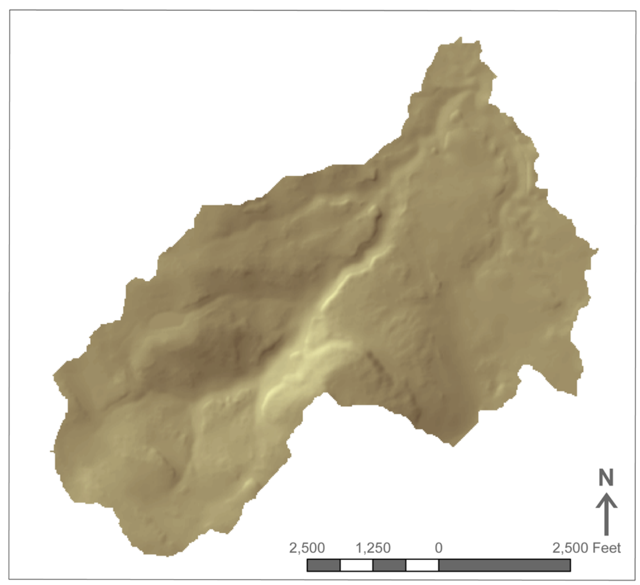

(d) Pre-incision DEM with 14 percent etching

Figure 4.5: Franks Creek: DEMs of pre-incision valley topographic surface with various degrees of etching. All units in feet.

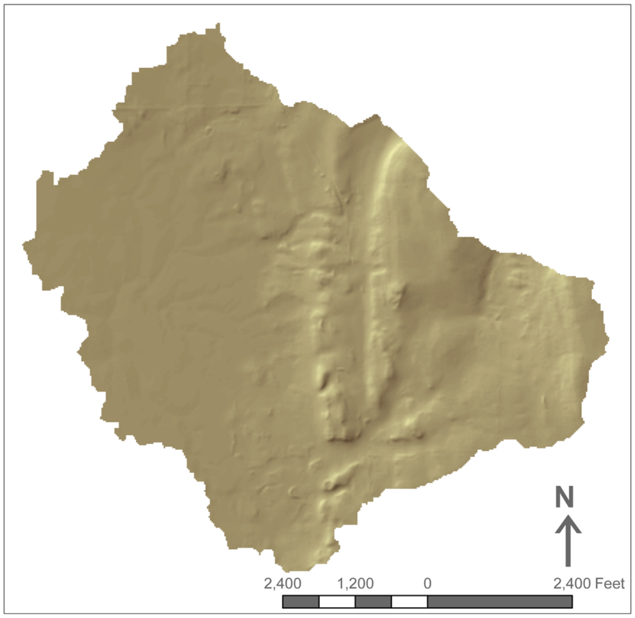

(a) Pre-incision DEM with 3.5 percent etching

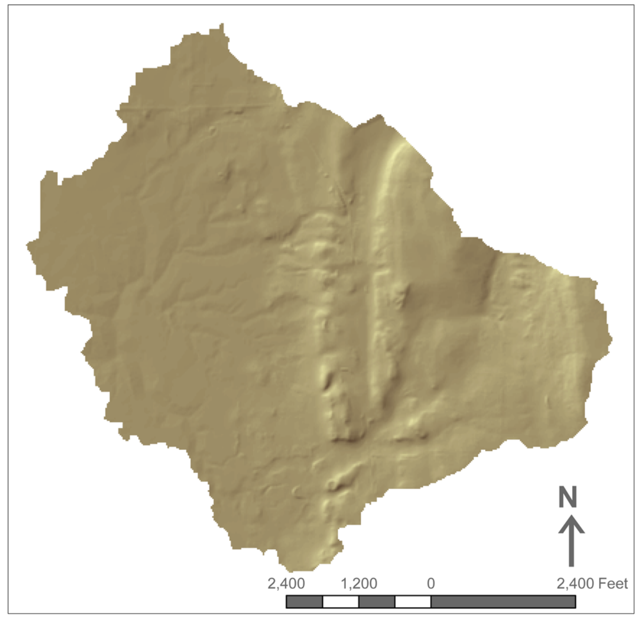

(b) Pre-incision DEM with 7 percent etching

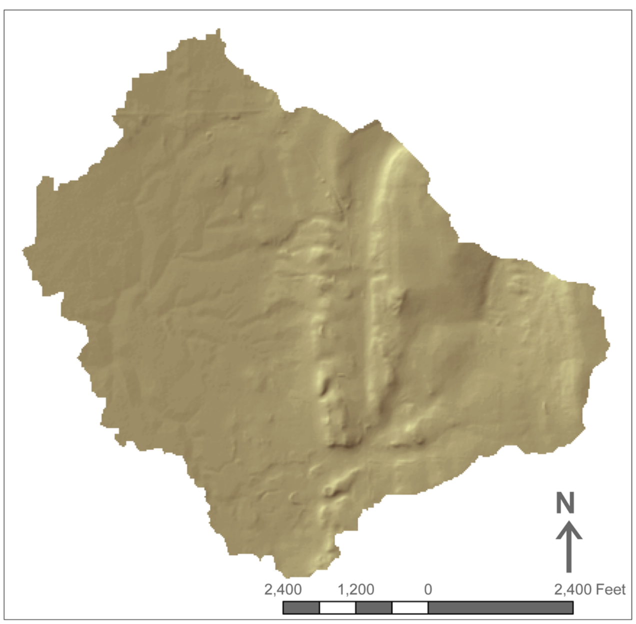

(c) Pre-incision DEM with 7 percent random etching

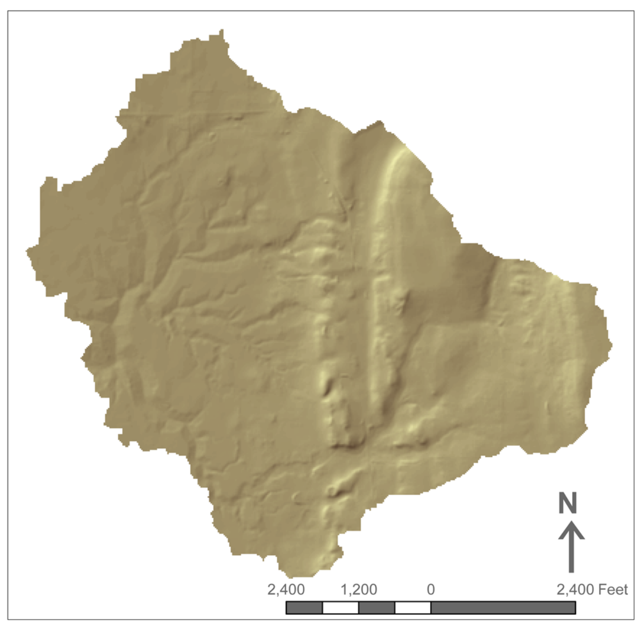

(d) Pre-incision DEM with 14 percent etching

Figure 4.6: Validation site: DEMs of pre-incision valley topographic surface with various degrees of etching. All units in feet.

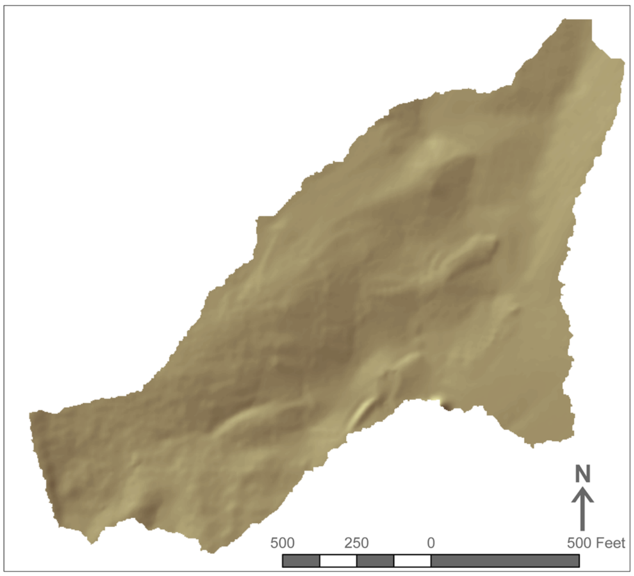

(a) Pre-incision DEM with 3.5 percent etching

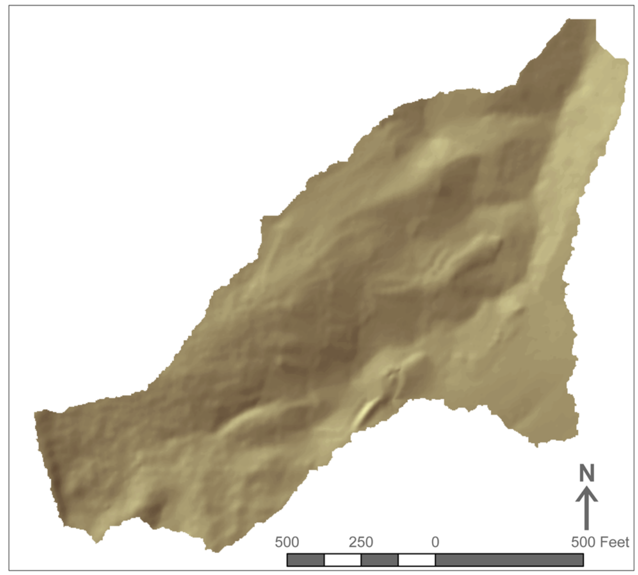

(b) Pre-incision DEM with 7 percent etching

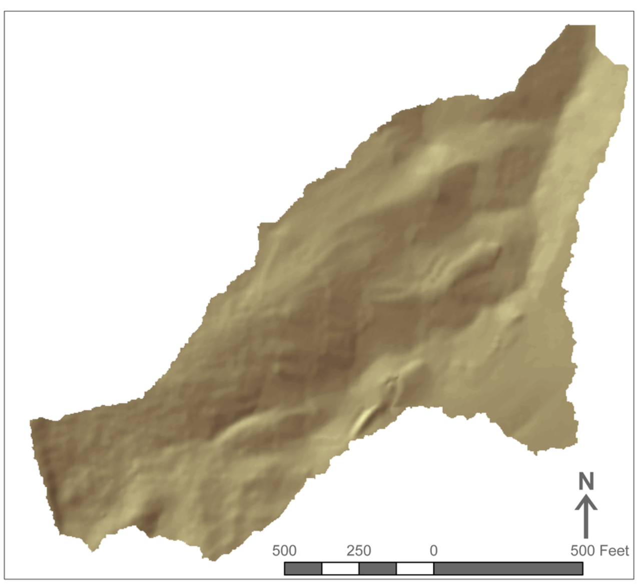

(c) Pre-incision DEM with 7 percent random etching

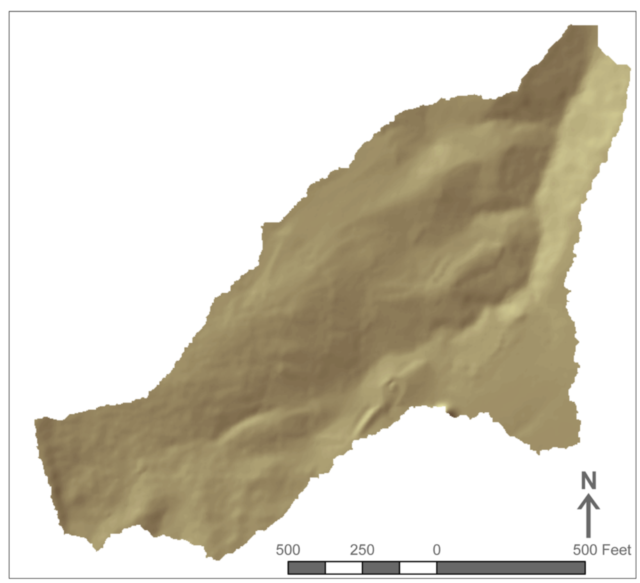

(d) Pre-incision DEM with 14 percent etching

Figure 4.7: Gully: DEMs of pre-incision valley topographic surface with various degrees of etching. All units in feet.

Randall (1980). Randall's bedrock contour map partially extends into each of the three modeling areas as shown in Figure 4.8. Using Randall's data control points as a guide, we extended the contours to the edge of the three drainage basins. Unfortunately, Randall's bedrock contour map did not extend into the western portion of the Franks Creek watershed and the eastern portion of Area 6, where the bedrock surface is exposed or close to the present-day surface. In these two areas, we determined the depth to bedrock by subtracting the thickness of the soil layer from the LiDAR surface elevations at each grid node. We used soil layer thickness data provided in the NRCS gSSURGO database (*Soil Survey Staff*, 2017) for this task. We combined the bedrock surface information from the two data sources to generate the topographic maps, which we then smoothed and converted to DEMs using the 'topo-to-raster' interpolation technique (*ESRI*, 2014). Depth-to-bedrock for all three model domains is shown in Figure 4.9.

The starting point for the regolith (shallow surface soils/sediments) layer was data taken from the NRCS gSSURGO database. Its thickness was assumed to be equal to the thickness of the NRCS soil units as measured down to a depth of approximately five feet by the NRCS soil scientists. Throughout the eastern portion of the Franks Creek watershed, the gully area, and the western portion of Area 6, the soil units were measured to be five-feet thick. Only in the western portion of the Franks Creek watershed and the eastern portion of Area 6 were soil units measured at less than five feet (i.e., in the zero to five-foot range). To account for the variability of the soil unit thickness in these areas, we used a range of zero to five feet for the regolith thickness parameter in the sensitivity and calibration model runs. Also, due to a lack of information on the age of alluvial fans, we included them as part of the thick unlithified glacial sediments layer, instead of within the regolith layer.

4.3 Downcutting History

Observations that constrain the incision of Buttermilk Creek since deglaciation provide key information to the modeling effort by supplying the time-variable elevation of the watershed outlet. Incision of the watershed after retreat of glacial ice occurred in response to the lowering of the junction of Franks Creek and Buttermilk Creek; thus, the timing of the incision of the outlet serves as a boundary condition to the model runs. In order to be usable in the EMS, the incision history constrained by geomorphic and geochronologic evidence must be supplied as value pairs of time and elevation above modern river level. Under Study 1, the EWG deveoped two alternative scenarios of river incision for use in the models (Figure 4.10). They are:

- **Scenario 1: Meander Scenario.** The first scenario, termed the Meander Scenario, is predominantly based on the dates from the Abandoned Meander site (*Wilson and Young*, 2018). This scenario also uses a combination of observations of sediment burial (OSL) and buried wood (^{14}C) dating to indicate that Buttermilk Creek had reached its present grade approximately 2.5 ka (thousand years before 1950). This interpretation assumes that the dates on buried wood do not represent preservation of the absolute oldest point in time that Buttermilk Creek occupied its current grade. Thus, it uses the sediment burial (OSL) date of 2.5 ka as the point at which Buttermilk Creek occupied its current grade. The Abandoned Meander is located upstream of the Franks

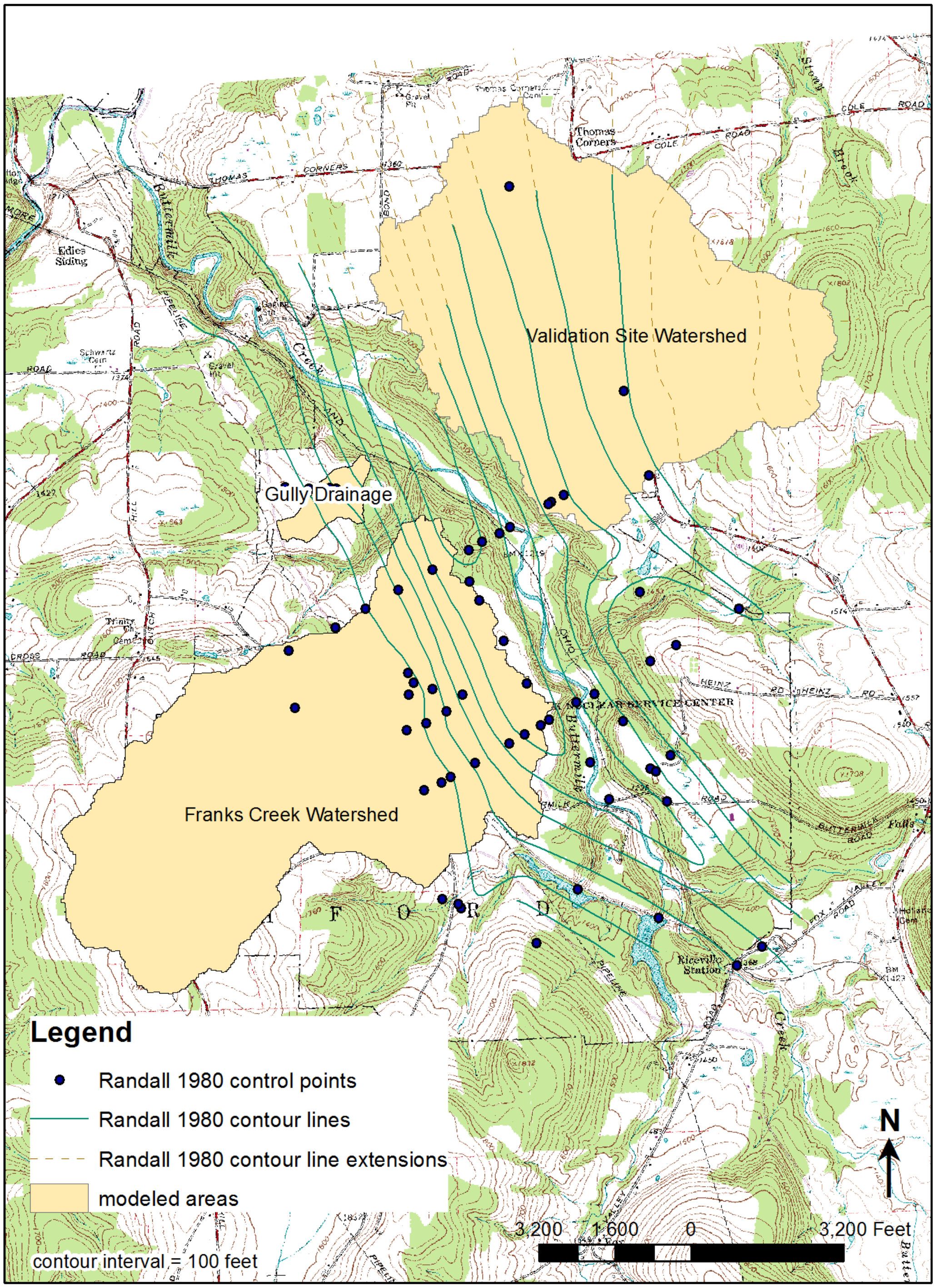

Figure 4.8: Randall's bedrock contour map showing extensions into the three model domains. Scale is in feet.

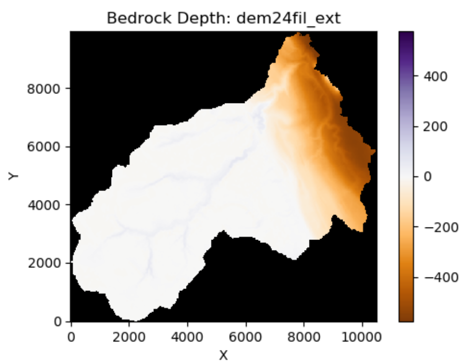

(a) Franks Creek Watershed domain

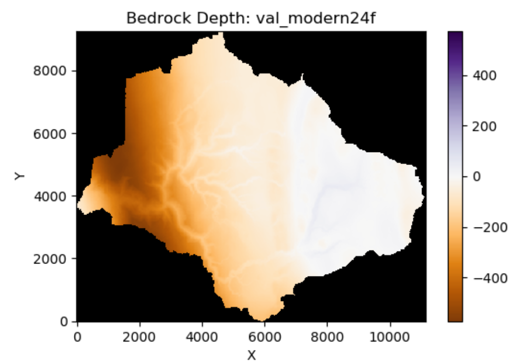

(b) Validation domain

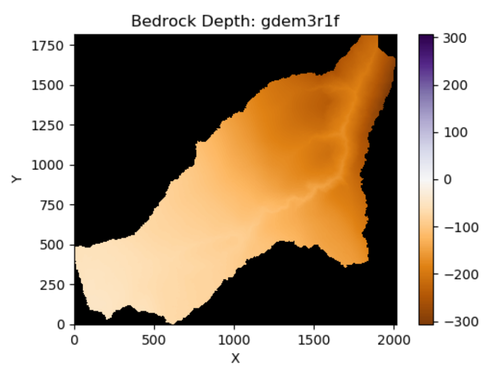

(c) Gully domain

Figure 4.9: Depth to bedrock from modern topography in all three considered domains. Orange indicates that bedrock is below the modern topography and purple indicates that bedrock is exposed at the surface. All units in feet.

Creek-Buttermilk Creek junction and thus the elevation of Buttermilk Creek at this location does not correspond exactly to the elevation of the Franks Creek-Buttermilk Creek junction. However, the model only requires elevation of the channel relative to the modern channel elevation. This was determined by subtracting the elevations of Abandoned Meander sites from the modern elevation of Buttermilk Creek at the Abandoned Meander.

- **Scenario 2: Buttermilk Context Scenario.** An alternative scenario, termed the Buttermilk Context Scenario, differs from the Meander Scenario in three ways. First, it projects all observations to the junction of Franks Creek and Buttermilk Creek using the slope of the 13 ka age line and the elevation and gradient of modern Buttermilk Creek. Elevations of the channel above the modern river level are then determined by subtracting the elevations from the modern elevation of Buttermilk Creek at its junction with Franks Creek. Second, it includes a date and elevation pair from the Heinz Trench site HT-7 at 3.785 ka and 42 feet above the modern channel elevation. Finally, it considers two additional observations in order to make a different interpretation of the slowing of the incision as Buttermilk Creek approached its current grade: a date of 1.653 ka at the Tree Farm Site located at 16 feet above modern river level and a date of 2.128 ka at site HT-33 located seven feet above modern river level. Taken in concert with the OSL and buried wood ^{14}C observations an age elevation point of 2.3 ka and 14 feet above modern river level is used. This indicates that incision slowed but did not stop in the period $\sim$2.5 ka to the present.

These two scenarios are quite similar and both are considered to be equally viable. Moreover, sensitivity analysis (Chapter 7) demonstrated that the erosion models are insensitive to the differences between the two scenarios. Given the similarity between the scenarios and the erosion models' insensitivity, the scenarios were averaged for use as the watershed-outlet boundary condition in the calibration runs, and as a starting point for developing scenarios of future downcutting over the next 10,000-year period.

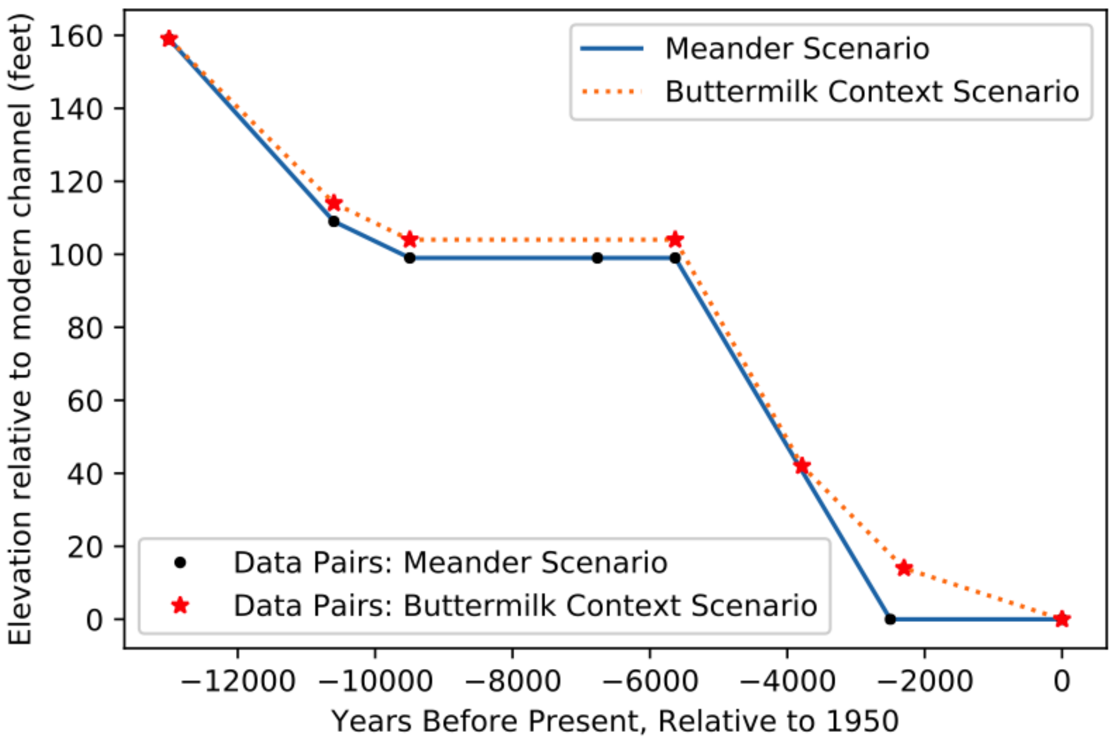

Figure 4.10: Graphical Summary of Alternative Incision Histories

Chapter 5

Input Parameters

5.1 Introduction

The erosion models require specification of input parameters. These are numerical values that describe material properties and the processes of rainfall, runoff, and erosion, and thereby control the behavior of the models. In order to perform sensitivity analysis and calibration, it is necessary to identify reasonable ranges for each parameter. These ranges also provide constraints to the calibration process: it is assumed that the most appropriate value lies somewhere within the specified range. For sensitivity analysis, the parameter ranges provide the bounds within which model sensitivity is assessed. Parameter ranges also influence the quantification of sensitivity by providing a reference scale for changes in parameter values, as discussed further in Chapter 7.

This chapter presents the parameter ranges used in sensitivity analysis and calibration, along with the rationale for those ranges. In considering these parameter estimates, it is important to bear in mind that the purpose is simply to establish plausible upper and lower bounds for each parameter. The parameter values and probability distributions used in model projection (Chapter 11) are obtained through a process of calibration, rather than by *a priori* selection, as discussed in Chapter 8.

Parameters and their corresponding symbols are listed alphabetically in Table 5.1. Parameter ranges are summarized in Table 5.2.

5.2 Hillslope Process Parameters

Here the term "hillslope processes" represents those processes responsible for producing soil, and transporting soil and sediment downslope primarily due to the work of gravity, as opposed to stresses exerted by surface-water flow. The Erosion Modeling Suite uses four alternative component models to describe the rate of downslope material transport. Each of these component models consists of a mathematical expression for the volume rate of soil transport per unit slope width, which we will represent using the symbol q_h. These component models and their equations and parameters are as follows:

1. **Linear soil creep law** (default option used in most models). The rate of soil creep

is proportional to the local slope gradient, $\nabla\eta$.

$$q_h = -D\nabla\eta \tag{5.1}$$

Parameters: soil-creep coefficient D.

2. **Depth-dependent linear soil creep law.** The rate of soil creep is a linear function of the local slope gradient, and an exponential function of the local soil thickness, H. The latter allows the soil flux to drop to zero where no soil is present.

$$q_h = -D\left[1 - \exp(-H/H_0)\right]\nabla\eta \tag{5.2}$$

Parameters: soil-creep coefficient D and characteristic transport depth H_0.

3. **Taylor series soil creep law.** The soil creep rate law includes a series of nonlinear terms term designed to represent the acceleration in downslope flux when gradient is close to a specified critical gradient, S_c.

$$q_h = DS\left[1 + \sum_{i=1}^{N}\left(\frac{S}{S_c}\right)^{2i}\right], \tag{5.3}$$

where $S = -\nabla\eta$ is the slope gradient, and N is the user-specified number of terms.

Parameters: soil-creep coefficient D and critical slope gradient S_c. The number of terms N could also be considered a parameter. In this study, N has been set to seven as a compromise between numerical stability and the desired behavior of the flux law.

4. **Depth-dependent Taylor series soil creep law.** This combines the cubic formulation above with soil-depth dependence.

$$q_h = DS\left[1 - \exp(-H/H_0)\right]\left[1 + \sum_{i=1}^{N}\left(\frac{S}{S_c}\right)^{2i}\right] \tag{5.4}$$

Parameters: soil-creep coefficient D, characteristic transport depth H_s, and critical slope gradient S_c.

For component models 2 and 4 above, it is also necessary to calculate the production of potentially mobile material (here simply referred to as “soil”) from the underlying rock or glacial sediment. As described in Chapter 3, the function used to represent the rate of soil production, P, in these models is

$$P = P_0 \exp\left(-\frac{H}{H_s}\right). \tag{5.5}$$

Here the parameters are the maximum soil production rate, P_0, and the characteristic depth scale H_s.

Collectively, among the various component hillslope models above, there are five parameters that require ranges to be specified: D, P_0, H_s, H_0, and S_c. In addition, some models require specification of a starting soil thickness, H_{init}, as an initial condition. The following subsections describe the ranges identified for use in sensitivity analysis and model calibration, and the rationale for choosing them.

5.2.1 Soil Creep Rate Coefficient, D

All of the models in the Erosion Modeling Suite include a soil-creep rate coefficient, D. This parameter represents the efficiency with which soil is transported downslope, for a given slope gradient. It has dimensions of length squared per time, and estimates in the literature are often reported in square meters per year, square cm per year, or square meters per thousand years. It appears in the equations describing soil flux. For example, in models that use a linear, non-depth-dependent formulation, the equation for soil volume flux per unit contour width, q_h, is

$$q_h = -D\nabla\eta. \tag{5.6}$$

where η is land surface elevation, and ∇ is the derivative (gradient) operator in two dimensions.

Because many models assume hillslope evolution is a diffusion-like process, this efficiency term is often referred to as *hillslope diffusivity*. A variety of techniques have been used to estimate values of D in different settings. These methods range from fitting theoretical hillslope profiles to degraded scarps (e.g., *Nash*, 1980; *Hanks et al.*, 1984) to the use of cosmogenic nuclide measurements in conjunction with mass-balance models (e.g., *McKean et al.*, 1993; *Small et al.*, 1999).

Most estimates of D fall in the range 10^{-4} to 10^{-2} m^{2}y^{-1} (Table 5.3). One of the highest published values, 0.036 ± 0.0055 m^{2}y^{-1}, was obtained by *McKean et al.* (1993) using ^{10}Be analysis at a site in central California. Estimates on the order of 10^{-4} m^{2}y^{-1} have been derived from sites in the Negev and Sinai deserts (*Begin*, 1992). For purposes of sensitivity analysis, it is desirable to cover the full range of observed values. For this reason, the range adopted is $10^{-6.3}$ to $10^{-1.3}$ m^2/y, or about 5×10^{-7} to about 0.05. The lower end lies below the lower range of field estimates; this allows a test of the (unlikely) possibility that soil creep is largely ineffective at the site.

5.2.2 Maximum Soil Production Rate, P_0

Several studies have used cosmogenic radionuclide analysis to estimate maximum soil production rates, which corresponds to the erosion-model parameter P_0. Table 5.4 lists field-estimated rates (in m/yr) together with the associated lithology and field settings. These studies are summarized as follows:

- 2.68×10^{-4} *Heimsath et al.* (2001a)
  Oregon Coast Range, in humid-temperate, hilly landscape underlain by relatively uniform, unweathered arkosic sandstone and siltstone.

- 7.7×10^{-5} *Heimsath et al.* (1997, 1999)
  Tennessee Valley in Marin County, California. Underlying bedrock is greywacke.

- 1.43×10^{-4} *Heimsath et al.* (2001b)
  Southeastern highlands of Australia, characterized by cool climate and heavy rainfall. Underlying bedrock types are Ordovician metasediments and granite.

- 1×10^{-3} *Heimsath et al.* (2012)
  San Gabriel Mountains in California.

- $7{\times}10^{-6}$ *Small et al.* (1997, 1999)
  Alpine environments across the western US. Lithologies represented are granite and gneiss.

The range of these studies spans 7×10^{-6} to 10^{-3} m/yr, with the lowest rate in a rocky, high alpine environment, and the highest in a warm, mediterranean climate. Based on these studies, a reasonable bracketing range for calibration and sensitivity analysis, rounding to the outermost factors of ten, is 10^{-6} to 10^{-3} m/yr.

5.2.3 Soil Production Characteristic Depth Scale, H_s

Studies have shown the soil production decay depth to be approximately 0.5 m in a number a sites around the world (*Rosenbloom and Anderson*, 1994; *Pelletier and Rasmussen*, 2009; *Heimsath et al.*, 1997, 1999, 2001a,b). Here a bounding range of 0.2–0.7 m is adopted.

5.2.4 Transport Depth Scale, H_0

This parameter is defined in *Johnstone and Hilley* (2015) as the scaling depth of the velocity profile of soil. In their study they use values of H_0 between 0.12 and 0.33 m. Where soil thickness is much larger than H_0, only a fraction of the soil profile is mobile, and the transport rate is not limited by soil availability. Conversely, when H_0 is much greater than the soil depth, soil moves as plug flow and the transport rate is limited by the soil thickness.

As of this writing, there are very few quantitative estimates available for H_0. Models of frost creep (soil creep caused by repeated cycles of soil freezing and dilation followed by collapse upon melting) predict that the characteristic transport depth scales with the depth to which freeze-thaw cycles penetrate during winter (e.g., *Anderson et al.*, 2013), but these models are restricted to a single process only. At West Valley, it is likely that soil creep results from a combination both of freezing-related processes and of biological processes, with the latter including animal burrowing, and soil displacement by root growth and tree fall. For vegetation-related soil disturbance processes, it seems reasonable to assume that the characteristic transport depth should be similar to the depth of the rooting zone, which is commonly on the order of approximately half a meter (though occasional individual roots may penetrate much more deeply). In view of the values considered by *Johnstone and Hilley* (2015), and the informal field inference that soil disturbance processes commonly tend to penetrate to a meter or less, the recommended range for H_0 is 0.1 and 1 m.

5.2.5 Threshold Slope Gradient, S_c

The nonlinear hillslope transport law includes a "critical slope" parameter, S_c. This parameter represents the gradient near which the downslope soil flux becomes significantly greater than a simple linear formulation between gradient and flux would predict. The equivalent parameter in the more familiar Andrews-Bucknam equation represents the gradient at which soil flux becomes infinite; the equation is undefined for gradients steeper than this value. In the nonlinear transport function used in this study, however, the parameter S_c has a somewhat different meaning. For example, gradients at or above S_c are perfectly allowable in the present formulation. For this reason, S_c is best thought of as a calibration parameter that influences the gradient of rapidly eroding hillslopes, rather than as a strict threshold.

Published estimates of S_c in the Andrews-Bucknam equation include 0.6 (from sandpile experiments; *Roering et al.* (2001)), and 1.2–1.4 (from terrain analysis in Oregon and California; 1.4, 1.2, and 1.25, respectively, in *Roering et al.* (1999, 2007); *Ganti et al.* (2012)). These estimates are likely to be on the high end for West Valley, where valley side-slope gradients on the order of 20–25° (gradient of 0.36–0.47) are common. Furthermore, numerical experiments with the nonlinear hillslope erosion component demonstrate that there are cases in which the valley side-slope gradient may be substantially higher than S_c, particularly when the basal downcutting rate is relatively fast. Therefore, for purposes of sensitivity analysis and calibration, a range of S_c from 0.1 to 1.25 is adopted.

5.2.6 Initial Soil Thickness, H_{init}

Models that explicitly track a soil layer need to specify the starting thickness of the soil, H_{init}. Although H_{init} is an initial condition rather than a process parameter, it is useful to include it in sensitivity analyses. A reasonable basis for its range is the soil thickness in the Franks Creek watershed as mapped by the U.S. Department of Agriculture's Gridded Soil Survey Geographic database (gSSURGO) (*Soil Survey Staff*, 2017). According to this database, soils in the area commonly range from 1 to 5 feet in thickness. Therefore this range is adopted for purposes of sensitivity analysis.

5.3 Precipitation Parameters

Several models in EMS use a stochastic representation of precipitation, runoff, and surface water discharge. These models treat precipitation intensity, p, as a random variable. The stochastic model is implemented numerically by dividing a global time step of duration T_g into n_t sub-time-steps of duration T_g/n_t. For each sub-time-step, a precipitation intensity p is drawn at random from a Weibull distribution, whose survival function is also known as the stretched exponential distribution. The distribution's survival function, or the probability $Pr(P > p)$ that a given precipitation intensity will be greater than some value p is

$$Pr(P > p) = \exp\left[-\left(\frac{p}{P_*}\right)^c\right], \tag{5.7}$$

where P_* is a scale parameter and c is a shape parameter. The scale parameter is related to the mean daily precipitation intensity p_d by

$$P_* = \frac{p_d}{\Gamma(1 + 1/c)}, \tag{5.8}$$

where $\Gamma()$ is the gamma function.

Once a precipitation intensity has been selected for a sub-time-step, water erosion is applied for a fraction F of the sub-step duration. Here F is an intermittentcy factor that represents the fraction of an average year that precipitation occurs, defined as the total number of days with measurable precipitation divided by the total number of days in the year

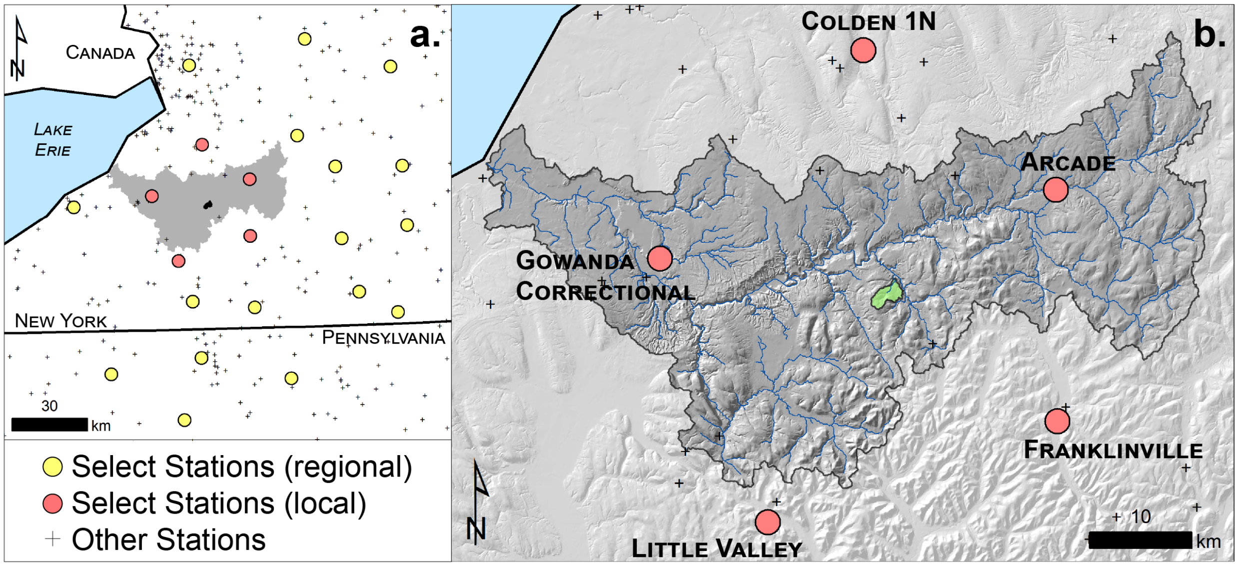

Figure 5.1: Regional (a) and local (b) maps of GHCN stations used in this analysis. Red symbols show the closest stations to the study site with long, complete records with which to estimate daily precipitation parameters. Yellow symbols show stations used to compare estimates from points to those from daily, gridded precipitation. Frank's Creek is highlighted in green in (b) for reference.

(365.25). Collectively, models that include stochastic precipitation have three precipitation parameters: the mean daily precipitation intensity, p_d, the distribution shape factor, c, and the fraction of wet days, F.

To estimate these parameters for this study, empirical analysis of daily precipitation statistics (p_d, c, F) is based on a subset of meteorological stations selected from the Global Historical Climatology Network (GHCN) v.3.22 (*Menne et al.*, 2012). Daily data was downloaded from the NOAA NCDC server (`ftp.ncdc.noaa.gov/pub/data/ghcn/daily/`). Within a 30-km radius of the Frank's Creek watershed, there are 29 GHCN stations, six of which record more than 40 years of observations. We used five of these six stations as representative of local hydro-climatic conditions for the study site (one was excluded because it had less than 60% completeness from 1941–2010) (red stations in Figure 5.1). To compare point observations of precipitation (i.e., GHCN) against gridded precipitation products such as PRISM (*Daly et al.*, 2008) and GRIDMET (*Abatzoglou*, 2013), we supplemented local estimates of precipitation parameters with a regional analysis of stations within a 90-km radius of study site that have continuous records over a reference period of 1981–2010 (>95% complete; yellow stations in Figure 5.1a).

Figure 5.2 illustrates how parametric estimates for mean daily precipitation intensity (p_d), the precipitation shape factor (c), and the fraction of wet days (F) vary in time for the two longest records (>70 years of observations) near Frank's Creek. The two sites are a similar distance away from the study site (Figure 5.1b), yet the Franklinville station is 15% dryer than the Little Valley station. Below, we provide a more detailed description for how parameters are estimated, how they vary in space and time, and how they compare to gridded precipitation data products.

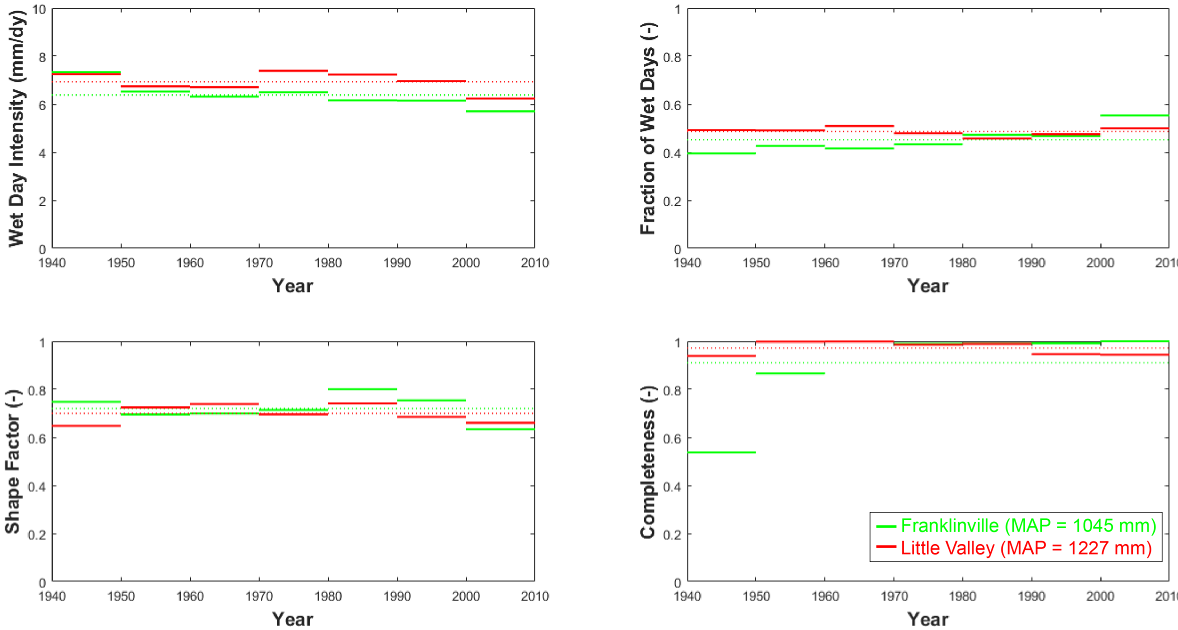

Figure 5.2: Time-varying estimates (10-year intervals) of daily precipitation parameters from the two local GHCN stations (Figure 5.1) which have semi-continuous records since the 1940's. Mean daily precipitation intensity (top left panel), daily precipitation shape factor (bottom left), fraction of wet days (top right panel), and the completeness of the record over each interval (bottom right panel) are shown. Dashed lines show the mean value.

5.3.1 Mean Daily Precipitation Intensity, p_d

Mean daily precipitation intensity (p_d) is estimated using the average value for all non-zero days over a given time interval. For the reference period of 1941–2010, the spatial average of p_d for the five local stations (red symbols in Figure 5.1) is 6.50 mm/day (2σ=0.61), where station records are, on average, 79% complete. At two of these stations, records were long enough to calculate time-varying estimates of p_d (top left panel in Figure 5.2) over 10-yr intervals. There is no trend in p_d (mean value = 6.93 mm/day; 2σ=0.81) at the wetter site (Little Valley). There is weak decreasing trend in p_d (mean value = 6.38 mm/day; 2σ=1.01) at the drier site (Franklinville). The range of values used in the model calibration range from 5 to 12 mm/day and is much larger than the historic range of values.

5.3.2 Precipitation Shape Factor, c

While the stretched exponential distribution performs well in describing the full distribution of events, we follow the lead of *Wilson and Toumi* (2005) and fit the parametric model to only those events larger than the 95th percentile (*Rossi et al.*, 2016). This allows for the distribution to account for apparent heavy-tailed behavior observed in some daily rainfall distributions (*Laherrere and Sornette*, 1998). To estimate c, we linearize equation 5.7 by taking the natural log of both sides twice. This yields a ln-transformed version of equation 5.7 that can be evaluated using least squares regression of empirical exceedance frequencies. The slope of the regression line is an estimate of c. Figure 5.3 shows how well probability

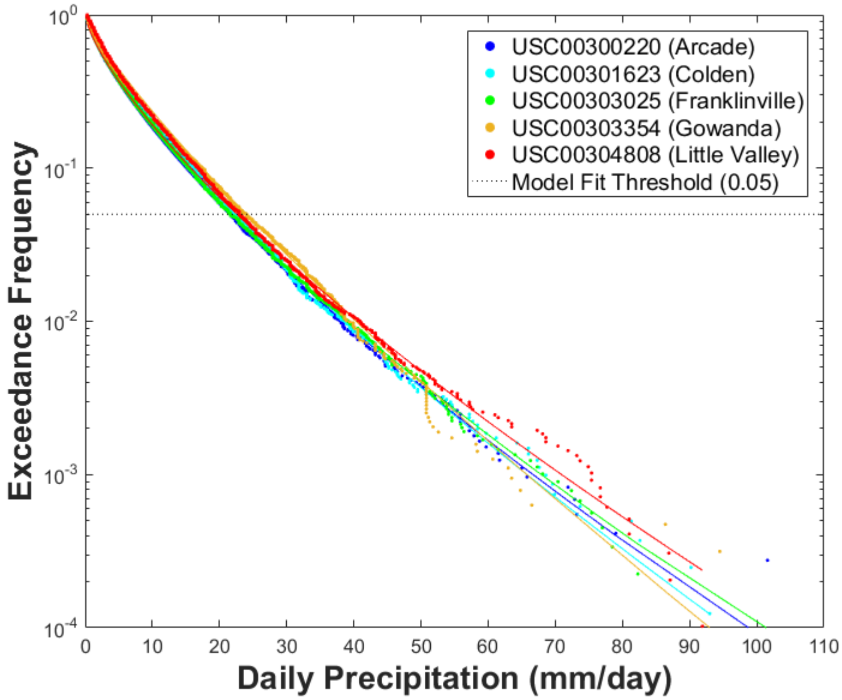

Figure 5.3: Exceedance frequency plot shows empirical data from five local stations (points) along with the associated best-fit, parametric models. Fits are based on least-squares regression of ln-transformed data larger than the 95th percentile (dashed line)

distributions are characterized for the five GHCN stations near Frank's Creek using this approach.

For the reference period of 1941–2010, the spatial average of c for the five local stations (red symbols in Figure 5.1) is 0.77 (2σ=0.03), where station records are, on average, 79% complete. At two of these stations, records were long enough to calculate time-varying estimates of c (bottom left panel in Figure 5.2) over 10-yr intervals. There is no trend in c (mean value = 0.70; 2σ=0.07) at the wetter site (Little Valley). There is also no trend in c (mean value = 0.72; 2σ=0.11) at the drier site (Franklinville). The range of values used in the model calibration range from 0.6 to 0.8 and captures the historic range of values.

5.3.3 Fraction of Wet Days, F

The fraction of wet days (F) is estimated by taking the ratio of all non-zero days against all days for a given time interval. For the reference period of 1941–2010, the spatial average of F for the five local stations (red symbols in Figure 5.1) is 0.46 (2σ=0.04), where station records are, on average, 79% complete. At two of these stations, records were long enough to calculate time-varying estimates of F (top right panel in Figure 5.2) over 10-yr intervals. There is no trend in F (mean value = 0.49; 2σ=0.04) at the wetter site (Little Valley). There is weak increasing trend in F (mean value = 0.45; 2σ=0.11) at the drier site (Franklinville). The range of values used in the model calibration range from 0.2 to 0.6 and is much larger than the historic range of values.

5.3.4 Comparison of Meteorological Station to Gridded Precipitation

Because climate futures will be based on gridded precipitation data (*Abatzoglou*, 2013), we also compared estimates of precipitation parameters from meteorological stations with the corresponding precipitation parameters derived from the gridded data product, GRIDMET (*Abatzoglou and Brown*, 2012). This 4-km spatial resolution, daily temporal resolution, historic data product is based on high spatial resolution PRISM data (*Daly et al.*, 2008) and high temporal resolution regional reanalysis data for the contiguous U.S. (*Abatzoglou and Brown*, 2012). Using a reference period of 1981–2010 (30-yr overlapping time period between GRIDMET and GHCN daily data), we compared precipitation statistics derived from gridded data with those derived from meteorological station data that had near continuous coverage over the reference period (i.e., >95% complete). The 19 locations that met this criterion included the yellow stations in Figure 5.1a and the nearby Little Valley and Franklinville stations shown in Figure 5.1b. GRIDMET data includes a higher fraction of very low daily values as compared to the GHCN daily data. We found that by ignoring values below 0.8 mm/day in GRIDMET, we were able to better match estimates of both p_d and F among GRIDMET and GHCN daily data.

5.4 Basin Hydrology Parameters

Several of the EMS models require parameters that represent aspects of drainage basin hydrology. Models that use a stochastic representation of precipitation also include a mean soil infiltration capacity parameter, I_m, which represents the rate at which precipitation can infiltrate into the soil. This parameter appears in the equation for the rate of runoff generation, r:

$$r = p - I_m(1 - e^{-p/I_m})\,. \tag{5.9}$$

Non-stochastic models that use variable source-area hydrology require specification of soil saturated hydraulic conductivity, K_{sat}, effective recharge rate, R_m, and soil thickness, H_{init} (unless soil thickness is explicitly tracked, in which case the current value at a given grid cell is used). These three parameters appear in the definition of effective drainage area, A_{eff},

$$A_{eff} = Ae^{-K_{sat}H_{init}\Delta x S/R_m A}, \tag{5.10}$$

where A is drainage area, S is local topographic gradient, and Δx is flow width (in this case, grid cell width). It is important to recognize that the three parameters K_{sat}, H_{init}, and R_m can be combined to form a single, lumped parameter (called α; see Appendix A.2.3). However, they are broken out for purposes of sensitivity analysis in order to examine their individual roles. One EMS model, BasicStVs, combines stochastic precipitation with variable source area hydrology. In this model, the actual precipitation rate is used in place of R_m. Collectively, the basin hydrology parameters that require specification of ranges are: I_m, K_{sat}, and R_m (the soil-thickness parameter H_{init} has already been covered in Section 5.2.6).

5.4.1 Soil Infiltration Capacity, I_m

The soil infiltration capacity represents the maximum sustained rate at which rainfall can infiltrate into the soil without generating surface runoff. It is equivalent to the saturated hydraulic conductivity of surface soil, with the caveat that use of daily precipitation in stochastic-precipitation models means that the infiltration capacity parameter represents an *effective* value: the maximum infiltration rate averaged over a day and over the area of the watershed in question. For purposes of sensitivity analysis and calibration, ranges for this parameter are based on infiltrometer measurements on various materials at the site performed by the Erosion Working Group (*Bennett*, 2017).

The Erosion Working Group conducted 37 infiltration-rate measurements at three field locations within the site area (*Bennett*, 2017). Infiltration rates ranged widely, from 0.5 ± 0.9 mm/hr on the finest-grained, most consolidated sediment, to 852.7 ± 59.6 mm/hr on the coarsest-grained, least consolidated material. The ensemble average among all measured infiltration rates was 32.8 ± 59.1 mm/hr. The range measured at the West Valley site is broadly consistent with measured infiltration rates for glacial till in other locations, with reported ranges spanning ∼0.004 to ∼200 mm/hr (∼0.4 mm/hr from *Strobel* (1993); ∼0.04–40 mm/hr from *Mohanty et al.* (1994); and ∼2–200 mm/hr from *Ronayne et al.* (2012)).

Based on the in-situ measurements obtained at the West Valley site, the range assigned to I_m for use in sensitivity analysis is 0.5–830 mm/hr. The equivalent values in meters per year (the units reported in Table 5.2 and used in erosion-model input files) are 4.28 and 7280, respectively.

5.4.2 Recharge Rate, R_m

Non-stochastic models that include variable source-area hydrology include a recharge rate parameter, R_m (equation 5.10). This parameter represents a time-averaged rate of water infiltration, and it controls the potential for water flow in the subsurface: the bigger the recharge rate, the less the capacity for subsurface flow and the more overland flow. Recharge rate can be considered part of a lumped parameter, α, defined as

$$\alpha = K_{sat} H_{init} \Delta x / R_m, \tag{5.11}$$

which has dimensions of length squared and can be thought of as a "saturation area scale." Nonetheless, the elements of α are entered as separate parameters in the relevant EMS models, and ranges are given for each (except Δx, which is model grid cell width).

To calculate the saturation area scale, it is useful to consider published estimates of recharge rates through glacial till. Two studies that are relevant are those of *Daniels et al.* (1991), who reported a range of recharge rates from 0.035 to 0.051 m/yr, and *Bauer and Mastin* (1997), who reported 0.04 to 0.19 m/yr. These rates represent recharge into an aquifer: water that has infiltrated below the root zone, and escaped transpiration losses. Flow through the shallow subsurface is presumably generally larger than aquifer recharge, because some water in the shallow subsurface will be picked up by transpiration or contribute to stream flow before without reaching an aquifer. For this reason, one can consider the lower end of groundwater recharge estimates for glacial sediments to place an approximate minimum bound on shallow subsurface flow.

The mean annual precipitation, which at the West Valley site is about 1 m/yr, provides an upper limit to shallow subsurface recharge. Using the low end of the recharge studies listed above as a lower bound, and the local mean annual precipitation at the West Valley site as an upper bound, the range of R_m used in sensitivity analysis is 0.03 m/yr to 1 m/yr.

5.4.3 Saturated Hydraulic Conductivity, K_{sat}

The hydraulic conductivity of soils, K_{sat}, is used to calculate shallow subsurface flow capacity in models that use variable source area hydrology. Ranges for this parameter are based on two sources: data from the United States Department of Agriculture (USDA) Natural Resources Conservation Service (NRCS) gSSURGO database for soils that are found within the Franks Creek drainage basin (*Soil Survey Staff*, 2017), and measurements of infiltration capacity for glacial till reported by *Mohanty et al.* (1994). The gSSURGO database includes representative K_{sat} measurements over 160 soil units. Taking the 10th and 90th percentiles of these data, the representative K_{sat} ranges from 7×10^{-4} mm/s to 10^{-2} mm/s. Measurements reported by *Mohanty et al.* (1994) range from 10^{-6} to 10^{-2} mm/s, which spans the gSSURGO data but has a smaller lower end. Using the larger of these ranges, the upper and lower values applied in sensitivity analysis are 10^{-6} mm/s (0.032 m/y) and 10^{-2} mm/s (316 m/y), respectively.

5.5 Fluvial Process Parameters

We use the term "fluvial processes" to refer to the processes by which sediment and rock are detached from the bed of a stream or gully, transported down the channel, and (possibly) deposited. Our models combine these processes, or simplified representations of them, to describe changes in elevation of the channel bed through time. The Erosion Modeling Suite uses two overarching types of fluvial erosion models, each of which may have several different parameterizations. The two basic model types are:

1. The stream power/shear-stress family of models. In these models, changes in river bed elevation through time $\partial\eta/\partial t$ are driven by water quantity and channel slope, under the assumption that the water energy slope is approximately equivalent to the channel bed slope. The basic form of these models is:

$$\frac{\partial \eta}{\partial t} = -\left(\omega - \omega_c\left(1 - e^{\omega/\omega_c}\right)\right), \tag{5.12}$$

   where the erosion-rate term ω is a function of either drainage area, A,

$$\omega = KA^m S^n, \tag{5.13}$$

   or water discharge, Q,

$$\omega = K_q Q^m S^n. \tag{5.14}$$

   In equations 5.12–5.14, the change in channel bed elevation with time is calculated from the upstream drainage area (A) or discharge (Q), the channel bed slope S, and a constant (K or K_q) describing the erodibility of the channel bed. ω_c represents an erosion threshold that must be exceeded in order for significant bed lowering to occur. Equation 5.12 describes only bed erosion, not aggradation, and therefore holds only when $\partial\eta/\partial t \leq 0$. As discussed in Appendix A, the Erosion Modeling Suite uses several different forms of Equation 5.12 which require different parameters. The different models are listed below.

(a) Basic stream power ($m = 0.5$, $n = 1$, $\omega_c = 0$).

(b) Stream power with variable area exponent m ($n = 1$, $\omega_c = 0$).

(c) Threshold stream power ($m = 0.5$, $n = 1$, $\omega_c \neq 0$).

(d) Shear stress ($m = 1/3$, $n = 2/3$, $\omega_c = 0$).

(e) Incision-depth-dependent threshold ($m = 0.5$, $n = 1$, $\omega_c \neq 0$).

(f) Stochastic hydrology (Q calculated by hydrological model components, $n = 1$).

(g) Stochastic-threshold (Q calculated by hydrological model components, $n = 1$, $\omega_c \neq 0$).

(h) Variable source area hydrology as described in Equation 5.10, with $m = 0.5$ and $n = 1$, both with and without an erosion threshold.

(i) Basic stream power with different erodibility parameters (K) for areas overlying bedrock and areas overlying glacial till deposits, both with and without an erosion threshold.

(j) Shear stress with an incision-depth-dependent threshold ($m = 1/3$, $n = 2/3$, $\omega_c \neq 0$).

(k) Shear stress with stochastic hydrology (Q calculated by hydrological model components, $m = 1/3$, $n = 2/3$).

(l) Shear stress with variable source area hydrology as described in Equation 5.10, with $m = 1/3$ and $n = 2/3$.

(m) Shear stress with different erodibility parameters (K) for areas overlying bedrock and areas overlying glacial till deposits.

(n) Stochastic hydrology (Q calculated by hydrological model components, $n = 1$) with an incision-depth-dependent erosion threshold.

(o) Variable source area hydrology as described in Equation 5.10, with $m = 0.5$ and $n = 1$, with an incision-depth-dependent erosion threshold.

(p) Basic stream power with different erodibility parameters (K) for areas overlying bedrock and areas overlying glacial till deposits, with an incision-depth-dependent erosion threshold.

(q) Variable source area hydrology as described in Equation 5.10 with stochastic hydrological inputs, $m = 0.5$ and $n = 1$.

(r) Variable source area hydrology as described in Equation 5.10, with $m = 0.5$ and $n = 1$, and different erodibility parameters (K) for areas overlying bedrock and areas overlying glacial till deposits.

The mathematical formulations for these various options are discussion in Appendix A.

2. The entrainment-deposition model. In the entrainment-deposition model, changes in bed elevation are the sum of bed erosion by sediment entrainment E_s and bedrock erosion E_r, and bed aggradation by sediment deposition D_s:

$$\frac{\partial \eta}{\partial t} = \frac{D_s - E_s}{1 - \phi} - (1 - F_f) E_r. \tag{5.15}$$

In Equation 5.15, ϕ is sediment porosity and F_f is the fraction of bedrock eroded that may be considered "wash load". All wash load is assumed to pass out of the model domain. Sediment entrainment is governed by upstream drainage area and channel bed slope such that

$$E_s = \left(K_s A^m S^n - \omega_{cs}\left(1 - e^{-\omega/\omega_{cs}}\right)\right)\left(1 - e^{-H/H_*}\right) \tag{5.16}$$

where K_s is the sediment erodibility constant, ω_{cs} is the erosion threshold for sediment, H is the thickness of sediment on the channel bed, and H_* is the bedrock roughness length scale. As such, sediment entrainment depends on the availability of sediment on the channel bed. (Note that stochastic-precipitation models use water discharge Q in place of drainage area A.) Similarly, bedrock erosion is:

$$E_r = \left(K_r A^m S^n - \omega_{cr}\left(1 - e^{-\omega/\omega_{cr}}\right)\right) e^{-H/H_*}, \tag{5.17}$$

where K_r is the bedrock erodibility constant and ω_{cr} is the erosion threshold for bedrock (and again, some models use Q in place of A). Sediment deposition is a function of sediment settling velocity V and the ratio of volumetric sediment flux to volumetric water discharge Q_s/Q:

$$D_s = V\frac{Q_s}{Q}. \tag{5.18}$$

The Erosion Modeling Suite includes erosion-deposition models to address both the bedrock-alluvial case as described above, as well as the simpler, sediment-only case. In the case of river erosion into sediment, Equation 5.15 simplifies considerably to:

$$\frac{\partial \eta}{\partial t} = \frac{D_s - E_s(1 - F_f)}{1 - \phi}. \tag{5.19}$$

where F_f is the fraction of entrained sediment that becomes wash load. The sediment-only case was developed by *Davy and Lague* (2009), and the coupled sediment and bedrock case was developed by *Shobe et al.* (2017). The Erosion Modeling Suite uses several different forms of the entrainment-deposition model, which require different parameters. Those different models are listed below.

(a) Entrainment-deposition with sediment only ($m = 0.5$, $n = 1$, $\omega_{cs} = 0$).

(b) Entrainment-deposition with an erosion threshold ($\omega_{cs} \neq 0$).

(c) Entrainment-deposition with shear-stress-based sediment entrainment ($m = 1/3$, $n = 2/3$).

(d) Entrainment-deposition with an incision-depth-dependent erosion threshold ($\omega_{cs} \neq 0$).

(e) Entrainment-deposition with fine sediment ($F_{fs} \neq 0$).

(f) Entrainment-deposition with stochastic precipitation and discharge.

(g) Entrainment-deposition with variable source area hydrology as described in Equation 5.10.

(h) Entrainment-deposition with bedrock (Equation 5.15).

(i) Entrainment-deposition with different erodibility parameters (K) for areas overlying bedrock and areas overlying glacial till deposits.

Between the stream power and entrainment-deposition models described above, the following require specified ranges: the family of substrate erodibility parameters (e.g., K), the family of erosion thresholds (e.g., ω_c), parameters governing the incision-depth-dependent erosion threshold, the fraction of wash load when material is entrained from bedrock (F_f), sediment porosity ϕ, and sediment settling velocity V (or its dimensionless equivalent V_c). The following subsections describe the ranges identified for use in sensitivity analysis and model calibration, and the rationale for choosing them.

5.5.1 Simple Stream Power Erosion Coefficient, K

The erosion coefficient K encompasses several influences on erosion, including material properties, hydrology, and channel geometry. K is set in part by rock properties such as tensile strength, and fracture density at the sub-meter to meter scale. K also incorporates the effects of precipitation rate, runoff efficiency, and discharge variability. K may also subsume constants from empirical scaling relationships that are built into the stream power model. For example, all of the Erosion Modeling Suite models assume that channel width scales with volumetric water discharge, and that the coefficient governing that scaling relationship is incorporated into K.

Several studies have attempted to use comparisons between numerical models and real landscapes to invert for K, and we have used these results to set the bounds on K. Because the specific parameterization of the stream power model determines the units of K, we have used a reference slope and drainage area to convert published K values to common dimensions $[y^{-1}]$. We use a minimum K of 1×10^{-6} and a maximum of 1×10^{-1}.

5.5.2 Till Erosion Coefficient, K_1

Till has the potential to be more erodible than bedrock (i.e., higher erosion coefficient). For till, we use the same range of erosion coefficients as in the simple stream power model. We use a minimum K_1 of 1×10^{-6} and a maximum of 1×10^{-1}.

5.5.3 Rock Erosion Coefficient, K_2

Rock has the potential to be less erodible than till (i.e., lower erosion coefficient). We use a range that is two orders of magnitude lower than the ranges for K and K_1, under the rationale that bedrock alone will be substantially less erodible than the mix of rock and till represented by the single value of K in the simple stream power model. We use a minimum K_2 of 1×10^{-8} and a maximum of 1×10^{-3}.

5.5.4 Discharge-Based Stream Power Erosion Coefficient, K_q

Using a discharge-based stream power erosion model results in an erosion coefficient K_q with different units and a somewhat different physical meaning than the simple stream power erosion coefficient K. K_q does not incorporate precipitation, runoff, or flow variability, as discharge is explicitly calculated by a stochastic discharge model. However, K_q still incorporates the rock and sediment properties and local flow conditions discussed above for K. The units of K_q are $[m^{-1/2}y^{-1/2}]$.

We obtained a range of K_q by converting from the basic stream power erosion coefficient K using the equation $K_q = \frac{K}{R^{1/2}}$ where R is annual runoff in meters per year. We used a range for R of 0.1016–2.032 m/yr. We therefore derived a minimum K_q of 7.03×10^{-7} and a maximum of 3.14×10^{-1}.

5.5.5 Shear-Stress Erosion Coefficient, K_{ss}

Using a shear-stress erosion model requires specification of an erosion coefficient K_{ss}, which has different units than the simple stream power erosion coefficient K. We converted values of K to K_{ss} by the equation:

$$K_{ss} = KA^{1/6}S^{1/3}, \tag{5.20}$$

where A and S are reference values of drainage area and slope, respectively. To derive a range for K_{ss}, we used two reference area values (10^6 and 10^7 m^2) and two reference slope values (0.01 and 0.1). Given the range of K described above, this calculation yields a range for K_{ss} of 2.14×10^{-6} to 6.81×10^{-1} $m^{1/3}y^{-1}$.

5.5.6 Shear-Stress Erosion Coefficient for Till, K_{ss1}

For till, we use the same range of erosion coefficients as in the shear stress model for uniform lithology. We use a minimum K_{ss} of 2.14×10^{-6} and a maximum of 6.81×10^{-1} $m^{1/3}y^{-1}$.

5.5.7 Shear-Stress Erosion Coefficient for Rock, K_{ss2}

We use a range that is two orders of magnitude lower than the ranges for K_{ss} and K_{ss1}, under the rationale that bedrock alone may be less erodible than the mix of rock and till represented by the single value of K_{ss} in the simple one-lithology model. We use a minimum K_{ss2} of 2.14×10^{-8} and a maximum of 6.76×10^{-3} $m^{1/3}y^{-1}$.

5.5.8 Stream Power Alluvium Entrainment Coefficient, K_s

In the entrainment-deposition models, sediment entrainment is treated separately from bedrock erosion. We expect that sediment in the study site is generally more erodible than bedrock, and thereby warrants higher values for the erosion/entrainment coefficient. We use a range of 1×10^{-2} to 1 y^{-1}.

5.5.9 Discharge-Based Alluvium Entrainment Coefficient, K_{qs}

Using a discharge-based erosion-deposition model results in an entrainment coefficient K_{qs} with different units and a different physical meaning than the simple entrainment-deposition coefficient K_s. K_{qs} does not incorporate the effects of flow variability, as discharge is explicitly calculated by a stochastic discharge model. However, K_{qs} still incorporates sediment properties and local flow conditions. The units of K_{qs} are $[m^{-1/2}y^{-1/2}]$.

We obtained a range of K_{qs} by converting from the basic entrainment-deposition coefficient K_s using the equation $K_{qs} = K_s/R^{1/2}$, where R is annual runoff in meters per year. We used a range for R of 0.1016–2.032 m/yr. We therefore derived a minimum K_q of 7.02×10^{-3} and a maximum of 3.14 $m^{-1/2}y^{-1/2}$.

5.5.10 Shear Stress Alluvium Entrainment Coefficient, $K_{s,ss}$

Using a shear-stress-based erosion-deposition model requires specification of an erosion coefficient $K_{s,ss}$, with different units than the simple erosion-deposition entrainment coefficient K_s. We converted values of K_s to $K_{s,ss}$ by the equation:

$$K_{s,ss} = K_s A^{1/6} S^{1/3}, \tag{5.21}$$

where A and S are reference values of drainage area and slope, respectively. To derive a range for $K_{s,ss}$, we used two reference area values (10^6 and 10^7 m^2) and two reference slope values (0.01 and 0.1). Given the range of K_s described above, this calculation yields a range for $K_{s,ss}$ of 2.14×10^{-2} to 6.81 $m^{1/3}y^{-1}$.

5.5.11 Drainage Area Exponent, m

The drainage area exponent m governs the importance of drainage area to channel bed erosion. A review by *Tucker and Whipple* (2002) suggests using a range from 0 to 1. We have adopted this range.

5.5.12 Erosion Threshold, ω_c

For models that do not explicitly account for rock/till layers, we use a range of channel erosion thresholds bounded by those found for rock and till (see below). This range of ω_c values has a minimum of 1×10^{-6} and a maximum of 1×10^{3} my^{-1}.

5.5.13 Erosion Threshold for Rock, ω_{c2}

The erosion threshold for bedrock should be at least as large as the threshold for motion of the median grain size (D_{50}), the erosion threshold for till (see below), and possibly larger. We use as a lower limit on the range of ω_{c2} the threshold value for till, 1×10^{-6} my^{-1}. As an upper limit, we use twice the threshold for motion of the D_{50}, 1×10^{3} my^{-1}.

5.5.14 Erosion Threshold for Till, ω_{c1}

To obtain a lower bound on the critical shear stress for till, we assume that ω_{c1} must be at least as high as the threshold needed to mobilize particles. The critical shear stress, τ_c, for entraining particles of median diameter D_{50} can be found from the Shields equation:

$$\tau_c = \theta_c(\sigma - \rho)gD_{50}. \tag{5.22}$$

Buffington and Montgomery (1997) found a lower limit of the critical Shields stress θ_c to be 0.03, agreeing with other studies. We use 0.08 as an upper limit to θ_c, again based on experimental data reviewed by *Buffington and Montgomery* (1997). Using this range for critical Shields stress, with sediment density σ = 2650 kg/m3 and D_{50} = 5 cm (*Bennett*, 2017) gives a range for critical shear stress of 24–64 Pa.

On-site field measurements using the Scour Depth method show a range of critical shear stress from 12 to 90 Pa. Therefore, we recommend using a range of 5 to 100 Pa to account for uncertainty in the estimate of D_{50}. We can convert the critical shear stress to critical stream power ω_{c1} for use in the stream power model:

$$\omega_{c1} = \tau_c U_{*c} = \tau_c^{3/2}/\rho^{1/2} = 0.031623\tau_c^{3/2}, \tag{5.23}$$

where ρ is fluid (water) density, and $U_{*c} = \sqrt{\tau_c/\rho}$. Using the values reported above, we obtain a range of $\omega_c = 0.35$ to $31.62\ my^{-1}$. However, we choose to expand our parameter range beyond that derived from field measurements to take into account the possibility that variations in till composition, bed roughness, and sediment grain size may alter ω_{c1}. We use a range of 1×10^{-6} to $1 \times 10^{3}\ my^{-1}$.

5.5.15 Rock-Till Contact Zone Width, W_c

The width of the contact zone between the rock and till layers is a parameter used to promote a smooth transition from one unit to the next, both to avoid numerical artifacts in the models and to honor the likelihood that the actual contact zone is rough and/or gradational. It turns out not to be a very influential parameter. We set the range W_c to 1–3 m.

5.5.16 Initial Erosion Threshold, ω_{c0}

Models in which the erosion threshold increases with progressive incision depth require specification of the initial threshold value. This is the value of the threshold before any incision has taken place. The same range is used for this parameter as for the threshold parameter ω_c in the fixed-threshold models.

5.5.17 Rate of Threshold Change with Depth, b

Gran et al. (2013) showed that the median grain size D_{50} can increase with increasing incision depth as the channel incises through glacial sediments and terraces. We therefore used the same rate of threshold change with incision depth for all substrates. The minimum is 0 (no change in threshold with depth) and the maximum of 20 y^{-1}.

5.5.18 Sediment Porosity, ϕ

Sediment porosity can range between two theoretical end-members. $\phi = 0$ occurs when all space in the sediment is taken up by rock mass and none by void space, and $\phi = 1$ when there is no sediment and all void space. All natural sediment beds fall between these two end-members, and we use the full range of 0 to 1.

5.5.19 Fraction of Fine Sediment in Eroded Material, F_f

The fraction of fine sediment can range from 0 to 1. $F_f = 0$ describes well-jointed bedrock or large gravels that release no fine sediment into permanent suspension. $F_f = 1$ describes erosion of completely fine-grained deposits such as loess, in which all particles may enter permanent suspension. We use the full range of 0 to 1.

5.5.20 Depth Scale for Bedrock Erosion under Alluvium, H_*

H_* is the characteristic depth of alluvial scour relevant for bedrock incision, which determines how much erosion can happen beneath a given thickness of sediment. The lower limit should be approximately the median grain size D_{50}, which is approximately 5 cm for the field site (*Bennett*, 2017). The upper limit should be approximately the characteristic flood depth, which is assumed to be on the order of 1 m. Therefore use a range for H_* of 0.05–1 m is used.

5.5.21 Sediment Deposition Coefficients, V and V_c

The deposition-rate coefficient is likely to be lower than still-water settling velocity of sediment in transport due to upward-directed turbulent forces in natural streams. A value of 0.001 m/y is used as a lower range for V, representing a system with very fine grained suspended sediment. An upper limit of 1 m/yr is used. Although this upper limit is low from the standpoint of an instantaneous clear-water settling velocity, it is here interpreted as a rough upper estimate of the maximum sustained channel sedimentation rate that one might expect for the Site (for example, where a stream enters a ponded body of water).

Models that use drainage area employ a normalized version of this parameter, defined as $V_c = V/\mathcal{R}$, where $\mathcal{R}$ is an effective runoff rate. Using a range of effective runoff rate from 0.1 to 2 m/yr yields a corresponding range of V_c from 0.0005 to 10.

Table 5.1: Parameters in the EMS Models.

Symbol	Description	Units	Models
b	rate of threshold change with depth	y^{-1}	Dd
c	precipitation distribution shape factor	-	St
D	soil creep coefficient	m^2y^{-1}	all
f	paleoclimate variation factor	-	Cc
F_f	fraction fines in eroded material	-	Hy
F	intermittency factor	-	St
H_*	depth scale for bedrock erosion under alluvium	m	Hy
H_0	soil transport depth scale	m	Sa
H_{init}	initial soil thickness	m	Sa
H_s	soil production depth scale	m	Sa
I_m	soil infiltration capacity	my^{-1}	St
K	simple stream power erosion coefficient	y^{-1}	all but Rt, Ss, St
K_1	till erosion coefficient	y^{-1}	Rt
K_2	rock erosion coefficient	y^{-1}	Rt
K_q	coefficient in discharge-based stream-power law	$m^{-1/2}y^{-1/2}$	St
$K_{q,ss}$	coefficient in discharge-based shear-stress law	$y^{-2/3}$	St
K_s	alluvium entrainment coefficient	y^{-1}	Hy (not HySt)
K_{ss}	shear-stress erosion coefficient	$m^{1/3}y^{-1}$	Ss
K_{ss1}	shear-stress coefficient for till	$m^{1/3}y^{-1}$	SsRt
K_{ss2}	shear-stress coefficient for rock	$m^{1/3}y^{-1}$	SsRt
K_{sat}	saturated hydraulic conductivity	my^{-1}	Vs
m	drainage area exponent	-	Vm
n	slope exponent	-	Vm
n_{ts}	number of sub-timesteps	-	St
p_d	mean daily precipitation rate	my^{-1}	St
P_0	maximum soil production rate	my^{-1}	Sa
R_m	recharge rate	my^{-1}	Vs
S_c	critical slope gradient	-	Ch
S_r	random seed	-, integer	St
T_s	climate constant date	y	Cc
V_c	sediment deposition coefficient	-	Hy
V	sediment deposition coefficient	my^{-1}	HySa
W_c	contact-zone width	m	Rt
ϕ	porosity	-	Hy
ω_c	erosion threshold	my^{-1}	Th
ω_{c1}	till erosion threshold	my^{-1}	RtTh
ω_{c2}	rock erosion threshold	my^{-1}	RtTh

Table 5.2: Parameter ranges used in sensitivity analysis.

Parameter	Units	Lower bound	Upper bound
b	y^{-1}	0.0	20.0
c	-	0.6	0.8
D	$m^2 y^{-1}$	5×10^{-7}	0.05
f	-	0.5	1.5
F_f	-	0.0	1.0
F	-	0.2	0.6
H_*	m	0.05	1.0
H_0	m	0.1	1.0
H_{init}	m	0.305	1.52
H_s	m	0.2	0.7
I_m	my^{-1}	4.28	7280
K	y^{-1}	10^{-6}	10^{-1}
K_1	y^{-1}	10^{-6}	10^{-1}
K_2	y^{-1}	10^{-8}	10^{-3}
K_q	$m^{-1/2} y^{-1/2}$	7.03×10^{-07}	3.41×10^{-1}
$K_{q,ss}$	$y^{-2/3}$	1.51×10^{-6}	2.14
K_s	y^{-1}	10^{-2}	10^{-0}
K_{ss}	$m^{1/3} y^{-1}$	2.14×10^{-6}	6.81×10^{-1}
K_{ss1}	$m^{1/3} y^{-1}$	2.14×10^{-6}	6.81×10^{-1}
K_{ss2}	$m^{1/3} y^{-1}$	2.14×10^{-8}	6.76×10^{-3}
K_{sat}	my^{-1}	0.03	300
m	-	0.0	1.0
n_{ts}	integer	1	20
p_d	my^{-1}	1.83	4.38
P_0	my^{-1}	10^{-6}	10^{-3}
R_m	my^{-1}	0.03	1.0
S_c	-	0.1	1.25
S_r	integer	-	-
V	my^{-1}	10^{-3}	10^{0}
V_c	-	4.90×10^{-4}	9.84
W_c	m	1.0	3.0
ϕ	-	0.0	1.0
ω_c	my^{-1}	10^{-6}	10^{3}
ω_{c1}	my^{-1}	10^{-6}	10^{3}
ω_{c2}	my^{-1}	10^{-6}	10^{3}

Table 5.3: Published estimates for hillslope diffusivity coefficient.

Source	D ($\mathbf{m^2\ y^{-1}}$)	**Location**
Nash 1980a	0.012	Emmet County, Michigan
Nash 1984	0.002	West Yellowstone, Montana
Nivière B 2000	0.0014	Upper Rhine Graben, Central Europe
Nivière B 1998	0.0015	Near Basel, Switzerland
Putkonen and O'Neal 2006	0.0005	Chillicothe, Ohio
Oehm 2005	0.0021	Switzerland
Oehm 2005	0.0031	Switzerland
Oehm 2005	0.0047	Switzerland
Oehm 2005	0.0003	Switzerland
Oehm 2005	0.0036	Japan
Oehm 2005	0.0093	Japan
Oehm 2005	0.0135	Japan
Oehm 2005	0.0059	Japan
Arrowsmith et al., 1998	0.0086	Carrizo Plain, California
Avouac and Peltzer, 1993	0.008	Hotan Region, Xinjiang, China
Callaghan, 2012	0.0002–0.0212	Chile
Carretier et al., 2002	0.0033	Mongolia
Hanks, 2000	0.001	Lost River, Idaho
Hughes et al., 2009	0.0088	Charwell Basin, New Zealand
Jungers et al., 2009	0.0331	Great Smoky Mountains, North Carolina
Perron et al., 2012	0.01	Allegheny Plateau, Pennsylvania
Perron et al., 2012	0.0124	Gabilan Mesa, California
Pierce and Colman, 1986	0.0021	Big Lost River Valley, Idaho
Reneau and Dietrich, 1991	0.0051	Southern Coast Range, Oregon
Reneau et al., 1989	0.0047	Clearwater River, Washington
Riggins et al., 2011	0.0394	Bodmin Moor, Cornwall, UK
Roering et al., 1999	0.0036	Sullivan Creek, Oregon
West et al., 2014	0.0067	Shale Hills, Pennsylvania
Richardson et al., 2015	0.0019	Great Smokey Mountains, North Carolina

Table 5.4: Published estimates of maximum soil production rate

Source	P_0 [m/yr]	Location
Heimsath et al. (2001a)	0.000268	Oregon Coast Range
Heimsath et al. (1997, 1999)	0.000077	Tennessee Valley, California
Heimsath et al. (2001b)	0.000143	Australia
Heimsath et al. (2012)	0.001	San Gabriel Mountains, California
Small et al. (1997, 1999)	0.000007	Western US

Chapter 6

Metrics for Model-Data Comparison

6.1 Introduction

In order to calibrate the erosion models to the Site, as well as to perform sensitivity analysis and validation, we require a method to compare observed and simulated topography. This chapter describes the metrics that are used for model-data comparison.

We began by testing a set of statistical metrics derived from the digital terrain data. These included a group of metrics that have been previously used in comparisons of observed and modeled topography. For example, in a comparison of simulated landforms with terrain produced in a scaled laboratory experiment, *Hancock and Willgoose* (2001) used the hypsometric curve, width function, cumulative area distribution, and area-slope relationship as evaluation metrics. *Howard and Tierney* (2012) used statistical moments of elevation, slope, divergence (the Laplacian of elevation), and profile and planform curvature to compare observed and modeled topography.

For comparison between observed and simulated topography in the upper Franks Creek watershed, we tested a set of statistical metrics inspired by the above referenced studies, with some modifications. The test metrics included hypsometry, cumulative area distribution, chi-elevation statistics (an updated form of area-slope statistic, discussed below), and the first two statistical moments of elevation and gradient. Trial calibrations, however, showed that these metrics did not always perform as desired: in certain cases, for example, these metric scores indicated a good model fit when visual inspection showed the model to be relatively poor, and conversely.

As an alternative approach, we developed a method for model evaluation based on direct cell-by-cell comparison of the elevations. What makes such an approach feasible for the West Valley site is the fact that remnants of the post-glacial topography are reasonably well preserved. This preservation allows reconstruction of the watershed paleo-topography, as discussed in Chapter 4. An important source of uncertainty in studies like that of *Howard and Tierney* (2012), where paleo-topography is poorly known, is that it becomes difficult for models to reproduce the observed planform configuration of the drainage networks: the statistical shape may be accurate, but the locations of particular tributaries tend to be sensitive to the initial topography (e.g., *Ijjász-Vásquez et al.*, 1992). It is this problem that motivates the use of statistical metrics. In the case of upper Franks Creek, however, we find that when a post-glacial reconstruction is used as an initial condition, the erosion models generally do a good job of reproducing the major outlines of the modern stream network. Hence, it becomes feasible to test models using a more direct cell-by-cell comparison. We therefore developed an approach that divides the target landscape into a set of patches, and evaluates a given model simulation by measuring the sum-of-squares difference between observed and simulated present-day elevation values.

6.2 Overview of Patch-Based Elevation Metric

The approach involves direct comparison between a digital elevation model of the area of interest, and the simulation of the terrain after 13,000 years of post-glacial landform development. To perform the comparison, the modeled area is first divided into a set of 20 patches. A score is assigned to each patch based on a weighted sum-of-squares difference between observed and modeled grid cell elevations within the patch in question. This score is considered to be one *observation*. An objective function is then defined as the sum-of-squares differences among all 20 individual patch scores. The methods for delineating patches, weighting individual grid cells, and defining the objective function are described in the following.

6.3 Dividing Model Domain into Patches

In order to perform statistical analysis of model calibration results, it is useful to arrange the data such that they form a number of observations that is greater than the number of parameters in any one model, but considerably less than the number of grid cells in the digital elevation model. With the number of grid cells on the order of 10^5, treating each cell as a unique observation would make analyses such as the construction of variance-covariance matrices impractical. On the other hand, having fewer observations than parameters would clearly be undesirable. To surmount this problem, we divided the grid cells in the watershed domain into 20 individual patches, each of which is treated as an individual observation.

We seek to identify landscape patches that represent characteristic landform elements, such as canyons cut in till, bedrock uplands, and so forth. We used a semi-automated method to identify these patches. The cells in the DEM were divided into categories based on two criteria: elevation, and the χ (chi) index value. The χ index is a geomorphic metric that represents an upstream integral of weighted drainage area (*Perron and Royden*, 2013). It is defined as

$$\chi = \int_0^x \left(\frac{A_0}{A(x)} \right)^{m/n} dx. \tag{6.1}$$

The integral is taken in the upstream direction, from a given point starting on a stream profile (considered to be $x = 0$) to a particular streamwise distance x upstream of that point. The drainage area at point x is $A(x)$, and A_0 is a reference drainage area (for our purposes, its value is unimportant). For the exponent m/n we adopt a commonly used value of 0.5.

The χ index is used in our definition of patches because it tends to increase systematically as one moves from main branches of the channel network, up into tributaries, and finally

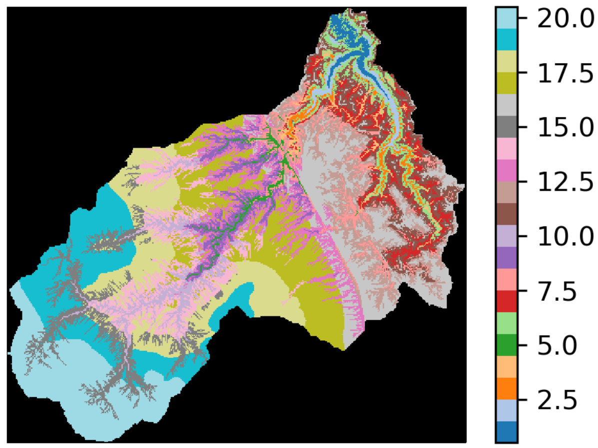

Figure 6.1: Chi-elevation based patches in the upper Franks Creek watershed. Each color represents one patch; patch numbers are listed in the bar at right.

onto hillslopes. In other words, it is sensitive to position within a drainage network, and is therefore useful in delineating different characteristic elements of a drainage basin.

We divided the catchment DEM into five χ index categories based on percentile of the chi value (0–5, 5–20, 20–50, 50–100). Within each of these chi-domains, we divided the domain into four elevation bands, again based on percentile (0–25, 52–50, 50–75, 75–100). A map showing the resulting 20 distinct landscape patches in a digital elevation model of the upper Franks Creek watershed is presented in Figure 6.1. We make patch division based on chi and elevation percentiles in order to construct equivalent metrics in the three different model domains we consider: Upper Franks Creek, Validation Site, Gully Site (Figures 6.1–6.3).

6.4 Scoring Individual Patches

For each patch, a model mis-fit score is calculated as the sum-of-squares difference between observed and modeled elevations in the patch's grid cells. The (squared) mis-fit score P_j for patch j is defined by

$$P_j^2 = \sum_{i=1}^{N_j} w_i \left(\eta_i^{\text{obs}} - \eta_i^{\text{sim}}\right)^2 , \tag{6.2}$$

where η_i^{obs} is the observed elevation at cell i, η_i^{sim} is the simulated elevation at cell i, N_j is the number of grid cells in patch j, and w_i is a weighting factor defined below (equation 6.4).

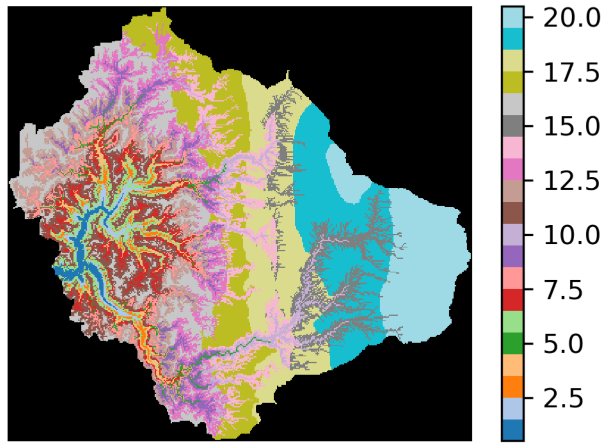

Figure 6.2: Chi-elevation based patches in the Validation watershed. Each color represents one patch; patch numbers are listed in the bar at right.

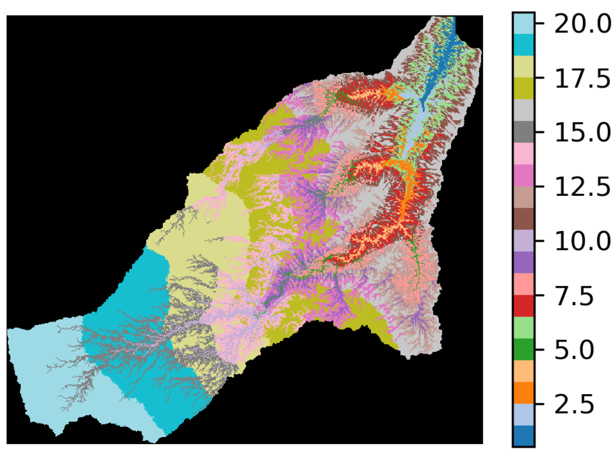

Figure 6.3: Chi-elevation based patches in the Gully watershed. Each color represents one patch; patch numbers are listed in the bar at right.

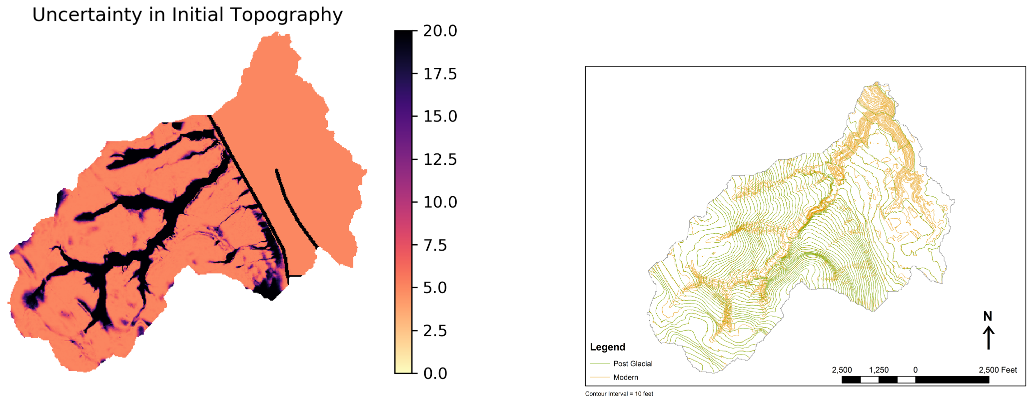

(a) uncertainty map (b) postglacial and modern topography

Figure 6.4: Map of assumed uncertainty in initial post-glacial topography, compared with contour map showing topography past and present. Scale is in feet.

6.5 Definition of the Objective Function

The objective function is defined simply as the sum of the squared patch scores:

$$F_{\text{obj}} = \sum_{j=1}^{M} P_j^2. \tag{6.3}$$

The objective function therefore includes the combined misfits of all 20 patches. The patch scores, P_j^2, themselves are weighted equally, but their individual grid cells take on different weights depending on the size of the patch and an estimate of the uncertainty associated with post-glacial erosion at a particular cell.

The weighting of individual grid cells is designed to acknowledge varying degrees of uncertainty in the modern terrain as a reflection of post-glacial erosion and construction of the postglacial topography. Figure 6.4 shows a map of estimated elevation-change uncertainty, σ (feet), assigned to grid cells in the upper Franks Creek DEM. In the plateau areas of the landscape, geologic evidence suggests that the terrain has not changed very much in terms of elevation relative to a datum in the underlying rock column. Along the lower reaches of streams that cut the plateau surface (such as Franks Creek), the total depth of post-glacial erosion is reasonably well known because the plateau provides a reference surface. Thus, the elevation-change uncertainty associated with these locations is considered to be relatively low. For purposes of grid-cell weighting, we assign an elevation-change uncertainty of 5 feet in these locations (Figure 6.4).

In the upper parts of the Quarry-Franks-Erdman drainage network, above the glacial till plateaus, we lack a geologic marker surface. The incised valleys in these locations might have been carved since the last glacial retreat, or they might have been carved earlier, or some combination of the two. Because we do not know their incision history, these locations have a higher elevation-change uncertainty. For purposes of grid-cell weighting, a value of 20 feet is assigned based on the depth of these features relative to the surrounding hillslopes (Figure 6.4). We also assign a relatively large (20-foot) uncertainty to locations of strong

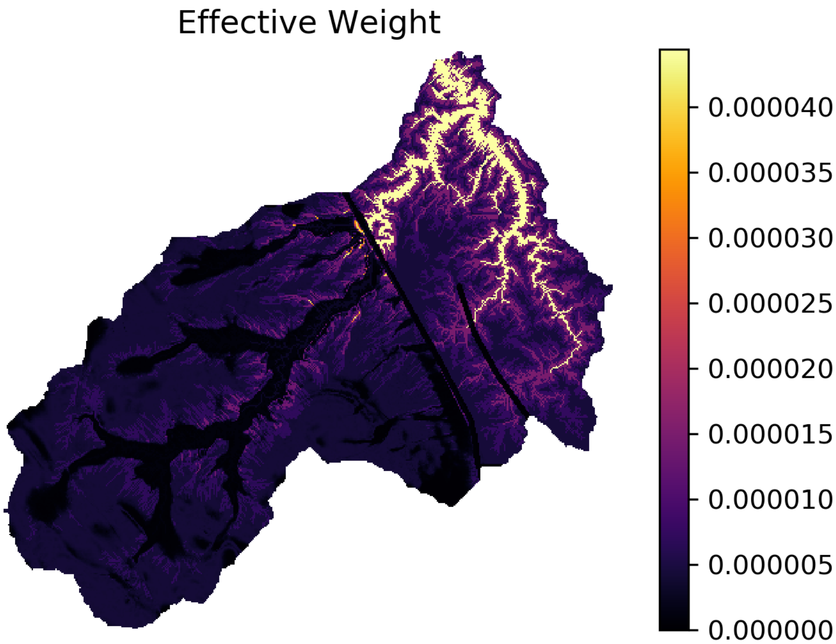

Figure 6.5: Effective weight assigned to grid cells in upper Franks Creek digital elevation model. Weights combine estimated uncertainty in initial topography with number of grid cells in each patch, as discussed in text. Units are ft^{-2}.

anthropogenic modification, including Rock Springs Road and an elevated road-bed within the site premises.

To calculate weight factors for individual grid cells, the elevation-change uncertainty is combined with the total number of grid cells in a particular patch. The weight factor for cell i which belongs in patch j is

$$w_i = \frac{1}{\sigma_i^2 N_j}, \tag{6.4}$$

where σ_i is the elevation-change uncertainty assigned to cell i (feet) and N_j is the total number of grid cells in patch j. Including the number of cells in the patch provides a method for weighting some patches more than others. This allows us to identify certain landscape elements having particular importance to the model calibration, by adjusting the size of the patch in question. For example, patches that contain the lower reaches of Franks Creek, Quarry Creek, and Erdman Brook are considered to be especially important because they reflect rapid post-glacial downcutting in the glacial materials that underlie the site. Terrain features to the southwest of Rock Springs Road carry less importance for purposes of model testing and calibration, and so a larger number of grid cells per patch is used in these areas. The net result is an effective-weight map that emphasizes the incised channels and gullies within the till plateau area (Figure 6.5).

6.6 Discussion

Our metrics are based on direct cell-by-cell comparison, rather than on statistical properties derived from the digital terrain model. As noted above, this approach is made possible by the fact that the map positions of the streams at the Site (Quarry Creek, Franks Creek, and Erdman Brook) appear to have been relatively stable during the post-glacial period.

Use of terrain patches allows us to organize a very large data set (consisting of roughly 100,000 grid cells within the Upper Franks Creek watershed, and a similar number for the validation site) into a manageable number (20) of aggregated observations. This data-organization process simplifies the analysis and calibration procedure while retaining use of all cell elevations within the watershed. The weighting technique makes it possible to emphasize certain key areas of the landscape, notably the till plateaus and (in particular) the stream channels and gullies incised into them.

The elevation-based objective function defined in this chapter is used as the target in model calibration, as described in Chapter 8. The objective function is also used in analyzing model sensitivity to input parameters and initial and boundary conditions (Chapter 7). In addition, a similar metric is defined for the validation watershed and used in model-validation testing, as described in Chapter 9.

Chapter 7

Sensitivity Analysis

7.1 Introduction

Effective use of a computational environmental model requires a sound understanding of the model's behavior and the role of its input parameters in governing that behavior. Sensitivity analysis provides a formalized method for documenting a model's behavior by systematically varying model inputs and measuring the impact of those variations on model output. This chapter describes sensitivity analyses that were conducted on erosion process models in the Erosion Modeling Suite (EMS; Chapter 3). The goals of sensitivity analysis were as follows:

1. as a test of simulated dynamics and to provide a deeper understanding of the behavior of each model by documenting the relative influence of each parameter on model solutions,
2. assess the degree to which alternative reconstructions of post-glacial topography (initial condition topography) influence model behavior,
3. evaluate the degree to which different plausible outlet-lowering histories influence model behavior,
4. identify which parameters are important enough to be included in calibration, and which show sufficiently limited sensitivity that they can be held constant,
5. help guide priorities for future data collection.

To meet these objectives, a systematic sensitivity analysis was conducted, using the Method-of-Morris (MoM) screening method. The analysis was applied to each of the single-element and two-element erosion process models in EMS. The models were run for two drainage basins: the ∼4 km^2 Franks Creek watershed, and a smaller (∼15.4 ha) basin known informally as the Gully Watershed. The analyses were performed by running models forward in time from a reconstructed paleotopography at ∼13 ka to the present, and using a weighted difference of observed and modeled topography as the metric for model behavior (see Chapter 6). In order to evaluate the influence of initial and boundary conditions, the analysis runs used two different reconstructions for geo-historical lowering of the watershed outlet, and several alternative reconstructed initial topographic surfaces (see Chapter 4).

7.2 Methodology

7.2.1 Morris One-at-a-Time (MOAT) Screening

Global sensitivity measures are calculated using the Method of Morris (MoM) (*Morris*, 1991), which is closely related to Elementary Effects (EEj) (*Saltelli et al.*, 2008) and the Latin Hypercube variant One-At-Time (LH-OAT) method of *Van Griensven et al.* (2006). The MoM was designed to screen parameters into three primary categories, those parameters with effects on an outcome that are (a) negligible, (b) linear and additive, and (c) non-linear.

For MoM in a k dimensional input parameter space, the input space is first partitioned into p levels creating a grid of p^k points. From this starting parameter value, MoM makes $k+1$ model evaluations in which only one parameter value changes at a time. This results in number of parameter +1 runs per sequence. The elementary effect for input parameter i, $d_i(x)$ is calculated as

$$d_i(x) = \frac{y(x + \Delta e_i) - y(x)}{\Delta} \,. \tag{7.1}$$

where e_i is the i^{th} coordinate vector, $y(x)$ represents the evaluation of the model at base parameter set x, and Δ is the step size. Dakota implements MoM with Δ calculated as

$$\Delta = \frac{p}{2(p-1)} \tag{7.2}$$

for an input parameter range scaled to $[0,1]$ such that Δ represents a step size of a bit less than 1/2 the parameter range. In each sequence, a parameter value only changes once and thus the sequence of model runs forms what can be thought of as a stair-case pattern in multi-dimensional parameter space.

In a MoM study, a set of r independent sequences are evaluated. *Morris* (1991) and *Saltelli et al.* (2004) recommend using a value of four to ten for r, and we used $r = 10$. This results in $r(k+1)$ model evaluations used to construct r elementary effects for each of k input parameters. These sequences are generated randomly, and thus we set the random seed as a parameter so that the results are fully reproducible.

As discussed by *Saltelli et al.* (2004, pg. 102), the selection of appropriate values for p is an open problem. Considering a large value for p results in a large number of levels, many of which are not explored if the value for r is also not large. However, for parameter input spaces with low k, a small value of p results in an increased likelihood that two sequences are not independent. For our application, we set $p = (10k) + 1$.

MoM produces two global statistics for each input parameter based on the set of elementary effects: the first, μ^*, measures the overall parameter importance and the other, σ^* provides an overall global measure of importance variability [see *Saltelli et al.* (2008), p. 117]. These measures are defined as

$$\mu_i^* = \frac{1}{r}\sum_{j=1}^{r} |d_i^{(j)}| \tag{7.3}$$

and

$$\sigma_i^* = \sqrt{\frac{1}{r}\sum_{j=1}^{r} (|d_i^{(j)}| - \mu_i^*)^2} \,. \tag{7.4}$$

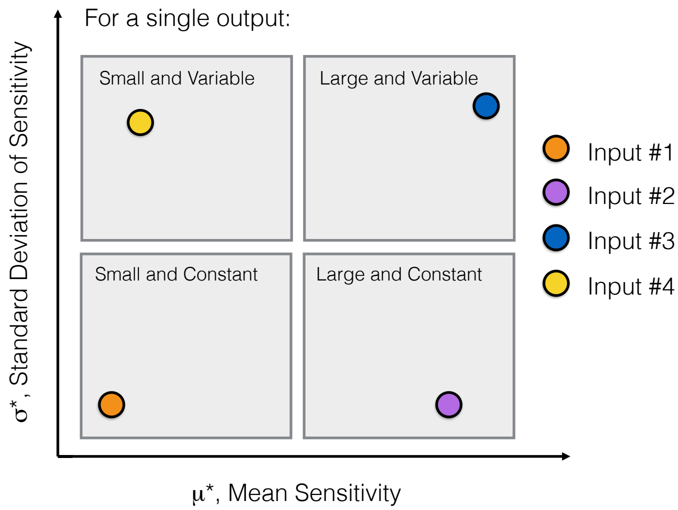

Figure 7.1: Cartoon μ^* vs σ^* plot to assist in describing appropriate interpretation of the Method of Morris results.

One would expect μ^* to identify the same important and unimportant parameters as other methods such as DELSA and Sobol' (*Borgonovo et al.* (2017) provides a review of selected methods), and was chosen for this work because other global methods tend to require more model runs.

7.2.2 Guide to interpretation of MoM results

Figure 7.1 provides a cartoon of a μ^* vs σ^* plot. Four example inputs have (μ^* , σ^*) pairs for a single output plotted. Recall that the intention of the MoM is to screen parameters into three primary categories, those parameters with effects on an outcome that are (a) negligible, (b) linear and additive, and (c) non-linear.

A large μ^* value indicates a large mean value for calculated elementary effects while a large σ^* value indicates elementary effect sizes that are highly variable across parameter space. Thus, a parameter such as Input #1 that has a low value for both μ^* and σ^* has a negligible effect on the output. A parameter such as Input #2, which has a high value for μ^* but a low value for σ^* indicates a parameter with a large effect that is similar across parameter space—that is, a parameter with a linear and additive effect. Input #3 has a large value for both μ^* and σ^*, which indicates that the parameter is both influential and interacts non-linearly with other parameters. A parameter such as Input #4, would be interpreted to have a small average effect but large variability.

7.2.3 Experimental Design

We ran the MoM sensitivity analyses for each combination of the following: process model (36), watershed domain (2), outlet downcutting trajectory (2), and postglacial topography initial condition (5 and 6 for the Gully and Franks watersheds, respectively). As it was developed based on calibration results of the initial 36 models, no sensitivity analysis was done on model 842. Table 7.1 lists the parameters varied for each model in the sensitivity analysis.

Table 7.1: Parameters varied in the sensitivity analysis for each model. Parameter symbols are defined in Chapter 5 and Appendix A.

Model ID	# of Parameters	Parameters Symbols
000	2	$\log_{10} K$, D
001	3	$\log_{10} K$, m, D
002	3	$\log_{10} K$, $\log_{10} \omega_c$, D
004	2	$\log_{10} K_{ss}$, D
008	4	$\log_{10} K$, $\log_{10} \omega_c$, b, D
00C	4	$\log_{10} K_{ss}$, $\log_{10} \omega_c$, b, D
010	4	$\log_{10} K$, $\log_{10} V_c$, ϕ, D
012	5	$\log_{10} K$, $\log_{10} \omega_c$, $\log_{10} V_c$, ϕ, D
014	4	$\log_{10} K_{ss}$, $\log_{10} V_c$, ϕ, D
018	6	$\log_{10} K$, $\log_{10} \omega_c$, b, $\log_{10} V_c$, ϕ, D
030	5	$\log_{10} K$, $\log_{10} V_c$, F_f, ϕ, D
040	3	$\log_{10} K$, D, S_c
100	8	$\log_{10} K_q$, D, p_d, F, I_m, n_{ts}, c, S_r
102	9	$\log_{10} K_q$, $\log_{10} \omega_c$, D, p_d, F, I_m, n_{ts}, c, S_r
104	8	$\log_{10} K_{q,ss}$, D, p_d, F, I_m, n_{ts}, c, S_r
108	10	$\log_{10} K_q$, $\log_{10} \omega_c$, b, D, p_d, F, I_m, n_{ts}, c, S_r
110	10	$\log_{10} K_q$, $\log_{10} V$, ϕ, D, p_d, F, I_m, n_{ts}, c, S_r
200	5	$\log_{10} K$, D, H_{init}, R_m, K_{sat}
202	6	$\log_{10} K$, $\log_{10} \omega_c$, D, H_{init}, R_m, K_{sat}
204	5	$\log_{10} K_{ss}$, D, H_{init}, R_m, K_{sat}
208	7	$\log_{10} K$, $\log_{10} \omega_c$, b, D, H_{init}, R_m, K_{sat}
210	7	$\log_{10} K$, $\log_{10} V_c$, ϕ, D, H_{init}, R_m, K_{sat}
300	9	$\log_{10} K_q$, D, H_{init}, p_d, F, n_{ts}, c, S_r, K_{sat}
400	6	$\log_{10} K$, D, H_0, H_{init}, P_0 , H_s
410	10	$\log_{10} K_2$, $\log_{10} K_s$, $\log_{10} V_c$, ϕ, H_*, D, H_0, H_{init}, P_0 , H_s
440	7	$\log_{10} K$, D, H_0, H_{init}, P_0 , H_s, S_c
600	8	$\log_{10} K$, D, H_0, H_{init}, P_0 , H_s, R_m, K_{sat}
800	4	$\log_{10} K_2$, $\log_{10} K_1$, W_c, D
802	6	$\log_{10} K_2$, $\log_{10} K_1$, $\log_{10} \omega_{c2}$, $\log_{10} \omega_{c1}$, W_c, D
804	4	$\log_{10} K_{ss2}$, $\log_{10} K_{ss1}$, W_c, D
808	6	$\log_{10} K_2$, $\log_{10} K_1$, $\log_{10} \omega_c$, b, W_c, D
810	6	$\log_{10} K_2$, $\log_{10} K_1$, W_c, $\log_{10} V_c$, ϕ, D
840	5	$\log_{10} K_2$, $\log_{10} K_1$, W_c, D, S_c
A00	7	$\log_{10} K_2$, $\log_{10} K_1$, W_c, D, H_{init}, R_m, K_{sat}
C00	8	$\log_{10} K_2$, $\log_{10} K_1$, W_c, D, H_0, H_{init}, P_0 , H_s
CCC	3	$\log_{10} K$, f, D

To assess the sensitivity of the objective function to the outlet downcutting trajectory and initial condition, we ran the same parameter set sequences within each combination of downcutting trajectory and initial condition. This was accomplished by using the same random seed value for all initial and downcutting combinations for a given model. This allowed us to calculate a modified mean effect μ^* and standard deviation σ^* that measures the sensitivity of the objective function to the downcutting history and initial condition. The calculation of these elementary effects used the "7% etch" initial condition as the base case and lowering history 1.

7.3 Computational considerations

Use of the MoM for sensitivity analysis on the Franks Creek and Gully Domains required on order of 53,000 model evaluations, each of which takes a minimum of about 30 minutes (model evaluation time depends on which model is being evaluated as well as model time and space resolution). Application of the DELSA method as a follow up to the MOAT screening method was originally planned. However, to fully apply DELSA in a framework with 36 models, 2 boundary conditions, 5 or 6 initial conditions, and between two and eleven input parameters would have greatly exceeded the available computational resources.

7.4 Results

This section reviews primary findings from the sensitivity analysis. The details of the results are given in Appendix B, which lists in tabular form μ^* and σ^* for each model, parameter, initial condition, and downcutting history.

7.4.1 Example of plots provided in Appendix B

Figure 7.2 provides an example of the type of figures presented in Appendix B. The figures come in pairs, with one pair per model. The first figure of each pair plots the modified mean sensitivity, μ^*, against the standard deviation, σ^*, for each parameter in the model. Colors are used to indicate parameters; symbols denote different initial topographies. The second figure of each pair highlights sensitivity to initial topography and downcutting history. Parameters are shown in gray, with the sensitivity to initial topography plotted in green and the sensitivity to downcutting history shown in red.

Along with these figures, tables of the equivalent information are also provided. The tables show the values of μ^* and σ^* for each sensitivity-test series.

7.4.2 Primary finding #1: Objective function not sensitive to details of lowering history or postglacial topography

In general, the sensitivity to the difference between the two baselevel lowering histories is minimal. This is indicated by low mean-effect scores for lowering history, as compared with the scores for the most important parameters. Mean-effect scores for parameters in eight of

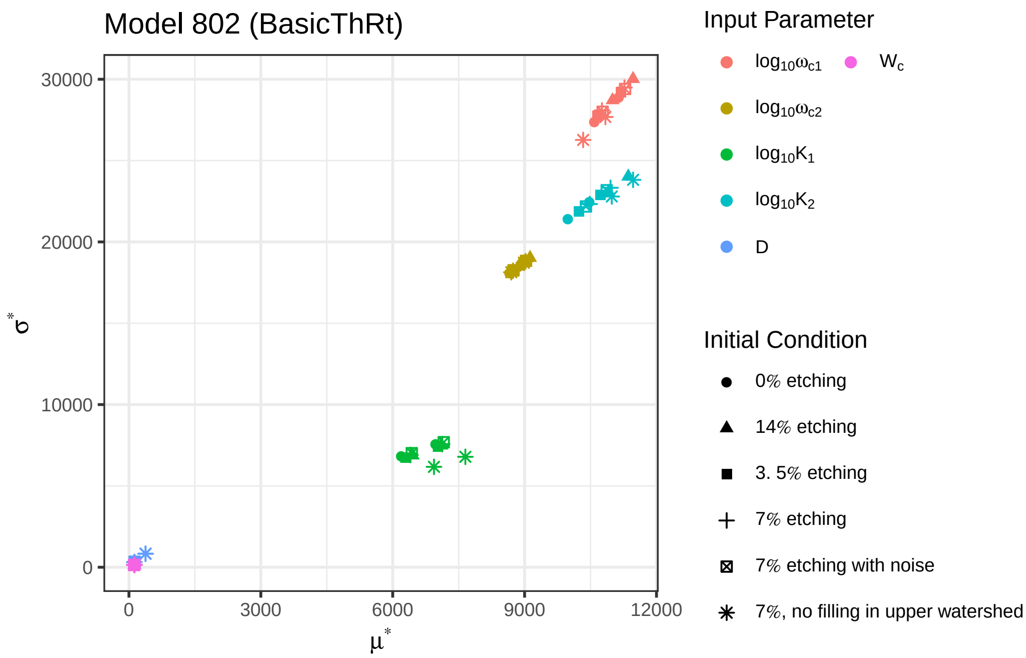

(a) Input parameter sensitivity plot for model 802 in Franks Creek Watershed (SEW domain). Colors represent Method of Morris sensitivity analysis results for model input parameters. Shape represents postglacial topography and the two lowering histories considered are not distinguished. Thus two markers are present for each color-symbol combination.

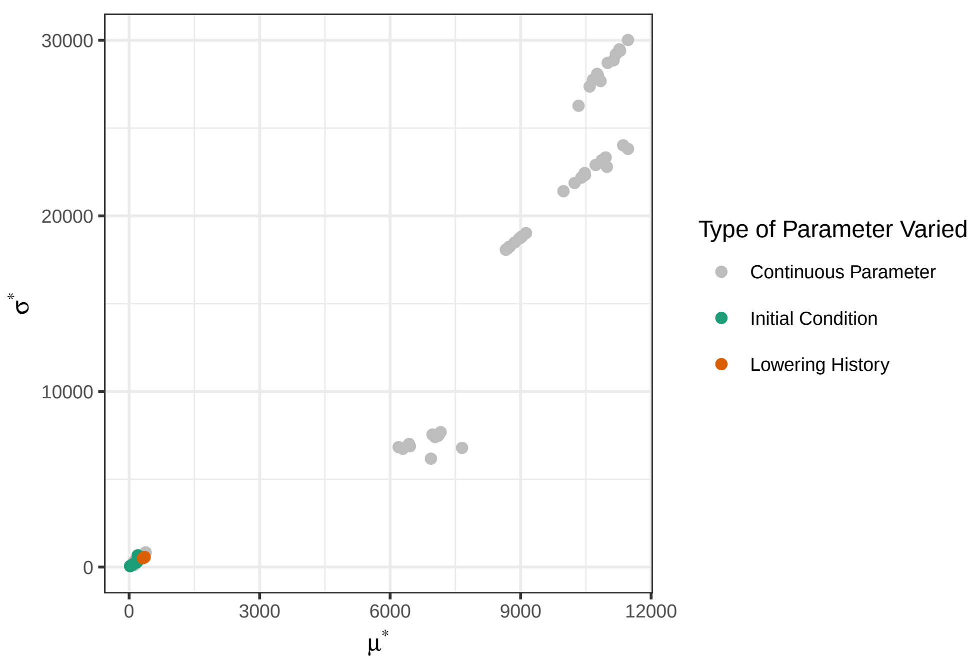

(b) Parameter, initial condition, and lowering sensitivity plot for model 802 in Franks Creek Watershed (SEW domain). Colors represent parameter, initial condition, or lowering history sensitivities. The parameter sensitivities of the upper panel are shown in gray for context. Initial condition "7% etching" and lowering history "1" were used as references value initial and boundary condition sensitivity calculations.

Figure 7.2: Sensitivity analysis summary for model 802 in Franks Creek Watershed (SEW domain)

the erosion models are shown in the form of bar graphs in Figure 7.3. For each graph, the columns represent individual parameters, which are color-coded in the legend to the right of the figure. The model number appears at the top of each graph. The vertical axis (height of the bars) shows the average sensitivity score, μ^*, among all initial conditions and lowering histories for a particular model. The eight models shown include the best performing two-element models (see Chapter 8).

The last column on the right of each graph shows the sensitivity to the choice of lowering history. In all cases, the difference between the two baselevel lowering histories has much less influence than do the most important parameters.

The effect of initial topography, shown in the next-to-last column on the right of each graph, is similarly low relative to the most influential parameters. The low sensitivity shown for eight models in Figure 7.3 is common among all the models (Appendix B). Whereas there are a few circumstances in which the modified mean sensitivity to initial topography rises a bit higher, in most cases the initial topography is among the least influential effects.

7.4.3 Primary finding # 2: Only a small number of parameters exert strong influence on the models with respect to the objective function

Across the three dozen models tested, sensitivity with respect to the objective function tends to be dominated by just a few parameters. The erodibility coefficient(s) nearly always have a strong influence on model output, as measured by the objective function. In the eight models illustrated in Figure 7.3, for example, the erodibility coefficient parameters (K_1, K_2, K_{ss1}, and K_{ss2}) rank among the most influential for each model. This is not a surprising finding, given that the erodibility coefficient governs the speed and extent of water erosion. For models that include an erosion threshold(s), the threshold parameter or parameters tend to exert a strong influence on the model's output (again, as measured by the objective function). For example, model 802 is a variation on the basic rock-till model that includes an erosion threshold for each of the two lithologies. For this model, the four most important parameters are the two erodibility coefficients (green bars) and the two erosion thresholds (orange bars).

For models that use stochastic precipitation, the water erosion rate is influenced by several parameters, all of which are associated with moderately high values of modified mean sensitivity (see Appendix B). The modified erodibility coefficient, K_q, is important because it represents the material's susceptibility to erosion. The parameters that describe precipitation frequency and magnitude, F and p_d, respectively, matter because they influence surface water discharge. The soil infiltration capacity tends to be associated with high sensitivity because it has a nonlinear influence on runoff generation. One can think of these parameters, which appear explicitly only in the stochastic models, as components of the "bulk" erodibility coefficient that is used in the other models. In other words: K is always an important parameter, and for those models that split K into several components, its components are also influential.

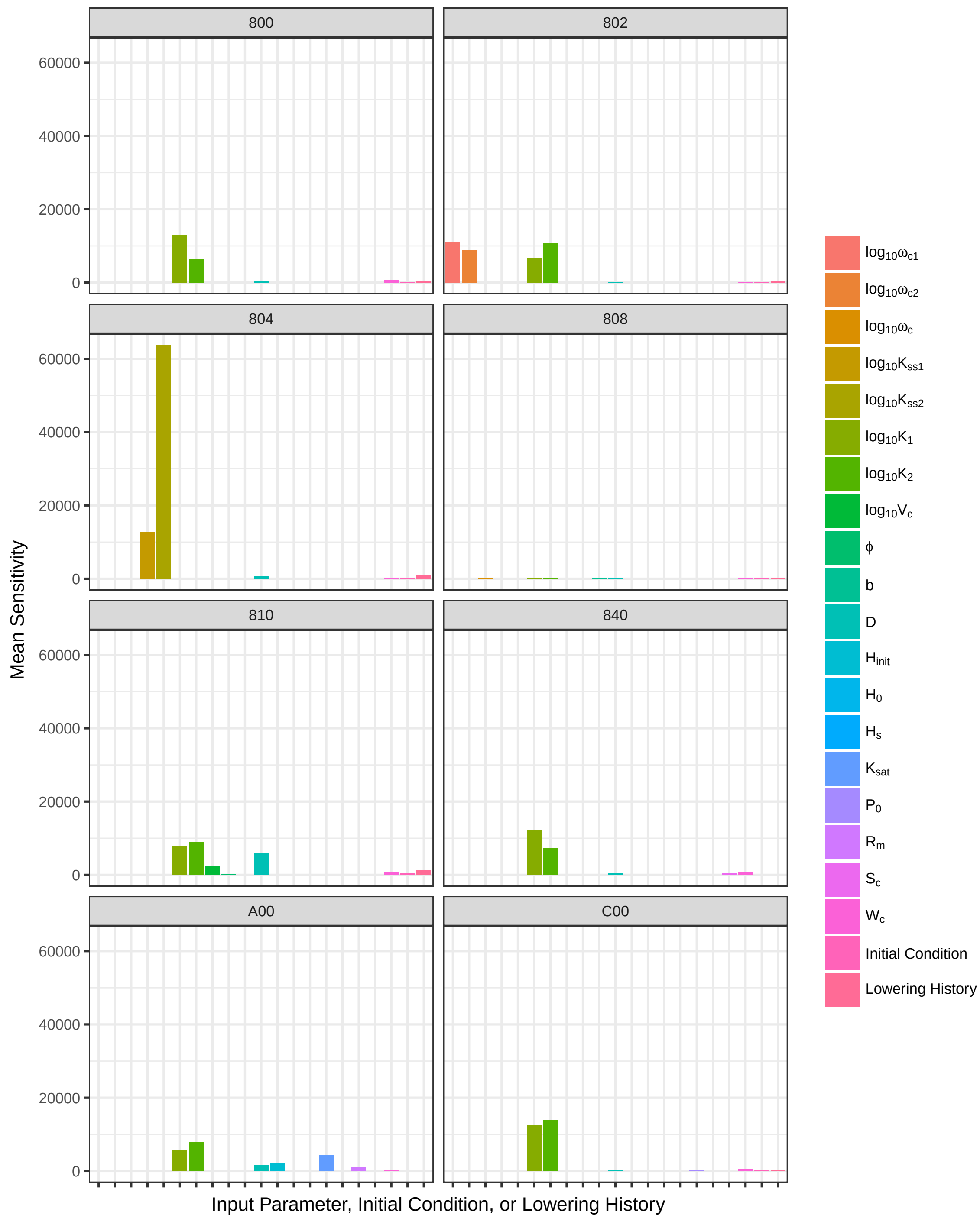

Figure 7.3: Bar chart illustrating mean sensitivity for different parameters for eight selected models. Vertical axis shows the mean value of μ^* averaged across 6 initial conditions and 2 lowering histories for each model.

7.4.4 Primary finding #3: Sensitivity of the components of the objective function is consistent with model physics.

The use of discrete landscape patches as components in the objective function (Chapter 6) allows us to examine how each parameter influences the behavior of the model with respect to a given patch. As an illustration of how parameter sensitivity varies with location, Figure 7.4 shows sensitivity scores for each patch for model BasicThRt (802). This model is among those that perform best in calibration and validation tests (see Chapters 8 and 9). It distinguishes between till and rock and includes erosion threshold parameters for both lithologies (ω_{c1} AND ω_{c2} for till and rock, respectively). The panels in Figure 7.4 are colored according to whether the patch lies primarily in the rock area (purple) or till area (orange) (see inset). As expected, the areas within the till zone show strong sensitivity to the erodibility factor for till (K_1) and the erosion threshold for till (ω_{c1}), and little or no sensitivity to the corresponding parameters for rock. Conversely, in the upper portion of the watershed where bedrock dominates, the model shows strong sensitivity to rock erodibility K_2 and rock erosion threshold ω_{c2}. The model's behavior in many of these rock dominated areas is also sensitive to the parameters for till, and especially to the till erosion threshold. This sensitivity reflects the fact that the rock-dominated area lies in the upper part of the watershed, where erosion rates and patterns depend in part on what is happening downstream. For example, when till is easy to erode in a particular model run (because K_1 is high or/and ω_{c1} is low), rapid erosion on the lower branches of the Quarry-Franks Creek network will propagate upstream to the bedrock portion of the watershed, and thus tend to produce more rapid erosion there as well.

At the West Valley Site, the areas of greatest concern are the plateaus that lie within the till zone, to the southeast of Quarry Creek and west and north of Franks Creek. These areas are represented by the "orange zone" in Figure 7.4. Model sensitivity results for this area in particular is broadly consistent with sensitivity for the objective function as a whole: those parameters that directly influence stream and gully erosion, and in particular the erodibility coefficient(s) and erosion threshold(s), tend to be the most important. Among these parameters, those that apply to till are generally more important.

7.4.5 Influence of hillslope transport parameters

The hillslope transport efficiency coefficient, D, appears in all models. This parameter sets the rate at which hillslopes decline. The log-transformed coefficient, $\log D$, is rarely among the most influential parameters. Nonetheless, we treat it as a calibration because it is the primary—and, for many models, only—parameter to describe the rate of downslope motion on hillslopes. Sensitivity to D is illustrated in the μ^*–σ^* plots shown in Appendix B.

The threshold gradient parameter S_c, which represents the gradient near and above which soil transport accelerates more-than-linearly with gradient, appears in models that use a nonlinear hillslope transport law. In general, these models show relatively little sensitivity to S_c (see Appendix B, plots and tables for BasicCh (040), BasicChSa (440), and BasicChRt (840)).

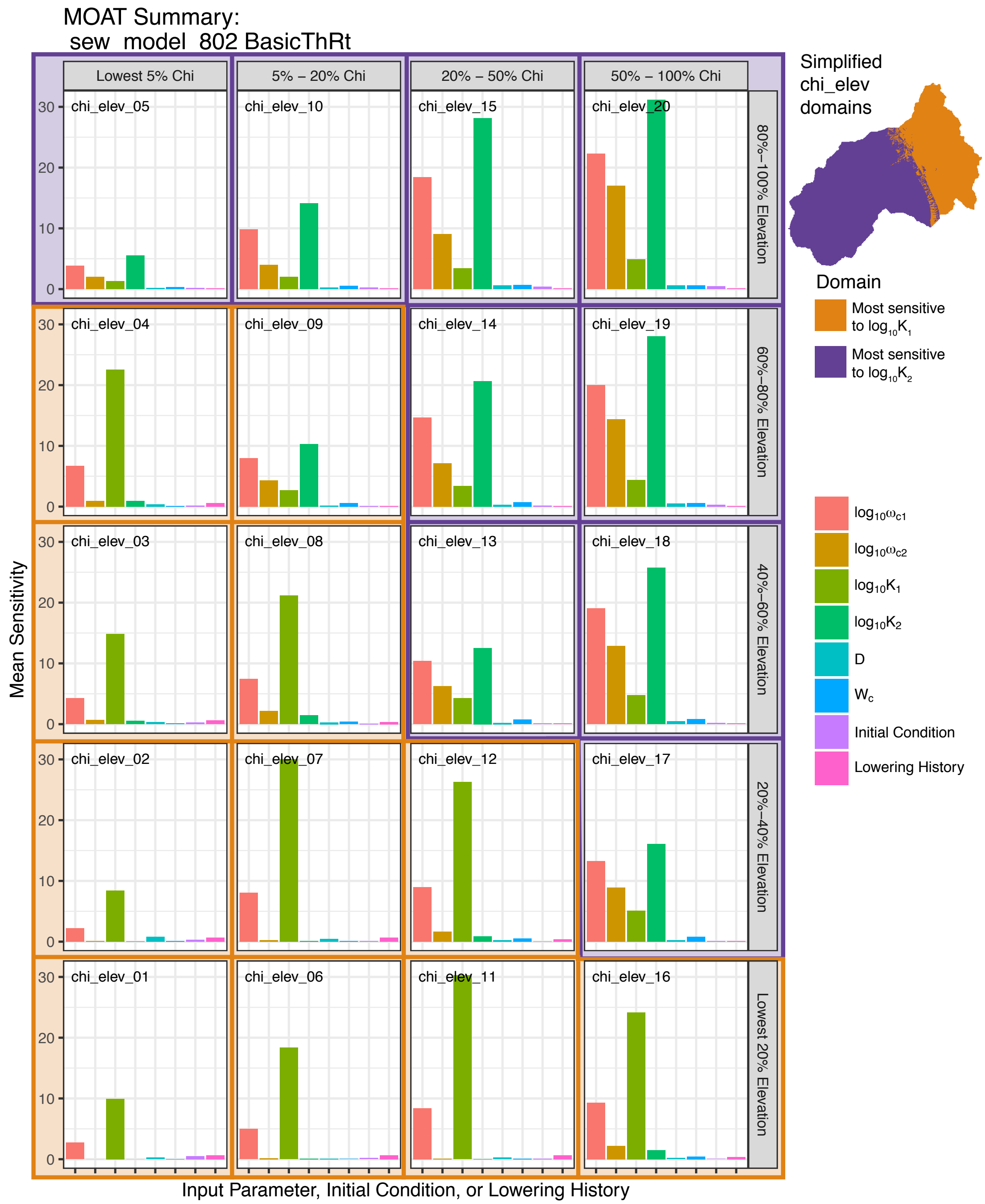

Figure 7.4: Sensitivity for individual terrain patches.

7.5 Gully domain sensitivity analysis

The foregoing sensitivity analysis pertains to a model domain that spans the Franks Creek watershed at a grid resolution of 24 feet per grid cell. An additional sensitivity analysis was conducted on a much smaller watershed—the Gully Watershed presented in Chapter 4—at a grid resolution of three feet per grid cell. This smaller, finer-scale domain was studied in order to prepare for the possibility of conducting erosion projections on small gully watersheds at high spatial resolution. Initial calibration tests on this small gully domain at high spacial resolution, however, showed that models run more slowly (in some cases considerably so), despite the reduced domain size. For this reason, the model calibrations for the gully-scale domain were not completed. However, a full sensitivity analysis was completed.

7.6 Parameters set constant in calibration

Several parameters proved to have little influence on the models; in other words, the analysis showed low sensitivity as measured by the objective function. These parameters were held to constant values in the calibration process, which reduces the computational and analytical complexity of calibration. Table 7.2 lists these parameters, and the models in which they were set to fixed values.

The random seed used in stochastic precipitation models was treated as a parameter in the sensitivity analysis in order to test the influence of the particular random sequences used. The seed value turned out to have uniformly low influence. This finding implies that the differences between one random sequence and another (both drawn from the same underlying distribution) has little impact on model output. The random seed was held constant in calibration.

Models with a dynamic soil layer are relatively insensitive to the characteristic soil thickness, H_0. This parameter represents the length scale over which weathering rate declines; prior studies suggest it is on the order of a few decimeters, and for calibration it was set to 0.5 m.

Models that include variable source-area (VSA) hydrology, as well as those with a dynamic soil layer, use the parameter H_{init}. For dynamic-soil models, this is the starting soil thickness at the beginning of a run. For VSA models, it is the assumed soil thickness for purposes of calculating shallow subsurface flow capacity. In both cases, the models show little sensitivity to the parameter. In calibration, it is set to 1.5 m (about 5 feet), based on the observed thickness of soils at the Site (see Chapter 4).

Models that include VSA hydrology also specify a recharge rate, R_m. This parameter is one of three that control subsurface flow capacity, with the others being soil thickness (H_{init}, or dynamic if applicable) and saturated hydraulic conductivity, K_{sat}. These three parameters effectively form a single lumped parameter (see Chapter 5), and it is necessary only to calibrate one of them. The recharge R_m is therefore held constant at 0.5 m/y (roughly half the site's mean annual precipitation) while K_{sat} is retained as a calibration parameter.

The models are generally insensitive to the width of the contact zone between glacial sediments and bedrock, W_c. For calibration, it is held fixed at 1 m.

The entrainment-deposition models include as a parameter the porosity of bed material,

ϕ. This parameter turns out to have little impact, and is fixed at 0.3 for calibration.

Six models with stochastic precipitation show little sensitivity to either the precipitation distribution shape factor, c, or to the number of sub-time-steps used in the numerical algorithm, n_{ts}. Both parameters are held fixed in calibrating these models.

7.6.1 Sensitivity to paleoclimate variation

One model, BasicCc (CCC), incorporates climate variation through time, as described in Appendix A. This model allows the erodibility coefficient for water erosion to either increase or decrease over time, reaching a stable value after a specified period of time has elapsed. This treatment is designed to explore the importance of uncertainty in past climate during the 13,000 year period used for model calibration. In the sensitivity analysis runs conducted with this model, the erodibility coefficient was set to stabilize at 5,000 years into the model run, representing 8,000 years ago. This corresponds to the time when, according to the TRACE21ka long-period climate model simulation presented in Chapter 3, the annual precipitation rate and its apportionment among various forms became approximately steady (see Figure 3.1). Allowing erodibility to vary systematically (either increasing or decreasing, depending on parameter choice) provides a test of the degree to which variation in the amount and/or form of precipitation during the first 5,000 years of a 13,000-year model run influence the model output. The range for the adjustment factor was 50% to 150%; in other words, the erodibility coefficient at the beginning of each sensitivity run could be as much as 1.5 times its final value or as little as half of its final value.

What this range implies in terms of precipitation variation depends on what one assumes about factors such as precipitation variability and runoff generation mechanisms (see Chapter 11 for more on this issue). If one assumes a linear relation between precipitation and erodibility, then the range used in sensitivity analysis is rather large relative to the magnitude of fluctuations calculated by the TRACE21ka simulations for the period 13,000 to 8,000 years ago in western New York (on the order of 15% variation in annual precipitation; see Figure 3.1).

The results of these sensitivity tests showed that climate-driven variation over time in the erodibility coefficient has only a small influence on the model's output as measured by the objective function (Appendix B, Figure B.36). As in the case of most models, the erodibility coefficient itself has a strong influence on the output. This is the case in part because the feasible range for the parameter is wide, spanning several orders of magnitude, as discussed in Chapter 5. But regardless of the base value chosen for this parameter, variation in time by $\pm 50\%$ has a negligible impact on model output. In light of this result, the calibration procedure assumed a steady climate over the calibration period (Chapter 8).

Table 7.2: Parameter values fixed for calibration runs. Units for parameters are given in Table 5.1.

Parameter Name	Fixed Value	Model
H_0	0.5	BasicSa BasicHySa BasicChSa BasicSaRt
H_{init}	1.5	BasicVs BasicThVs BasicSsVs BasicDdVs BasicHyVs BasicStVs BasicSa BasicHySa BasicChSa BasicVsSa BasicVsRt BasicSaRt
R_m	0.5	BasicVs BasicThVs BasicSsVs BasicDdVs BasicHyVs BasicVsSa BasicVsRt
S_r	1908	BasicSsSt
	3850	BasicThSt
	5098	BasicSt
	845	BasicDdSt
	9032	BasicStVs
	9879	BasicHySt

Table 7.2: (continued)

Parameter Name	Fixed Value	Model
W_c	1	BasicRt BasicThRt BasicSsRt BasicDdRt BasicHyRt BasicChRt BasicVsRt BasicSaRt
ϕ	0.3	BasicHy BasicThHy BasicSsHy BasicDdHy BasicHyFi BasicHySt BasicHyVs BasicHySa BasicHyRt
c	0.75	BasicSt BasicThSt BasicSsSt BasicDdSt BasicHySt BasicStVs
n_{ts}	10	BasicSt BasicThSt BasicSsSt BasicDdSt BasicHySt BasicStVs

7.7 Summary and Conclusions

The erosion models show very little sensitivity, as measured by the objective function, to the difference between the two lowering histories (Figure 4.10). This finding motivates the use of a single, averaged history in the calibration procedure. The models also show little sensitivity to reconstructed post-glacial topography: the differences between the six different post-glacial surfaces have little impact on the objective function.

Globally, the most important parameters are those that control channel and gully erosion: the erodibility coefficient(s) and (where present) erosion threshold(s). The stochastic-precipitation models also tend to be sensitive to parameters that influence water erosion. These parameters include precipitation frequency and intensity, and soil infiltration capacity.

The variation in parameter sensitivity among landscape patches mirrors the spatial distribution of rock and till. Not surprisingly, parameters that relative to rock have little or no impact within the till-mantled area in the lower portion of the Franks Creek watershed. In the bedrock-dominated upper portion of the watershed, parameters associated with both rock and till are influential. The influence of till-related parameter arises because erosion downstream (in the till area) affects erosion upstream (in the bedrock area). Overall, the differences in sensitivity among different terrain patches make sense given the distribution of material properties and the physical processes in the models.

The sensitivity analysis enabled identification of a set of low-sensitivity parameters that were set constant for purposes of calibration. Deactivating these insensitive parameter reduces the computation time and analytical complexity required for calibration.

Finally, sensitivity analysis revealed that the basic erosion model is not strongly sensitive to temporal variations in precipitation of the magnitude that paleoclimate model results suggest for the 13 ka to 8 ka calibration period. This finding provides support for assuming a stationary effective precipitation in the recent geologic past for purposes of model calibration.

Chapter 8

Model Calibration

8.1 Introduction

Simulation requires that all model inputs be defined. Model inputs include numerical definition of initial and boundary conditions, system geometry, and the parameters described in Chapter 5. Models can be classified as *predictive models* and *calibrated models* based on how model input values are obtained (*Hill and Tiedeman*, 2007; *Wilcock and Iverson*, 2003). When it is possible to determine model inputs accurately using measured values, the model is referred to as *predictive*. However, it is often not possible to determine model inputs at the appropriate space or time scale, if at all, and in this case model input values must be determined by modifying model inputs so that the model outputs are able to match readily measurable equivalents, which are also called observations. This type of model is referred to as a *calibrated model*, and the process used to determine input values is called calibration or inverse modeling. Formally, inverse modeling provides a mechanism for modifying input values to improve the match between model outputs and observations. In general, it is expected that results from predictive models are accurate in a wider range of circumstances, and that calibrated models are limited to the circumstances during which observations are obtain. Predictive models are very rare when simulating environmental systems; in practice, calibrated models are common.

The models described in this work are calibrated. The processes involved in reproducing the erosion in the last 13,000 years are similar to the processes important to forecasting erosion over the next 10,000 years. This similarity between observations and forecasts makes the model design more likely to yield accurate results.

Basic features of model calibration include definition of what is not changed during calibration (described in previous chapters), what is changed, how the effects of changes are evaluated, and how the changes are made. For the calibration procedure used in this study, changes are made to parameter values, while the post-glacial initial topography and outlet lowering history are fixed (based on results from sensitivity analysis, reported in Chapter 7). As discussed in Chapter 4, the Erosion Working Group reports *Wilson and Young* (2018) and *Bennett* (2017) provide data that constrain the initial conditions (the post-glacial topography; e.g., Figure 4.2), and boundary conditions (specifically, the rate and timing of Buttermilk Creek incision; Figure 4.10). The parameter values are continuous, and suitable parameter values for each model are determined by *parameter optimization*.

Real-valued parameters can be estimated using formal optimization methods. In these methods, an equation is defined that compares model-simulated values to observations (see Chapter 6). The values of the identified parameters are then iterative varied in order to minimize the equation. The equation is called an *objective function*. The set of parameters that produce the "best" match of the model to the observations are those that minimize the objective function. A *calibration algorithm* (also called an *optimization algorithm*) is used to accomplish the minimization. Many calibration algorithms exist. A technical summary of the calibration algorithms used in this Report is provided in Section 8.7. It is important to keep in mind that a calibration algorithm knows nothing of internal model physics or details of objective-function calculation. A calibration algorithm simply minimizes the objective function by modifying the values of identified parameters, given a set of constraints such as reasonable parameter ranges. A completed calibration will yield measures of model fit (typically the objective function value, see Section 8.5 for a complete discussion) and an estimate of the optimal parameter values along with their associated uncertainty.

The remainder of this Chapter is organized as follows. Section 8.2 provides background information about the optimization methods used in this work. Section 8.3 describes the multi-model calibration approach. Sections 8.4 and 8.5 define the metrics used to compare calibrated models. Because the objective-function surface used in this study contains local minima, and many of the models include common ingredients, it is necessary to establish operational criteria for a successful calibration; these criteria are described in Section 8.6. Section 8.7 provides technical background on the algorithms used for model calibration. Section 8.8 presents the results, and Section 8.9 discusses implications.

Identifying a viable calibration strategy for the erosion models was challenging, and we explored a number of alternative calibration algorithms. Section 8.10 describes the effort undertaken for calibration of the Gully Domain, and the reasons why work on this domain did not progress beyond calibration. Finally, additional technical information regarding model calibration is given in Appendix C, which includes tables and figures that support and extend this chapter.

8.2 Background Information on Optimization Methods

This section briefly describes four issues of concern for the optimization method used in this work: (1) the objective function; (2) parameter hyperspace, constraints, and prior information; (3) local minima; (4) local and global optimization methods; and (5) complex model evaluations and surrogate models

The objective function used for erosion-model calibration (equation 6.3) is the sum of squared residual values, where a residual is one observed value minus its associated simulated value. This is a common type of objective function used in the study of over-determined systems (systems in which there are more observations than free parameters). There are two types of least-squares problems: ordinary least squares, in which the residuals are linear in all unknowns, and nonlinear least squares, in which residuals are not linear in all unknowns.

The linear case has a closed-form solution, while the nonlinear problem is determined through numerical methods. Confidence intervals on the estimated parameters are calculated using the variance of the least-squares estimator, which measure how closely the simulated values match the observations.

A single objective function was useful in this work because all metrics used in the objective function were functions of the DEM of modern topography. Individual terms of the objective function were evaluated to understand model misfit patterns and its source and potential reduction.

The objective function can be calculated for all sets of parameter values, and can thus be calculated everywhere in parameter space. The idea of an objective-function surface is often useful and is referred to in this work. If a model has two parameters, the parameter values can be plotted along two axes (one for each parameter) and the objective-function value plotted on a third axis. In this circumstance the objective-function surface can be visualized and looks much like a topographic surface. In the optimization, the goal is to determine the lowest value of the objective function surface and its associated parameter values.

The goal of model calibration is to find the set of model input parameters that minimizes the objective function. This is equivalent to finding the *global minimum* of the objective function surface in a parameter hyperspace with a number of dimensions equal to the number of estimated parameters. Depending on the problem, the parameter space may be unconstrained and have no limits, or constrained to only a portion of parameter space. In our application, parameter space is constrained by parameter ranges from the literature (Table 5.2).

Unless it is possible to prove that the objective function is convex in the considered portion of parameter space, it is not possible to know whether *local minima* in the objective function surface are present. For a function that has an analytical expression, a typical way to demonstrate convexity is to prove that the second derivative is always greater than or equal to zero. In the context of the landscape evolution models and the objective function used in this report, no analytical expression exists that relates the input parameter values to the objective function. Thus it is not possible to prove or disprove convexity *a priori*. When convexity is not guaranteed, it is not possible to know whether the parameter set produced by an optimization algorithm represents the *global minimum* or one of an unknown number of possible *local minima*. To address this issue in the context of our multi-model calibration effort, we created a set of criteria for determining whether a calibration is successful (Section 8.6).

There are two major classes of optimization methods: local or gradient-based methods, and global methods. Both are used in this work. Local methods use either analytical or numerical gradients of the objective function with repect to parameters to determine how to move from a starting place in parameter space to a minimum point. Local methods are advantageous because they typically require a relatively small number of model function evaluations. However, mechanisms to escape potential local minima are not always reliable. Global methods use sampling approaches. They perform model runs for a series of parameter value sets. Often they use one set of results to identify new sets of parameter values to evaluate, and iterate until a specified convergence criterion has been achieved. While global methods are less prone to inadvertently identifying a local minimum as the final result, they can take many tens to thousands of times longer than a local method. The models run in this work are computationally demanding, and a combination of local and global methods was found to perform well.

Finally, we discuss two approaches to obtaining the simulated values needed to evaluate the objective function surface: using only complex model evaluations, or constructing a surrogate. Here we refer to using a full EMS model to evolve topography and then evaluating its objective function as a *complex model evaluation.* A typical model evaluation takes ≈30 minutes or more, which is too long to use a global optimization method given computational capacity considerations. An alternative is to use a smaller number of complex model evaluations to construct a statistical fit that serves as a *surrogate model.* The optimization method then evaluates, and depending on the method, refines, the surrogate. In this study, the approach that proved to be the most practical involved using a combination of surrogate and complex-model evaluation methods. (In the text below, if no note is made about the use of a surrogate, then the method in question used complex-model evaluations).

8.3 Methodological Approach and Overview

The calibration procedure considered 37 alternative landscape evolution models; these models are outlined in Chapter 3 and described in detail in Appendix A. Each of these 37 alternative models has between two and ten free parameters (Table 7.1). Based on the results of the sensitivity analysis, in most models some parameter values were held constant in calibration (Table 7.2), so that the number of estimated parameters is between two and seven (Table 8.1). The objective function used for calibration is given by equation 6.3.

The results of the sensitivity analysis presented in Chapter 7 indicated that neither the choice of post-glacial topography (Figures 4.2–4.5) nor the choice of downcutting history (Figure 4.10) had a significant effect on the objective function. As the two downcutting histories are similar, for the calibration effort we used an average between the two of them. Based on exploratory assessment we chose to use the initial topography with 7% etching in the glacial fill area and no filling in the upper bedrock portions of the watershed (option 6 in Table 4.1). These exploratory assessments concluded that the calibration results are not sensitive to the degree of filling in the upper watershed. This result is sensible, as the objective function places little importance on the upper portion of the watershed (Figure 6.5) and has large uncertainty for the channelized portions of its initial watershed (Figure 6.4).

The starting hypothesis for the calibration procedure was that it would be possible to successfully calibrate the suite of models using only the Gauss-Newton algorithm, a computationally frugal local algorithm (Section 8.7.1) (*Hill and Tiedeman*, 2007, pages 68, 77). As the EMS landscape evolution models run on the Franks Creek domain at the resolution described in Chapter 4 take on order 30 minutes or more, a computationally frugal method is a necessity in this application. However, preliminary trials with the Gauss-Newton algorithm described in Section 8.8.3 demonstrated many small local minima, which meant that the local method alone was not practical. We determined that calibration can be achieved through a hybrid calibration method that uses a surrogate-based global method, followed by a local method. The global method is the surrogate-based Efficient Global Optimization (EGO) algorithm (*Jones et al.*, 1998) (Section 8.7.3), which was used to find the region of the global minimum. A gradient-based local method is then used with the complex model to refine the search (Section 8.7.2). Examination of selected models suggested that this approach is able to identify optimal parameter sets that meet the success criteria defined in Section 8.6). However, we found that parameter confidence intervals calculated using linear theory were too large (in some cases by an order of magnitude or more). This occurred because objective-functions surfaces were often flat near the minima, where the gradients used by linear methods are calculated, while the objective function becomes steeper some distance from the minimum point. These effects would likely lead to inaccurate uncertainty measures for projections in linear confidence intervals were used. Thus, we applied Bayesian calibration on a surrogate of the model (Section 8.7.4) to construct final estimates for the probability distribution of parameter values of a subset of models.

Finally, some of the methods described above, such as Latin Hypercube sampling, have a component that includes random number generation. When Dakota uses random number generation, a random seed value is needed. In this work the seed is set as a parameter in the input file so that the value can be easily retrieved, and re-used as needed so that the results presented fully reproducible (in other words, if one repeated our calculations using the same random seed, one should obtain exactly the same results).

Table 8.1: Free parameters for each model for calibration. Parameter symbols are defined in Table 5.1.

Model ID	Number of Free Parameters	Free Parameter Symbols
000	2	$\log_{10} K$, D
001	3	$\log_{10} K$, m, D
002	3	$\log_{10} K$, $\log_{10} \omega_c$, D
004	2	$\log_{10} K_{ss}$, D
008	4	$\log_{10} K$, $\log_{10} \omega_c$, b, D
00C	4	$\log_{10} K_{ss}$, $\log_{10} \omega_c$, b, D
010	3	$\log_{10} K$, $\log_{10} V_c$, D
012	4	$\log_{10} K$, $\log_{10} \omega_c$, $\log_{10} V_c$, D
014	3	$\log_{10} K_{ss}$, $\log_{10} V_c$, D
018	5	$\log_{10} K$, $\log_{10} \omega_c$, b, $\log_{10} V_c$, D
030	4	$\log_{10} K$, $\log_{10} V_c$, F_f, D
040	3	$\log_{10} K$, D, S_c
100	5	$\log_{10} K_q$, D, p_d, F, I_m
102	6	$\log_{10} K_q$, $\log_{10} \omega_c$, D, p_d, F, I_m
104	5	$\log_{10} K_{q,ss}$, D, p_d, F, I_m
108	7	$\log_{10} K_q$, $\log_{10} \omega_c$, b, D, p_d, F, I_m
110	6	$\log_{10} K_q$, $\log_{10} V$, D, p_d, F, I_m
200	3	$\log_{10} K$, D, K_{sat}
202	4	$\log_{10} K$, $\log_{10} \omega_c$, D, K_{sat}
204	3	$\log_{10} K_{ss}$, D, K_{sat}
208	5	$\log_{10} K$, $\log_{10} \omega_c$, b, D, K_{sat}
210	4	$\log_{10} K$, $\log_{10} V_c$, D, K_{sat}
300	5	$\log_{10} K_q$, D, p_d, F, K_{sat}
400	4	$\log_{10} K$, D, P_0 , H_s
410	7	$\log_{10} K_2$, $\log_{10} K_s$, $\log_{10} V_c$, H_*, D, P_0 , H_s
440	5	$\log_{10} K$, D, P_0 , H_s, S_c
600	6	$\log_{10} K$, D, H_0, P_0 , H_s, K_{sat}
800	3	$\log_{10} K_2$, $\log_{10} K_1$, D
802	5	$\log_{10} K_2$, $\log_{10} K_1$, $\log_{10} \omega_{c2}$, $\log_{10} \omega_{c1}$, D
804	3	$\log_{10} K_{ss2}$, $\log_{10} K_{ss1}$, D
808	5	$\log_{10} K_2$, $\log_{10} K_1$, $\log_{10} \omega_c$, b, D
810	4	$\log_{10} K_2$, $\log_{10} K_1$, $\log_{10} V_c$, D
840	4	$\log_{10} K_2$, $\log_{10} K_1$, D, S_c
842	6	$\log_{10} K_2$, $\log_{10} K_1$, $\log_{10} \omega_{c2}$, $\log_{10} \omega_{c1}$, D, S_c
A00	4	$\log_{10} K_2$, $\log_{10} K_1$, D, K_{sat}
C00	5	$\log_{10} K_2$, $\log_{10} K_1$, D, P_0 , H_s
CCC	3	$\log_{10} K$, f, D

8.4 Confidence Regions for the Objective Function

In equation 6.3 we defined the objective function. Objective functions are inherently statistical quantities, and when objective function values from different models are compared this statistical character needs to be considered. This is accomplished by comparing confidence regions around objective-function minima. The upper bound of the $(1-\alpha)100$-percent confidence interval can be calculated as in *Hill and Tiedeman* (2007, pg 178, equation 8.14, page 178, Table 8.2),

$$\text{upper limit} = F_{\text{obj}} + s^2 c_{(1-\alpha)100} \tag{8.1}$$

where s^2 is the calculated error variance, defined as

$$s^2 = \frac{F_{\text{obj}}}{N_d + N_{pr} - N_p} \tag{8.2}$$

and $c_{(1-\alpha)100}$ is a critical value. Here N_d is the number of observations, N_{pr} is the number of prior information values, and N_p is the number of input parameters for a given model.

Confidence intervals based on critical values from the Student-t distribution are typically agreed on as too small, while those with critical values from the F distribution are too large. Thus we present both as bounding values for confidence intervals.

8.5 Metrics of Model Evaluation

In addition to the objective function F_{obj} defined in equation 6.3, we use the maximum likelihood objective function F'_{obj} and the corrected Akaike Information Criterion AIC_c in this Report (*Akaike*, 1973, 1974; *Sugiura*, 1978; *Poeter and Hill*, 2007). These model comparison metrics are provided alongside F_{obj} in Table 8.2.

In most cases, the maximum likelihood objective function varies coincidentally with the value of the objective function (*Hill and Tiedeman*, 2007, Appendix A). It is used in this work to calculate the AIC_c, and can be calculated as,

$$F'_{\text{obj}} = (N_d + N_{pr}) \ln 2\pi - \ln|\omega| + F_{\text{obj}} \tag{8.3}$$

where $|\omega|$ is the determinant of the weight matrix. In our application, $N_d = 20$ and $N_{pr} = 0$. As we weight each patch equally (as defined in Chapter 6), in our application ω is a vector of ones of length N_d.

F_{obj} and F'_{obj} contain information about model-data fit, but contain no information about the number of free parameters in a given model. Models with more free parameters are expected to perform better than models with fewer free parameters, all else equal, simply because there are more fitting parameters. The new parameters can only be considered to significantly improve the model if the improvement is "sufficient"; in other words, if the improvement in objective function is more than would be expected from the addition of an extra fitting parameter. Several model-comparison metrics have been developed that combine the objective function with a penalization based on the number of free parameters. With these metrics, the definition of "enough" is that the improved model fit needs to overcome the penalty incurred by the added parameters.

Following the recommendations of *Burnham and Anderson* (2003, page 66), we use the AIC$_c$, which is defined as

$$\mathrm{AIC}_c = F'_{\mathrm{obj}} + 2N_p + \frac{2N_p(N_p+1)}{N_d + N_{pr} - N_p - 1} \ . \tag{8.4}$$

where N_p is the number of parameters in the model. Thus, a model with more parameters will be penalized by having a higher value of AIC$_c$, all else equal.

8.6 Definition of Multi-Model Calibration Success

Five criteria are used to determine whether the calibration of a particular model was successful:

Criterion 1: The simulated terrain evolution should make sense given the process representation within the specific model. For example, a model that uses a linear creep law is expected to simulate plateau edges that are smoother than the real ones. Simulations that contradicted basic understandings such as this would be suspect.

Criterion 2: The best-fit parameters obtained from the calibration should not fall on the boundaries of the imposed parameter space. If the best-fit value of a particular parameter ends up at the high or low extreme of its range, a contradiction is evident. One possible explanation for such an outcome would be that the model is not correctly representing processes related to the parameter, and as a result the parameter is "trying to make up for" this model deficiency. An exception to this general rule is the case of insensitive parameters that have such minimal influence that nearly any value would produce the same objective function; in this case, the calibrated best-fit value makes little difference, and values near the edge of the range are considered permissible.

Criterion 3: Any multi-element model that would mimic the Basic model if some parameters were set to specific values should have an equal or lower best-fit objective-function score. For example, model BasicVm is identical to Basic in all respects except that it treats the drainage-area exponent m as a calibration parameter, rather than fixing it at 1/2 (see Appendix A). Because $m = 1/2$ falls within the assigned parameter range, it is possible for BasicVm to exactly mimic Basic. For models in this category, their best-fit objective function score should be at least as good (i.e., at least as small) as the score for Basic. Failure of such a model to out-perform Basic would indicate that the calibration became stuck in a local minimum in objective-function space. The exceptions to this criterion are cases for which the parameter space does not allow a model to mimic Basic. For example, although model BasicVs would theoretically reduce to Basic if its hydraulic conductivity parameter were allowed to become zero, the assignment of a range for conductivity that does not include zero precludes the model from reproducing the behavior of the Basic model.

Criterion 4: Any multi-element model whose range includes one or more simpler models should out-perform the simpler model(s). For example, model BasicRtTh, which uses an erosion threshold ("Th") and treats rock and till separately ("Rt"), should out-perform both BasicRt and BasicTh. (This is a generalization of Criterion 3.)

Criterion 5: A model calibration should be able to complete in a reasonable amount of time. "Reasonable completion time" was considered to be 24 hours on one core of the

University of Colorado Summit heterogeneous supercomputing cluster (https://www.rc.colorado.edu/resources/compute/summit). The 24 hour limit is due to the wall-time limits for entry into the standard queue on Summit. We did a small number of tests to determine whether relaxing this limit from 24 hours to 7 days resulted in increased completion and it did not. Seven days is the longest possible job time on Summit so increasing job length beyond this limit was not possible.

Of the 37 models for which calibration was attempted, the inability of some to meet criteria 3 and 4 resulted in the redesign of the calibration method used. Once this was accomplished, 34 of the models met all five criteria. Calibration jobs for three of the 37 models failed to complete within 24 hours, and showed signs that completion would require considerably more than 24 hours. These jobs were therefore not continued, and calibration of these models was considered unsuccessful. Further discussion of the three models that did not calibrate is given in Section 8.8.

8.7 Calibration Algorithms

In this section we provide information about the four optimization algorithms used in the final results. We discuss two local methods, Gauss-Newton and NL2SOL, and two global methods, Efficient Global Optimization and Bayesian calibration. As with the sensitivity analysis, calibration was performed using methods available through the Dakota Package (*Adams et al.*, 2017a).

8.7.1 Gauss-Newton

The Gauss–Newton algorithm is an optimization method that modifies Newton's method for finding the minimum of a function to address nonlinear least squares problems. Here nonlinear least squares refers to a problem for which a set of data is used to find the values of a set of unknown input values to a nonlinear function in an over-determined context. The Gauss–Newton algorithm is only applicable to objective functions that are the sum of squared residual values; however, it does not require knowledge of the second derivatives.

Quoting from the Dakota User Manual, version 6.6, *Adams et al.* (2017a, page 149):

> Dakota's Gauss-Newton algorithm consists of combining an implementation of the Gauss-Newton Hessian approximation (see Section 7.2) with full Newton optimization algorithms from the OPT++ package (*Meza et al.*, 2007) (see Section 6.2.1.1). The exact objective function value, exact objective function gradient, and the approximate objective function Hessian are defined from the least squares term values and gradients and are passed to the full-Newton optimizer from the OPT++ software package. As for all of the Newton-based optimization algorithms in OPT++, unconstrained, bound-constrained, and generally-constrained problems are supported. However, for the generally constrained case, a derivative order mismatch exists in that the nonlinear interior point full Newton algorithm will require second-order information for the nonlinear constraints whereas the Gauss-Newton approximation only requires first order information for the least squares terms.

8.7.2 NL2SOL

After our initial work using only the Gauss-Newton method, we explored a number of global methods and eventually settled on a hybrid approach that first uses the Efficient Global Optimization (EGO) algorithm to locate an approximate minimum using a surrogate, and then uses gradient-enabled NL2SOL to refine the identified minimum using complex model evaluations. We elected to use NL2SOL instead of the Gauss-Newton method because our problem is highly nonlinear and has non-zero residuals. The Dakota Documentation states that: "Least squares solvers may experience difficulty when the residuals at the solution are significant, although experience has shown that Dakota's NL2SOL method can handle some problems that are highly nonlinear and have nonzero residuals at the solution" (*Adams et al.*, 2017a, pg 147).

Additional information about the NL2SOL method comes from the Dakota User Guide, version 6.6, *Adams et al.* (2017a, page 150):

> The NL2SOL algorithm (*Dennis et al.*, 1981) is a secant-based least-squares algorithm that is q-superlinearly convergent. It adaptively chooses between the Gauss-Newton Hessian approximation and this approximation augmented by a correction term from a secant update. NL2SOL tends to be more robust (than conventional Gauss-Newton approaches) for nonlinear functions and "large residual" problems, i.e., least-squares problems for which the residuals do not tend towards zero at the solution.

This method was developed in the 1980s based on a need for a nonlinear least-squares algorithm that would be more reliable than Gauss-Newton or Levenberg-Marquardt in large residual cases.

8.7.3 Efficient Global Optimization (EGO)

We found success with the *Efficient Global Optimization* algorithm (*Jones et al.*, 1998), which is a global method that uses a surrogate. Quoting from the Dakota Users Manual, *Adams et al.* (2017a, page 129),

> Efficient Global Optimization (EGO) is a global optimization technique that employs response surface surrogates (*Jones et al.*, 1998; *Huang et al.*, 2006). In each EGO iteration, a Gaussian process (GP) approximation for the objective function is constructed based on sample points of the true simulation. The GP allows one to specify the prediction at a new input location as well as the uncertainty associated with that prediction. The key idea in EGO is to maximize an Expected Improvement Function (EIF), defined as the expectation that any point in the search space will provide a better solution than the current best solution, based on the expected values and variances predicted by the GP model. It is important to understand how the use of this EIF leads to optimal solutions. The EIF indicates how much the objective function value at a new potential location is expected to be less than the predicted value at the current best solution. Because the GP model provides a Gaussian distribution at each predicted point,

expectations can be calculated. Points with good expected values and even a small variance will have a significant expectation of producing a better solution (exploitation), but so will points that have relatively poor expected values and greater variance (exploration). The EIF incorporates both the idea of choosing points which minimize the objective and choosing points about which there is large prediction uncertainty (e.g., there are few or no samples in that area of the space, and thus the probability may be high that a sample value is potentially lower than other values). Because the uncertainty is higher in regions of the design space with few observations, this provides a balance between exploiting areas of the design space that predict good solutions, and exploring areas where more information is needed. There are two major differences between our implementation and that of *Jones et al.* (1998): we do not use a branch and bound method to find points which maximize the EIF. Rather, we use the DIRECT algorithm. Second, we allow for multiobjective optimization and nonlinear least squares including general nonlinear constraints. Constraints are handled through an augmented Lagrangian merit function approach (see Surrogate-Based Minimization chapter in Dakota Theory Manual (*Adams et al.*, 2017b).

8.7.4 Bayesian Calibration using Delayed Rejection Metropolis Hastings Markov Chain Monte Carlo

After successfully identifying optimal parameter sets using a hybrid EGO-NL2SOL method, we assessed whether the linear parameter confidence intervals were reasonable. After determining that they were not reasonable, we identified Bayesian calibration using a surrogate as an appropriate method to determine parameter confidence intervals.

In Bayesian calibration, a *prior distribution* of a parameter set θ is updated based on data in a Bayesian framework to determine a *posterior distribution*. We used the distribution identified by hybrid EGO-NL2SOL as our prior distribution. Following *Adams et al.* (2017a, pg 105, Section 5.8), we present a basic overview of Bayesian calibration followed by a description of the specific implementation we used.

Consider a prior distribution for parameters $f_\theta(\theta)$. The likelihood function $\mathcal{L}(\theta; d)$ describes the support for parameter values based on data d. Bayes Theorem (*Jaynes and Bretthorst*, 2003) is used to write an expression for the posterior parameter distribution $f_{\theta|d}(\theta|d)$,

$$f_{\theta|d}(\theta|d) = \frac{f_\theta(\theta)\mathcal{L}(\theta; d)}{f_D(d)} \,. \tag{8.5}$$

The likelihood function implemented in Dakota takes the difference between modeled and observed quantities as Gaussian. As with many Bayesian calibration implementations, Dakota uses Markov Chain Monte Carlo (MCMC) sampling to estimate the posterior parameter distribution and provides four implementations of Bayesian calibration. Each of these implementations provides a number of different options and functionalities. We use the Delayed Rejection Adaptive Metropolis (DRAM; *Haario et al.*, 2006) sampling method within the Quantification of Uncertainty for Estimation, Simulation, and Optimization (QUESO) package (*Prudencio and Schulz*, 2012). Note that so far no assumptions as to the nature of the posterior parameter distribution have been made.

Bayesian calibration methods require tens to hundreds of thousands of model evaluations for the MCMC sampling method to estimate the posterior parameter distribution. This is not feasible given our model run times, and thus we needed to use a method that supported the use of a surrogate. At the conclusion of a successful Bayesian calibration an empirical estimate of the posterior distribution is produced. In our application, this estimate has 100,000 samples.

We chose the QUESO-DRAM implementation because QUESO is the only Bayesian calibration method in Dakota that provides the ability to adaptively refine a surrogate. This means that after doing an initial set of complex model samples, QUESO-DRAM preforms a MCMC estimation of the posterior density, identifies a set of new parameter values at which to do complex model evaluations, updates the surrogate, and then refines the MCMC posterior estimate. Given our use of a surrogate and the highly nonlinear nature of our objective function, we decided that adaptive refinement was a good quality to have in a calibration method. It is important to note that no convergence criteria exist for Bayesian calibration with an adaptively refined surrogate in Dakota. Thus we performed 10 adaptive refinement steps and manually assessed the stability of the solution (see Figure 8.7 for example results and Appendix C for the complete set of results). We used Dakota's default values for the Gaussian Process surrogate, and dictated that the initial surrogate be constructed based on a Latin Hypercube sampling with twenty times the number of free parameter points.

We chose to use the DRAM sampling algorithms because the Dakota online reference manual states: "If the user knows very little about the proposal covariance, using DRAM is a recommended strategy. The proposal covariance is adaptively updated, and the delayed rejection may help improve low acceptance rates."

Note that it was not computationally feasible to make projections with the full 100,000 sample estimate of the posterior distribution. In projection we constrain uncertainty associated with parameter calibration by making 1000 complex model evaluations for each model, using those model evaluations to construct a surrogate of projected quantities, and then sampling from that surrogate.

8.8 Results

8.8.1 Overview

The first attempt at calibrating the suite of 37 alternative models used the Gauss-Newton algorithm described in Section 8.7.1. The results of this method provided evidence for solutions that identified local minima nowhere near the global minimum, and therefore did not meet Criterion 3 or 4 for calibration success. This effort also yielded evidence that the topographically based objective function contains many small local minima, and thus would likely benefit from a surrogate method to help smooth over these small-amplitude variations. This discovery motivated the use of the hybrid approach described above, which applies EGO followed by NL2SOL.

NL2SOL only gives confidence estimates based on linear theory. Because the objective function turns out to be relatively flat in some dimensions at the minimum point, these linear-

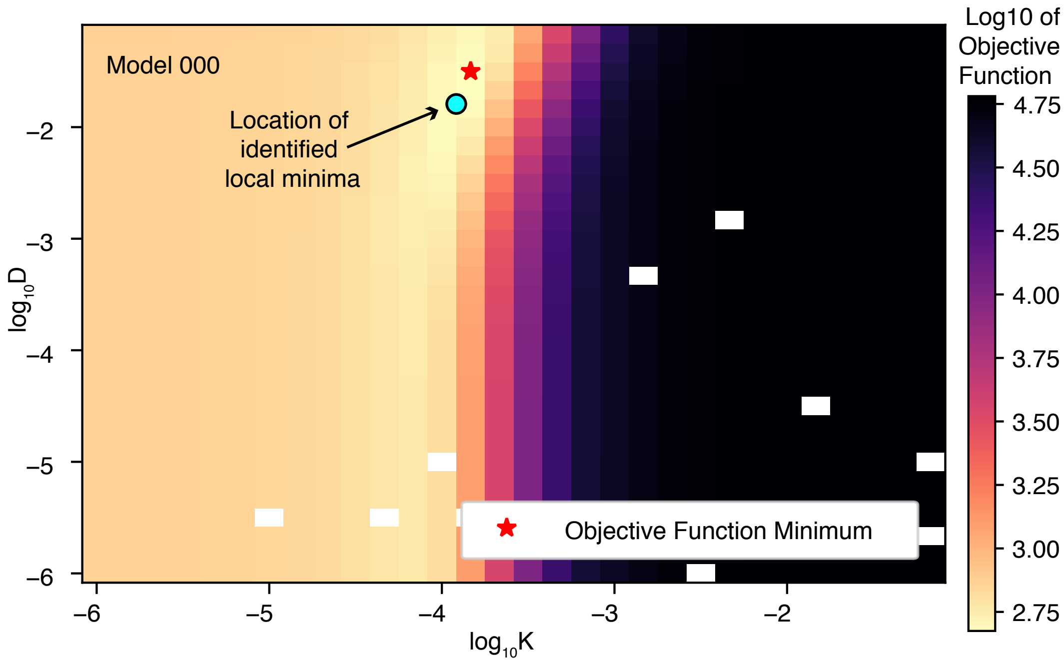

Figure 8.1: Objective function surface for model Basic (000) characterized by a grid search of size 31x31 (a total of 961 model evaluations). White squares indicate model evaluations that had not completed when the graphic was rendered.

estimate confidence intervals are larger than they should be given the actual shape of the objective function. Because an important outcome of the calibration effort is the estimation of parameter confidence intervals, we sought a more appropriate method for estimating the posterior parameter distributions. This led to the choice of Bayesian calibration on a Gaussian process surrogate using the DRAM sampling algorithm in the QUESO package, as described above.

8.8.2 Nature of Basic Model (000) Objective Function Surface

Before undertaking calibration efforts for any model, we made a grid search of 961 (31x31) points on model Basic (000) in order to characterize the objective function surface for this model. We chose Basic for this exercise for two reasons. First it is one of only two dual-parameter models in the 37 model suite (all other models have three or more parameters). Because the parameter space is restricted to two dimensions, we can populate the parameter space more densely with a given number of model evaluations and can visualize its objective function on a 2D plot. Second, model Basic contains two ingredients that are present (in some form) in all of the models: D a parameter controlling soil gravitational transport, and K, a parameter controlling the efficiency of water erosion. (Note: the water erosion coefficient takes different forms in different models, but its role is fundamentally similar among all models; see Chapter 5).

The Basic objective function surface shows three primary domains (Figure 8.1). First, in tan and on the left, is a flat region with objective function values that are relatively low, but not as low as the global minimum. This region corresponds to model runs in which little or no erosion occurred. The existence of a corresponding relatively flat zone on the objective-function surface makes sense given that the overall shape of the postglacial topography and the modern topography are similar: models with little erosion get a moderate score that reflects their "success" in not eroding the preserved plateau remnants. Second, in black and on the right, is a region with very high objective function values. In this region, too much erosion occurred due to high values of K, the parameter that controls the ability of rivers to incise. Finally, in between these two regions, lies a narrow band of lower objective values (in yellow on Figure 8.1). For low values of D, the location of this trough is only influenced by the value of K. For higher values of D, we see that the orientation of the trough is influenced by both D and K. Adjacent to the global minimum point (shown with a red star) is a region with similarly low objective function values. We examined the objective function for local minima and (at the scale of our grid search) found one at slightly lower K and D values than those that correspond to the global minimum identified in the grid search (this local minimum is shown with a cyan circle in Figure 8.1).

Examining this objective function surface, we can conclude that the objective function is non-Gaussian for the Basic model. We can also conclude that there are large regions of parameter space that are quite flat. Thus careful choice of convergence criteria and algorithm step size are likely to be important in the success of applying a gradient-based method like Gauss-Newton. While the grid search illustrated in Figure 8.1 reveals one local minimum in the vicinity of the global minimum, there are likely others that are not apparent at this resolution, and it is not yet clear how extensive such features are in the objective function.

8.8.3 Initial Calibration Attempt with Gradient-Based Algorithm

In each step of the calibration procedure, we began our efforts using only model Basic (000), then extended the method to model BasicRt (800) (a three-parameter model), and finally extended the method to all models. In this way we were able to first work with a calibration method on the computationally fastest model, which is also one of the only two-parameter models in the 37-model suite.

Initial Gauss-Newton model runs with model Basic (000) successfully found the approximate location of the global minimum shown in Figure 8.1. However, calibrations of other models did not meet Criteria 3 or 4 for calibration success. These criteria state that a model that can subsume other models through parameter choice should calibrate to have an objective-function value that is at least as good as those of the simpler model(s). It was a challenge to get model Basic (000) to successfully find the global minimum. Getting this method to work took careful identification of appropriate step sizes, starting locations, and convergence criteria (see the Dakota .in files for all values used). In initial calibrations of Basic as well as follow-on trial calibrations with other models, we found that many models produced calibration results with unrealistically low K and D values, resulting in little to no erosion (shaded region in lower left of Figure 8.2).

In order to understand this issue, we made a high-resolution series of parameter studies on the Basic model. Figure 8.3 shows two transects in the vicinity of the objective function minimum determined based on a grid search (Figure 8.1). The results confirm the presence of many small local minima in the vicinity of the objective function minimum. Based on this result we decided to pursue an alternative method for calibration that is more robust to

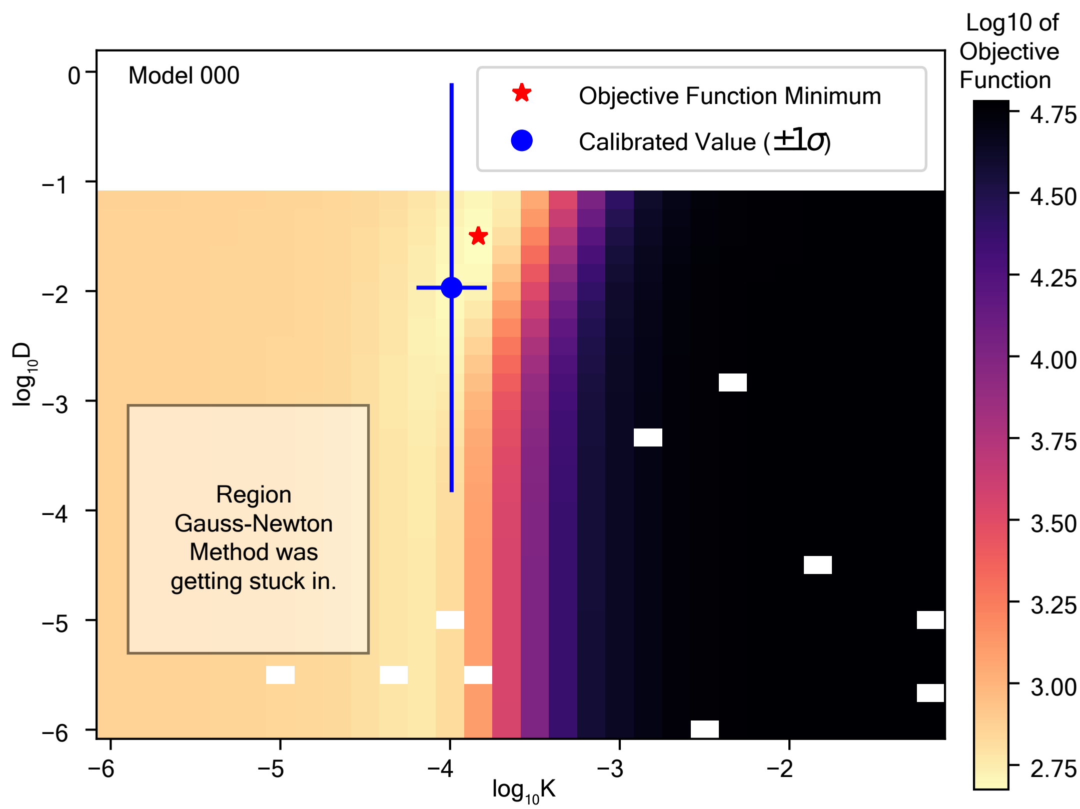

Figure 8.2: Objective function surface for model Basic (000) characterized by a grid search of size 31x31 (a total of 961 model evaluations). Red star indicates the objective function minimum based on the grid search and the blue circle indicates the result of EGO-NL2SOL calibration (with 1σ error bars). White squares indicate model evaluations that had not completed when the graphic was rendered.

the presence of local minima.

It is important to note that these results highlight the information gained by being able to carefully characterize the properties of the objective-function surface. While our ultimate results presented in Section 8.8.4 meet the success criteria listed in Section 8.6, we were not able to interrogate the objective function surfaces of all models in the same way we assessed the Basic model. As we discuss in Section 8.9, a likely improvement to the approach is to further refine the objective function such that the local minima are reduced or eliminated. We were also unable to diagnose the source of this property of the objective function (e.g., is it a true property of this sort of model or is a model artifact such as those described by *Kavetski and Kuczera* (2007); *Clark and Kavetski* (2010); *Kavetski and Clark* (2010)).

8.8.4 Calibration of Models with a Hybrid Global Surrogate and Gradient-Based Algorithm

After attempting calibration with the Gauss-Newton method, we explored calibration with a number of non-surrogate global methods available in Dakota, including Adaptive Mesh, Direct, and Basinhopping. We finally found a workable calibration methodology that first uses the EGO surrogate based global method described in Section 8.7.3 and then uses the NL2SOL method described in Section 8.7.2. We settled on this method because it was the first calibration method that we tried that provided results that met the criteria for calibration success identified in Section 8.6.

We verified that the hybrid EGO-NL2SOL method found the correct region of the objective function minimum for model Basic and model BasicRt. In Figure 8.2 we show the objective function surface, grid search minimum objective function, and the calibrated value using EGO-NL2SOL. As is evident from this figure, this method did not find the global minimum, but found a local minimum very close to the global minimum earlier identified in Figure 8.1. Given that we are unable to demonstrate convexity for our models, and run times prohibit comprehensive grid search, we must accept that an unknown number of subsequent solutions are local minima. However, we designed the success criteria carefully with this reality in mind.

Of the 37 models for which calibration was attempted, we were able to successfully calibrate 34 of them. The objective function values as well as the upper bounds of the calibration confidence intervals are shown in Figure 8.4. The objective function at the end of the EGO method (prior to refinement using NL2SOL), the final objective function, the upper bound of the confidence intervals constructed both with the Student T and the F distribution, the maximum likelihood objective function, and the AIC$_c$ are all presented in Table 8.2. Additional tables listing the parameter confidence intervals estimated using NL2SOL are presented in Appendix C. Figure 8.5 demonstrates that the addition of NL2SOL after EGO results in finding deeper objective function minima than EGO2 alone. Figure 8.6 shows an example of a calibrated model. Additional figures like this one, for every successfully calibrated model, can be found in Appendix C. These figures show modeled modern topography, the amount of cumulative erosion from postglacial to present, the difference between modern actual and modeled topography, and the pattern of the residuals that go into the objective function calculation.

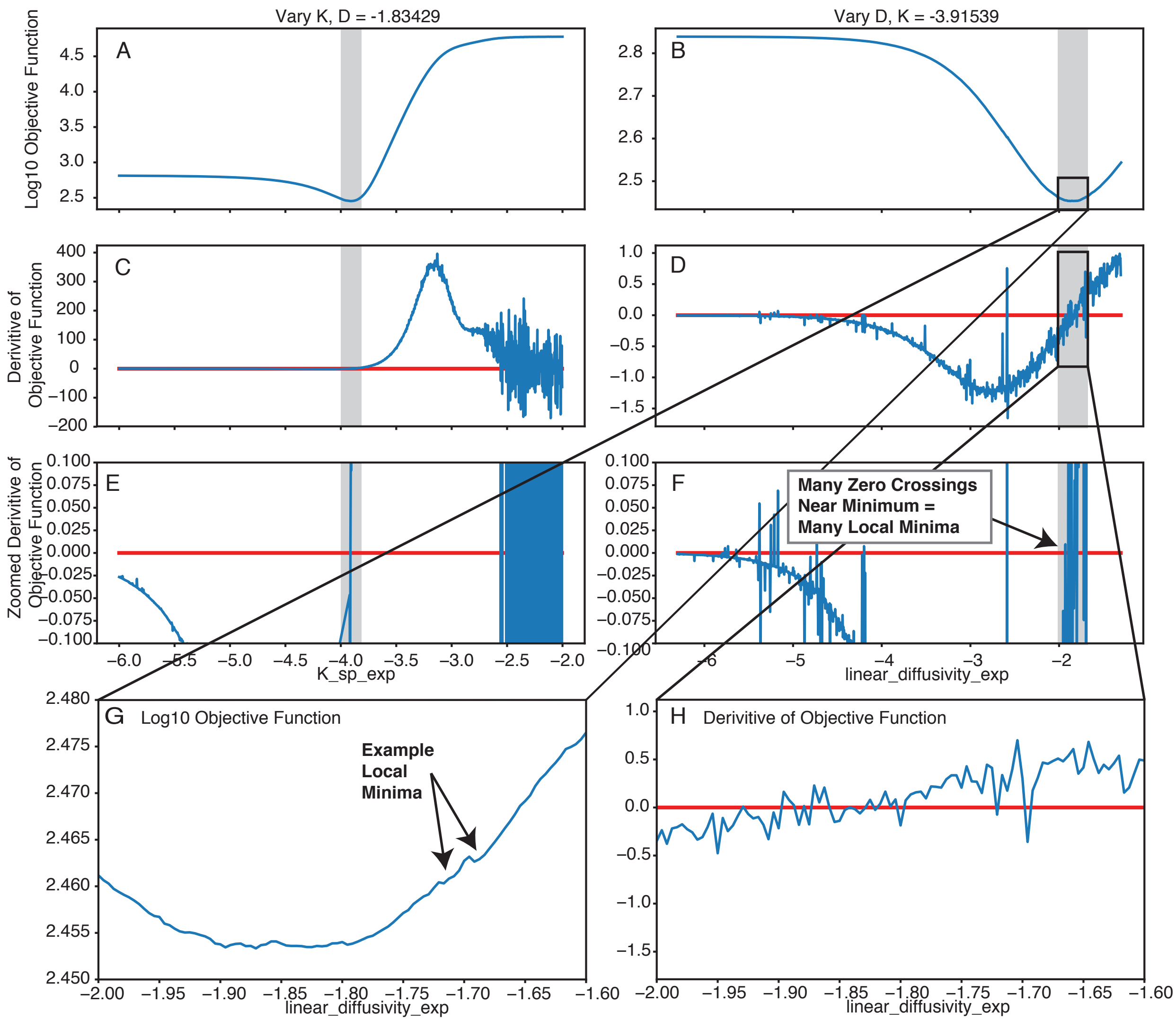

Figure 8.3: Line parameter study of Model 000 Basic that was evaluated in order to understand the properties of the objective function surface. The left-hand column shows a parameter study in which K was varied and D was fixed and the right-hand column shows a parameter study in which D was varied and K was fixed. The top two panels (A and B) show the $\log_{10}$ of the objective function while the second row of panels (C and D) show the first derivative of the objective function. The third row of panels (E and F) show a zoomed in version of panels C and D. Finally panels G and H show close ups of portions of panels B and D. As panel G shows, the objective function is bumpy, and this is manifested in multiple zero crossings in panel H. While these only show bumps in 1D, they are an indication that true local minima in 2D exist.

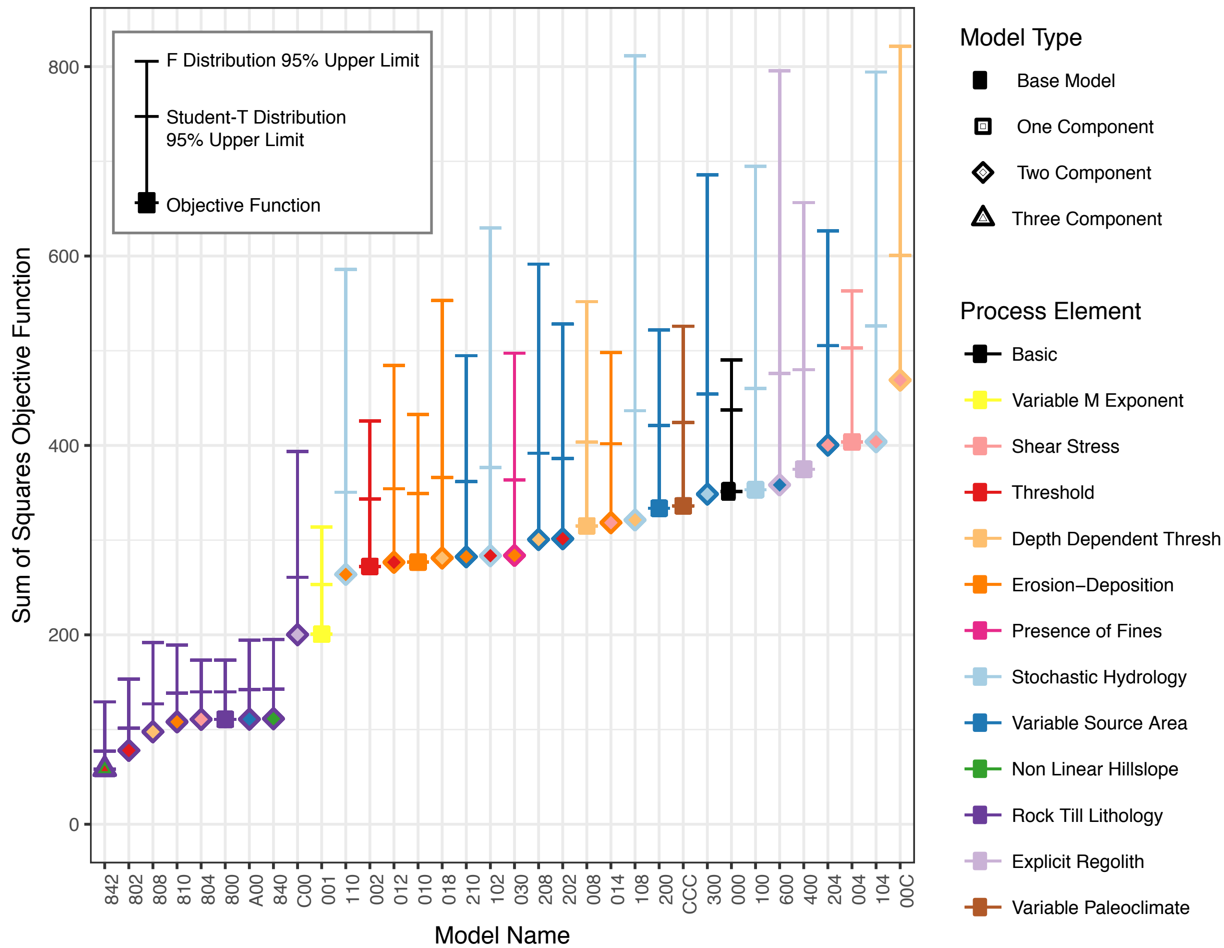

Figure 8.4: Summary of results from the EGO-NL2SOL calibration. Each model is represented by a single symbol and models are ranked from best on the left to worst on the right. Colors indicate model ingredients and both the Student-T and F distribution uncertainty estimates are presented.

The three models that did not successfully calibrate are BasicCh (040), BasicHySa (410), and BasicChSa (440). These three calibration failures appear to be the result of numerical stability and performance constraints in these particular models. Model BasicHySa is the least numerically stable model of the suite of 37 models, and examination of model log files indicated that it was not able to achieve consistently stable numerical solutions with the given parameter ranges and model timestep used. Models BasicCh and BasicChSa have an internal routine that reduces sub-time-step duration when needed to ensure numerical stability. When slopes are especially steep, the solution routine can demand very small internal timesteps, which in turn leads to prohibitively long run times. Because the most successful models turned out to be those that incorporate separate rock and till lithologies, and the three uncalibrated models lack this feature, it is likely that they would not have scored well had their calibrations completed.

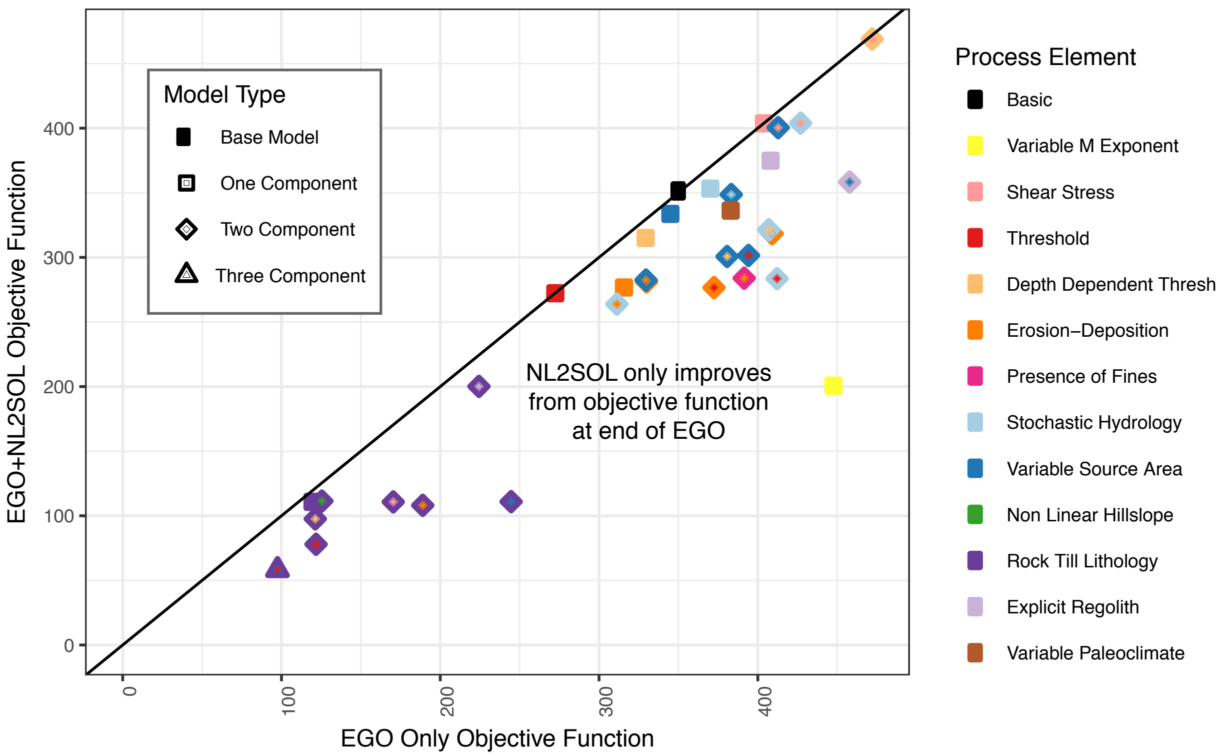

Figure 8.5: Comparison of objective function value at the end of EGO portion and at the combined end of hybrid EGO-NL2SOL calibration. As expected, addition of NL2SOL finds deeper minima that EGO alone. For reference a 1:1 line is shown.

Table 8.2: Summary of calibration results with the EGO + NL2SOL hybrid method for the Upper Franks Creek watershed domain. Models are ranked in order of final objective function.

Model ID	F_{obj} (EGO only)	F_{obj} (EGO + NL2SOL)	F_{obj} + $s^2 c_{95}$ (Student T)	F_{obj} + $s^2 c_{95}$ (F distribution)	Maximum Likelihood	AIC$_c$
842	97.5	58.2	77.3	129.2	106.0	124.4
802	121.8	77.9	101.5	153.3	123.9	138.2
808	121.3	97.6	127.1	192.0	143.5	157.8
810	189.0	108.1	138.4	189.3	152.2	162.9
804	170.4	110.7	139.7	173.2	153.0	160.5
800	119.6	110.8	139.8	173.3	153.1	160.6
A00	244.6	110.9	142.1	194.3	155.0	165.7
840	125.4	111.4	142.7	195.2	155.5	166.2
C00	224.4	200.1	260.8	393.7	246.1	260.4
001	447.6	200.7	253.2	313.9	243.0	250.5
110	311.2	263.8	350.5	585.8	311.6	330.0
002	272.5	272.3	343.5	425.8	314.5	322.0
012	372.5	276.6	354.3	484.6	320.7	331.4
010	315.7	276.7	349.2	432.8	319.0	326.5
018	329.9	281.1	366.3	553.0	327.1	341.4
210	329.6	282.5	361.8	494.8	326.6	337.2
102	412.1	283.5	376.7	629.6	331.3	349.8
030	391.4	283.9	363.6	497.3	328.0	338.7
208	380.7	300.7	391.7	591.5	346.6	360.9
202	394.1	301.5	386.2	528.2	345.6	356.3
008	329.4	315.0	403.5	551.8	359.1	369.8
014	409.0	318.4	401.8	498.0	360.7	368.2
108	406.9	321.3	436.7	811.4	371.0	394.3
200	344.9	333.6	421.0	521.8	375.9	383.4
CCC	382.9	336.2	424.2	525.8	378.4	385.9
300	383.3	348.6	454.2	685.8	394.6	408.9
000	351.7	351.4	437.6	490.2	391.8	396.5
100	370.1	353.2	460.2	694.8	399.2	413.5
600	457.8	358.3	476.0	795.6	406.1	424.6
400	408.0	374.7	480.0	656.4	418.9	429.5
204	412.8	400.5	505.4	626.5	442.8	450.3
004	403.8	403.8	502.8	563.3	444.2	448.9
104	427.0	403.8	526.1	794.3	449.7	464.0
00C	472.0	468.9	600.6	821.4	513.0	523.7

8.8.5 Determining Posterior Parameter Distribution for Most Successful Models with a Bayesian calibration Algorithm

One consistent feature of the EGO-NL2SOL results is that the parameter confidence intervals (i.e., blue bars in Figure 8.2) are larger than expected given prior information about parameter values and the overall shape of the objective function surface (see Tables in Appendix C). For example, in Figure 8.2 there is a large region with low objective function values that extends parallel to the D-axis, which would indicate that uncertainty in D is high. However, the extent of the blue bars—which only present 1σ—is much larger than the uncertainty in D that one would expect given the shape of the objective function surface. This result is likely due to the rather flat area around the objective function minimum (on the D axis), as the confidence interval is related to the curvature.

If we were only interested in identifying the optimal parameter value set for each model, issues with the confidence intervals might be ignored. However, an important result of our calibration effort is parameter confidence intervals, because these intervals provide a way to identify the component of uncertainty in projection associated with uncertainty in calibration.

Thus we undertook Bayesian calibration using the QUESO-DRAM method provided in Dakota and described by Section 8.7.4. We used the Bayesian calibration method on only the subset of nine models identified in Chapter 10 as appropriate for projection. The QUESO-DRAM method successfully completed for eight of the nine models. Model BasicRtCh (840) did not complete because the QUESO-DRAM algorithm wanted to make complex model evaluations in parts of parameter space where low S_c values made the runs too long to complete execution in a reasonable time frame. The primary result of Bayesian calibration is an empirical estimate of the joint posterior paramter distribution. Figure 8.7 provides an example of such as joint posterior distribution for the parameters in model BasicRtTh (802) after ten iterations of surrogate refinement. See Appendix C for tables showing the first four moments of the estimated distributions after ten iterations.

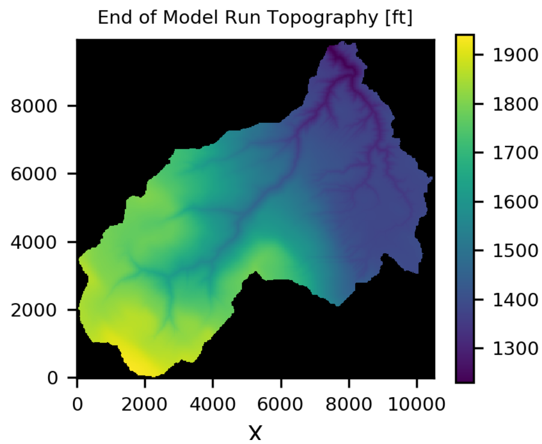

(a) Modeled modern topography.

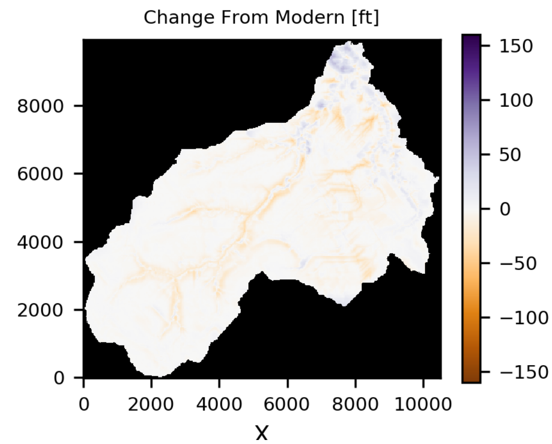

(b) Modeled modern topography minus actual modern topography. Purple indicates that modeled topography is above actual topography and orange indicates that modeled topography is below actual topography.

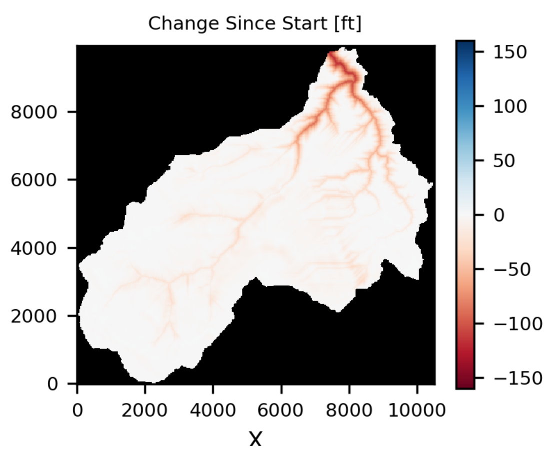

(c) Cumulative erosion from 13 ka to modern. Red indicates that erosion occurred, and blue indicates that deposition occurred.

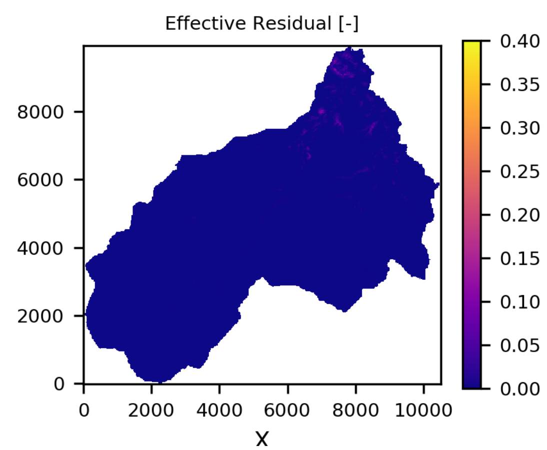

(d) Effective residual value at each grid node used in objective function calculation.

Figure 8.6: Calibration results summary for Model 842 showing spatially distributed values at the end of the 13 ka to present model run with calibrated parameter values in Franks Creek Watershed (SEW domain).

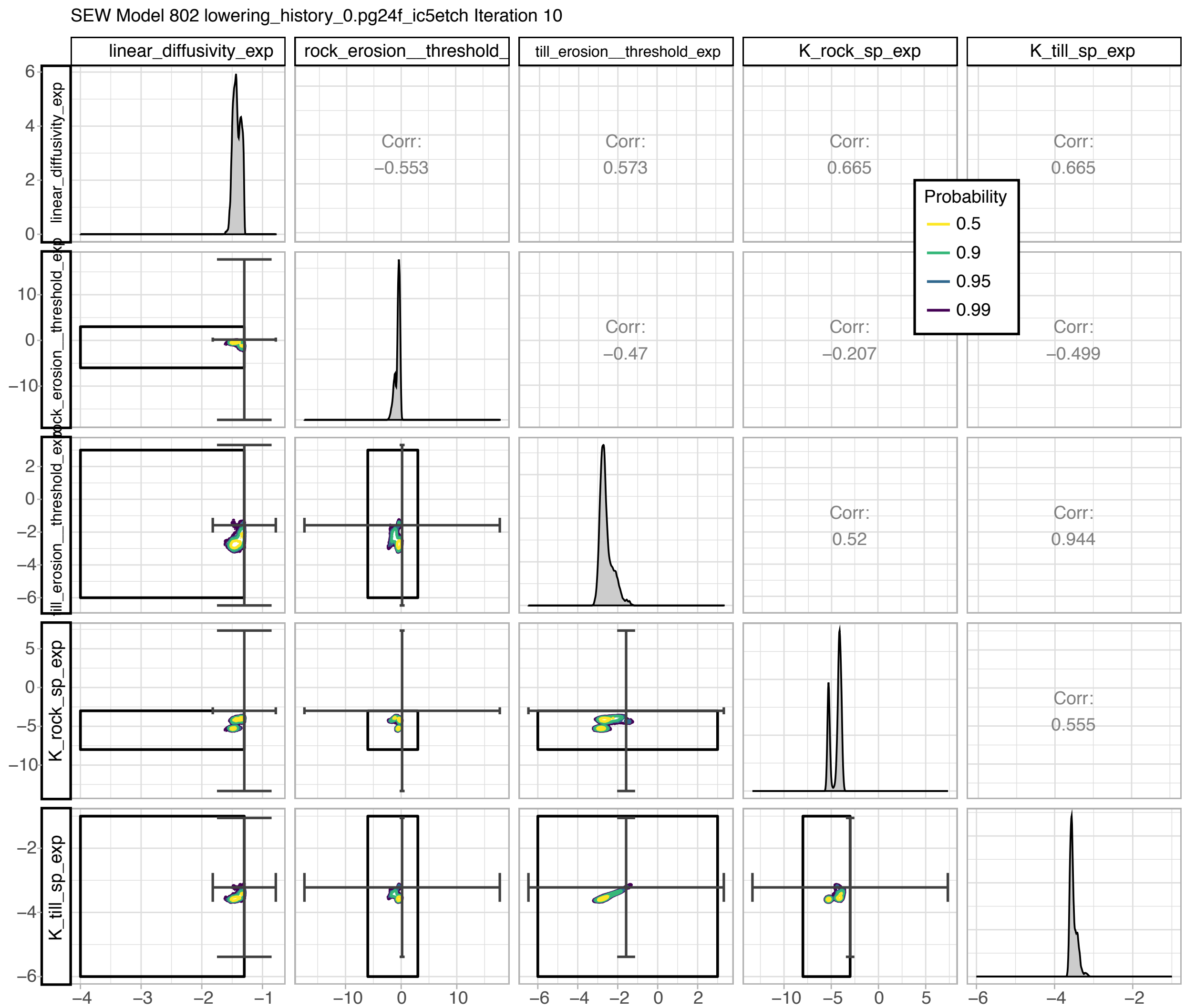

Figure 8.7: Posterior parameter distribution for model BasicRtTh at the end of ten iterations of surrogate refinement. Each row or column represents one of the five input parameters to this model such that the diagonal displays the marginal distribution of each parameter. The upper half of the matrix displays the parameter correlation and the colored lines present the two dimensional marginal distributions. The black box indicates the reasonable parameter range and the error bars indicate the 2σ confidence interval provided by EGO-NL2SOL.

8.9 Discussion

The discussion of calibration results is divided into three main subsections: identification of model ingredients that provide substantial model improvement, additional findings, and technical notes.

8.9.1 Model Ingredients that Improve Calibration Performance

Recall that one intention of the systematic variation of model ingredients used to construct the suite of 37 alternative landscape evolution models was to identify which ingredients improved model performance and how ingredients interacted to influence model results.

The calibration results overwhelmingly support the conclusion that models for the Franks Creek domain that differentiate between bedrock and glacial-related sediments (referred to informally here as "till") perform better than models that do not. These models all include the Rt component of Table A.2. This is evident in the group of best performing models, which all have purple outlines in Figure 8.4. The effect of including the Rt ingredient on the results is that the erodibility coefficient for bedrock by water is allowed to be smaller than that for till. This permits the incision of the channel network into the till plateau without extensive incision of the upper watershed.

To illustrate this conclusion, we contrast results from model Basic (000) and model BasicRt (800), which differ only in the inclusion of the Rt component (Figure 8.8). As the objective function puts more weight on erosion in the lower part of the drainage network and adjacent plateau, the calibrated model Basic over-incises in the upper parts of the watershed in order to do some incision in the lower part of the watershed. This results in modeled modern topography that has not incised enough in the lower part of the watershed but has incised too much in the upper part of the watershed. In contrast, model BasicRt has two values for erodibility, and is thus able to incise more in the lower part of the watershed while not incising excessively in the upper, bedrock-underlain portions of the watershed. There are still flaws in model BasicRt's performance. For example, the valley it incises into the till plateau is too narrow (shown by purple values adjacent to the valley in Figure 8.8d). The overly narrow valleys in both models reflect the use of a simple linear diffusion law for hillslope transport, rather than nonlinear law with a specified slope threshold (see Appendix A). Additionally, model BasicRt erodes more than it should in areas between channels, over much of the watershed (shown by light orange color over most of the domain in the right hand column).

Among the suite of eight two-element Rt models, the most successful are those two that include an erosion threshold, BasicRtTh (802) and BasicRtDd (808). To illustrate the improvement in model performance that comes from adding a threshold, we contrast model BasicRt and BasicRtTh in Figure 8.9. Model BasicRtTh includes two additional parameters that model BasicRt lacks: an erosion threshold for glacial sediments, and an erosion threshold for bedrock. In model BasicRtDd, which allows the erosion threshold to increase with progressive incision, it is the rate of change of threshold value with incision depth that varies between rock and glacial sediments.

In Figure 8.9 the calibrated models maintain incision of the main channels in the till plateau but do not over-erode away from the main channels. This is evident in the decrease

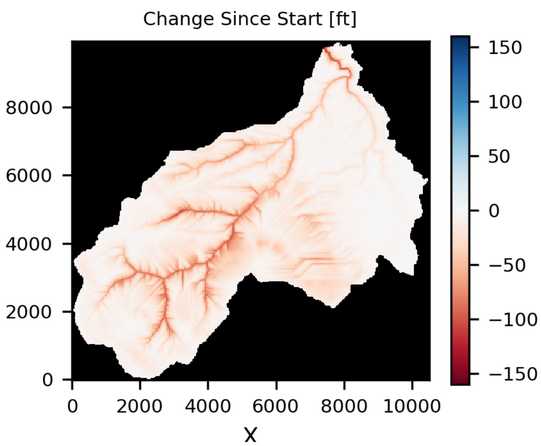

(a) Cumulative erosion from 13ka to present, Model Basic (000).

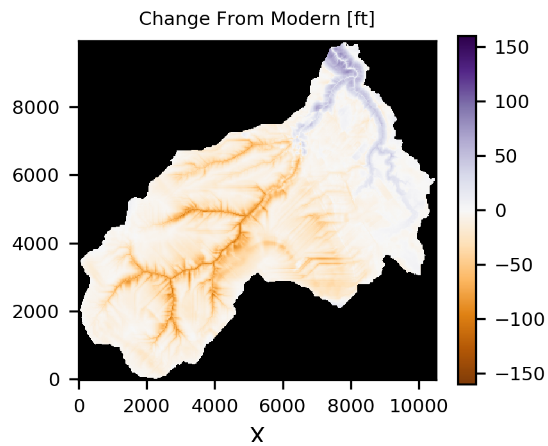

(b) Modeled modern topography minus actual modern topography, Model Basic (000).

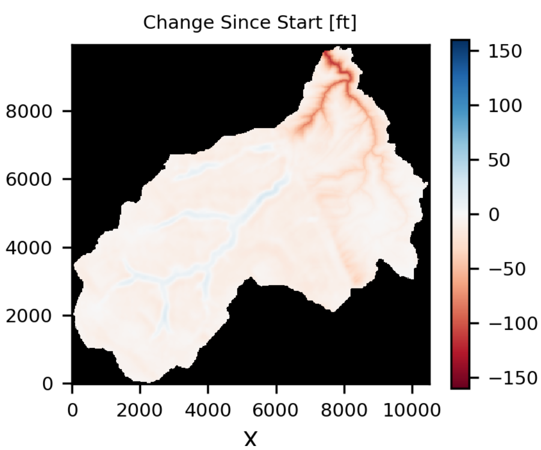

(c) Cumulative erosion from 13ka to present, Model BasicRt (800)

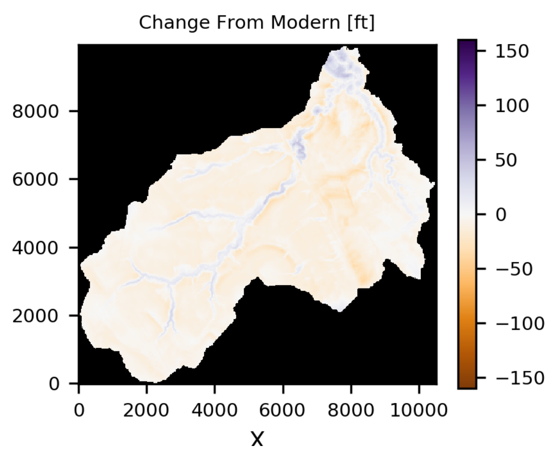

(d) Modeled modern topography minus actual modern topography, Model BasicRt (800).

Figure 8.8: Comparison of calibration results for models Basic and BasicRt. Left hand column indicates cumulative erosion from 13 ka to modern. Red indicates that erosion occurred, and blue indicates that deposition occurred. Right hand column shows modeled modern topography minus actual modern topography. Purple indicates that modeled topography is above actual topography and orange indicates that modeled topography is below actual topography.

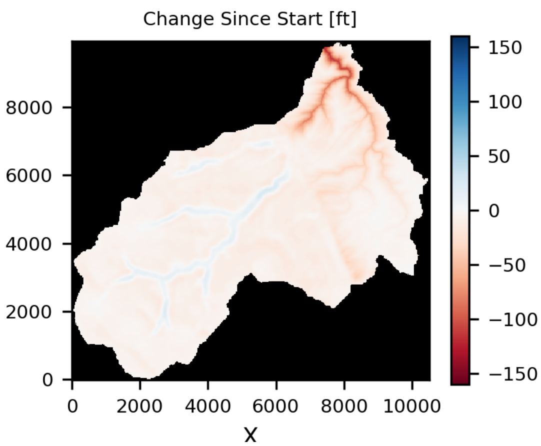

(a) Cumulative erosion from 13ka to present, Model BasicRt (800).

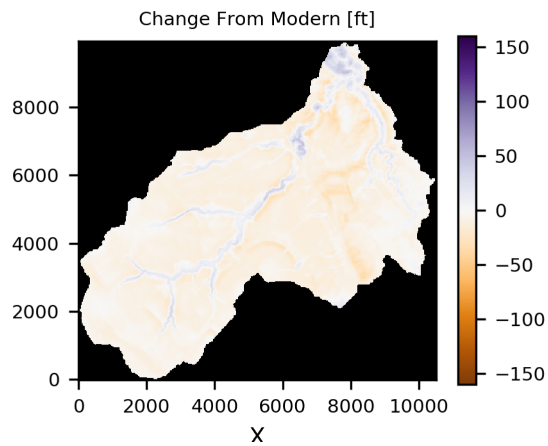

(b) Modeled modern topography minus actual modern topography, Model BasicRt (800).

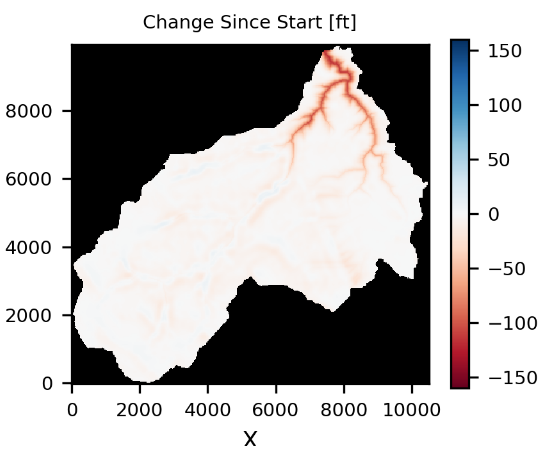

(c) Cumulative erosion from 13ka to present, Model BasicRtTh (802)

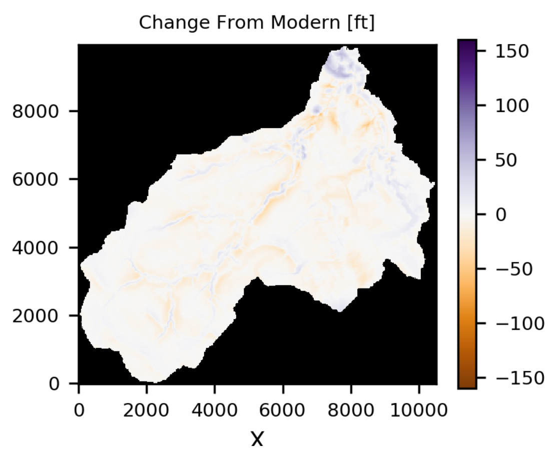

(d) Modeled modern topography minus actual modern topography, Model BasicRt (802).

Figure 8.9: Comparison of calibration results for models BasicRt and BasicRtTh. Left hand column indicates cumulative erosion from 13 ka to modern. Red indicates that erosion occurred, and blue indicates that deposition occurred. Right hand column shows modeled modern topography minus actual modern topography. Purple indicates that modeled topography is above actual topography and orange indicates that modeled topography is below actual topography.

in total erosion from panel (b) to panel (d) in the areas away from the main channels. The problem of insuffìcent erosion along the side-slopes of lower Franks Creek remains, but as in the case of model Basic, this is to be expected because neither BasicRt or BasicRtTh has a mechanism to create planar hillslopes.

Given the preliminary success of model BasicRtTh and the anticipated improvement the nonlinear hillslope component would provide due to the planar slopes adjacent to Franks Creek, we created a new model, BasicRtThCh (842). This model retains the rock-till map and use of erosion thresholds, and it also adds a nonlinear (Taylor series) model of downslope soil motion (see Appendix A for details on the formulation of this model). The nonlinear law has the property that it tends to create planar side-slopes with a gradient close to a specified threshold gradient, S_c. In Figure 8.10 we contrast the results of this new model with model BasicRtTh.

Two interesting subtleties in these calibration results are worth discussing. First, model BasicRtCh—which combines a nonlinear hillslope law with a rock-till map—does not perform substantially better than model BasicRt. Moreover, the calibrated value of its threshold gradient (S_c) parameter is at the upper limit of the permitted parameter range. This is an indication that in calibration BasicRtCh is attempting to recover the diffusive end member presented by BasicRt (Table C.30). We conclude that this occurs because without a threshold to prevent water erosion and incision away from the main channels, stream reaches with small contributing area in the upper part of the watershed experience water erosion and then create steep slopes that result in nonlinear hillslope motion. This then results in too much erosion in the upper part of the watershed and poor objective function values. One potential solution would be to modify the nonlinear hillslope component to allow for a spatially variable S_c, with different values assigned to bedrock and till domains.

Second, model BasicVm (001) does much better than all other single-component models except BasicRt. This result makes sense given the location of weaker till material in the lower elevation and higher drainage area portions of the model domain. The process change present in model BasicVm is a variable drainage area exponent. In model Basic, the value for m is set at 0.5 which means that, for a given channel slope, erosion is proportional to drainage area to the one-half power. This has the effect of more channel incision by water erosion in the downstream reaches of the major streams, where drainage area is larger. In the case of Franks Creek, these downstream reaches happen to correspond to the areas with thick till and deep incision. The calibrated value of m in BasicVm is 0.86, which describes a faster downstream increase (relative to the behavior if m were smaller) in the efficiency of water erosion with increasing drainage area. In other words, the calibration of model BasicVm uses a higher-than-expected value of m to compensate for the assumption of uniform lithology and allow the lower reaches of channels that cross the till plateau to incise more deeply. This property of model BasicVm is illustrated by Figure 8.11, which contrasts calibration results from models Basic, BasicVm, and BasicRt.

8.9.2 Additional findings

Here we expand on the primary calibration findings to summarize second-order conclusions related to which model ingredients are important (or not) to successful model performance.

One might expect that stochastic hydrology models (ingredient St), which have three free

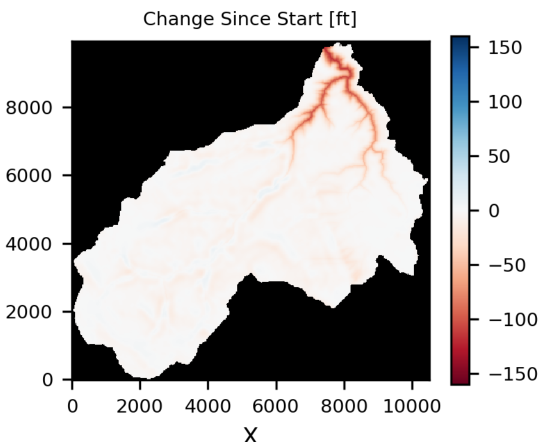

(a) Cumulative erosion from 13ka to present, Model BasicRtTh (802).

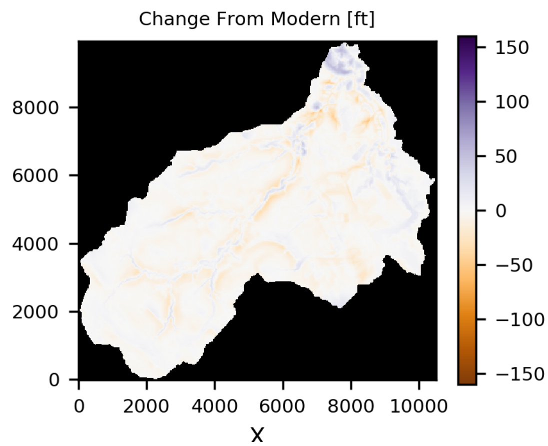

(b) Modeled modern topography minus actual modern topography, Model BasicRtTh (802).

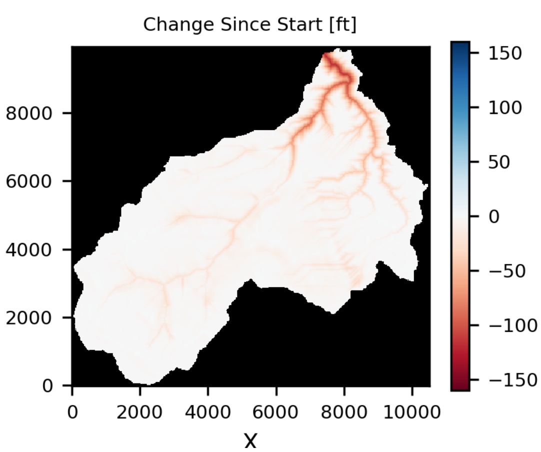

(c) Cumulative erosion from 13ka to present, Model BasicRtThCh (842)

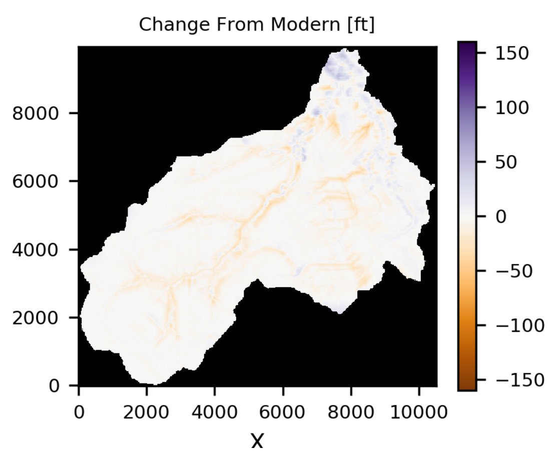

(d) Modeled modern topography minus actual modern topography, Model BasicRtThCh (842).

Figure 8.10: Comparison of calibration results for models BasicRtTh and BasicRtThCh Left hand column indicates cumulative erosion from 13 ka to modern. Red indicates that erosion occurred, and blue indicates that deposition occurred. Right hand column shows modeled modern topography minus actual modern topography. Purple indicates that modeled topography is above actual topography and orange indicates that modeled topography is below actual topography.

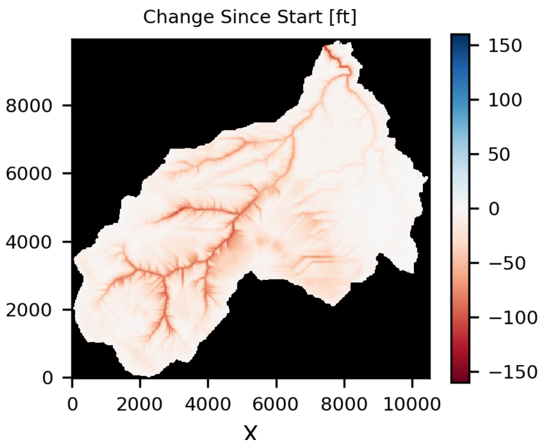

(a) Cumulative erosion from 13ka to present, Model Basic (000)

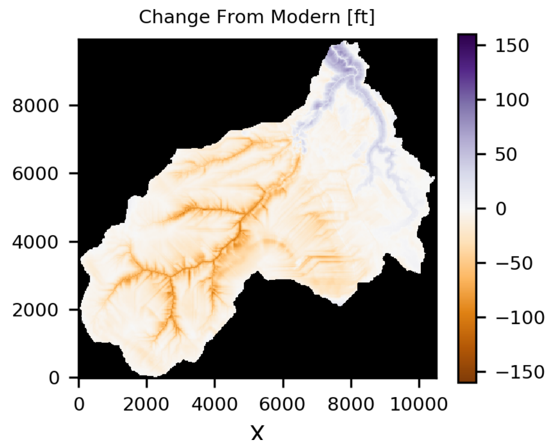

(b) Modeled modern topography minus actual modern topography, Model Basic (000).

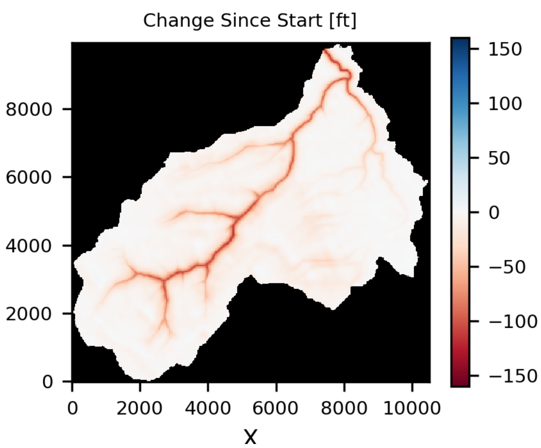

(c) Cumulative erosion from 13ka to present, Model BasicVm (001)

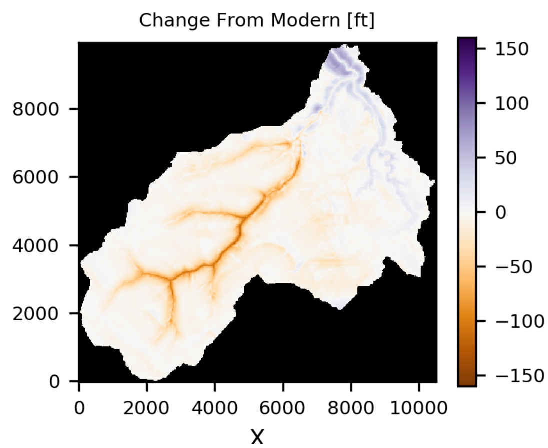

(d) Modeled modern topography minus actual modern topography, Model BasicVm (001).

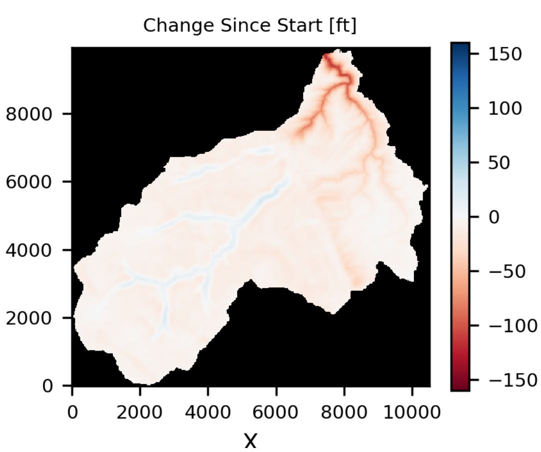

(e) Cumulative erosion from 13ka to present, Model BasicRt (800).

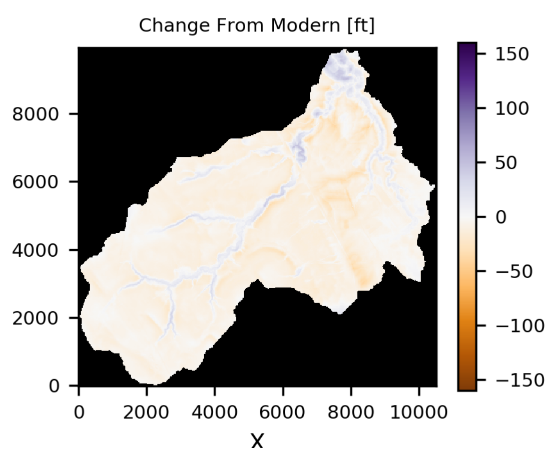

(f) Modeled modern topography minus actual modern topography, Model BasicRt (800).

Figure 8.11: Comparison of calibration results for models Basic, BasicVm, and BasicRt. See caption for Figure 8.10 for further explaination of Figure layout.

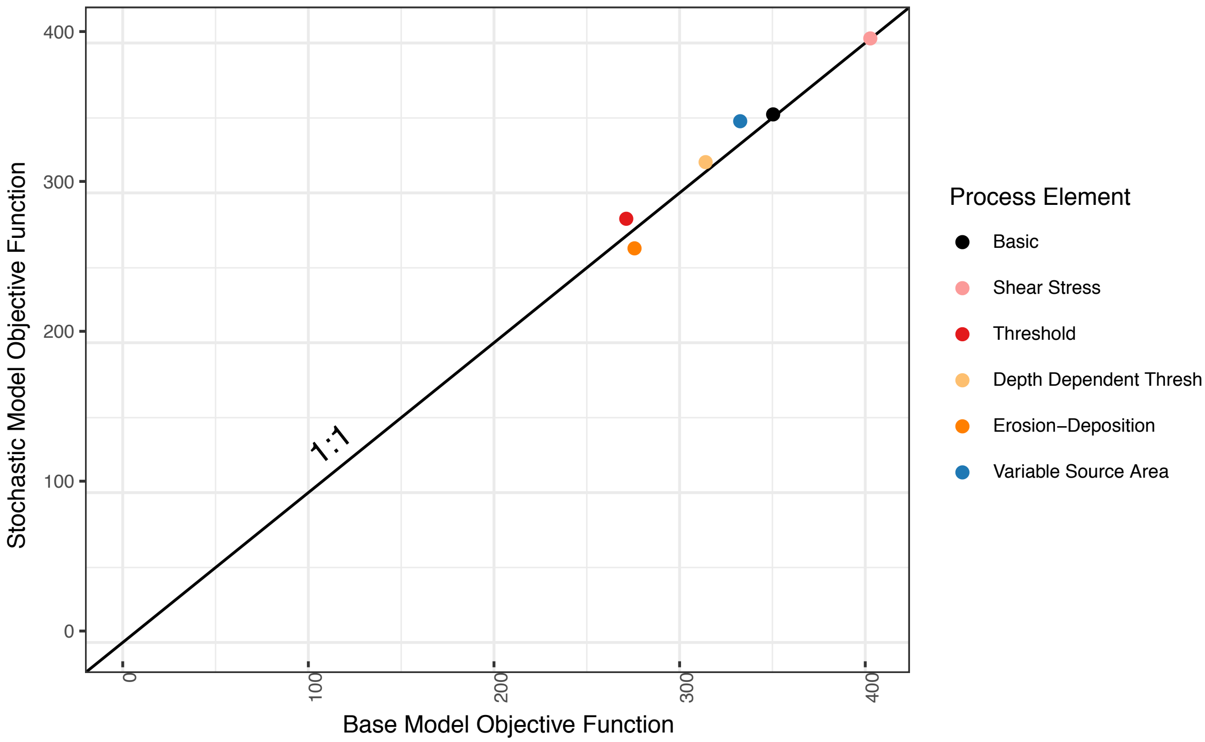

Figure 8.12: Comparison between base models and stochastic models for the six model pairs that include adding the St ingredient. Colors indicate the non-stochastic model ingredient. For reference a 1:1 line is shown.

parameters that control rainfall intensity and frequency, would be able to beat their deterministic counterparts. Our suite of 37 models includes six pairs of stochastic/deterministic models—that is, models that are identical in every respect except that one is deterministic and the other is stochastic (Figure 8.12). Examining the relative performance of these pairs permits us to identify whether explicitly treating stochastic variability in runoff improves model results. We find that stochastic models do not calibrate any better than their deterministic counterparts, even given their additional free parameters. We interpret this as an indication that explicitly treating the rainfall distribution does not provide additional explanatory power in this region. This result indicates that use of an "effective" erodibility factor appropriately subsumes the effects of sequences of high and low runoff.

None of the models that explicitly treat soil perform especially well. Examination of the resulting modeled topography (for example, for model BasicRtSa (C00) in Figure 8.13) indicates that the major drainages have cut steep-sided channels. Examination of the output files indicates that adjacent to these channels is a thin soil layer. Recall that in this model in order for bedrock to move by linear diffusion it must first weather to soil. We interpret the relatively poor performance of models with a dynamic soil layer to indicate that even with the highest justifiable soil production rates, soil cannot form fast enough in this model to keep up with rapid river incision. The model fails to account for the fact that the glacial material is capable of failing and moving downslope without first being transformed into soil by various weathering processes. A clear next step to improve this model would be to allow

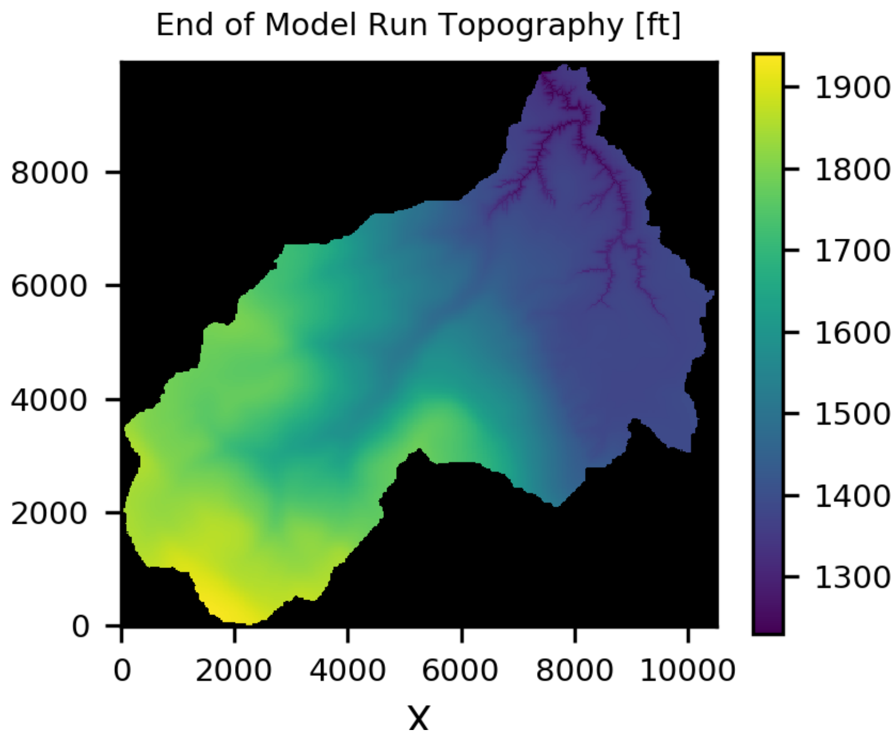

Figure 8.13: Calibrated simulation of modern topography using model BasicRtSa, which uses a dynamic soil layer together with a rock-till map.

soft lithologies such as till to move downslope through hillslope processes, and configure the model with two transport coefficients: a larger one that applies to soil, and a smaller one that permits the till to move without being first converted to soil.

Finally, we note that model BasicCc (CCC), which permits variation in K as a function of time in order to simulate paleoclimatic variations, only improves from Basic slightly. The relative insensitivity to time-variation in K is consistent with the finding from sensitivity analysis that such variations have a relatively weak impact on the model output, as measured by the objective function.

8.9.3 Technical Notes

Here we summarize a number of findings associated with the technical issues we faced in calibrating the EMS models.

The EMS models have a number of parameters that are process-critical but have little influence on the objective function. An example of such a parameter is the linear diffusivity coefficient D. In calibration, this parameter was associated with large uncertainties when using a least-squares method for calculating confidence intervals. For this sort of parameter, Bayesian calibration provides a more effective means of quantifying uncertainty bounds. Ultimately, this is an indication that the objective function could be refined such that it becomes more sensitive to process-critical parameters like D. The development of such objective functions for comparing observed and simulated topography is an open area of research.

Some calibration parameters are highly correlated with one another, which implies that changing one can have a similar effect on model output as changing the other. For example, the till erodability factor and the till threshold show a correlation coefficient of 0.944 (Figure 8.7). Such high correlation makes calibration challenging because the calibration algorithm can get the same objective function value by changing the two parameters in concert. Correlation among parameters was one of the motivating factors for the Bayesian calibration algorithm described above.

Finally, the objective function we developed has many local minima. Even with extensive effort to find a workable calibration method, the results comparing the grid search and final parameter value of EGO-NL2SOL on model Basic indicate that the calibration algorithm found only a local minimum, albeit one very close to the global minimum. In our use-case, in which it is not possible to prove convexity for any of our models, the possibility of local minima is a known issue. It was beyond the scope of this work to fully diagnose the origin of these minima. However, these results indicate that an avenue by which to improve this work would be to identify smoother, more robust objective functions.

8.10 Calibration on the Gully Domain

As we developed the calibration methodology presented in this chapter, we applied it in tandem to Franks Creek watershed and the Gully domain. However, we were not able to calibrate a model for the gully domain due to a combination of factors. In this section we discuss them so that future work can benefit from our attempt.

When we calibrated the models for the gully domain, the model ranking did not meet the success criteria outlined in Section 8.6. This result might indicate that the objective function we constructed does not provide information for successful calibration when using the gully domain. In performing a full sensitivity analysis on the gully domain, we found that the erosion models displayed similar responses regardless of which domain was used.

One reason we think the objective function may be behaving differently between the two domains is the absense of near-surface bedrock in the gully domain. While Franks Creek and the validation site have two regions, associated with rock and till, respectively, the gully site is underlain by till throughout.

Finally, we ran into substantial computational issues running the Ch variant (nonlinear hillslope) models on the gully domain. The Franks Creek results indicate that nonlinear hillslope transport is an important model ingredient for capturing the shape of the valley side-walls. This particular process component has an internal stability criterion in which internal time-step size depends on local slope and grid size. The reduction of grid size from 24 feet to 3 feet meant that a gully-domain model that included the nonlinear hillslope component could generally only compute a few hundred years in the alloted 24 hour compute time.

Chapter 9

Validation

9.1 Introduction

In the opening to Chapter 8 we introduced a distinction between a *predictive model* and a *calibrated model*. While sufficient external information exists to determine input values in a *predictive model*, determination of appropriate model inputs in a *calibrated model* is done through minimization of the difference between model output and measured values. As a *calibrated model* is calibrated to a particular model domain (or domains) and with specific boundary and initial conditions, it is reasonable to assess how well the model performs in a context for which it was not calibrated. This is the purpose of validation. In this chapter we describe the site that was selected for validation (Section 9.2), methods (Section 9.3), results (Section 9.4), and discussion (Section 9.5).

9.2 Description of Site Selection

An ideal validation site would be a catchment of similar size to the Franks Creek watershed, with a similar lithologic composition and history of baselevel lowering. Several candidate watersheds within and near the Buttermilk Creek drainage basin were considered. Among these, the watershed that most closely satisfies the three criteria—similarity in size, geology, and baselevel history—is the basin of an un-named right-bank tributary to Buttermilk Creek that joins the main stream about 800 m downstream (streamwise distance) from the Buttermilk-Franks junction (Chapter 4, Figure 4.1). Based on the 24-foot resolution digital elevation models used in this study, the validation drainage basin has an area of approximately 4.65 km^2, as compared with an area of 4.82 km^2 for Franks Creek. Total relief in the validation watershed is 182 m, slightly lower than but comparable to the 218 m of relief in Franks Creek. Both basins are underlain by bedrock in their upper portions, while the lower portions are underlain by late Pleistocene glacial sediments. The geomorphology of both watersheds consists of steep-walled ravines and gullies etched into remnants of the once-continuous till-complex surface. For these reasons, the selected watershed meets the similarity criteria for validation testing.

The validation watershed meets Buttermilk Creek in a wide river reach. As our model was not designed to directly simulate the widening of Buttermilk Creek, we chose to use a location slightly upstream from the Buttermilk-un-named tributary junction as the outlet node for the modeling domain.

9.3 Methods

In order to evaluate model runs for the validation watershed, we prepared alternative post-glacial topographies (Figures 4.3 and 4.6) and depth-to-bedrock maps (Figure 4.9) following the same methodologies applied to the calibration watershed. We also constructed the Chi-Elevation category map used for the objective function calibration (Figure 6.2).

We then ran each of the 34 calibrated models on the five alternative validation domain postglacial topographies and calculated the objective function. This resulted in $5 \times 34 = 170$ model evaluations. The same downcutting history used for calibration was used for validation.

9.4 Results

We present the cross-postglacial topography mean of the validation objective function values in Table 9.1. For clarity, the models are ranked from best performing (lowest objective function value) to worst performing. The calibration objective function value is plotted against the validation objective function value in Figure 9.1.

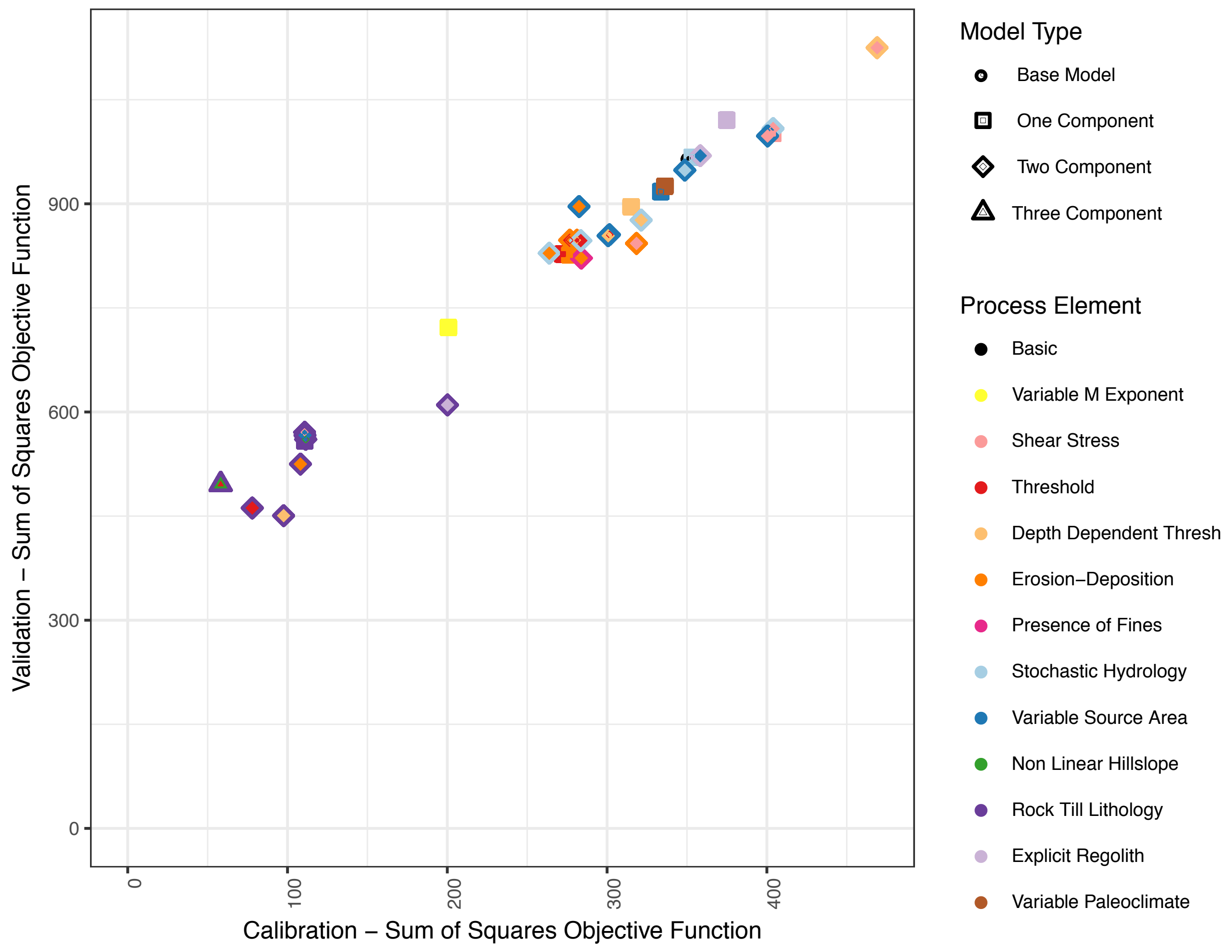

Figure 9.1: Plot of calibration versus validation objective-function scores for each of the calibrated models. Model elements are indicated by colors; number of elements in each model is indicated by symbol type.

Table 9.1: Validation Objective Function Values. Objective function values are the mean across the five alternative initial conditions.

Model ID	Objective Function
808	450.640176
802	461.646562
842	495.611220
810	524.939991
800	558.322166
840	560.507663
A00	566.412249
804	570.799904
C00	610.184357
001	721.750024
030	821.750563
010	826.342955
002	827.527859
110	828.744276
014	842.873243
102	846.943187
018	847.449768
012	847.517228
208	853.923977
202	855.496911
108	876.488396
008	895.675689
210	896.032790
200	917.558437
CCC	925.315176
300	948.357741
000	966.129410
100	966.978425
600	969.230806
204	997.668649
004	1001.341568
104	1008.459355
400	1020.548658
00C	1124.868764

Example figures of the three best and three worst validation runs are shown in Figures 9.2 and 9.3.

9.5 Discussion

We draw two primary conclusions from the validation effort. First, the validation results support the conclusion that the models that include a distinction between rock and till—the "800 model variants"—perform substantially better than other models. This can be seen in the large break between the cluster of points with purple outlines and the remaining models. Model BasicVm (yellow square) is the next-best performer, and as discussed in Section 8.9 this occurs because of the similarity between drainage area and the distribution of rock and till in the watershed. This permits BasicVm to approximate having a lower erodibility in the lower part of the watershed.

Second, the clear distinction in calibration score between BasicRtThCh (842) and the remaining Rt models is not as clear in the validation scores. Model BasicRtDd (808) is the best overall validation performer, followed by BasicRtTh (802), and BasicRtThCh (842). The fact that each of these models includes an erosion threshold supports the conclusion that a threshold is an important ingredient in a successful model for this domain. The validation results, however, do not provide support for the conclusion that model BasicRtThCh is significantly better than the other 800-variant models.

In Chapter 10 we synthesize the calibration and validation results to identify models for use in erosion projections.

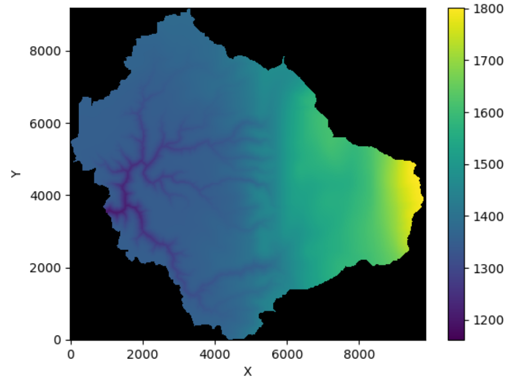

(a) Model BasicRtDd (808) run for the validation domain with initial condition vpg_14fr3 (14% etching). The objective function score was 257.

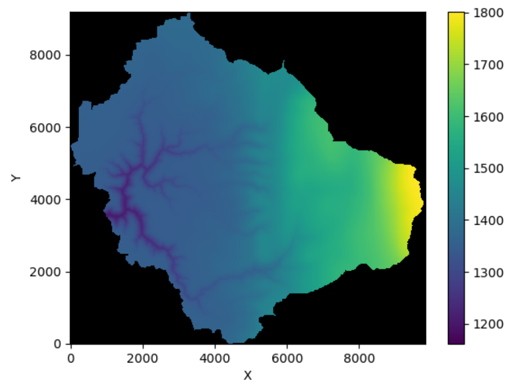

(b) Model BasicRtTh (802) run for the validation domain with initial condition vpg_14fr3 (14% etching). The objective function score was 267.

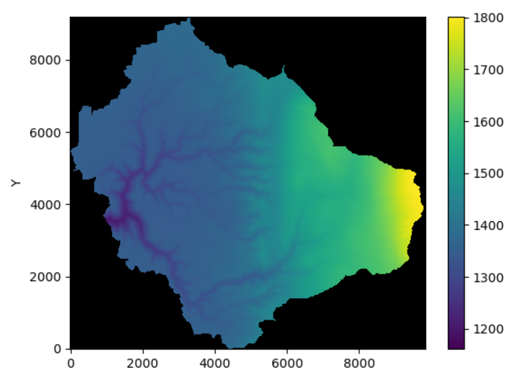

(c) Model BasicRtDd (842) run for the validation domain with initial condition vpg_14fr3 (14% etching). The objective function score was 292.

Figure 9.2: Three lowest objective function scores on the validation domain

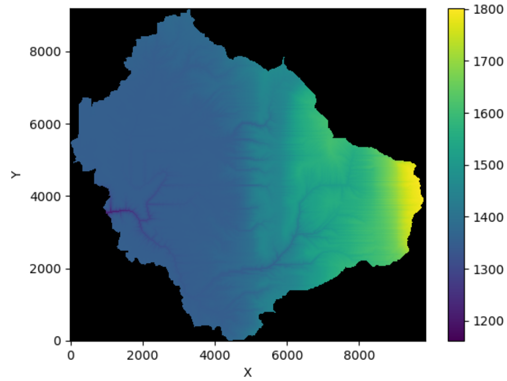

(a) Model BasicSa (040) run for the validation domain with initial condition vpg_0fr3 (0% etching). The objective function score was 1384.

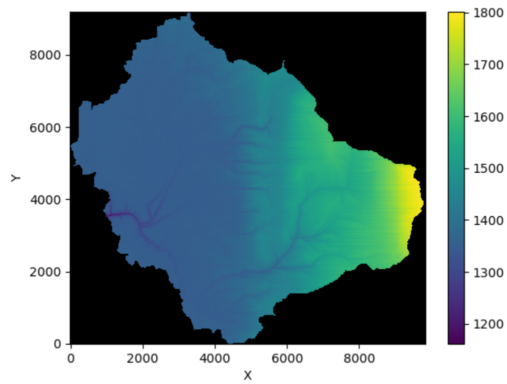

(b) Model BasicStSs (104) run for the validation domain with initial condition vpg_0fr3 (0% etching). The objective function score was 1400.

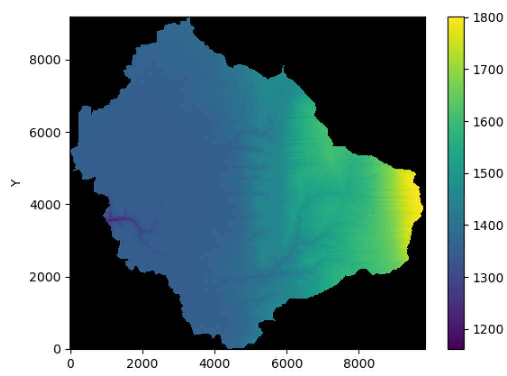

(c) Model BasicDdSa (00C) run for the validation domain with initial condition vpg_0fr3 (0% etching). The objective function score was 1422.

Figure 9.3: Three highest objective function scores on the validation domain.

Chapter 10

Model Selection

10.1 Introduction

In this section we outline the approach taken to synthesize the results of the calibration and validation efforts to determine which models are appropriate to use for projection.

10.2 Methods

Following *Burnham and Anderson* (2003) we use the AIC$_c$ difference Δ as a basis for assessing model probability. The AIC$_c$ difference for model i, Δ_i is defined as

$$\Delta_i = \mathrm{AIC}_{c,i} - \mathrm{AIC}_{c,\min} \tag{10.1}$$

over all models in the set (*Burnham and Anderson*, 2003, page 71). Here AIC$_{c,\min}$ is the minimum value of AIC$_c$ among all models in the set. Based on the set of Δ_i values for candidate models, model probabilities p_i can be assigned with the following equation:

$$p_i = \frac{\exp\left(-\frac{1}{2}\mathrm{AIC}_{c,i}\right)}{\sum_{r=1}^{R} \exp\left(-\frac{1}{2}\mathrm{AIC}_{c,i}\right)} \tag{10.2}$$

where R is the total number of models in the set. For a definition of AIC$_c$ see Section 8.5, equation (8.3).

10.3 Results and Discussion

Based on the calibration and validation results, we consider our candidate model set to be the nine rock-till models. Table 10.1 provides calculated values of Δ_i and p_i for each of these nine models. Note that these values apply to calibration results rather than validation results.

Based on model probabilities alone (Table 10.1) only model BasicRtThCh (842) should be used for projections. However, the calculation of model probabilities does not take into account the validation results, which show that models such as BasicRtDd (808) and BasicRtTh (802) do better than model 842 on validation. We do not, however, have a formal

Table 10.1: Model probabilities based on AIC_c

Model ID	AIC_c	Δ_i	p_i
842	124.4	0.0	0.999
802	138.2	13.7	0.001
808	157.8	33.4	0.000
804	160.5	36.1	0.000
800	160.6	36.1	0.000
810	162.9	38.4	0.000
A00	165.7	41.3	0.000
840	166.2	41.8	0.000
C00	260.4	136.0	0.000

approach for combining the calibration and validation results into a model probability value similar to p_i.

Based on this analysis, we use two different methods for evaluating the projection results, and for quantifying and mapping their associated uncertainties. The first approach uses model 842 only. The second approach uses the entire set of nine 800-variant models, considering each model to have equal probability. Results from both methods are presented in Chapter 11.

Chapter 11

Erosion Projections

11.1 Introduction

This chapter presents model-based estimates of potential future erosion at the Site and the uncertainties around those estimates. The goal of the analysis is to provide erosion-model projections of cumulative erosion across the Site, up to 10,000 years into the future, together with quantitative uncertainty bounds on those projections. The primary sources of uncertainty that were formally considered in the analysis include the following:

1. **Uncertainty in model structure:** addressed by using multiple erosion models.

2. **Uncertainty in model input parameters:** addressed by surrogate-based Monte Carlo simulation (at selected points only due to computation considerations).

3. **Uncertainty in modern topography, together with uncertainty arising from landscape management:** addressed with ensembles that apply random perturbations to the modern topography.

4. **Uncertainty in future climate:** addressed with three future-climate scenarios based on climate-model projections for the region.

5. **Uncertainty in future downcutting on Buttermilk Creek:** addressed with three future-downcutting scenarios based on geologic data.

To develop the erosion projections and quantify these five sources of uncertainty, more than 24,000 erosion-model runs were executed. Sixteen thousand of these were used to construct the surrogate models used to estimate parameter uncertainty based on the MCMC posterior parameter distributions presented in Section 8.8.5. Eight thousand were used to construct an experiment in which 100 runs with slightly different modern topography were run for each combination of model, climate future, and downcutting future. The resulting analyses provide projections and uncertainties at 100-year increments for each 24-foot grid cell within the model domain, which represents the Franks Creek drainage basin. The one exception to this is that, due to computational constraints, parameter uncertainty was only calculated for a set of 25 selected points around the Site, and only for seven of the nine selected models. Note, however, that the erosion model runs used for this part of projection save the topography everywhere, every 100 years, and could be used to repeat the surrogate construction and sampling procedure for any desired grid cell.

One source of uncertainty not listed above is the potential for stream capture of Franks Creek, either from propagation of nearby gullies or widening of the Buttermilk valley. An exhaustive analysis of possible future geomorphic interactions between the Buttermilk valley and the Franks Creek system was not possible, given current limitations in data and modeling technology. However, a set of idealized model experiments was run to explore the potential consequences of stream capture from the east or southeast.

The scenarios that address future climate change are necessarily constrained by the limits of contemporary climate science. The climate modeling community has developed projections out to the year 2100, based on alternative fossil-fuel emissions scenarios (e.g, *Taylor et al.*, 2012). Exploration by climate modelers beyond that time horizon is necessarily more limited and speculative. Some attempts have been made to investigate the potential longevity of anthropogenic warming, with some evidence that surface warming generated by 21st-century emissions may persist for thousands of years (*Solomon et al.*, 2009). Given the unquantifiable uncertainties involved in long-term future climate, the climate scenarios used in the future-erosion projections are best thought of as sensitivity experiments. Part of their utility lies in comparing the magnitude of climate-related uncertainty with other sources of uncertainty.

Likewise, the three scenarios for future downcutting on Buttermilk Creek, which provides the baselevel for Franks Creek and its tributaries, are also somewhat speculative. As described below, they were developed on the basis of available geologic data, by essentially extrapolating the faster and slower rates observed in the recent geologic past. These scenarios are also best thought of as sensitivity experiments that give an indication of how uncertainty related to downcutting compares with uncertainty that arises from other sources.

A Monte Carlo analysis of uncertainty arising from the posterior parameter distribution constructed in Section 8.8.5 parameters requires especially large numbers of model runs. Section 11.4.1 describes how this was accomplished by using process-based erosion model runs to construct surrogate models for predicted quantities. The heavy computational cost for these analyses meant that projections of parameter uncertainty had to be restricted to a small number of locations at the Site, and the two end-member combinations of climate future and downcutting future.

The present analysis is designed to address the first four sources of uncertainty listed in Chapter 1: experimental (via parameter uncertainty analysis), estimation (also by parameter analysis), temporal (through future-climate and future-downcutting scenarios), and theoretical (by use of multiple models). We have not attempted to quantify geologic or cognitive uncertainties, but instead have assumed that the interpretations of geologic features that inform this study are correct. The analysis does not address uncertainty in the depth-to-bedrock map that was used as an input to the models. Nor has it been possible to address uncertainty arising from the simplification involved in treating the Site's geological materials as two uniform lithologic types (rock and sediment). Finally, the analysis does not address uncertainty arising from the possibility of major changes in future land use, such as might substantially alter rates and/or patterns of surface-water runoff.

While the results of the sensitivity analysis presented in Chapter 7 concluded that the objective function used in calibration was not sensitive to the variations in postglacial topography reconstructions or postglacial to present downcutting history, we do not consider these findings to have direct bearing on the likely sensitivity of predicted quantities to uncertainty in model to *future* initial topography or future downcutting patterns. This is simply because the sensitivity analysis results assessed sensitivity *with respect to the objective function*, and not with respect to the predicted quantities we discuss in this chapter. In particular, the quantification of uncertainty in projections described in this chapter focuses on at-a-point erosion, rather than the broad-scale amount and general spatial distribution that the objective function addresses. The variations in initial condition presented here and in Chapter 7 were also constructed to test completely different things; Chapter 7 addressed uncertainty in our ability to reconstruct the postglacial topography, whereas the projection analysis attempts to capture uncertainty in plateau drainage reconstruction by making perturbations to the initial topography.

We also note that the findings discussed in this chapter are a result of two distinct efforts: first, research on reasonable boundary conditions to use with the model suite (Section 11.3), and second, the experimental design used to assess and partition uncertainty associated with considered sources (Section 11.4). With additional information about the future boundary conditions than we had access to, other projection efforts could employ the same experimental design but with different boundary conditions. Likewise, the boundary conditions presented here could be used in a different experimental design.

The remainder of this chapter is divided into several sections. Section 11.2 describes the construction of initial conditions based on LiDAR observations. Section 11.3 develops scenarios for future climate and future downcutting in the Buttermilk valley. This section also describes two stream capture scenarios. Section 11.4 describes the overall experimental design and methodology. One method employed required considerable computation such that we were not able to employ it at all model grid cells. Instead we focused on 25 select sites that are described in Section 11.5. The results and discussion are presented in Section 11.6. These include the assessment of uncertainty due to model structure, climate future, downcutting future, and perturbations to initial topography (Section 11.6.1). Next we assess uncertainty associated with model calibration (Section 11.6.2) and make erosion projections with uncertainty at the 25 sites (Section 11.6.3). Finally we present maps of expected erosion and uncertainty through time (Section 11.6.4) and explore the impact of stream capture from two locations (Section 11.6.5). We conclude with a summary (Section 11.7).

11.2 Initial Conditions

We created the initial topographic surface from high-resolution LiDAR data. As described in *Cortes* (2016), the Agencies collected LiDAR data during November of 2015. The data were subsequently processed and filtered to yield a topographic surface representing bare earth with a vertical accuracy of ± 0.132 feet. We entered the LiDAR filtered bare earth LAS files and hydrologic break line file into ArcMap's 3D Analyst software package (*ESRI*, 2014) to create a digital terrain model (DTM) of the Franks Creek watershed. DEMs were generated from the DTM at a variety of grid cell sizes (3, 6, 12, 24, and 48 feet) for use in computational speed tests. Based on the results, we selected a DEM with a 24-foot grid cell spacing to use as the initial condition in the projection runs. This present-day DEM of the

Franks Creek watershed is shown in Figure 11.5.

11.3 Future Boundary Conditions

11.3.1 Projection of Downcutting History

Modeling projections require time-versus-elevation time-series of the river outlet for use as boundary conditions. Multiple time-series are desirable because they make it possible to bound the range of viable river incision rates and thus account for the inevitable uncertainty associated with long-term projections. To this end, we developed three time-versus-elevation scenarios for use as alternative boundary conditions in the modeling projection runs. The scenarios are based on the incision history information provided by EWG's geological field analysis (*Wilson and Young*, 2018), and available information about the geology in northern Cattaraugus County.

As discussed in Chapter 4, the EWG collected age-dating observations, which made it possible to construct time-versus-elevation histories of the Franks Creek outlet since deglaciation. As shown in Figure 4.10, these data provided the basis for two equally viable alternatives for the lowering history. Both scenarios show a similar pattern of alternating fast-slow incision rates (i.e., rapid incision during the first 2,000 years, followed by slow incision for roughly 5,000 years near an elevation of roughly 1,300 feet, followed by rapid incision for roughly 3,000 years, and then slow incision for that last 2,500 years near an elevation of roughly 1,200 feet). The two scenarios are quite similar and both are considered equally viable. Moreover, sensitivity analysis (Chapter 7) demonstrated that the erosion models are insensitive to the differences between the two scenarios. Given the similarity between the scenarios and the erosion models' insensitivity, we averaged the scenarios for use as the watershed-outlet boundary condition in the forward modeling runs and as the starting point for projecting the boundary condition over the next 10,000-year period.

To understand the significance of the alternating fast-slow incision rate pattern shown in the time-versus elevation plot of the Franks Creek outlet, we reviewed available information concerning the Paleozoic bedrock stratigraphic section in the vicinity of the WNYNSC. This effort revealed a bedrock sequence composed of interbedded shales, siltstones, and sandstones of the Upper Devonian Canadaway and Conneaut Groups (*Rickard*, 1975). Individual beds within these groups are typically less than 1.6 feet thick, with the exception of massive sandstones that may be up to 6.6 feet thick *Zadins* (1997).

The presence of siltstone- and sandstone-bearing strata in the vicinity of the WNYNSC provides a plausible explanation for the periods of slower incision observed in the time-versus-elevation plot of the Franks Creek outlet because these sections of strata are significantly more resistant to erosion than the surrounding sections composed primarily of shale. To determine the elevations of the erosion-resistant siltstone- and sandstone-bearing units in the vicinity of the WNYNSC, we reviewed studies of the bedrock stratigraphy by *Tesmer* (1963), *Smith and Jacobi* (2001) and the United States Geological Survey (*Bergeron*, 1985). Tesmer's study mapped bedrock units west of the WNYNSC. His mapping extended across Chautauqua County and into western Cattaraugus County. It included the Shumla and Laona Siltstone Members of the Canadaway Group, which consist of up to 35 feet of mainly

Table 11.1: Excerpt from Summary Well Log 69-USGSS1-5

Borehole Depth (feet)	Elevation (feet)	Thickness (feet)	Description
169-175	1,200-1,194	6	Shale, weathered
175-356	1,194-1,013	181	Shale interbedded with numerous thin layers (most less than 0.01 ft but some up to 0.1 ft) of medium to coarse-grained siltstone
356-527	1,013-842	171	Shale, as above but with much less interbedded siltstone
527-730	842-639	203	Sharpstone conglomerate (1 foot); shale interbedded with thin layers of siltstone; and thicker beds of siltstone interbedded with silty shale

quartzose siltstone with beds seldom more than a few inches in thickness. Exposures of siltstone in Quarry Creek at approximately 1,300 feet above sea level likely belong to the Shumla member and beds near the elevation of the current Buttermilk Creek bed likely belong to the Laona member (personal communication with R. Fakindiny, 2017). Smith and Jacobi mapped bedrock units east of the WNYNSC. Their mapping includes the Rushford siltstone member of the Canadaway Group, which is characterized by two thick sandstone packets separated by interbedded gray shales and thin sandstones. In Figure 9 of their report, they show a cross section that extends from Big Indian Creek, which is northwest of the WNYNSC, to Cameron, which is east of the WNYNSC. This cross section shows the Rushmore siltstone member connecting to the Laona siltstone member, implying that the siltstone is continuous across this portion of western New York and present north of the WNYNSC. Inspection of a USGS summary well log (69-USGS1-5) (*Bergeron*, 1985) compiled from wells drilled near the WNYNSC reveals a resistant member composed of shale interbedded with numerous thin layers of siltstone at an elevation of approximately 1,200 feet above sea level (see Table 11.1), which is close to the current elevation of Buttermilk Creek's river bed at its confluence with Franks Creek.

Using the time-versus-elevation time-series for the postglacial to present time period shown in Figure 4.10 as a guide, and the assumption that the periods of slower incision were caused by the more resistant siltstone layers, it appears that it took roughly 5,000 years for the Buttermilk Creek channel to erode through the Shumla siltstone member during the 10,600 to 5,600 BP time period in the vicinity of the Franks Creek outlet. This equates to an incision rate of approximately 0.007 feet/y assuming a thickness of 35 feet. Likewise it appears that Buttermilk Creek has eroded through about the first 13 feet of the second resistant siltstone section during the last 2,500 BP time period (i.e., assuming an elevation of 1,181 feet at the junction of Buttermilk Creek with Franks Creek and a top elevation of the

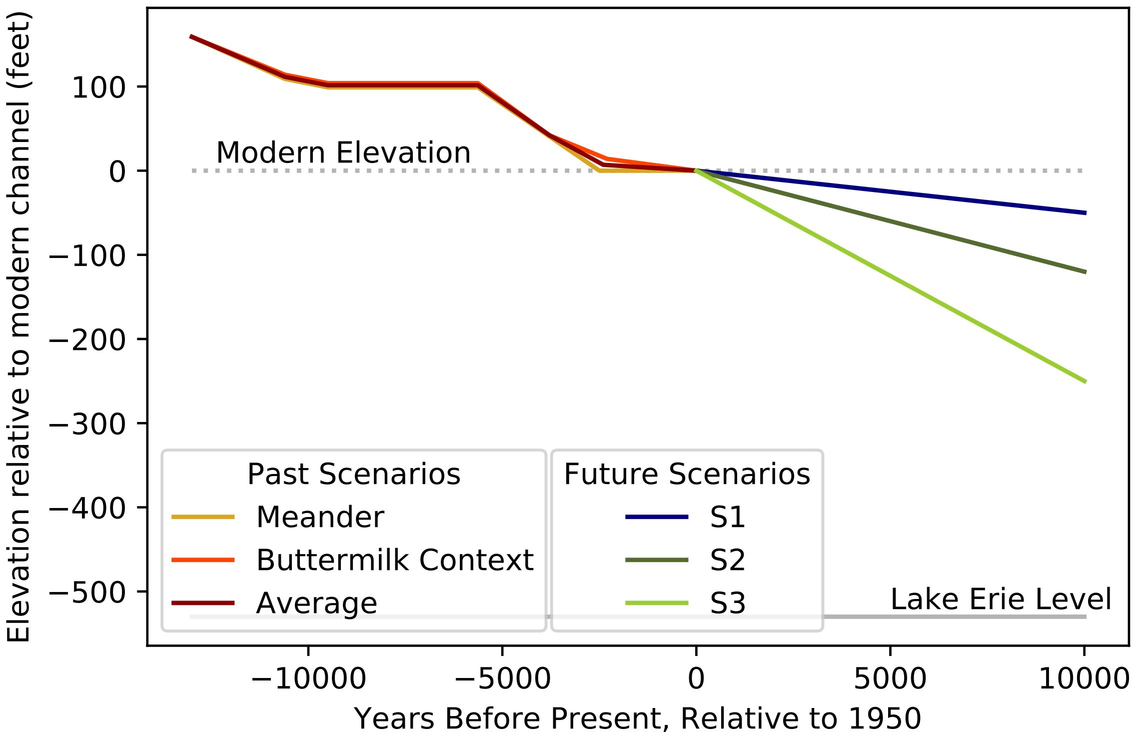

Figure 11.1: Incision Rate Scenarios for Projection Modeling Runs

second resistant section of 1,194 feet), which equates to an incision rate of approximately 0.005 feet/y. This rate is within the range estimated for the two viable lowering history alternatives during the geologically recent (post-2500 BP) time period (i.e., 0.0 and 0.006 feet/y). To incise through the remaining 168-foot thickness of the second resistant unit at its current incision rate would take roughly 35,000 years.

Based on this rationale, we selected three scenarios to use as boundary condition inputs for the projection runs. Figure 11.1 shows the time-versus-elevation plots of the river outlet for each of the three scenarios. Here and elsewhere in this Report we will refer to these scenarios interchangeably as “downcutting futures” and “lowering futures.” The details of the three scenarios are as follows:

- Scenario 1 (S1) assumes Buttermilk Creek will continue to incise at its current rate of 0.005 feet/y. Using this assumption, the river will incise an additional 50 feet of the second resistant unit during the next 10,000 year period.

- Scenario 2 (S2) assumes Buttermilk Creek will incise at a rate of 0.012 feet per year, which is the average rate of incision over the past 13,000 year period. Using this assumption, the river will incise an additional 120 feet during the next 10,000 years.

- Scenario 3 (S3) assumes Buttermilk Creek will incise at a rate of 0.025 feet/y, which is the average rate of incision through the less-resistant shale sections of the time-verses-elevation plot over the past 13,000 year period. In other words, this scenario assumes the second resistant unit will be composed of less resistant shale units for the next 10,000 years. Using this assumption, the river will incise an additional 250 feet during the next 10,000 years.

11.3.2 Construction of Climate Futures

In the models used for erosion projection, the influence of changing precipitation climatology manifests as changes in the lumped erosion coefficient K (or K_{ss} in the shear-stress version of the water-erosion law). Based on climate variables available in climate projections, precipitation climatology is represented in terms of the fraction of wet days (average number of precipitation days per year divided by the number of days in a year), and by the mean and frequency distribution of wet-day precipitation depth or intensity.

In order to represent changes in climate as changes in the lumped erosion coefficient, it is necessary to identify how precipitation statistics will change in the future and how these changes result in changes in the erosion coefficient K (or K_{ss}). We first describe the conversion of precipitation statistics into an erodibility coefficient before presenting anticipated changes in precipitation statistics and discussing details of implementation.

Conversion of Precipitation Statistics into Erodibility Coefficient for Climate Futures

Precipitation Parameters and Distribution

The precipitation model considers the fraction of wet days, F, and the frequency distribution of precipitation depth on wet days. For daily average precipitation intensity, we assume that the complementary cumulative distribution function is a stretched exponential:

$$Pr(P > p) = \exp\left[-\left(p/\lambda\right)^{c}\right] \tag{11.1}$$

where c is the shape factor and λ is the scale factor. The corresponding probability density function is a Weibull distribution. The mean wet-day precipitation depth p_d is related to the scale factor by

$$p_d = \lambda\Gamma(1 + 1/c) \tag{11.2}$$

where Γ is the gamma function.

Definition of K and K_{ss}

The basic erosion law considered here is:

$$E = KA^{1/2}S \tag{11.3}$$

where E is channel erosion rate, A is contributing drainage area, and S is local channel gradient. In this definition, K has dimensions of inverse length. Four of the models used in projection use the above equation directly, while four others include $KA^{1/2}S$ as one term in their governing erosion law (for example, in models that add a threshold [802, 808, and 842] or a deposition term [810]). The equivalent expression in the projection model that uses shear-stress scaling (804) is

$$E = K_{ss}A^{1/3}S^{2/3}. \tag{11.4}$$

Here, we present the approach used to relate changes in K to changes in p_d. A similar approach follows for K_{ss}, using the appropriate values for the area and slope exponents.

Deriving a relation between K, p_d, and F requires defining an underlying hydrology model. We start by noting that drainage area serves as a surrogate for discharge, Q. We can therefore write an instantaneous version of the erosion law as

$$E_i = K_q Q^{1/2} S. \tag{11.5}$$

This formulation represents the erosion rate during a particular daily event with daily-average discharge Q, as opposed to the long-term average rate of erosion, E. We next assume that discharge is the product of runoff rate, r, and drainage area:

$$Q = rA. \tag{11.6}$$

Combining these we can write

$$E_i = K_q r^{1/2} A^{1/2} S. \tag{11.7}$$

This equation establishes the dependence of short-term erosion rate on catchment-average runoff rate, r.

Next we need to relate runoff rate to precipitation rate. A common method is to acknowledge that there exists a soil infiltration capacity, I_c, such that when $p < I_c$, no runoff occurs, and when $p > I_c$,

$$r = p - I_c. \tag{11.8}$$

An advantage of this simple approach is that I_c can be measured directly or (as discussed below) inferred from stream-flow records.

To relate short-term ("instantaneous") erosion rate to the long-term average, one can first integrate the erosion rate over the full probability distribution of daily precipitation intensity. This operation yields the average erosion rate produced on wet days. To convert this into an average that includes dry days, we simply multiply the integral by the wet-day fraction F. Thus, the long-term erosion rate by water can be expressed as:

$$E = F \int_{I_c}^{\infty} K_q (p - I_c)^{1/2} A^{1/2} S f(p) dp, \tag{11.9}$$

where $f(p)$ is the probability density function (PDF) of daily precipitation intensity. By equating the above definition of long-term erosion E with the simpler definition in equation (11.5), we can solve for the effective erosion coefficient, K:

$$K = F K_q \int_{I_c}^{\infty} (p - I_c)^{1/2} f(p) dp. \tag{11.10}$$

In this case, what is of interest is the *change* in K given some change in precipitation frequency distribution $f(p)$. Suppose we have an original value of the effective erodibility coefficient, K_0, and an original precipitation distribution, $f_0(p)$. Given a future change to a new precipitation distribution $f(p)$, we wish to know what is the ratio of the new effective erodibility coefficient K to its original value. Using the definition of K above, the ratio of old to new coefficient is:

$$\frac{K}{K_0} = \frac{\int_{I_c}^{\infty} (p - I_c)^{1/2} f(p) dp}{\int_{I_c}^{\infty} (p - I_c)^{1/2} f_0(p) dp} \tag{11.11}$$

Thus, if we know the original and new precipitation distributions, we can determine the resulting change in K.

We assume that the daily precipitation intensity PDF is given by the Weibull distribution (see Chapter 5),

$$f(p) = \frac{c}{\lambda}\left(\frac{p}{\lambda}\right)^{(c-1)} e^{-(p/\lambda)^c}. \tag{11.12}$$

The above definition can be substituted in the integrals in equation (11.11). We are not aware of a closed-form solution to the resulting integrals. Therefore, the erosion models used for projection apply a numerical integration to convert the input values of F, c, and p_d (the last of which can change from timestep to timestep) into a corresponding new value of K.

Identification of Suitable Infiltration Capacity

To apply equation (11.11), it is necessary to define an infiltration capacity, I_c. The time scale to which this infiltration capacity applies is daily, and the spatial scale is the watershed. In other words, I_c as used here represents a daily precipitation threshold for runoff generation at the watershed scale. In general, it is expected to be smaller than point-based instrumental measurements. Therefore, the on-site measurements reported by *Bennett* (2017) should provide an upper bound.

As a means of constraining watershed-scale effective infiltration capacity, we consider estimates of mean annual storm runoff in the region reported by *DOE and NYSERDA* (2010, Appendix F). These estimates ranged from 0.2 to 0.6 m/y, with most estimates closer to the lower end. Because 0.2 m/y is the more common value and more broadly representative of watershed runoff coefficients, we consider this the best current estimate. Equipped with this information, one can ask: given the known daily precipitation statistics for the area, what is the effective infiltration capacity that would produce the correct observed mean annual storm runoff? To answer this question, we note that the mean annual storm runoff can be derived from the above hydrologic model as follows:

$$R_a = F\int_{I_c}^{\infty}(p - I_c)f(p)dp. \tag{11.13}$$

To find the effective daily watershed-scale infiltration capacity I_c consistent with the estimated actual value of $R_a = 0.2$ m/y, we performed numerical integration of equation (11.13). Using the precipitation parameters of $p_d = 6.5$ mm/d, $F = 0.46$, and $c = 0.77$, we calculated the corresponding values of R_a for a range of I_c from 0 to 20 mm/d. The value of I_c that best matches $R_a = 0.2$ m/y is 15 mm/d, or 0.625 mm/h. This falls within the range of the instantaneous, at-a-point measurements reported by *Bennett* (2017); it is close to the low end of that range, as expected for an effective value that applies to watershed-scale, 24-hour precipitation. If in the above calculation one instead uses the parameters for Climate Scenario 1 (described below, $p_d = 6.3$ mm/d, $F = 0.48$, $c = 0.82$), the corresponding I_c is 13.5 mm/d, or 0.563 mm/h. As expected, the minor differences in choice of precipitation parameters has only a small impact on estimated I_c. For purposes of projection, we use the larger value (15 mm/d), which will slightly increase the sensitivity of K to changes in p_d.

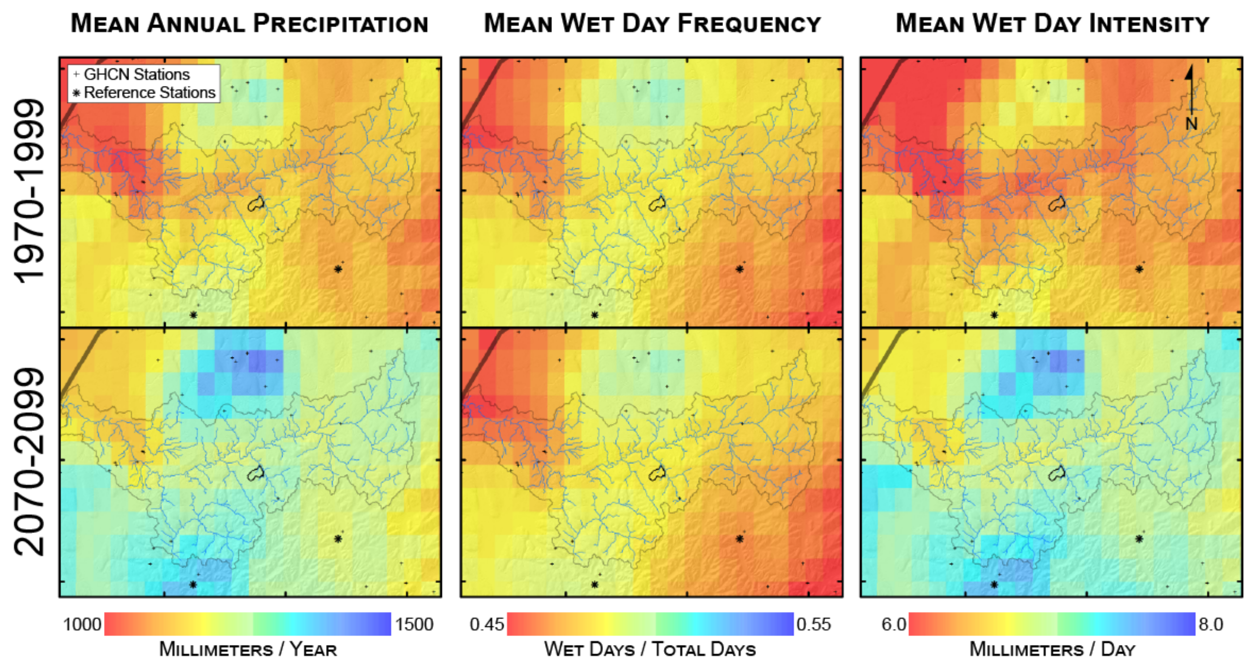

Figure 11.2: 30-year climate normals derived from MACAv2-METDATA daily for mean annual precipitation (left), mean wet day frequency >0.8 mm/day (center), and mean wet day intensity >0.8 mm/day (right). Top panels are based historic training results (1970-1999) and bottom panels are based on RCP 8.5 (2070-2099). Black crosses are locations of all GHCN stations with the two shown in Figure 5.2 highlighted as large stars. Tick marks on maps are in 15 mile increments and the Frank's Creek watershed is shown using a bold black line.

Future stochastic precipitation parameter values

As described in the prior section, the modeling projections require estimates for how parameters describing stochastic precipitation will change through time. To address this, we build on the latest suite of models coordinated by the Coupled Model Inter-Comparison Project 5 (CMIP5) as best estimates for how climate will change through the 21st century, including changes in precipitation (*Taylor et al.*, 2012). Over 40 different modeling groups contributed to this effort. Given the coarse spatial resolution of the General Circulation Models (GCMs) included in CMIP5, we adopt the downscaled product of *Abatzoglou and Brown* (2012) for CMIP5 climate projections in Franks Creek. Daily precipitation for 20 of the CMIP5 models (one ensemble run only) are included in this downscaled data product. Below, we briefly articulate the rationale for using these data and how they relate to model projections.

The climate futures used in this study rest on two robust outcomes of global climate modeling studies. First, the timescale of response of global temperature to a reduction in carbon dioxide emissions is long (*Solomon et al.*, 2009; *Matthews and Caldeira*, 2008). For example, *Solomon et al.* (2009) showed that even if carbon emissions are set to zero at 2100, increased global temperatures are effectively irreversible for at least the next 1,000 years, regardless of emissions scenario. This result arises due to a quasi-equilibrium maintenance of atmospheric carbon dioxide above pre-industrial values (around 40% of peak emissions) combined with slower heat loss to the oceans, both of which are linked to the physics of ocean mixing (*Solomon et al.*, 2009). Second, changes in global precipitation are strongly linked to global temperature. While global-scale circulation slows down in a warmer world, the increased water holding capacity of atmosphere has important implications on spatio-temporal patterns of intense precipitation (*Held and Soden*, 2006; *O'Gorman and Schneider*, 2009; *Trenberth*, 2011). Given the importance of event-scale precipitation on the hydrology and erosion models used in this study, we focus the rest of our description of climate futures on the response of daily precipitation statistics to anthropogenic climate change.

Two of the more robust hydroclimatic responses to anthropogenic climate change in global models are an increase in the magnitude of precipitation extremes (*O'Gorman and Schneider*, 2009; *Trenberth*, 2011) alongside an increase in dryness, due to lower precipitation frequency and increased evaporative demand (*Trenberth*, 2011; *Dai*, 2013). One explanation for these seemingly disparate responses is that, for global increases in temperature, mean annual precipitation increases more slowly than precipitation intensities (*Giorgi et al.*, 2011). This basic system behavior (i.e., increases in both precipitation intensities and in dry spell lengths) is corroborated by the latest CMIP5 experiments (*Lau et al.*, 2013). However, how this global increase in hydroclimatic intensity translates into local or regional water balances is complex. To address this, we use the Multivariate Adapted Constructed Analogs (MACA) daily precipitation data product(*Abatzoglou and Brown*, 2012).

The MACA method is a statistical downscaling of GCMs that has shown skill in resolving heterogeneous meteorological conditions in the contiguous U.S. The success of the method lies in its multivariate approach in downscaling physical variables and its reliance on synoptic-scale (historic) analogs instead of interpolation (*Abatzoglou and Brown*, 2012). To train the method, a spatio-temporally uniform historic dataset is needed. In this study, we used MACAv2-METDATA daily, which was trained on the historic gridded dataset METDATA over the years 1979–2012 (*Abatzoglou*, 2013). Projections on trained models require specification of a Representative Concentration Pathway (RCP) that represents how humans will alter carbon emissions throughout the 21st century. MACA downscaling has been done for two of these pathways (RCP 4.5 and RCP 8.5). Documentation for this downscaling method can be found at `https://climate.northwestknowledge.net/MACA/`. Figure 11.2 shows the 30-year climate normals derived for 1970–1999 (MACA historic; top panels) and 2070–2099 (MACA RCP 8.5; bottom panels). Mean annual precipitation, mean wet day frequency (>0.8 mm/day), and mean wet day intensity (>0.8 mm/dy) are shown from left to right. While there is substantial spatial heterogeneity in all three precipitation metrics due to topography, coastal proximity, and large-scale circulation patterns, Figure 11.2 shows two main patterns that have implications for climate futures: (1) mean annual precipitation increases throughout the region over the next century; (2) increases are driven by changes in the mean precipitation intensity, with very little change in the mean wet day frequency.

Figure 11.3 shows 30-year moving averages (i.e., climatic averages) for mean precipitation, mean wet day intensity (>0.8 mm/day), and mean wet day frequency (>0.8 mm/day) for two emissions scenarios (RCP 4.5 and RCP 8.5). RCP 4.5 emissions peak in the mid-21st century and then decline. RCP 8.5 emissions rise throughout the 21st century and represent the largest magnitude warming considered in CMIP5. Note that values before 2006 are those trained on the historic GRIDMET dataset. Figure 11.3 illustrates in more detail what is driving the 100-year change in climate normals observed in Figure 11.2, namely that

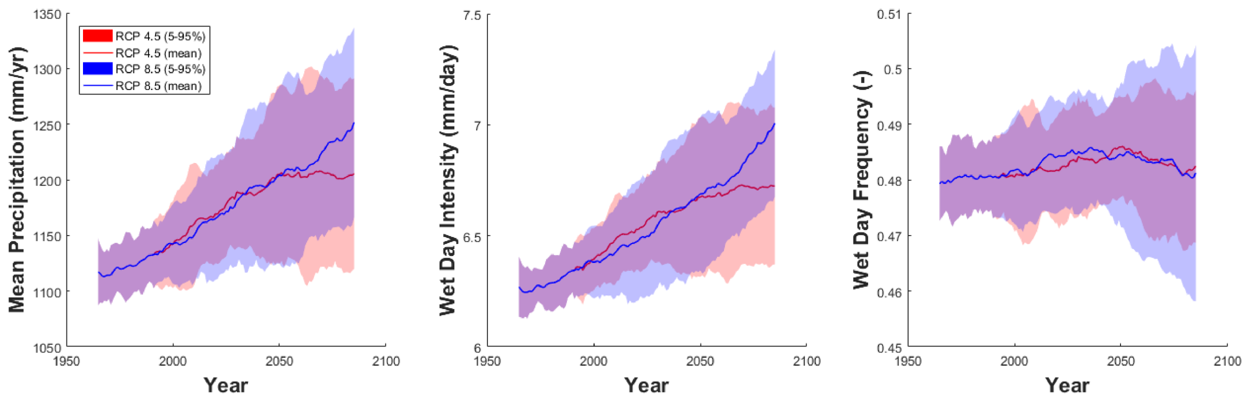

Figure 11.3: 30-year moving averages of mean annual precipitation (left), mean wet day intensity (center), and mean wet day frequency (right) for the MACA grid cell encompassing Frank's Creek. Ensemble averages (n=20) are shown as solid red (RCP 4.5) and blue lines (RCP 8.5). Shaded areas are 1.64 times the standard deviation of model runs representing the 5th to 95th percentile range.

increases in mean annual precipitation vary in concert with increases in wet day intensity. Furthermore, this time series of climatic averages show that increases in wet day intensity (and mean annual precipitation) stabilize midway through the RCP 4.5 scenario and continue to increase throughout the RCP 8.5 scenario.

Based on this rationale, the modeling team selected three climate scenarios to use as boundary condition inputs for the projection runs. The wet day intensities (p_d) vary among climate scenarios and drive changes in mean annual precipitation due to climate change. The wet day frequency (F) was set to a constant value based on the results of the MACA analysis (see Figure 11.3 right panel). The shape of the wet day precipitation (c) distribution was set to a constant value based on historic values (1970-1999) of the MACA grid cell over Frank's Creek. This decision was based on the observation that MACA values were within the range of values of observed at nearby meteorological stations and that model sensitivity to c is low.

- Climate Scenario 1 (C1) assumes no change in parametric values for historic estimates of daily precipitation parameters (p_d = 6.3 mm/d; $F = 0.48$; $c = 0.82$). This is a baseline condition that allows for evaluation of how projected climate change scenarios impact erosion projection uncertainties.

- Climate Scenario 2 (C2) assumes a linear change in parametric values from historic estimates of daily precipitation parameters (p_d = 6.3 mm/d; $F = 0.48$; $c = 0.82$) to those corresponding to Representative Concentration Pathway 4.5 (p_d = 6.7 mm/d; $F = 0.48$) in the first 100 years of model time. RCP 4.5 assumes carbon emissions peak ≈2040 and then decline.

- Climate Scenario 3 (C3) assumes a linear change in parametric values from historic estimates of daily precipitation parameters (p_d = 6.3 mm/d; $F = 0.48$; $c = 0.82$) to those corresponding to Representative Concentration Pathway 8.5 (p_d = 7.0 mm/d;

$F = 0.48$) in the first 100 years of model time. RCP 8.5 assumes carbon emissions continue to increase throughout the 21st century.

These climate scenarios all used a shape factor value of $c = 0.82$ and an infiltration capacity of I_m=5.5 m/yr.

Implementation of Climate-to-Erodibility Conversion

In the erosion models used for projection, Climate Scenarios 2 and 3 are implemented as follows. The rate and duration of increase in p_d over time are given as input parameters. At each time step, the model calculates (1) an updated value of mean daily precipitation intensity, and (2) a corresponding updated value of K, relative to its starting value K_0, using equation (11.11). After the first 100 years of model time, p_d and K become constant.

The effect of these climate scenarios is a modification of the erodibility coefficients. For the RCP 4.5 scenario, the erodibility increases over the first 100 years to 110% of the value used in the constant climate scenario. In the RCP 8.5 scenario the erodibility increases to 124% of the constant climate value.

11.3.3 Stream Capture Scenarios

Stream capture occurs when a stream is diverted from its own bed, and flows instead down the bed of a neighboring stream. A lower elevation stream eroding laterally into an interfluvial area between its bed and an adjacent higher elevation stream bed can cause stream capture. At the Site, this situation may occur on the South Plateau where Franks Creek runs parallel to Buttermilk Creek (near the SDA). The altitude of Franks Creek at the eastern corner of the SDA is approximately 1,358 feet. The altitude of Buttermilk Creek in this area ranges from 1,230 to 1,250 feet. Thus, there is a height difference between the two drainages of up to 131 feet. The interfluvial distance between the two streams varies along the length of Franks Creek and is on the order of a little over a thousand feet.

A study of past and present erosional processes by the West Valley EWG speculated on the potential for capture of upper Franks Creek by widening of the Buttermilk Creek valley (*Wilson and Young*, 2018). The report notes that the reach of Buttermilk Creek adjacent to the Heinz Creek fan appears to have migrated westward over time, at an estimated rate of approximately 0.03 m per year. Given a distance of about 300 m from the plateau edge at this location to Franks Creek, if the rate were sustained over time, the migrating plateau edge could intercept upper Franks Creek in roughly 8,000 to 11,000 years. The drainage divide between the plateau edge would be intercepted beforehand, in roughly 4,000-5,000 years. Although there are reasons to doubt that the geologically recent westward rate would be sustained for that length of time (see discussion in *Wilson and Young*, 2018), it is nonetheless of interest to explore what such a capture might mean in terms of erosion in the captured area.

Another potential scenario involving capture concerns a series of steep gullies located southeast of the SDA. The head of the nearest of these lies approximately 200 m from the sharp bend in upper Franks Creek that bounds the east corner of the SDA. We are not aware of estimates of the long-term average rate of headward propagation of these features. As

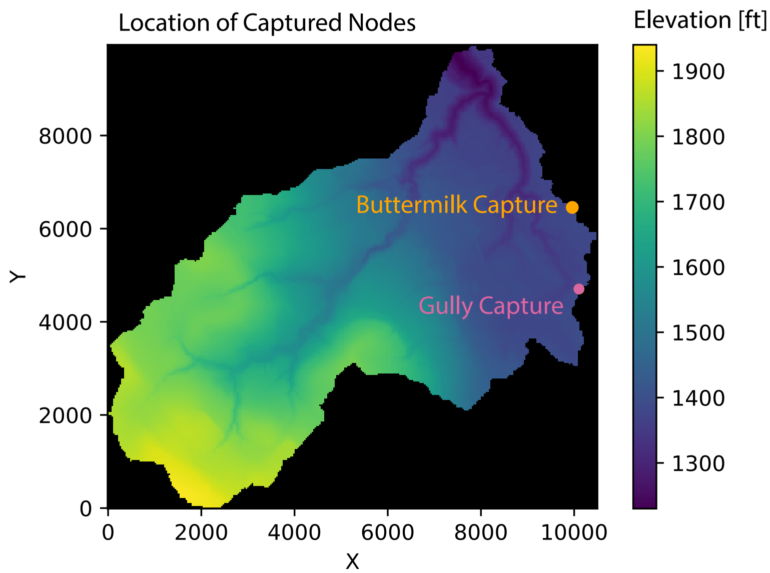

Figure 11.4: Location of nodes used to simulate stream capture.

discussed in the EWG Study 2 Report (*Bennett*, 2017), long-term gully growth measurements are not available at this time, but short-term measurements (measured over a five-year period) yielded an average rate of gully incision of 0.0064 ± 0.0124 m/ha-y. During this time period, changes in gully morphology and rates of soil loss from the inner gullies were comparable to previously reported values at the Site. Nonetheless it is of interest to consider what might happen were such propagation to lead to a capture event some time within the next 10,000 years.

To assess what might happen in either of these capture scenarios, we designed a series of model experiments to determine the sensitivity of projected topography to stream capture in two locations and multiple times. Capture is represented in the model by converting one of the model grid nodes on the watershed perimeter to an active outlet point. The point is then lowered over time, representing progressive erosion of a point of land that is in direct contact with the Buttermilk Creek valley.

The experiments consider two different captured outlet nodes: one representing capture of Upper Franks Creek by Buttermilk Creek due to the widening of Heinz Creek Fan, and the other representing capture due to a gully in the southeast portion of the watershed (Figure 11.4). The nine selected models discussed in Chapter 10 were used in these experiments. For a full mathematical description of how we calculated the rate of lowering at the capture point and the end-of-capture time based on the topography at the two capture sites, see Appendix D.

Given the current information related to rates of lateral motion of Buttermilk Creek in the vicinity of the Heinz Creek fan and rates of gully incision southeast of the SDA, it seems unlikely that capture of Franks Creek by either of these neighboring drainages will occur sooner than ∼4,000 years in the future. We elected to explore the impact of capture at each of these points, with scenarios that have capture beginning at each of five different points in time: 100, 2000, 4000, 6000 and 8000 years in the future. The inclusions of the early (100 year) and late (8000 year) scenarios is not an indication that we have confidence that capture may occur at these times. Instead, the capture scenario start times are best viewed as a sensitivity analysis that indicates the degree of risk of capture at two different locations, the extent to which that risk depends on when capture occurs, and the likely consequences if capture were to take place.

11.4 Experimental Design and Methods

This section describes the experimental design and methods we employed to construct projections with uncertainty out to 10,000 years in the future at the site. We discuss three numerical experiments: in the first part of Section 11.4.1 we describe the main experiment used to assess the expected value and uncertainty in erosion associated with model selection, future climate, future downcutting, and human modification to the plateau surface; the next part describes the methods used to assess uncertainty associated with the parameter calibration presented in Chapter 8; finally, we describe the approach used to explore the impacts of stream capture on the Site.

Based on the results of the experiments we estimate the proportion of uncertainty in future erosion that arises due to uncertainty in model structure, climate future, and downcutting future. At the selected sites we also assess uncertainty associated with model calibration. This is discussed in Section 11.4.2, with a full mathematical derivation presented in Appendix E.

Recall that a conclusion of Chapter 10was that there are two reasonable options in terms of models to use for projections: only model BasicRtThCh (842), or all nine models that include the Rt component. As model BasicRtThCh is included in the nine-model set, we can easily assess the results for each of these two model-choice options with the computation associated with the nine-model set. In this chapter, we will refer to the nine-model set as "all nine 800 variants" as model BasicRt has model code 800. We will refer to the single model as "only model 842".

For reference, the nine-model set includes the following models:

- BasicRt (800)
- BasicRtTh (802)
- BasicRtSs (804)
- BasicRtDd (808)
- BasicRtHy (810)
- BasicRtCh (840)
- BasicRtThCh (842)
- BasicRtVs (A00)
- BasicRtSa (C00)

Refer to Table A.2 and Appendix A for additional information about each model.

For all erosion model evaluations described in this section, the topography over the entire model domain at the modeled resolution of 24 feet was saved every 100 years and is provided in the calculation package. This effort resulted in many model evaluations and thus we carefully optimized file saving in order to minimize required storage space. Each saved topography file takes about 1.5 MB, such that each complete model run takes 150 MB.

11.4.1 Experiments

Main Experiment

The first experiment assesses uncertainty in future erosion across the modeled domain due to model structure, climate future, downcutting future, and human modification to the plateau surface. For each of the nine 800 variants we made 900 model evaluations, corresponding to 100 evaluations for each combination of three climate future and three downcutting futures. Model parameters were set to the expected value resulting from the hybrid EGO-NL2SOL method. The 100 evaluations within each model-climate-downcutting combination varied only in uncorrelated, mean zero, standard deviation five-foot noise applied over the entire domain. The addition of random noise is intended to represent perturbations in the surface drainage patters on the plateau that may result from relatively minor human modification to the surface. Five feet was chosen as the standard deviation size because this aspect of the experiment is meant to represent movement of material by bulldozers, construction of new roads or ditches, or demolition of existing structures. In this experiment, the random seed used for noise construction is set as a parameter value so the results are fully reproducible. In addition to the 100 evaluations with random topographic perturbations, we made one run per model-climate-lowering combination with no noise added to the starting (modern) topography.

This experiment required 8,181 erosion model evaluations and resulted in a fully balanced experiment that assesses the impact of each of three *treatments*: model, climate, and downcutting. This balanced experimental design permits us to take advantage of the ANOVA method for assessing the uncertainty associated with the three different treatments and their interactions.

Combining the results of these model evaluations based on the multimodel inference theory layed out in *Burnham and Anderson* (2003) requires assigning probabilities to each model. In the case of using only model 842, this is trivial; it receives a probability of one. In the context of using all nine 800 model variants, this is not trivial. We don't want to use the model probabilities presented in Table 10.1 because they do not include information about the validation results. As we were unable to identify a theoretically justified method for assigning these probabilities, we assigned each model an equal probability of 1/9.

Parameter Calibration Experiment

A second set of model evaluations was done to estimate uncertainty in projected quantities associated with parameter calibration. In Section 8.8.5 we produced posterior parameter distributions that represent the uncertainty in calibrated parameter values. Each of these empirical posterior distributions has 100,000 samples. Ultimately our focus is not the parameter values, but on how the uncertainty in the parameter values propagates into the uncertainty in projected quantities.

It was not computationally feasible for us to make 100,000 model evaluations for each model-climate-lowering combination. Even if it were feasible, this would present a tremendous storage issue (100,000 model evaluations = 15 TB of storage). We determined that it was possible for us to compute and store 1,000 model evaluations for each model and the two end-member combinations of climate and downcutting future (the least conservative pair: constant climate and the slowest downcutting future, scenario 1; and the most conservative pair: RCP85 and the fastest downcutting future, scenario 2). This resulted in 14,000 complex model evaluations. Thus we determined that the best way to constrain the uncertainty associated with model calibration was to use the complex model evaluations to construct a Gaussian process surrogate of projected values and then sample from that surrogate at the 100,000 parameter sets provided by the posterior distribution. We would have preferred to undertake an experiment that was fully balanced with respect to model structure, climate future, and lowering future like that described in Section 11.4.1, or a single experiment that combined all sources of uncertainty, but this was simply not feasible.

The 1,000 model evaluations were made by a Latin Hypercube design constrained to the region in parameter space that contained the posterior distribution. We used the MCMC posterior mean plus or minus three standard deviations to set the Latin Hypercube extent. These model evaluations serve as the basis for constructing a surrogate for the elevation of each grid node at each of the 101 time steps from modern to +10,0000 years, at a time resolution of 100 years.

Another computation and storage consideration that we faced was where in the model domain we could fully assess parameter uncertainty through constructing the surrogate. The model domain has ∼100,000 grid cells, and the construction and sampling on the surrogate takes ∼10 minutes and creates a sample file that is ∼150 MB. Note here that this corresponds 29-node-days on Summit's 24-core nodes.

We decided to constrain the full assessment of parameter uncertainty to 25 selected points chosen to represent areas of concern on the Site as well as key geomorphic features such as gully heads (Section 11.5). As the complex model runs save the topography everywhere, it is possible to extend the surrogate construction and sampling to all nodes, but we did not have sufficient resources to undertake this effort.

We were able to attempt this effort with eight of the nine models (840 did not successfully construct a posterior parameter distribution). Of these eight models, we have omitted model 810 because its results indicated that the posterior included samples in parts of parameter space that were poorly constrained and unreasonably extrapolated. We did not have sufficient time to fully diagnose this surrogate-extrapolation issue, but we suspect that this was due to highly non-linear behavior associated with the parameter V_{sc}. In order to calculate the combined uncertainty associated with calibration we needed to have values for models and 810, and 840 and so we applied an average of the seven successful models.

Stream Capture Experiment

In Section 11.3.3 we outlined the basis for considering scenarios related to future capture of Franks Creek. We made 180 model evaluations to explore the impact of stream capture. We considered all nine 800 variants, the two end-member climate future and lowering future combinations, two capture locations, and five capture start times (100, 2000, 4000, 6000, and 8000 years in the future). Appendix D provides additional detail about implementation and a derivation of how rates were calculated.

11.4.2 Uncertainty Partitioning

The experiment presented in Section 11.4.1 was designed based on similar work in climate projection uncertainty analysis, such that we could separate out the uncertainty in future erosion that arises from each source of uncertainty. *Hawkins and Sutton* (2009) and *Yip et al.* (2011) describe how the ANOVA method can be used to partition the uncertainty in climate model projections that arises due to model structure and future scenario. Following this work, we employ ANOVA to partition the uncertainty in our projections. Appendix E contains a formal derivation of the equations used to calculate all discussed sources of uncertainty.

In the case of using only model 842, we calculate the uncertainty associated with model calibration, climate future, lowering future, and the interaction between lowering future and climate future at the 25 select sites. As this case only considers one model, there is no uncertainty associated with model structure. In addition we present maps of projected value, uncertainty components, and "total*" uncertainty. As we were not able to make fully distributed estimates of uncertainty associated with model calibration, we use the term *total* uncertainty* to mean the uncertainty for all components *except* model calibration.

In the case of using all nine 800 variants, we calculate all of the sources of uncertainty present in the 842-only case. In addition, we calculate the uncertainty associated with model structure, the interactions between model structure and climate future, model structure and downcutting future, and the three-way interaction between model structure, climate future, and downcutting future.

When considering all nine 800 variants, we had to make one additional decision in partitioning the uncertainty associated with the relationship between model structure and model calibration. As discussed in *Burnham and Anderson* (2003, pg 160) (based on the work of *Buckland et al.* (1997)), because our alternative models are all calibrated on the same dataset, it is reasonable to expect that there is some correlation between uncertainty associated with model structure and the uncertainty associated with model calibration. Taking the conservative approach that these two sources of uncertainty perfectly covary, *Buckland et al.* (1997) derive an expression for the combined uncertainty due to model structure and calibration (their Equation 9, reproduced as Equation E.34). They also provide an expression for uncertainty if independence can be assumed (their Equation 10, reproduced as Equation E.35). We calculate and partition uncertainty based on both approaches.

11.5 Locations considered for detailed analysis

We completed a detailed parameter uncertainty assessment at 25 points within the Franks Creek model domain. The 25 selected points are located on the North and South Plateaus, as shown in Figure 11.5. We selected points that are near the waste burial areas and facilities with stored radioactive waste, such as the New York State-Licensed Disposal Area (SDA), Nuclear Regulatory Commission-Licensed Disposal Area (NDA), lagoons 2 and 3, the process building, high level waste tanks, and the groundwater plume.[1] In addition, we selected a few points near the edge of the plateaus to assist in determining gully advance and rim widening rates of the Quarry Creek, Franks Creek, and Erdman Brook stream channels. Although we selected 25 specific points for this assessment, it is possible using these models to complete a detailed parameter uncertainty assessment at any other points of interest within the Franks Creek model domain.

[1]However, it should be noted that the lagoons, their radiological inventory, and surrounding soils will be excavated, disposed offsite, and the excavations backfilled with clean soil during Phase 1 decommissioning of the WVDP. The source area of the groundwater plume will also be excavated, disposed offsite, and the excavation backfilled with clean soil during Phase 1 decommissioning. The remainder of the plume, which is principally Sr-90 with a half-life of 28.8 years, will have decayed away before it can be impacted by gully or valley-wall migration from adjacent streams.

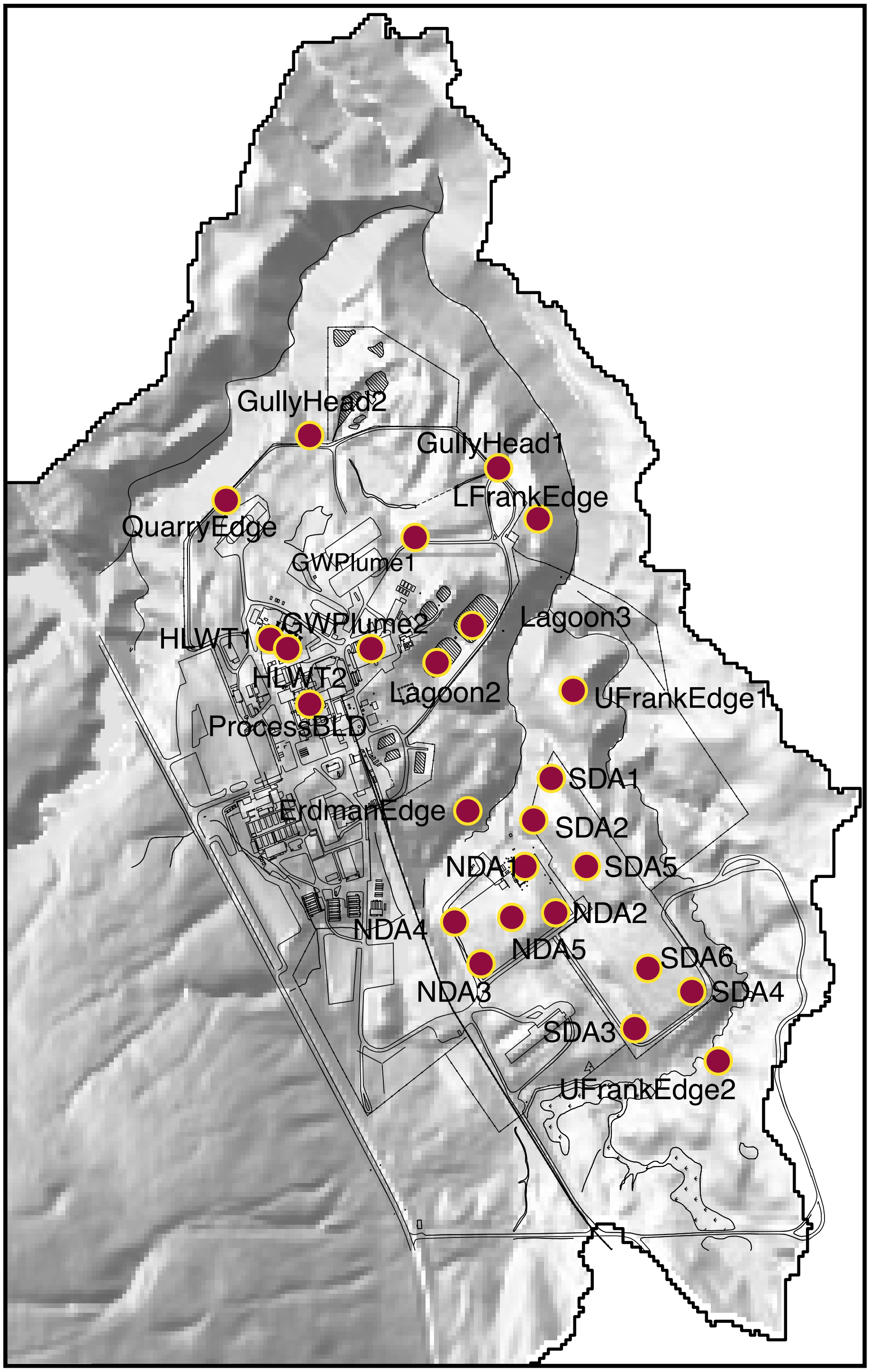

Figure 11.5: Map of northeastern portion of Franks Creek watershed model domain with the locations of 25 analysis sites noted as red dots and text specifying the name used for each site.

11.6 Results and Discussion

In this section, we present and discuss the results of the projection effort. This section is divided into five major parts. First we illustrate the impact of model structure, climate future, downcutting future, and initial condition noise on erosion projections (Section 11.6.1). We then discuss the results of the surrogate-based method to assess uncertainty associated with model calibration (Section 11.6.2). At each of the 25 selected analysis points we calculate expected erosion and uncertainty through time before partitioning the uncertainty in projections (Section 11.6.3). Next we present maps of erosion projections and uncertainty through time (Section 11.6.4). Finally we present the results of the stream capture experiments (Section 11.6.5).

11.6.1 Illustration of model structure, climate future, downcutting future, and initial condition on future erosion

Here we present a summary of the effect of model structure, climate future, downcutting future, and initial condition on the patterns of erosion at +10,000 years. While subsequent analysis will quantitatively assess the expected value and uncertainty associated with each of these components, we think it is useful to highlight the variability through maps of erosion patterns. The results of this section come from the experiment described in Section 11.4.1.

Effects of model structure

Figure 11.6 shows end of model run (+10,000 years) cumulative elevation for the conservative pair of climate and lowering scenarios for all nine considers 800 variant models. The broad pattern of erosion is similar—little erosion has occurred in the upper part of the watershed while the channel network in the lower part of the watershed continues to incise.

There are, however, substantial differences in the nature of incision within the till plateau. Models with thresholds (802, 808, 842) project less erosion on the till plateau surfaces than those models with no threshold. Model 842, the only model with both model physics and calibrated parameter values that permit non-linear hillslope transport, shows incision distributed over the entirety of the incised valleys. This contrasts with other models in which incision is more substantial at the bottom of the valleys. Model C00 stands out as focusing all erosion on the center of the channel. Recall from Chapter 8 that this model must convert till to soil in order to move it. While we considered removing this model from the suite based on calibration, it performed well enough in validation that we kept it in the nine-model suite. However, its projection of only limited erosion on valley side-walls should be viewed with skepticism, as reflects the unrealistic assumption that glacial sediment must be fully weathered into soil before being transported.

Effects of climate and downcutting scenario

Figure 11.7 shows end-of-run (+10,000 years) cumulative elevation for model BasicRtThCh (842) for all nine combinations of climate and lowering scenarios. Changing from the constant climate scenario to the RCP 8.5 scenario (indicated by differences between the maps

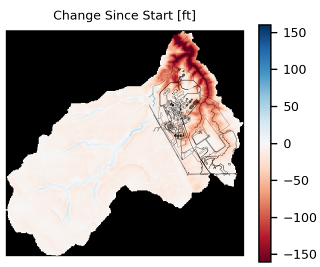

(a) Model 800

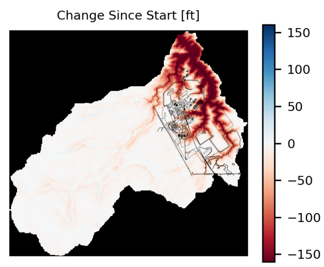

(b) Model 802

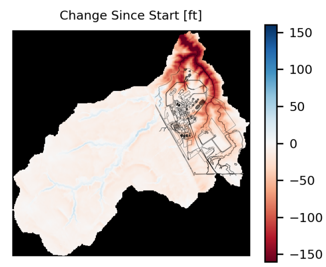

(c) Model 804

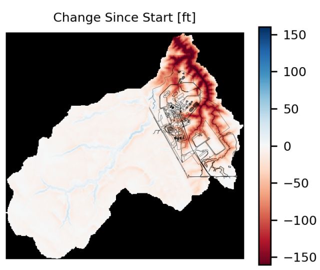

(d) Model 808

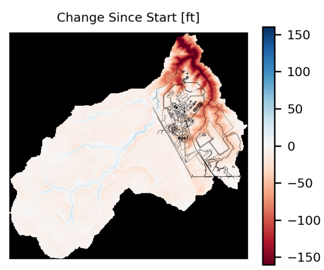

(e) Model 810

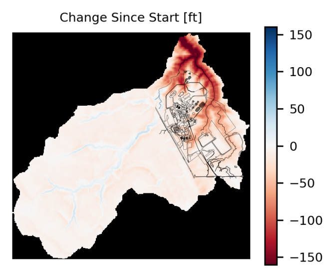

(f) Model 840

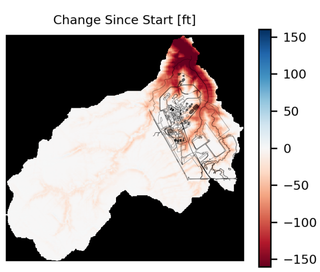

(g) Model 842

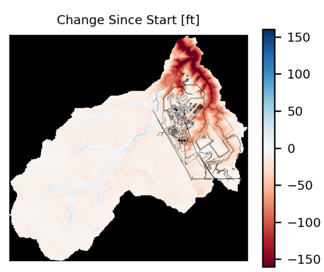

(h) Model A00

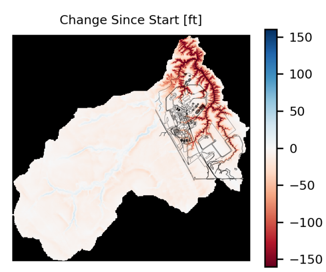

(i) Model C00

Figure 11.6: Cumulative erosion depth at +10,000 years (feet) for the EGO-NL2SOL estimated parameters for all nine 800 variants using lowering future 3 and RCP 8.5. Note that the color scale is the same in all panels.

in the left column and those in the right column) results in increased cumulative erosion along the main drainage side-slopes and in plateau-edge gullies. Differences in cumulative erosion among the three lowering scenarios are indicated by the differences between images in different rows, with the lower row representing the most rapid baselevel downcutting.

As expected, a larger amount of erosion occurs in the scenarios with greater downcutting rates and with a larger change in climate. This result makes sense in the context of the model physics. The lower reaches of the major incised valleys in the till plateau are most impacted by the variations in downcutting rate, whereas regions with steep slopes and/or large drainage area are most impacted by climate-related changes in erosional efficiency.

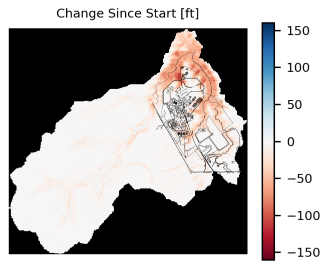

(a) Lowering future 1, Constant Climate

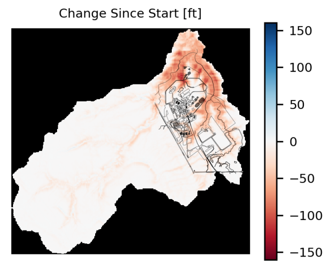

(b) Lowering future 1, RCP 4.5

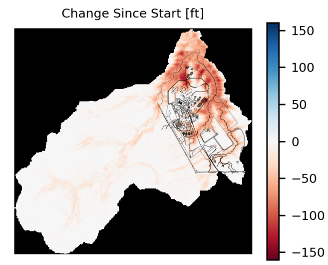

(c) Lowering future 1, RCP 8.5

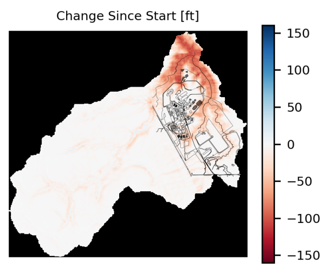

(d) Lowering future 2, Constant Climate

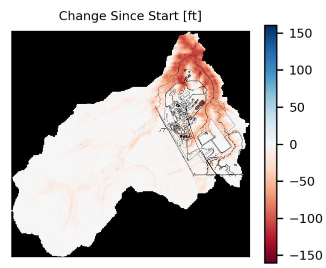

(e) Lowering future 2, RCP 4.5

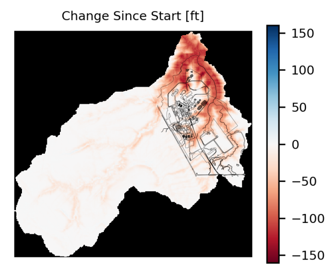

(f) Lowering future 2, RCP 8.5

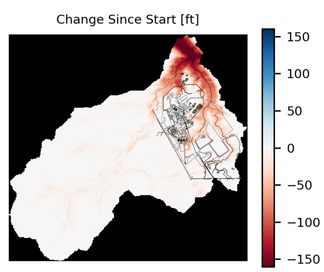

(g) Lowering future 3, Constant Climate

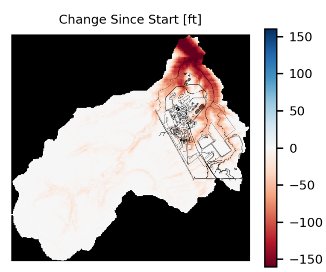

(h) Lowering future 3, RCP 4.5

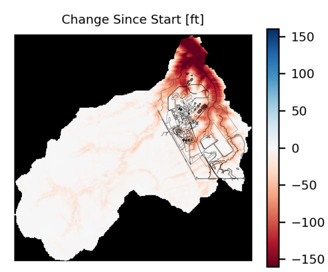

(i) Lowering future 3, RCP 8.5

Figure 11.7: Cumulative erosion depth at +10,000 years (feet) for the EGO-NL2SOL estimated parameters for model 842 for each of the nine climate and downcutting scenarios. Downcutting scenarios are constant across rows and climate scenarios are constant across columns. Note that the color scale is the same in all panels.

Effect of initial topography perturbations

Figure 11.8 shows end-of-run (+10,000 years) cumulative erosion for four model evaluations made with model BasicRtThCh (842) and the conservative pair of climate and lowering scenarios. The only difference between the four subfigures is the random noise placed on the surface of the topography as part of model setup. While the broad pattern of erosion is the same in all four model realizations, the location of the small gullies that line the edge of the till plateau surface varies. We interpret these results to indicate that (a) we were successful in capturing uncertainty associated with modification of the plateau surface hydrology; (b) uncertainty in this modification will primarily affect the plateau edges, with some impact as well on particular locations in the interior north plateau that may or may not be subject to gully propagation; and (c) routing of storm runoff on the plateau surfaces can impact the relative growth rates of gullies along the plateau rim.

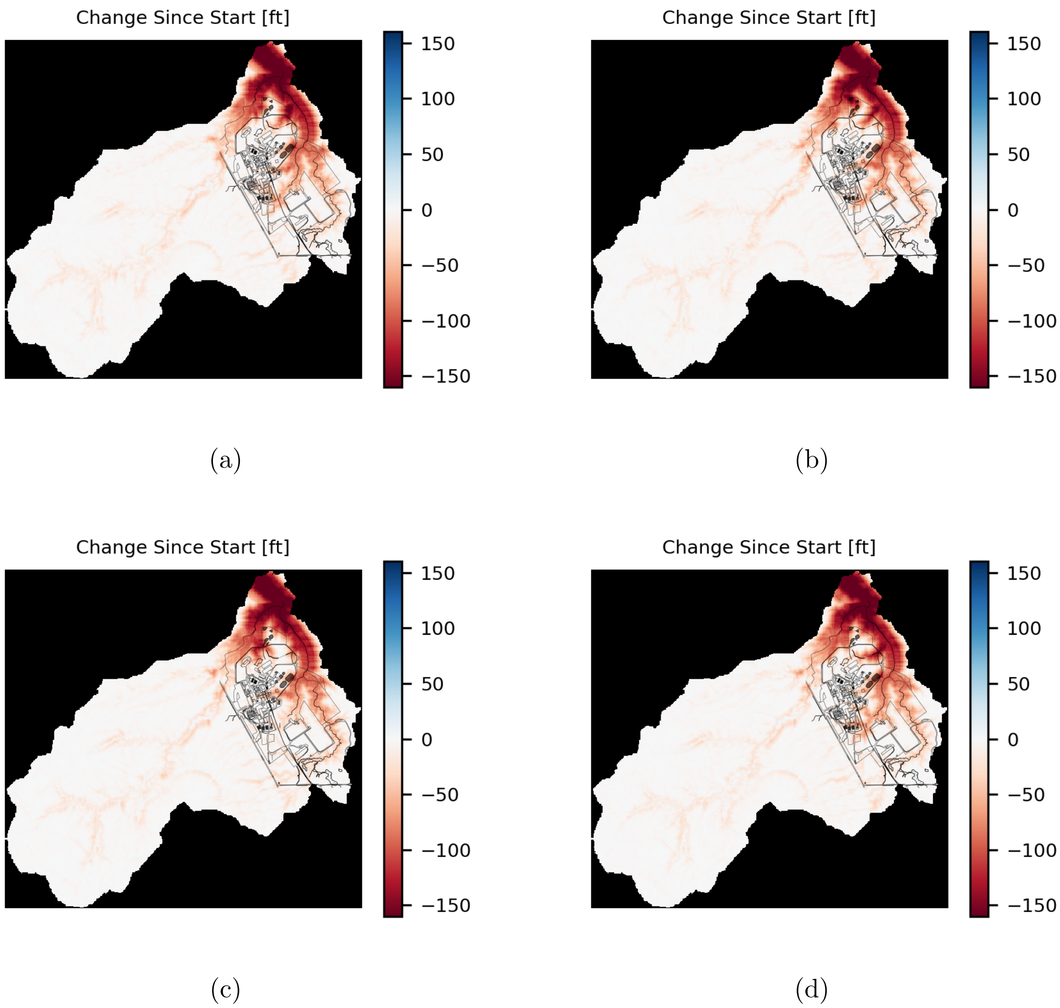

Figure 11.8: Cumulative erosion depth at +10,000 years (feet) for four of the 100 model evaluations run with random noise placed on the modern surface for the model 842, downcutting scenario 3, RCP85 climate scenario. Note that the color scale is the same in all panels.

11.6.2 Parameter Calibration Experiment

Next, we consider the results of the parameter calibration experiment described in Section 11.4.1. We calculated the expected value, variance, and 95% confidence interval at each of the 25 analysis points at every 100 years for each of the seven 800 variant models for which we were able to successfully construct distributions of predicted quantities. We show two example figures from two sites that illustrate the type of results produced by this experiments.

In Figure 11.9 we show results for the Lagoon3 analysis point. Here and elsewhere we show a gray box for reference that has its upper limit at the modern surface and its lower limit at a 50 ft depth. Based on Figure 11.6 it is not surprising that the expected value for erosion through time varies depending on the model used. As expected the amount of uncertainty from parameter choice grows through time. In contrast, consider the results at analysis point SDA4 (Figure 11.10). At this site, the expected value for erosion is low and does not vary substantially from model-to-model.

The confidence intervals associated with model 842 in some cases show abrupt changes through time (for example, at point SDA4) (Figure 11.10). One potential source of this pattern is the nonlinear diffusion component (present in this model but not the other six), which may be rapidly moving material into and out of this particular grid cell. An alternative potential source is unevenness in the surrogate for this model, caused by the nonlinear behavior associated with the hillslope-process component.

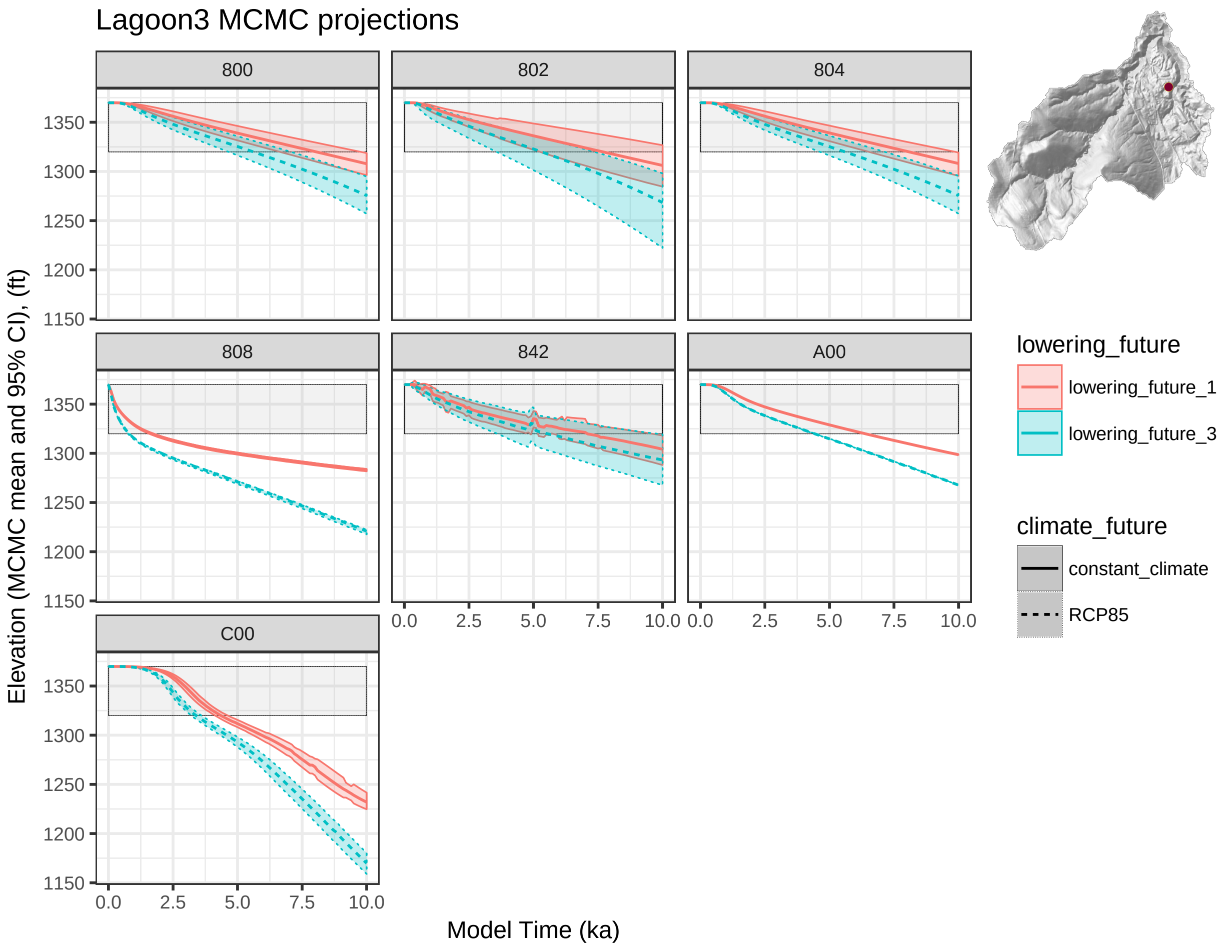

Figure 11.9: Summary figure illustrating the mean and 95% confidence intervals for topographic elevation as a function of time at Lagoon3. Inset map shows the location of Lagoon3 within the model domain with modern topography as a base-map. The gray box is a 50 foot deep reference box that extends below the modern surface. Climate future is shown with line style and and downcutting future scenario is shown with line type and capture start time is shown with color.

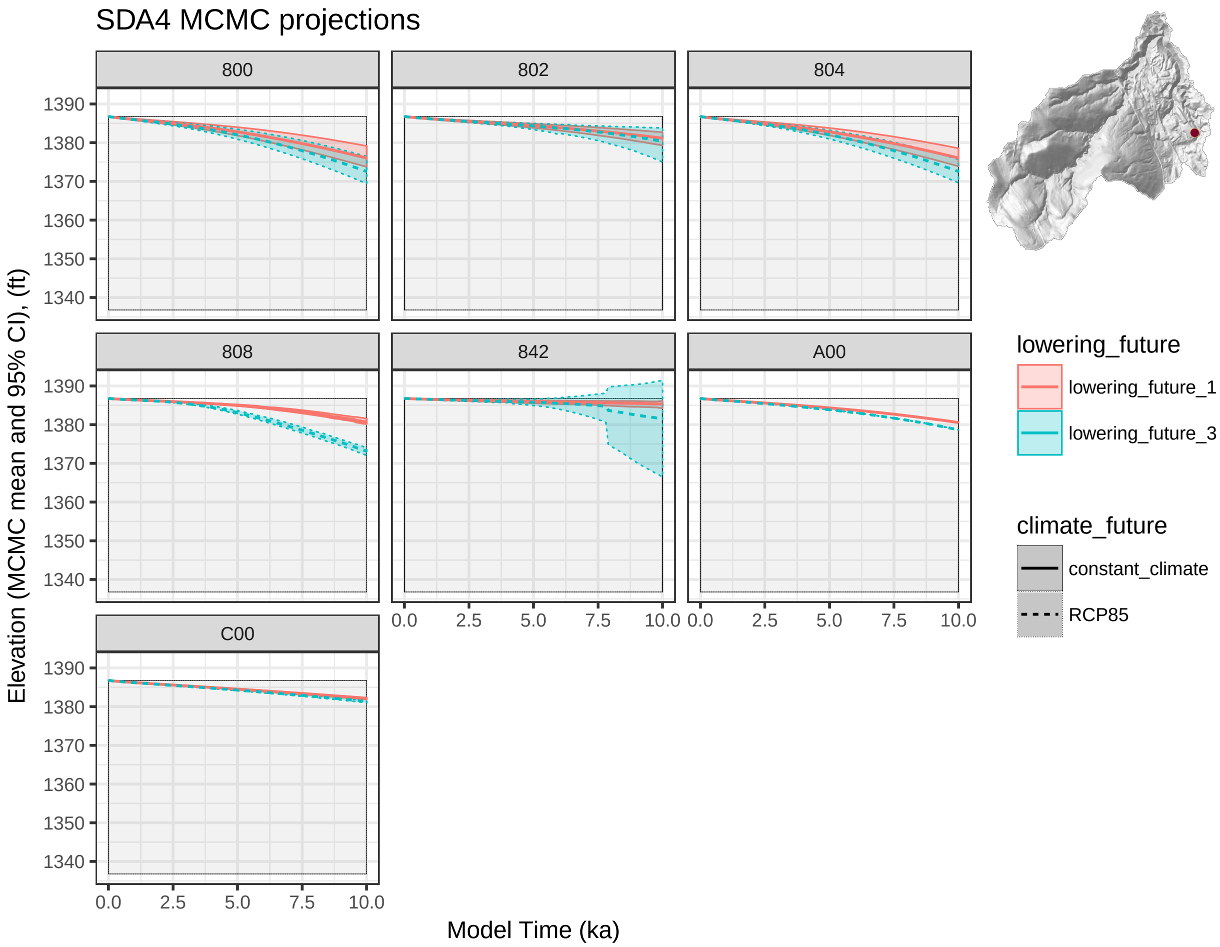

Figure 11.10: Summary figure illustrating the mean and 95% confidence intervals for topographic elevation as a function of time at SDA4. Inset map shows the location of SDA4 within the model domain with modern topography as a base-map. The gray box is a 50 foot deep reference box that extends below the modern surface. Climate future is shown with line style and and downcutting future scenario is shown with line type and capture start time is shown with color.

11.6.3 Projections and partitioned uncertainty at analysis sites

Based on combining the results of the experiments described in the main experiment (Section 11.4.1) and the parameter calibration uncertainty experiment (Section 11.4.1) using the methods described in detail in Appendix E we present time series of expected erosion and total uncertainty, as well as each addressed source of uncertainty. We consider three cases for calculating and partitioning the uncertainty in model projections: Case 1, in which we only consider model 842; Case 2a, in which we consider all nine 800 variant models and assume that their calibration and model structure uncertainties are independent; and Case 2b, which is identical to Case 2a except that we consider model calibration and structure uncertainties as correlated.

Figure 11.11 shows the expected value and 95% confidence interval for elevation of each of the 25 sites calculated use each of the three methods listed above. Individual figures associated with each panel are provided in Appendix F. The presented mean and standard deviation values at 200, 500, 1000, and 10,000 years are provided in Table 11.2. The amount of erosion varies substantially from point to point, as does the total uncertainty in erosion.

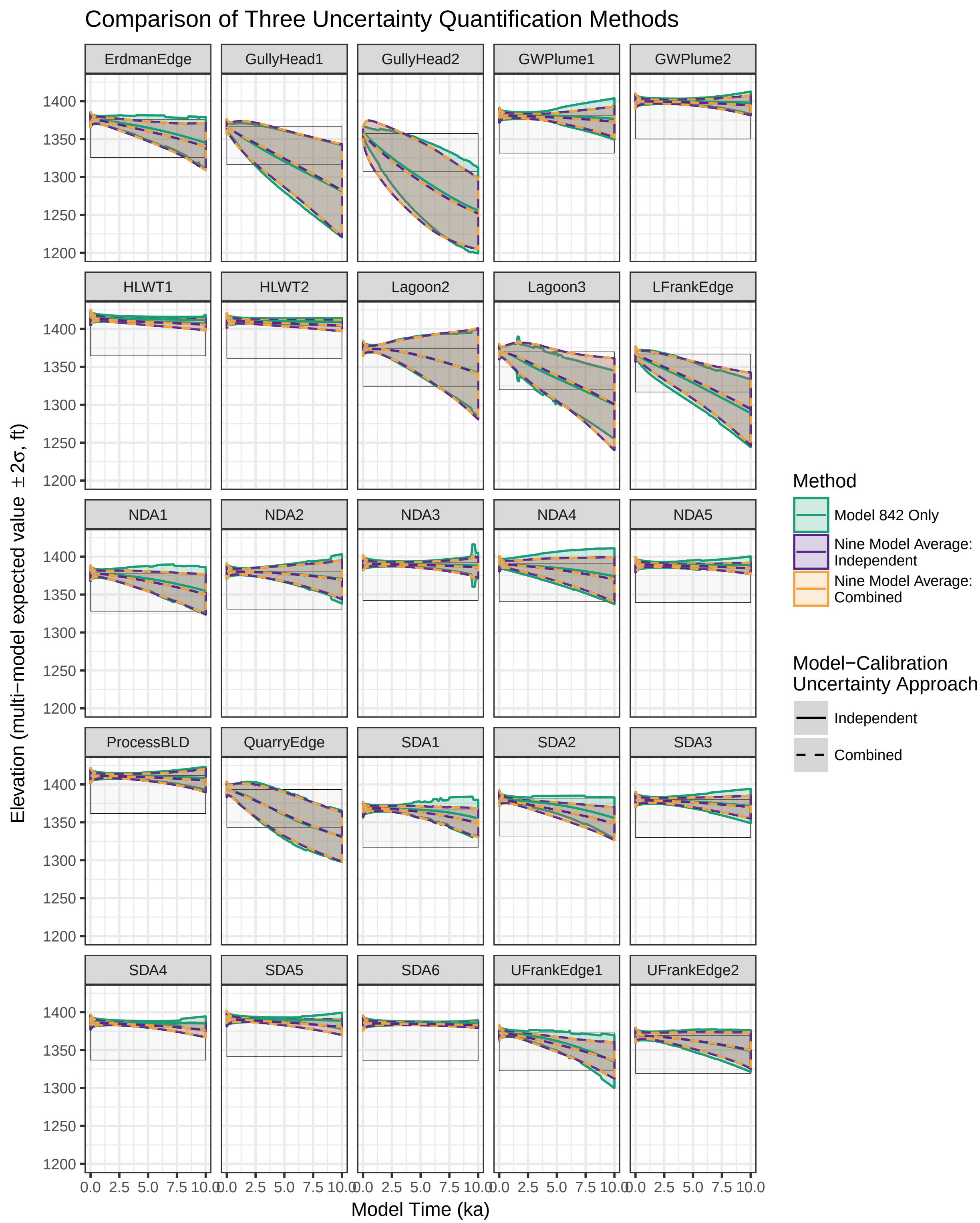

Figure 11.11: Summary of projections at each of the 25 analysis sites showing expected elevation and uncertainty through time. The gray box is a 50-ft deep reference box that extends below the modern surface. Note that both the x and y axis limits are constant. Three expected values and 95% confidence regions are shown that corresponds to the two approaches to model selection (only 842 and all nine 800 variants) and the two approaches to model structure and calibration uncertainty (independent or covarying). A close-up of each panel is presented in Appendix F

Table 11.2: Mean and standard deviation for expected depth of erosion at the 25 detailed analysis points at 200, 500, 1000, and 10,000 years in the future. Positive values indicate erosion and negative values indicated deposition. Projections using both multi-model approaches (model 842 only and all nine 800 model variants) are presented. Presented standard deviation includes all considered sources of uncertainty.

		+200 years		+500 years		+1000 years		+10,000 years	
		μ [ft]	σ [ft]	μ [ft]	σ [ft]	μ [ft]	σ [ft]	μ [ft]	σ [ft]
Location	Approach								
ErdmanEdge	Model 842 Only	-0.16	3.03	0.15	2.72	0.85	2.86	30.57	17.07
	All nine 800s	0.05	2.92	0.43	2.26	1.59	2.40	35.49	15.52
GullyHead1	Model 842 Only	2.72	3.32	5.34	4.57	10.26	7.25	85.31	30.31
	All nine 800s	2.54	4.13	5.39	5.68	9.75	8.38	84.19	30.47
GullyHead2	Model 842 Only	1.14	5.03	6.14	6.75	13.18	9.36	101.62	28.25
	All nine 800s	3.74	9.30	8.84	12.98	16.41	15.97	105.52	23.52
GWPlume1	Model 842 Only	0.08	3.26	0.17	2.82	0.27	2.42	4.94	13.70
	All nine 800s	0.21	2.88	0.38	1.94	0.60	1.51	8.77	10.26
GWPlume2	Model 842 Only	-0.03	3.14	0.06	2.67	0.14	2.20	2.24	7.42
	All nine 800s	0.17	2.87	0.25	1.89	0.36	1.41	5.61	6.53
HLWT1	Model 842 Only	0.06	3.12	0.23	2.67	0.46	2.24	3.00	3.39
	All nine 800s	0.23	2.83	0.78	1.86	1.59	1.44	9.07	3.80
HLWT2	Model 842 Only	0.08	3.06	0.19	2.59	0.30	2.16	1.97	2.73
	All nine 800s	0.31	2.80	0.43	1.87	0.66	1.47	6.65	3.77
Lagoon2	Model 842 Only	0.11	3.01	0.22	2.57	0.42	2.43	32.00	28.50
	All nine 800s	0.21	2.86	0.43	1.95	0.71	2.18	33.44	30.02
Lagoon3	Model 842 Only	0.24	3.26	0.93	4.22	3.84	6.72	69.97	22.54
	All nine 800s	0.42	3.52	1.27	4.50	3.43	6.91	69.25	30.26
LFrankEdge	Model 842 Only	2.01	3.46	4.73	5.19	8.95	7.04	77.94	22.38
	All nine 800s	1.35	3.34	3.44	3.91	6.95	5.40	72.46	24.09
NDA1	Model 842 Only	0.05	3.34	0.24	2.87	0.62	2.80	23.23	15.62
	All nine 800s	0.17	2.96	0.41	2.15	1.02	2.16	27.72	13.32
NDA2	Model 842 Only	0.05	3.39	0.17	2.86	0.36	2.43	10.10	16.28
	All nine 800s	0.26	2.89	0.40	2.04	0.54	1.78	11.22	12.80
NDA3	Model 842 Only	0.64	3.35	0.86	2.82	1.10	2.31	4.05	8.54
	All nine 800s	0.82	2.86	1.31	1.88	1.63	1.40	6.25	6.70
NDA4	Model 842 Only	0.25	3.42	0.57	3.48	1.08	4.16	16.42	18.42
	All nine 800s	0.43	2.98	0.85	2.28	1.45	2.57	20.73	14.88
NDA5	Model 842 Only	-0.08	3.32	-0.05	2.78	-0.01	2.26	0.65	5.82
	All nine 800s	0.01	2.93	0.09	1.92	0.22	1.40	4.90	3.74
ProcessBLD	Model 842 Only	0.22	3.09	0.29	2.63	0.36	2.17	3.54	7.54
	All nine 800s	0.25	2.85	0.41	1.90	0.55	1.44	6.52	7.72
QuarryEdge	Model 842 Only	0.55	3.55	1.79	4.36	4.33	6.34	61.57	16.92
	All nine 800s	0.85	3.48	2.32	4.37	5.19	6.46	62.48	16.22

Table 11.2: (cont'd.)

Location	Approach	+200 years μ [ft]	σ [ft]	+500 years μ [ft]	σ [ft]	+1000 years μ [ft]	σ [ft]	+10,000 years μ [ft]	σ [ft]
SDA1	Model 842 Only	-1.18	3.29	-1.43	2.77	-1.67	2.28	11.23	12.20
	All nine 800s	-1.08	2.83	-1.62	1.88	-1.86	1.45	17.43	9.35
SDA2	Model 842 Only	1.07	3.08	1.51	2.62	2.15	2.26	26.38	13.65
	All nine 800s	1.10	2.85	2.28	1.97	3.87	1.72	33.64	10.82
SDA3	Model 842 Only	0.41	3.41	0.57	2.89	0.77	2.44	8.44	11.36
	All nine 800s	0.44	2.80	0.73	1.85	0.94	1.45	9.98	7.52
SDA4	Model 842 Only	0.11	3.00	0.23	2.50	0.37	2.04	1.60	4.64
	All nine 800s	0.40	2.86	0.72	1.84	1.12	1.33	10.25	4.80
SDA5	Model 842 Only	0.48	3.34	0.65	2.81	0.81	2.29	2.93	5.34
	All nine 800s	0.69	2.88	1.06	1.88	1.44	1.38	11.12	5.27
SDA6	Model 842 Only	0.09	3.13	0.18	2.59	0.28	2.05	0.61	2.00
	All nine 800s	0.39	2.84	0.56	1.84	0.69	1.32	3.07	1.87
UFrankEdge1	Model 842 Only	0.09	3.13	0.30	2.63	0.74	2.21	38.00	17.45
	All nine 800s	0.37	2.81	0.86	1.84	1.86	1.50	36.53	11.92
UFrankEdge2	Model 842 Only	0.05	3.35	0.30	3.02	0.68	2.88	20.53	13.79
	All nine 800s	0.00	2.93	0.08	2.16	0.44	2.06	19.49	12.13

Examining the projections at SDA4 provides a detailed example for one of the biggest differences between the 842-only projections and the all-800 model suite (Figure 11.12). Model 842 projects very little erosion at this location for the entire modeled time period. This contrasts with the multi-model suite, which shows moderate erosion throughout the modeled time period, with uncertainty in projections increasing through time. Model 842 has both a stream incision threshold and non-linear hillslopes. In model 842, incision of Franks Creek, Quarry Creek, and Erdman Brook is more decoupled from erosion of the plateau surface as compared with the behavior of models without stream incision thresholds and linear hillslopes. This is because the non-linear hillslope component permits creating and mainlining the sharp plateau edge. For erosion of site SDA4 to occur in model 842, incision of the bounding creeks must be sufficient for the hillslopes to respond by moving the plateau edge to the location of SDA4. In contrast, models with linear hillslope transport create a rounded plateau edge, which results in tighter coupling between stream incision and hillslope response.

Before we separate out each of the sources of uncertainty, recall that standard deviations are not additive. Variances are additive, however, and thus the combination of two standard deviations σ_1 and σ_2 into the total standard deviation σ_t is accomplished by

$$\sigma_t = \sqrt{\sigma_1^2 + \sigma_2^2}. \tag{11.14}$$

For each of the cases we present two figures, the first of which shows the standard deviation associated with each of the uncertainty components, as well as the total standard deviation (in absolute value) at each of the 25 analysis points (Figures 11.13, 11.15, and 11.17). We present this figure first to orient the reader to the relative magnitude of uncertainty and the rate of change of uncertainty through time at each of the sites. Second, we present the proportion of variance at each analysis location (Figures 11.14, 11.16, and 11.18). This second set of figures is intended to illustrate how the proportion—but not the total amount—of uncertainty changes through time at each site.

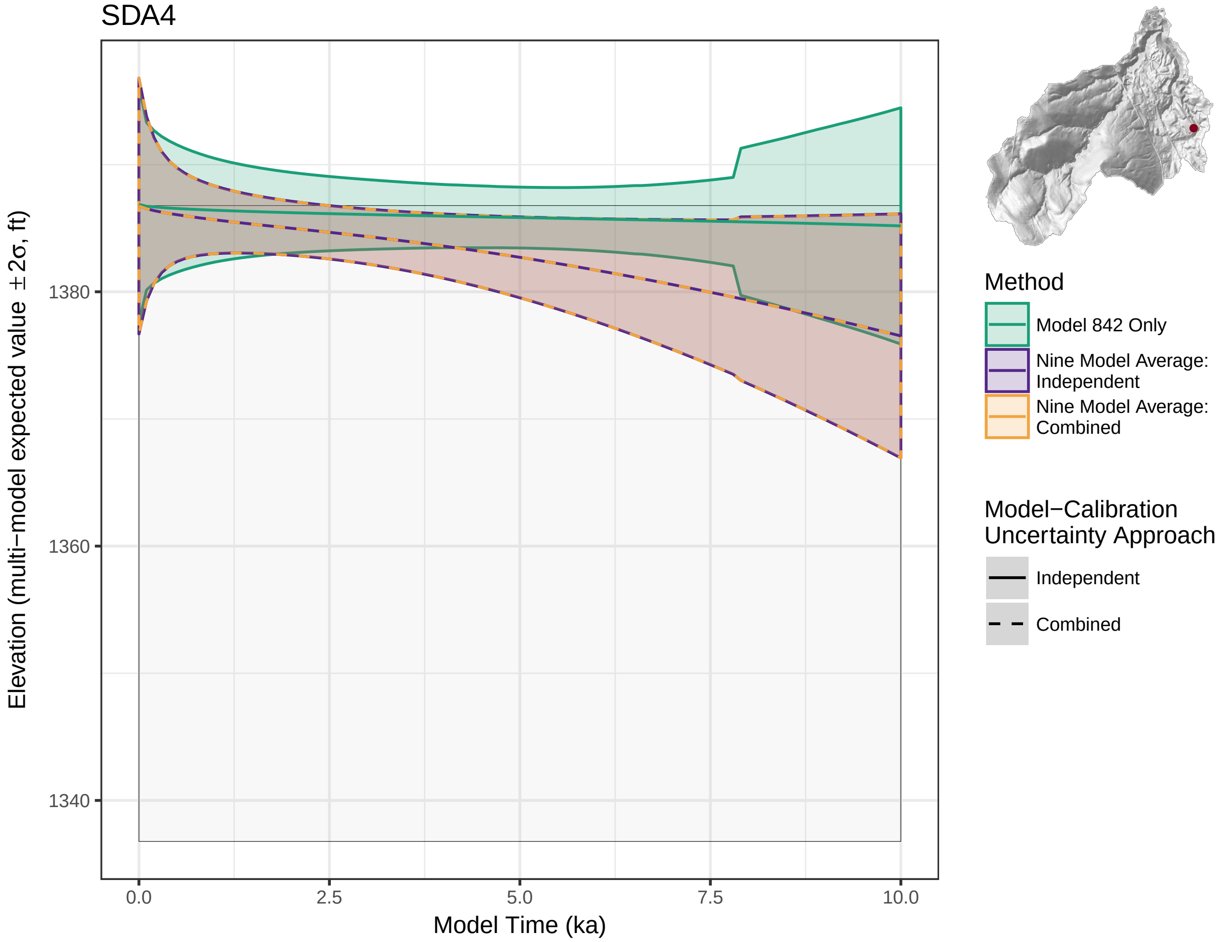

Figure 11.12: Summary of projections at SDA4 showing expected elevation and uncertainty through time. The gray box is a 50 foot deep reference box that extends below the modern surface. Note that both the x and y axis limits are constant. Three expected values and 95% confidence regions are shown that corresponds to the two approaches to model selection (only 842 and all nine 800 variants) and the two approaches to model structure and calibration uncertainty (independent or covarying).

Case 1: Model 842 only

Figure 11.13 shows the standard deviation associated with each source of uncertainty for the case of considering just model 842 for projections. The locations of each of the 25 sites are shown in Figure 11.5. As expected, uncertainty grows through time at all sites. We note that because we initialized the model runs with some noise, the uncertainty associated with initial condition decreases somewhat at first as higher-frequency variations (that is, the random variations imposed on the initial topography) are diffused away. As this case only considered model 842, no model-structure uncertainty is presented. Figure 11.14 shows the proportion of uncertainty through time.

These two Figures illustrate a few important points. First, the amount of uncertainty through time varies a great deal depending on location. The two gully-head sites have a total standard deviation of 30 feet by 10,000 years, while some of the SDA sites have a cumulative erosion of 5 feet or less. Second, the temporal pattern of uncertainty growth varies across the 25 points. Some points see the uncertainty grow linearly in time (e.g., UFrankEdge1), some points see uncertainty grow and then level off (e.g., QuarryEdge), and others see more complicated temporal patterns (e.g., Lagoon3).

Examining Figure 11.14, it is clear that uncertainty in the modern topography dominates at many of the sites. Note here that uncertainty in the initial topography is *not* just uncertainty in measuring the topography, but rather represents uncertainty in how human modification of the plateau surface will impact the patterns of surface water drainage.

Over time, the proportion of uncertainty that is associated with model calibration tends to increase. (Note that the irregularity in the contribution of calibration uncertainty probably reflects irregularity in the surrogate used to represent model 842; the irregularity is absent or much less pronounced for other models). At sites along the plateau edge, the proportion of uncertainty associated with future climate also increase over time. At some sites, such as SDA 2 and UFrankEdge1, uncertainty related to future climate grows to become the second- or third-largest contributor to total uncertainty. At other sites (particularly those located far from the plateau rims), climate-related uncertainty is relatively minor. Uncertainty related to Buttermilk Creek lowering is a minor contributor at all locations; its greatest contribution appears at LFrankEdge, which is one of the closest to the outlet among the 25 locations.

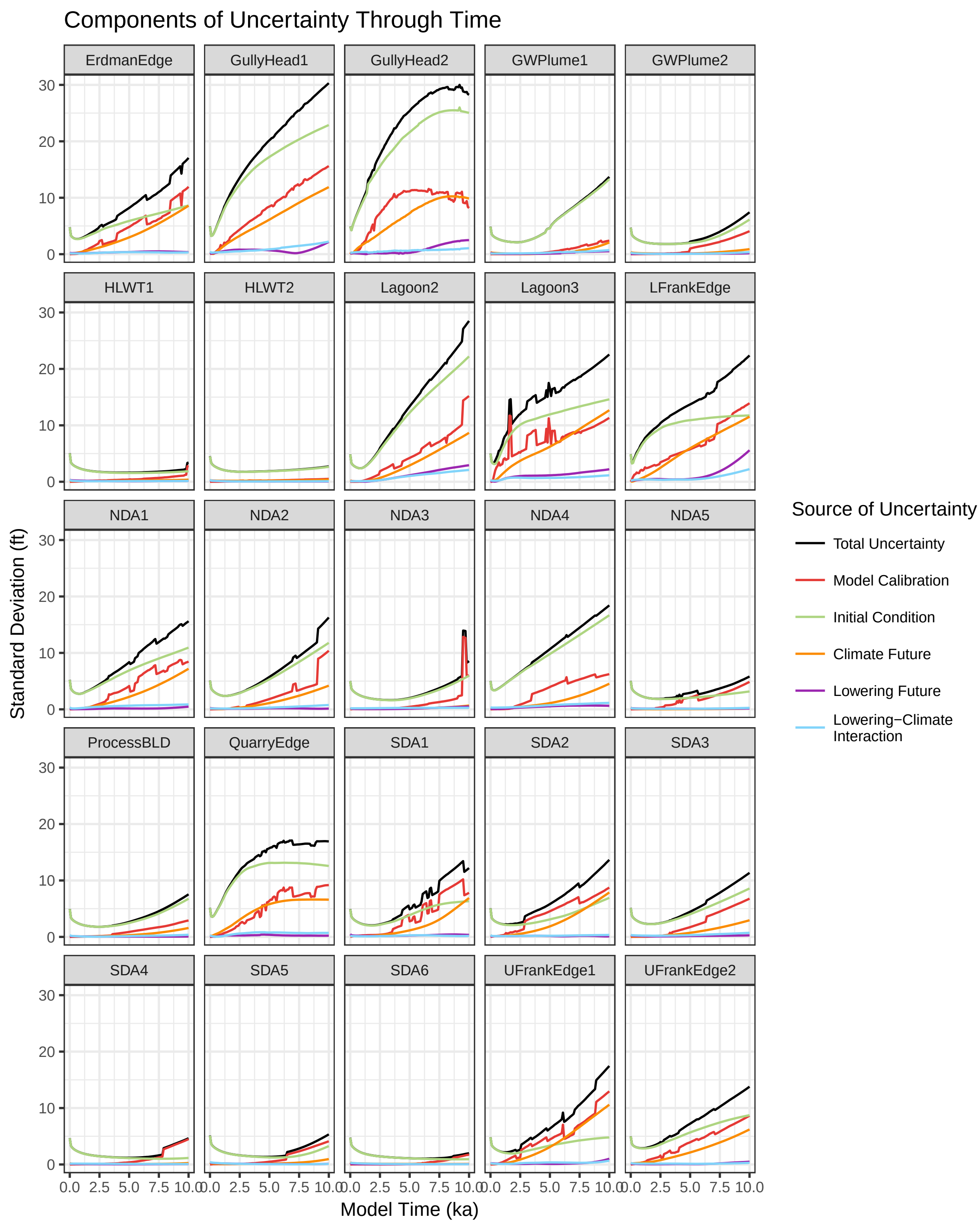

Figure 11.13: Standard deviation (feet) for all components of uncertainty for predictions made with only model 842 at each of the selected analysis sites.

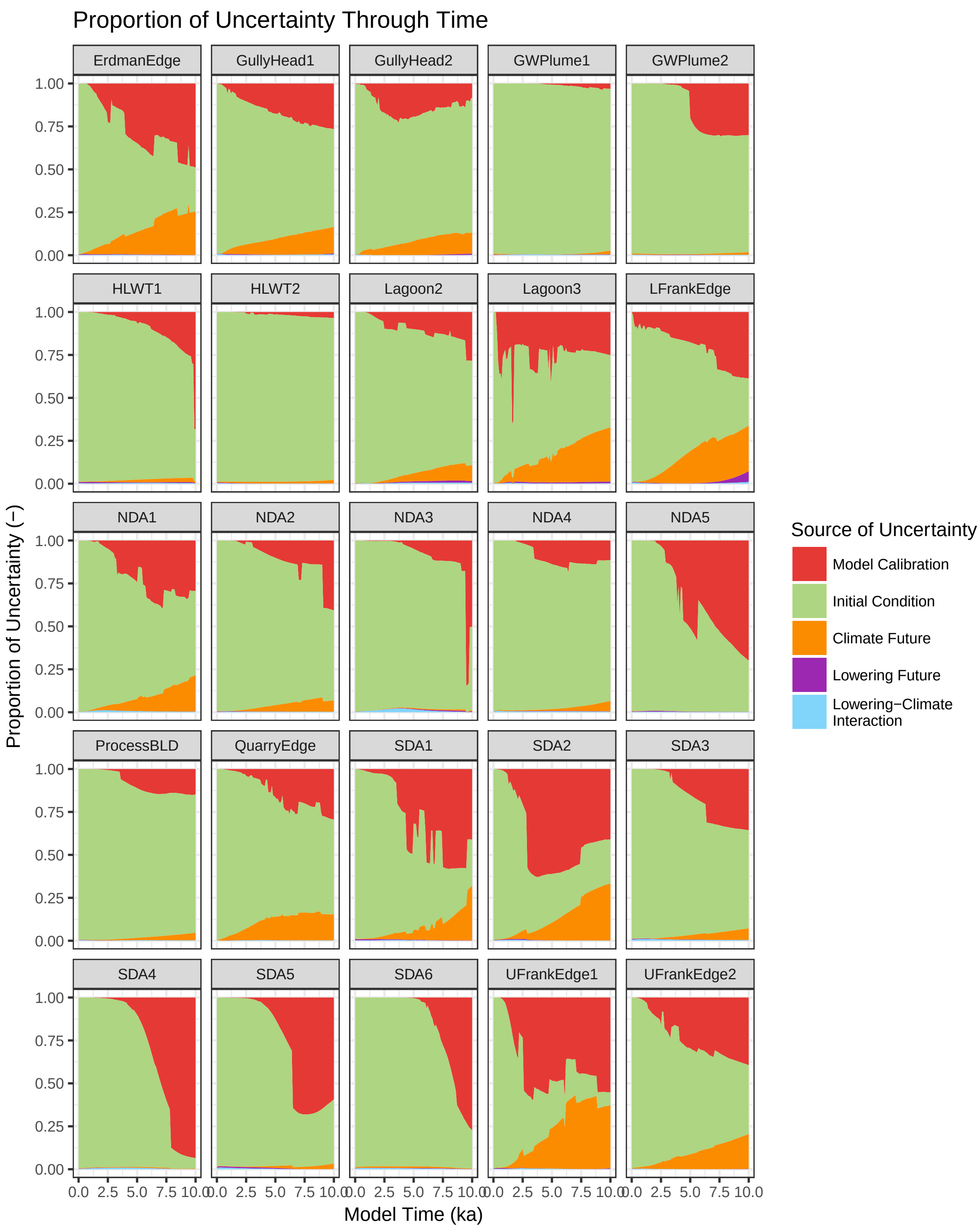

Figure 11.14: Proportion of variance associated with all components of uncertainty for predictions made with only model 842 at each of the selected analysis sites.

Case 2a: All nine 800 variants, independent model structure and calibration

Next we consider the absolute and scaled uncertainties associated with using all nine 800 variants. Here we first assume that model structure and calibration are independent. Figure 11.15 shows the absolute value of the components of uncertainty through time while Figure 11.16 presents the scaled proportions.

As in the prior case, in which we only considered model 842, the uncertainty in initial topography dominates at first. However, uncertainty in model structure quickly grows to dominate the proportion of uncertainty at many of the locations. Model-structure uncertainty is generally greater than model-calibration uncertainty at all points in time; however, at a few sites, calibration uncertainty grows to exceed model-structure uncertainty (e.g., Lagoon2, LFrankEdge).

Interestingly, at a few sites, the proportion of uncertainty associated with model structure grows quickly and then decreases. This occurs at sites GullyHead1 and GullyHead2, which are adjacent to Quarry Creek or Franks Creek. Examination of the projection model output indicates that in the beginning and middle of the projection time period, there is divergence among the nine considered models, as models with and without thresholds and with and without non-linear hillslopes respond differently. However, after the initial amount of erosion occurs, there is convergence between the models. This makes sense because these sites are located right on the edge of the plateau. How they transition from being the plateau edge to being part of a gully channel will vary from model to model, but once they have become part of the channel, the models behave in a similar way.

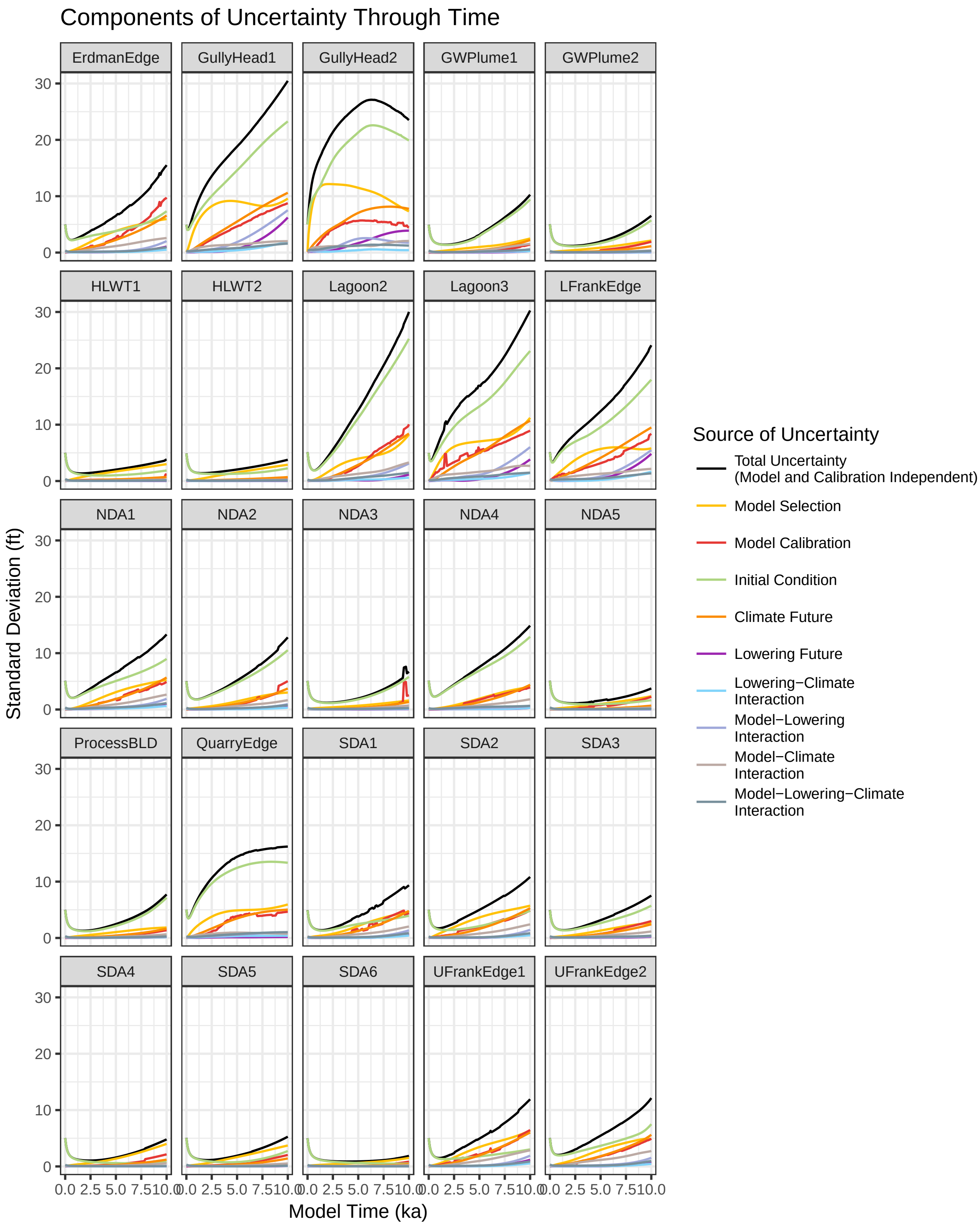

Figure 11.15: Standard deviation (feet) for all components of uncertainty for predictions made with all nine 800 variants at each of the selected analysis sites. This case assumes independent model structure and calibration uncertainty

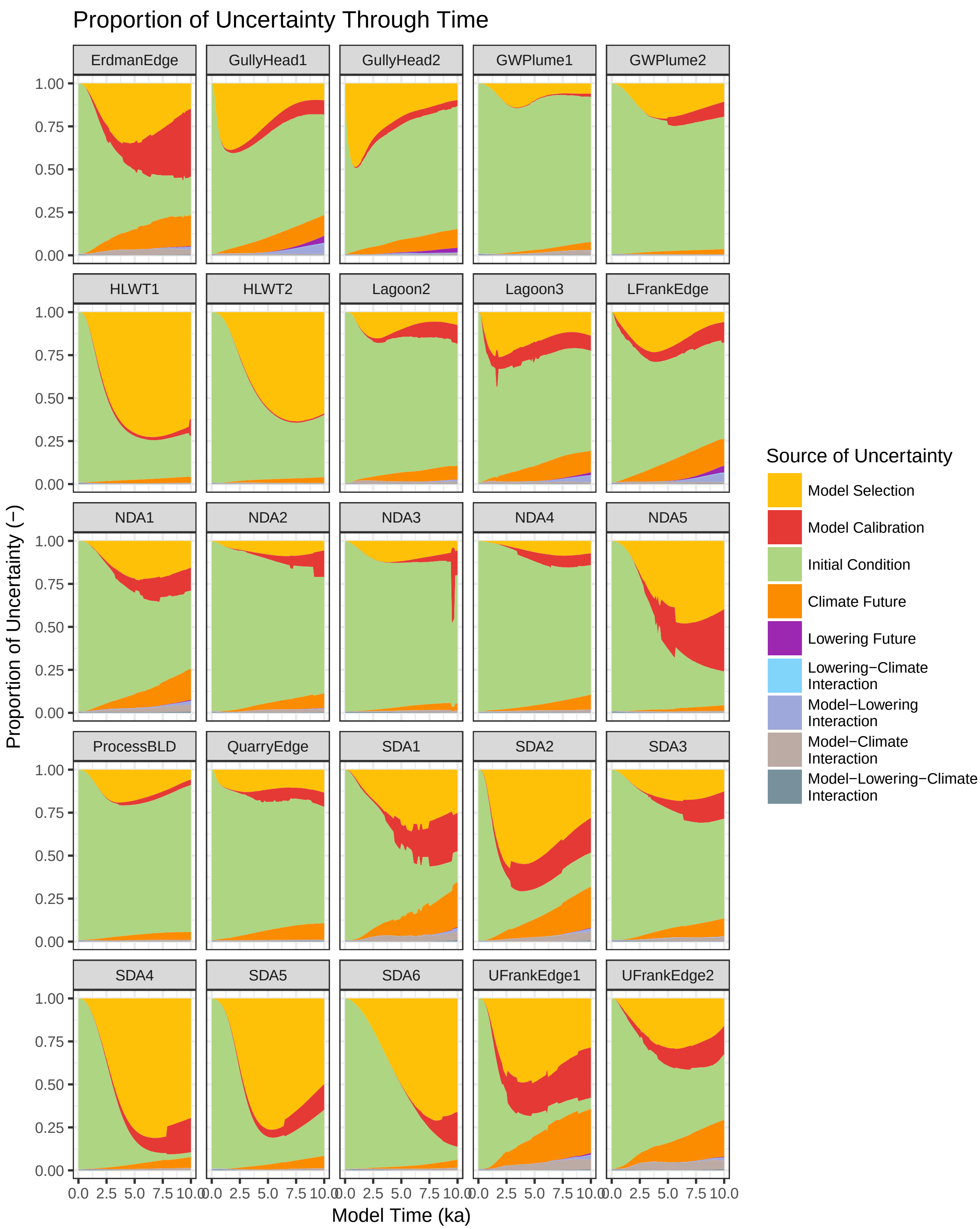

Figure 11.16: Proportion of variance associated with all components of uncertainty for predictions made with all nine 800 variants at each of the selected analysis sites. This case assumes independent model structure and calibration uncertainty

Case 2b: All nine 800 variants with covariance

Finally, we consider all nine 800 variants under the alternative assumption that there may be covariance between the model structure and model calibration uncertainties that derives from the fact that all models were calibrated with the same dataset (*Buckland et al.*, 1997; *Burnham and Anderson*, 2003). Figure 11.17 shows the absolute value of the components of uncertainty through time while Figure 11.18 presents the scaled proportions.

The primary result of these analyses is that the total uncertainty is functionally identical between the results presented here and in Case 2a. This can also be seen in Figure 11.11 in that the two all-800 variant model approaches plot on top of one another. This does not necessarily mean that the model structure-uncertainty and model-calibration uncertainty are not correlated. We interpret this to have occurred because the model-calibration uncertainty is generally smaller than the model-structure uncertainty.

In summary, the uncertainty partitioning analysis at the 25 analysis points indicates a few major conclusions. First, there is substantial variation in the amount of uncertainty in erosion at each site. Second, there is variation in the temporal patterns of uncertainty growth. We identified that initial condition and model structure (for 800s cases) dominate the projection uncertainty, with initial condition being more important in the first portion of the model period and model structure being most important at the end of the modeled time period. Calibration uncertainty is the next most important, followed by uncertainty in downcutting future and climate future. Two- and three-way interactions between model lowering and climate are negligible.

These conclusions make sense in the context of the figures presented at the beginning of this section. For example, we can contrast Figure 11.6, in which the nine models are contrasted for a given climate future and lowering future, and Figure 11.7, in which all nine climate-downcutting scenarios are shown for model 842. The difference in resulting topography between the multiple models is much larger than the differences across downcutting histories. Differences between the climate scenarios are hard to distinguish. Finally, if we also consider Figure 11.8, we can see that for sites along the plateau margins, the reorganization of surface drainage that occurred due to the initial-condition perturbations can have a strong impact on at-a-point future erosion. This finding reflects the fact that relatively subtle changes to the topography on the north plateau (for example) can have a large impact on the relative supply of surface-water drainage to particular proto-gullies along the plateau rim.

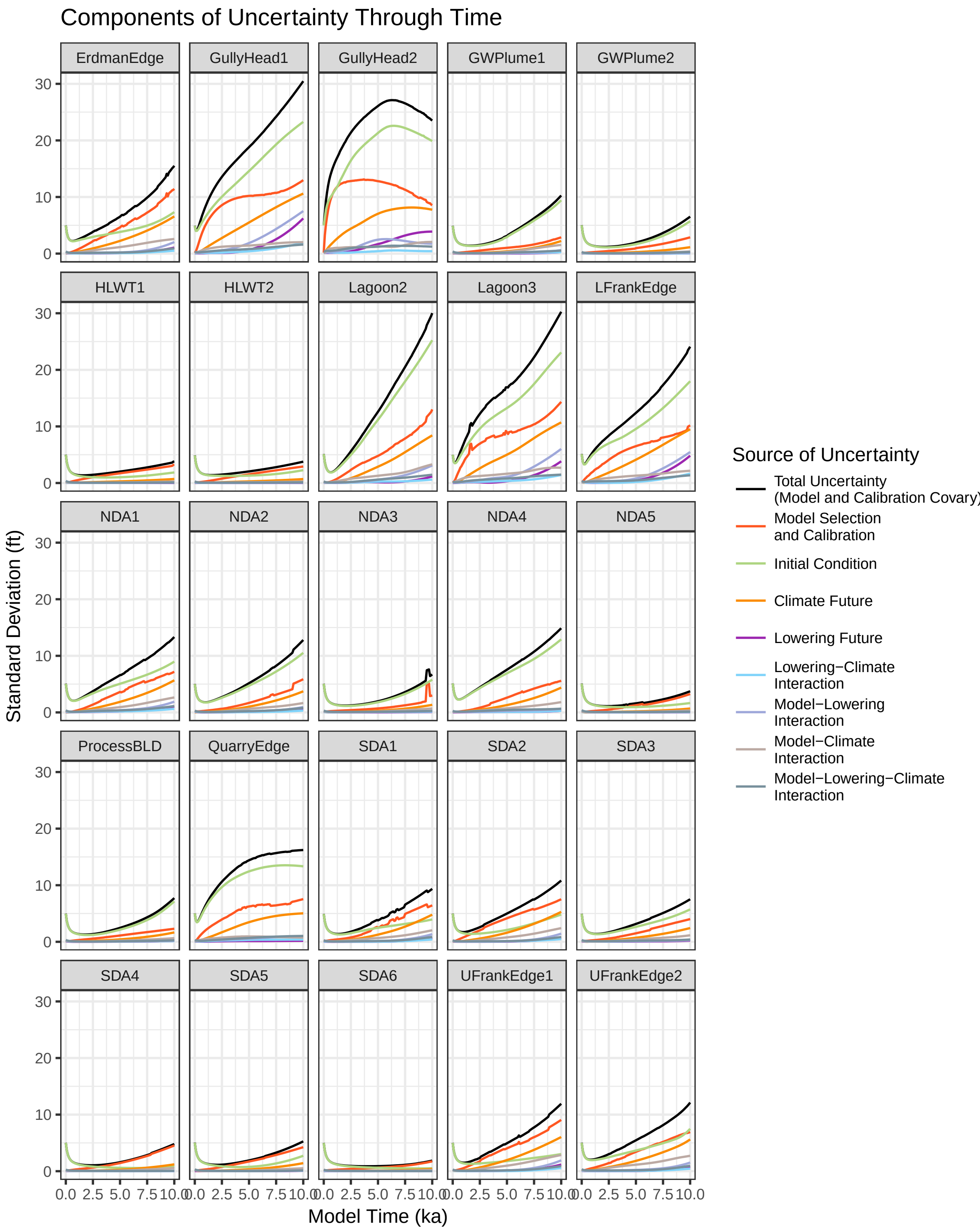

Figure 11.17: Standard deviation (feet) for all components of uncertainty for predictions made with all nine 800 variants at each of the selected analysis sites. This case assumes covariance between model structure and calibration uncertainty

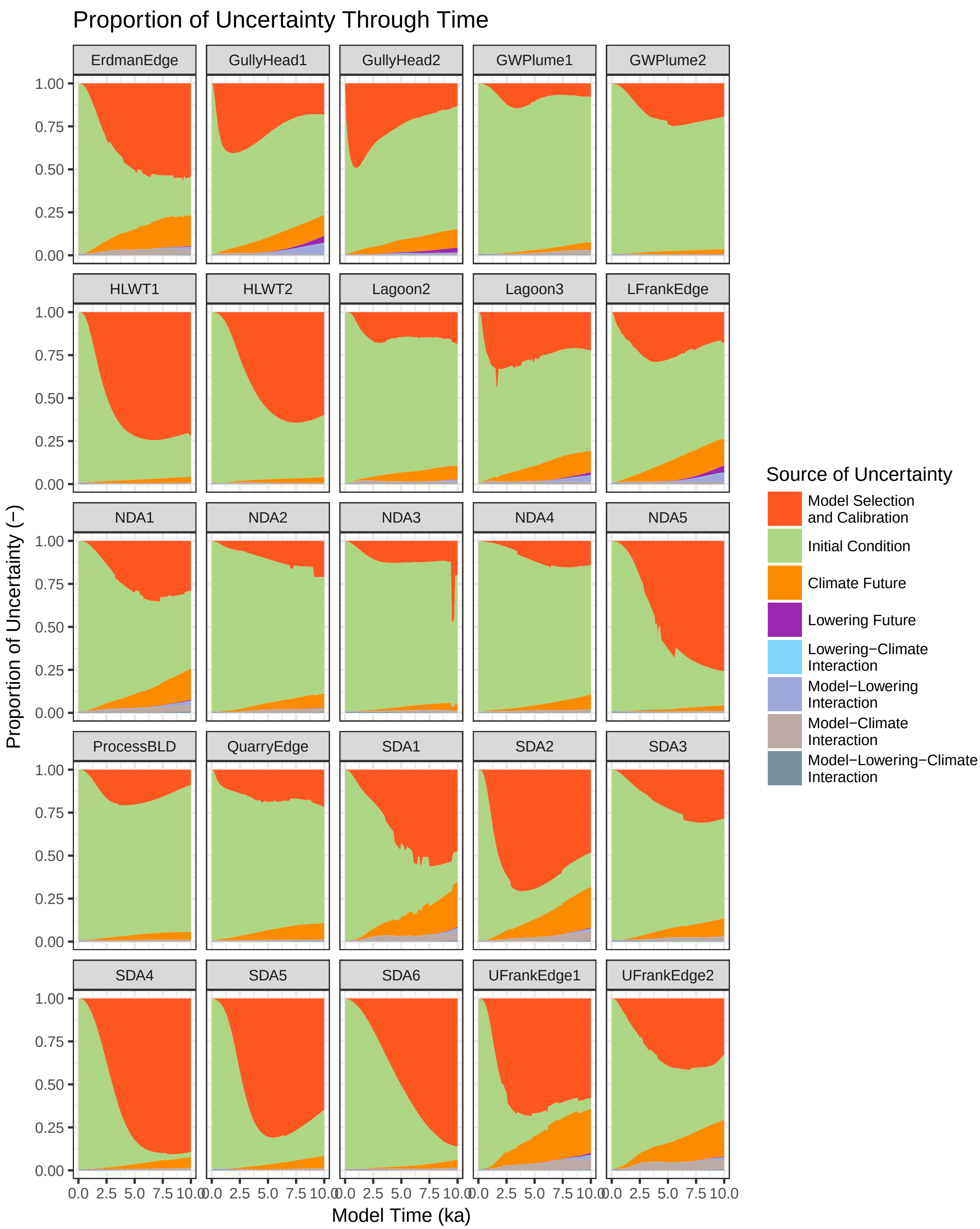

Figure 11.18: Proportion of variance associated with all components of uncertainty for predictions made with all nine 800 variants at each of the selected analysis sites. This case assumes covariance between model structure and calibration uncertainty

11.6.4 Maps of erosion projections and uncertainty through time

The uncertainty partitioning figures presented in the prior section document the proportion of uncertainty associated with model calibration in the context of other sources of uncertainty. Model calibration uncertainty is larger than uncertainty associated with climate future or downcutting future, but generally lower than that associated with model structure or perturbation to initial condition topography. The results of Section 11.6.3 also show that there is substantial variation in uncertainty across space and time.

Here we present maps of expected erosion through time over the entire model domain. As in the prior section we consider two cases: use of only model 842, and use of all nine model-800 variants. While we cannot constrain uncertainty associated with parameter calibration over the entire domain, we can constrain all other sources of uncertainty. We also note that while we could calculate the uncertainty associated with various interaction effects over the entire domain, the prior analysis revealed that their contribution is minimal. Thus we focus here on uncertainty associated with model structure (in the all-800s case), climate future, downcutting future, and initial condition. We use the term *total* uncertainty* to indicate the uncertainty that includes just these components.

We present projections at six time periods: 200, 500, 1000, 2000, 5000, and 10,000 years in the future. One set of figures shows expected erosion and total* uncertainty at all six times. A second set shows expected erosion plus and minus 1σ (where 1σ = total* uncertainty equivalent to one standard deviation). A third set shows expected erosion plus and minus 2σ. Finally, a fourth set shows each of the the components of uncertainty at 1000 and 10,0000 years. Table 11.3 provides a guide to what is presented in each figure.

Table 11.3: Guide to prediction map figures

Figure Type	only model 842	all nine 800 variants
Expected erosion & total* uncertainty	Figures 11.19 and 11.20	Figures 11.26 and 11.27
Expected erosion $\pm 1\sigma$	Figures 11.21 and 11.22	Figures 11.28 and 11.29
Expected erosion $\pm 2\sigma$	Figures 11.23 and 11.24	Figures 11.30 and 11.31
Uncertainty components	Figure 11.25	Figure 11.32

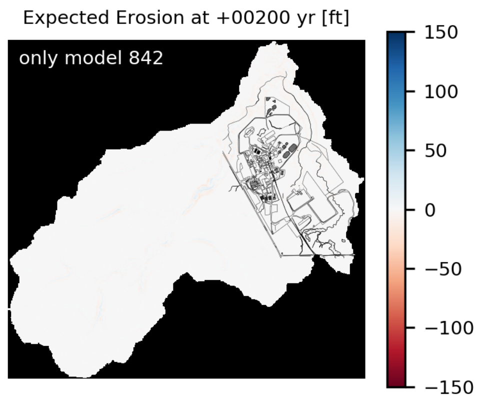

(a) Expected erosion at 200 years

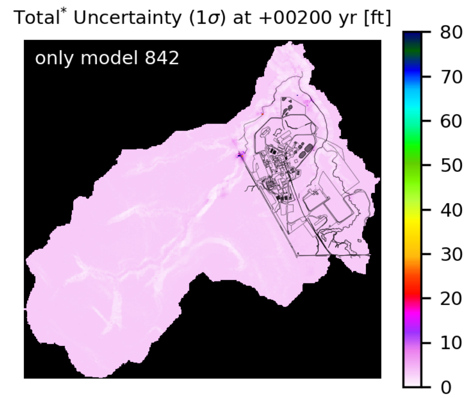

(b) Total* uncertainty at 200 years

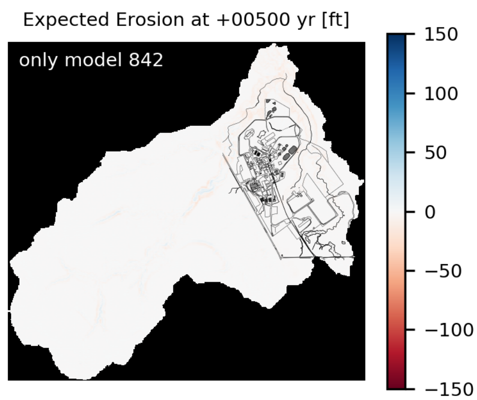

(c) Expected erosion at 500 years

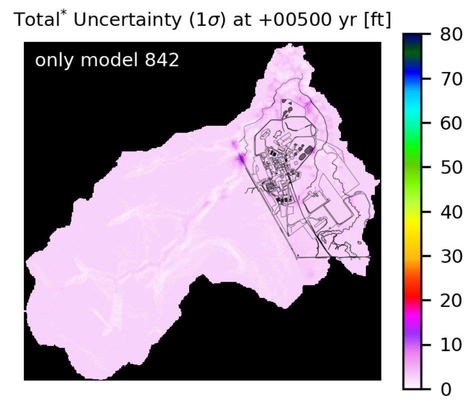

(d) Total* uncertainty at 500 years

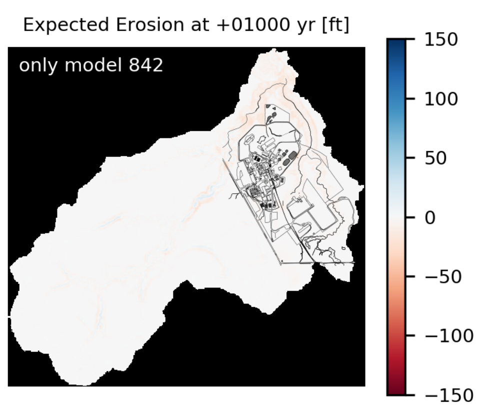

(e) Expected erosion at 1000 years

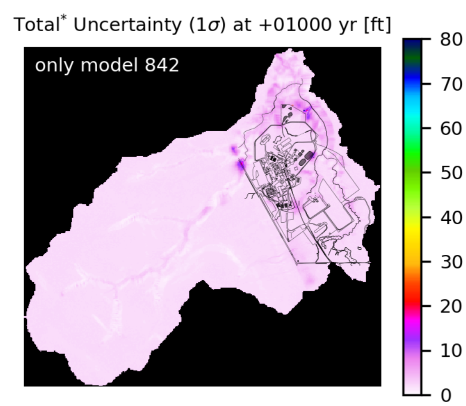

(f) Total* uncertainty at 1000 years

Figure 11.19: Maps of expected erosion and total* uncertainty in erosion at 200, 500, and 1000 years in the future for model 842 only.

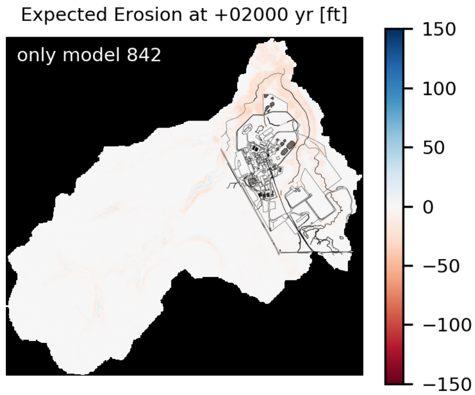

(a) Expected erosion at 2000 years

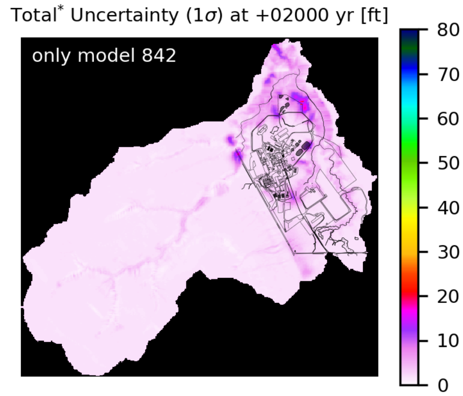

(b) Total* uncertainty at 2000 years

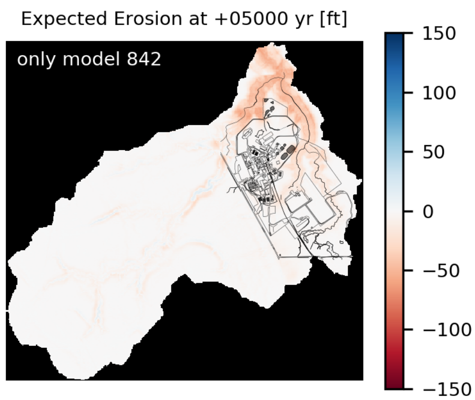

(c) Expected erosion at 5000 years

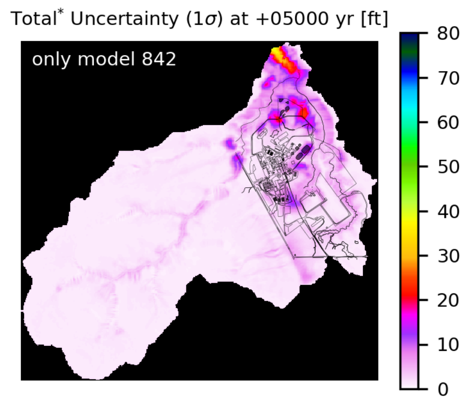

(d) Total* uncertainty at 5000 years

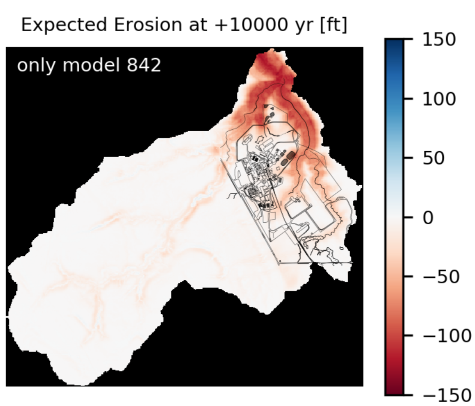

(e) Expected erosion at 10000 years

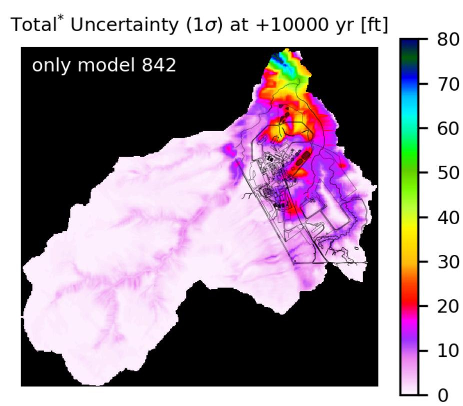

(f) Total* uncertainty at 10000 years

Figure 11.20: Maps of expected erosion and total* uncertainty in erosion at 2000, 5000, and 10000 years in the future for model 842 only.

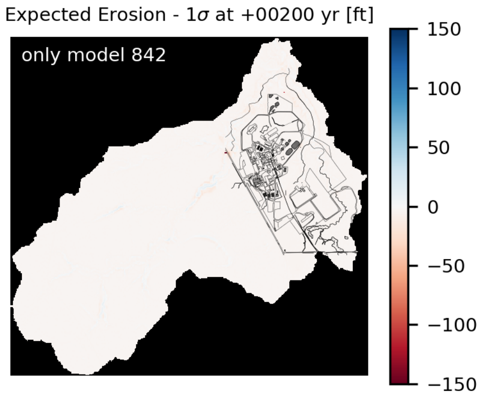

(a) Expected erosion -1σ at 200 years

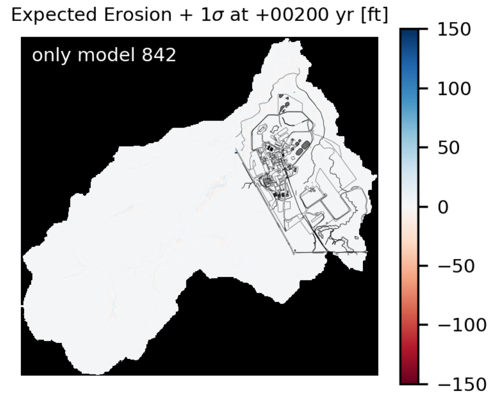

(b) Expected erosion $+1\sigma$ at 200 years

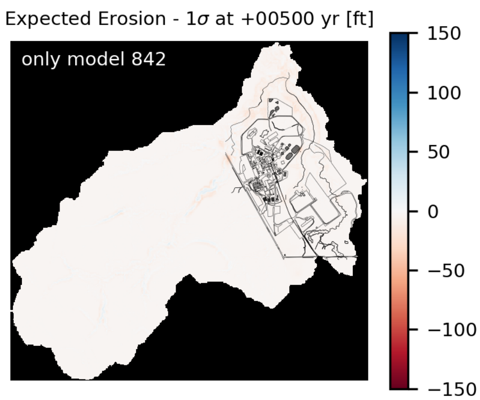

(c) Expected erosion -1σ at 500 years

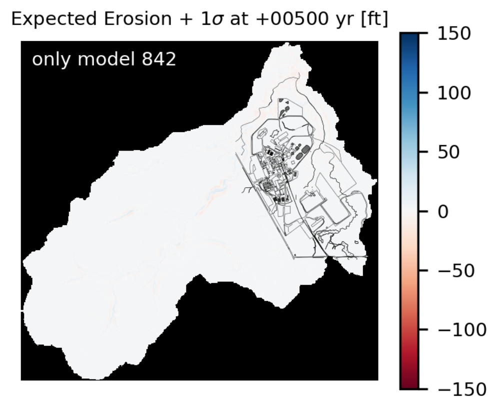

(d) Expected erosion $+1\sigma$ at 500 years

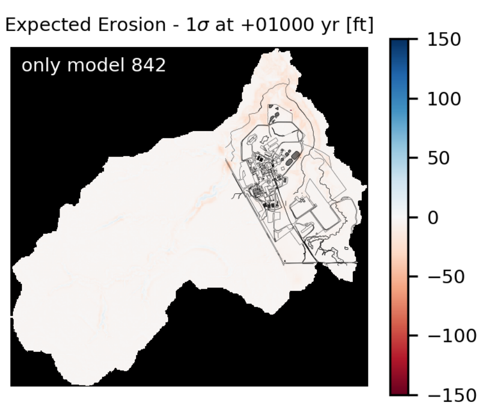

(e) Expected erosion -1σ at 1000 years

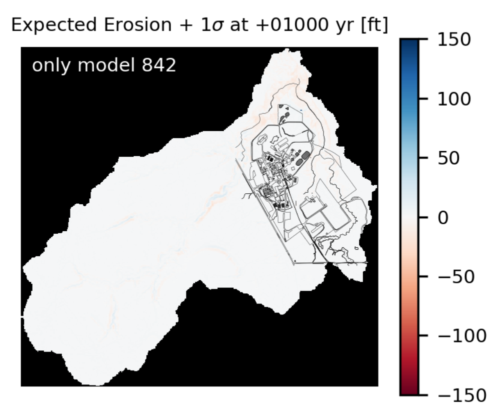

(f) Expected erosion $+1\sigma$ at 1000 years

Figure 11.21: Maps of expected erosion plus and minus 1σ at 200, 500, and 1000 years in the future for model 842 only.

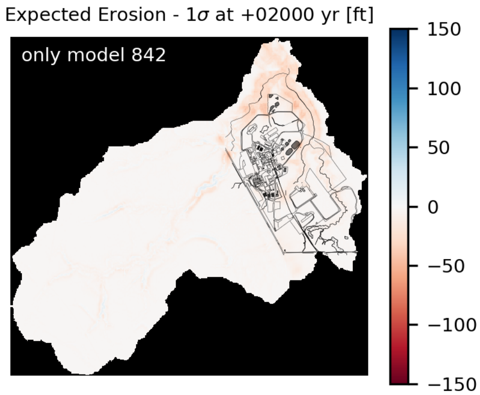

(a) Expected erosion -1σ at 2000 years

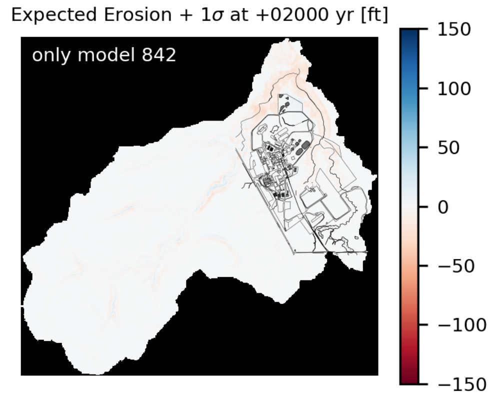

(b) Expected erosion $+1\sigma$ at 2000 years

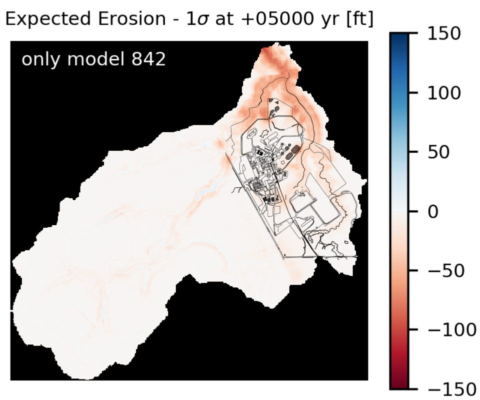

(c) Expected erosion -1σ at 5000 years

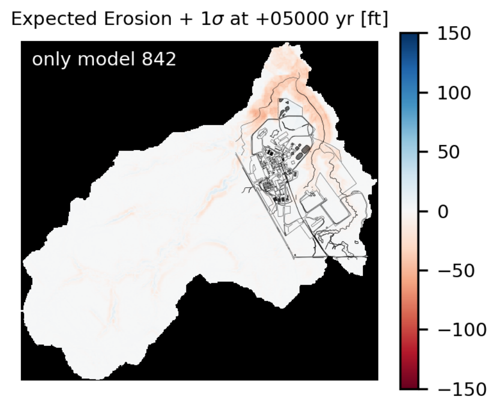

(d) Expected erosion $+1\sigma$ at 5000 years

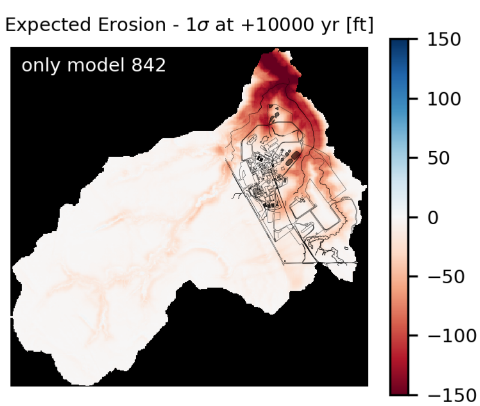

(e) Expected erosion -1σ at 10000 years

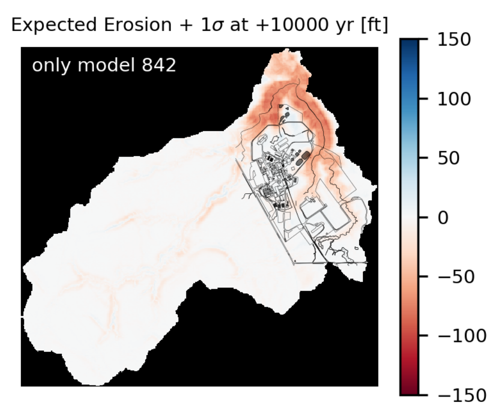

(f) Expected erosion $+1\sigma$ at 10000 years

Figure 11.22: Maps of expected erosion plus and minus 1σ at 2000, 5000, and 10000 years in the future for model 842 only.

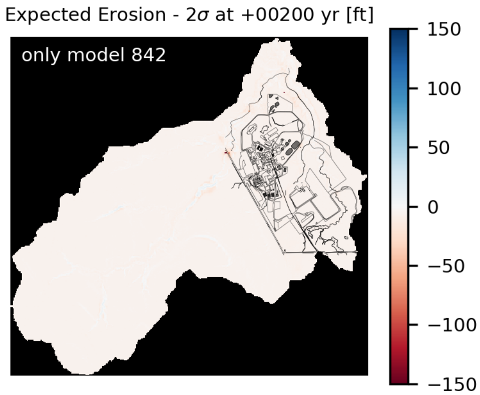

(a) Expected erosion -2σ at 200 years

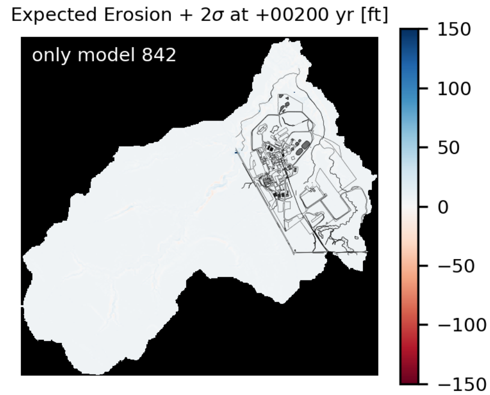

(b) Expected erosion $+2\sigma$ at 200 years

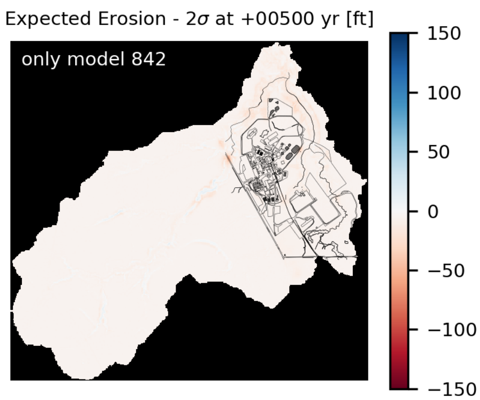

(c) Expected erosion -2σ at 500 years

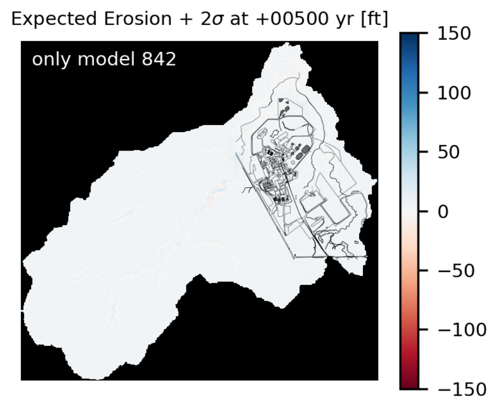

(d) Expected erosion $+2\sigma$ at 500 years

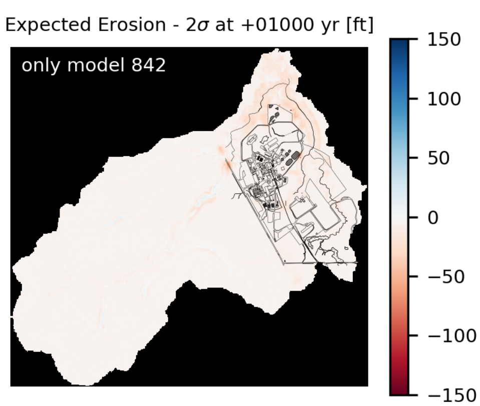

(e) Expected erosion -2σ at 1000 years

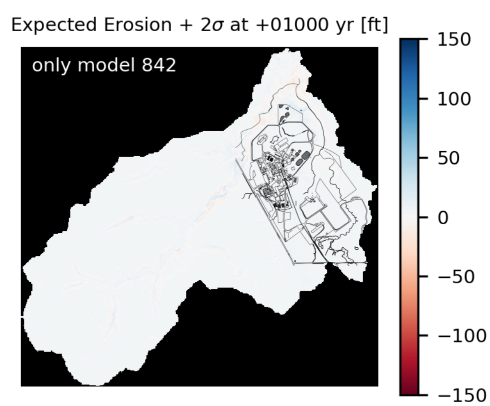

(f) Expected erosion $+2\sigma$ at 1000 years

Figure 11.23: Maps of expected erosion plus and minus 2σ at 200, 500, and 1000 years in the future for model 842 only.

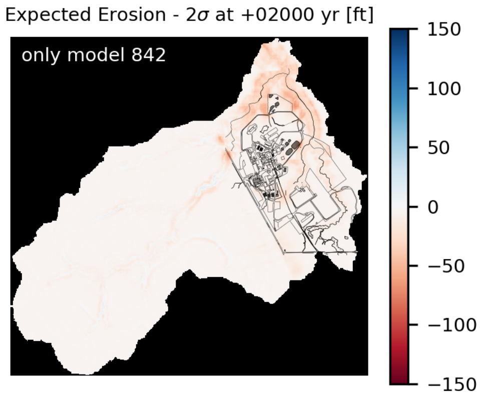

(a) Expected erosion -2σ at 2000 years

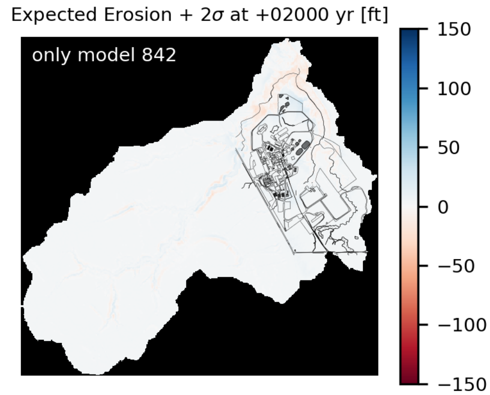

(b) Expected erosion $+2\sigma$ at 2000 years

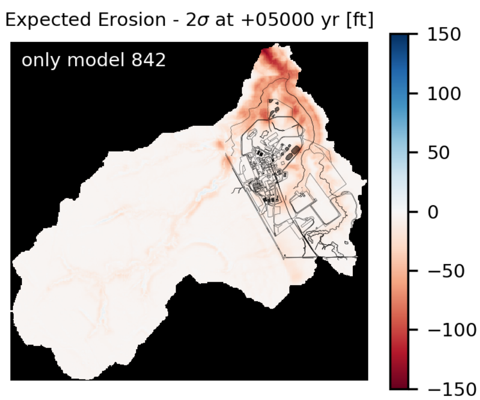

(c) Expected erosion -2σ at 5000 years

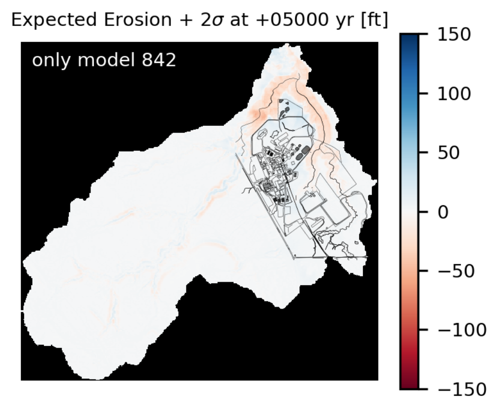

(d) Expected erosion $+2\sigma$ at 5000 years

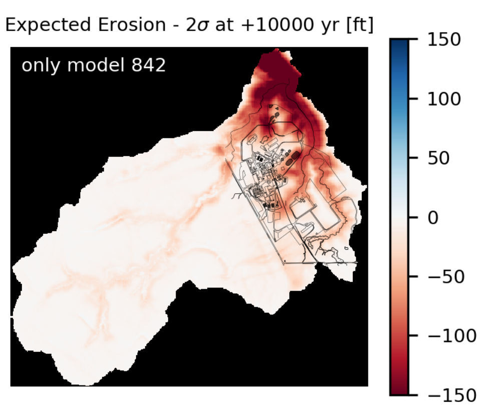

(e) Expected erosion -2σ at 10000 years

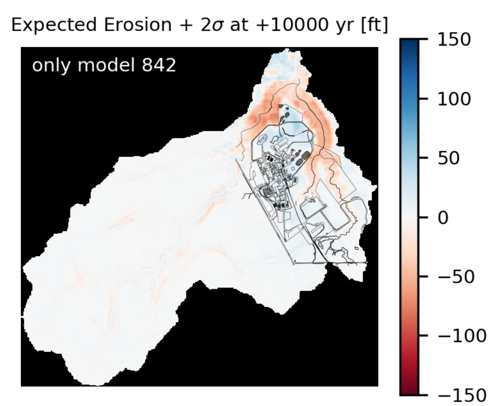

(f) Expected erosion $+2\sigma$ at 10000 years

Figure 11.24: Maps of expected erosion plus and minus 2σ at 2000, 5000, and 10000 years in the future for model 842 only.

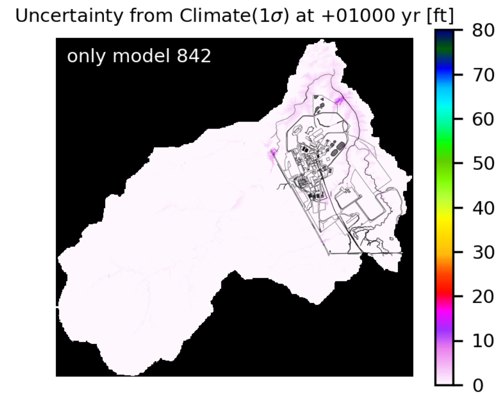

(a) Uncertainty associated with climate future at 1000 years

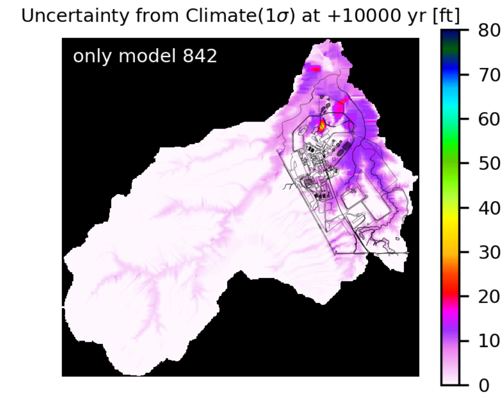

(b) Uncertainty associated with climate future at 10000 years

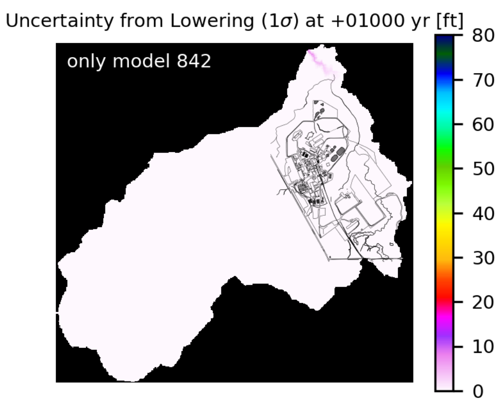

(c) Uncertainty associated with lowering future at 1000 years

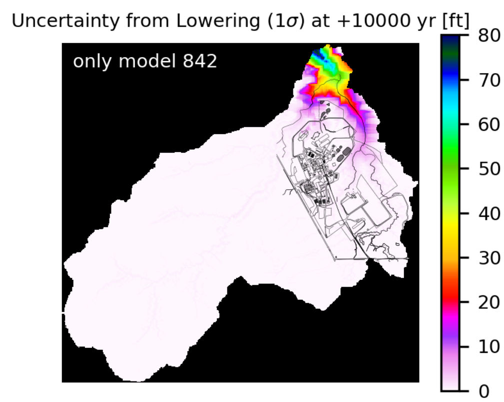

(d) Uncertainty associated with lowering future at 10000 years

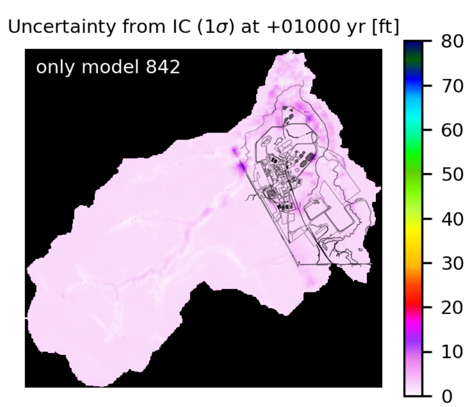

(e) Uncertainty associated with initial topography at 1000 years

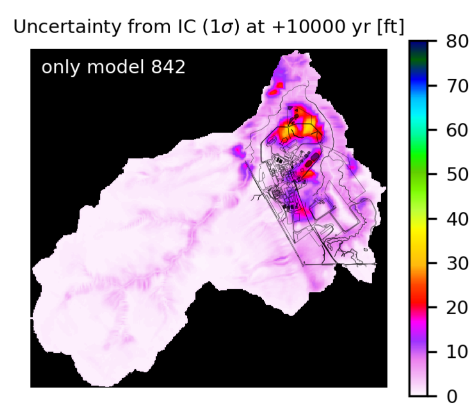

(f) Uncertainty associated with initial topography at 10000 years

Figure 11.25: Components of uncertainty at 1000 and 10000 years in the future for model 842 only.

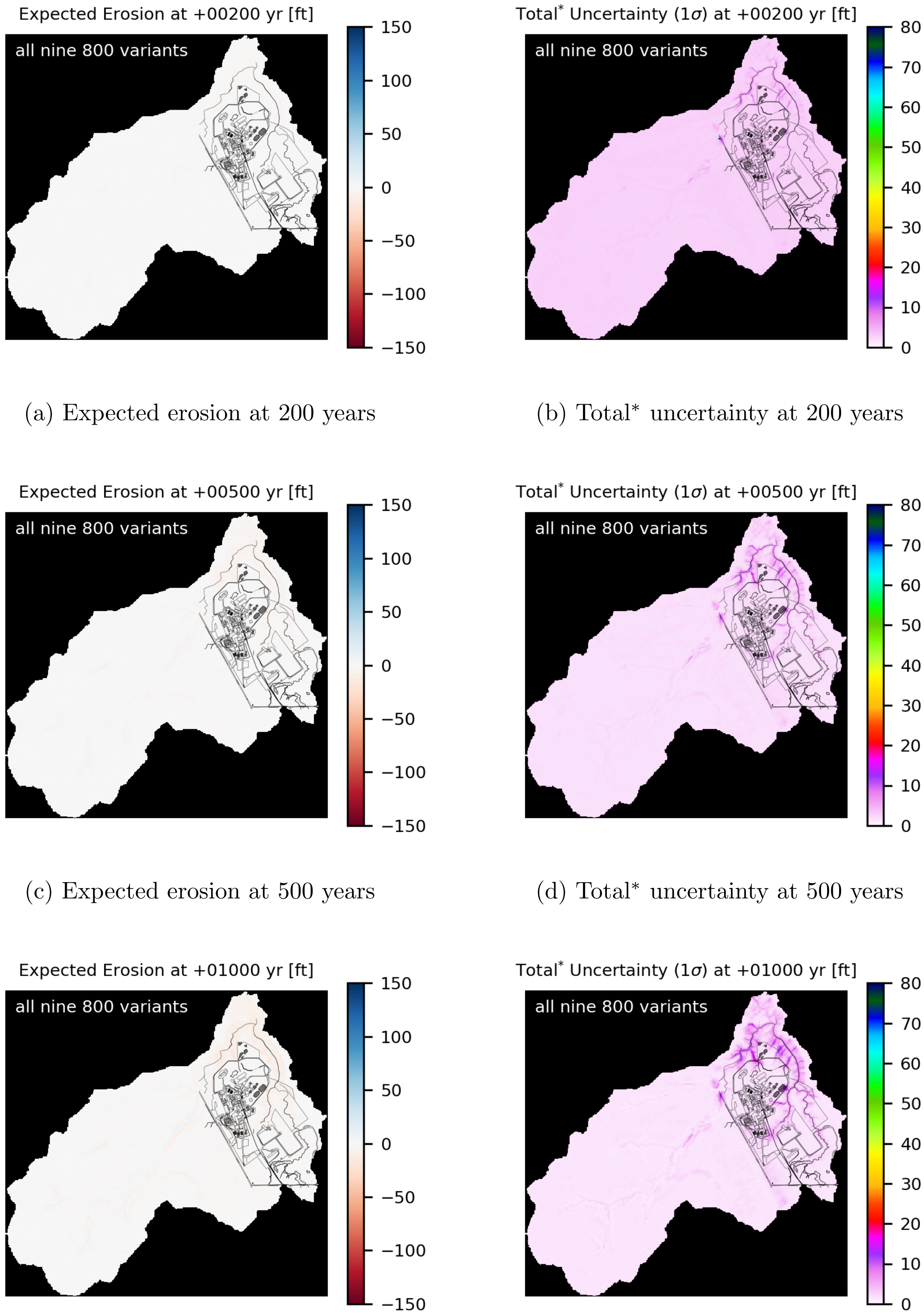

(a) Expected erosion at 200 years

(b) Total* uncertainty at 200 years

(c) Expected erosion at 500 years

(d) Total* uncertainty at 500 years

(e) Expected erosion at 1000 years

(f) Total* uncertainty at 1000 years

Figure 11.26: Maps of expected erosion and total* uncertainty in erosion at 200, 500, and 1000 years in the future for the combination of all nine 800 variants.

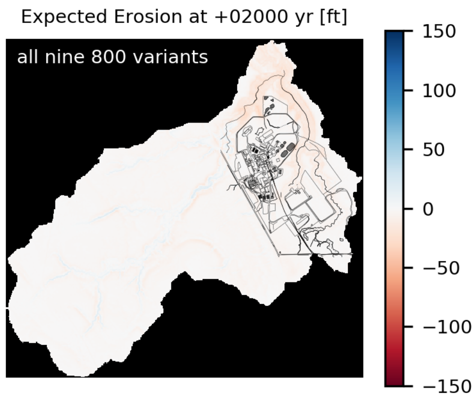

(a) Expected erosion at 2000 years

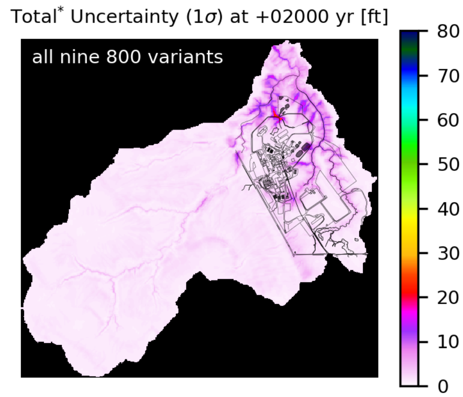

(b) Total* uncertainty at 2000 years

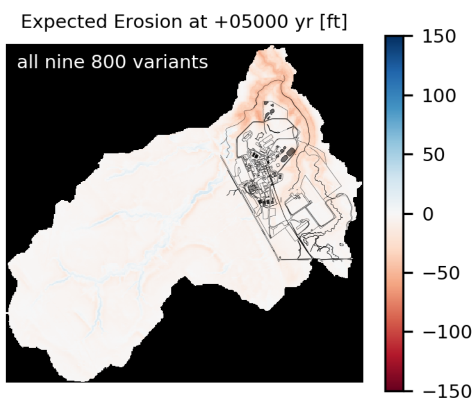

(c) Expected erosion at 5000 years

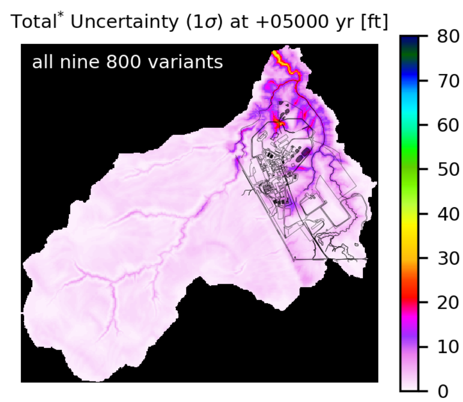

(d) Total* uncertainty at 5000 years

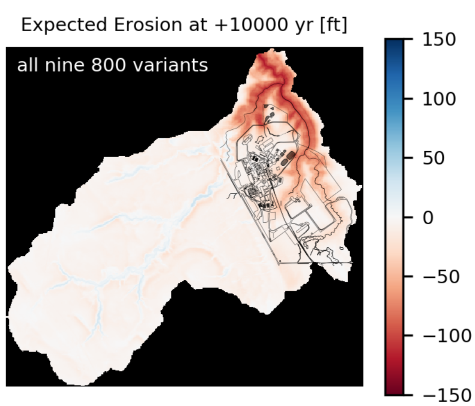

(e) Expected erosion at 10000 years

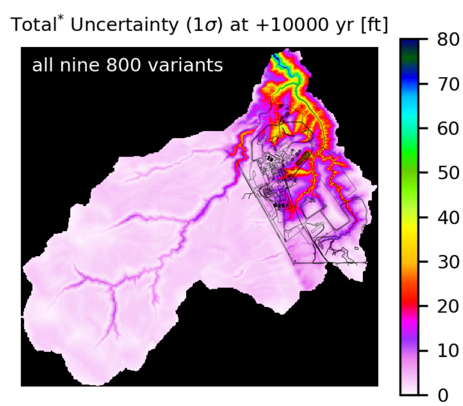

(f) Total* uncertainty at 10000 years

Figure 11.27: Maps of expected erosion and total* uncertainty in erosion at 200, 500, and 1000 years in the future for the combination of all nine 800 variants.

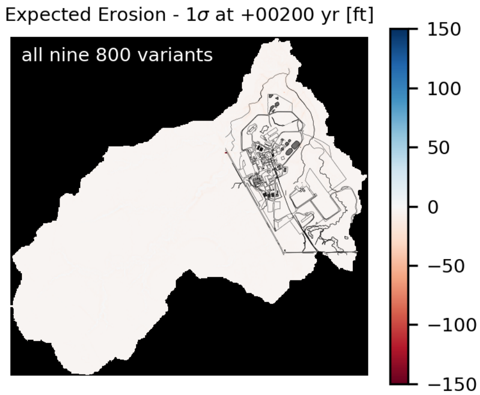

(a) Expected erosion -1σ at 200 years

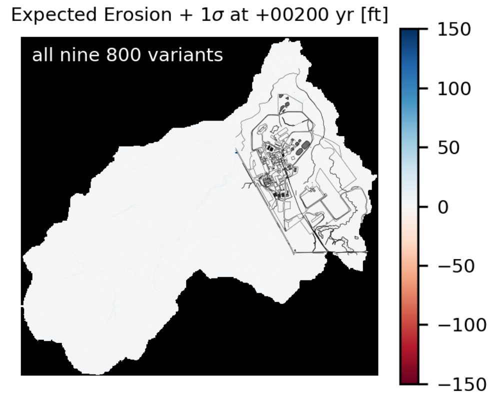

(b) Expected erosion $+1\sigma$ at 200 years

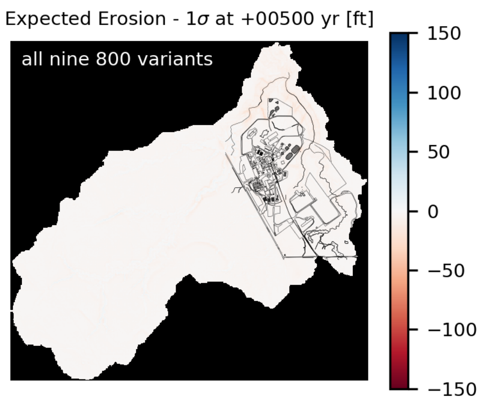

(c) Expected erosion -1σ at 500 years

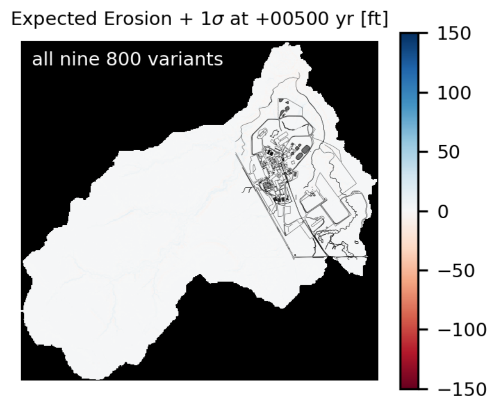

(d) Expected erosion $+1\sigma$ at 500 years

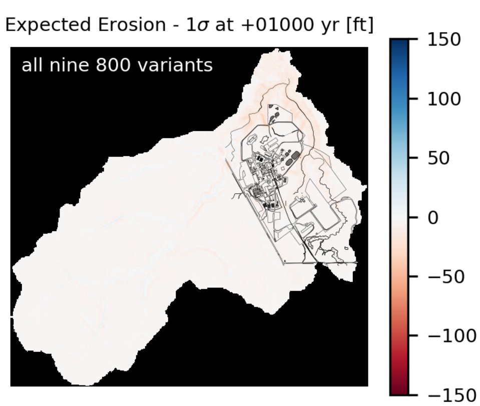

(e) Expected erosion -1σ at 1000 years

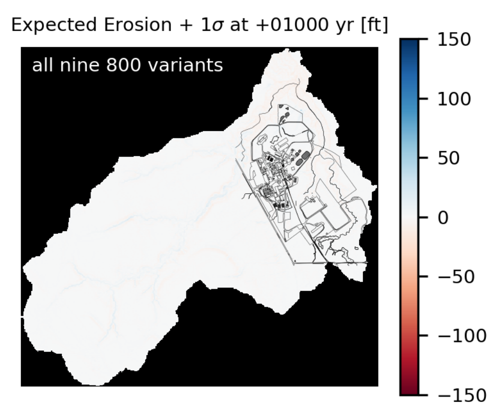

(f) Expected erosion $+1\sigma$ at 1000 years

Figure 11.28: Maps of expected erosion plus and minus 1σ at 200, 500, and 1000 years in the future for the combination of all nine 800 variants.

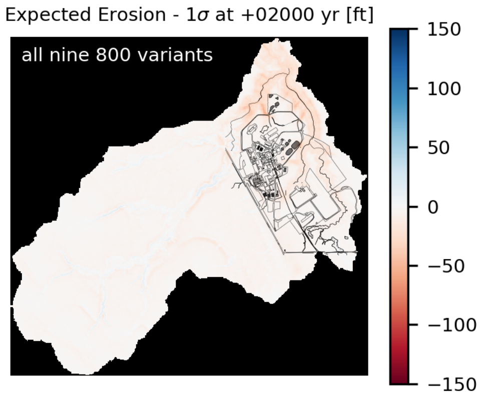

(a) Expected erosion -1σ at 2000 years

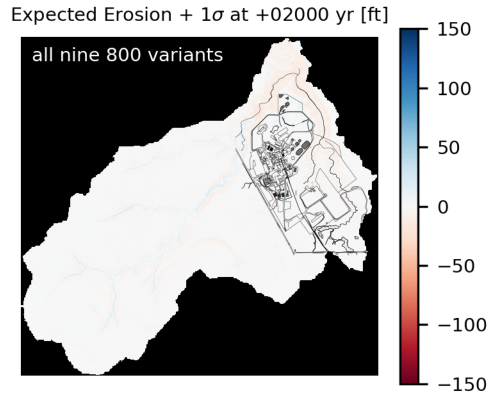

(b) Expected erosion $+1\sigma$ at 2000 years

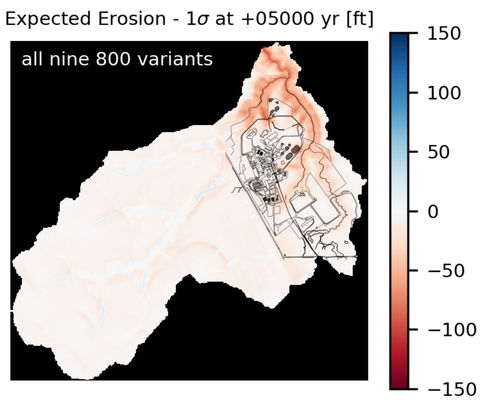

(c) Expected erosion -1σ at 5000 years

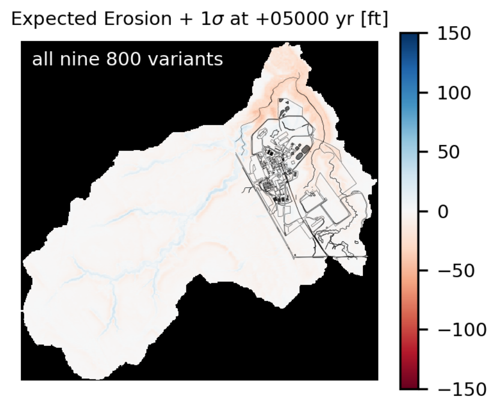

(d) Expected erosion $+1\sigma$ at 5000 years

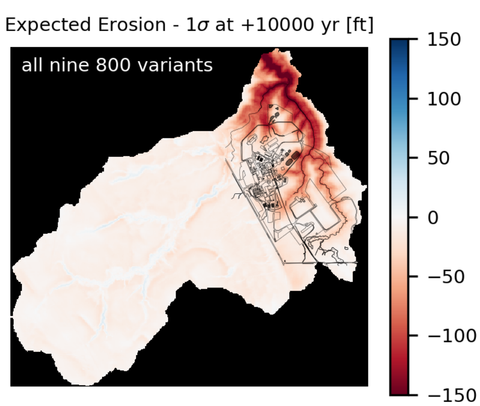

(e) Expected erosion -1σ at 10000 years

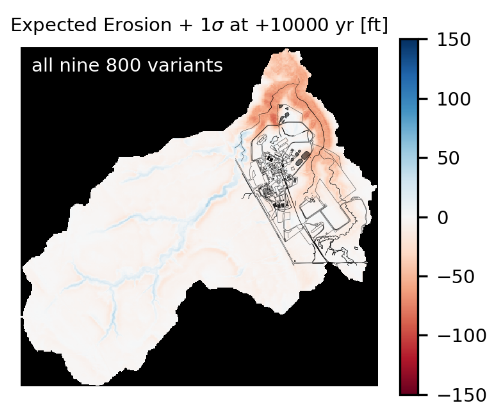

(f) Expected erosion $+1\sigma$ at 10000 years

Figure 11.29: Maps of expected erosion plus and minus 1σ at 2000, 5000, and 10000 years in the future for the combination of all nine 800 variants.

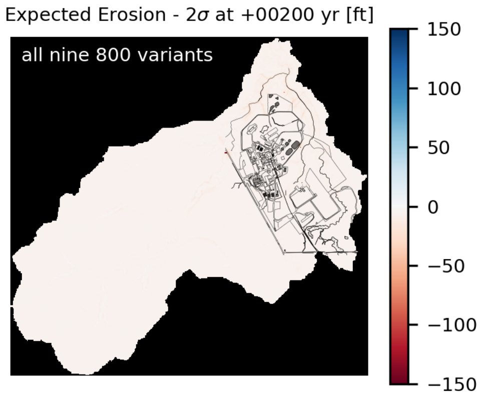

(a) Expected erosion -2σ at 200 years

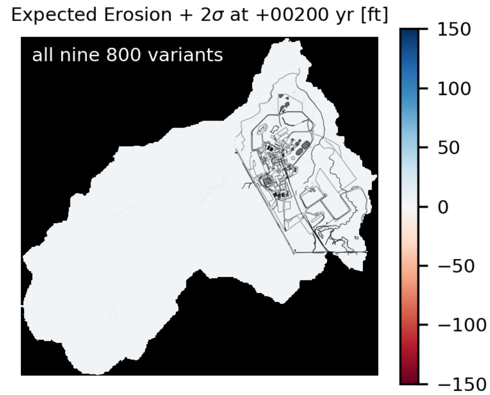

(b) Expected erosion $+2\sigma$ at 200 years

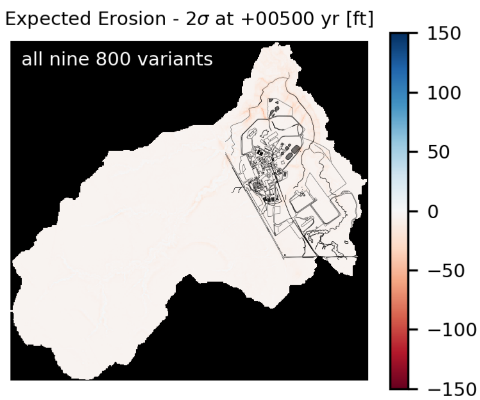

(c) Expected erosion -2σ at 500 years

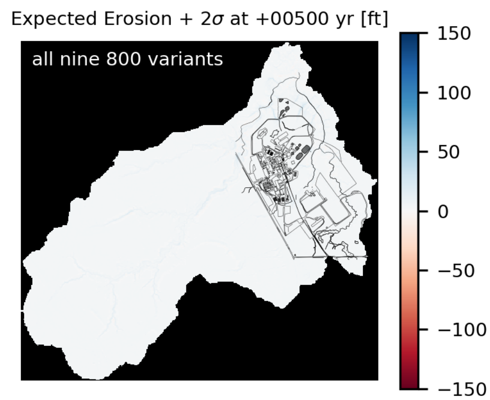

(d) Expected erosion $+2\sigma$ at 500 years

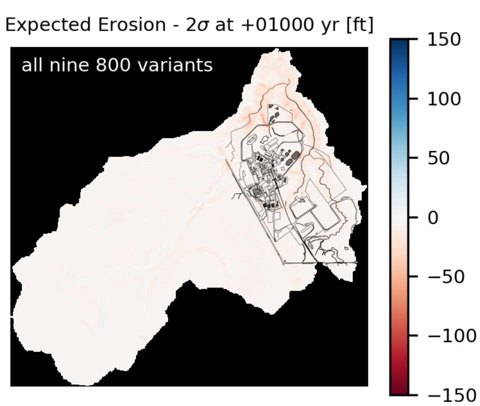

(e) Expected erosion -2σ at 1000 years

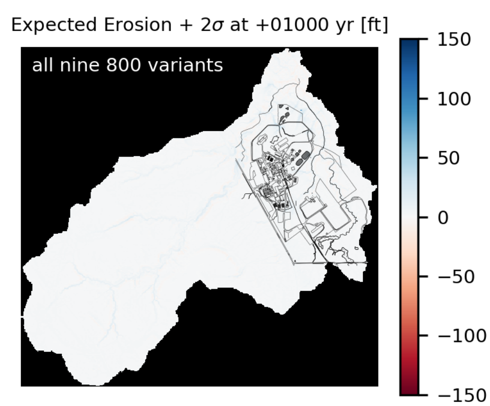

(f) Expected erosion $+2\sigma$ at 1000 years

Figure 11.30: Maps of expected erosion plus and minus 2σ at 200, 500, and 1000 years in the future for the combination of all nine 800 variants.

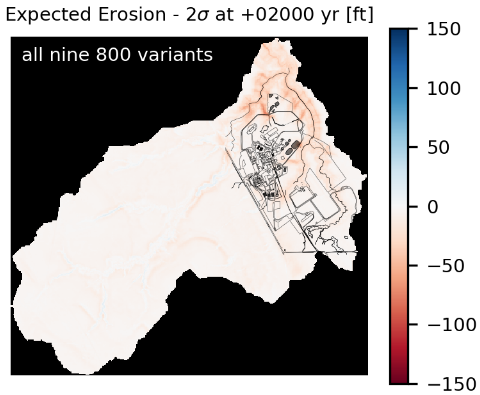

(a) Expected erosion -2σ at 2000 years

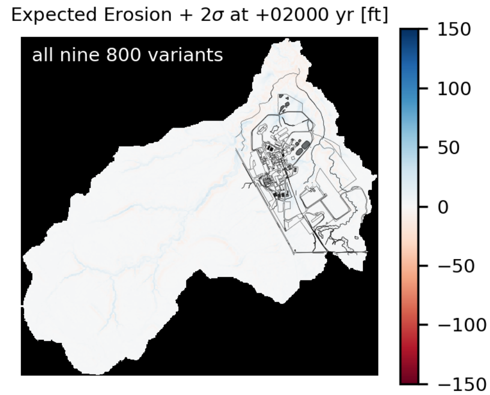

(b) Expected erosion $+2\sigma$ at 2000 years

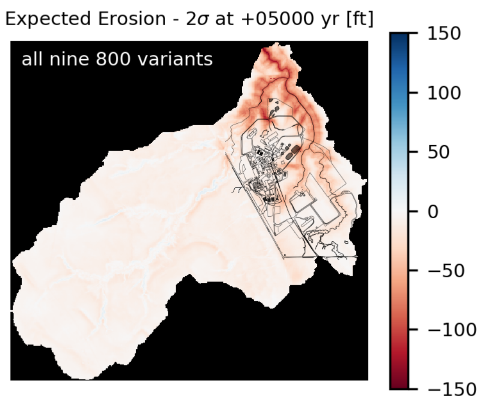

(c) Expected erosion -2σ at 5000 years

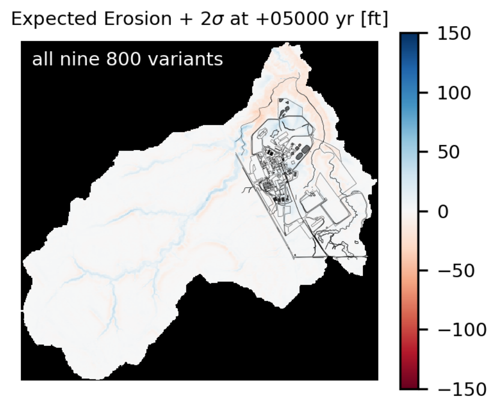

(d) Expected erosion $+2\sigma$ at 5000 years

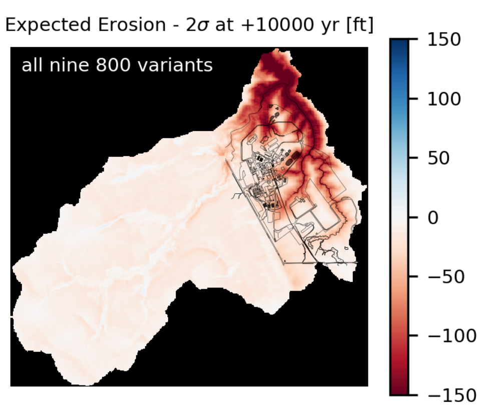

(e) Expected erosion -2σ at 10000 years

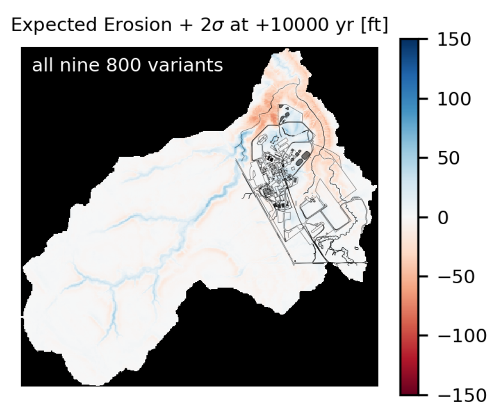

(f) Expected erosion $+2\sigma$ at 10000 years

Figure 11.31: Maps of expected erosion plus and minus 2σ at 2000, 5000, and 10000 years in the future for the combination of all nine 800 variants.

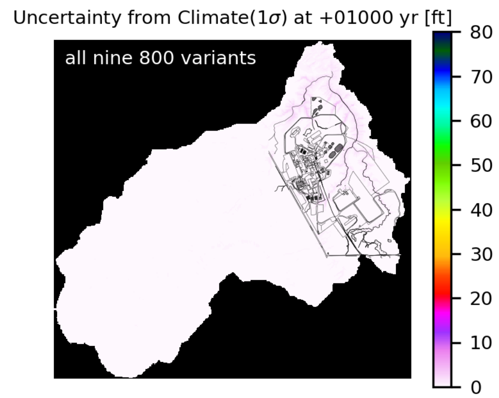

(a) Uncertainty associated with climate future at 1000 years

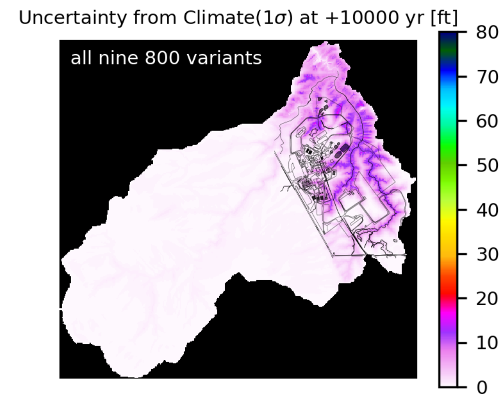

(b) Uncertainty associated with climate future at 10000 years

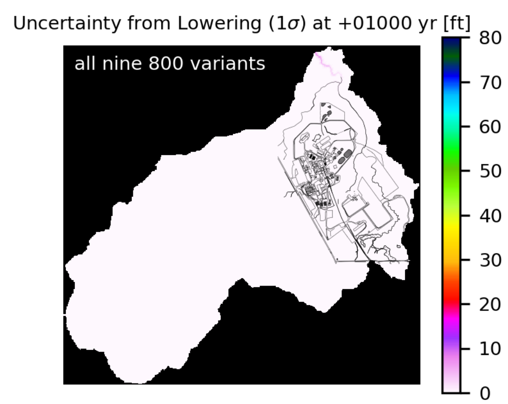

(c) Uncertainty associated with lowering future at 1000 years

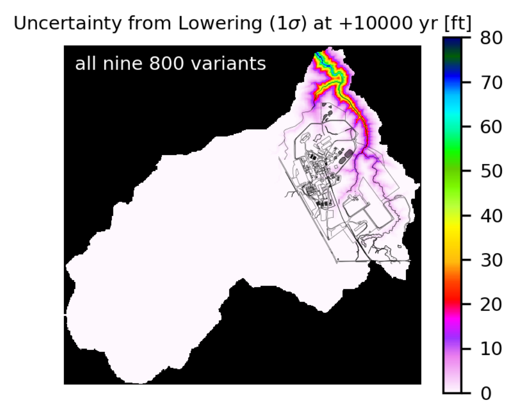

(d) Uncertainty associated with lowering future at 10000 years

Figure 11.32: Components of uncertainty at 1000 and 10000 years in the future for the combination of all nine 800 variants.

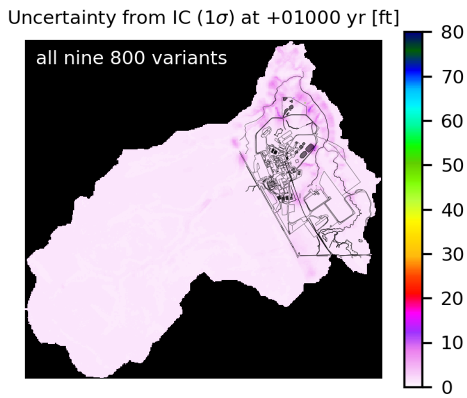

(e) Uncertainty associated with initial topography at 1000 years

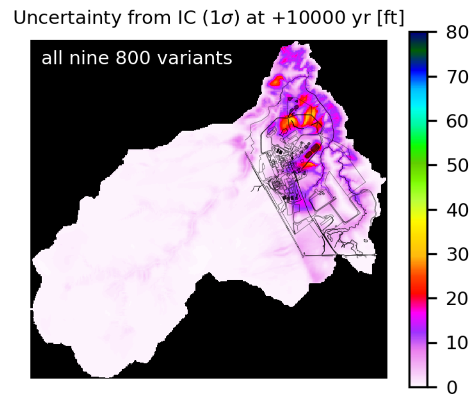

(f) Uncertainty associated with initial topography at 10000 years

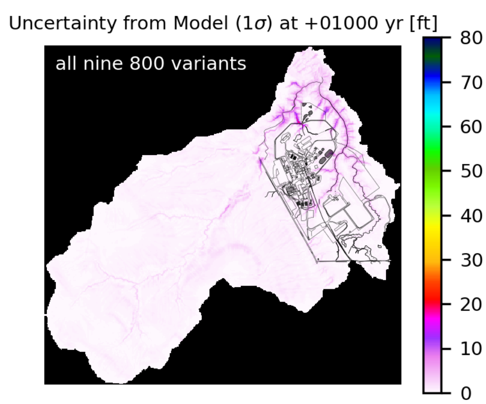

(g) Uncertainty associated with model structure at 1000 years

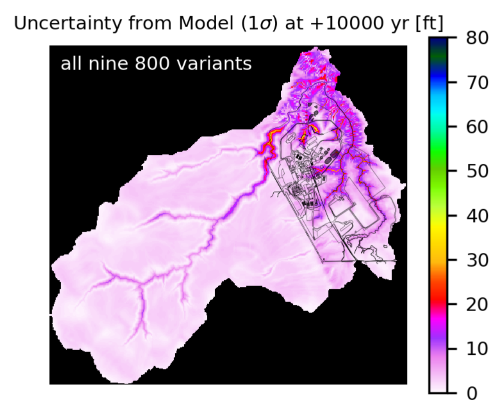

(h) Uncertainty associated with model structure at 10000 years

Figure 11.32: Components of uncertainty at 1000 and 10000 years in the future for the combination of all nine 800 variants (cont'd).

Discussion of erosion and uncertainty maps

Here we summarize the key points associated with the results presented in Figures 11.19–11.32. While there are differences between the model-842 and all-800 results, the basic projection made in both cases is similar. As an illustration, Figure 11.33 shows where the models project erosion of greater than 20 feet in both the expected erosion and at the conservative (worst case) 95% confidence bound. The top row shows model 842 only, and the bottom row shows the all-800 multi-model average. While there are slight differences in the extent of the zone predicted to have more than 20 feet of erosion, these differences are relatively minor.

The model projections identify that the sites most vulnerable to future erosion fall along the rims of the two plateaus. The projections consistently show greater erosion on the north plateau than on the south plateau. This is consistent with continued erosion of the steep side-slopes along the lower reaches of Franks Creek and Quarry Creek. The interior of the north plateau may also be vulnerable to propagation of gully erosion from either the northwest or the northeast rim. Continued incision of Erdman Brook results in erosion along the adjacent plateau edges, including the area of the lagoons (which, however, will have been excavated and backfilled with clean soil during Phase 1 decommissioning). On the south plateau, the northwest edge of the SDA and NDA, and the northeast edge of the SDA, are the most vulnerable to erosion. These erosion projections provide support for decommissioning planning for the Site, including potential selective exhumation of the NDA and SDA in areas vulnerable to erosion.

Based on the results of the uncertainty partitioning at each of the 25 sites, there appear to be substantial variations in the patterns of uncertainty components across the sites. Figures 11.25 and 11.32 depict the spatial patterns of the constrained uncertainty components. In general, the largest contributions to uncertainty arise from model structure and parameters, and from perturbations to the initial topography. Uncertainty related to future climate ranks next; at some locations, its contribution is minor, and at others it is the second or third most important contributor. Uncertainty arising from differences in the Buttermilk Creek lowering scenarios constitutes only a small element of the total mapped uncertainty.

The uncertainty with respect to future downcutting in both cases (model 842 only, and all 800 models) is focused in the lower portion of the watershed and is largest at the watershed outlet. Consideration of the dynamics of channel longitudinal-profile evolution helps to clarify these results. The signal of incision downstream is initially transmitted upstream through the steepening of the channel gradient. It takes time for the signal of downstream incision to propagate upstream and on to the plateaus. The regions that show the least uncertainty with respect to lowering future are those regions that have not yet received the signal of downstream incision.

Uncertainty that results from initial condition perturbations is focused on the plateau edges and the main valley side-slopes. The primary impact these perturbations have on the resulting topography is to shift the location of the small gullies that form and incise on the plateau edge (Figure 11.8). Thus portions of the plateau edge where shifting drainage can result in a particular gully receiving more or less drainage from the plateau (and hence more erosive power) are associated with high uncertainty.

Finally, we note two conclusions related to the maps of uncertainty in model structure.

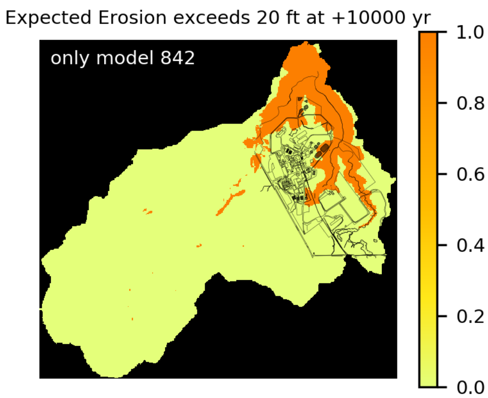

(a) Expected erosion at 10000 years, model 842 only.

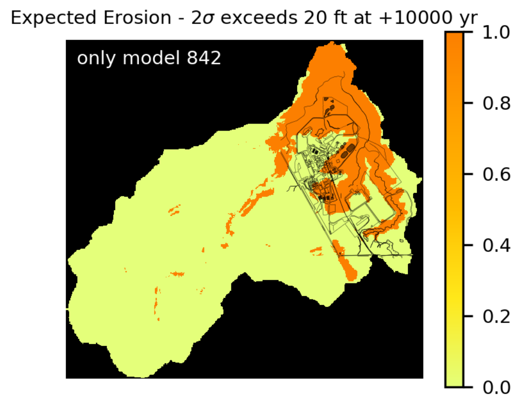

(b) Expected erosion plus 2σ at 10000 years, model 842 only.

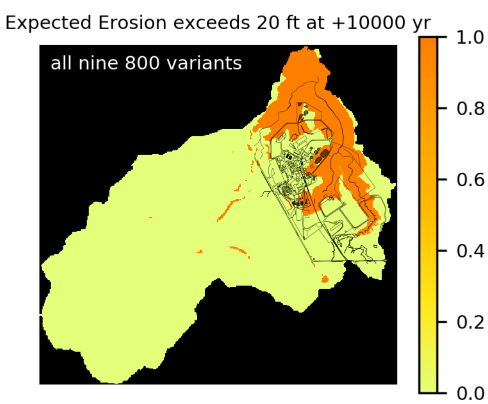

(c) Expected erosion at 10000 years, all 800 variants.

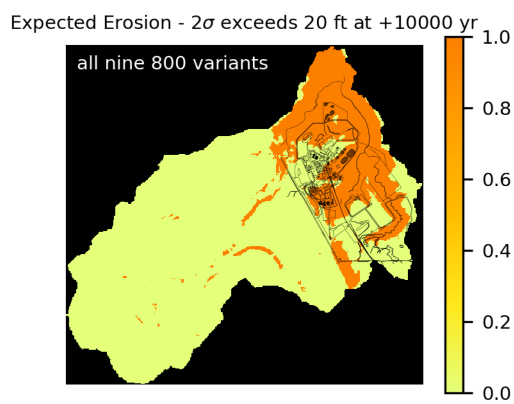

(d) Expected erosion plus 2σ at 10000 years, all 800 variants.

Figure 11.33: Regions of the map domain (in orange) where where expected erosion (left hand column) and expected erosion plus 2σ (95% worst case confidence bound, right hand column) exceeds 20 feet at 10000 years. Top row shows results from model 842 only and bottom row shows results from all 800 variants.

First, this uncertainty map shows significant uncertainty in the upper part of the watershed (indicated by the medium-purple colors that appear in the upper reaches of Quarry Creek and its tributaries). This is due to the combination of models that have erosion thresholds (802, 808, 842) and models without thresholds (all others) in our nine-model set. The models with thresholds will do less water erosion in the small-drainage-area portions of the watershed. It also reflects, in part, differences in the calibrated values of rock erodibility and (where applicable) the rock-erosion threshold among the models. A second notable feature in the spatial pattern of model-structure uncertainty is large uncertainty along the main channel margins. This feature makes sense when we consider that the nine-model suite effectively contains three different approaches to modeling the steep hillslopes. Most models use linear diffusion, model 842 uses nonlinear diffusion, and model C00 requires that material is first converted to soil before it can be transported by hillslope processes.

11.6.5 Stream Capture Experiment

The final numerical experiment we conducted was related to the potential for stream capture to impact erosion in Franks Creek watershed. We conducted two sets of experiments: one considered stream capture through the widening of Buttermilk Creek in the vicinity of Heinz Creek Fan, and the other considered capture by a gully in the south east portion of the watershed. Recall that these experiments were not designed to formally assess expected erosion given an assigned probability of stream capture, nor do they address the uncertainty in such erosion projections. Instead, these results represent an exploration of the sensitivity of capture scenarios on erosion projections.

Figures 11.34 and 11.35 show the results of the capture scenarios for the Buttermilk and gully scenarios, respectively. These model evaluations used the most conservative (worst case) climate and downcutting futures. The runs were conducted using all nine models; the erosion maps are shown for model 842. We show the resulting pattern of erosion at the end of the model time period for capture scenarios in which capture starts in 100, 2000, 4000, and 6000 years.

For the Buttermilk Creek capture scenario, even if capture begins at the unreasonably imminent time of 100 years in the future, very little erosion attributable to the capture has occurred (Figure 11.34). Until the capture point can gain increased drainage area, it only will erode with hillslope processes; in this scenario, the lowering around the capture point is insufficient to penetrate into the Upper Franks Creek valley. In contrast, once capture initiates at the southeast capture point, rapid erosion at that location is able to more quickly gain drainage area and incise (Figure 11.35).

We closely examined the impact of the capture scenarios on each of the 25 analysis points. Here we present the example of the impact of Buttermilk Creek capture on analysis site Lagoon3 (Figure 11.36) and gully capture on SDA4 (Figure 11.37).

At Lagoon3, all but one of the time-elevation lines for each of the two considered climate-lowering scenario combinations plot on top of each other. This is an indication that erosion at Lagoon3 is not impacted by "proto-capture" near Buttermilk Creek, even if that capture began only 100 years in the future. The one line that does not over-plot is the line for the fastest downcutting future combined with a capture that starts at +100 years, for model 842. Because this model includes non-linear hillslope transport law, it responds more quickly

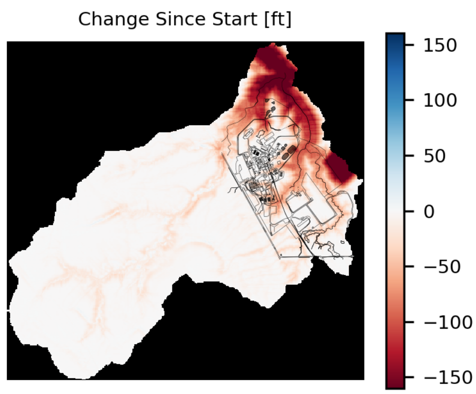

(a) 100 year start time

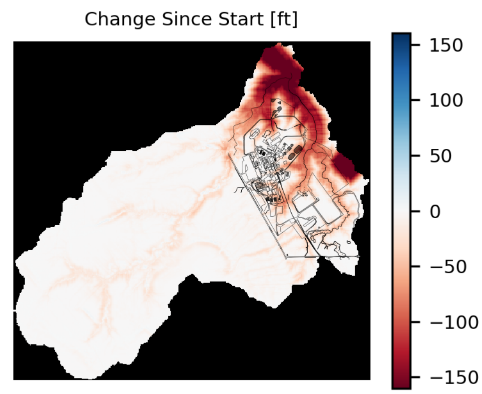

(b) 2000 year start time

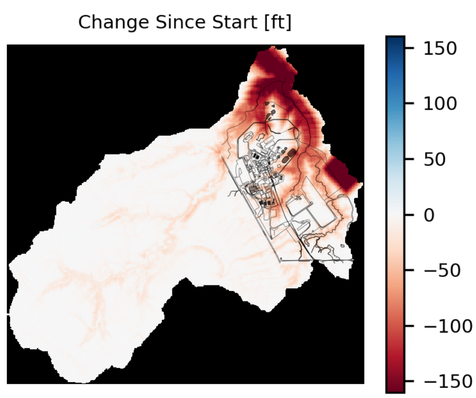

(c) 4000 year start time

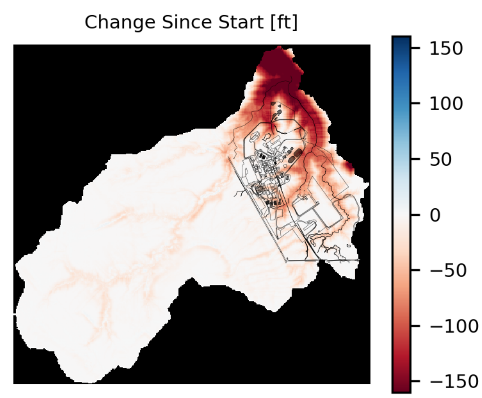

(d) 6000 year start time

Figure 11.34: Cumulative erosion depth at +10,000 years (feet) for the Buttermilk Creek capture point with model 842. The scenario with a starting time of 8000 years is not shown for simplicity. These model runs used the most conservative downcutting and climate scenarios (fastest downcutting and RCP85).

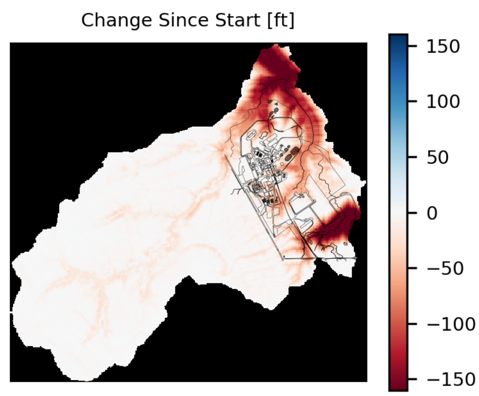

(a) 100 year start time

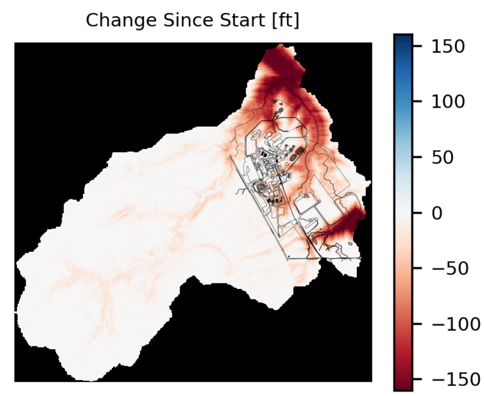

(b) 2000 year start time

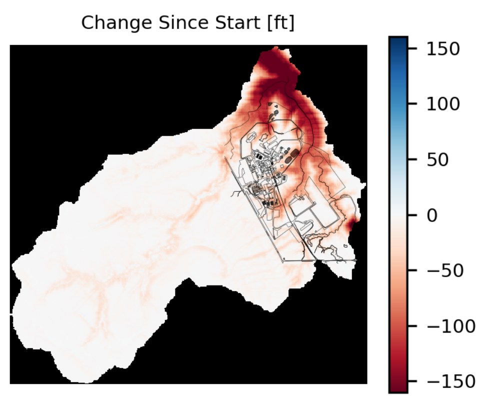

(c) 4000 year start time

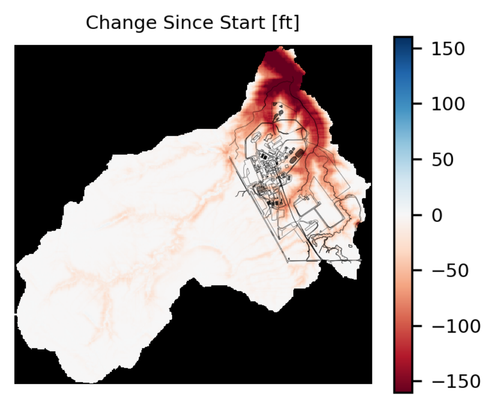

(d) 6000 year start time

Figure 11.35: Cumulative erosion depth at +10,000 years (feet) for the southeast gully capture point with model 842. The scenario with a starting time of 8000 years is not shown for simplicity. These model runs used the most conservative downcutting and climate scenarios (fastest downcutting and RCP85).

than the others to the proto-capture event. Most analysis sites show the same negligible response to both Buttermilk Creek capture and the southeast gully capture that Figure 11.36 illustrates.

The most substantial response among the capture scenarios is the response of SDA4 to early gully breaching in the southeast. SDA4 is located on the southeast corner of the SDA and is close to the gully breach point. Again the response is largest for model 842. In the scenario in which capture starts in only 100 years, SDA4 is impacted around by 5000 years after capture starts, and rapidly erodes in response to its new, lower baselevel. In the scenario in which capture starts in 2000 years, the SDA analysis point is impacted by about 6000 years after capture starts. Other models show only slight sensitivity to the capture scenarios.

These results indicate that stream capture by Buttermilk Creek is unlikely to have an impact on the Site over the next 10,000 years, unless lateral erosion along Buttermilk were to bring the edge of the valley into much closer proximity to Franks Creek than the position represented by the modeled capture point (technical limitations have made it impossible to explore the possibility of valley-wall propagation into the interior of the model domain). In a worse-case-scenario, capture by the gully to the southeast of the SDA may start to increase the rate of erosion at the southeastern corner of the SDA about 6000 years after capture begins.

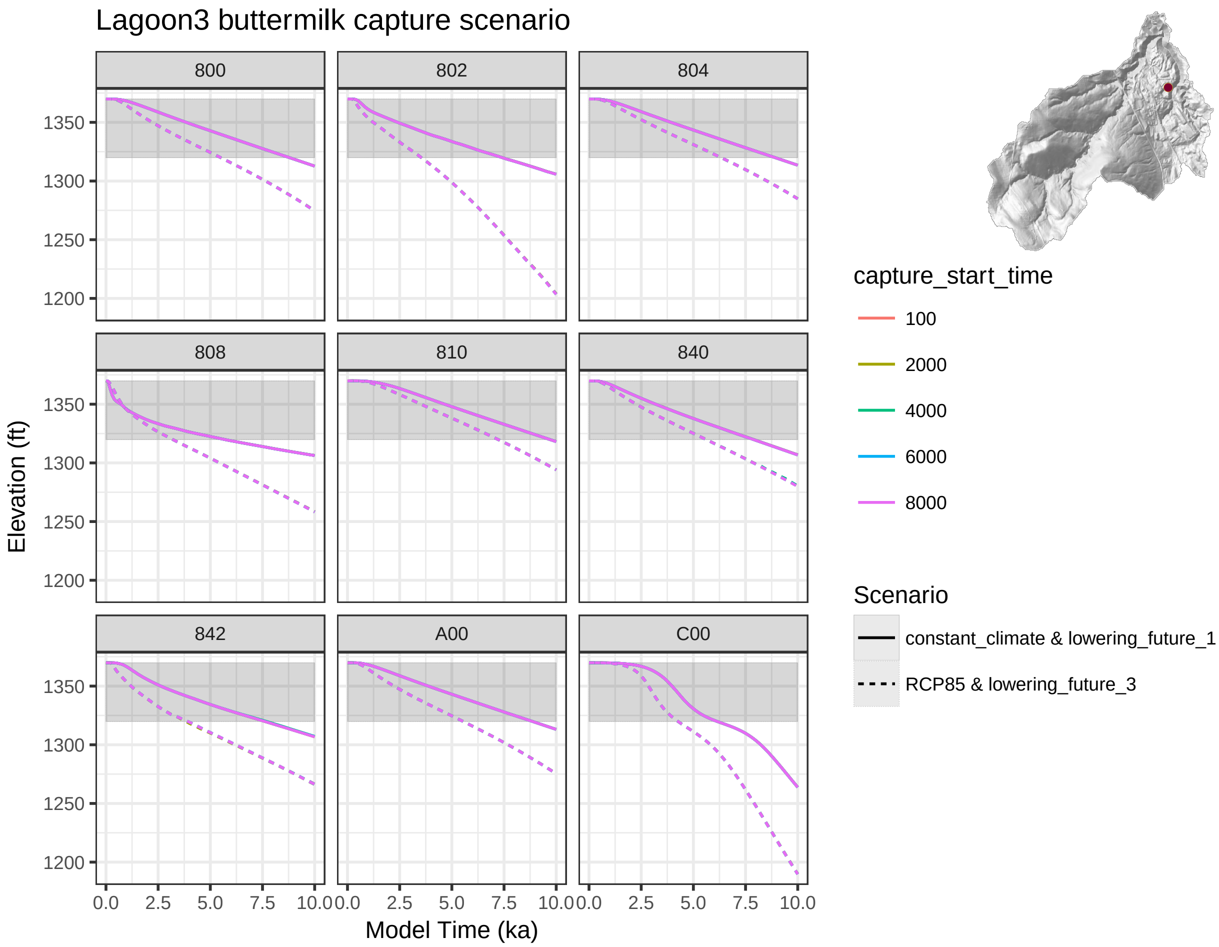

Figure 11.36: Summary figure illustrating the impact of the Buttermilk capture scenario at multiple times and in all nine 800 variant models at the Lagoon3 analysis point. Inset map shows the location of Lagoon3 within the model domain with modern topography as a base-map. The gray box is a 50 foot deep reference box that extends below the modern surface. Climate future and downcutting future scenario is shown with line type and capture start time is shown with color. When only one color is visible, all lines are plotting on top of each other.

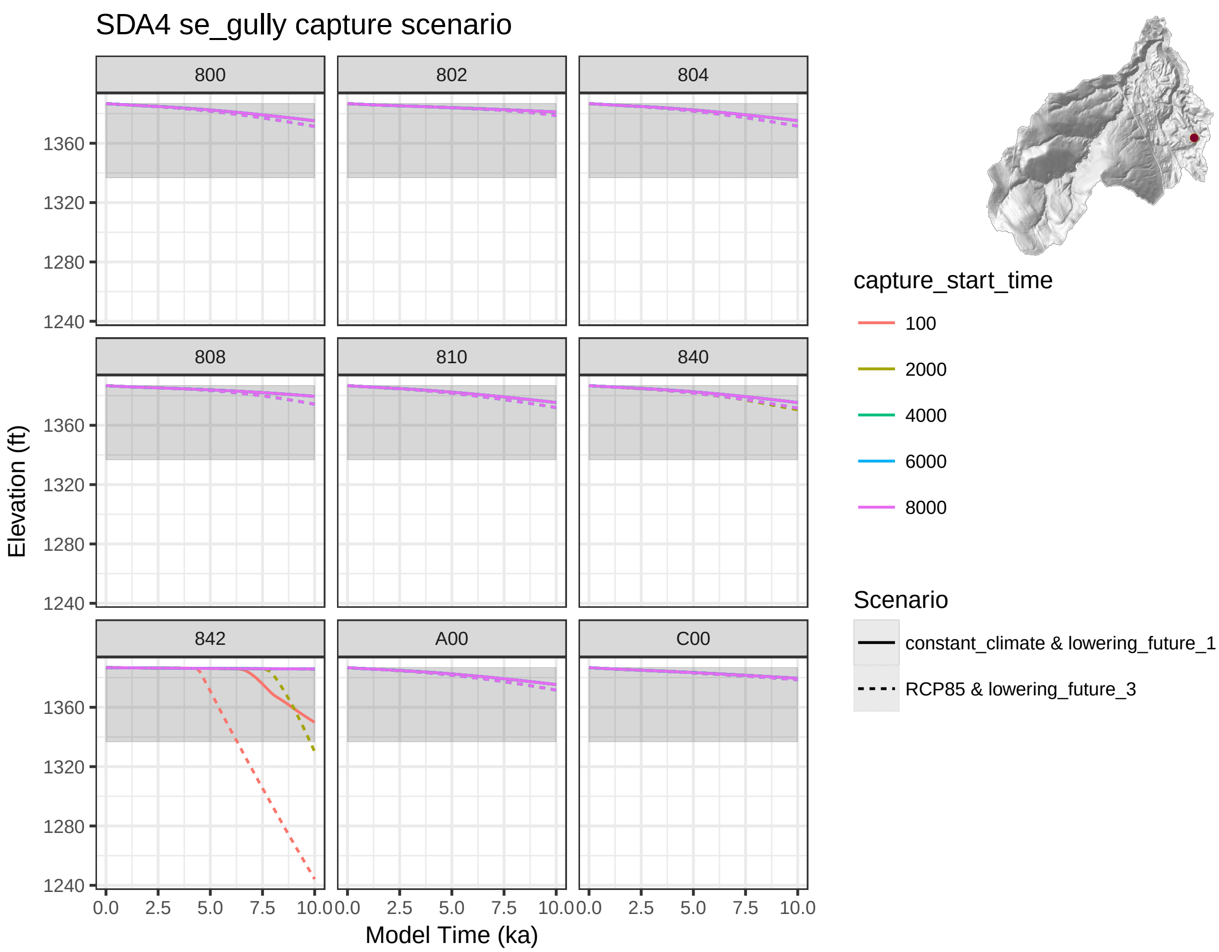

Figure 11.37: Summary figure illustrating the impact of the SE gully capture scenario at multiple times and in all nine 800 variant models at the SDA4 analysis point. Inset map shows the location of Lagoon3 within the model domain with modern topography as a basemap. The gray box is a 50 foot deep reference box that extends below the modern surface. Climate future and downcutting future scenario is shown with line type and capture start time is shown with color. When only one color is visible, all lines are plotting on top of each other.

11.7 Summary

This section summarizes the major points illustrated by the projection and uncertainty quantification results.

1. The sites most vulnerable to future erosion fall along the rims of the two plateaus, and consistently show greater erosion on the north plateau as compared with the south plateau. The interior of the north plateau may also be vulnerable to future erosion by gully headward propagation.

2. Model structure, modification of surface drainage, and model calibration are the major sources of uncertainty in projections.

3. Uncertainty in future climate varies in its relative contribution to the total at-a-point uncertainty. At some locations, it is the second or third most important contributor, whereas at others (generally those located further from main drainages) its contribution is relatively minor.

4. Uncertainty in the downcutting of the downstream fluvial system (Buttermilk Creek) is small relative to other sources of uncertainty.

5. The basic patterns of projected erosion and uncertainty are similar between the two alternative approaches for making projections (using only model 842 versus using all nine model-800 variants).

6. Stream capture by lateral erosion of Buttermilk Creek is unlikely to result in a change in erosion pattern in the next 10,000 years.

7. Stream capture by a gully in the southeastern portion of the model domain would start to impact the southeastern portion of the SDA approximately 6,000 years after capture starts.

Chapter 12

Analysis and Implications

12.1 Feasibility of long-term erosion projection

The results described in the preceding chapters demonstrate that it is feasible, with today's generation of landscape evolution models, to make projections of long-term cumulative erosion with quantified uncertainties. One outcome of this effort is a roadmap for how to develop such projections in a comprehensive manner that honors the important sources of uncertainty. The essential ingredients in the approach we have developed include:

1. Identification of multiple candidate models that are justified by the nature of the Site and the scope of the current scientific understanding

2. Sensitivity analysis to document model responses to different inputs, and identify key contributing factors as well as inputs that have relatively little input

3. Calibration, using an efficient surrogate-based approach, as a means both to identify an optimal parameter set for each model, and to evaluate quantitatively the performance of each model

4. Validation testing at an independent but geomorphically similar site, so as to test the transferability of models and assess their relative ranking

5. Quantification of future-climate uncertainty through construction of multiple future climate scenarios

6. Quantification of uncertainty in future baselevel forcing through construction of geologically feasible baselevel futures

7. Quantification of uncertainty in model structure, through selection and parallel analysis of a small ensemble of high-ranking models

8. Quantification of uncertainty arising from topographic perturbations, through ensemble modeling

9. Quantification of parameter uncertainty through Markov-Chain Monte Carlo modeling on model surrogates

This combination of steps provides spatially and temporally distributed projections of future changes in elevation and the uncertainty associated with these changes.

Although some elements of our approach are specific to the West Valley Site, the individual procedures above are generic in nature. They could in principle be applied to other locations where erosional exhumation of toxic and/or radiological materials is of concern. The key differences between sites may lie in the nature of data available, and the specific geological and geomorphic history. In the particular case of the West Valley Site, one of the elements that made this approach possible is the existence of well-preserved remnants of the post-glacial plateau surface. This provided a basis for reconstructing the postglacial topography which was necessary for model calibration.

The erosion models are necessarily fairly simple in their structure, reflecting limitations in contemporary scientific understanding as well as in computing capabilities. Nonetheless, the results from the past-to-present calibration and validation procedures demonstrate that several of the models have sufficient predictive power to capture the major elements of post-glacial landscape evolution at the Site.

12.2 Relative vulnerability of site locations

In general, the model projections show that the areas of greatest vulnerability to future erosion tend to fall along the rims of the two plateaus. A composite projection, including $\pm 2\sigma$ uncertainties, highlights areas of particular vulnerability (Figures in Section11.6.4). Of the two plateaus, the projections consistently show greater erosion on the north, because the valleys that bound it (lower Quarry Creek and lower Franks Creek) are deeper, with steeper side-slopes, than those that bound the South Plateau (upper Franks Creek and Erdman Brook).

The composite model projections also suggest that the interior of the North Plateau may be vulnerable to propagation of gully erosion, either from the northwest or the northeast rim. The area in and around the lagoons is also projected to be vulnerable to propagation of erosion from Erdman Brook. However, these lagoons, their radionuclide inventory, and associated contaminated soil will have been removed and the excavation backfilled with clean soil during Phase 1 decommissioning of the WVDP.

The margins of the South Plateau are also projected to be vulnerable. The northwest sides of the SDA and NDA, and the northeast edge of the SDA, appear to be the most vulnerable parts of these two disposal areas. Regarding these and other areas of vulnerability, the erosion models and projections will be an additional analytical tool to support Phase 2 decommissioning alternative development and Phase 2 decision making for the WNYNSC.

Under most scenarios, the interior of the South Plateau (including parts of the SDA and NDA) is projected to have experienced less than 20 feet of cumulative erosion at 10,000 years, at the 95% confidence level. Although this may seem like a surprising finding, it reflects in part the fact that the South Plateau is bounded by relatively small tributaries (Erdman Brook and Upper Franks Creek), and is located well upstream of the basin outlet. Smaller tributaries have lower drainage area and take longer to adjust to changes in baselevel.

12.3 Sources of uncertainty

Sources of uncertainty in the erosion projections vary from location to location in their relative importance. However, in general, the largest uncertainties in single-point erosion rates arise from uncertainty in initial topography, in model structure, and in the calibration of model parameters. The influence of minor ($\pm$5') topographic variations is surprisingly large. At first glance, this result might appear to be at odds with the finding that uncertainty in paleo-topography has a negligible influence on modeled paleo-to-modern landscape evolution. However, a key difference is that the projection uncertainty refers to uncertainty at a particular point, whereas the paleo-to-modern result concerns the overall large-scale erosion pattern. In fact, small perturbations to the terrain have little influence on the projected broad-scale pattern of erosion, but they can have a strong influence on erosion rates at particular points, particularly around the plateau rims. The at-a-point sensitivity arises because small perturbations in the topography can alter the direction of surface water drainage on the plateau surface, and thereby potentially shift the locations where surface water spills over the plateau rim. These spill points tend to grow into gullies: the more surface-water drainage a proto-gully receives, the more rapidly it will grow, and in the course of growing, rob its neighbors of their own surface-water supply.

Model-structure and model-parameter-calibration uncertainties also tend to make up a large contribution to the overall uncertainty budget. Broadly speaking the existence of model-structure uncertainty arises in this case because the scientific community presently lacks a consensus view on what is the proper mathematical structure for a long-term erosion model given the time scale, processes, and materials at the site of interest. Conducting projections with the nine different erosion models identified through calibration and validation tests provided a way to quantify this source of uncertainty.

The uncertainty in model parameter values estimated through calibration also translates into a significant source of uncertainty in erosion projections. As a general rule, the parameters in long-term erosion models are difficult to measure directly. For some parameters, such as the hillslope transport coefficient (D; see Chapter 5), this is because the process of interest is too slow to measure with sufficient precision to establish a coherent parameter estimate. Other parameters, such as the threshold for material detachment under hydraulic stress, can be measured, but the translation between a point-based, "instantaneous" field measurement and the long-term effective value—integrated over time and space—is often not straightforward. Thus, field measurements can help reduce parameter uncertainty by constraining what ranges are reasonable, but some degree of uncertainty in scaling inevitably remains.

Uncertainty arising from future downcutting on Buttermilk Creek primarily manifests in the lower reaches of Franks and Quarry Creeks, and the small gullies that drain to them. In general, it presents a less significant source of uncertainty than model structure, model parameters, or initial topography.

The contribution of uncertainty arising from potential future climate change varies by location. At some of the 25 points selected for detailed analysis, climate-related uncertainty ranks as the second or third most important source; at other points, climate-related uncertainty is a relatively minor contributor. In part, the finding that future-climate uncertainty is subsidiary to other sources reflects the nature of the climate-change scenarios used: in the absence of better information, the scenarios assumed no further change in precipitation beyond the 21st century. This assumption primarily reflects a lack of clear information or guidance from the climate-science community about potential change beyond that time horizon. In that sense, the three climate-change scenarios are best viewed as sensitivity experiments. What they show is that sensitivity to the magnitude of precipitation change that has been forecast for the 21st century under the high-emissions scenario (RCP 8.5) of the Intergovernmental Panel on Climate Change (IPCC) is relatively modest as compared with other sources of uncertainty.

Two additional factors contribute to the somewhat limited role of future precipitation in the overall uncertainty budget. First, there is a relatively small projected spread in changes in precipitation intensity—from zero (stable climate) to an increase of a little over 10%. This manifests in a change in the lumped erosion efficiency pattern of 24% in the RCP 8.5 scenario (10% in the RCP 4.5 scenario). This modest span is in contrast with much larger uncertainty in some of the model parameters (see Chapters 5 and 11). The second factor concerns the relationship between precipitation intensity and rates of erosion by channelized flow. This relationship, which is explored in Chapter 11, involves at least two nonlinear components. The transformation of precipitation into surface flow is thresholded in the sense that low precipitation rates tend to infiltrate or be intercepted by vegetation canopy, whereas higher rates can generate disproportionately more runoff. In the precipitation-to-erodibility function discussed in Chapter 11, this phenomenon is described with a soil infiltration capacity function. All else equal, the nonlinearity involved should tend to amplify the erosional impact of changes in precipitation. On the other hand, increases in surface water flow volume in channel networks tend to be apportioned between deepening of flow (which increases erosive potential) and widening of flow (which offsets part of the potential increase in depth, and can increase frictional resistance). Thus, for example, a doubling in stream discharge would normally be expected to result in less than a doubling of the tractive stress that drives particle detachment and sediment transport. This hydraulic effect appears in the erosion laws in the form of a square root of discharge or drainage area. The net result of these two effects—one that tends to amplify the effect of increasing precipitation, and one that tends to dampen it—is that a small increase in precipitation intensity is projected to result in only a modest increase in erosional efficiency. The most important caveat to this conclusion is that the underlying hydrologic model that supports it is highly simplified; a more sophisticated approach would require long-term data on runoff and on-site stream flow that do not appear to exist at present.

Further reduction in uncertainty regarding the hydrologic and erosional parameters in particular would require additional data. Data on stream flow and sediment transport, on scales from single gullies to drainages the size of Franks Creek could provide a clearer picture of the site's hydrology and response to precipitation inputs. Likewise, continued monitoring of terrain change through repeated LiDAR surveys holds the potential to map changes over periods of 10 years or more, with the signal of progressive topographic change becoming clearer as the time baseline between surveys grows.

12.4 Potential impact of stream capture

The potential for stream capture was evaluated with an ensemble of model runs that explored two scenarios: capture from a point to the southeast, near the right-angle bend in upper Franks Creek, and to the east as a result of widening of the Buttermilk Valley. Only a few of the ensemble members project effective capture of upper Franks Creek by a gully to the southeast, leading to significantly increased erosion (formation of a new ravine) along the southeast flank of the south plateau. Such capture occurred in the models only when the initial breaching of the drainage divide began early ($\leq$4,000 into the future), and only with models that include nonlinear hillslope transport. Later onset of divide breaching never produced capture, either because of insufficient lowering at the capture point, or because ongoing incision along Franks Creek made capture more difficult, or both. None of the runs in the ensemble produced a successful capture from the east.

Collectively, the stream-capture run ensemble results suggest that stream capture from the east or south is possible, but requires early or rapid lateral erosion. The primary consequence of capture from the southeast is formation of a deep ravine along the portion of Franks Creek that flows from Rock Springs Road to the southeast corner of the SDA. Such a ravine would erode into the south side of the SDA.

A caveat regarding capture modeling is that the approach used was highly simplified, and in each case restricted to a single potential capture point. Erosion models like those employed in this study do not naturally lend themselves to representing progressive lateral migration of a bounding valley such as Buttermilk Creek. The scenarios did not consider wholesale removal of the divide between Franks and Buttermilk, nor was it possible to model continued lateral erosion of the single capture point, as a representation of lateral erosion by a future Buttermilk Creek. Implementing such scenarios in the future might be feasible, but would require a non-trivial investment in software engineering to develop and test the necessary routines to represent the progressive "planation" of a gradually expanding surface along one side of a model's gridded domain.

12.5 Lessons from multi-model comparison

The multi-model comparison and evaluation provides some interesting lessons about which effects are and are not important in modeling long-term landscape evolution in this type of environment and time scale. One lesson is that there is a significant contrast in erodibility between bedrock and glacial sediments. The strength of the contrast was not obvious in prospect, because the bedrock consists primarily of shale (a relatively weak lithology) and the glacial sediments primarily of cohesive, clay-rich till (a relatively strong material as sediments go). Yet models that incorporate a layer of glacial sediments overlying bedrock perform significantly better than those that do not. Adding a distinction between rock and glacial sediment to a model produces a bigger increase in explanatory power than any other element.

The models also tend to perform somewhat better with the inclusion of an erosion threshold, which is a finding consistent with erosion and sediment transport physics. All else being equal, the erosion rate projected by a model that includes erosion thresholds will tend to slow down more over time as slopes decline.

The best-performing model included, in addition to rock and till units and an erosion threshold, a nonlinear representation of gravitational mass transport. This expression is expected to do a better job at capturing rapid ravine-side slumping than the simpler linear diffusion formula used by the majority of models.

There were also several optional model elements that did *not* significantly improve performance. One such element was stochastic precipitation: models that used this more sophisticated approach generally performed about as well as their simpler equivalents. This finding indicates that capturing a quasi-random spectrum of storm events does not add to the predictive power of these particular models, for this particular site. The finding supports the view that use of a "lumped" erosion law for channel erosion can be viewed as encapsulating the average erosional behavior over many storm events.

Another element that generally brought little or no improvement was the use of variable-source area (VSA) hydrology. The lack of improvement from this particular element may indicate that the clay-rich soils at the site tend to have low permeability, such that substantial shallow subsurface flow is rare. An additional or alternative interpretation is that the VSA model element does not account for the thin soils on steep side-slopes, and therefore under-predicts runoff generation on these slopes.

Models with a dynamic soil layer generally under-perform their simpler equivalents. These models effectively ignore the fact that the glacial sediments are weak enough to be transported on ravine and gully side-slopes without first having been converted into granular soil by weathering processes.

The model analysis presented in this report has only considered a small subset of possible permutations and combinations of the dozen or so model elements that have been developed. Future refinement of erosion models for the site could explore additional combinations.

Identifying models that preformed poorly was not possible *a priori* and only became clear after testing and calibration. Further iterations of model development, sensitivity analysis, calibration, and model assessment—including exploration of a broader range of process and material combinations—could be used to improve the overall quality of the multi-model suite.

12.6 Limitations and potential improvements

No environmental model can provide a complete representation of the full complexity of a natural system. The best a model can do is capture the major processes and trends in the system. In this section, we highlight several limitations of this study, and discuss potential improvements and additions that could be addressed in future work.

None of the erosion models used in this study accounts for lateral erosion by streams, which can lead to valley widening. For this reason, the model projections do not address the possibility that the streams bounding the Site—Franks Creek, Quarry Creek, and Erdman Brook—could undergo valley-floor widening and thereby drive additional back-wearing of their valley walls. Combining vertical and lateral erosion in landscape evolution models is a research frontier, and those few attempts that have been made are currently in an exploratory stage (e.g., *Langston and Tucker*, 2018). An implication of this limitation for the present study is that the model forecasts may under-predict the lateral retreat of ravine walls. To address this limitation in a performance assessment, one simple approach would be to estimate a potential widening rate and add this rate to the model-projected rate for locations near the edge of a ravine.

Another potential limitation concerns the routing of surface water. The erosion models used in this study used a so-called single-direction routing scheme, in which surface water in a particular grid cell will drain to one and only one neighboring cell. This approach works well for channel networks but tends to over-predict the degree of flow concentration on hillslopes, potentially leading to formation of closely spaced gully features rather than a more distributed pattern of erosion. This limitation could be addressed through the use of a multi-direction flow-routing scheme. Fast algorithms for landscape evolution models with multi-direction routing are not yet available.

The study described in this report is designed to address long-term, progressive erosion. It does not address single "catastrophic" events, such as a large, deep-seated landslide, or a powerful earthquake (which could trigger landsliding). Assessing the potential risk arising from such events would require a different kind of approach from the one we have used. For example, risk posed by large, deep-seated landslides would be better addressed through a geotechnical analysis.

The study has also not addressed "extreme" future climate scenarios. For example, possibility of a renewed ice age within the next 10,000 years has not been considered. The analysis has also not addressed the prospect of continued fossil-fuel emissions beyond the year 2100, which could lead to warming beyond that forecast by the climate-model ensemble used in the MACA database (Chapter 11). Similarly, the analysis has not considered the outer bounds of the confidence intervals in the 21st-century climate scenarios provided in MACA, though the models' limited sensitivity to precipitation increases suggests that this particular source of uncertainty is subsidiary to other sources.

The erosion models used in this study represent the site's geologic materials in a highly simplified manner. The nine models used in erosion projections treat the site as being composed of two primary materials: bedrock, and glacial sediment. This treatment neglects much of the complexity within these two broad units; for example, differences among till and interstadial sedimentary units are not accounted for, nor are variations in resistance among sedimentary rock strata. This simplified treatment of lithology represents a tradeoff between realism and analytical complexity. As noted in Chapter 5, the computational cost of a model rises exponentially with the number of parameters. Because each unique geologic unit would require its own set of parameters, this cost becomes prohibitive for more than two or three units (in this case, up to three units have been considered: rock, soil, and glacial sediments). Overall, the computing cost required to achieve the results described in this report amounted to over 1.3 *million* compute hours. Given this cost, it was simply not feasible to include additional geologic units beyond these three.

The erosion models also used a highly simplified treatment of site hydrology. For example, they do not account explicitly for event hydrographs. (Early tests with a dynamic hydrology model demonstrated that simulations on a sub-storm-event time scale required far more computation time that was feasible). Experiments with model variants that included additional aspects of hydrology—the variable-source "VSA" models and the stochastic-precipitation models—showed that these elements do not add significant explanatory value. However, while this finding provides some confidence that a simplified approach to surface-water hydrology is warranted, it does not rule out the possibility that some other, more sophisticated, representation of site hydrology might lead to improved performance. One limitation in this regard is a lack of data. Very few measurements of runoff or stream flow at or near the site are available, and such datasets that exist have short records (some of these datasets are reviewed in the 2010 Final Environmental Impact Statement, Appendix F).

12.7 Potential use of process-based erosion modeling in probabilistic performance assessment

The products of this research have potential utility for probabilistic analysis of future erosion. The model output produced by this project includes projection of erosion at each grid cell in 100-year time increments, out to 10,000 years. Accompanying this model output are composite expected values of erosion produced from (1) a combination of all 9 selected models, and (2) from the combined scenarios using the top-calibrated model BasicChRtTh (model 842). The output also includes, for each grid cell, expected erosion plus and minus one and two standard deviations, as calculated from all sources of uncertainty except model-parameter uncertainty.

Additional information is provided for each of the 25 selected points discussed in Chapter 11. For the grid cells in which these points fall, the total uncertainty budget also includes, for three of the models, the resultant projection uncertainty deriving from model parameters.

With these model results, an analyst interested in formulating probability distributions of cumulative erosion at a specific location and time in the future would have a variety of options. For example, one could derive a mean and standard deviation by using the composited expected value and the associated 1- or 2-σ uncertainty bounds. Alternatively, an analyst could select only the projections associated with a particular climate scenario, downcutting scenario, or model. If one wanted rates instead of cumulative erosion depth, these could be obtained easily by simply dividing the projected change in elevation at a point by the applicable time interval. If lateral rates of erosion were needed (for example, as a representation of backwearing of a ravine wall), one could extract the projected vertical rate and use the slope gradient at the particular location to calculate the corresponding lateral rate. The key point is that the computational strategy for this project has been designed to provide flexibility in the use of model outputs for probabilistic analysis of erosion.

Finally, although it was not possible to compute parameter-related uncertainty for every model, grid cell, and time interval, the procedures for performing these calculations have been carefully documented, so that they can be applied to additional locations if needed.

12.8 Potential use of process-based erosion modeling to support Phase 2 decision making for the WNYNSC

The erosion models and associated projections provide an additional analytical tool to support Phase 2 development of decommissioning alternatives and decision making. The erosion models could be used, for example, to analyze potential consequences of modifications to the Site terrain that would alter the pathways of surface-water and sediment flow, and thereby influence rates and patterns of future erosion.

Part III

Appendices

Appendix A

Erosion Modeling Suite (EMS) 1.0

[1]

Computational models of long-term drainage basin and landscape evolution have a wide range of applications in geomorphology, ranging from addressing fundamental questions about how climatic and tectonic processes shape topography, to performing engineering assessments of landform stability and potential for hazardous-waste containment (see, e.g., reviews by *Coulthard*, 2001; *Pazzaglia*, 2003; *Martin and Church*, 2004; *Willgoose*, 2005; *Codilean et al.*, 2006; *Bishop*, 2007; *Willgoose and Hancock*, 2011; *Pelletier*, 2013; *Temme et al.*, 2013; *Valters*, 2016). Although the basic principles of drainage basin evolution are reasonably well understood—such as the fundamental concept that erosion is driven by gravitational and water-runoff processes, the latter of which depend strongly on surface gradient and water flow—there remains uncertainty concerning the appropriate forms of the governing transport laws under any particular set of materials and environmental conditions (*Dietrich et al.*, 2003). This situation creates a need for comparative testing, in order to gauge the overall performance of various model formulations, to identify knowledge gaps in areas where models perform poorly, and to assess which transport laws are most appropriate for various types environment conditions, time scale, and spatial scale.

To date, there have been relatively few studies that have systematically compared and tested alternative transport laws, and those that do usually address only a single, quasi-one-dimensional landform element, such as the shape of an idealized hillslope (*Roering*, 2008), or the longitudinal profile of a particular stream channel (*Tomkin et al.*, 2003; *van der Beek and Bishhop*, 2003; *Valla et al.*, 2010; *Attal et al.*, 2011; *Hobley et al.*, 2011; *Gran et al.*, 2013). Models that combine hillslope and channel processes—often referred to as Landscape Evolution Models (LEMs)—can simulate the formation of three-dimensional landforms that arise from interaction of multiple processes, and in principle comparative testing ought to be straightforward (*Hancock et al.*, 2010). Yet the algorithms behind these models commonly differ from one another in multiple ways, which makes one-to-one comparison difficult. For example, if two model codes differ simultaneously in their treatments of hydrology, sediment transport, and material properties, diagnosing any differences in their performance would require dis-entangling each of these effects. To help solve this problem, it would be useful to

[1]This Appendix contains a version of a draft of manuscript that was prepared for submission to the journal Geoscientific Model Development.

have a software framework in which an investigator could alter one "process ingredient" at a time, and thereby conduct meaningful sensitivity analyses and comparisons with data.

The Erosion Modeling Suite (EMS) is a Python-language software product that is designed to help meet this need. EMS version 1.0 provides two resources for exploring alternative process models for landscape evolution. First, EMS 1.0 includes a collection of 37 distinct computational models for the long-term (order 10^4 years) evolution of drainage basin topography; most of these models vary from a simple "base" model in just one or two particular elements. Second, EMS includes source code for a generic template model, implemented as a Python class and intended for use as a base class from which specific models are derived. This erosion-model template enables modelers to craft and apply their own rule sets without needing to re-invent the overarching software framework or the various necessary utility functions. EMS 1.0 builds on the Landlab Toolkit (*Hobley et al.*, 2017), using Landlab Components to represent individual hillslope, hydrologic, and channel process components, and taking advantage of Landlab to handle common tasks such as input and output management.

Earth's landscapes are incredibly diverse, and the scientific questions that they pose are equally diverse. No one model, or even a general framework like EMS, can hope to encompass all of this diversity. EMS 1.0 was originally created to address landscape evolution in a humid-temperate, soil-mantled, post-glacial environment with moderate relief (order 10^2 m, on a horizontal scale of order 10^4 m) and relatively rapid erosion rates (10^{-4} to 10^{-2} m/yr), over a time scale of order 10^4 years. The choices of algorithms and process laws among the constituent models reflect this motivation. Nonetheless, EMS has been designed provide a sufficiently generic platform that it could be readily adapted to address a range of other scales and environments. This paper presents and describes EMS version 1.0, including its basic structure, mathematical underpinnings, software implementation, and the 37 constituent models.

A.1 General Structure of an EMS Model

An EMS model begins with a gridded representation of topography. By default, a regular raster grid is used, but the basic framework could readily be modified to accommodate Landlab's hex/trigonal and irregular Delaunay-Voronoi grid types. The elevation, and possibly regolith thickness, at each grid node evolves according to a specified set of erosion and/or sediment transport laws, which vary from model to model. In this section, we start by outlining the governing equations in a generic form. We then examine the software framework that implements common elements among all EMS models. The subsequent section then presents the collection of process laws and algorithms that are used to represent hillslope erosion, hydrology, water erosion, and material properties. The governing equations for all 37 models in EMS 1.0 are listed in Section A.5.

A.1.1 A Note on Terminology

The word "model" can have multiple meanings in scientific computing, and indeed in science generally. Some definitions are therefore in order. Here we will use the term *mathematical* *model* to mean a set of governing equations, which in this case describe landscape evolution under a given set of assumed process dynamics, materials, and boundary conditions. Under this definition, two mathematical models may have governing equations that are structurally quite similar, but which are nonetheless considered to be distinct models either because certain constants take on different values, or because a term is included in one version but not the other. For example, as described below, water erosion is commonly treated as proportional to either hydraulic power or hydraulic stress. We consider these to be distinct mathematical models, despite the fact that the difference lies only in the choice of two exponent values in the governing equation.

Each *mathematical model* contains terms that represent individual processes (or closely related collection of processes), such as erosion by surface water flow. The mathematical representation for an individual process will be referred to as a *process law* or *rate law*. By this definition, a *mathematical model* in EMS consists of a set of *process laws* embedded within an overall mass-conservation equation.

The term *numerical model* is used here to refer to a numerical algorithm that solves a particular mathematical model by marching forward in time from a given initial condition. The term *model program* will refer to a set of source-code files that performs the calculations needed to implement a *numerical model*. In some cases in EMS 1.0, a single *model program* can be configured to implement two or more *numerical models*, depending on its input parameters. For example, in EMS 1.0 the same model program can be configured to represent either a stream-power or shear-stress representation of water erosion. The combination of a model program plus the inputs that control this type of choice will be referred to as a *model configuration*.

A.1.2 Basic Ingredients and Governing Equation

Topography in an EMS model is represented as a two-dimension field of elevation values, $\eta(x, y, t)$. The general governing equation describes the rate of change of η as the sum of two terms: one representing erosion (or deposition) by water-driven processes, and one representing gravitational ("hillslope") processes:

$$\frac{\partial \eta}{\partial t} = -E_W - E_H \tag{A.1}$$

where E_W is the rate of erosion (or deposition, if negative) by water-driven processes such as channelized flow, and E_H is the rate for gravitationally driven processes such as soil creep and shallow landsliding (the subscript H stands for "hillslope," recognizing that gravitational processes will tend to be most important on hillslopes). Water erosion is assumed to depend on local slope gradient, S, water discharge, Q (which in many of EMS' models will be treated using drainage area as a surrogate, as discussed below), and material properties. Erosion or accumulation by gravitational processes is assumed to be a function of gradient, material properties, and (in some models) soil thickness.

A.1.3 Soil-Tracking Models

As described in Section A.2.5, several of EMS' models also explicitly track a layer of regolith, defined here as unconsolidated and potentially mobile sediment, such as soil or alluvium. Here, for simplicitly we will refer to this material as soil, keeping in mind that our operational definition is more general that the one commonly used by soil scientists. The land surface height is the sum of bedrock elevation, η_b, and soil thickness, H:

$$\eta = \eta_b + H. \tag{A.2}$$

Here too the term "bedrock" is used in its broadest possible sense, and may include for example cohesive sedimentary material such as glacial till. The time rate of change of soil thickness is the difference between the rate soil production and erosion,

$$\frac{\partial H}{\partial t} = P - E_{WHS}, \tag{A.3}$$

where P is the rate of soil production from bedrock, and E_{WHS} denotes the total rate of soil erosion (or accumulation, if negative) resulting from water-driven and gravity-driven transport processes. Similarly, the rate of change of bedrock surface height is the sum of soil production rate (scaled by any density contrast between rock and soil), and the rate of bedrock incision by running water, E_{WR}:

$$\frac{\partial \eta_b}{\partial t} = -\frac{\rho_s}{\rho_r} P - E_{WR}. \tag{A.4}$$

The above equation simply says that the rate of lowering of the bedrock surface is the sum of the rate of rock-to-soil conversion and the rate of removal by water erosion.

A.1.4 Multi-Lithology Models

Nine EMS models allow for spatial juxtaposition of two different lithologies, L_1 and L_2. Layer L_1 is assumed to overlie L_2, but it may be absent (thickness zero) at any particular location. Let $\eta_{L2}(x, y, t)$ denote the elevation of the top of L_2, and $T_{L1}(x, y, t)$ represent the thickness of L_1. Then the land surface elevation (in the absence of an explicit soil layer) is given by:

$$\eta = \eta_{L2} + T_{L1}. \tag{A.5}$$

In models that honor both a soil layer and two different lithologies, the surface elevation is:

$$\eta = \eta_{L2} + T_{L1} + H, \tag{A.6}$$

in which case we also have the height of the bedrock surface as

$$\eta_b = \eta_{L2} + T_{L1}. \tag{A.7}$$

Where the top layer exists, it lowers as a result of water erosion and (if soil is tracked) rock-to-soil conversion. This can be expressed mathematically as

$$\frac{\partial T_{L1}}{\partial t} = -\delta_L (E_W + P) \tag{A.8}$$

where δ_L is a spatially varying function equal to 1 where $L_1 > 0$, and 0 elsewhere (here P is considered to be zero in non-soil-tracking models). The rate of change of elevation of the top of L_2 is given by

$$\frac{\partial \eta_{L2}}{\partial t} = -(1 - \delta_L)(E_W + P), \tag{A.9}$$

which simply means that the lower layer L_2 is vulnerable to erosion and weathering wherever the top layer is missing (for example, having been eroded through). Note that for reasons reflecting the original application of EMS, within the source code and input files the top layer is referred to as 'till' and the bottom layer as 'rock.' Note also that the BasicHySa model allows simultaneous water erosion of soil and rock, as discussed below.

A.2 Process Formulations

Each model in the EMS 1.0 collection has four elements, reflecting the model's treatment of hillslope processes, surface-water hydrology, erosion by running water, and material properties. The possible formulations for each of these elements are constructed around a set of binary choices. Each choice represents a decision about how a particular element might be formulated. For example, the downhill soil transport rate could be represented as either a linear or nonlinear function of local slope gradient, while the lithology could be treated as being uniform, or divided into two distinct types as discussed in Section A.1.4. The binary-choice design makes it possible to test the behavior of one alternative model element at a time. The binary options that form the basis for the EMS 1.0 constituent models are listed in Table A.1. In Table A.1, option B in each row usually represents a more sophisticated choice than option A: one that may bring more realism, but also generally involves more parameters (one exception being the choice between stream power and shear stress formulations for channel incision, as discussed below).

Each of EMS's models uses Landlab Components to implement the numerical algorithms behind channel erosion, hillslope processes, and water-flow routing. The components used are briefly identified by name in the following descriptions of EMS model ingredients. The software architecture that supports this component-based approach is then discussed further in Section A.3. Further information about Landlab and its component-modeling capability is provided by *Hobley et al.* (2017).

Table A.1: Binary options for process formulations and boundary conditions.

Category	**Option A**	**Option B**
Hillslope processes	linear transport law	nonlinear transport law
Surface-water hydrology	deterministic	stochastic
	uniform runoff	variable source area runoff
Channel/gully erosion	$m = 1/2$	variable m
	$\omega_c = 0$	$\omega_c > 0$
	stream power	shear stress
	constant ω_c	ω_c increases with incision depth
	detachment-limited	sediment-tracking
	uniform sediment*	fine vs. coarse[a]
Material properties	no separate soil layer	tracks soil layer $H(x, y, t)$
	homogeneous lithology	two lithologies
Paleoclimate	constant climate	time-varying K

[a] only applies to sediment-tracking model (see text).

Table A.2: Summary of individual models in the EMS 1.0 collection.

Model configuration	**Model program**[a]	**Element varied #1**	**Element varied #2**
Basic		-	-
BasicVm	Basic	variable m	-
BasicTh		threshold	-
BasicSs	Basic	shear stress[b]	-
BasicDd		$\omega_{ct} \propto$ incision depth	-
BasicHy		entrainment-deposition[c]	-
BasicCh		nonlinear creep	-
BasicSt		stochastic runoff	-
BasicVs		VSA[d]	-
BasicSa		tracks soil/alluvium	-
BasicRt		tracks two lithologies	-
BasicCc		K varies over time	-
BasicThHy	BasicHy	variable ω_c	entrainment-deposition
BasicThSt		variable ω_c	stochastic runoff
BasicThVs		variable ω_c	VSA
BasicThRt		variable ω_c	tracks two lithologies
BasicSsDd	BasicDd	shear stress	$\omega_{ct} \propto$ incision depth
BasicSsHy	BasicHy	shear stress	entrainment-deposition
BasicSsSt	BasicSt	shear stress	stochastic runoff
BasicSsVs	BasicVs	shear stress	VSA
BasicSsRt	BasicRt	shear stress	tracks two lithologies
BasicDdHy		$\omega_{ct} \propto$ incision depth	entrainment-deposition
BasicDdSt		$\omega_{ct} \propto$ incision depth	stochastic runoff
BasicDdVs		$\omega_{ct} \propto$ incision depth	VSA
BasicDdRt		$\omega_{ct} \propto$ incision depth	tracks two lithologies
BasicHyFi	BasicHy	entrainment-deposition	variable fraction fines
BasicHySt		entrainment-deposition	stochastic runoff
BasicHyVs		entrainment-deposition	VSA
BasicHySa		entrainment-deposition	tracks soil/alluvium
basicHyRt		entrainment-deposition	tracks two lithologies
basicChSa		nonlinear creep	tracks soil/alluvium
basicChRt		nonlinear creep	tracks two lithologies
basicStVs		stochastic runoff	VSA
basicVsSa		VSA	tracks soil/alluvium
basicVsRt		VSA	tracks two lithologies
basicSaRt		tracks soil/alluvium	tracks two lithologies

[a] If different
[b] Shear stress version of water erosion term
[c] Entrainment-deposition (“hybrid”) water erosion law
[d] Variable source-area hydrology

A.2.1 Basic Model

The simplest of the component models in EMS is known as the Basic model. Its governing equation for land-surface elevation $\eta(x, y, t)$ is:

$$\frac{\partial \eta}{\partial t} = -KA^{1/2}S + D\nabla^2\eta, \tag{A.10}$$

where K is a coefficient with dimensions of inverse time, A is upstream contributing drainage area, S is gradient in the steepest down-slope direction, and D is a soil-creep coefficient with dimensions of length squared per time. Here the first term on the right represents channel and gully erosion, while the second term represents erosion or deposition by gravitational mass movement. An example of a landscape simulated using the EMS Basic model is shown in Figure A.1.

The channel incision term in the Basic model (equation A.10) is based on the widely used stream-power formulation (*Howard et al.*, 1994; *Whipple and Tucker*, 1999), in which the long-term average rate of channel downcutting is taken to be proportional to hydraulic power per unit bed area. Drainage area appears as a surrogate for effective water discharge; the 1/2 power reflects the assumption that discharge per unit channel width scales as the square root of drainage area. A key assumption is that erosion rate is limited by the capacity to detach and remove material, rather than by along-stream variations in the capacity to transport sediment. The second term on the right is the popular linear diffusion law for hillslopes.

Although the Basic model is rather simple, having just two parameters (K and D), it represents a formulation that has been widely used in geomorphic models (e.g., *Miller and Slingerland*, 2006; *Miller et al.*, 2007; *Perron et al.*, 2009; *Pelletier*, 2010; *Duvall and Tucker*, 2015). The equations are common solved numerically on a regular or irregular grid. The drainage area factor is normally evaluated using a downslope routing algorithm in which the water output from one grid cell is passed to one or more downhill neighboring cells (see, for example, review in *Tucker and Hancock*, 2010). Despite its simplicity, this two-parameter model has been shown to reproduce first-order properties of drainage basin topography, including dendritic drainage networks, concave-upward channel longitudinal profiles, and convex-upward hillslopes.

The EMS Basic model uses a regular (raster) grid, which may be initialized using an input Digital Elevation Model (DEM) or generated as a rectangular grid of user-specified dimensions and spacing with superimposed random noise (Figure A.1). Drainage area is calculated using a single-direction, eight-neighbor ("D8") flow-routing algorithm. This flow-routing procedure is handled by the Landlab FlowDirector and FlowAccumulator components.

Depressions in the topography are resolved using a routing algorithm that passes flow across them without modifying their elevation values. The algorithm is implemented by Landlab's DepressionFinderAndRouter component; the current (Landlab 1.1, early 2018) version is based on (*Tucker et al.*, 2001).

One arrives at the EMS Basic model by choosing option A for each item in Table A.1. In the following sub-sections, we review the various options that EMS offers for alternative treatment of hillslope processes, surface-water hydrology, channel incision, materials, and boundary conditions.

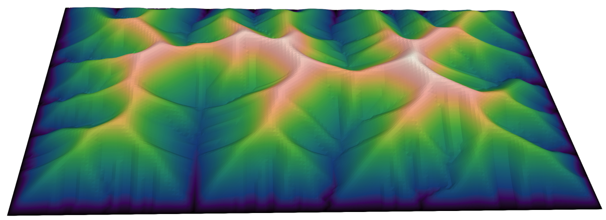

Figure A.1: Three dimensional view of simulated topography using the Basic model. Landscape represents a condition of dynamic equilibrium between erosion and material uplift relative to the fixed model boundaries.

A.2.2 Hillslope Processes

To model hillslope evolution processes in a soil-mantled landscape, we use components of varying complexity that treat soil transport as a diffusion-like process in which sediment flux is governed by topographic gradient. EMS offers two alternative soil-flux rules with which to model the downslope transport of soil and its dependence on topographic gradient: linear and nonlinear. In addition, as discussed previously, EMS also allows for the option of explicitly tracking a dynamic soil layer. This option is provided to address the possibility that soil may become thin enough to limit flux, and this limitation may in turn influence the rate and pattern of landscape evolution. Inclusion of a dynamic soil layer requires that one provide a term for soil production from the underlying lithology (P in equation A.3), and furthermore that the flux law be modified to account for the local soil thickness such that flux goes smoothly to zero as thickness vanishes.

Continuity law for soil creep

The simplest forms of the so-called "geomorphic diffusion" equation (*Dietrich et al.*, 2003) assume transport-limited conditions in which the production rate of soil is always much greater than the transport rate; thus, transport rate does not depend in any way on soil availability or thickness. In this case, the hillslope term in the continuity equation (A.1) is:

$$E_H = \frac{1}{1-\phi} \nabla q_s \tag{A.11}$$

where q_s is the soil volume flux per unit width, and ϕ is the porosity of the soil, and the ∇ operator represents differentiation in two horizontal directions ($\nabla = \partial/\partial x + \partial/\partial y$).

Linear creep law

A variety of formulas exist for the soil flux, q_s. The simplest and most common formula treats the soil transport rate as a simple linear function of topographic gradient, using a transport efficiency constant, D':

$$q_s = -D'\nabla\eta \tag{A.12}$$

where $\nabla\eta$ is the slope gradient. Using this flux rule with equation A.11, the hillslope term in the continuity equation becomes:

$$E_H = -D\nabla^2\eta \tag{A.13}$$

where D, sometimes referred to as hillslope diffusivity, is equivalent to $D'/(1-\phi)$ and has dimensions of L^2/T. This simplest form of the evolution equation for soil creep on hillslopes results in convex-upward topography at steady state.

Nonlinear creep law

A more complex version of the creep law for soil-mantled slopes involves a non-linear relationship between soil flux and topographic gradient. The non-linear formulation captures accelerated creep and shallow landsliding as gradient approaches an effective angle of repose for loose granular material. Several nonlinear creep-transport laws have been suggested in the literature. The most popular of these is the Andrews-Bucknam equation (*Andrews and Bucknam*, 1987), which performs reasonably well when compared with experimental and field data (*Roering et al.*, 1999, 2001; *Roering*, 2008). One problem with the Andrews-Bucknam law, however, is that the flux divergences when the slope gradient, S, equals the threshold gradient S_c, and is undefined for $S > S_c$. This property makes it challenging to incorporate in a landscape evolution model, where other processes may produce gradients equal to or greater than S_c. Some authors have addressed this problem with a modified form that avoids divergence at gradient $S = S_c$ (e.g., *Carretier and Lucazeau*, 2005).

EMS uses a truncated Taylor Series formulation for soil flux, which was derived by *Ganti et al.* (2012) for the Andrews-Bucknam law. The flux is given by

$$q_s = DS\left[1 + \left(\frac{S}{S_c}\right)^2 + \left(\frac{S}{S_c}\right)^4 + ... \left(\frac{S}{S_c}\right)^{2N}\right] \tag{A.14}$$

where $S = -\nabla\eta$ is topographic gradient (positive downhill), D is the transport efficiency factor, and S_c is a critical gradient. The user specifies the number of terms N to be used in the approximation. The nonlinear flux rule results in convex-up topography for shallow slopes, and transitions to linear hillslopes for steeper slopes. An example EMS simulation using the nonlinear creep law is shown in Figure A.2.

Linear depth-dependent creep law

For models that explicitly track a soil layer $H(x, y, t)$, one needs to modify the creep law to incorporate a relationship between flux, q_s, and local soil thickness. EMS uses an approach proposed by *Johnstone and Hilley* (2015), in which the flux decays exponentially as soil thickness approaches zero,

$$q_s = -D\left[1 - \exp\left(-\frac{H}{H_0}\right)\right]\nabla\eta, \tag{A.15}$$

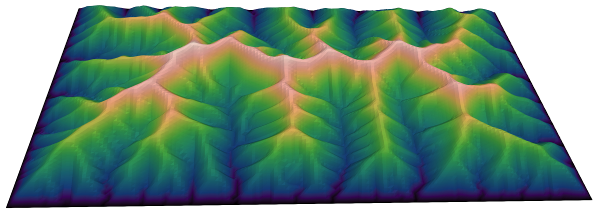

Figure A.2: Three dimensional view of simulated topography using the BasicCh model, which uses a nonlinear (Taylor Series) hillslope transport law. Landscape represents a condition of dynamic equilibrium between erosion and material uplift relative to the fixed model boundaries.

where H_0 represents the soil thickness for which q_s shrinks to $(1-1/e)$ of its maximum value for a given slope gradient. (Note that in the original formulation of *Johnstone and Hilley* (2015), D is treated as the product of H_0 and a transport coefficient with dimensions of length per time; here we lump them together as D).

Nonlinear depth-dependent creep law

We can modify the nonlinear flux rule (equation A.14) to accommodate soil, again assuming an exponential velocity distribution in the subsurface (*Johnstone and Hilley*, 2015):

$$q_s = DS\left[1 - \exp\left(-\frac{H}{H_0}\right)\right]\left[1 + \left(\frac{S}{S_c}\right)^2 + \left(\frac{S}{S_c}\right)^4 + ...\left(\frac{S}{S_c}\right)^{2N}\right]. \tag{A.16}$$

This approach is somewhat similar to that used by *Roering* (2008) in a study that compared the predictions of a nonlinear, depth-dependent flux law with observed hillslope forms.

Soil production

Models that track a layer of soil must include an expression to specify the rate at which soil is produced from the underlying parent material. The most commonly applied formula, and the one used by EMS' soil-tracking models, treats the rate of soil production from the underlying lithology as an inverse-exponential function of soil thickness (*Ahnert*, 1976; *Heimsath et al.*, 1997; *Small et al.*, 1999):

$$P = P_0 \exp(-H/H_s) \tag{A.17}$$

where P_0 is the maximum production rate (with dimensions of length per time), and H_s is a depth-decay constant on the order of decimeters.

A.2.3 Hydrology

Treatments of surface-water hydrology in landscape evolution models are commonly quite simple, reflecting the need for both simplicity and computational efficiency. Erosion formulae normally require specification of water discharge or (less commonly) depth. The most common parameterization is to use contributing drainage area, A, as a surrogate for surface-flow discharge, Q. This is the default option in EMS' models. Operationally, this means that the water-erosion law includes A (see Section A.2.4 below), and that the erosion law's parameters embed information about climatic factors such as precipitation frequency and intensity, as well as material properties such as soil infiltration capacity (e.g., *Tucker*, 2004).

Drainage area can measured from digital elevation data using standard routing methods. In EMS 1.0, each model uses the common "D8" routing method, in which each grid cell is assigned to flow toward whichever of its eight surrounding neighbors lies in the direction of steepest descent. Water routing across closed depressions is handled using a lake-fill algorithm implemented by the Landlab DepressionFinderAndRouter component. Once drainage directions have been assigned, contributing drainage area at a given grid cell i is calculated by adding up the area of all cells whose flow eventually passes through i, plus the area of i itself.

Variable source-area hydrology

In vegetated, humid-temperate regions, storm runoff is commonly produced by the saturation-excess mechanism, in which rain falls on areas that have become saturated (*Dunne and Black*, 1970). Such areas tend to occur in locations with either gentle topography, large contributing area, or both. Because the source area for runoff generation is both limited in spatial extent and varies over time, the phenomenon has come to be known as variable source-area hydrology, or VSA for short. Previous modeling studies have suggested that VSA can impact long-term landform evolution, as steeper upland areas tend to experience less intense and/or less frequent erosion and sediment transport by runoff (*Ijjasz-Vasquez et al.*, 1993; *Tucker and Bras*, 1998). For this reason, EMS 1.0 includes a set of models that provide a relatively simple treatment of VSA. This treatment is based on the approach of *O'Loughlin* (1986) and *Dietrich et al.* (1993), and is similar to the TOPMODEL concept of *Beven and Kirkby* (1979). Each element on the landscape is considered to have an upper permeable soil layer of thickness H and saturated hydraulic conductivity K_{sat}. The soil layer is assumed to overlie relatively impermeable material. From Darcy's Law, the maximum shallow subsurface flow discharge when the soil is fully saturated is the product of conductivity, depth, and local hydraulic gradient, which is assumed to be equal to topographic gradient, S. The maximum subsurface discharge per unit contour width is therefore given by:

$$q_{ss} = K_{sat} H S = T S \tag{A.18}$$

where $T = K_{sat} H$ is the soil transmissivity. Next, we consider a recharge rate, R, which represents the average rate of water input per unit area (dimensions of length per time). The total unit discharge is the product of recharge and drainage area per unit contour length, a:

$$q_{tot} = a R. \tag{A.19}$$

Using these two principles, the surface water unit discharge, q, is:

$$q = \begin{cases} 0 & \text{if } aR < TS \\ aR - TS & \text{otherwise.} \end{cases} \tag{A.20}$$

This threshold-based approach has been used, for example, in models that explore how hillslope hydrology influences landform evolution (*Ijjasz-Vasquez et al.*, 1993; *Tucker and Bras*, 1998). One drawback, however, is that the use of mathematical thresholds in numerical models can complicate the calibration process by creating "numerical daemons": sharp discontinuities in a model's response surface (i.e., the n-dimensional surface that describes a particular model output quantity as a function of its n input parameters) (e.g., *Kavetski and Kuczera*, 2007; *Hill et al.*, 2016). In this particular case, we can create a smoothed version of (A.20) without any loss of realism, by positing that within any given patch of land there is actually a distribution of effective recharge rates. The simplest strictly positive probability distribution is an exponential function

$$p(R) = (1/R_m)e^{-R/R_m}, \tag{A.21}$$

where $p(R)$ is the probability density function of R, and R_m is the mean recharge rate. The mean surface-water unit discharge can then be found by integrating as follows:

$$\bar{q} = \int_{R_c}^{\infty} q(R)p(R)dR = aR_m e^{TS/R_m a}, \tag{A.22}$$

where $R_c = TS/a$ is the minimum recharge needed to produce surface runoff.

It is useful to re-cast this in terms of an effective contributing area, A_{eff}, defined as

$$A_{eff} = \frac{q\Delta x}{R_m} = Ae^{-T\Delta x S/R_m A} \tag{A.23}$$

where Δx represents flow width (in a gridded digital elevation model, it would be natural to use cell width). By this definition, the effective drainage area is always less than or equal to the actual drainage area, reflecting the fact that some of the water runs through the shallow subsurface rather than across the surface as overland (or channelized) flow. Where slope gradient is small or drainage area is large, the effective area approaches the actual area. If the surface is flat ($S = 0$), the exponential factor equals unity and $A_{eff} = A$, reflecting the fact that no water can be conveyed by shallow subsurface flow. Conversely, where S is large and/or A is small—as might be the case in steep headwater areas—the effective drainage area becomes much smaller than the actual area, indicating that most of the incoming water is traveling beneath the surface rather than contributing to overland flow.

A final step is to note that one can collapse the various factors in (A.23) into a single parameter, $\alpha = T\Delta x/R_m$. This parameter has dimensions of length squared; we will refer to it henceforth as the *saturation area scale*. A high value of α represents soils that have a large capacity to carry subsurface flow, relative to the recharge rate; a low value reflects a more limited subsurface flow capacity.

Seven of EMS' models implement variable source-area hydrology by using A_{eff}, as defined in (A.23), in place of drainage area, A (Table A.2). One of these (BasicVsSa) also explicitly

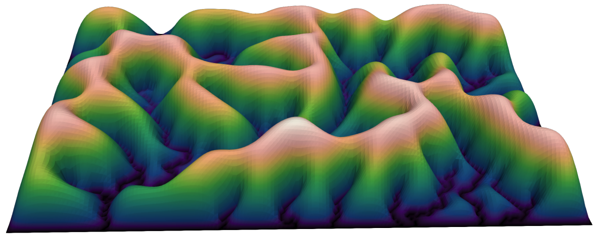

Figure A.3: Three dimensional view of simulated topography using the BasicVs model, which represents variable source-area hydrology by calculating water erosion using an effective drainage area, as defined in equation (A.23). Landscape represents a condition of dynamic equilibrium between erosion and material uplift relative to the fixed model boundaries.

tracks a soil layer, and the time- and space-varying thickness of this soil layer is used to calculate T $(= K_{sat}H(x, y, t))$ in this particular model. An eighth model (BasicStVs) also uses a stochastic treatment of precipitation; in this model, the randomly generated precipitation rate p is used for R_m in equation (A.23).

An example simulation with an EMS model (BasicVs) that includes a variable source-area component is shown in Figure A.3. The only difference in formulation between this example and the Basic model illustrated in Figure A.1 is that BasicVs calculates channel erosion using effective drainage area, A_{eff}, as defined in equation (A.23), in place of total drainage area. The result is a drainage network bounded by steep, convex-upward ridges. These ridges are sufficiently steep that $A_{eff} \ll A$, so that their erosion is dominated by soil creep. The bases of the hills represent locations where water emerges from the shallow subsurface to become surface flow that feeds the channel network.

Stochastic precipitation and runoff

Many landscape evolution models use an *effective discharge* approach, in which a single value of precipitation or runoff (either given explicitly or embedded in a lumped rate coefficient) is used as a surrogate for the full range of runoff-producing events (e.g., *Willgoose et al.*, 1991b; *Kooi and Beaumont*, 1994; *Tucker and Slingerland*, 1997). This approach has the advantages of simplicity and computational efficiency, but also has limitations. For example, the appropriate effective discharge may vary in space and time (*Huang and Niemann*, 2006). One solution is to use a stochastic treatment of precipitation and/or discharge, in which events are drawn from a specified probability distribution (*Tucker and Bras*, 2000; *Snyder et al.*, 2003; *Tucker*, 2004; *Lague et al.*, 2005).

In order to facilitate comparison between models with deterministic and stochastic treatments of water discharge, EMS 1.0 includes a set of six models that implement a stochastic precipitation algorithm. The aim of the algorithm is not to reproduce individual storm events, but rather to capture a spectrum of runoff and stream-flow events of varying frequency and magnitude. The frequency of occurrence of rainfall is described using an intermittency factor, F, which is defined as the fraction of rain days per year, and a mean daily precipitation rate, p_d.

Thus, the mean annual precipitation, p_{ma} is given as

$$p_{ma} = F \, p_d \, . \tag{A.24}$$

The probability distribution of daily precipitation rate, p, is modeled using a stretched exponential survival function,

$$Pr(P > p) = \exp\left[- \left(\frac{p}{P_*} \right)^c \right] , \tag{A.25}$$

where c is a shape parameter and P_* is a scale parameter. Use of the stretched exponential function is based on *Rossi et al.* (2016), who found that the function provides a good approximation for daily rainfall distributions in the continental US and Puerto Rico. *Wilson and Toumi* (2005) argued that theoretical considerations suggest $c \approx 2/3$, while *Rossi et al.* (2016) found a mean value of $c = 0.74$ for weather stations in the continental US.

The shape parameter P_* associated with a mean daily precipitation rate p_d and shape factor c is given by

$$P_* = \frac{p_d}{\Gamma(1 + \frac{1}{c})} , \tag{A.26}$$

where Γ is the gamma function.

To describe the frequency-magnitude spectrum probabilistically in EMS' stochastic models, time is discretized into a series of steps of duration δt. During each step, an "event" with precipitation rate p is drawn at random from the cumulative distribution in equation (A.25). One of two approaches is then used to calculate the corresponding runoff rate, r. The first approach, which is the default used in five of the six stochastic models, assumes a mean soil infiltration capacity I_m. The rate of runoff is calculated as

$$r = p - I_m(1 - e^{-p/I_m}) \, . \tag{A.27}$$

This formulation is a smoothed version of the simple threshold approach $r = \max(p - I_m, 0)$, which has been used in prior studies to represent infiltration-excess overland flow generation (e.g., *Tucker and Bras*, 2000). The smoothed version avoids the sharp discontinuity at $p = I_m$, and is arguably more realistic as it honors natural variability in soil infiltration capacity. The runoff rate approaches zero when $p \ll I_m$, and approaches p when $p \gg I_m$.

The second approach uses the variable source-area runoff generation model described in Section A.2.3, using p in place of recharge R_m. This approach is used only in model BasicStVs (Table A.2).

A.2.4 Water Erosion

Several different expressions have been proposed as models for long-term channel incision (and for erosion by surface water more generally). EMS 1.0 was originally designed to address erosion into cohesive sediments (including glacial till) and clastic sedimentary rocks with a relatively high fracture density, both of which are prone to erosion by hydraulic detachment of sediment grains and fracture-bounded fragments ("plucking"). This focus guided the choice of water-erosion laws in EMS 1.0. Each EMS model uses one of two main types of erosion law: a simple area-slope detachment formula (sometimes referred to in the literature as the *stream power* family of erosion laws (e.g., *Howard et al.*, 1994; *Whipple and Tucker*, 1999)), and an erosion formula that accounts for sediment discharge, particle entrainment from the bed, and particle deposition onto the bed. Within these two broad categories, EMS models express several variations in form; for example, some include a threshold term, and in some of these the threshold increases with progressive incision depth. Each variation is presented and discussed in the sections below. Here, we start with a description of the simplest formulation, which serves as the default choice.

The area-slope (a.k.a., stream power) family of models derives from the assumption that the erosion rate, E_W, depends primarily on the hydraulic gradient, S, and the water discharge, Q,

$$E_W = k_1 Q^M S^N - \Omega_c \tag{A.28}$$

where k_1 is a coefficient that depends on material properties, channel geometry, and other factors, and Ω_c is a threshold below which no erosion occurs (in practice, the threshold is often assumed negligible, or its effects are taken to be subsumed in the exponents). The exponents M and N reflect the nature of the erosional processes; for example, *Whipple et al.* (2000a) argued that different values may be appropriate for abrasion-dominated and for plucking-dominated systems. The discharge exponent M also embeds information about channel geometry. Often, drainage area A is used as a surrogate for discharge. One limitation of equation (A.28) is that it does not allow for sediment deposition; for this reason, it is sometimes referred to as a *detachment-limited* law (a term first coined by *Howard* (1994)), reflecting the assumption that the rate of downcutting is limited by the rate at which material can be detached and removed.

Despite the simplicity of equation (A.28), its various permutations have shown reasonable success when tested against field observations (*Stock and Montgomery*, 1999; *Whipple et al.*, 2000b; *Kirby and Whipple*, 2001; *Snyder et al.*, 2000; *Lavé and Avouac*, 2001; *Tomkin et al.*, 2003; *van der Beek and Bishhop*, 2003; *Duvall et al.*, 2004; *Loget et al.*, 2006; *Whittaker et al.*, 2007; *Attal et al.*, 2008; *Yanites et al.*, 2010; *Attal et al.*, 2011; *Hobley et al.*, 2011; *Gran et al.*, 2013). Landscape evolution models that the generic stream-power approach are able to reproduce basic properties of erosional landscapes, such as dendritic channel networks with concave-upward longitudinal profiles (e.g., *Howard*, 1994; *Whipple and Tucker*, 1999; *Tucker and Whipple*, 2002).

One of the most commonly used versions of equation (A.28) is obtained by making the following assumptions: (1) the rate of downcutting depends on stream power per unit surface area; (2) effective discharge is proportional to drainage area; (3) channel width is proportional to the square root of discharge; and (4) the erosion threshold is negligible. Under these conditions, the erosion law becomes:

$$E_W = K A^{1/2} S, \tag{A.29}$$

where K is a coefficient that includes information about precipitation and hydrology as well as material properties and channel geometry. The simplicity of equation (A.29)—it has only one parameter—together with its ability to reproduce common features of drainage basins and networks have led to its widespread use in landscape evolution studies (e.g.,

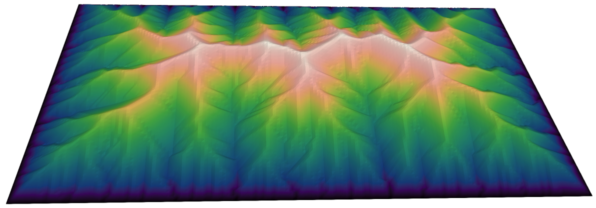

Figure A.4: Three dimensional view of simulated topography using the BasicVm model, with the drainage area exponent m set to 0.25 (as opposed to the default value of 0.5 used in Basic). Landscape represents a condition of dynamic equilibrium between erosion and material uplift relative to the fixed model boundaries.

Duvall and Tucker, 2015). One might think of it as the "model to beat": to justify a more complex formulation, one would ideally need to demonstrate that such a formulation performs distinctly better.

Equation (A.28), which we will refer to as the simple unit stream power law, forms the default choice for water erosion in EMS' models. It is used in this basic form by six of EMS' models (Table A.2). By also providing models with alternative (often more complex) erosion laws to (A.28), EMS' model collection allows one both to compare the behavior of several different formulations, and to test their performance against data. In other words, EMS is designed to enable systematic, quantitative hypothesis testing among a collection of different fluvial erosion laws. In the following sub-sections, we describe the variations and alternatives to simple unit stream power among the EMS 1.0 models. The complete governing equations for each of the EMS 1.0 models are given in Appendix A.

Variable area/discharge exponent

The area exponent $m = 1/2$ on the simple unit stream power model derives from the assumptions that effective discharge is linearly related to drainage area, channel width is proportional to the square root of discharge, and roughness is uniform. Although these are reasonable for many drainage basins, one can gain additional flexibility by treating m as a calibration parameter. EMS 1.0 provides the option of varying m in the water erosion law, such that:

$$E_W = KA^m S. \tag{A.30}$$

This option is operationalized simply by using the Basic model but setting m to a value other than 1/2 (in other words, BasicVm is implemented as a parameter variation rather than as a separate program). An example simulation using $m = 1/4$ is shown in Figure A.4.

Erosion threshold

Bed-load sediment transport is well known to exhibit threshold-like behavior, in which the transport rate is negligible until a certain minimum hydraulic tractive stress is reached, at

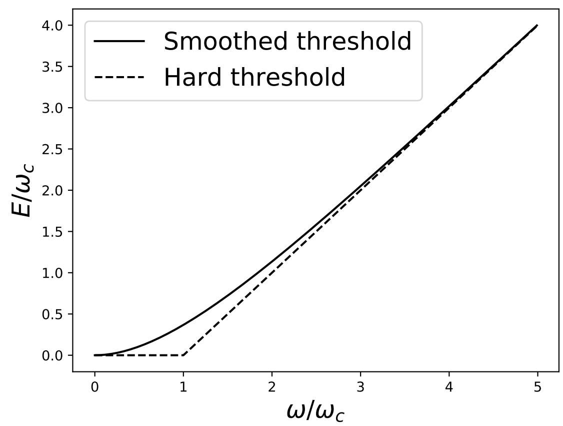

Figure A.5: Illustration of the functional form of the smoothed-threshold erosion law (equation A.31), compared with the more traditional hard-threshold formulation.

which point significant transport begins. Similar behavior applies to the erosion of highly cohesive sediment (e.g., *Julien*, 1998), and presumably also to bedrock (though the value of the operative threshold in the latter case is not well known). For this reason, models of landscape or longitudinal channel profile evolution often include a threshold term below which no erosion takes place.

Several EMS models include a threshold in the water-erosion law. In order to promote mathematically smooth behavior, and avoid numerical daemons associated with threshold-type equations (e.g., *Kavetski and Kuczera*, 2007), the basic thresholded erosion law in EMS uses an exponential smoothing function. EMS' thresholded erosion laws take the form:

$$E_W = \omega - \omega_c(1 - e^{-\omega/\omega_c}). \tag{A.31}$$

Here ω represents the erosion rate that would occur in the absence of a threshold, and is a function of slope gradient and either drainage area or discharge. For example, for those models that add a threshold term to the area-slope erosion in equation A.29, ω is defined as

$$\omega = KA^{1/2}S. \tag{A.32}$$

The factor ω_c is a threshold with dimensions of length per time. The functional form of the smooth-threshold erosion function (equation A.31) is illustrated in Figure A.5. A constant threshold term in included in the water-erosion laws for five of EMS' constituent models (Table A.2). Several others use a space- and time-varying threshold, as we describe next.

Depth-dependent erosion threshold

In a study of river incision into glacial deposits following ice recession in the US upper midwest, *Gran et al.* (2013) found evidence for an erosion threshold that increased with progressive incision depth. They attributed this to a downstream increase in median grain diameter resulting from enrichment of coarse gravel in bed material as the channel cuts through glacial deposits and the valley widens. In comparing alternative long-profile evolution models with the observed profile, they found that the best match was achieved when the erosion threshold was allowed to increase linearly as a function of cumulative incision depth. Inspired by the findings of *Gran et al.* (2013), EMS 1.0 includes the option to allow the erosion threshold ω_{ct} to increase with erosion depth according to:

$$\omega_{ct}(x, y, t) = \max(\omega_c + bD_I(x, y, t), \omega_c) \tag{A.33}$$

where D_I is the cumulative incision depth at location (x, y) and time t, ω_c is the threshold when no incision has taken place yet, and b (with dimensions of inverse time) sets the rate at which the threshold increases with progressive incision depth. As before, an exponential term is used to smooth the threshold, such that the water erosion rate approaches zero when $\omega \ll \omega_c$, and asymptotes to $\omega - \omega_c$ when $\omega \gg \omega_c$ (Figure A.5). The max function is included to prevent the threshold from decreasing in locations where hillslope processes produce net deposition (i.e., negative incision).

Shear-stress erosion law

Two important and commonly used measures of the erosional potential of stream flow are unit stream power and shear stress. The first represents the rate of energy dissipation per unit surface area, while the second represents the hydraulic traction force per unit area. Erosion rates in cohesive or rocky material tend to correlate strong with both quantities (e.g., *Howard and Kerby*, 1983; *Whipple et al.*, 2000b), and both are widely used as the basis for long-term erosion laws. To support studies that compare and test these two approaches, EMS 1.0 allows one to configure the erosion law to represent bed shear stress rather than unit stream power. This is accomplished simply by changing the exponents on discharge (or drainage area) and channel gradient in equation (A.28). If one uses the Manning equation to describe channel roughness and assumes that channel width is proportional to the square root of discharge, the applicable exponent values are $M = 3/5$ and $N = 7/10$ (*Howard and Kerby*, 1983; *Howard*, 1994). Use of the Darcy-Weisbach roughness law leads to a slightly different values, $M = 1/3$ and $N = 2/3$, which we uses in the examples that accompany EMS 1.0 documentation.

In EMS 1.0, the choice of exponent values is set using an input file, and so separate code is not needed to implement the shear-stress option. Nonetheless, we consider the stream-power and shear-stress formulations to form distinct mathematical models. For this reason, we include in Table A.2 several "models" that manifest a shear-stress-based erosion law, even though they share the same source code as other models on the list. As described further below, we also provide example scripts and equilibrium tests for each one, even where two models share source code but use different input configurations.

Sediment-tracking entrainment-deposition hybrid model

The sediment-tracking model, following *Davy and Lague* (2009), computes changes in river bed elevation resulting from competition between entrainment of bed material into the water column and deposition from the water column onto the bed. The governing equations, derived from a mass balance, state that changes in channel bed elevation η over time are driven by bed material erosion E and bed material deposition D:

$$\frac{\partial \eta}{\partial t} = \frac{-E + D_s}{1 - \phi} \tag{A.34}$$

where E and D_s are volumetric fluxes of bed material per unit bed area representing entrainment from the bed and deposition onto the bed, respectively, and ϕ is the porosity of bed material. Equation A.34 is coupled with conservation of sediment concentration in the water column of depth h:

$$\frac{\partial (c_s h)}{\partial t} = E - D_s - \frac{\partial q_s}{\partial \hat{x}} \tag{A.35}$$

where $\hat{x}$ represents distance along the path of flow. The above states that sediment in the water column involves a balance between erosion, deposition, and the streamwise spatial gradient in sediment flux per unit width, q_s. Again following *Davy and Lague* (2009), we assume that the time rate of change of sediment in the water column is negligible (as it is meant to represent an average over time), so that

$$q_s = \int_0^{\hat{x}} [E(\hat{x}) - D_s(\hat{x})]\, d\hat{x}. \tag{A.36}$$

In other words, the sediment flux at a particular downstream point $\hat{x}$ is the integral of all the erosion minus deposition that has taken place upstream.

The erosion flux E may be written in a number of ways, but in general depends on water discharge Q (or drainage area as a proxy), bed slope S, and some parameter or set of parameters describing the erodibility of the channel bed. Two common approaches, both of which are used in the erosion modeling suite, are to make E a function of unit stream power or shear stress, both of which can be expressed in the form of equation (A.28). Using drainage area in place of discharge, and setting the scaling exponents M and N to 0.5 and 1.0, respectively, gives the simplest and most frequently employed stream power erosion law (equation A.29). If instead $M = 1/3$ and $N = 2/3$, one obtains a shear-stress erosion rule, as discussed in Section A.2.4. The entrainment term may also include a threshold, and that threshold may be constant or may vary with incision depth or with lithology.

Sediment deposition flux D_s is a function of the concentration of sediment in the water column c_s and the effective settling velocity V of the sediment particles. Adding that c_s is the volumetric sediment flux divided by the volumetric water flux, the deposition flux may be written:

$$D_s = V \frac{Q_s}{Q} \tag{A.37}$$

where Q is volumetric water discharge and Q_s is volumetric sediment discharge (equal to q_s times flow width). Importantly, V is the net settling velocity after accounting for upward-directed turbulence and sediment concentration gradients in the water column. *Davy and Lague* (2009) separate the latter effects into a dimensionless parameter d^* such that $D_s = d^* V Q_s / Q$, but here for simplicity we combine both effects into an effective settling velocity V.

The entrainment-deposition model provides greater flexibility than detachment-limited models in that it can freely transition between detachment-limited and transport-limited behavior, depending on the relative importance of the erosion and deposition fluxes (for this reason, models of this type are sometimes known as "hybrid" models). If the deposition flux is negligible relative to the erosion flux, model behavior becomes detachment-limited. In the opposite case, the model expresses transport-limited behavior. The entrainment-deposition model is therefore uniquely able to treat landscapes that may exhibit both types of behavior at different points in space and time, at the cost of only a single extra parameter (V) relative stream-power type models. For a full description of the entrainment-deposition model and its implications, see *Davy and Lague* (2009).

Entrainment-deposition hybrid model with fine sediment

In the entrainment-deposition approach proposed by *Davy and Lague* (2009), all material eroded from the channel bed is included in sediment flux and deposition calculations. While this fully mass-conservative approach is a useful general case, it neglects the fact that clay- and silt-sized sediment may have such a low settling velocity as to be remain permanently suspended until and unless they enter a body of standing water. A simple modification to the entrainment-deposition model allows for treatment of a scenario in which the finest fraction of eroded sediment is in permanently from the erosional landscape upon entrainment. In the general case, the change in Q_s along the river is written:

$$\frac{\mathrm{d}Q_s}{\mathrm{d}x} = E\mathrm{dx} - D_s\mathrm{dx}. \tag{A.38}$$

where dx is the width of flow. To account for permanently suspendable fine sediment, represented as a fraction of total bed sediment F_f, we simply exclude the fine sediment from the sediment flux and write:

$$\frac{\mathrm{d}Q_s}{\mathrm{d}x} = (1 - F_f)\, E\mathrm{dx} - D_s\mathrm{dx} \tag{A.39}$$

such that the material incorporated into the sediment flux is reduced in proportion to the amount of fine sediment on the bed. This approach is simple and efficient, but would likely be limited in settings with very high proportions of fine sediment, as large concentrations of even very fine grains in the water column may inhibit further sediment entrainment.

Entrainment-deposition model with bedrock and alluvium

One weakness of the erosion-deposition model described above is its limitation to a single type of bed material. For example, one can configure the parameters to represent erodible material such as loose sediment, or resistant material such as indurated bedrock, but not both at once. This limitation means that the basic form of the entrainment-deposition model cannot honor the reality that many bedrock-incising rivers are blanketed by alluvium, nor can it be used to assess the relative contributions of sediment entrainment and bedrock erosion to channel morphology and sediment flux. One potential solution is to use the erosion-deposition model in conjunction with a substrate layering system (i.e., a layer of sediment overlying bedrock), in which each layer is defined by its own erodibility factor and erosion threshold (e.g., *Carretier et al.*, 2016). However, such an approach does not allow the simultaneous erosion of sediment and bedrock, which can occur in real rivers when the alluvial cover is spatially discontinuous and/or intermittent in time. Some recent modeling approaches allow a smooth transition between alluviated and bare-bedrock beds, and simultaneous evolution of the sediment and bedrock surfaces (*Lague*, 2010; *Zhang et al.*, 2015;

Shobe et al., 2017). *Lague* (2010) tracked sediment thickness and allowed progressively more bedrock erosion as sediment thickness H declined relative to median grain size D_{50}. He tested both exponential and linear models for the relationship between bedrock exposure and the ratio H/D_{50}. *Zhang et al.* (2015) compared sediment thickness to a statistical description of the macro-scale bedrock roughness to determine the probability of bedrock being exposed. The probability of bedrock exposure increased with declining sediment thickness and increasing bedrock surface roughness.

For the erosion modeling suite we adopt the approach of *Shobe et al.* (2017) (the Stream Power with Alluvium Conservation and Entrainment [SPACE] model), who also used an exponential expression describing increases in bedrock exposure as sediment thickness declines relative to bedrock surface roughness. The SPACE model tracks topographic elevation η as well as bedrock surface elevation η_b and sediment thickness H, such that

$$\frac{\partial \eta}{\partial t} = \frac{\partial \eta_b}{\partial t} + \frac{\partial H}{\partial t}. \tag{A.40}$$

Changes in sediment thickness are treated identically to the erosion-deposition model (equation A.34), and changes in bedrock height are driven by bedrock erosion E_r (there is no deposition of bedrock):

$$\frac{\partial \eta_r}{\partial t} = -E_r. \tag{A.41}$$

Erosion and deposition of sediment are computed using the same approach as used in the more basic entrainment-deposition model, with the addition of a factor that limits the rate of sediment entrainment, E_s, as sediment availability declines:

$$E_s = K_s A^{1/2} S \left(1 - e^{-H/H_*}\right). \tag{A.42}$$

where K_s is an entrainment coefficient for alluvium. Here H_* is the bedrock surface roughness length scale. Large H_* corresponds to a rough bedrock surface and vice versa.

The SPACE model includes a similar formulation for the bedrock, where bedrock erosion becomes more efficient as sediment thickness declines:

$$E_r = K_r A^{1/2} S e^{-H/H_*}. \tag{A.43}$$

Here, r subscripts denote bedrock parameters. Adding bedrock erosion to the entrainment-deposition model requires that eroded bedrock material be added to sediment flux calculations:

$$\frac{\mathrm{d}Q_s}{\mathrm{d}A(\hat{x})} = E_s + (1 - F_f)\, E_r - D_s. \tag{A.44}$$

where $A(\hat{x})$ represents drainage area, which increases as a function of streamwise distance $\hat{x}$. The factor F_f indicates the proportion of the bedrock that is made up of fine sediment such that it goes into permanent suspension and is no longer included in model calculations. Q_s therefore only includes grains not considered "fine."

As demonstrated by *Shobe et al.* (2017), the SPACE model is capable of transitioning between detachment-limited and transport-limited behavior. In a further advance over basic entrainment-deposition models, SPACE can model bare-bedrock channels, fully alluvial channels, and mixed bedrock-alluvial channels, allowing the transition between these states to be set by sediment flux and erosive power. SPACE enables modeling of channels that may alternate between bedrock, bedrock-alluvial, and alluvial states in response to changing tectonic forcing, climate, or sediment supply conditions. For a full derivation and discussion of the SPACE model, as well as a development of steady-state analytical solutions, see *Shobe et al.* (2017).

How the alternative hydrology models influence EMS' erosion laws

For those models that use variable-source area hydrology, the drainage area factor in the water-erosion law is replaced by effective drainage area, A_{eff}, as defined by equation (A.23). Models that use stochastic hydrology replace A with $Q = rA$, using r as defined in equation (A.27).

One model, BasicStVs, combines stochastic runoff generation with variable source-area hydrology. With this model, as in the variable-source model more generally, the capacity to carry subsurface discharge is defined as

$$Q_{ss} = TS\Delta x, \tag{A.45}$$

where as before T is transmissivity, S is surface gradient, and Δx is flow width. Assuming interception loss and leakage to deeper groundwater are negligible, the total discharge produced by a storm event with rainfall rate p is

$$Q_{tot} = pA. \tag{A.46}$$

The surface discharge, Q, should then be the difference between these two quantities, or zero if $Q_{ss} > Q_{tot}$. However, a simple "either-or" differencing formulation is somewhat unrealistic (given small-scale natural variability in T), and if implemented numerically would risk creating numerical daemons in the model's response surface. To avoid these issues, the BasicStVs model uses the exponentially smoothed formula

$$Q = Q_{tot} - Q_{ss}[1 - \exp(-Q_{tot}/Q_{ss})], \tag{A.47}$$

so that $Q \to 0$ when $Q_{tot} \ll Q_{ss}$, and $Q \to Q_{tot}$ when $Q_{tot} \gg Q_{ss}$. The form of this equation is similar to that of the smooth-threshold erosion law illustrated in Figure A.5. Substituting the definitions of Q_{tot} and Q_{ss} above,

$$Q = pA - TS\Delta x[1 - \exp(-pA/TS\Delta x)]. \tag{A.48}$$

The precipitation rate calculated for each stochastic event is used to calculate Q, which is then used as the discharge factor in the erosion law $E_W = K_q Q^{1/2} S$.

A.2.5 Material Properties

Soil and alluvium

One of the binary options listed in Table A.1 is the ability to track explicitly a dynamic soil layer. Models that use this option implement the depth-dependent form of the applicable soil-creep law (i.e., either the linear or nonlinear form).

When the dynamic-soil option is used in combination with a sediment-tracking entrainment-deposition erosion law (model BasicHySa), the SPACE model is used in place of the simpler (single-material-type) entrainment-deposition law. In all other cases, the use of a dynamic soil layer does not directly influence the water-erosion law.

When dynamic soil is combined with variable source-area hydrology (model BasicVsSa), the actually soil thickness at each point $H(x, y, t)$ is used to calculate transmissivity. In this particular model, therefore, there is effectively a single hydrologic parameter, β, defined as $\beta = K_{sat}\Delta x / R_m$, and having dimensions of length.

Multiple lithologies

With two-lithology models, the material-dependent parameters in the water-erosion equation, including the coefficient (K, K_{ss}, or K_q) and, if applicable, the threshold (ω_c), vary in space and time as a function of the local surface elevation, η, in relation to the elevation of the contact between lithologies 1 and 2, $\eta_C(x, y)$. If $\eta > \eta_C$, lithology 1 is exposed at the surface; otherwise, the surface unit is lithology 2.

To preserve smoothness in the numerical solution, we allow there to be a finite "contact zone" within which the two lithologies are both considered to influence the material erodibility; one might imagine this zone as representing a gradational transition from one unit to another, or alternatively an uneven contact surface. We define a weight factor w that defines the relative influence of each of the two lithologies:

$$w(x, y, t) = \frac{1}{1 + \exp\left(-\frac{(\eta - \eta_C)}{W_c}\right)}. \tag{A.49}$$

Here, w represents the influence of lithology 1, and $1 - w$ describes the influence of lithology 2. At each location, the channel erosion rate coefficient is calculated by applying this weight factor. For example, in model BasicRt, which uses the simple unit stream power formula, the rate coefficient K is calculated as

$$K(\eta, \eta_C) = wK_1 + (1 - w)K_2 \tag{A.50}$$

where K_1 and K_2 are the rate coefficients associated with each lithology, and W_c is the contact-zone width.

A.2.6 Climate and Baselevel Boundary Conditions

All EMS 1.0 models include a rudimentary ability to control baselevel change by specifying either a constant or time-varying rate of baselevel lowering. This method of baselevel control is only available when a model is configured to represent a drainage basin with a single outlet location. The outlet location can be specified by the user, or identified automatically (a feature that takes advantage of Landlab's *watershed boundary condition* functionality). The elevation of the outlet point lowers through time at the user-specified rate or time-series of rates.

One model (BasicCc) provides the ability to change parameter K linearly through time, as a simple representation of paleoclimate variation. The representation of change is as follows. At the beginning of a model run, K is assumed to be larger or smaller than its final value (K_0) by a factor f; if $f > 1$, K starts out larger than K_0 (representing a more erosive climate) and declines through time, and conversely if $f < 1$. K stops changing after a time period T_s, whereupon it assumes its final value K_0. Mathematically, this linear variation in K is

$$K(t) = \begin{cases} \mu t + fK_0, & \text{when } t < T_s, \\ K_0 & \text{otherwise.} \end{cases} , \tag{A.51}$$

where $\mu = (1 - f)K_0/T_s$ is the rate of change.

A.2.7 Pairwise Process Combinations

As noted earlier, the various process-model options described above can be arranged into a set of 12 binary choices (Table A.1). EMS 1.0 is designed to support experimentation and hypothesis testing among these (and other) alternative formulations. The number of possible unique combinations among this set of 12 options is unweildy (2^{12}, though some are not physically sensible). In creating the individual EMS model configurations, we used an approach that focuses on single and pairwise variations on the Basic (simplest) model, which is the first entry in Table A.2. The next 11 entries are models or model configurations that differ from Basic in just one element. The remaining entries represent pairwise combinations. Not all possible pairwise combinations are included. Instead, the pairwise process combinations selected represent those for which we thought there might be nonlinear interactions between the two process elements—in other words, those combinations where we expected the whole to be greater (or less) than the sum of the parts. An example of such a nonlinear interaction that has been explored in the literature is temporal variability in water discharge in a river system where the erosion process is strongly thresholded (*Tucker and Bras*, 2000; *Snyder et al.*, 2003; *DiBiase et al.*, 2010). This particular combination is represented in EMS by model BasicThSt.

The particular list of model choices in Table A.2 is not meant to be exhaustive. The EMS software was designed to be easily extensible as needed for any given application, so that for example if a researcher wishes to explore combinations that are not included in the present collection of models, or to add a new process formulation, he or she can do so with relative ease. In the next section, we describe how the software is designed to promote extensibility.

A.3 Software Implementation

A.3.1 Overview

In creating a software product that manifests not one but rather dozens of potential model configurations, efficiency and reuse are key design considerations. To meet this goal, EMS 1.0 uses an object-oriented approach to its high-level design. An EMS model is implemented as a Python class. The class that implements any particular EMS model inherits from a common base class called ErosionModel. Here we describe the main functions of the base class, the typical structure of the derived class, and the use of a driver program to configure and execute an EMS model.

A.3.2 ErosionModel Base Class

The ErosionModel base class takes care of operations that are common to all EMS model programs. This includes handling of parameter inputs, reading and configuring input topography (if used), and implementing baselevel lowering (Table A.3). The base class also provides method functions to support model execution, at three different levels of granularity: running a single step of specified duration, running many steps over a specified amount of time (for example, to run a model continually between pauses for output), and to execute a complete run.

The Community Surface Dynamics Modeling System (CSDMS) has promoted use of an interface standard known as the Basic Model Interface (BMI) for geoscientific numerical models (*Peckham et al.*, 2013). Although EMS does not yet fully implement a BMI, its model-control functions follow the conventions used by the Landlab Toolkit, which themselves have a close parallel with the main BMI model-control functions. The EMS `initialize` method is fully compatible with the BMI method of the same name, which takes as an argument a string containing the name of a parameter-input file (EMS' version can alternatively accept a Python dictionary containing parameter name-value pairs). The EMS `run_one_step` method serves the same function as BMI's `update`, but accepts step size as an argument. EMS' `run_for` is similar to BMI's `update_until` (the former takes a duration whereas the latter takes an absolute time).

Table A.3: Base class methods. Run-control methods in top part of table.

Name	Purpose
__init__	Initialize model
run_one_step[a]	Execute one time step of duration dt
run_for	Call run_one_step repeatedly to execute model for given total duration
run	Execute complete model run, pausing periodically to write output
finalize	Clean up prior to ending execution
write_output	Write output to netCDF file
calculate_cumulative_change	Calculate cumulative node-by-node changes in elevation
update_outlet	Update outlet node elevation
read_topography	Read and return topography from file, as a Landlab grid and field
setup_rectangular_grid	Create and configure rectangular grid based on input parameters
setup_time_varying_precip	Set up to handle time variation in precipitation and related parameters
get_parameter_from_exponent	Converts exponent to parameter value ($p \rightarrow 10^p$)
check_walltime[b]	Check walltime and save model out if near end of time
pickle_self	Create restart file using Python *pickle*
__get_state__	Get ErosionModel state from pickled state˙dict
__set_state__	Set ErosionModel state for pickling

[a] empty function intended to be overridden by child class.

[b] used to create a restart file on high-performance computing systems that limit job execution time.

A.3.3 Derived Classes and use of Landlab Components

Two features make the process of writing a new model program in EMS relatively fast and efficient: the ability to inherit functionality from the ErosionModel base class, and the use of Process Components in the Landlab Toolkit to handle individual process laws. Having already discussed the base class, it is useful to say a few words about Landlab. The Landlab Toolkit is a Python-language software library designed to support efficient creation, exploration, and modifiction of two-dimensional numerical models of earth-surface processes (*Hobley et al.*, 2017). Landlab accomplishes this by using a CSDMS-inspired plug-and-play method, in which the functionality needed for a numerical implementation of a single process is encapsulated in a standard-format *Process Component*. Process Components are implemented as Python classes. Landlab also uses an object-oriented approach to grid creation and management, so that a simulation grid is encapsulated as a Python object. Components normally interact with a Grid object, and share *fields* (arrays) of grid-linked

```
# Test inputs for model 802: basic with threshold plus two lithologies
run_duration: 1000.0
output_interval: 1000.0
dt: 10.0
DEM_filename: '../../topo_data_for_testing/dem48_fillClip_ascii.txt'
rock_till_file__name: 'test_rock_till_contact_elev.txt'
output_filename: 'model_802_basicThRt_test_output'
rock__erodibility: 0.0
till__erodibility: 0.00025
rock_erosion__threshold: 1.0e-6
till_erosion__threshold: 1.0e-6
contact_zone__width: 1.0
m_sp: 0.5
n_sp: 1.0
linear_diffusivity: 0.108
```

Figure A.6: Example of an EMS input file (model BasicThRt).

data by creating attaching the necessary fields to a common grid. More information about Landlab can be found in *Hobley et al.* (2017).

EMS uses Landlab Components to implement its process laws. Each EMS model program is implemented as a class that derives from the ErosionModel base class. The model program's `__init__` method handles parameter retrieval, and instantiates the necessary Landlab Components. The model program's `run_one_step` method then advances each component in turn, normally by calling the component-level `run_one_step`. In addition to the definition of the model class, each EMS model program includes a short `main` function that allows the model program to be run in a stand-alone fashion (as opposed to being instantiated and run from an outside script, which can also be done). This simple design allows the main model program files to be quite short, often with between 100 and 300 lines, many of which are comments or blanks.

A.3.4 Model and Class Naming Scheme

The naming scheme for the classes that implement the individual EMS models starts with the name "Basic" and then adds a two-letter code for each element in which the model differs from the Basic model (Table A.2). For example, the BasicTh model uses a threshold formula for water erosion, but is otherwise identical to the Basic model. Model BasicThRt uses a threshold and also implements two separate lithologies (here, "Rt" stands for "rock and till," a name that reflects the original motivation for this particular capability).

A.4 Input/output Formats and Semantics

EMS 1.0 provides two options for handling input of parameter values and run-control options. Parameters can be listed in an ASCII-text input file, using YAML format ("Yet Another Macro Language"), as in the example in Figure A.6. The name of the input file is then passed as an argument when a model object is instantiated. Alternatively, parameter name-value pairs can be entered in a Python dictionary and passed as an input when the model object is instantiated.

If a user wishes to read in a digital elevation model (DEM) to use as the initial topography, the name of the DEM file is given as a parameter in the input file or dictionary. As of EMS 1.0, the file must be in ESRI ASCII format. EMS 1.0 treats the DEM as a watershed, using Landlab's watershed setup functionality. Any grid nodes with elevation values equal to -9999 (the ESRI "no-data" code) are set to *closed boundary* status (for more on Landlab grids, see *Hobley et al.*, 2017). The user may optionally specify a particular grid node as the watershed outlet, using Landlab's standard node-numbering scheme. Otherwise, an outlet node will be identified automatically. If the user does not specify the name of a DEM file, EMS will create a rectangular grid and initialize its elevation field with uncorrelated random noise (drawn from a uniform distribution ranging between 0 and 1 grid-length units). For two-lithology ("Rt") models, the user must also provide an ESRI ASCII file containing the elevations of the contact between the two units at each grid node.

Gridded output is written in netCDF format. The base name for the output files must be specified as an input parameter. When an EMS model runs, output is written at regular intervals, with the frequency set by the user via an input parameter. One file is created for every output interval; these files are numbered sequentially. An EMS output file contains all of the grid fields used in that particular model, which is to say all the grid fields created by that model's Landlab Components plus any created in the main model program.

Unique names are assigned to each EMS input parameter and each data field. EMS 1.0 parameter and field names are listed in Table A.4, together with their equivalent mathematical symbols. EMS 1.0 follows the naming conventions used by Landlab (see *Hobley et al.*, 2017). These conventions are loosely based on the CSDMS Standard Names (*Peckham et al.*, 2013), whose syntax uses an "object plus value" pattern (for example, *topographic__elevation*). Both Landlab and EMS 1.0 names seek a balance between brevity, information content, and consistency with the CSDMS Standard Names. Many of the EMS/Landlab names are shorter than their full Standard Name equivalents (which can be quite lengthy), but are designed to be similar enough to allow one-to-one automated mapping. Examples of input-parameter names are shown in the input file example in Figure A.6. Similar principles apply to the field names, which are encoded in the netCDF output files.

Table A.4: EMS parameter names and unit dimensions.

Symbol	Name	Dimensions
b	thresh_change_per_depth	T^{-1}
c	precip_shape_factor	-
D	linear_diffusivity	L^2T^{-1}
f	climate_factor	-
F_f	F_f	-
F	intermittency_factor	-
H_*	H_star	L
H_0	soil_transport_decay_depth	L
H_{init}	initial_soil_thickness	L
H_s	soil_production_decay_depth	L
I_m	infiltration_capacity	LT^{-1}
K	K_sp	T^{-1}
K_1	K_till_sp	T^{-1}
K_2	K_rock_sp	T^{-1}
K_q	K_stochastic	$L^{-1/2}T^{-1/2}$
$K_{q,ss}$	K_stochastic_ss	$T^{-2/3}$
K_s	K_sed_sp	T^{-1}
K_{ss}	K_ss	$L^{1/3}T^{-1}$
K_{ss1}	K_till_ss	$L^{1/3}T^{-1}$
K_{ss2}	K_rock_ss	$L^{1/3}T^{-1}$
K_{sat}	K_hydraulic_conductivity	$LT^{-1})$
m	m_sp	-
n	n_sp	-
n_{ts}	number_of_sub_time_steps	integer
p_d	mean_storm__intensity	LT^{-1}
P_0	max_soil_production_rate	LT^{-1}
R_m	recharge_rate	LT^{-1}
S_c	slope_crit	-
S_r	random_seed	integer
T_s	climate_constant_date	T
V_c	v_sc	-
V	v_s	LT^{-1}
W_c	contact_zone__width	L
ϕ	phi	-
ω_c	erosion__threshold[a]	LT^{-1}
ω_{c1}	till_erosion__threshold	LT^{-1}
ω_{c2}	rock_erosion__threshold	LT^{-1}

[a] becomes field rather than single-value parameter in Dd models.

Table A.5: Selected EMS field names, corresponding mathematical symbols, and unit dimensions.

Symbol	Name	Dimensions
A	`drainage_area`	L^2
A_{eff}	`effective_drainage_area`[a]	L^2
D_I	`cumulative_erosion__depth`	L
H	`soil__depth`[b]	L
K	`substrate__erodibility`[c]	T^{-1}
P	`soil_production__rate`[b]	LT^{-1}
Q	`surface_water__discharge`[d]	L^3T^{-1}
Q_s	`sediment__flux`[e]	L^3T^{-1}
S	`topographic__steepest_slope`	-
η	`topographic__elevation`	L
η_b	`bedrock__elevation`[b]	L
η_C	`rock_till_contact__elevation`	L
ω_c	`erosion__threshold`[f]	LT^{-1}

[a] used in most models with variable source area hydrology
[b] used in models with dynamic soil layer
[c] used in several two-lithology models
[d] used in stochastic models
[e] used in entrainment-deposition models
[f] used in depth-dependent threshold models, and models that include two lithologies as well as an erosion threshold

A.5 Governing Equations for each EMS 1.0 Model

A.5.1 Basic

The governing equation for elevation change in the Basic model is:

$$\frac{\partial \eta}{\partial t} = -KA^{1/2}S + D\nabla^2\eta, \tag{A.52}$$

Parameters: K and D.

A.5.2 BasicVm

BasicVm modifies the Basic model by allowing a variable drainage-area exponent, m:

$$\frac{\partial \eta}{\partial t} = -KA^{m}S + D\nabla^2\eta, \tag{A.53}$$

Note that the units of K depend on m, so that the value of K used in BasicVm cannot be meaningfully compared to K used in models with a fixed area exponent of 1/2, unless of course m happens to equal 1/2.

Parameters: K, D, and m.

A.5.3 BasicTh

BasicTh adds a threshold to the water erosion term in the Basic model:

$$\frac{\partial \eta}{\partial t} = -[\omega - \omega_c(1 - e^{-\omega/\omega_c})] + D\nabla^2\eta, \tag{A.54}$$

$$\omega = KA^{1/2}S \tag{A.55}$$

The threshold is smoothed such that the water erosion term approaches zero when $\omega \ll \omega_c$, and asymptotes to $\omega - \omega_c$ as $\omega \gg \omega_c$.

Parameters: K, D, and ω_c.

A.5.4 BasicSs

BasicSs uses area and slope exponents of 1/3 and 2/3, respectively, which reflects the assumption that water erosion rate is proportional to boundary shear stress (see, e.g.,):

$$\frac{\partial \eta}{\partial t} = -K_{ss}A^{1/3}S^{2/3} + D\nabla^2\eta. \tag{A.56}$$

It is otherwise equivalent to Basic. Note that there is no unique source code that implements BasicSs; rather, one simply uses Basic but changes the exponent parameters.

Parameters: K_{ss} and D.

A.5.5 BasicDd

BasicDd includes a threshold to the water erosion term that increases with progressive incision depth (see main text):

$$\frac{\partial \eta}{\partial t} = -[\omega - \omega_c(1 - e^{-\omega/\omega_c})] + D\nabla^2\eta, \tag{A.57}$$

$$\omega = KA^{1/2}S, \tag{A.58}$$

$$\omega_{ct}(x, y, t) = \max(\omega_c + bD_I(x, y, t), \omega_c). \tag{A.59}$$

Parameters: K, D, b, and ω_c.

A.5.6 BasicHy

BasicHy uses a sediment-tracking ("hybrid") water-erosion law:

$$(1 - \phi)\frac{\partial \eta}{\partial t} = \frac{VQ_s}{A} - KA^{1/2}S + D\nabla^2\eta, \tag{A.60}$$

$$Q_s = \int_0^s \left(\left[KA^{1/2}S\right]_s - \left[\frac{VQ_s}{A}\right]_s \right) ds, \tag{A.61}$$

where ϕ is bed material porosity. Parameters: K, D, V, and ϕ.

A.5.7 BasicCh

BasicCh uses a nonlinear law for hillslope erosion and transport:

$$\frac{\partial \eta}{\partial t} = -KA^{1/2}S - \nabla q_h, \tag{A.62}$$

$$q_h = DS\left[1 + \sum_{i=1}^{N}\left(\frac{S}{S_c}\right)^{2i}\right], \tag{A.63}$$

where S_c is a critical slope gradient and N is the number of terms used. Parameters: K, D, S_c.

A.5.8 BasicSt

BasicSt uses a stochastic representation of precipitation, in which the rainfall rate p is a random variable. The evolution equation is

$$\frac{\partial \eta}{\partial t} = -K\hat{Q}^{1/2}S + D\nabla^2\eta. \tag{A.64}$$

The discharge, $\hat{Q}$, associated with a particular value of p is

$$\hat{Q} = p - I_m\left(1 - e^{-p/I_m}\right), \tag{A.65}$$

The probability distribution of p is given by a stretched exponential survival function

$$Pr(P > p) = \exp\left[-\left(\frac{p}{p_0}\right)^c\right], \tag{A.66}$$

with shape parameter c and scale parameter p_0.

Parameters: K, D, I_m, p_0, c.

A.5.9 BasicVs

The BasicVs model implements variable source area runoff using the "effective area" approach described in Section A.2.3:

$$\frac{\partial \eta}{\partial t} = -KA_{eff}^{1/2}S + D\nabla^2\eta, \tag{A.67}$$

$$A_{eff} = Ae^{-\alpha S/A} \tag{A.68}$$

Parameters: K, D, α.

A.5.10 BasicSa

BasicSa modifies the Basic model by explicitly tracking a dynamic soil layer of thickness $H(x, y, t)$. Its governing equations are:

$$\eta = \eta_b + H, \tag{A.69}$$

$$\frac{\partial H}{\partial t} = P_0 \exp(-H/H_*) - \delta(H)KA^{1/2}S - \nabla q_s, \tag{A.70}$$

$$\frac{\partial \eta_b}{\partial t} = -P_0 \exp(-H/H_*) - (1 - \delta(H))KA^{1/2}S, \tag{A.71}$$

$$q_s = -D\left[1 - \exp\left(-\frac{H}{H_0}\right)\right]\nabla\eta. \tag{A.72}$$

The function $\delta(H)$ is used to indicate that water erosion will act on soil where it exists, and on the underlying lithology where soil is absent. To achieve this, $\delta(H)$ is defined to equal 1 when $H > 0$ (meaning soil is present), and 0 if $H = 0$ (meaning the underlying parent material is exposed).

Parameters: K, D, P_0, H_*, H_0.

A.5.11 BasicRt

BasicRt modifies Basic by allowing for two lithologies, as described in Sections A.1.4 and A.2.5.

$$\frac{\partial \eta}{\partial t} = -K(\eta, \eta_C)A^{1/2}S + D\nabla^2\eta, \tag{A.73}$$

$$K(\eta, \eta_C) = wK_1 + (1 - w)K_2, \tag{A.74}$$

$$w = \frac{1}{1 + \exp\left(-\frac{(\eta - \eta_C)}{W_c}\right)} \tag{A.75}$$

where W_c is the contact-zone width.

Parameters: K_1, K_2, D, W_c (plus specification of $\eta_C(x,y)$).

A.5.12 BasicCc

BasicCc uses the same governing equation as Basic, but allows the parameter K to vary through time according to a linear function:

$$K(t) = \begin{cases} \mu t + fK_0, & \text{when } t < T_s, \\ K_0 & \text{otherwise.} \end{cases}, \tag{A.76}$$

$$\mu = (1-f)K_0/T_s. \tag{A.77}$$

Parameters: K_0, D, f (factor by which K is larger ($f > 1$) or smaller ($f < 1$) than K_0 at $t = 0$), and T_s (time at which K becomes constant).

A.5.13 BasicThHy

This model uses a sediment-tracking (hybrid) water-erosion law, with a smoothed threshold on the entrainment term:

$$\frac{\partial \eta}{\partial t} = \frac{VQ_s}{A} - E_s + D\nabla^2\eta, \tag{A.78}$$

$$Q_s = \int_0^{A(\hat{x})} \left(E_s(\hat{x}) - \frac{VQ_s}{A(\hat{x})} \right) dA(\hat{x}) \tag{A.79}$$

$$E_s = \omega - \omega_c(1 - e^{-\omega/\omega_c}), \tag{A.80}$$

$$\omega = KA^{1/2}S \tag{A.81}$$

Parameters: K, D, ω_c, V.

A.5.14 BasicThSt

The land surface evolution equation is:

$$\frac{\partial \eta}{\partial t} = -\left[\hat{\omega} - \omega_c(1 - e^{-\hat{\omega}/\omega_c})\right] + D\nabla^2\eta, \tag{A.82}$$

$$\hat{\omega} = K_q\hat{Q}^{1/2}S. \tag{A.83}$$

The discharge, $\hat{Q}$, associated with a particular value of p is

$$\hat{Q} = p - I_m\left(1 - e^{-p/I_m}\right), \tag{A.84}$$

The probability distribution of p is given by a stretched exponential survival function

$$Pr(P > p) = \exp\left[-\left(\frac{p}{p_0}\right)^c\right], \tag{A.85}$$

with shape parameter c and scale parameter p_0.

Parameters: K, D, ω_c, I_m, p_0, c.

A.5.15 BasicThVs

The BasicThVs model implements variable source area runoff using the "effective area" approach plus a threshold on the water-erosion law:

$$\frac{\partial \eta}{\partial t} = -\left[\omega - \omega_c(1 - e^{-\omega/\omega_c})\right] + D\nabla^2\eta, \tag{A.86}$$

$$\omega = KA_{eff}^{1/2}S, \tag{A.87}$$

$$A_{eff} = Ae^{-\alpha S/A} \tag{A.88}$$

Parameters: K, D, ω_c, α.

A.5.16 BasicThRt

BasicThRt modifies Basic by allowing for two lithologies, and applying a threshold to the channel incision law:

$$\frac{\partial \eta}{\partial t} = -\left[\omega - \omega_c(1 - e^{-\omega/\omega_c})\right] + D\nabla^2\eta, \tag{A.89}$$

$$\omega = K(\eta, \eta_C)A^{1/2}S, \tag{A.90}$$

$$K(\eta, \eta_C) = wK_1 + (1 - w)K_2, \tag{A.91}$$

$$\omega_c(\eta, \eta_C) = w\omega_{c1} + (1 - w)\omega_{c2}, \tag{A.92}$$

$$w = \frac{1}{1 + \exp\left(-\frac{(\eta - \eta_C)}{W_c}\right)} \tag{A.93}$$

where W_c is the contact-zone width.

Parameters: K_1, K_2, D, ω_{c1}, ω_{c2}, W_c (plus specification of $\eta_C(x, y)$).

A.5.17 BasicSsDd

BasicSsDd uses a thresholded shear-stress formula for channel erosion:

$$\frac{\partial \eta}{\partial t} = -[\omega - \omega_{ct}(1 - e^{-\omega/\omega_{ct}})] + D\nabla^2\eta, \tag{A.94}$$

$$\omega = K_{ss}A^{1/3}S^{2/3}, \tag{A.95}$$

$$\omega_{ct}(x, y, t) = \max(\omega_c + bD_I(x, y, t), \omega_c). \tag{A.96}$$

Parameters: K_{ss}, D, b, and ω_c.

A.5.18 BasicSsHy

This model uses an entrainment-deposition formula, with an incision term based on shear stress rather than simple unit stream power:

$$\frac{\partial \eta}{\partial t} = \frac{VQ_s}{A} - K_{ss}A^{1/3}S^{2/3} + D\nabla^2\eta, \tag{A.97}$$

$$Q_s = \int_0^{A(\hat{x})} \left(K_{ss}A^{1/3}S^{1/3} - \frac{VQ_s}{A}\right) dA \tag{A.98}$$

Parameters: K_{ss}, D, and V.

A.5.19 BasicSsVs

The BasicSsVs model uses a shear-stress law in combination with variable source area runoff, which is implemented using the "effective area" approach described in Section A.2.3:

$$\frac{\partial \eta}{\partial t} = -K_{ss} A_{eff}^{1/3} S^{2/3} + D\nabla^2 \eta, \tag{A.99}$$

$$A_{eff} = Ae^{-\alpha S/A} \tag{A.100}$$

Parameters: K_{ss}, D, α.

A.5.20 BasicSsRt

BasicSsRt combines a shear-stress erosion law with two lithologies:

$$\frac{\partial \eta}{\partial t} = -K_{ss}(\eta, \eta_C) A^{1/3} S^{2/3} + D\nabla^2 \eta, \tag{A.101}$$

$$K_{ss}(\eta, \eta_C) = wK_{ss1} + (1-w)K_{ss2}, \tag{A.102}$$

$$w = \frac{1}{1 + \exp\left(-\frac{(\eta - \eta_C)}{W_c}\right)} \tag{A.103}$$

where W_c is the contact-zone width.

Parameters: K_{ss1}, K_{ss2}, D, W_c (plus specification of $\eta_C(x, y)$).

A.5.21 BasicDdHy

This is a sediment-tracking (hybrid) erosion law with a depth-dependent threshold:

$$\frac{\partial \eta}{\partial t} = \frac{VQ_s}{A} - [\omega - \omega_{ct}(1 - e^{-\omega/\omega_{ct}})] + D\nabla^2 \eta, \tag{A.104}$$

$$Q_s = \int_0^A \left([\omega - \omega_c(1 - e^{-\omega/\omega_c})] - \frac{VQ_s}{A} \right) dA, \tag{A.105}$$

$$\omega = KA^{1/2} S, \tag{A.106}$$

$$\omega_{ct}(x, y, t) = \max(\omega_c + bD_I(x, y, t), \omega_c). \tag{A.107}$$

Parameters: K, D, V, b, and ω_c.

A.5.22 BasicDdSt

This model uses stochastic precipitation, and the water-erosion law includes a depth-dependent threshold:

$$\frac{\partial \eta}{\partial t} = -[\omega - \omega_{ct}(1 - e^{-\omega/\omega_{ct}})] + D\nabla^2\eta, \tag{A.108}$$

$$\omega = K_q \hat{Q}^{1/2} S, \tag{A.109}$$

$$\omega_{ct}(x, y, t) = \max(\omega_c + bD_I(x, y, t), \tag{A.110}$$

$$\hat{Q} = p - I_m \left(1 - e^{-p/I_m}\right), \tag{A.111}$$

$$Pr(P > p) = \exp\left[-\left(\frac{p}{p_0}\right)^c\right]. \tag{A.112}$$

Parameters: K_q, D, I_m, p_0, c, ω_c, b.

A.5.23 BasicDdVs

Model BasicDdVs uses variable source-area hydrology, and an erosion threshold that increases with progressive erosion depth:

$$\frac{\partial \eta}{\partial t} = -[\omega - \omega_{ct}(1 - e^{-\omega/\omega_{ct}})] + D\nabla^2\eta, \tag{A.113}$$

$$\omega = K A_{eff}^{1/2} S, \tag{A.114}$$

$$A_{eff} = A e^{-\alpha S/A}, \tag{A.115}$$

$$\omega_{ct}(x, y, t) = \max(\omega_c + bD_I(x, y, t). \tag{A.116}$$

Parameters: K, D, ω_c, b, and α.

A.5.24 BasicDdRt

BasicDdRt modifies Basic by allowing for two lithologies, and applying a depth-dependent threshold to the channel incision law. Unlike BasicThRt, the (initial) threshold is taken to be uniform across the two lithologies; the rate of increase in threshold with depth (b) is also assumed uniform.

$$\frac{\partial \eta}{\partial t} = -\left[\omega - \omega_{ct}(1 - e^{-\omega/\omega_{ct}})\right] + D\nabla^2\eta, \tag{A.117}$$

$$\omega = K(\eta, \eta_C) A^{1/2} S, \tag{A.118}$$

$$K(\eta, \eta_C) = wK_1 + (1 - w)K_2, \tag{A.119}$$

$$\omega_{ct}(x, y, t) = \max(\omega_c + bD_I(x, y, t), \tag{A.120}$$

$$w = \frac{1}{1 + \exp\left(-\frac{(\eta - \eta_C)}{W_c}\right)} \tag{A.121}$$

where W_c is the contact-zone width.

Parameters: K_1, K_2, D, ω_c, b, W_c (plus specification of $\eta_C(x, y)$).

A.5.25 BasicHyFi

This is a version of BasicHy that allows some fraction of eroded material to form "fines" that are permanently suspended and do not form part of the coarse sediment flux Q_s:

$$\frac{\partial \eta}{\partial t} = \frac{VQ_s}{A} - KA^{1/2}S + D\nabla^2\eta, \tag{A.122}$$

$$Q_s = \int_0^A \left(K(1-F_f)A^{1/2}S - \frac{VQ_s}{A} \right) dA \tag{A.123}$$

Parameters: K, D, V, F_f.

A.5.26 BasicHySt

$$\frac{\partial \eta}{\partial t} = \frac{V_q Q_s}{\hat{Q}} - K_q \hat{Q}^{1/2}S + D\nabla^2\eta, \tag{A.124}$$

$$Q_s = \int_0^A \left(K_q \hat{Q}^{1/2}S - \frac{VQ_s}{A} \right) dA, \tag{A.125}$$

$$\hat{Q} = A\left[p - I_m\left(1 - e^{-p/I_m}\right)\right], \tag{A.126}$$

$$Pr(P > p) = \exp\left[-\left(\frac{p}{p_0}\right)^c\right]. \tag{A.127}$$

Parameters: K_q, V_q, D, I_m, p_0, c.

A.5.27 BasicHyVs

Sediment-tracking (hybrid) model that uses variable source-area hydrology:

$$\frac{\partial \eta}{\partial t} = \frac{VQ_s}{A_{eff}} - KA_{eff}^{1/2}S + D\nabla^2\eta, \tag{A.128}$$

$$Q_s = \int_0^A \left(KA_{eff}^{1/2}S - \frac{VQ_s}{A_{eff}} \right) dA, \tag{A.129}$$

$$A_{eff} = Ae^{-\alpha S/A}. \tag{A.130}$$

Parameters: K, D, V, α.

A.5.28 BasicHySa

This model uses a continuous layer of soil/alluvium, which influences both hillslope transport and water erosion and transport. This model configuration uses the SPACE algorithm of

Shobe et al. (2017), whose governing equations can be summarized as:

$$\eta = \eta_b + H, \tag{A.131}$$

$$\frac{\partial H}{\partial t} = P_0 \exp(-H/H_*) + \frac{VQ_s}{A} - K_s A^{1/2} S(1 - e^{-H/H_*}) - \nabla q_h, \tag{A.132}$$

$$\frac{\partial \eta_b}{\partial t} = -P_0 \exp(-H/H_s) - K_r A^{1/2} S e^{-H/H_*}, \tag{A.133}$$

$$Q_s = \int_0^A \left(K_s A^{1/2} S(1 - e^{-H/H_*}) + K_r A^{1/2} S e^{-H/H_*} - \frac{VQ_s}{A} \right) dA, \tag{A.134}$$

$$q_h = -D \left[1 - \exp\left(-\frac{H}{H_0} \right) \right] \nabla \eta. \tag{A.135}$$

Parameters: K_s, K_r, H_*, V, D, H_0, P_0, H_s.

A.5.29 BasicHyRt

Sediment-tracking (hybrid) model with two lithologies:

$$\frac{\partial \eta}{\partial t} = \frac{VQ_s}{A} - KA^{1/2}S + D\nabla^2 \eta, \tag{A.136}$$

$$Q_s = \int_0^A \left(KA^{1/2}S - \frac{VQ_s}{A} \right) dA, \tag{A.137}$$

$$K(\eta, \eta_C) = wK_1 + (1 - w)K_2, \tag{A.138}$$

$$w = \frac{1}{1 + \exp\left(-\frac{(\eta - \eta_C)}{W_c} \right)} \tag{A.139}$$

Parameters: K_1, K_2, V, D, W_c.

A.5.30 BasicChSa

BasicChSa modifies the Basic model by explicitly tracking a dynamic soil layer of thickness $H(x, y, t)$, and using a nonlinear hillslope transport law. Its governing equations are:

$$\eta = \eta_b + H, \tag{A.140}$$

$$\frac{\partial H}{\partial t} = P_0 \exp(-H/H_s) - \delta(H) K A^{1/2} S - \nabla q_h, \tag{A.141}$$

$$\frac{\partial \eta_b}{\partial t} = -P_0 \exp(-H/H_s) - (1 - \delta(H)) K A^{1/2} S, \tag{A.142}$$

$$q_h = DS \left[1 - \exp\left(-\frac{H}{H_0} \right) \right] \left[1 + \sum_{i=1}^{N} \left(\frac{S}{S_c} \right)^{2i} \right]. \tag{A.143}$$

Parameters: K, D, S_c, P_0, H_s, H_0.

A.5.31 BasicChRt

This model uses nonlinear hillslope transport and two lithologies:

$$\frac{\partial \eta}{\partial t} = -K(\eta, \eta_C) A^{1/2} S - \nabla q_h, \tag{A.144}$$

$$K(\eta, \eta_C) = w K_1 + (1-w) K_2, \tag{A.145}$$

$$w = \frac{1}{1 + \exp\left(-\frac{(\eta - \eta_C)}{W_c}\right)}, \tag{A.146}$$

$$q_h = DS\left[1 - \exp\left(-\frac{H}{H_0}\right)\right]\left[1 + \sum_{i=1}^{N}\left(\frac{S}{S_c}\right)^{2i}\right]. \tag{A.147}$$

Parameters: K_1, K_2, D, S_c, W_c (plus specification of $\eta_C(x, y)$).

A.5.32 BasicStVs

BasicStVs uses a stochastic representation of precipitation, together with variable source-area hydrology:

$$\frac{\partial \eta}{\partial t} = -K\hat{Q}^{1/2} S + D\nabla^2 \eta, \tag{A.148}$$

$$\hat{Q} = pA - TS\Delta x[1 - \exp(-pA/TS\Delta x)], \tag{A.149}$$

$$T = K_{sat} H, \tag{A.150}$$

$$Pr(P > p) = \exp\left[-\left(\frac{p}{p_0}\right)^c\right]. \tag{A.151}$$

Parameters: K, D, p_0, c, K_{sat}, and H (the latter two effectively form a single lumped parameter, T, but each one needs to be specified in the input file).

A.5.33 BasicVsSa

This model combines variable source-area hydrology with a dynamic soil layer. Unlike other model configurations with variable source-area hydrology, here the actual soil thickness $H(x, y, t)$ is used to calculate transmissivity.

$$\eta = \eta_b + H, \tag{A.152}$$

$$\frac{\partial H}{\partial t} = P_0 \exp(-H/H_s) - \delta(H) K A_{eff}^{1/2} S - \nabla q_h, \tag{A.153}$$

$$\frac{\partial \eta_b}{\partial t} = -P_0 \exp(-H/H_s) - (1 - \delta(H)) K A_{eff}^{1/2} S, \tag{A.154}$$

$$q_h = -D\left[1 - \exp\left(-\frac{H}{H_0}\right)\right]\nabla \eta, \tag{A.155}$$

$$A_{eff} = A \exp\left(-\frac{-K_{sat} H \Delta x S}{R_m A}\right). \tag{A.156}$$

Parameters: K, K_{sat}, R_m, D, H_0, P_0, H_s.

A.5.34 BasicVsRt

BasicVsRt is a two-lithology model configuration that uses variable source-area hydrology:

$$\frac{\partial \eta}{\partial t} = -K(\eta, \eta_C) A_{eff}^{1/2} S + D\nabla^2 \eta, \tag{A.157}$$

$$K(\eta, \eta_C) = wK_1 + (1-w)K_2, \tag{A.158}$$

$$w = \frac{1}{1 + \exp\left(-\frac{(\eta - \eta_C)}{W_c}\right)}, \tag{A.159}$$

$$A_{eff} = A \exp\left(-\frac{-\alpha S}{A}\right). \tag{A.160}$$

Parameters: K_1, K_2, α, D, W_c (plus specification of $\eta_C(x, y)$).

A.5.35 BasicSaRt

This model configuration combines a dynamic soil layer and two lithologies:

$$\eta = \eta_b + H, \tag{A.161}$$

$$\frac{\partial H}{\partial t} = P_0 \exp(-H/H_*) - \delta(H) K A^{1/2} S - \nabla q_s, \tag{A.162}$$

$$\frac{\partial \eta_b}{\partial t} = -P_0 \exp(-H/H_*) - (1 - \delta(H)) K A^{1/2} S, \tag{A.163}$$

$$q_s = -D \left[1 - \exp\left(-\frac{H}{H_0}\right)\right] \nabla \eta, \tag{A.164}$$

$$K(\eta, \eta_C) = wK_1 + (1-w)K_2, \tag{A.165}$$

$$w = \frac{1}{1 + \exp\left(-\frac{(\eta - \eta_C)}{W_c}\right)}. \tag{A.166}$$

Parameters: K_1, K_2, P_0, H_s, D, H_0, W_c (plus specification of $\eta_C(x, y)$).

Appendix B

Sensitivity Analysis Calculations and Plots

B.1 Introduction

This Appendix contains the complete results from the sensitivity analysis procedure described in Chapter 7. The figures below plot the modified mean elementary effect μ^* against the effect standard deviation σ^* for each model, parameter, and effect (initial topography and outlet lowering history). In each figure pair, the first plot shows all parameters, color-coded by parameter and with symbols representing the initial topography used. The second plot highlights the effects of initial topography and outlet lowering history by showing only these effects in color, with the parameters shown in gray symbols. For a discussion of how to read these plots, see Chapter 7, Section 7.2.2.

The tables below list, for each parameter in each model, the modified mean elementary effect μ^* and the effect standard deviation σ^*. Results are listed for analyses using the upper Franks Creek watershed at 24 ft spatial resolution. There are three tables per model: one listing parameter sensitivities, one listing sensitivity to lowering history, and one listing sensitivity to initial topography. In the first table for each model, results are given for each parameter, each of the initial conditions, and both of the lowering histories. For example, Table B.1 lists results of sensitivity tests for the two parameters in model Basic (D and K). Two additional tables are provided for each model. The first contains results for tests of sensitivity to the lowering history (because lowering history 1 is used as the baseline for comparison, only lowering history 2 is listed; the results should be read as indicating the degree of sensitivity to a change from history 1 to history 2). For example, Table B.2 lists μ^* and σ^* for changes in lowering history on model Basic, for each of the six initial conditions. Finally, a table is provided for each model showing its sensitivity to initial condition, using the "7% etch" initial condition as a baseline. For example, Table B.3 lists sensitivity values for tests on the Basic model for each alternative initial condition (other than "etch 7%") and both of the lowering histories.

B.2 Sensitivity Results Figures for Upper Franks Creek Watershed

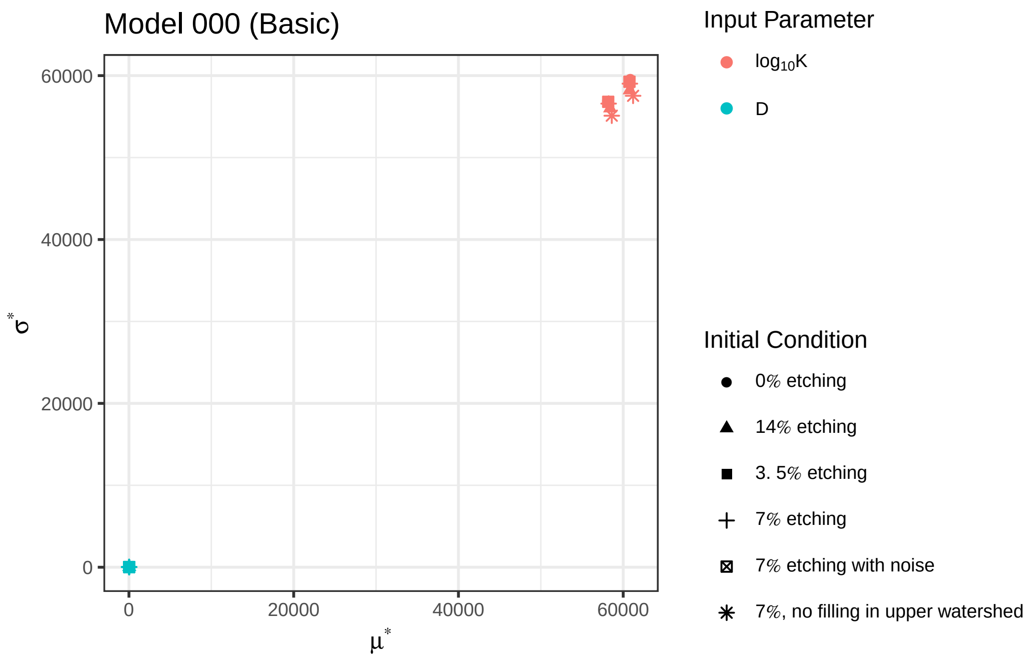

(a) Input parameter sensitivity plot for model 000 in Upper Franks Creek Watershed (SEW domain). Colors represent Method of Morris sensitivity analysis results for model input parameters. Shape represents postglacial topography and the two lowering histories considered are not distinguished. Thus two markers are present for each color-symbol combination.

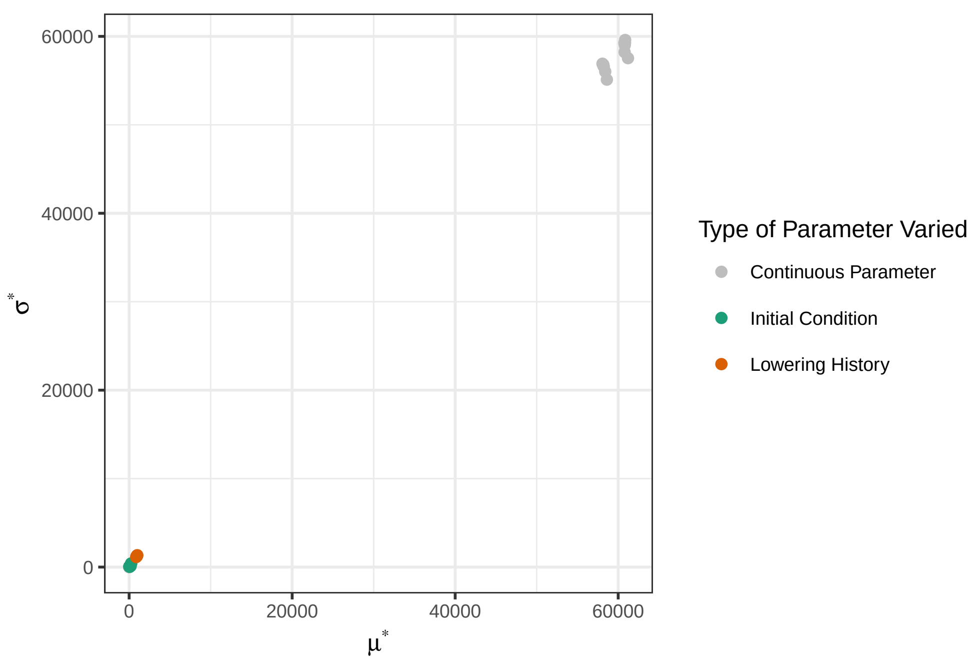

(b) Parameter, initial condition, and lowering sensitivity plot for model 000 in Upper Franks Creek Watershed (SEW domain). Colors represent parameter, initial condition, or lowering history sensitivities. The parameter sensitivities of the upper panel are shown in gray for context. Initial condition "7% etching" and lowering history "1" were used as references value initial and boundary condition sensitivity calculations.

Figure B.1: Sensitivity analysis summary for model 000 in Upper Franks Creek Watershed (SEW domain)

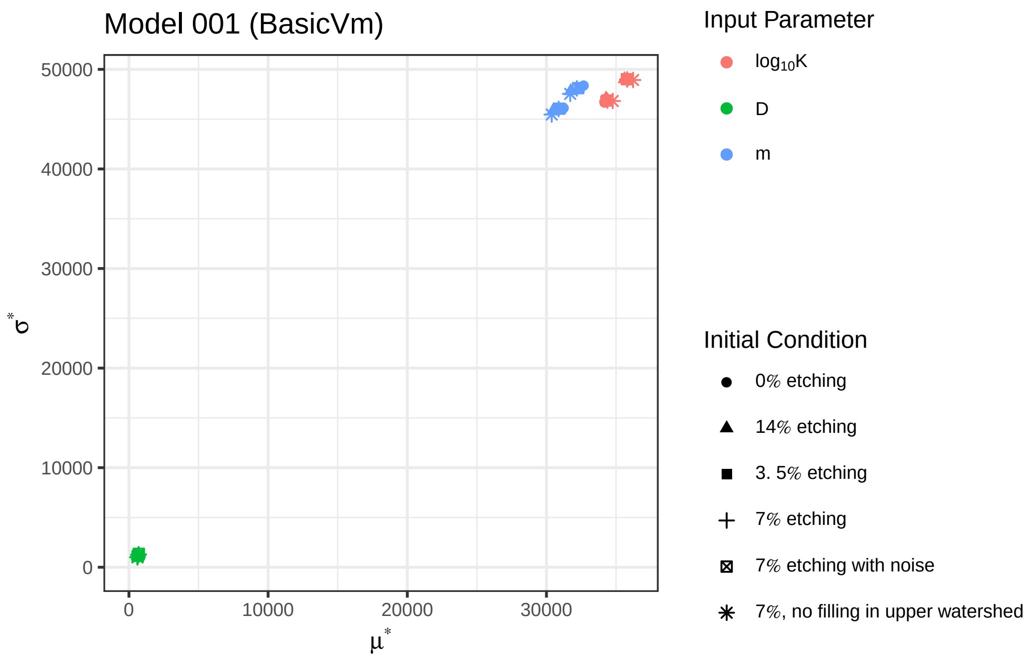

(a) Input parameter sensitivity plot for model 001 in Upper Franks Creek Watershed (SEW domain). Colors represent Method of Morris sensitivity analysis results for model input parameters. Shape represents postglacial topography and the two lowering histories considered are not distinguished. Thus two markers are present for each color-symbol combination.

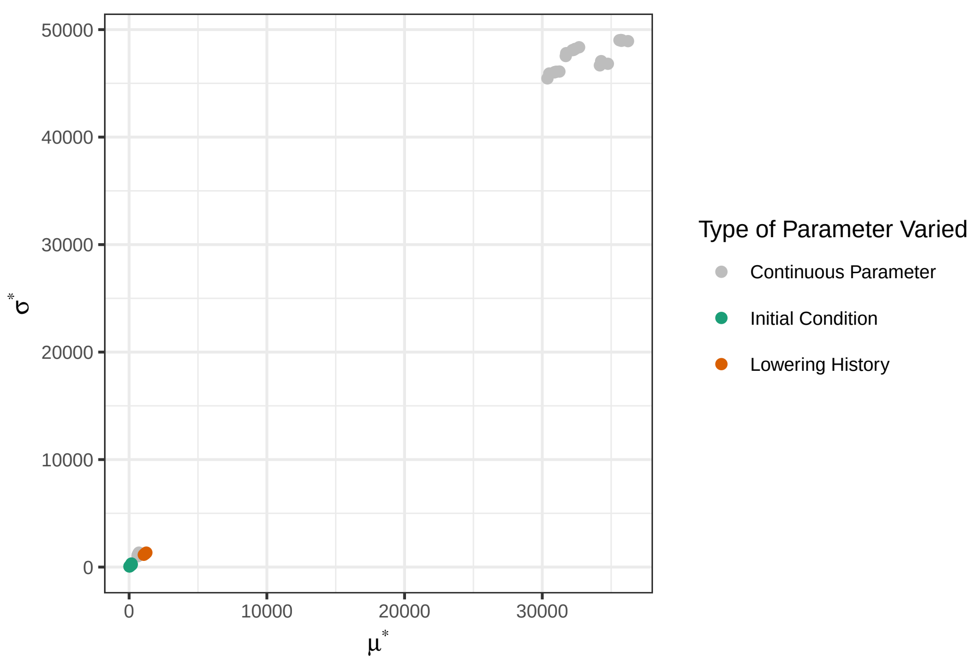

(b) Parameter, initial condition, and lowering sensitivity plot for model 001 in Upper Franks Creek Watershed (SEW domain). Colors represent parameter, initial condition, or lowering history sensitivities. The parameter sensitivities of the upper panel are shown in gray for context. Initial condition "7% etching" and lowering history "1" were used as references value initial and boundary condition sensitivity calculations.

Figure B.2: Sensitivity analysis summary for model 001 in Upper Franks Creek Watershed (SEW domain)

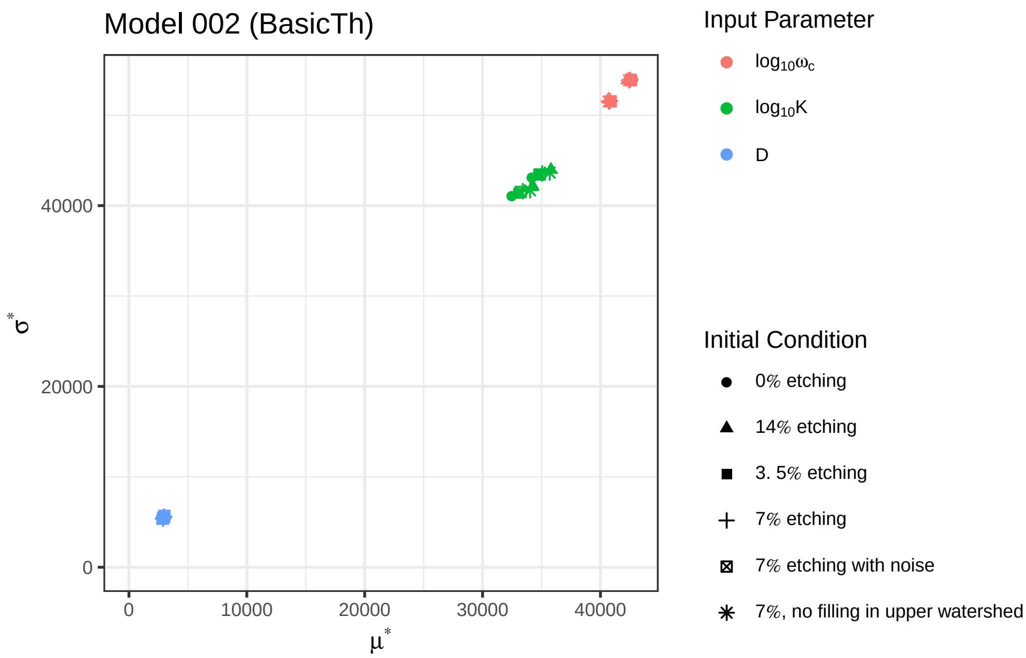

(a) Input parameter sensitivity plot for model 002 in Upper Franks Creek Watershed (SEW domain). Colors represent Method of Morris sensitivity analysis results for model input parameters. Shape represents postglacial topography and the two lowering histories considered are not distinguished. Thus two markers are present for each color-symbol combination.

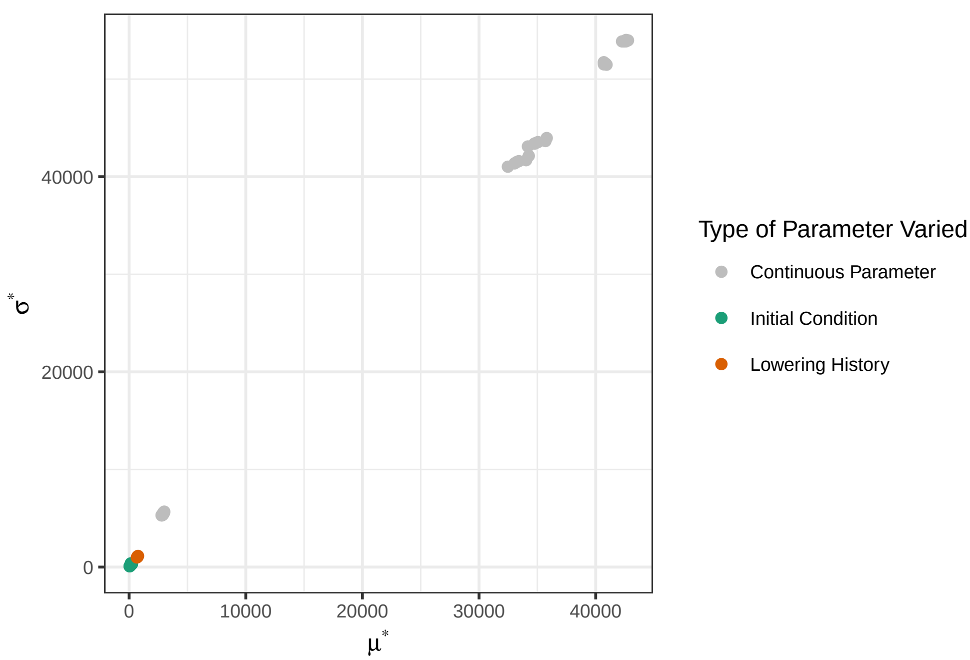

(b) Parameter, initial condition, and lowering sensitivity plot for model 002 in Upper Franks Creek Watershed (SEW domain). Colors represent parameter, initial condition, or lowering history sensitivities. The parameter sensitivities of the upper panel are shown in gray for context. Initial condition "7% etching" and lowering history "1" were used as references value initial and boundary condition sensitivity calculations.

Figure B.3: Sensitivity analysis summary for model 002 in Upper Franks Creek Watershed (SEW domain)

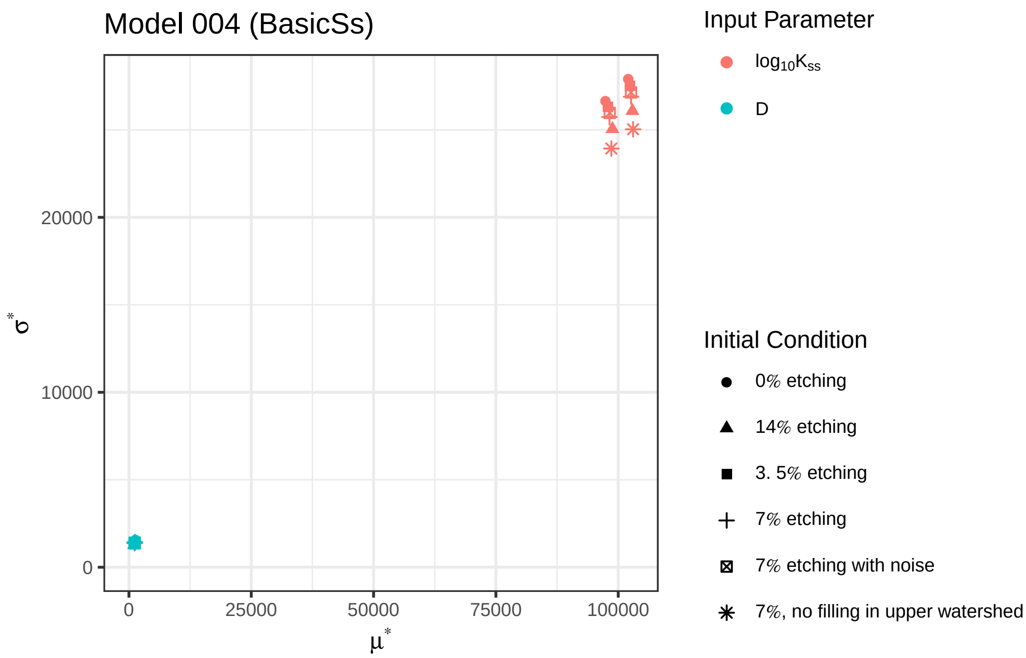

(a) Input parameter sensitivity plot for model 004 in Upper Franks Creek Watershed (SEW domain). Colors represent Method of Morris sensitivity analysis results for model input parameters. Shape represents postglacial topography and the two lowering histories considered are not distinguished. Thus two markers are present for each color-symbol combination.

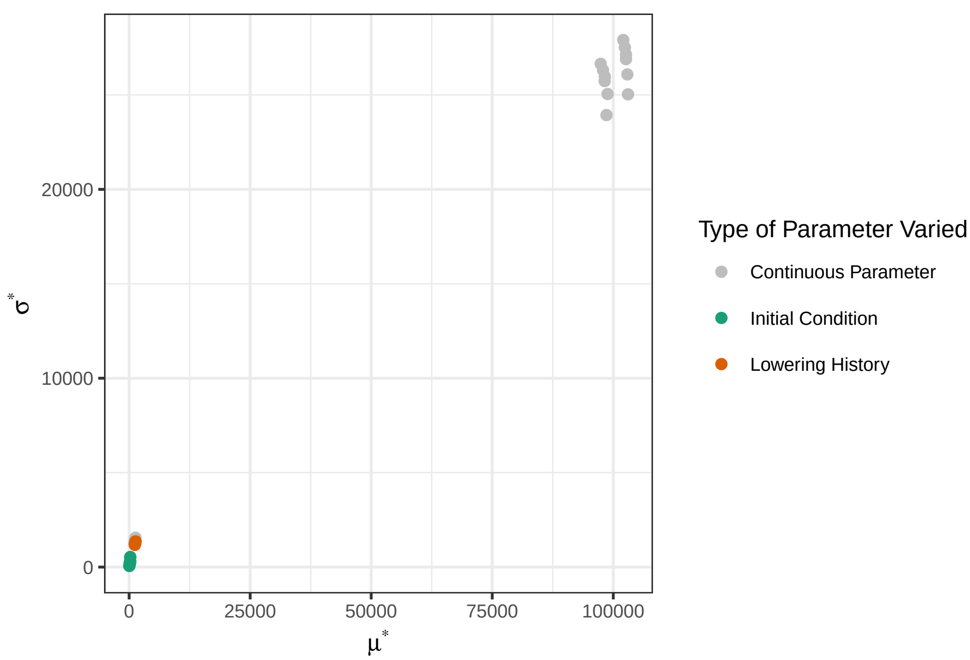

(b) Parameter, initial condition, and lowering sensitivity plot for model 004 in Upper Franks Creek Watershed (SEW domain). Colors represent parameter, initial condition, or lowering history sensitivities. The parameter sensitivities of the upper panel are shown in gray for context. Initial condition "7% etching" and lowering history "1" were used as references value initial and boundary condition sensitivity calculations.

Figure B.4: Sensitivity analysis summary for model 004 in Upper Franks Creek Watershed (SEW domain)

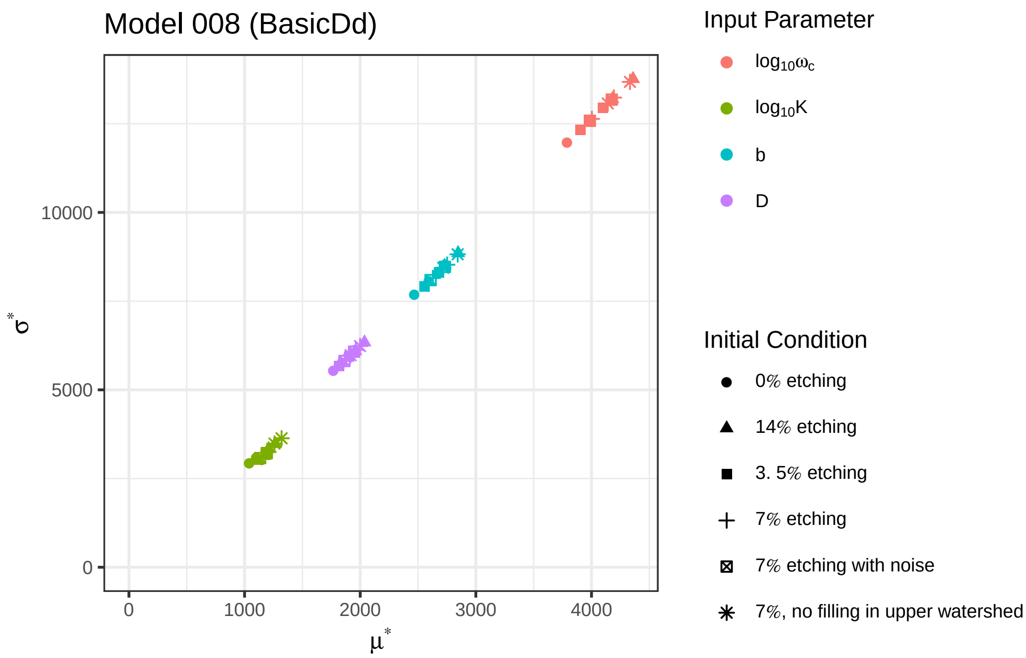

(a) Input parameter sensitivity plot for model 008 in Upper Franks Creek Watershed (SEW domain). Colors represent Method of Morris sensitivity analysis results for model input parameters. Shape represents postglacial topography and the two lowering histories considered are not distinguished. Thus two markers are present for each color-symbol combination.

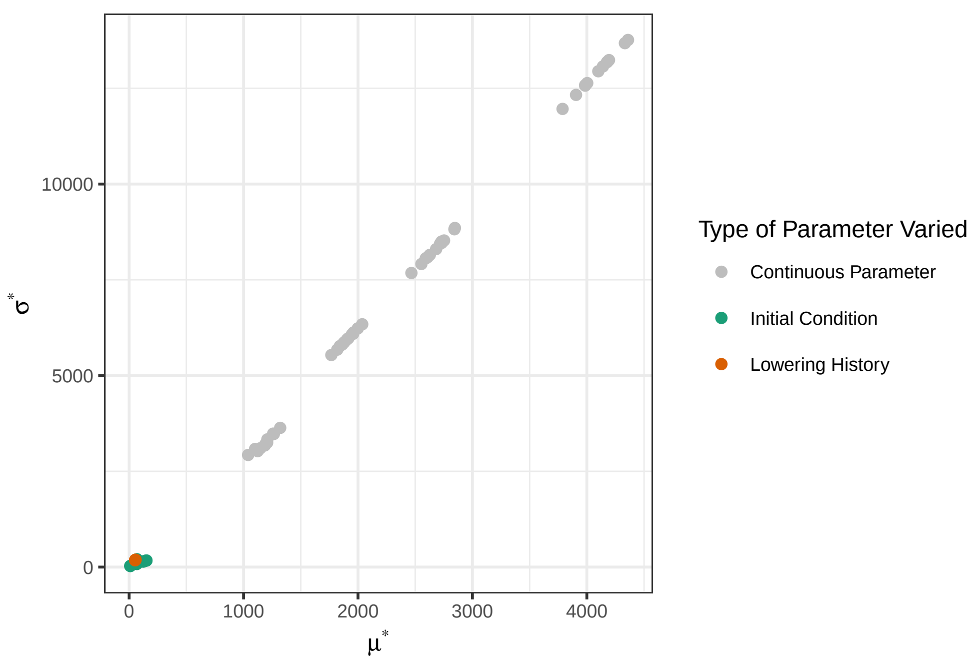

(b) Parameter, initial condition, and lowering sensitivity plot for model 008 in Upper Franks Creek Watershed (SEW domain). Colors represent parameter, initial condition, or lowering history sensitivities. The parameter sensitivities of the upper panel are shown in gray for context. Initial condition "7% etching" and lowering history "1" were used as references value initial and boundary condition sensitivity calculations.

Figure B.5: Sensitivity analysis summary for model 008 in Upper Franks Creek Watershed (SEW domain)

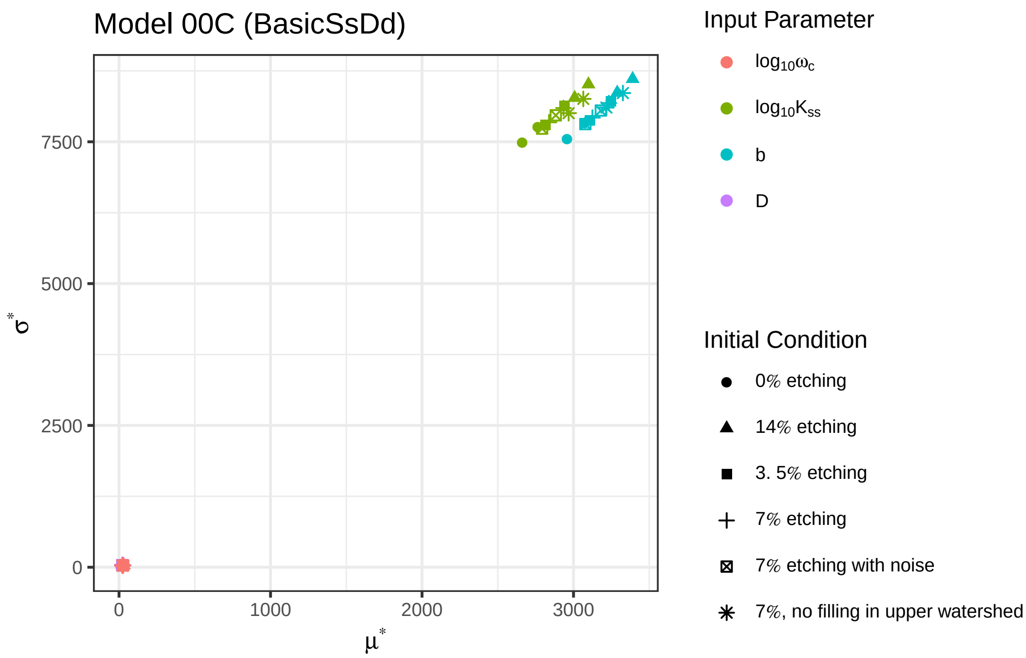

(a) Input parameter sensitivity plot for model 00C in Upper Franks Creek Watershed (SEW domain). Colors represent Method of Morris sensitivity analysis results for model input parameters. Shape represents postglacial topography and the two lowering histories considered are not distinguished. Thus two markers are present for each color-symbol combination.

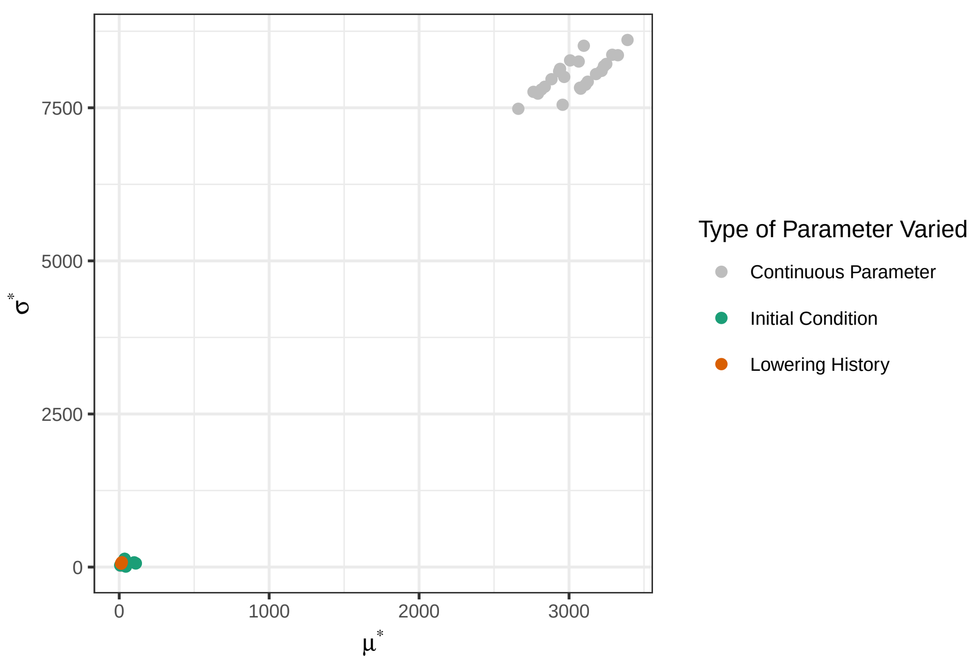

(b) Parameter, initial condition, and lowering sensitivity plot for model 00C in Upper Franks Creek Watershed (SEW domain). Colors represent parameter, initial condition, or lowering history sensitivities. The parameter sensitivities of the upper panel are shown in gray for context. Initial condition "7% etching" and lowering history "1" were used as references value initial and boundary condition sensitivity calculations.

Figure B.6: Sensitivity analysis summary for model 00C in Upper Franks Creek Watershed (SEW domain)

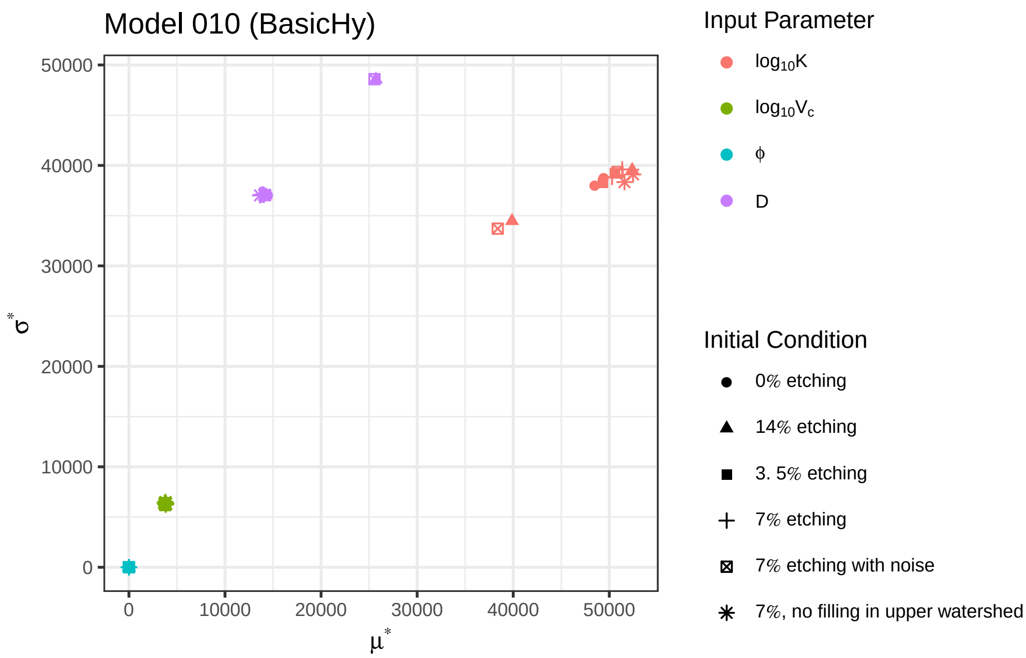

(a) Input parameter sensitivity plot for model 010 in Upper Franks Creek Watershed (SEW domain). Colors represent Method of Morris sensitivity analysis results for model input parameters. Shape represents postglacial topography and the two lowering histories considered are not distinguished. Thus two markers are present for each color-symbol combination.

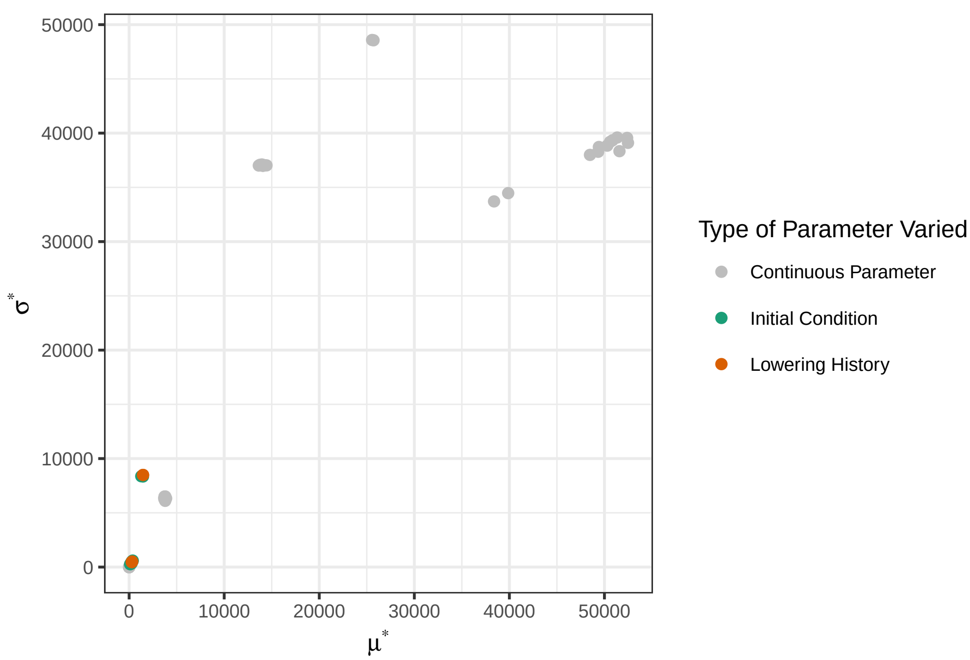

(b) Parameter, initial condition, and lowering sensitivity plot for model 010 in Upper Franks Creek Watershed (SEW domain). Colors represent parameter, initial condition, or lowering history sensitivities. The parameter sensitivities of the upper panel are shown in gray for context. Initial condition "7% etching" and lowering history "1" were used as references value initial and boundary condition sensitivity calculations.

Figure B.7: Sensitivity analysis summary for model 010 in Upper Franks Creek Watershed (SEW domain)

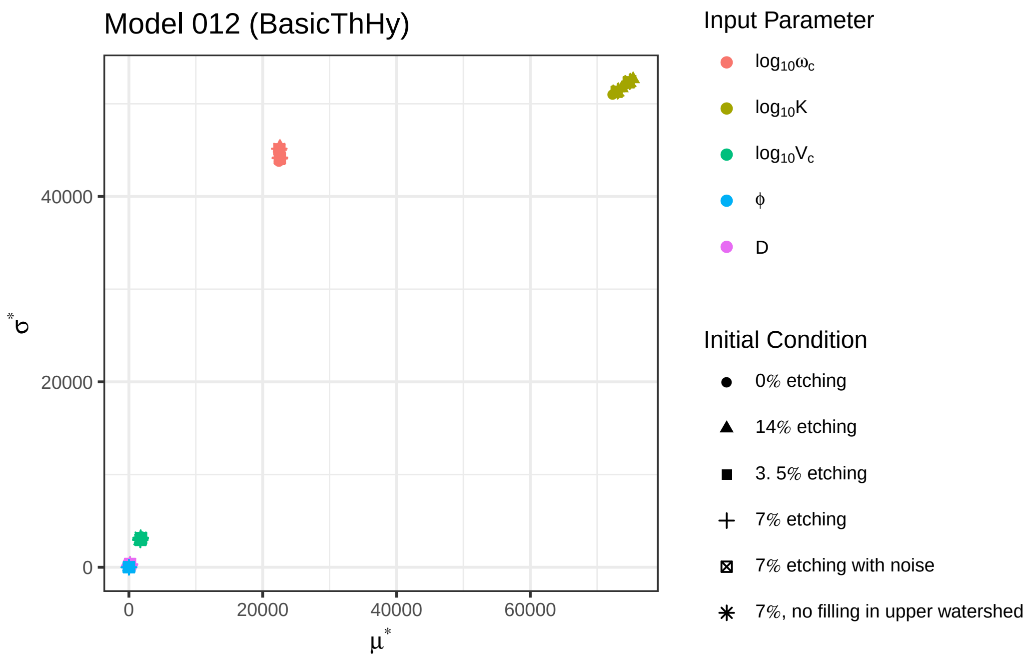

(a) Input parameter sensitivity plot for model 012 in Upper Franks Creek Watershed (SEW domain). Colors represent Method of Morris sensitivity analysis results for model input parameters. Shape represents postglacial topography and the two lowering histories considered are not distinguished. Thus two markers are present for each color-symbol combination.

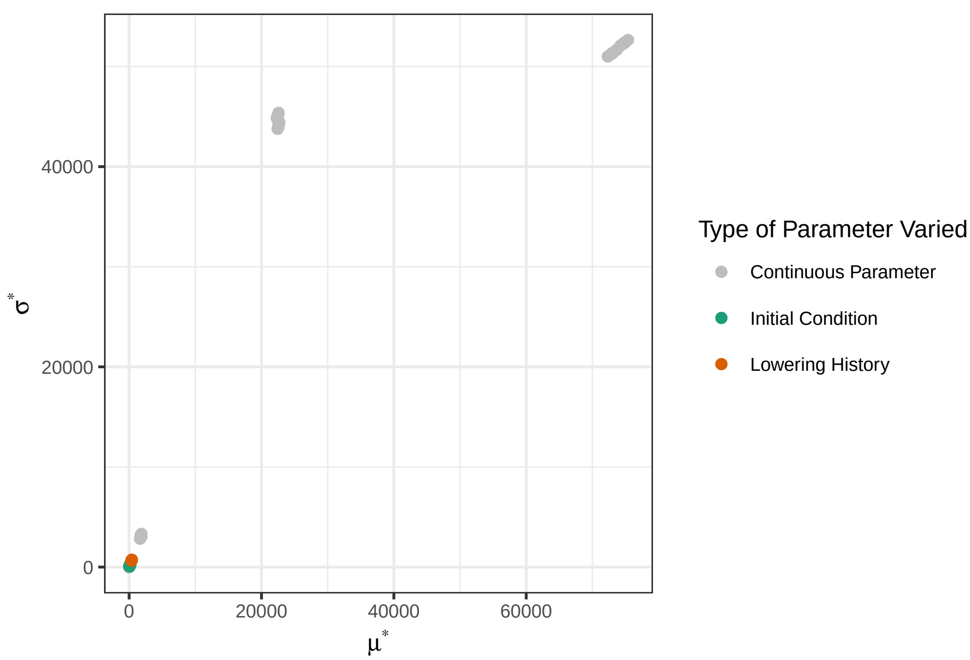

(b) Parameter, initial condition, and lowering sensitivity plot for model 012 in Upper Franks Creek Watershed (SEW domain). Colors represent parameter, initial condition, or lowering history sensitivities. The parameter sensitivities of the upper panel are shown in gray for context. Initial condition "7% etching" and lowering history "1" were used as references value initial and boundary condition sensitivity calculations.

Figure B.8: Sensitivity analysis summary for model 012 in Upper Franks Creek Watershed (SEW domain)

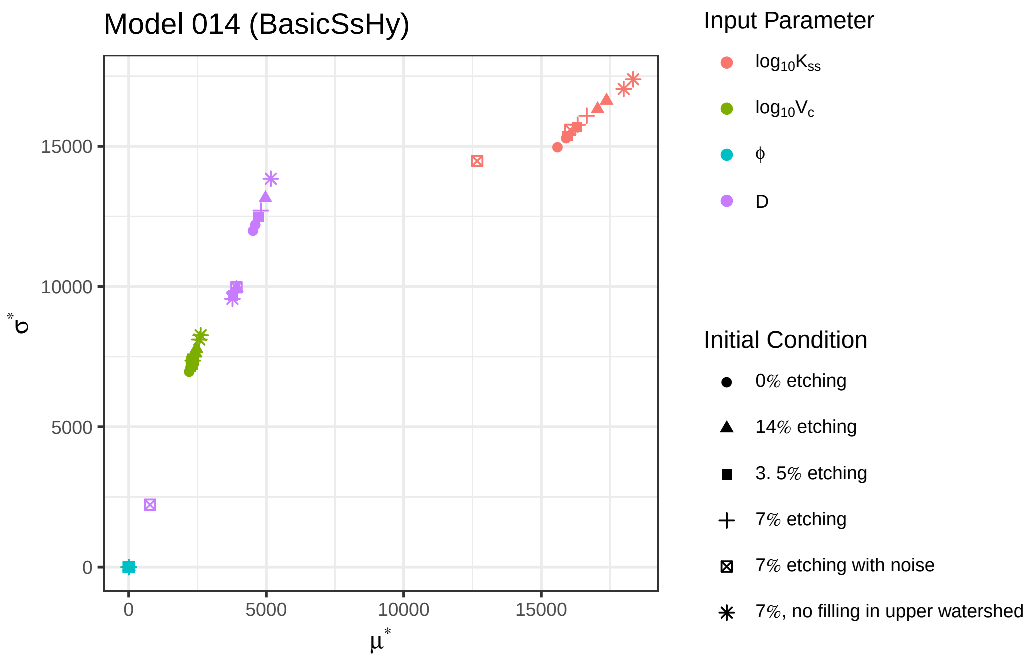

(a) Input parameter sensitivity plot for model 014 in Upper Franks Creek Watershed (SEW domain). Colors represent Method of Morris sensitivity analysis results for model input parameters. Shape represents postglacial topography and the two lowering histories considered are not distinguished. Thus two markers are present for each color-symbol combination.

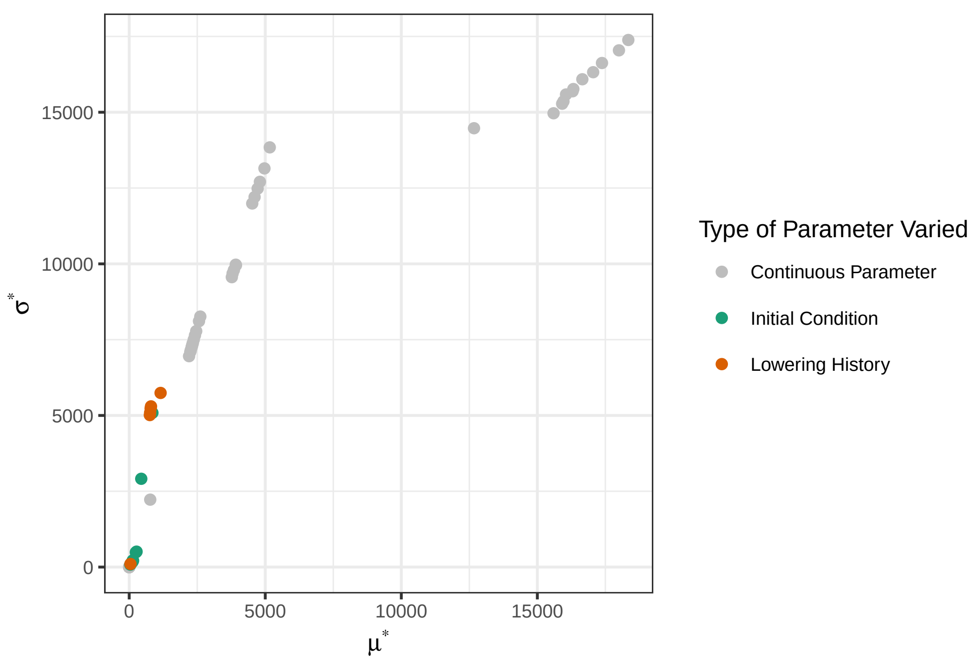

(b) Parameter, initial condition, and lowering sensitivity plot for model 014 in Upper Franks Creek Watershed (SEW domain). Colors represent parameter, initial condition, or lowering history sensitivities. The parameter sensitivities of the upper panel are shown in gray for context. Initial condition "7% etching" and lowering history "1" were used as references value initial and boundary condition sensitivity calculations.

Figure B.9: Sensitivity analysis summary for model 014 in Upper Franks Creek Watershed (SEW domain)

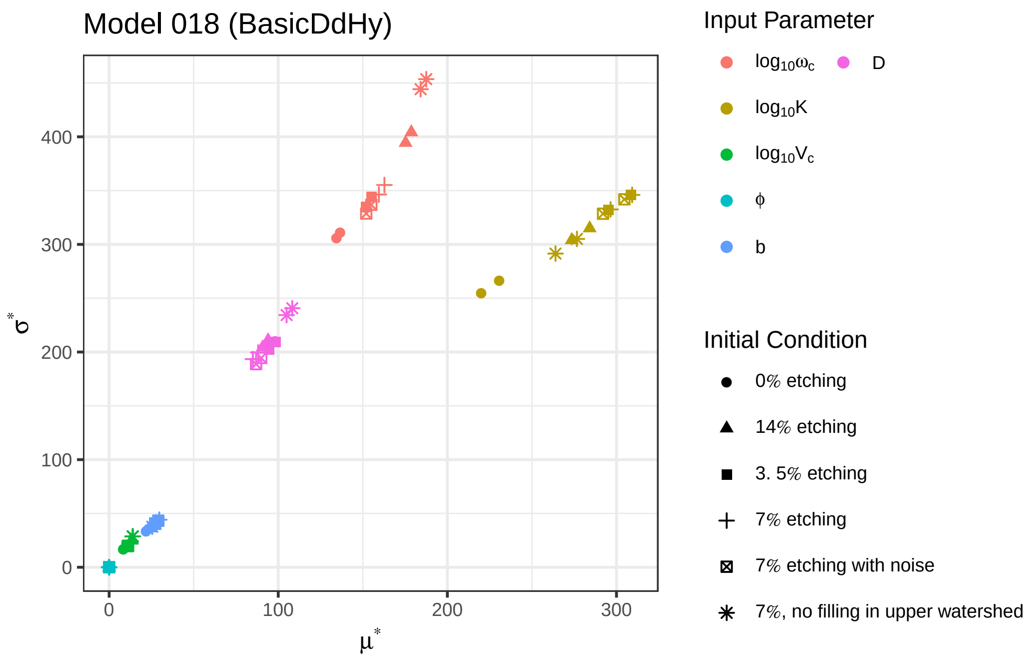

(a) Input parameter sensitivity plot for model 018 in Upper Franks Creek Watershed (SEW domain). Colors represent Method of Morris sensitivity analysis results for model input parameters. Shape represents postglacial topography and the two lowering histories considered are not distinguished. Thus two markers are present for each color-symbol combination.

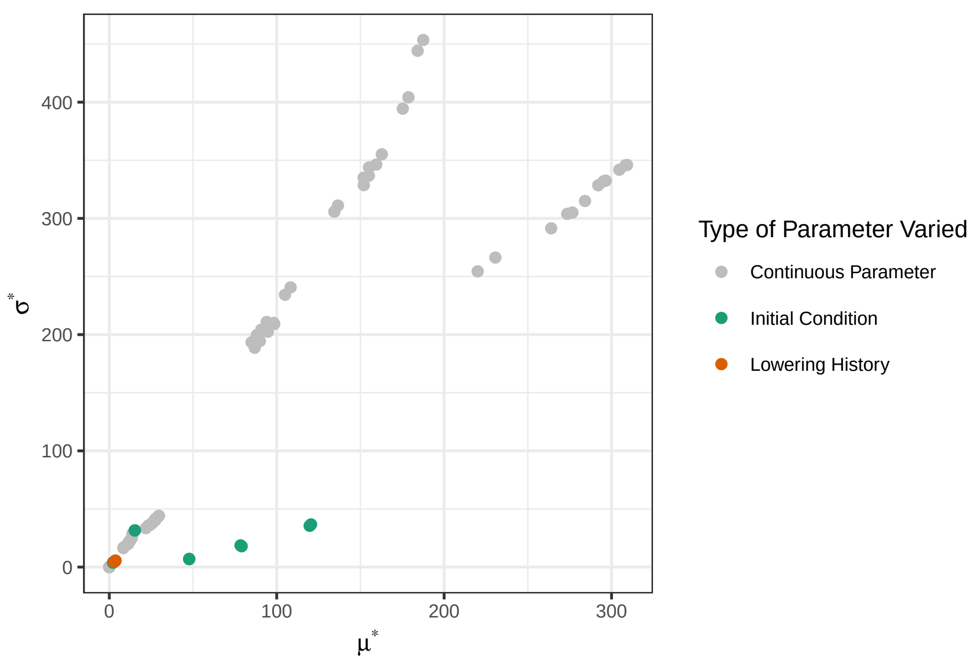

(b) Parameter, initial condition, and lowering sensitivity plot for model 018 in Upper Franks Creek Watershed (SEW domain). Colors represent parameter, initial condition, or lowering history sensitivities. The parameter sensitivities of the upper panel are shown in gray for context. Initial condition "7% etching" and lowering history "1" were used as references value initial and boundary condition sensitivity calculations.

Figure B.10: Sensitivity analysis summary for model 018 in Upper Franks Creek Watershed (SEW domain)

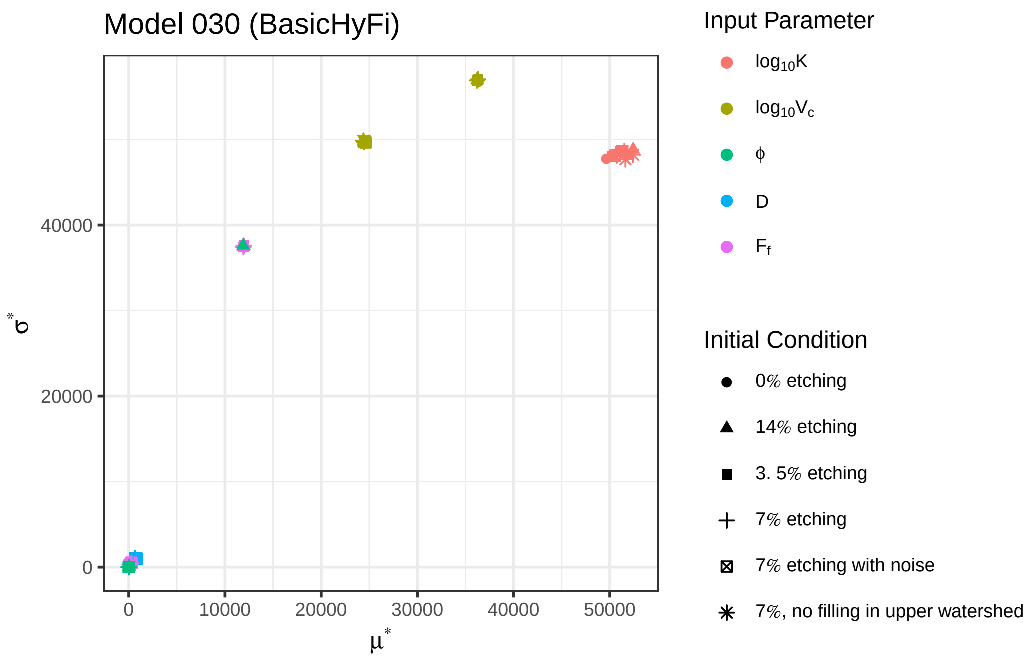

(a) Input parameter sensitivity plot for model 030 in Upper Franks Creek Watershed (SEW domain). Colors represent Method of Morris sensitivity analysis results for model input parameters. Shape represents postglacial topography and the two lowering histories considered are not distinguished. Thus two markers are present for each color-symbol combination.

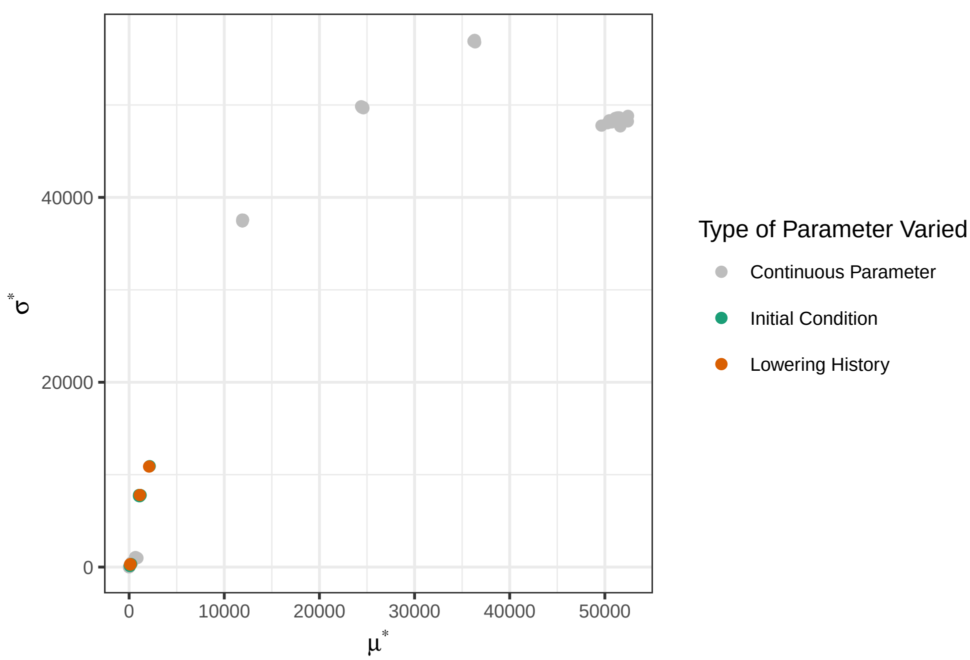

(b) Parameter, initial condition, and lowering sensitivity plot for model 030 in Upper Franks Creek Watershed (SEW domain). Colors represent parameter, initial condition, or lowering history sensitivities. The parameter sensitivities of the upper panel are shown in gray for context. Initial condition "7% etching" and lowering history "1" were used as references value initial and boundary condition sensitivity calculations.

Figure B.11: Sensitivity analysis summary for model 030 in Upper Franks Creek Watershed (SEW domain)

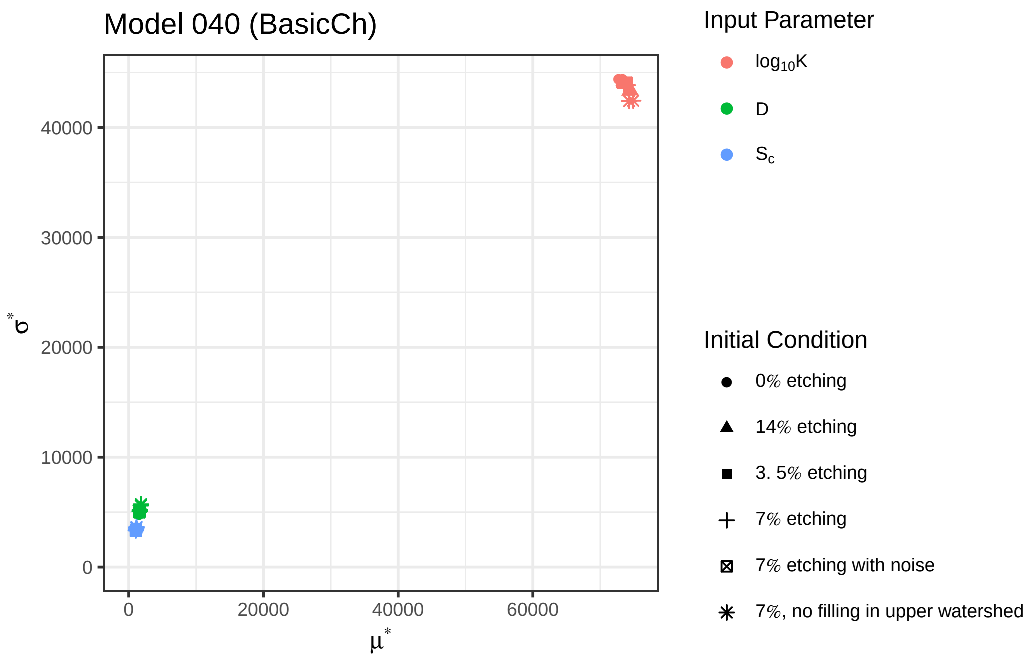

(a) Input parameter sensitivity plot for model 040 in Upper Franks Creek Watershed (SEW domain). Colors represent Method of Morris sensitivity analysis results for model input parameters. Shape represents postglacial topography and the two lowering histories considered are not distinguished. Thus two markers are present for each color-symbol combination.

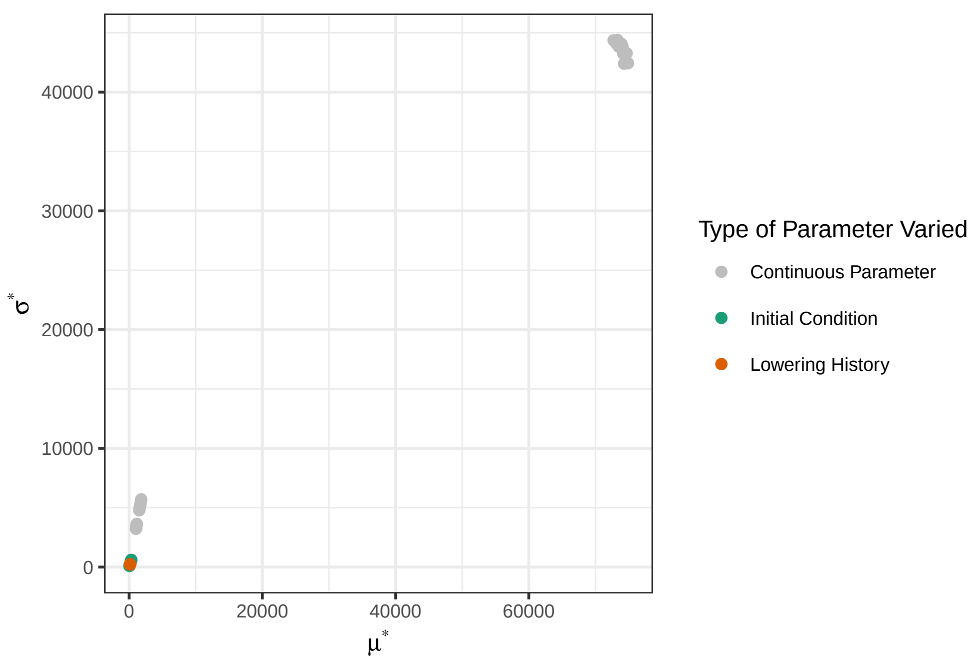

(b) Parameter, initial condition, and lowering sensitivity plot for model 040 in Upper Franks Creek Watershed (SEW domain). Colors represent parameter, initial condition, or lowering history sensitivities. The parameter sensitivities of the upper panel are shown in gray for context. Initial condition “7% etching” and lowering history “1” were used as references value initial and boundary condition sensitivity calculations.

Figure B.12: Sensitivity analysis summary for model 040 in Upper Franks Creek Watershed (SEW domain)

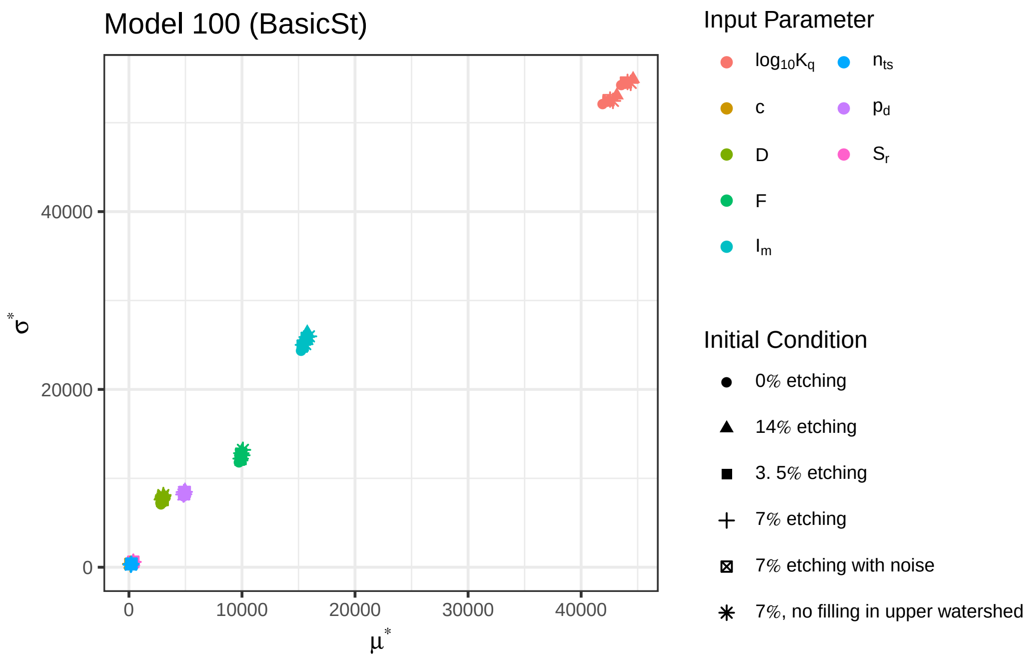

(a) Input parameter sensitivity plot for model 100 in Upper Franks Creek Watershed (SEW domain). Colors represent Method of Morris sensitivity analysis results for model input parameters. Shape represents postglacial topography and the two lowering histories considered are not distinguished. Thus two markers are present for each color-symbol combination.

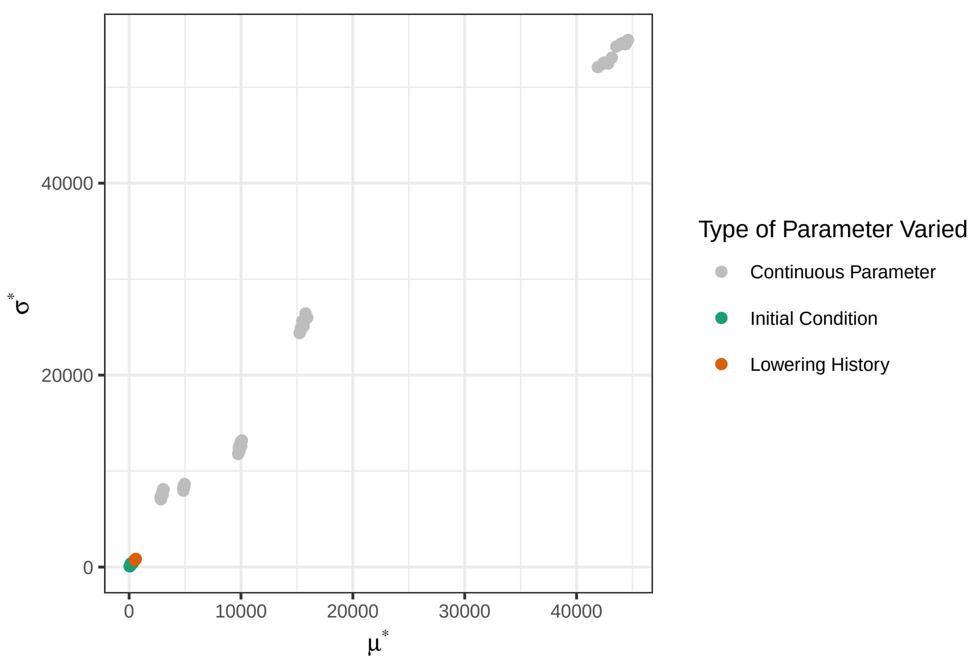

(b) Parameter, initial condition, and lowering sensitivity plot for model 100 in Upper Franks Creek Watershed (SEW domain). Colors represent parameter, initial condition, or lowering history sensitivities. The parameter sensitivities of the upper panel are shown in gray for context. Initial condition "7% etching" and lowering history "1" were used as references value initial and boundary condition sensitivity calculations.

Figure B.13: Sensitivity analysis summary for model 100 in Upper Franks Creek Watershed (SEW domain)

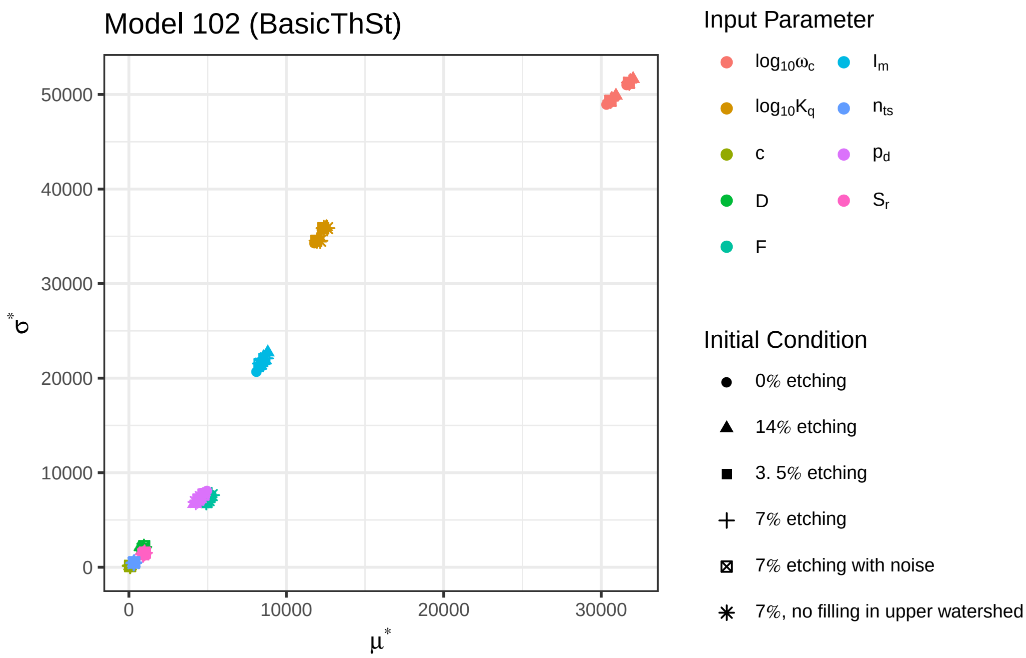

(a) Input parameter sensitivity plot for model 102 in Upper Franks Creek Watershed (SEW domain). Colors represent Method of Morris sensitivity analysis results for model input parameters. Shape represents postglacial topography and the two lowering histories considered are not distinguished. Thus two markers are present for each color-symbol combination.

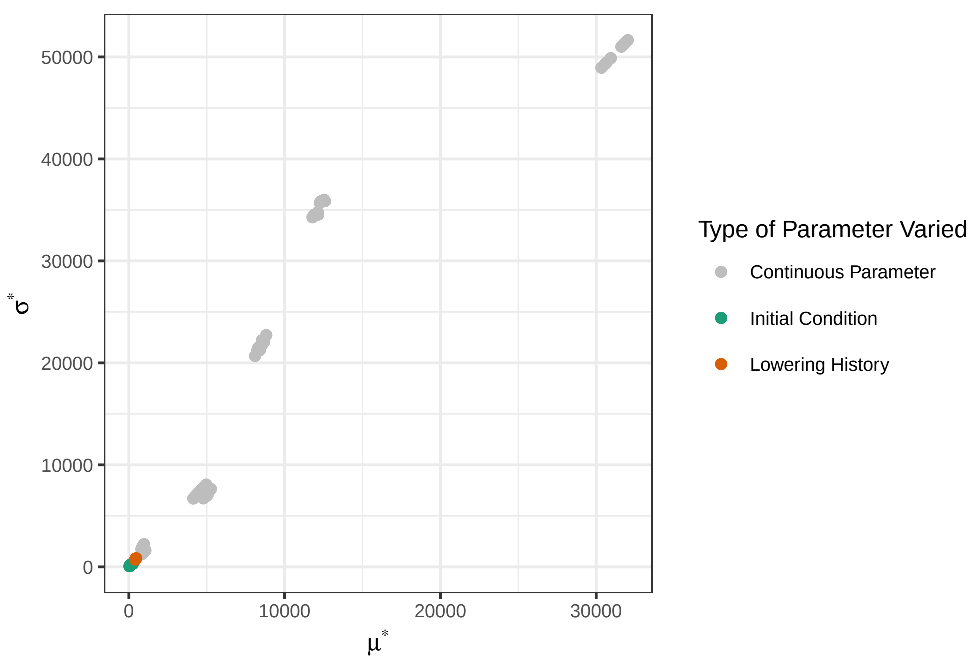

(b) Parameter, initial condition, and lowering sensitivity plot for model 102 in Upper Franks Creek Watershed (SEW domain). Colors represent parameter, initial condition, or lowering history sensitivities. The parameter sensitivities of the upper panel are shown in gray for context. Initial condition "7% etching" and lowering history "1" were used as references value initial and boundary condition sensitivity calculations.

Figure B.14: Sensitivity analysis summary for model 102 in Upper Franks Creek Watershed (SEW domain)

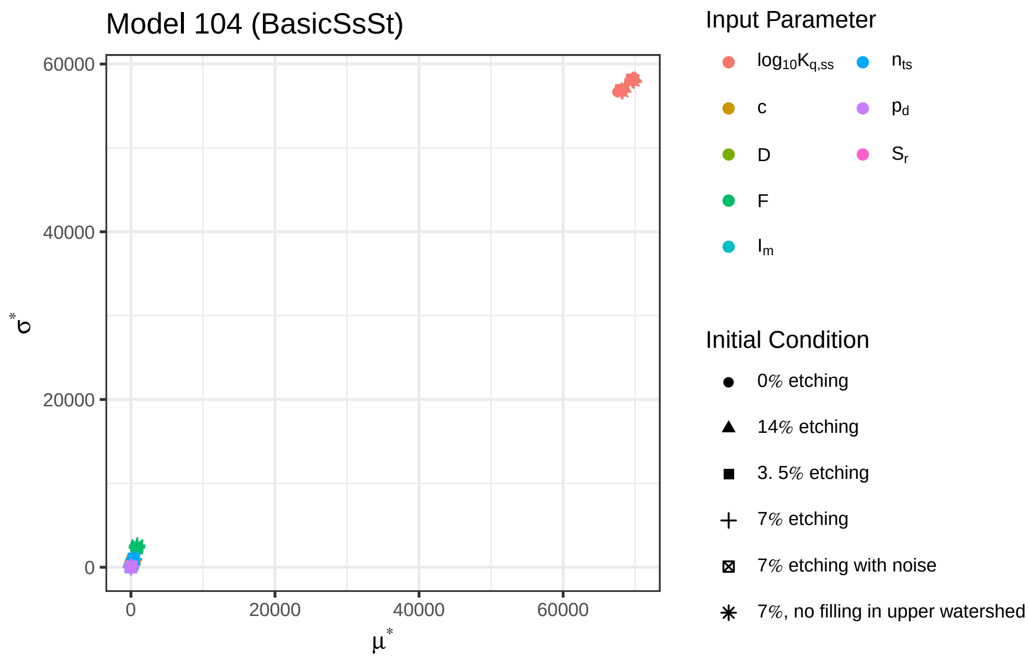

(a) Input parameter sensitivity plot for model 104 in Upper Franks Creek Watershed (SEW domain). Colors represent Method of Morris sensitivity analysis results for model input parameters. Shape represents postglacial topography and the two lowering histories considered are not distinguished. Thus two markers are present for each color-symbol combination.

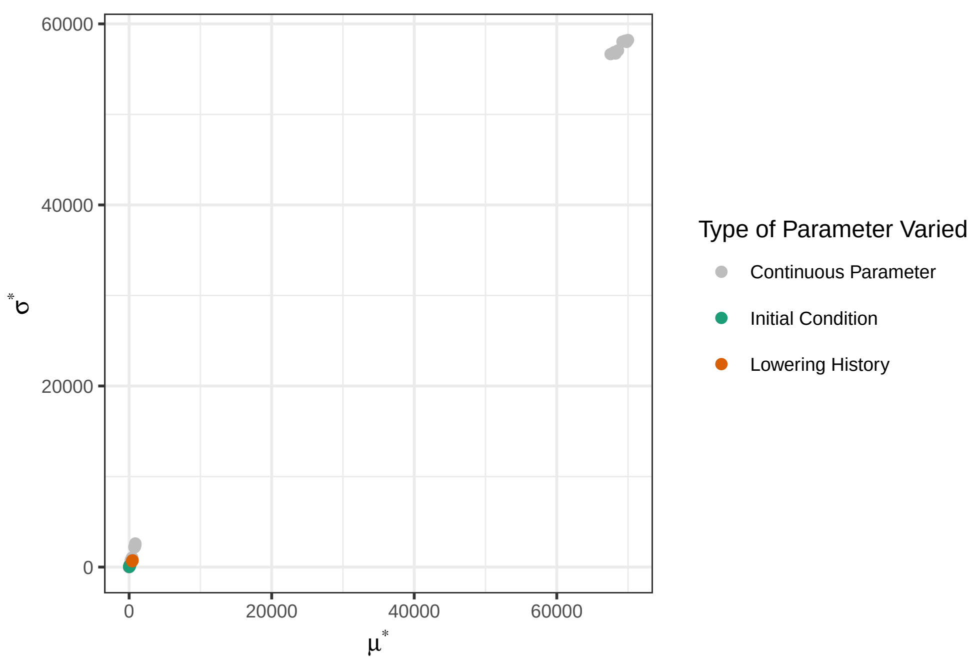

(b) Parameter, initial condition, and lowering sensitivity plot for model 104 in Upper Franks Creek Watershed (SEW domain). Colors represent parameter, initial condition, or lowering history sensitivities. The parameter sensitivities of the upper panel are shown in gray for context. Initial condition "7% etching" and lowering history "1" were used as references value initial and boundary condition sensitivity calculations.

Figure B.15: Sensitivity analysis summary for model 104 in Upper Franks Creek Watershed (SEW domain)

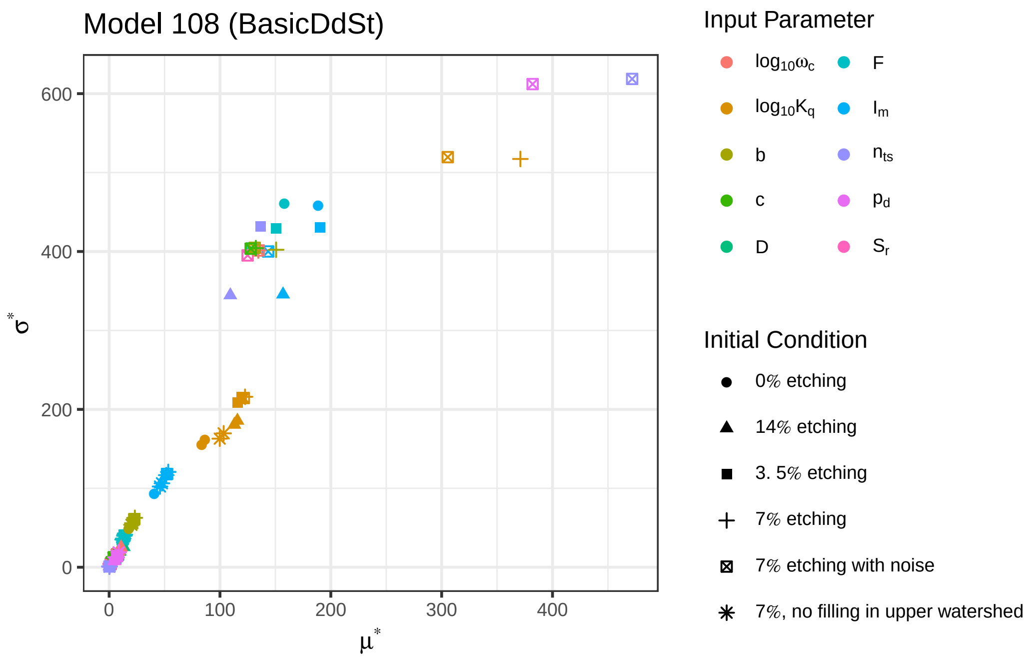

(a) Input parameter sensitivity plot for model 108 in Upper Franks Creek Watershed (SEW domain). Colors represent Method of Morris sensitivity analysis results for model input parameters. Shape represents postglacial topography and the two lowering histories considered are not distinguished. Thus two markers are present for each color-symbol combination.

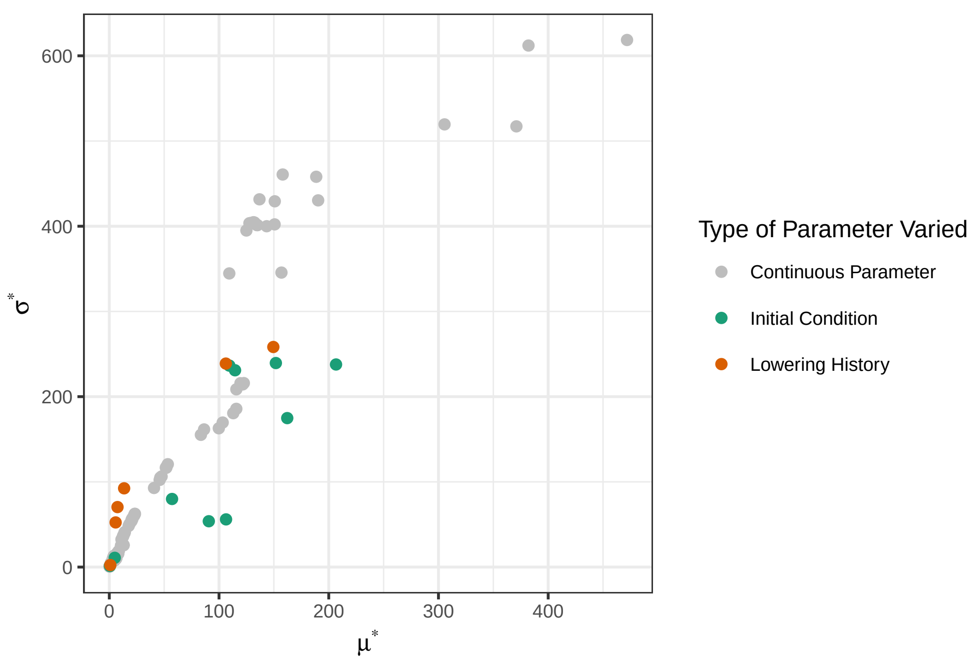

(b) Parameter, initial condition, and lowering sensitivity plot for model 108 in Upper Franks Creek Watershed (SEW domain). Colors represent parameter, initial condition, or lowering history sensitivities. The parameter sensitivities of the upper panel are shown in gray for context. Initial condition "7% etching" and lowering history "1" were used as references value initial and boundary condition sensitivity calculations.

Figure B.16: Sensitivity analysis summary for model 108 in Upper Franks Creek Watershed (SEW domain)

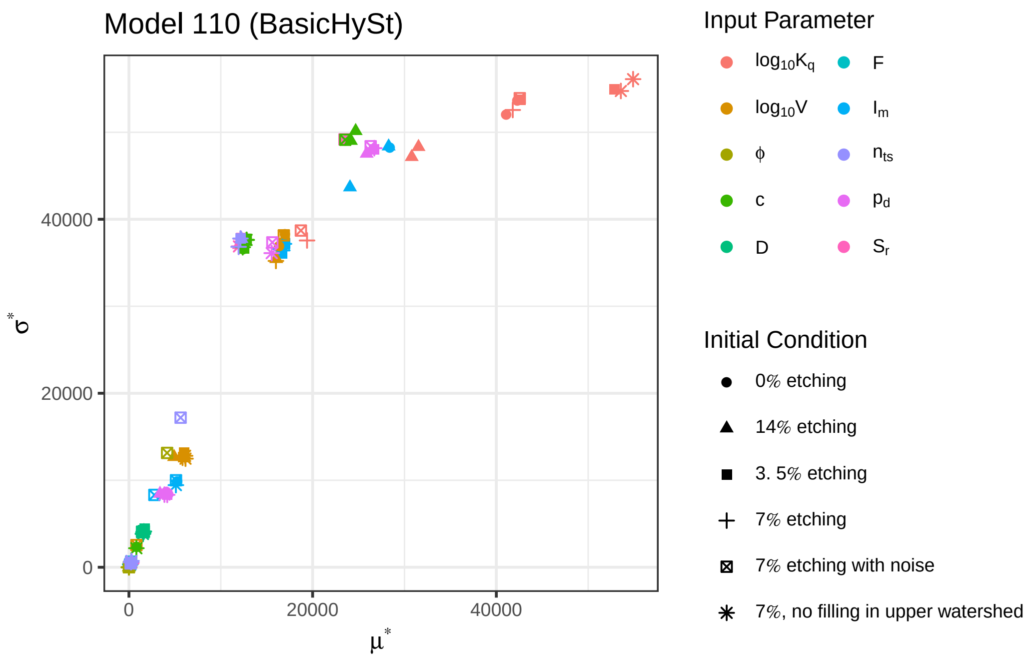

(a) Input parameter sensitivity plot for model 110 in Upper Franks Creek Watershed (SEW domain). Colors represent Method of Morris sensitivity analysis results for model input parameters. Shape represents postglacial topography and the two lowering histories considered are not distinguished. Thus two markers are present for each color-symbol combination.

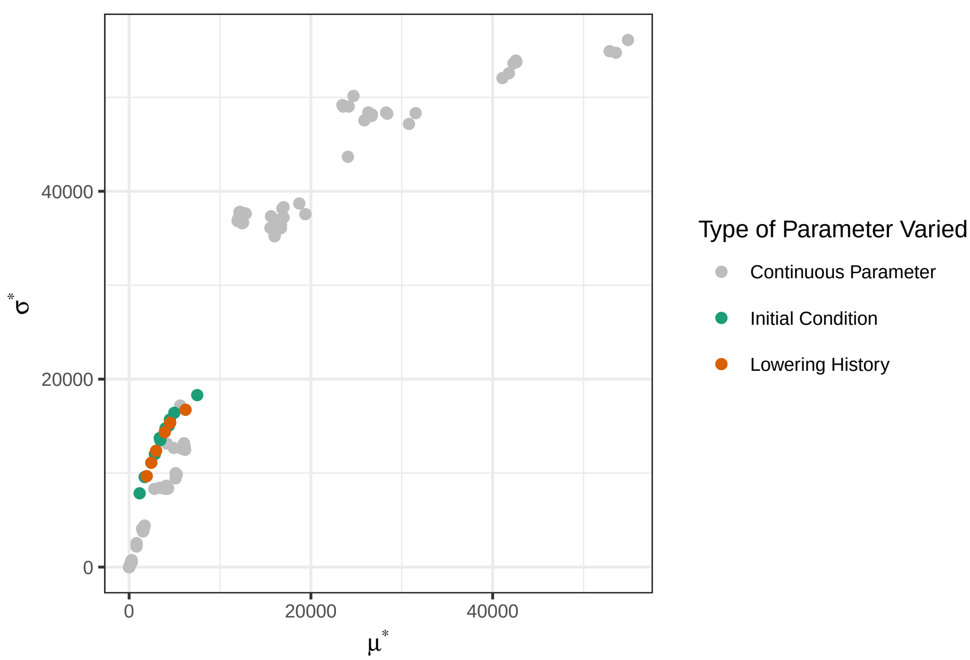

(b) Parameter, initial condition, and lowering sensitivity plot for model 110 in Upper Franks Creek Watershed (SEW domain). Colors represent parameter, initial condition, or lowering history sensitivities. The parameter sensitivities of the upper panel are shown in gray for context. Initial condition "7% etching" and lowering history "1" were used as references value initial and boundary condition sensitivity calculations.

Figure B.17: Sensitivity analysis summary for model 110 in Upper Franks Creek Watershed (SEW domain)

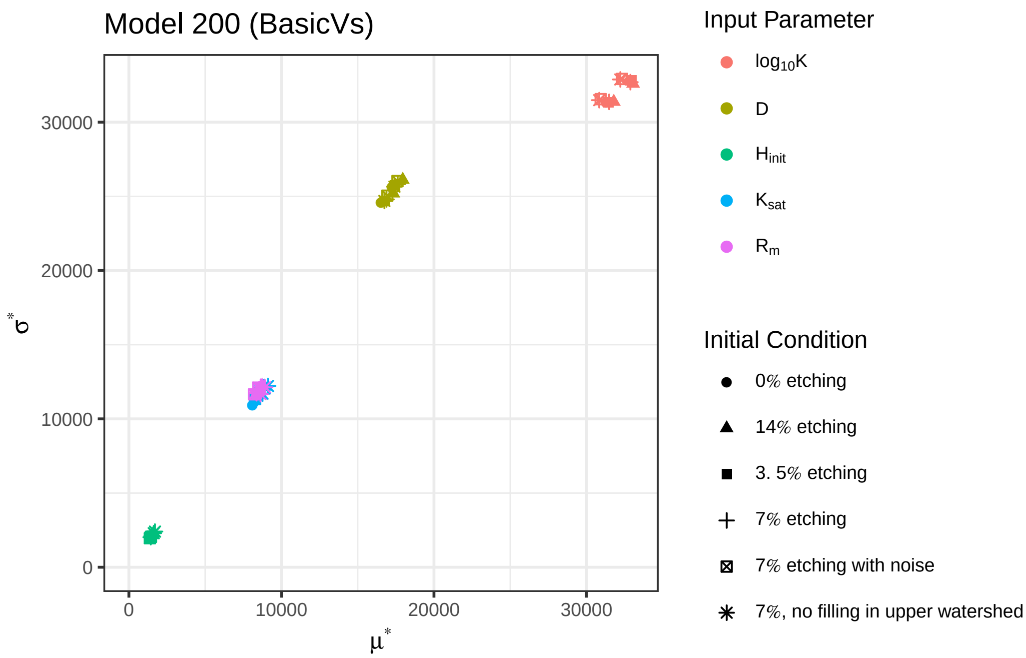

(a) Input parameter sensitivity plot for model 200 in Upper Franks Creek Watershed (SEW domain). Colors represent Method of Morris sensitivity analysis results for model input parameters. Shape represents postglacial topography and the two lowering histories considered are not distinguished. Thus two markers are present for each color-symbol combination.

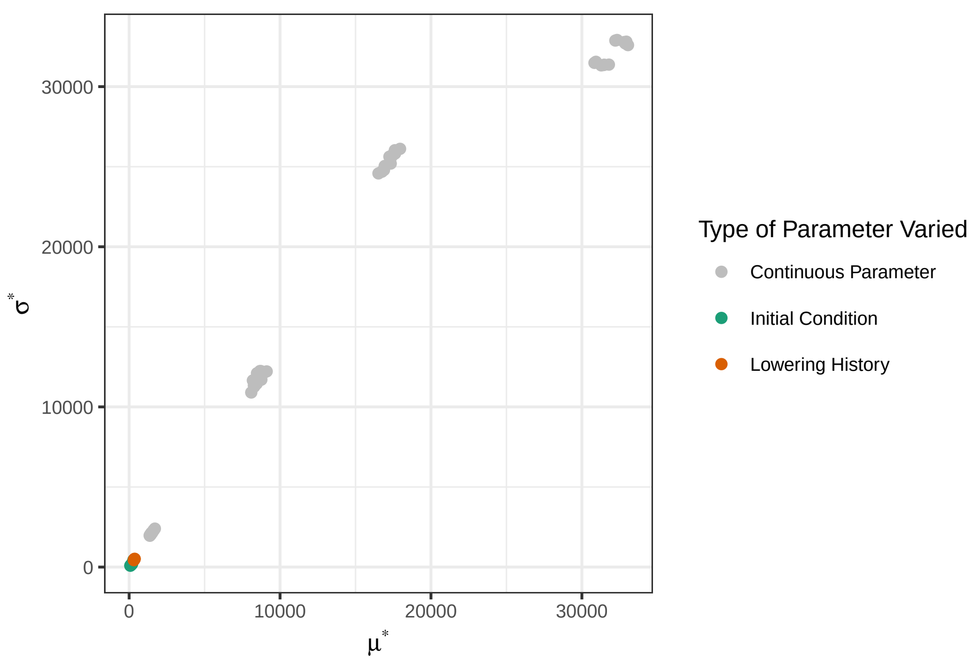

(b) Parameter, initial condition, and lowering sensitivity plot for model 200 in Upper Franks Creek Watershed (SEW domain). Colors represent parameter, initial condition, or lowering history sensitivities. The parameter sensitivities of the upper panel are shown in gray for context. Initial condition “7% etching” and lowering history “1” were used as references value initial and boundary condition sensitivity calculations.

Figure B.18: Sensitivity analysis summary for model 200 in Upper Franks Creek Watershed (SEW domain)

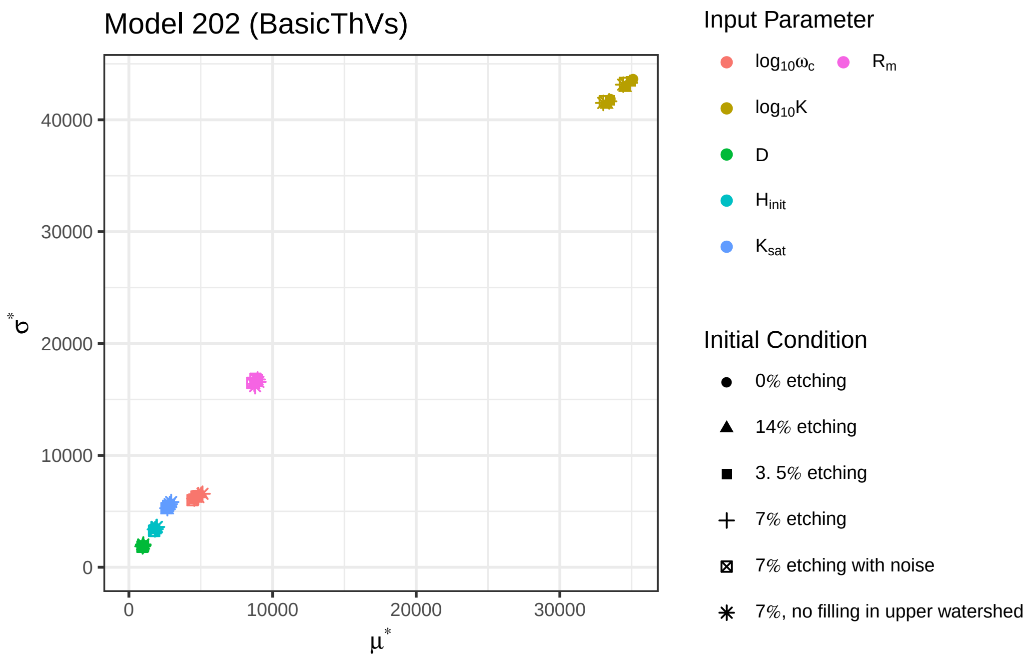

(a) Input parameter sensitivity plot for model 202 in Upper Franks Creek Watershed (SEW domain). Colors represent Method of Morris sensitivity analysis results for model input parameters. Shape represents postglacial topography and the two lowering histories considered are not distinguished. Thus two markers are present for each color-symbol combination.

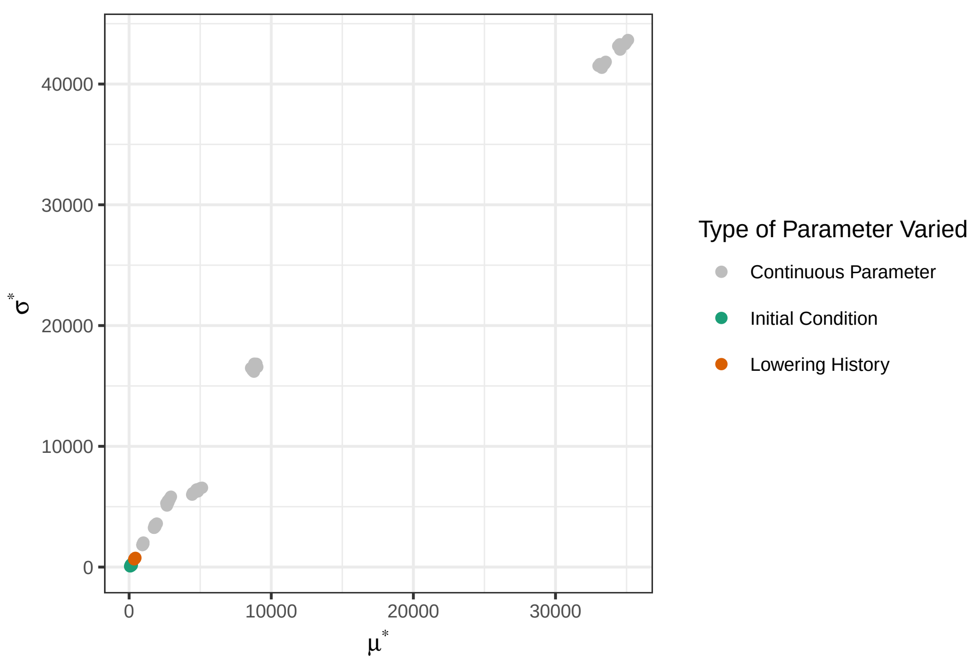

(b) Parameter, initial condition, and lowering sensitivity plot for model 202 in Upper Franks Creek Watershed (SEW domain). Colors represent parameter, initial condition, or lowering history sensitivities. The parameter sensitivities of the upper panel are shown in gray for context. Initial condition "7% etching" and lowering history "1" were used as references value initial and boundary condition sensitivity calculations.

Figure B.19: Sensitivity analysis summary for model 202 in Upper Franks Creek Watershed (SEW domain)

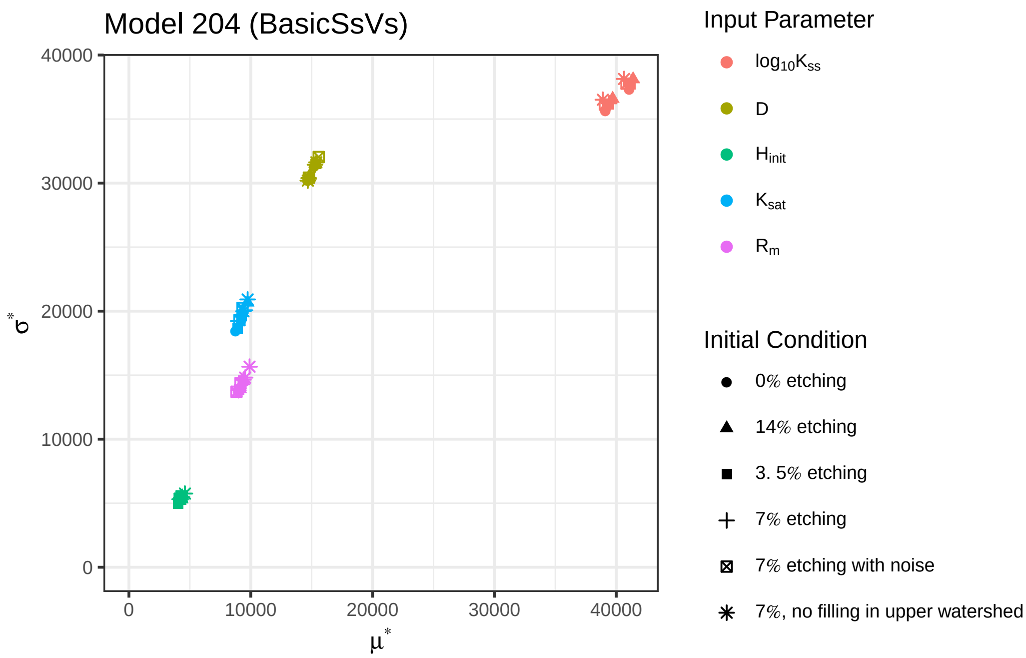

(a) Input parameter sensitivity plot for model 204 in Upper Franks Creek Watershed (SEW domain). Colors represent Method of Morris sensitivity analysis results for model input parameters. Shape represents postglacial topography and the two lowering histories considered are not distinguished. Thus two markers are present for each color-symbol combination.

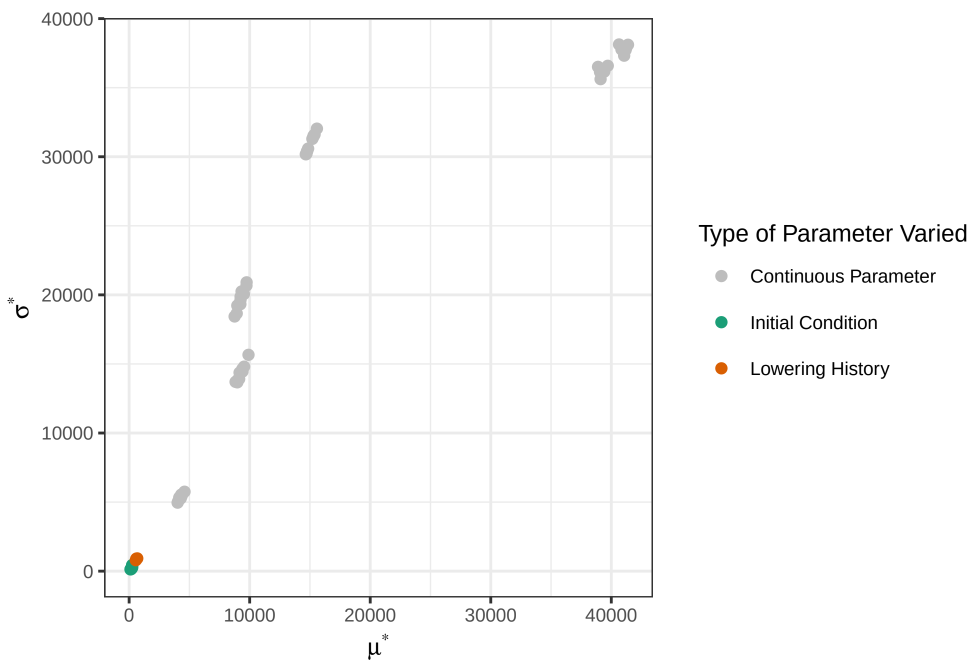

(b) Parameter, initial condition, and lowering sensitivity plot for model 204 in Upper Franks Creek Watershed (SEW domain). Colors represent parameter, initial condition, or lowering history sensitivities. The parameter sensitivities of the upper panel are shown in gray for context. Initial condition "7% etching" and lowering history "1" were used as references value initial and boundary condition sensitivity calculations.

Figure B.20: Sensitivity analysis summary for model 204 in Upper Franks Creek Watershed (SEW domain)

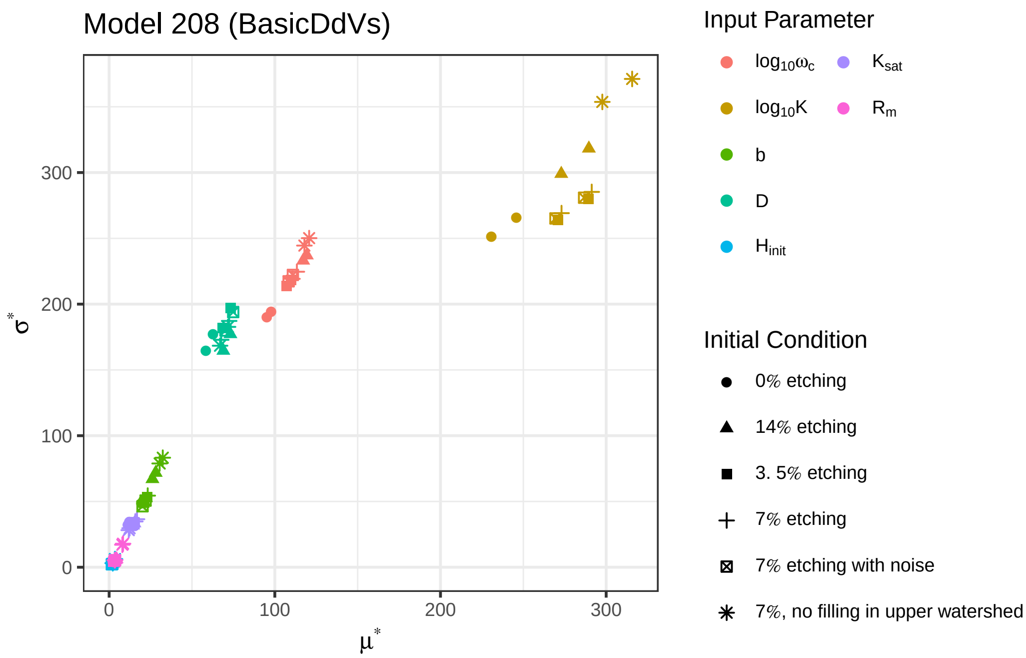

(a) Input parameter sensitivity plot for model 208 in Upper Franks Creek Watershed (SEW domain). Colors represent Method of Morris sensitivity analysis results for model input parameters. Shape represents postglacial topography and the two lowering histories considered are not distinguished. Thus two markers are present for each color-symbol combination.

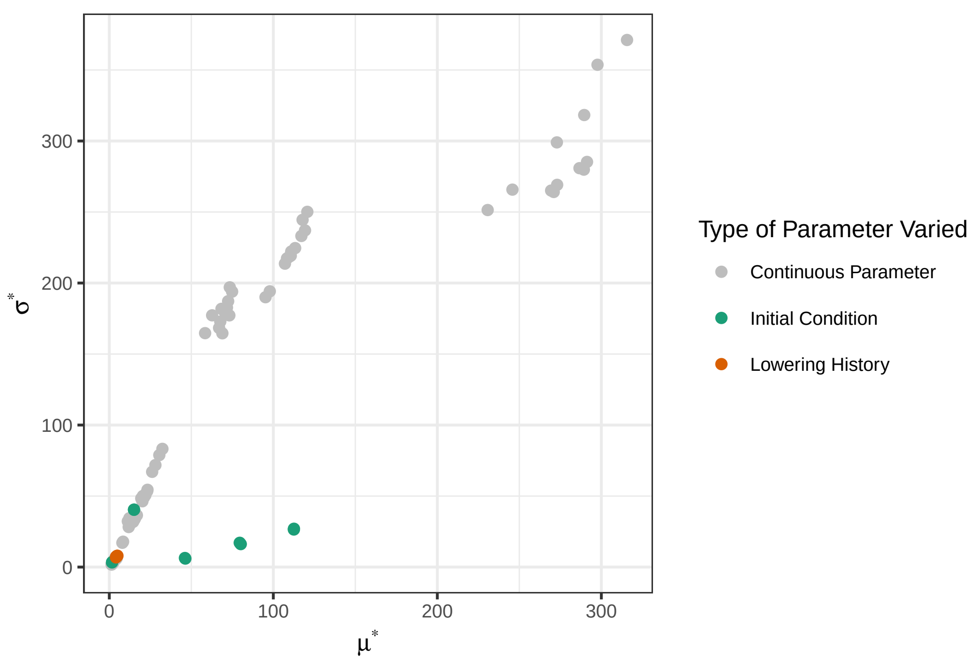

(b) Parameter, initial condition, and lowering sensitivity plot for model 208 in Upper Franks Creek Watershed (SEW domain). Colors represent parameter, initial condition, or lowering history sensitivities. The parameter sensitivities of the upper panel are shown in gray for context. Initial condition "7% etching" and lowering history "1" were used as references value initial and boundary condition sensitivity calculations.

Figure B.21: Sensitivity analysis summary for model 208 in Upper Franks Creek Watershed (SEW domain)

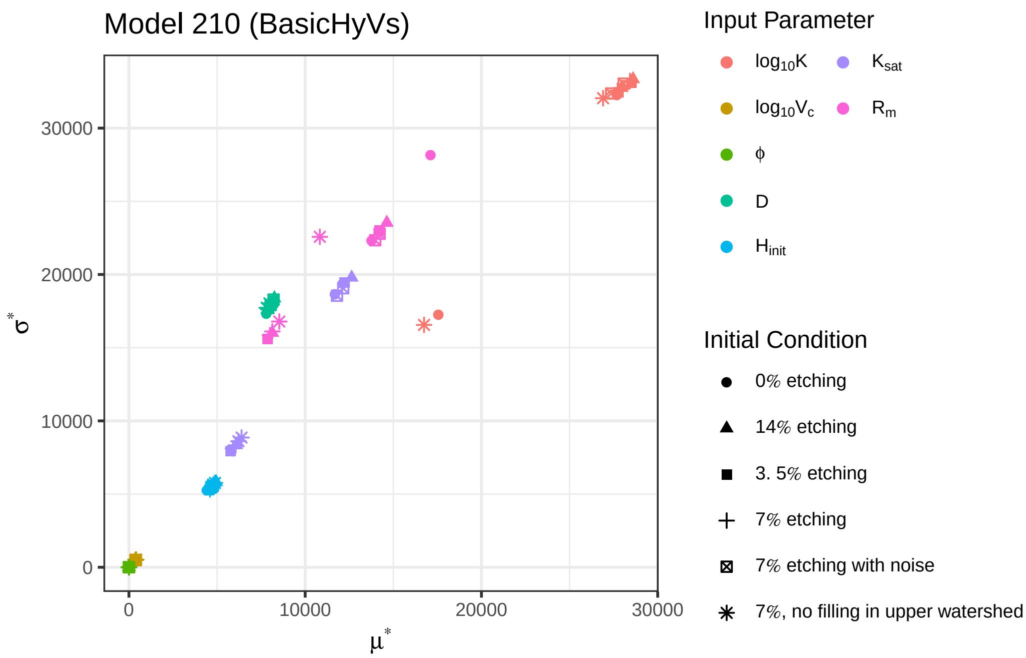

(a) Input parameter sensitivity plot for model 210 in Upper Franks Creek Watershed (SEW domain). Colors represent Method of Morris sensitivity analysis results for model input parameters. Shape represents postglacial topography and the two lowering histories considered are not distinguished. Thus two markers are present for each color-symbol combination.

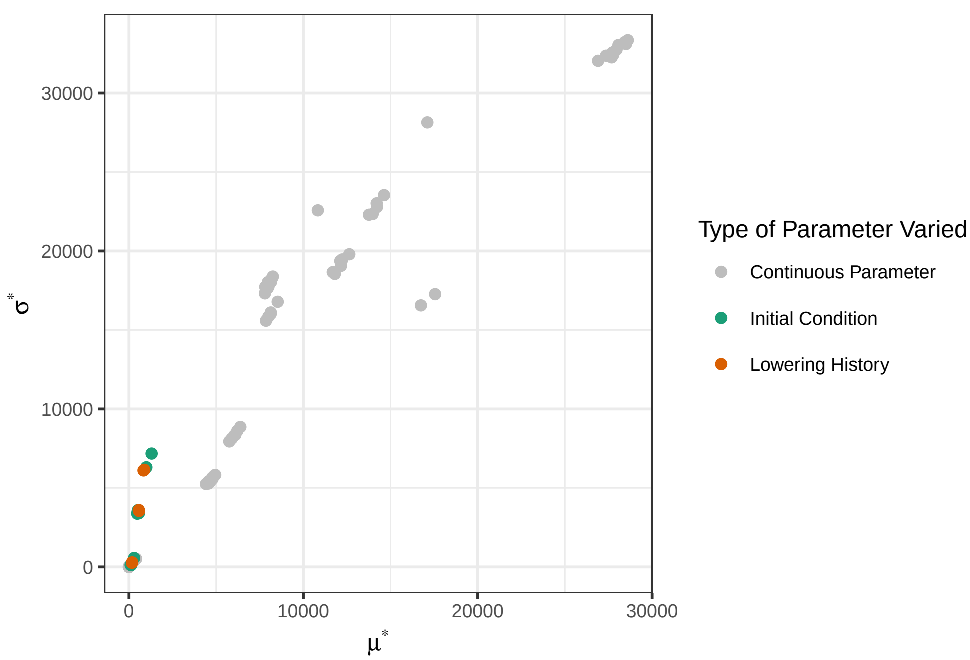

(b) Parameter, initial condition, and lowering sensitivity plot for model 210 in Upper Franks Creek Watershed (SEW domain). Colors represent parameter, initial condition, or lowering history sensitivities. The parameter sensitivities of the upper panel are shown in gray for context. Initial condition "7% etching" and lowering history "1" were used as references value initial and boundary condition sensitivity calculations.

Figure B.22: Sensitivity analysis summary for model 210 in Upper Franks Creek Watershed (SEW domain)

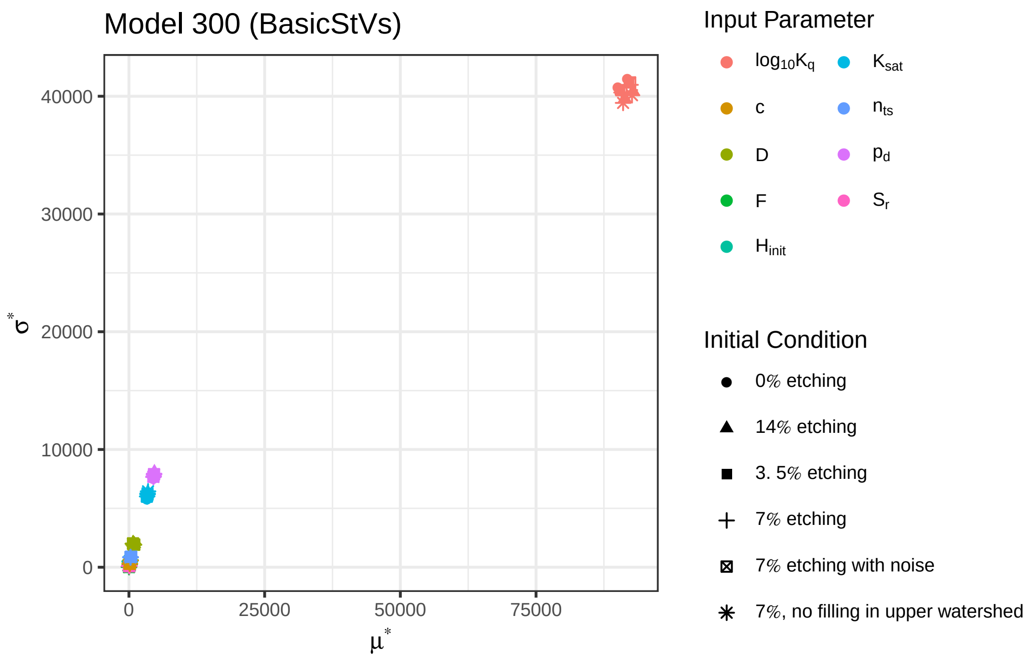

(a) Input parameter sensitivity plot for model 300 in Upper Franks Creek Watershed (SEW domain). Colors represent Method of Morris sensitivity analysis results for model input parameters. Shape represents postglacial topography and the two lowering histories considered are not distinguished. Thus two markers are present for each color-symbol combination.

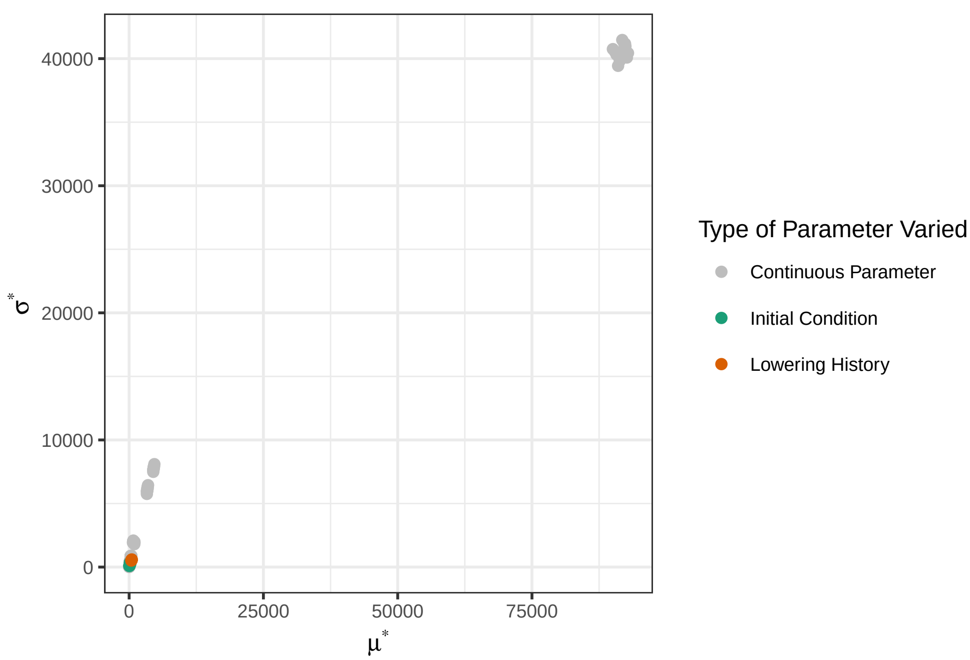

(b) Parameter, initial condition, and lowering sensitivity plot for model 300 in Upper Franks Creek Watershed (SEW domain). Colors represent parameter, initial condition, or lowering history sensitivities. The parameter sensitivities of the upper panel are shown in gray for context. Initial condition "7% etching" and lowering history "1" were used as references value initial and boundary condition sensitivity calculations.

Figure B.23: Sensitivity analysis summary for model 300 in Upper Franks Creek Watershed (SEW domain)

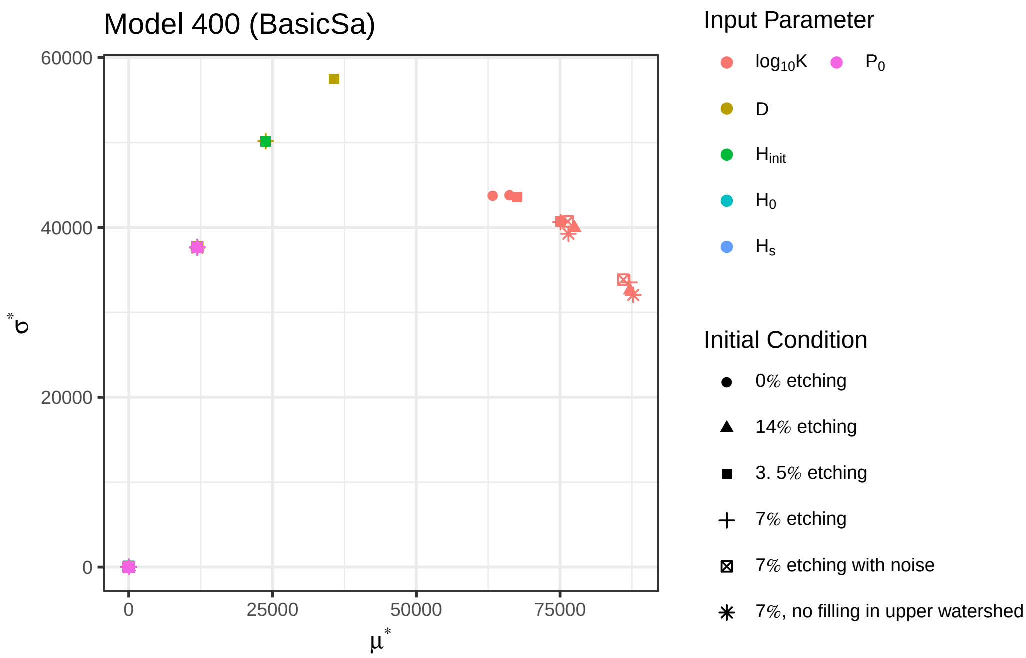

(a) Input parameter sensitivity plot for model 400 in Upper Franks Creek Watershed (SEW domain). Colors represent Method of Morris sensitivity analysis results for model input parameters. Shape represents postglacial topography and the two lowering histories considered are not distinguished. Thus two markers are present for each color-symbol combination.

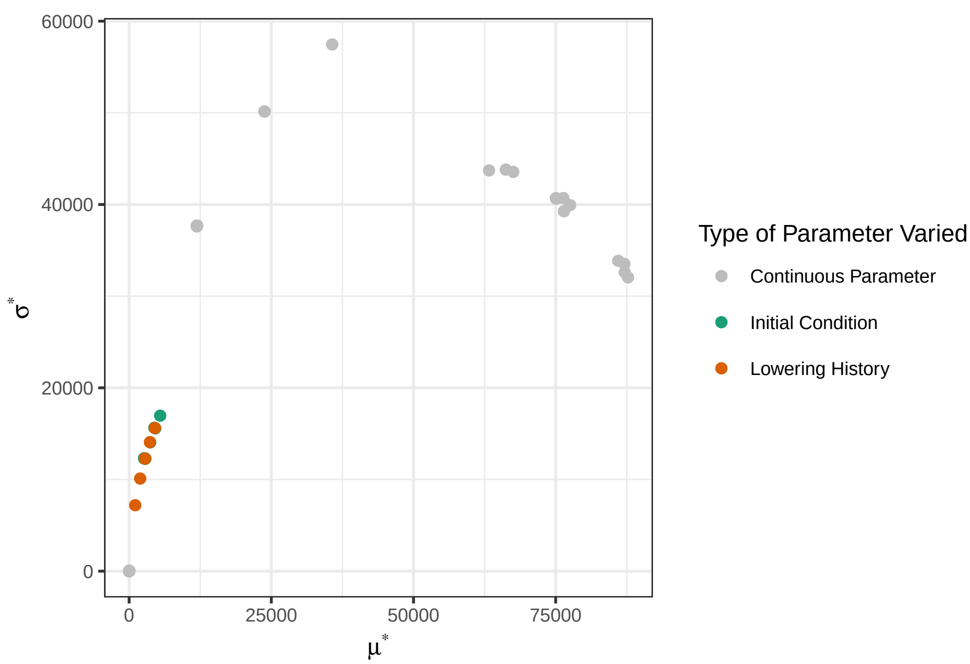

(b) Parameter, initial condition, and lowering sensitivity plot for model 400 in Upper Franks Creek Watershed (SEW domain). Colors represent parameter, initial condition, or lowering history sensitivities. The parameter sensitivities of the upper panel are shown in gray for context. Initial condition "7% etching" and lowering history "1" were used as references value initial and boundary condition sensitivity calculations.

Figure B.24: Sensitivity analysis summary for model 400 in Upper Franks Creek Watershed (SEW domain)

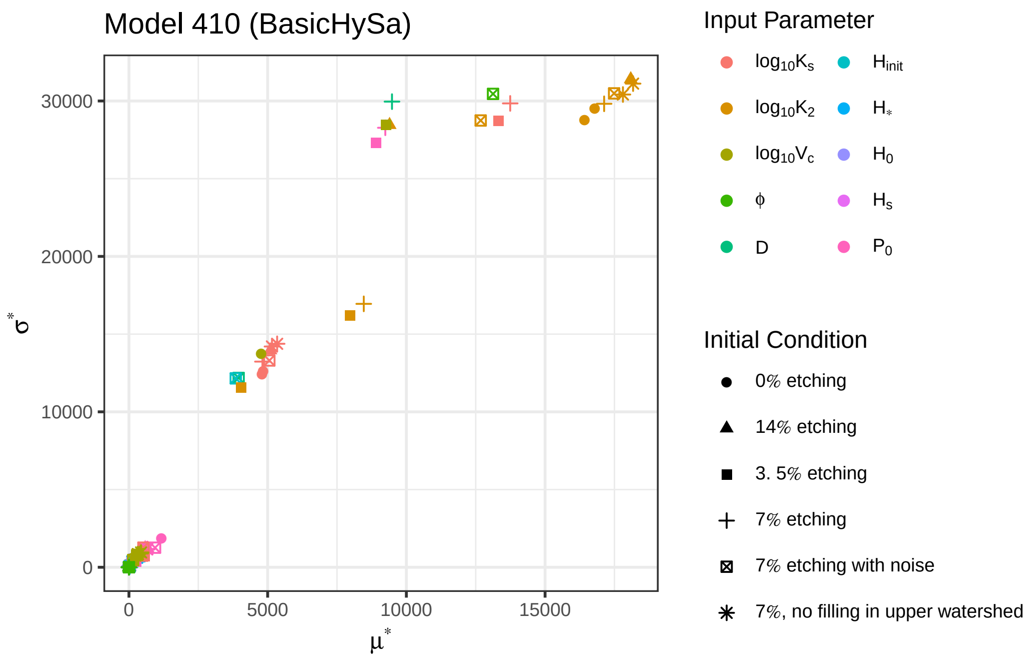

(a) Input parameter sensitivity plot for model 410 in Upper Franks Creek Watershed (SEW domain). Colors represent Method of Morris sensitivity analysis results for model input parameters. Shape represents postglacial topography and the two lowering histories considered are not distinguished. Thus two markers are present for each color-symbol combination.

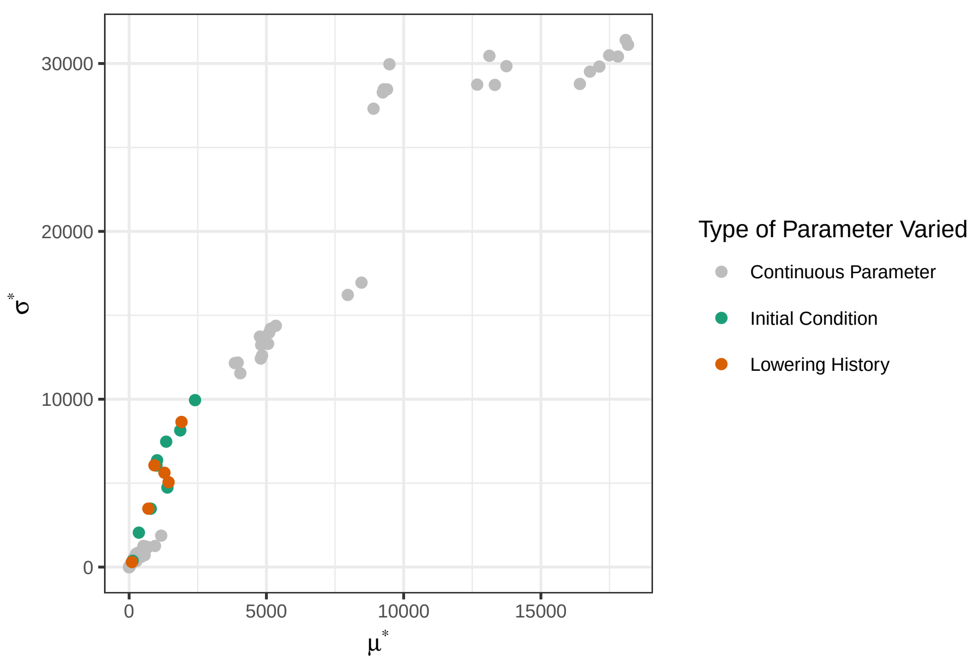

(b) Parameter, initial condition, and lowering sensitivity plot for model 410 in Upper Franks Creek Watershed (SEW domain). Colors represent parameter, initial condition, or lowering history sensitivities. The parameter sensitivities of the upper panel are shown in gray for context. Initial condition "7% etching" and lowering history "1" were used as references value initial and boundary condition sensitivity calculations.

Figure B.25: Sensitivity analysis summary for model 410 in Upper Franks Creek Watershed (SEW domain)

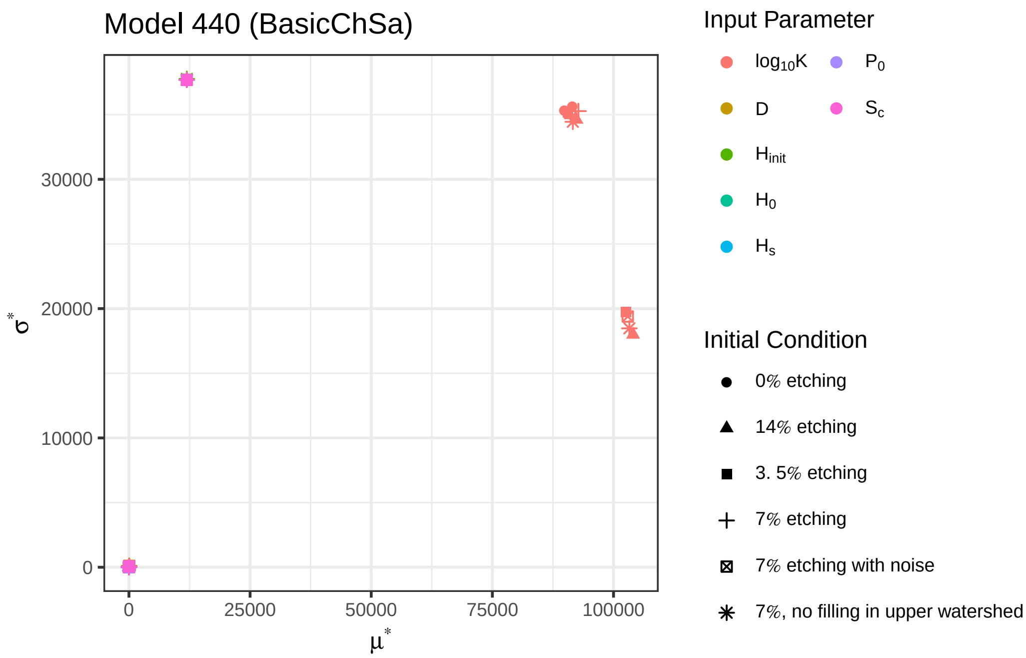

(a) Input parameter sensitivity plot for model 440 in Upper Franks Creek Watershed (SEW domain). Colors represent Method of Morris sensitivity analysis results for model input parameters. Shape represents postglacial topography and the two lowering histories considered are not distinguished. Thus two markers are present for each color-symbol combination.

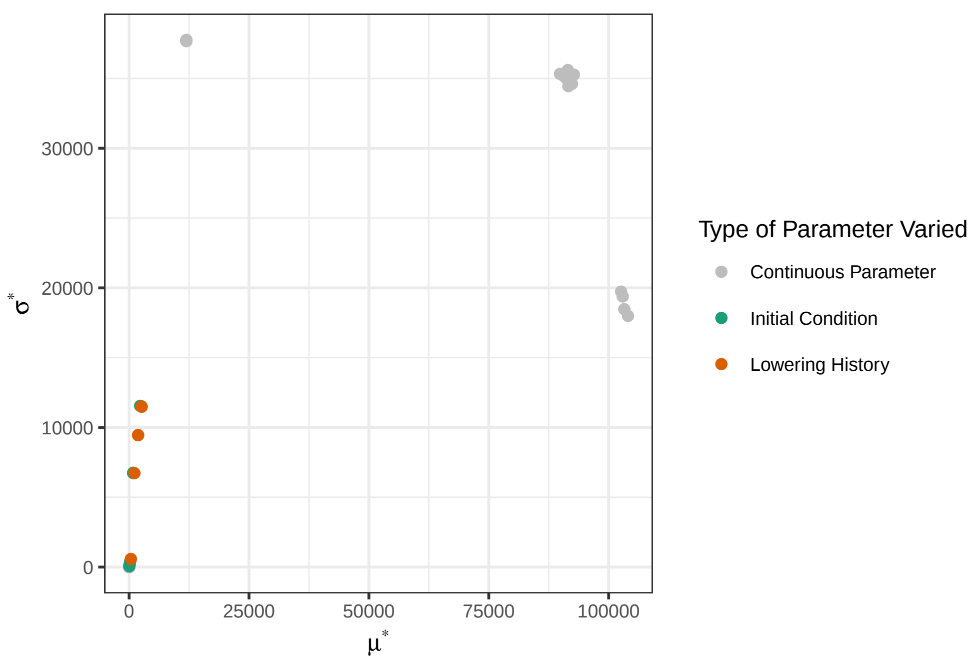

(b) Parameter, initial condition, and lowering sensitivity plot for model 440 in Upper Franks Creek Watershed (SEW domain). Colors represent parameter, initial condition, or lowering history sensitivities. The parameter sensitivities of the upper panel are shown in gray for context. Initial condition "7% etching" and lowering history "1" were used as references value initial and boundary condition sensitivity calculations.

Figure B.26: Sensitivity analysis summary for model 440 in Upper Franks Creek Watershed (SEW domain)

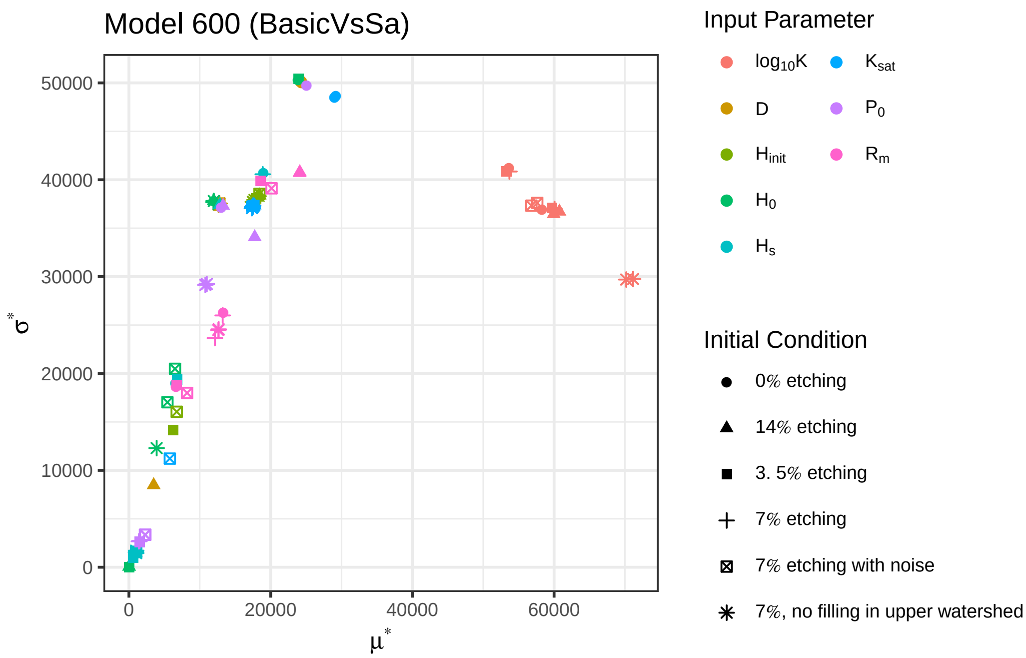

(a) Input parameter sensitivity plot for model 600 in Upper Franks Creek Watershed (SEW domain). Colors represent Method of Morris sensitivity analysis results for model input parameters. Shape represents postglacial topography and the two lowering histories considered are not distinguished. Thus two markers are present for each color-symbol combination.

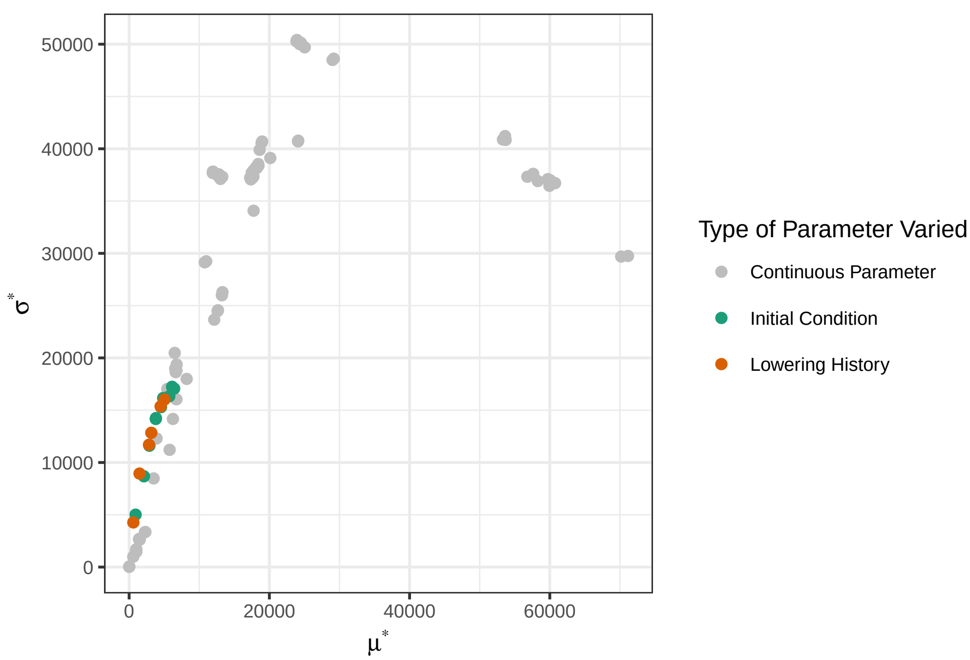

(b) Parameter, initial condition, and lowering sensitivity plot for model 600 in Upper Franks Creek Watershed (SEW domain). Colors represent parameter, initial condition, or lowering history sensitivities. The parameter sensitivities of the upper panel are shown in gray for context. Initial condition "7% etching" and lowering history "1" were used as references value initial and boundary condition sensitivity calculations.

Figure B.27: Sensitivity analysis summary for model 600 in Upper Franks Creek Watershed (SEW domain)

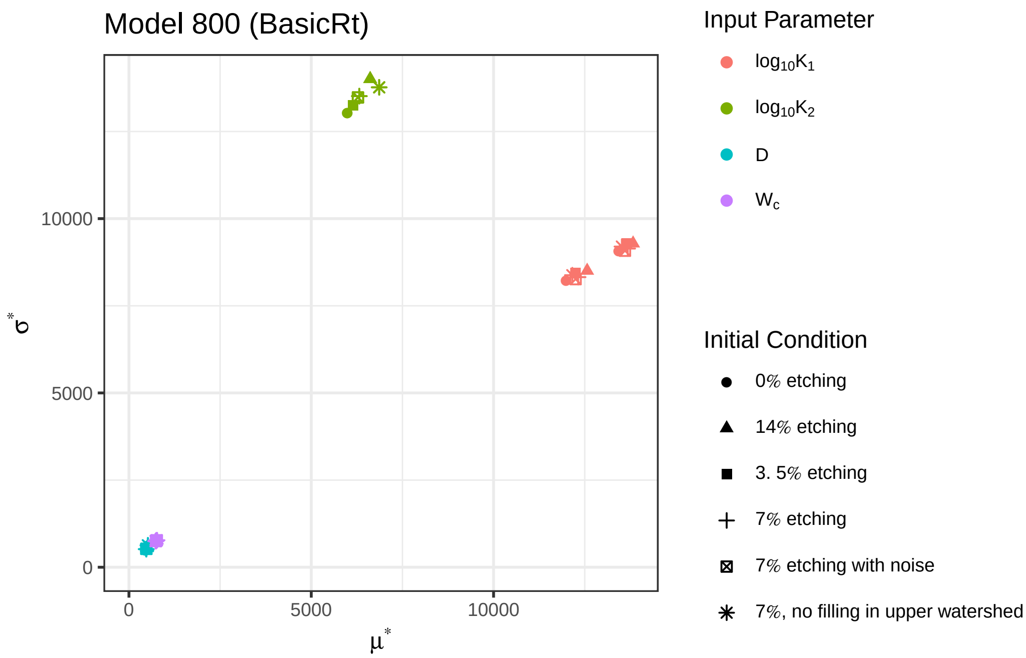

(a) Input parameter sensitivity plot for model 800 in Upper Franks Creek Watershed (SEW domain). Colors represent Method of Morris sensitivity analysis results for model input parameters. Shape represents postglacial topography and the two lowering histories considered are not distinguished. Thus two markers are present for each color-symbol combination.

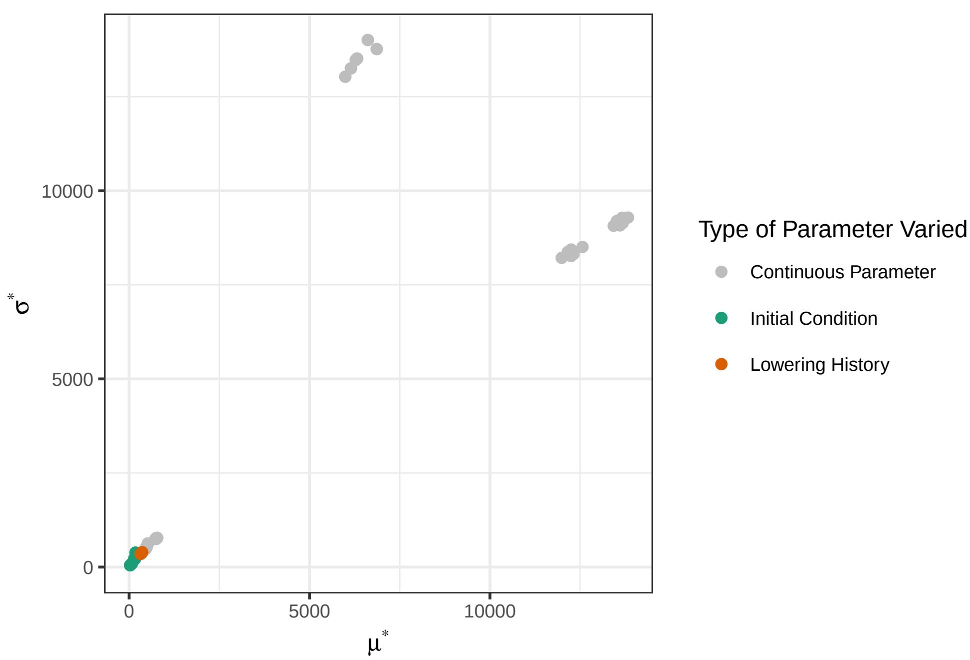

(b) Parameter, initial condition, and lowering sensitivity plot for model 800 in Upper Franks Creek Watershed (SEW domain). Colors represent parameter, initial condition, or lowering history sensitivities. The parameter sensitivities of the upper panel are shown in gray for context. Initial condition "7% etching" and lowering history "1" were used as references value initial and boundary condition sensitivity calculations.

Figure B.28: Sensitivity analysis summary for model 800 in Upper Franks Creek Watershed (SEW domain)

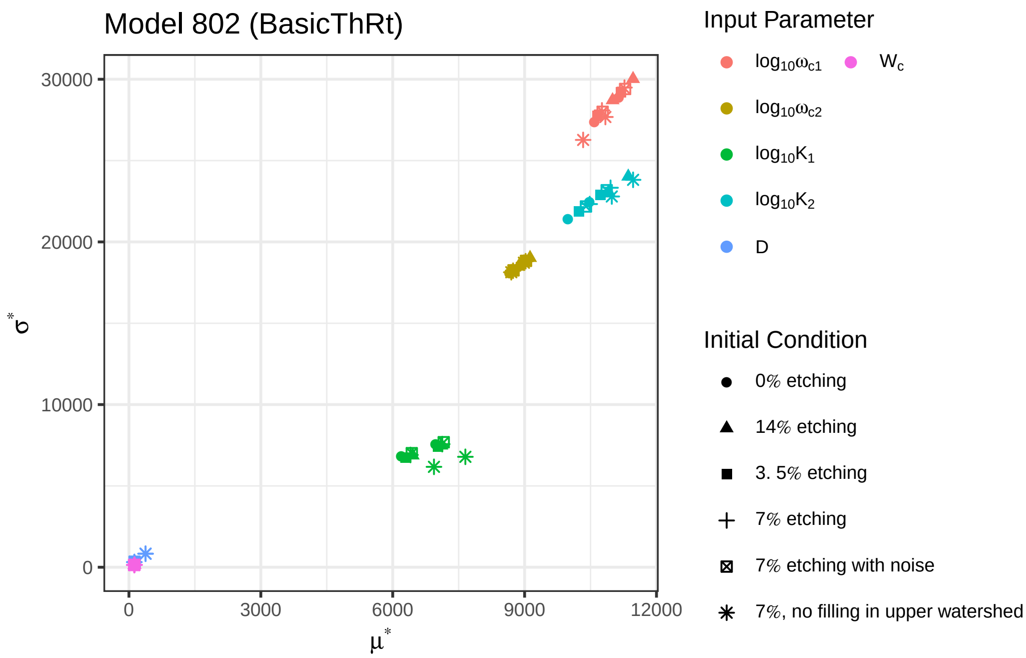

(a) Input parameter sensitivity plot for model 802 in Upper Franks Creek Watershed (SEW domain). Colors represent Method of Morris sensitivity analysis results for model input parameters. Shape represents postglacial topography and the two lowering histories considered are not distinguished. Thus two markers are present for each color-symbol combination.

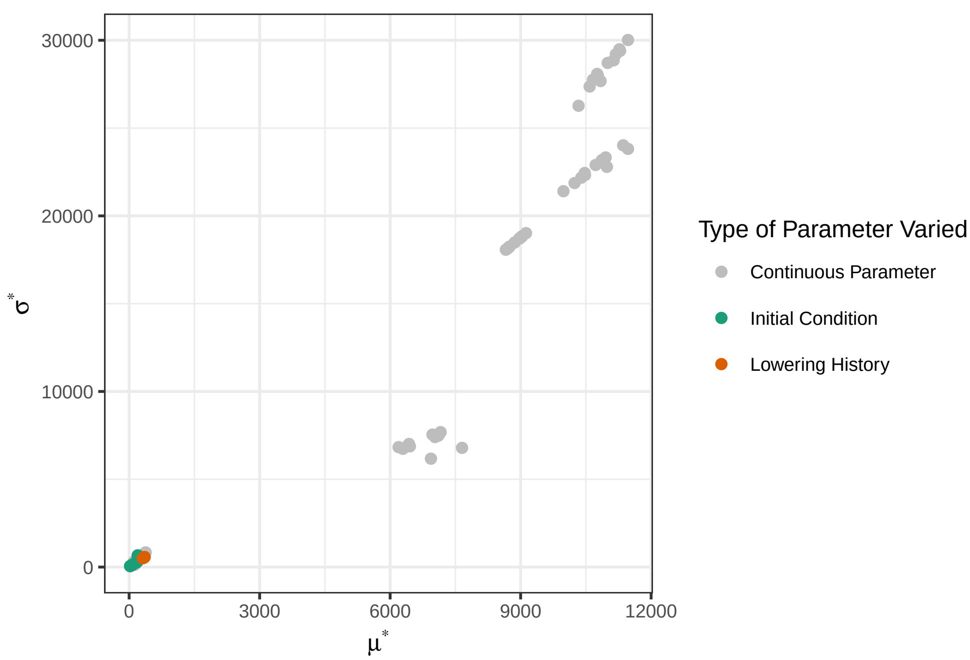

(b) Parameter, initial condition, and lowering sensitivity plot for model 802 in Upper Franks Creek Watershed (SEW domain). Colors represent parameter, initial condition, or lowering history sensitivities. The parameter sensitivities of the upper panel are shown in gray for context. Initial condition "7% etching" and lowering history "1" were used as references value initial and boundary condition sensitivity calculations.

Figure B.29: Sensitivity analysis summary for model 802 in Upper Franks Creek Watershed (SEW domain)

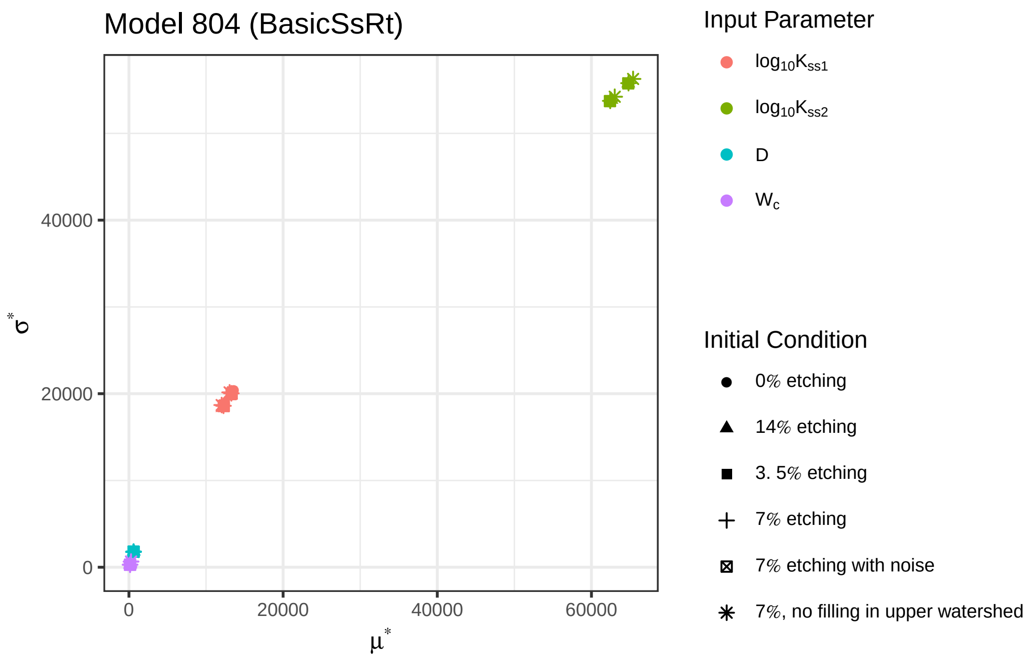

(a) Input parameter sensitivity plot for model 804 in Upper Franks Creek Watershed (SEW domain). Colors represent Method of Morris sensitivity analysis results for model input parameters. Shape represents postglacial topography and the two lowering histories considered are not distinguished. Thus two markers are present for each color-symbol combination.

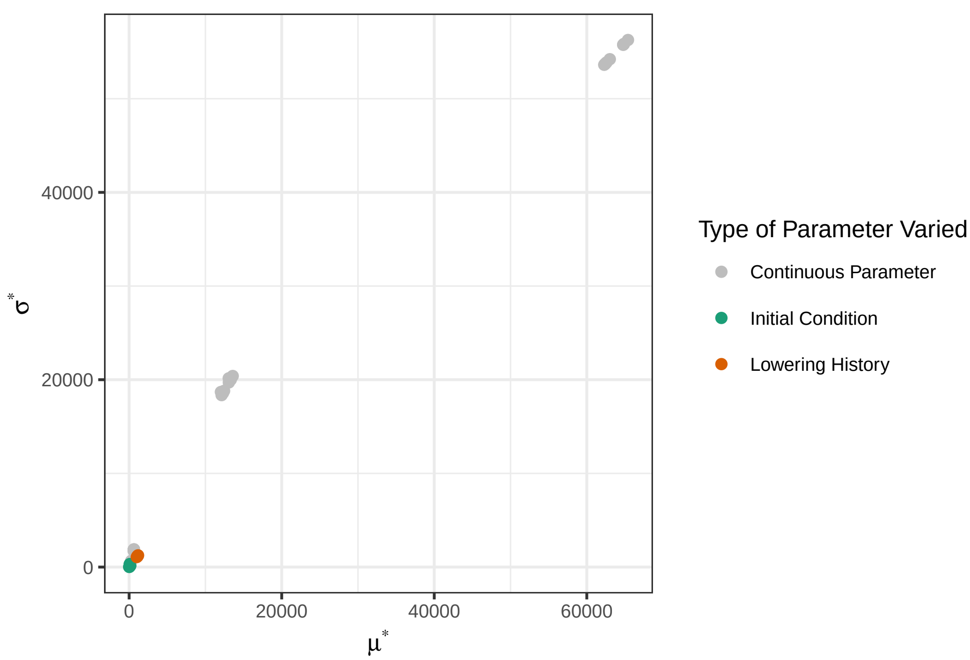

(b) Parameter, initial condition, and lowering sensitivity plot for model 804 in Upper Franks Creek Watershed (SEW domain). Colors represent parameter, initial condition, or lowering history sensitivities. The parameter sensitivities of the upper panel are shown in gray for context. Initial condition "7% etching" and lowering history "1" were used as references value initial and boundary condition sensitivity calculations.

Figure B.30: Sensitivity analysis summary for model 804 in Upper Franks Creek Watershed (SEW domain)

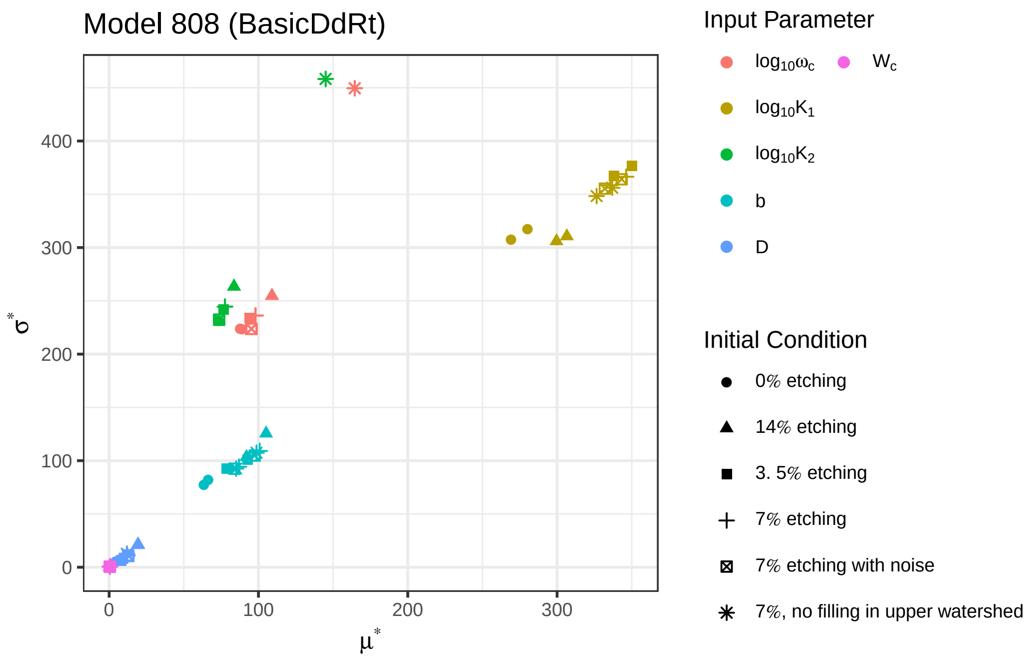

(a) Input parameter sensitivity plot for model 808 in Upper Franks Creek Watershed (SEW domain). Colors represent Method of Morris sensitivity analysis results for model input parameters. Shape represents postglacial topography and the two lowering histories considered are not distinguished. Thus two markers are present for each color-symbol combination.

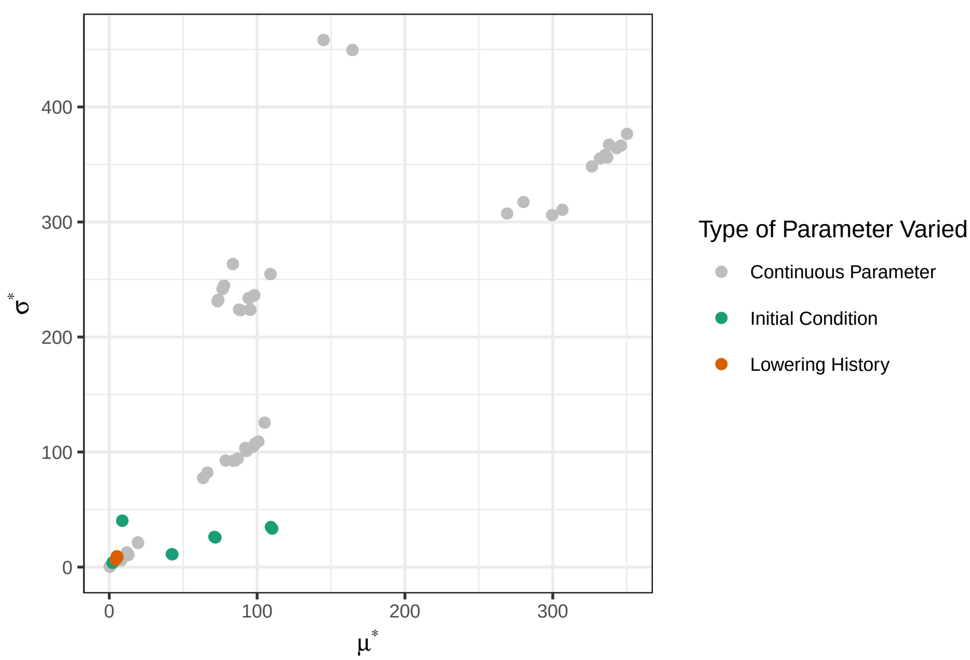

(b) Parameter, initial condition, and lowering sensitivity plot for model 808 in Upper Franks Creek Watershed (SEW domain). Colors represent parameter, initial condition, or lowering history sensitivities. The parameter sensitivities of the upper panel are shown in gray for context. Initial condition "7% etching" and lowering history "1" were used as references value initial and boundary condition sensitivity calculations.

Figure B.31: Sensitivity analysis summary for model 808 in Upper Franks Creek Watershed (SEW domain)

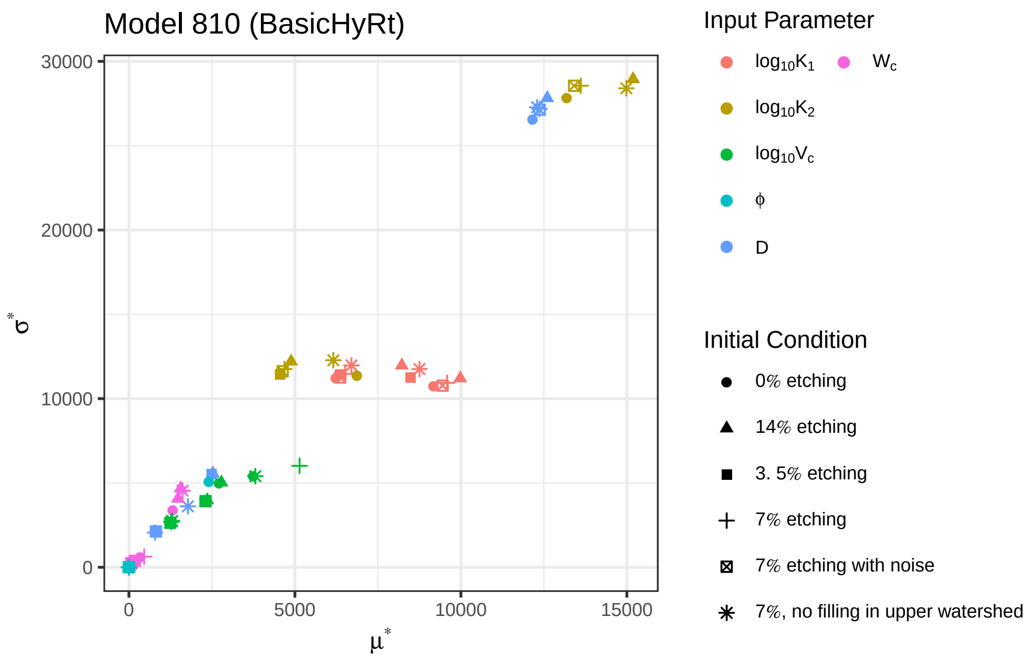

(a) Input parameter sensitivity plot for model 810 in Upper Franks Creek Watershed (SEW domain). Colors represent Method of Morris sensitivity analysis results for model input parameters. Shape represents postglacial topography and the two lowering histories considered are not distinguished. Thus two markers are present for each color-symbol combination.

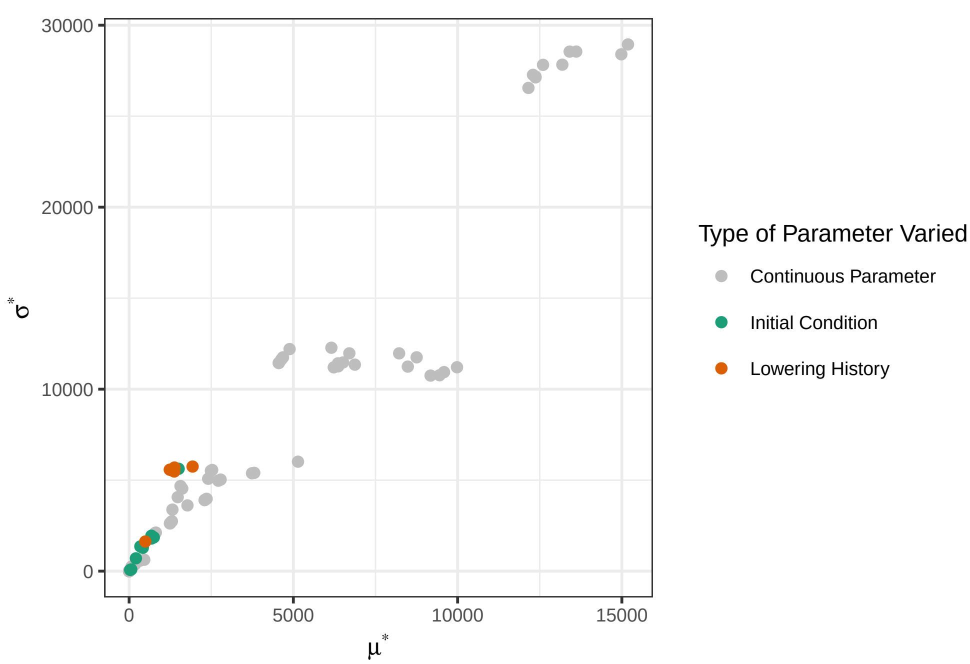

(b) Parameter, initial condition, and lowering sensitivity plot for model 810 in Upper Franks Creek Watershed (SEW domain). Colors represent parameter, initial condition, or lowering history sensitivities. The parameter sensitivities of the upper panel are shown in gray for context. Initial condition "7% etching" and lowering history "1" were used as references value initial and boundary condition sensitivity calculations.

Figure B.32: Sensitivity analysis summary for model 810 in Upper Franks Creek Watershed (SEW domain)

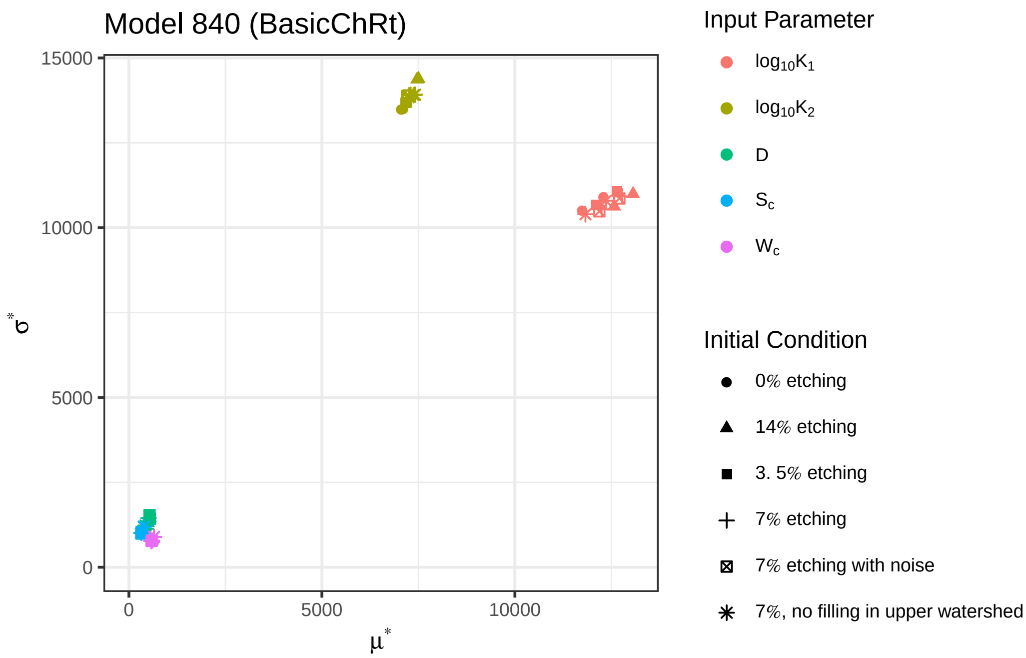

(a) Input parameter sensitivity plot for model 840 in Upper Franks Creek Watershed (SEW domain). Colors represent Method of Morris sensitivity analysis results for model input parameters. Shape represents postglacial topography and the two lowering histories considered are not distinguished. Thus two markers are present for each color-symbol combination.

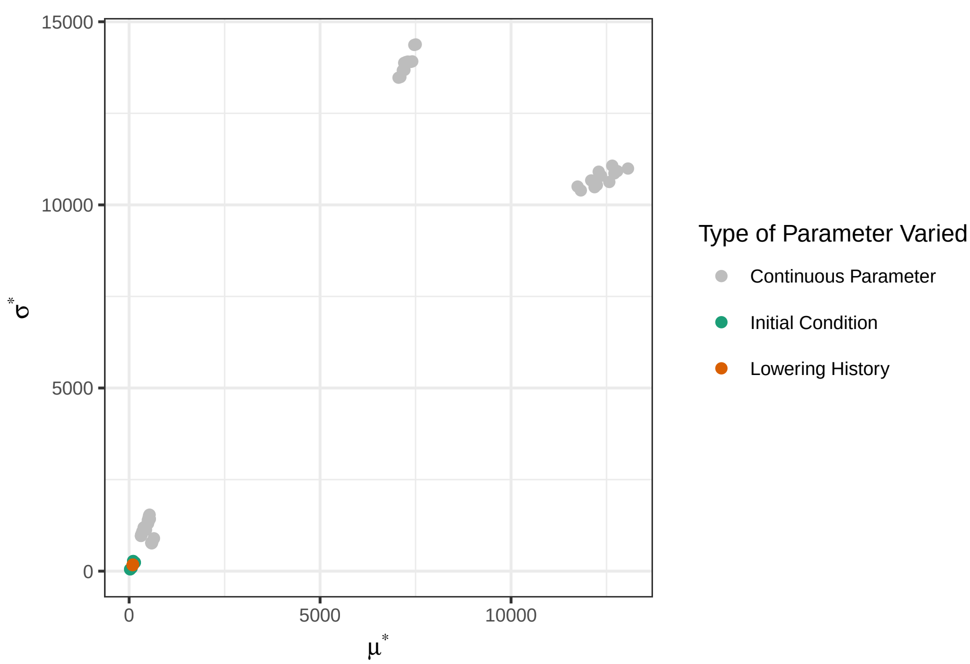

(b) Parameter, initial condition, and lowering sensitivity plot for model 840 in Upper Franks Creek Watershed (SEW domain). Colors represent parameter, initial condition, or lowering history sensitivities. The parameter sensitivities of the upper panel are shown in gray for context. Initial condition "7% etching" and lowering history "1" were used as references value initial and boundary condition sensitivity calculations.

Figure B.33: Sensitivity analysis summary for model 840 in Upper Franks Creek Watershed (SEW domain)

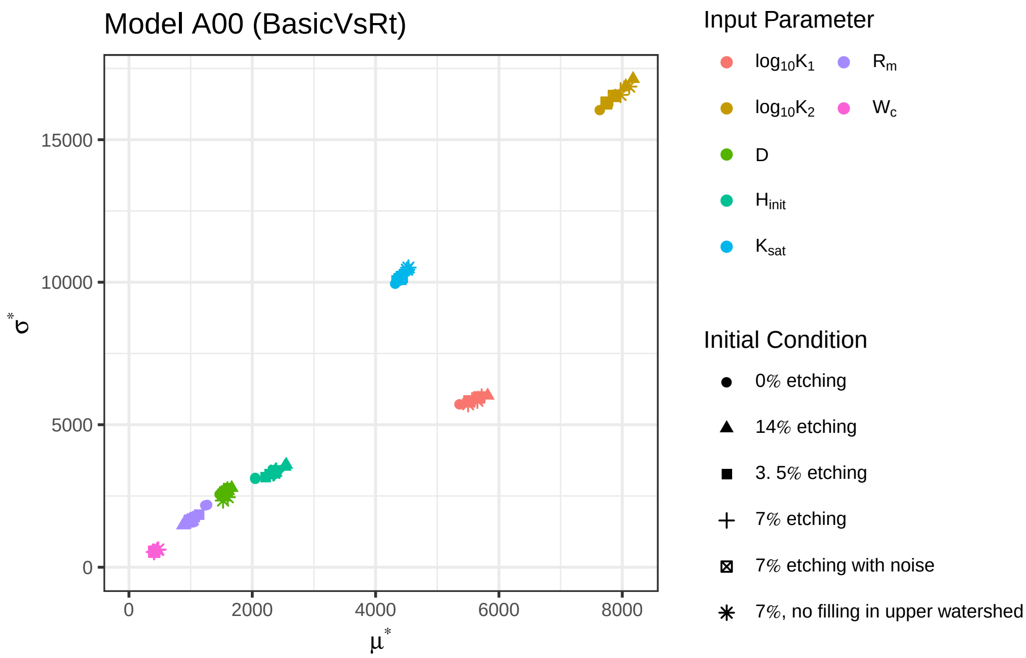

(a) Input parameter sensitivity plot for model A00 in Upper Franks Creek Watershed (SEW domain). Colors represent Method of Morris sensitivity analysis results for model input parameters. Shape represents postglacial topography and the two lowering histories considered are not distinguished. Thus two markers are present for each color-symbol combination.

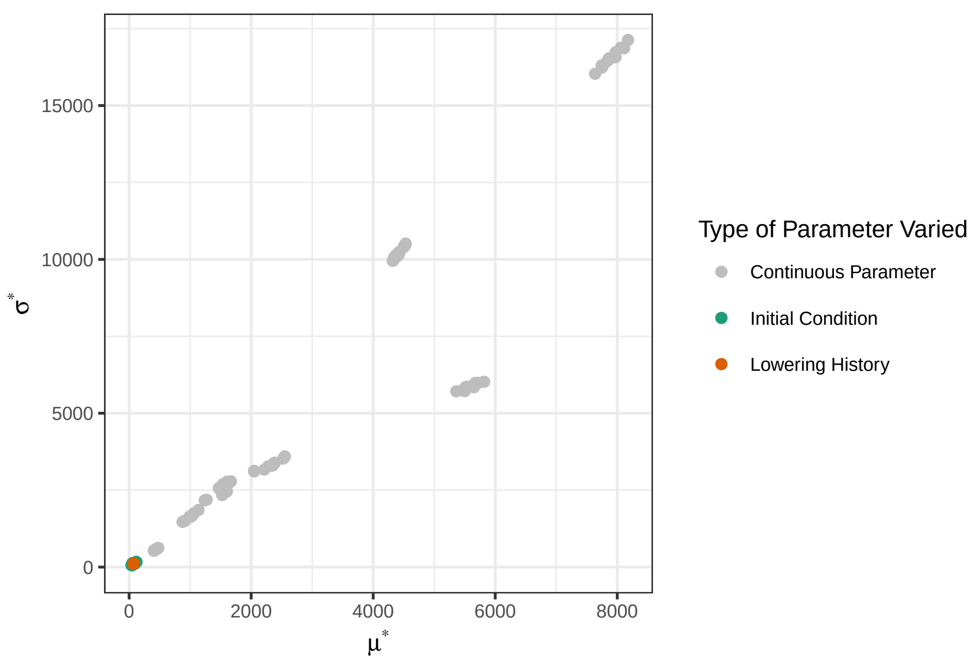

(b) Parameter, initial condition, and lowering sensitivity plot for model A00 in Upper Franks Creek Watershed (SEW domain). Colors represent parameter, initial condition, or lowering history sensitivities. The parameter sensitivities of the upper panel are shown in gray for context. Initial condition "7% etching" and lowering history "1" were used as references value initial and boundary condition sensitivity calculations.

Figure B.34: Sensitivity analysis summary for model A00 in Upper Franks Creek Watershed (SEW domain)

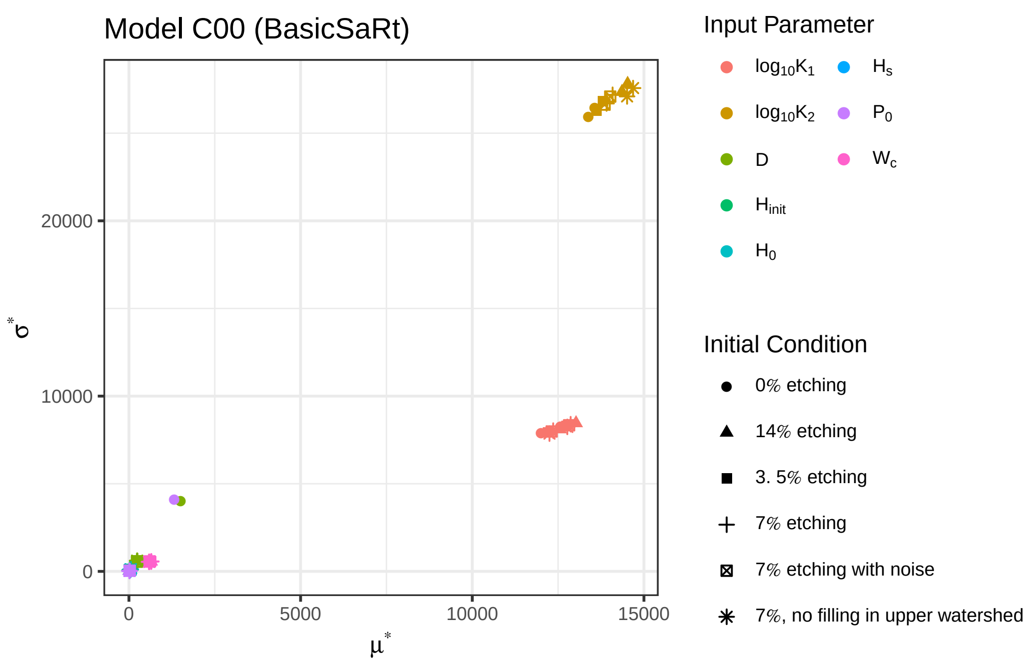

(a) Input parameter sensitivity plot for model C00 in Upper Franks Creek Watershed (SEW domain). Colors represent Method of Morris sensitivity analysis results for model input parameters. Shape represents postglacial topography and the two lowering histories considered are not distinguished. Thus two markers are present for each color-symbol combination.

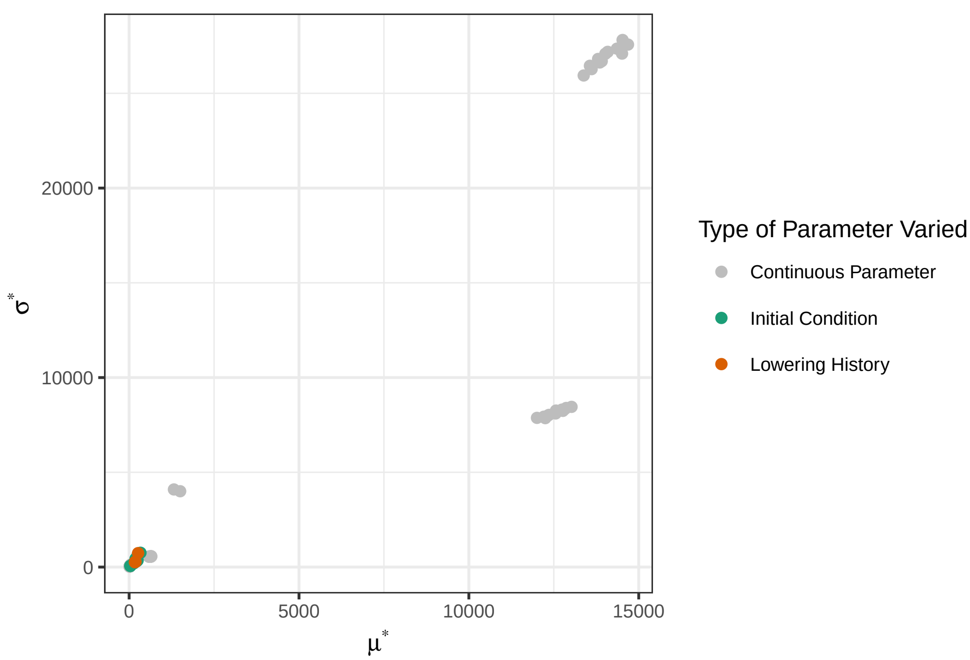

(b) Parameter, initial condition, and lowering sensitivity plot for model C00 in Upper Franks Creek Watershed (SEW domain). Colors represent parameter, initial condition, or lowering history sensitivities. The parameter sensitivities of the upper panel are shown in gray for context. Initial condition "7% etching" and lowering history "1" were used as references value initial and boundary condition sensitivity calculations.

Figure B.35: Sensitivity analysis summary for model C00 in Upper Franks Creek Watershed (SEW domain)

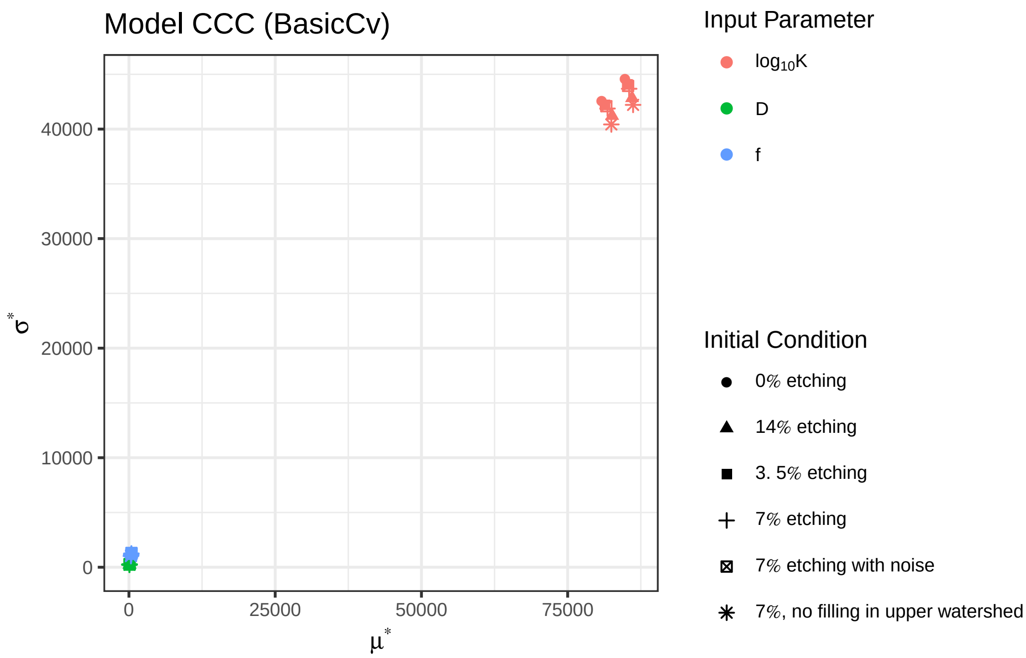

(a) Input parameter sensitivity plot for model CCC in Upper Franks Creek Watershed (SEW domain). Colors represent Method of Morris sensitivity analysis results for model input parameters. Shape represents postglacial topography and the two lowering histories considered are not distinguished. Thus two markers are present for each color-symbol combination.

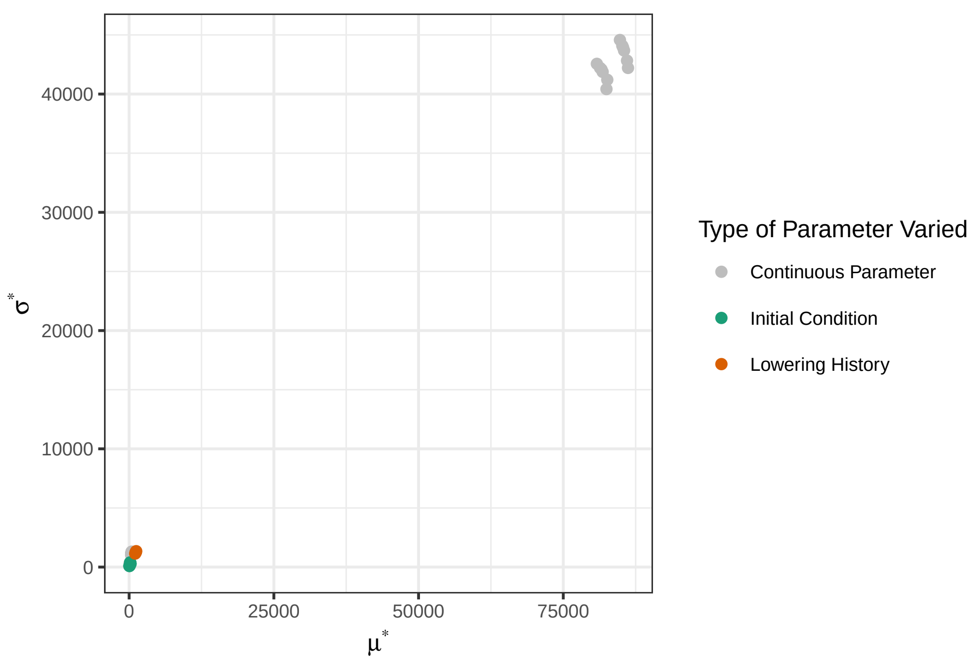

(b) Parameter, initial condition, and lowering sensitivity plot for model CCC in Upper Franks Creek Watershed (SEW domain). Colors represent parameter, initial condition, or lowering history sensitivities. The parameter sensitivities of the upper panel are shown in gray for context. Initial condition "7% etching" and lowering history "1" were used as references value initial and boundary condition sensitivity calculations.

Figure B.36: Sensitivity analysis summary for model CCC in Upper Franks Creek Watershed (SEW domain)

B.3 Tabulated Sensitivity Results for Upper Franks Creek Watershed

Table B.1: Parameter Sensitivity for Model 000, Basic South East Watershed Domain

Input	Lowering History	Initial Condition	μ^*	σ^*
D	1	0% etching	9.174×10^0	4.713×10^0
		3.5% etching	1.707×10^1	1.549×10^1
		7% etching	2.486×10^1	2.603×10^1
		7% etching with noise	2.492×10^1	2.547×10^1
		7%, no filling in upper watershed	2.691×10^1	2.632×10^1
		14% etching	4.057×10^1	4.276×10^1
	2	0% etching	6.629×10^0	5.723×10^0
		3.5% etching	1.592×10^1	1.538×10^1
		7% etching	2.530×10^1	2.435×10^1
		7% etching with noise	2.434×10^1	2.480×10^1
		7%, no filling in upper watershed	2.588×10^1	2.606×10^1
		14% etching	4.024×10^1	4.205×10^1
$\log_{10} K$	1	0% etching	5.807×10^4	5.691×10^4
		3.5% etching	5.816×10^4	5.673×10^4
		7% etching	5.823×10^4	5.659×10^4
		7% etching with noise	5.818×10^4	5.680×10^4
		7%, no filling in upper watershed	5.861×10^4	5.511×10^4
		14% etching	5.841×10^4	5.601×10^4
	2	0% etching	6.086×10^4	5.960×10^4
		3.5% etching	6.084×10^4	5.927×10^4
		7% etching	6.081×10^4	5.902×10^4
		7% etching with noise	6.076×10^4	5.925×10^4
		7%, no filling in upper watershed	6.120×10^4	5.754×10^4
		14% etching	6.078×10^4	5.822×10^4

Table B.2: Lowering History Sensitivity for Model 000, Basic South East Watershed Domain

Lowering History (Reference: History 1)	Initial Condition	μ^*	σ^*
2	0% etching	9.989×10^2	1.342×10^3
	3.5% etching	9.695×10^2	1.288×10^3
	7% etching	9.347×10^2	1.238×10^3
	7% etching with noise	9.331×10^2	1.241×10^3
	7%, no filling in upper watershed	9.379×10^2	1.239×10^3
	14% etching	8.662×10^2	1.136×10^3

Table B.3: Initial Condition Sensitivity for Model 000, Basic South East Watershed Domain

Initial Condition (Reference: 7% etch)	Lowering History	μ^*	σ^*
0% etching	1	8.337×10^1	1.124×10^2
	2	1.485×10^2	1.091×10^2
3.5% etching	1	3.731×10^1	4.694×10^1
	2	6.940×10^1	4.473×10^1
7% etching with noise	1	3.569×10^1	6.313×10^1
	2	3.950×10^1	6.717×10^1
7%, no filling in upper watershed	1	2.428×10^2	4.025×10^2
	2	2.455×10^2	4.046×10^2
14% etching	1	1.148×10^2	1.334×10^2
	2	1.786×10^2	1.093×10^2

Table B.4: Parameter Sensitivity for Model 001, BasicVm
South East Watershed Domain

Input	Lowering History	Initial Condition	μ^*	σ^*
D	1	0% etching	6.746×10^2	1.243×10^3
		3.5% etching	6.189×10^2	1.096×10^3
		7% etching	6.981×10^2	1.298×10^3
		7% etching with noise	6.426×10^2	1.145×10^3
		7%, no filling in upper watershed	6.023×10^2	1.010×10^3
		14% etching	6.241×10^2	1.126×10^3
	2	0% etching	6.793×10^2	1.255×10^3
		3.5% etching	6.573×10^2	1.173×10^3
		7% etching	6.794×10^2	1.231×10^3
		7% etching with noise	7.140×10^2	1.346×10^3
		7%, no filling in upper watershed	6.241×10^2	1.005×10^3
		14% etching	6.362×10^2	1.096×10^3
$\log_{10} K$	1	0% etching	3.418×10^4	4.668×10^4
		3.5% etching	3.426×10^4	4.682×10^4
		7% etching	3.438×10^4	4.686×10^4
		7% etching with noise	3.438×10^4	4.688×10^4
		7%, no filling in upper watershed	3.476×10^4	4.682×10^4
		14% etching	3.428×10^4	4.707×10^4
	2	0% etching	3.574×10^4	4.896×10^4
		3.5% etching	3.571×10^4	4.904×10^4
		7% etching	3.580×10^4	4.899×10^4
		7% etching with noise	3.578×10^4	4.901×10^4
		7%, no filling in upper watershed	3.622×10^4	4.893×10^4
		14% etching	3.561×10^4	4.902×10^4
m	1	0% etching	3.124×10^4	4.610×10^4
		3.5% etching	3.102×10^4	4.608×10^4
		7% etching	3.088×10^4	4.602×10^4
		7% etching with noise	3.092×10^4	4.605×10^4
		7%, no filling in upper watershed	3.038×10^4	4.546×10^4
		14% etching	3.051×10^4	4.592×10^4
	2	0% etching	3.267×10^4	4.836×10^4
		3.5% etching	3.239×10^4	4.820×10^4
		7% etching	3.219×10^4	4.809×10^4
		7% etching with noise	3.227×10^4	4.811×10^4
		7%, no filling in upper watershed	3.171×10^4	4.754×10^4
		14% etching	3.174×10^4	4.781×10^4

Table B.5: Lowering History Sensitivity for Model 001, BasicVm
South East Watershed Domain

Lowering History (Reference: History 1)	Initial Condition	μ^*	σ^*
2	0% etching	1.249×10^3	1.347×10^3
	3.5% etching	1.210×10^3	1.302×10^3
	7% etching	1.159×10^3	1.246×10^3
	7% etching with noise	1.163×10^3	1.254×10^3
	7%, no filling in upper watershed	1.160×10^3	1.248×10^3
	14% etching	1.065×10^3	1.144×10^3

Table B.6: Initial Condition Sensitivity for Model 001, BasicVm
South East Watershed Domain

Initial Condition (Reference: 7% etch)	Lowering History	μ^*	σ^*
0% etching	1	1.591×10^2	2.879×10^2
	2	1.831×10^2	2.440×10^2
3.5% etching	1	7.840×10^1	1.441×10^2
	2	9.282×10^1	1.237×10^2
7% etching with noise	1	2.112×10^1	5.670×10^1
	2	3.145×10^1	6.583×10^1
7%, no filling in upper watershed	1	1.717×10^2	3.197×10^2
	2	1.714×10^2	3.236×10^2
14% etching	1	1.643×10^2	2.766×10^2
	2	1.810×10^2	2.183×10^2

Table B.7: Parameter Sensitivity for Model 002, BasicTh
South East Watershed Domain

Input	Lowering History	Initial Condition	μ^*	σ^*
D	1	0% etching	2.781×10^3	5.308×10^3
		3.5% etching	2.796×10^3	5.289×10^3
		7% etching	2.898×10^3	5.418×10^3
		7% etching with noise	2.904×10^3	5.459×10^3
		7%, no filling in upper watershed	2.888×10^3	5.350×10^3
		14% etching	2.862×10^3	5.348×10^3
	2	0% etching	2.902×10^3	5.534×10^3
		3.5% etching	2.895×10^3	5.489×10^3
		7% etching	2.983×10^3	5.615×10^3
		7% etching with noise	3.009×10^3	5.683×10^3
		7%, no filling in upper watershed	2.988×10^3	5.559×10^3
		14% etching	2.960×10^3	5.516×10^3
$\log_{10} K$	1	0% etching	3.247×10^4	4.103×10^4
		3.5% etching	3.305×10^4	4.136×10^4
		7% etching	3.341×10^4	4.159×10^4
		7% etching with noise	3.323×10^4	4.150×10^4
		7%, no filling in upper watershed	3.404×10^4	4.169×10^4
		14% etching	3.426×10^4	4.214×10^4
	2	0% etching	3.419×10^4	4.310×10^4
		3.5% etching	3.474×10^4	4.339×10^4
		7% etching	3.505×10^4	4.355×10^4
		7% etching with noise	3.485×10^4	4.345×10^4
		7%, no filling in upper watershed	3.569×10^4	4.365×10^4
		14% etching	3.580×10^4	4.396×10^4
$\log_{10} \omega_c$	1	0% etching	4.093×10^4	5.147×10^4
		3.5% etching	4.084×10^4	5.160×10^4
		7% etching	4.082×10^4	5.157×10^4
		7% etching with noise	4.087×10^4	5.153×10^4
		7%, no filling in upper watershed	4.070×10^4	5.151×10^4
		14% etching	4.070×10^4	5.173×10^4
	2	0% etching	4.277×10^4	5.397×10^4
		3.5% etching	4.260×10^4	5.401×10^4
		7% etching	4.253×10^4	5.391×10^4
		7% etching with noise	4.259×10^4	5.387×10^4
		7%, no filling in upper watershed	4.243×10^4	5.386×10^4
		14% etching	4.226×10^4	5.386×10^4

Table B.8: Lowering History Sensitivity for Model 002, BasicTh
South East Watershed Domain

Lowering History (Reference: History 1)	Initial Condition	μ^*	σ^*
2	0% etching	7.632×10^2	1.143×10^3
	3.5% etching	7.443×10^2	1.107×10^3
	7% etching	7.186×10^2	1.068×10^3
	7% etching with noise	7.153×10^2	1.065×10^3
	7%, no filling in upper watershed	7.224×10^2	1.071×10^3
	14% etching	6.651×10^2	9.855×10^2

Table B.9: Initial Condition Sensitivity for Model 002, BasicTh
South East Watershed Domain

Initial Condition (Reference: 7% etch)	Lowering History	μ^*	σ^*
0% etching	1	2.360×10^2	3.389×10^2
	2	2.403×10^2	3.166×10^2
3.5% etching	1	9.976×10^1	1.470×10^2
	2	1.065×10^2	1.382×10^2
7% etching with noise	1	4.406×10^1	8.155×10^1
	2	4.698×10^1	8.833×10^1
7%, no filling in upper watershed	1	1.451×10^2	3.701×10^2
	2	1.467×10^2	3.786×10^2
14% etching	1	2.131×10^2	3.137×10^2
	2	2.040×10^2	2.790×10^2

Table B.10: Parameter Sensitivity for Model 004, BasicSs
South East Watershed Domain

Input	Lowering History	Initial Condition	μ^*	σ^*
D	1	0% etching	1.279×10^3	1.518×10^3
		3.5% etching	1.186×10^3	1.406×10^3
		7% etching	1.187×10^3	1.408×10^3
		7% etching with noise	1.148×10^3	1.363×10^3
		7%, no filling in upper watershed	1.163×10^3	1.380×10^3
		14% etching	1.074×10^3	1.273×10^3
	2	0% etching	1.310×10^3	1.554×10^3
		3.5% etching	1.213×10^3	1.439×10^3
		7% etching	1.213×10^3	1.439×10^3
		7% etching with noise	1.174×10^3	1.393×10^3
		7%, no filling in upper watershed	1.192×10^3	1.414×10^3
		14% etching	1.096×10^3	1.299×10^3
$\log_{10} K_{ss}$	1	0% etching	9.741×10^4	2.665×10^4
		3.5% etching	9.788×10^4	2.632×10^4
		7% etching	9.822×10^4	2.574×10^4
		7% etching with noise	9.827×10^4	2.597×10^4
		7%, no filling in upper watershed	9.860×10^4	2.394×10^4
		14% etching	9.883×10^4	2.505×10^4
	2	0% etching	1.021×10^5	2.791×10^4
		3.5% etching	1.024×10^5	2.752×10^4
		7% etching	1.026×10^5	2.690×10^4
		7% etching with noise	1.026×10^5	2.714×10^4
		7%, no filling in upper watershed	1.030×10^5	2.504×10^4
		14% etching	1.029×10^5	2.609×10^4

Table B.11: Lowering History Sensitivity for Model 004, BasicSs
South East Watershed Domain

Lowering History (Reference: History 1)	Initial Condition	μ^*	σ^*
2	0% etching	1.343×10^3	1.361×10^3
	3.5% etching	1.302×10^3	1.315×10^3
	7% etching	1.265×10^3	1.274×10^3
	7% etching with noise	1.256×10^3	1.268×10^3
	7%, no filling in upper watershed	1.272×10^3	1.276×10^3
	14% etching	1.172×10^3	1.175×10^3

Table B.12: Initial Condition Sensitivity for Model 004, BasicSs
South East Watershed Domain

Initial Condition (Reference: 7% etch)	Lowering History	μ^*	σ^*
0% etching	1	1.808×10^2	3.058×10^2
	2	2.272×10^2	2.959×10^2
3.5% etching	1	8.592×10^1	1.725×10^2
	2	1.276×10^2	1.612×10^2
7% etching with noise	1	3.747×10^1	5.943×10^1
	2	4.585×10^1	6.924×10^1
7%, no filling in upper watershed	1	2.244×10^2	5.185×10^2
	2	2.338×10^2	5.364×10^2
14% etching	1	1.622×10^2	2.329×10^2
	2	1.836×10^2	1.983×10^2

Table B.13: Parameter Sensitivity for Model 008, BasicDd
South East Watershed Domain

Input	Lowering History	Initial Condition	μ^*	σ^*
D	1	0% etching	1.767×10^3	5.536×10^3
		3.5% etching	1.819×10^3	5.677×10^3
		7% etching	1.879×10^3	5.867×10^3
		7% etching with noise	1.863×10^3	5.813×10^3
		7%, no filling in upper watershed	1.916×10^3	5.976×10^3
		14% etching	1.958×10^3	6.092×10^3
	2	0% etching	1.842×10^3	5.769×10^3
		3.5% etching	1.905×10^3	5.945×10^3
		7% etching	1.962×10^3	6.128×10^3
		7% etching with noise	1.947×10^3	6.076×10^3
		7%, no filling in upper watershed	1.999×10^3	6.233×10^3
		14% etching	2.037×10^3	6.339×10^3
$\log_{10} K$	1	0% etching	1.040×10^3	2.927×10^3
		3.5% etching	1.123×10^3	3.027×10^3
		7% etching	1.146×10^3	3.103×10^3
		7% etching with noise	1.134×10^3	3.076×10^3
		7%, no filling in upper watershed	1.259×10^3	3.485×10^3
		14% etching	1.208×10^3	3.334×10^3
	2	0% etching	1.101×10^3	3.084×10^3
		3.5% etching	1.185×10^3	3.177×10^3
		7% etching	1.206×10^3	3.248×10^3
		7% etching with noise	1.193×10^3	3.218×10^3
		7%, no filling in upper watershed	1.320×10^3	3.634×10^3
		14% etching	1.265×10^3	3.476×10^3
$\log_{10} \omega_c$	1	0% etching	3.788×10^3	1.196×10^4
		3.5% etching	3.906×10^3	1.233×10^4
		7% etching	4.003×10^3	1.264×10^4
		7% etching with noise	3.986×10^3	1.258×10^4
		7%, no filling in upper watershed	4.141×10^3	1.307×10^4
		14% etching	4.180×10^3	1.319×10^4
	2	0% etching	3.986×10^3	1.257×10^4
		3.5% etching	4.100×10^3	1.294×10^4
		7% etching	4.193×10^3	1.324×10^4
		7% etching with noise	4.175×10^3	1.318×10^4
		7%, no filling in upper watershed	4.333×10^3	1.368×10^4
		14% etching	4.360×10^3	1.376×10^4

Table B.13: (continued)

Input	Lowering History	Initial Condition	μ^*	σ^*
b	1	0% etching	2.467×10^3	7.679×10^3
		3.5% etching	2.554×10^3	7.913×10^3
		7% etching	2.628×10^3	8.151×10^3
		7% etching with noise	2.609×10^3	8.092×10^3
		7%, no filling in upper watershed	2.717×10^3	8.440×10^3
		14% etching	2.730×10^3	8.498×10^3
	2	0% etching	2.592×10^3	8.060×10^3
		3.5% etching	2.683×10^3	8.302×10^3
		7% etching	2.752×10^3	8.527×10^3
		7% etching with noise	2.732×10^3	8.466×10^3
		7%, no filling in upper watershed	2.843×10^3	8.819×10^3
		14% etching	2.847×10^3	8.854×10^3

Table B.14: Lowering History Sensitivity for Model 008, BasicDd
South East Watershed Domain

Lowering History (Reference: History 1)	Initial Condition	μ^*	σ^*
2	0% etching	5.381×10^1	1.866×10^2
	3.5% etching	5.635×10^1	1.912×10^2
	7% etching	5.462×10^1	1.855×10^2
	7% etching with noise	5.416×10^1	1.845×10^2
	7%, no filling in upper watershed	5.514×10^1	1.874×10^2
	14% etching	5.197×10^1	1.770×10^2

Table B.15: Initial Condition Sensitivity for Model 008, BasicDd
South East Watershed Domain

Initial Condition (Reference: 7% etch)	Lowering History	μ^*	σ^*
0% etching	1	1.506×10^2	1.711×10^2
	2	1.510×10^2	1.712×10^2
3.5% etching	1	6.760×10^1	8.629×10^1
	2	6.587×10^1	8.071×10^1
7% etching with noise	1	9.976×10^0	2.897×10^1
	2	1.044×10^1	3.003×10^1
7%, no filling in upper watershed	1	6.799×10^1	2.017×10^2
	2	6.855×10^1	2.035×10^2
14% etching	1	1.255×10^2	1.515×10^2
	2	1.228×10^2	1.431×10^2

Table B.16: Parameter Sensitivity for Model 010, BasicHy
South East Watershed Domain

Input	Lowering History	Initial Condition	μ^*	σ^*
D	1	0% etching	1.407×10^4	3.699×10^4
		3.5% etching	1.407×10^4	3.700×10^4
		7% etching	1.376×10^4	3.708×10^4
		7% etching with noise	2.556×10^4	4.859×10^4
		7%, no filling in upper watershed	1.364×10^4	3.702×10^4
		14% etching	2.571×10^4	4.856×10^4
	2	0% etching	1.445×10^4	3.703×10^4
		3.5% etching	1.411×10^4	3.705×10^4
		7% etching	1.395×10^4	3.711×10^4
		7% etching with noise	1.418×10^4	3.705×10^4
		7%, no filling in upper watershed	1.405×10^4	3.707×10^4
		14% etching	1.425×10^4	3.705×10^4
$\log_{10} K$	1	0% etching	4.848×10^4	3.800×10^4
		3.5% etching	4.934×10^4	3.828×10^4
		7% etching	5.029×10^4	3.885×10^4
		7% etching with noise	3.839×10^4	3.371×10^4
		7%, no filling in upper watershed	5.158×10^4	3.834×10^4
		14% etching	3.987×10^4	3.447×10^4
	2	0% etching	4.941×10^4	3.873×10^4
		3.5% etching	5.059×10^4	3.919×10^4
		7% etching	5.134×10^4	3.960×10^4
		7% etching with noise	5.085×10^4	3.934×10^4
		7%, no filling in upper watershed	5.248×10^4	3.911×10^4
		14% etching	5.238×10^4	3.956×10^4
$\log_{10} V_c$	1	0% etching	3.798×10^3	6.314×10^3
		3.5% etching	3.797×10^3	6.238×10^3
		7% etching	3.817×10^3	6.224×10^3
		7% etching with noise	3.787×10^3	6.192×10^3
		7%, no filling in upper watershed	3.889×10^3	6.334×10^3
		14% etching	3.792×10^3	6.107×10^3
	2	0% etching	3.724×10^3	6.506×10^3
		3.5% etching	3.710×10^3	6.419×10^3
		7% etching	3.724×10^3	6.411×10^3
		7% etching with noise	3.711×10^3	6.374×10^3
		7%, no filling in upper watershed	3.803×10^3	6.508×10^3
		14% etching	3.699×10^3	6.282×10^3

Table B.16: (continued)

Input	Lowering History	Initial Condition	μ^*	σ^*
ϕ	1	0% etching	0.000×10^0	0.000×10^0
		3.5% etching	0.000×10^0	0.000×10^0
		7% etching	0.000×10^0	0.000×10^0
		7% etching with noise	0.000×10^0	0.000×10^0
		7%, no filling in upper watershed	0.000×10^0	0.000×10^0
		14% etching	0.000×10^0	0.000×10^0
	2	0% etching	0.000×10^0	0.000×10^0
		3.5% etching	0.000×10^0	0.000×10^0
		7% etching	0.000×10^0	0.000×10^0
		7% etching with noise	0.000×10^0	0.000×10^0
		7%, no filling in upper watershed	0.000×10^0	0.000×10^0
		14% etching	0.000×10^0	0.000×10^0

Table B.17: Lowering History Sensitivity for Model 010, BasicHy
South East Watershed Domain

Lowering History (Reference: History 1)	Initial Condition	μ^*	σ^*
2	0% etching	2.765×10^2	4.651×10^2
	3.5% etching	3.198×10^2	5.127×10^2
	7% etching	2.878×10^2	4.587×10^2
	7% etching with noise	1.461×10^3	8.492×10^3
	7%, no filling in upper watershed	3.058×10^2	4.971×10^2
	14% etching	1.460×10^3	8.492×10^3

Table B.18: Initial Condition Sensitivity for Model 010, BasicHy
South East Watershed Domain

Initial Condition (Reference: 7% etch)	Lowering History	μ^*	σ^*
0% etching	1	3.614×10^2	5.585×10^2
	2	3.727×10^2	5.988×10^2
3.5% etching	1	1.846×10^2	3.645×10^2
	2	1.627×10^2	2.902×10^2
7% etching with noise	1	1.278×10^3	8.374×10^3
	2	1.036×10^2	2.684×10^2
7%, no filling in upper watershed	1	2.789×10^2	5.159×10^2
	2	2.479×10^2	4.447×10^2
14% etching	1	1.453×10^3	8.354×10^3
	2	2.590×10^2	3.537×10^2

Table B.19: Parameter Sensitivity for Model 012, BasicThHy
South East Watershed Domain

Input	Lowering History	Initial Condition	μ^*	σ^*
D	1	0% etching	1.549×10^2	3.404×10^2
		3.5% etching	1.343×10^2	2.721×10^2
		7% etching	1.389×10^2	2.704×10^2
		7% etching with noise	1.680×10^2	3.584×10^2
		7%, no filling in upper watershed	1.703×10^2	3.370×10^2
		14% etching	1.655×10^2	3.120×10^2
	2	0% etching	5.010×10^1	1.512×10^2
		3.5% etching	5.589×10^1	1.480×10^2
		7% etching	5.885×10^1	1.427×10^2
		7% etching with noise	5.618×10^1	1.344×10^2
		7%, no filling in upper watershed	6.787×10^1	1.693×10^2
		14% etching	7.300×10^1	1.624×10^2
$\log_{10} K$	1	0% etching	7.232×10^4	5.101×10^4
		3.5% etching	7.283×10^4	5.123×10^4
		7% etching	7.306×10^4	5.134×10^4
		7% etching with noise	7.292×10^4	5.129×10^4
		7%, no filling in upper watershed	7.318×10^4	5.142×10^4
		14% etching	7.369×10^4	5.168×10^4
	2	0% etching	7.425×10^4	5.210×10^4
		3.5% etching	7.470×10^4	5.231×10^4
		7% etching	7.486×10^4	5.238×10^4
		7% etching with noise	7.473×10^4	5.232×10^4
		7%, no filling in upper watershed	7.497×10^4	5.244×10^4
		14% etching	7.538×10^4	5.266×10^4
$\log_{10} V_c$	1	0% etching	1.846×10^3	3.173×10^3
		3.5% etching	1.859×10^3	3.045×10^3
		7% etching	1.715×10^3	2.943×10^3
		7% etching with noise	1.733×10^3	2.949×10^3
		7%, no filling in upper watershed	1.689×10^3	2.965×10^3
		14% etching	1.656×10^3	2.836×10^3
	2	0% etching	1.857×10^3	3.318×10^3
		3.5% etching	1.776×10^3	3.197×10^3
		7% etching	1.754×10^3	3.119×10^3
		7% etching with noise	1.824×10^3	3.146×10^3
		7%, no filling in upper watershed	1.753×10^3	3.198×10^3
		14% etching	1.733×10^3	3.030×10^3

Table B.19: (continued)

Input	Lowering History	Initial Condition	μ^*	σ^*
$\log_{10}\omega_c$	1	0% etching	2.244×10^4	4.378×10^4
		3.5% etching	2.256×10^4	4.397×10^4
		7% etching	2.258×10^4	4.420×10^4
		7% etching with noise	2.256×10^4	4.412×10^4
		7%, no filling in upper watershed	2.256×10^4	4.413×10^4
		14% etching	2.269×10^4	4.442×10^4
	2	0% etching	2.231×10^4	4.484×10^4
		3.5% etching	2.246×10^4	4.515×10^4
		7% etching	2.248×10^4	4.517×10^4
		7% etching with noise	2.250×10^4	4.509×10^4
		7%, no filling in upper watershed	2.248×10^4	4.513×10^4
		14% etching	2.259×10^4	4.537×10^4
ϕ	1	0% etching	0.000×10^0	0.000×10^0
		3.5% etching	0.000×10^0	0.000×10^0
		7% etching	0.000×10^0	0.000×10^0
		7% etching with noise	0.000×10^0	0.000×10^0
		7%, no filling in upper watershed	0.000×10^0	0.000×10^0
		14% etching	0.000×10^0	0.000×10^0
	2	0% etching	0.000×10^0	0.000×10^0
		3.5% etching	0.000×10^0	0.000×10^0
		7% etching	0.000×10^0	0.000×10^0
		7% etching with noise	0.000×10^0	0.000×10^0
		7%, no filling in upper watershed	0.000×10^0	0.000×10^0
		14% etching	0.000×10^0	0.000×10^0

Table B.20: Lowering History Sensitivity for Model 012, BasicThHy
South East Watershed Domain

Lowering History (Reference: History 1)	Initial Condition	μ^*	σ^*
2	0% etching	4.049×10^2	7.328×10^2
	3.5% etching	4.032×10^2	7.247×10^2
	7% etching	3.735×10^2	6.670×10^2
	7% etching with noise	3.762×10^2	6.760×10^2
	7%, no filling in upper watershed	3.777×10^2	6.800×10^2
	14% etching	3.574×10^2	6.428×10^2

Table B.21: Initial Condition Sensitivity for Model 012, BasicThHy
South East Watershed Domain

Initial Condition (Reference: 7% etch)	Lowering History	μ^*	σ^*
0% etching	1	1.898×10^2	2.491×10^2
	2	1.585×10^2	2.127×10^2
3.5% etching	1	7.449×10^1	9.495×10^1
	2	5.505×10^1	6.993×10^1
7% etching with noise	1	4.099×10^1	9.930×10^1
	2	3.499×10^1	9.401×10^1
7%, no filling in upper watershed	1	5.949×10^1	1.055×10^2
	2	6.617×10^1	1.291×10^2
14% etching	1	1.497×10^2	2.380×10^2
	2	1.341×10^2	2.419×10^2

Table B.22: Parameter Sensitivity for Model 014, BasicSsHy
South East Watershed Domain

Input	Lowering History	Initial Condition	μ^*	σ^*
D	1	0% etching	4.522×10^3	1.199×10^4
		3.5% etching	3.800×10^3	9.684×10^3
		7% etching	3.848×10^3	9.799×10^3
		7% etching with noise	3.916×10^3	9.974×10^3
		7%, no filling in upper watershed	3.772×10^3	9.562×10^3
		14% etching	3.924×10^3	9.954×10^3
	2	0% etching	4.608×10^3	1.220×10^4
		3.5% etching	4.720×10^3	1.248×10^4
		7% etching	4.803×10^3	1.271×10^4
		7% etching with noise	7.726×10^2	2.224×10^3
		7%, no filling in upper watershed	5.166×10^3	1.384×10^4
		14% etching	4.970×10^3	1.315×10^4
$\log_{10} K_{ss}$	1	0% etching	1.560×10^4	1.497×10^4
		3.5% etching	1.596×10^4	1.536×10^4
		7% etching	1.632×10^4	1.577×10^4
		7% etching with noise	1.605×10^4	1.559×10^4
		7%, no filling in upper watershed	1.800×10^4	1.704×10^4
		14% etching	1.705×10^4	1.632×10^4
	2	0% etching	1.591×10^4	1.528×10^4
		3.5% etching	1.630×10^4	1.569×10^4
		7% etching	1.665×10^4	1.609×10^4
		7% etching with noise	1.267×10^4	1.447×10^4
		7%, no filling in upper watershed	1.834×10^4	1.738×10^4
		14% etching	1.738×10^4	1.663×10^4
$\log_{10} V_c$	1	0% etching	2.200×10^3	6.956×10^3
		3.5% etching	2.264×10^3	7.158×10^3
		7% etching	2.328×10^3	7.359×10^3
		7% etching with noise	2.294×10^3	7.253×10^3
		7%, no filling in upper watershed	2.566×10^3	8.111×10^3
		14% etching	2.418×10^3	7.645×10^3
	2	0% etching	2.245×10^3	7.098×10^3
		3.5% etching	2.311×10^3	7.305×10^3
		7% etching	2.374×10^3	7.504×10^3
		7% etching with noise	2.339×10^3	7.395×10^3
		7%, no filling in upper watershed	2.614×10^3	8.263×10^3
		14% etching	2.462×10^3	7.782×10^3

Table B.22: (continued)

Input	Lowering History	Initial Condition	μ^*	σ^*
ϕ	1	0% etching	0.000×10^0	0.000×10^0
		3.5% etching	0.000×10^0	0.000×10^0
		7% etching	0.000×10^0	0.000×10^0
		7% etching with noise	0.000×10^0	0.000×10^0
		7%, no filling in upper watershed	0.000×10^0	0.000×10^0
		14% etching	0.000×10^0	0.000×10^0
	2	0% etching	0.000×10^0	0.000×10^0
		3.5% etching	0.000×10^0	0.000×10^0
		7% etching	0.000×10^0	0.000×10^0
		7% etching with noise	0.000×10^0	0.000×10^0
		7%, no filling in upper watershed	0.000×10^0	0.000×10^0
		14% etching	0.000×10^0	0.000×10^0

Table B.23: Lowering History Sensitivity for Model 014, BasicSsHy
South East Watershed Domain

Lowering History (Reference: History 1)	Initial Condition	μ^*	σ^*
2	0% etching	4.625×10^1	1.023×10^2
	3.5% etching	7.589×10^2	5.014×10^3
	7% etching	7.698×10^2	5.096×10^3
	7% etching with noise	1.154×10^3	5.744×10^3
	7%, no filling in upper watershed	8.008×10^2	5.301×10^3
	14% etching	7.879×10^2	5.231×10^3

Table B.24: Initial Condition Sensitivity for Model 014, BasicSsHy
South East Watershed Domain

Initial Condition (Reference: 7% etch)	Lowering History	μ^*	σ^*
0% etching	1	8.520×10^2	5.088×10^3
	2	1.318×10^2	2.203×10^2
3.5% etching	1	7.383×10^1	1.313×10^2
	2	6.171×10^1	1.073×10^2
7% etching with noise	1	4.053×10^1	8.256×10^1
	2	4.427×10^2	2.913×10^3
7%, no filling in upper watershed	1	2.701×10^2	5.101×10^2
	2	2.431×10^2	4.873×10^2
14% etching	1	1.425×10^2	2.135×10^2
	2	1.225×10^2	1.759×10^2

Table B.25: Parameter Sensitivity for Model 018, BasicDdHy
South East Watershed Domain

Input	Lowering History	Initial Condition	μ^*	σ^*
D	1	0% etching	9.414×10^1	2.036×10^2
		3.5% etching	9.467×10^1	2.026×10^2
		7% etching	8.499×10^1	1.934×10^2
		7% etching with noise	8.689×10^1	1.887×10^2
		7%, no filling in upper watershed	1.049×10^2	2.343×10^2
		14% etching	9.080×10^1	2.043×10^2
	2	0% etching	9.822×10^1	2.101×10^2
		3.5% etching	9.850×10^1	2.092×10^2
		7% etching	8.813×10^1	1.996×10^2
		7% etching with noise	8.994×10^1	1.945×10^2
		7%, no filling in upper watershed	1.083×10^2	2.407×10^2
		14% etching	9.401×10^1	2.109×10^2
$\log_{10} K$	1	0% etching	2.201×10^2	2.545×10^2
		3.5% etching	2.954×10^2	3.320×10^2
		7% etching	2.965×10^2	3.325×10^2
		7% etching with noise	2.921×10^2	3.285×10^2
		7%, no filling in upper watershed	2.639×10^2	2.915×10^2
		14% etching	2.735×10^2	3.039×10^2
	2	0% etching	2.306×10^2	2.663×10^2
		3.5% etching	3.084×10^2	3.458×10^2
		7% etching	3.093×10^2	3.460×10^2
		7% etching with noise	3.047×10^2	3.419×10^2
		7%, no filling in upper watershed	2.766×10^2	3.051×10^2
		14% etching	2.842×10^2	3.150×10^2
$\log_{10} V_c$	1	0% etching	8.353×10^0	1.636×10^1
		3.5% etching	1.123×10^1	2.044×10^1
		7% etching	1.206×10^1	2.228×10^1
		7% etching with noise	1.097×10^1	1.966×10^1
		7%, no filling in upper watershed	1.386×10^1	2.872×10^1
		14% etching	1.326×10^1	2.483×10^1
	2	0% etching	8.646×10^0	1.699×10^1
		3.5% etching	1.138×10^1	2.056×10^1
		7% etching	1.233×10^1	2.245×10^1
		7% etching with noise	1.122×10^1	1.996×10^1
		7%, no filling in upper watershed	1.404×10^1	2.870×10^1
		14% etching	1.356×10^1	2.530×10^1

Table B.25: (continued)

Input	Lowering History	Initial Condition	μ^*	σ^*
$\log_{10}\omega_c$	1	0% etching	1.344×10^2	3.058×10^2
		3.5% etching	1.519×10^2	3.351×10^2
		7% etching	1.595×10^2	3.464×10^2
		7% etching with noise	1.520×10^2	3.286×10^2
		7%, no filling in upper watershed	1.842×10^2	4.442×10^2
		14% etching	1.753×10^2	3.944×10^2
	2	0% etching	1.366×10^2	3.111×10^2
		3.5% etching	1.551×10^2	3.439×10^2
		7% etching	1.628×10^2	3.552×10^2
		7% etching with noise	1.550×10^2	3.368×10^2
		7%, no filling in upper watershed	1.875×10^2	4.535×10^2
		14% etching	1.787×10^2	4.042×10^2
ϕ	1	0% etching	0.000×10^0	0.000×10^0
		3.5% etching	0.000×10^0	0.000×10^0
		7% etching	0.000×10^0	0.000×10^0
		7% etching with noise	0.000×10^0	0.000×10^0
		7%, no filling in upper watershed	0.000×10^0	0.000×10^0
		14% etching	0.000×10^0	0.000×10^0
	2	0% etching	0.000×10^0	0.000×10^0
		3.5% etching	0.000×10^0	0.000×10^0
		7% etching	0.000×10^0	0.000×10^0
		7% etching with noise	0.000×10^0	0.000×10^0
		7%, no filling in upper watershed	0.000×10^0	0.000×10^0
		14% etching	0.000×10^0	0.000×10^0
b	1	0% etching	2.186×10^1	3.353×10^1
		3.5% etching	2.772×10^1	4.150×10^1
		7% etching	2.774×10^1	4.162×10^1
		7% etching with noise	2.722×10^1	4.075×10^1
		7%, no filling in upper watershed	2.550×10^1	3.764×10^1
		14% etching	2.425×10^1	3.620×10^1
	2	0% etching	2.341×10^1	3.584×10^1
		3.5% etching	2.946×10^1	4.392×10^1
		7% etching	2.965×10^1	4.417×10^1
		7% etching with noise	2.909×10^1	4.327×10^1
		7%, no filling in upper watershed	2.746×10^1	4.036×10^1
		14% etching	2.585×10^1	3.828×10^1

Table B.26: Lowering History Sensitivity for Model 018, BasicDdHy
South East Watershed Domain

Lowering History (Reference: History 1)	Initial Condition	μ^*	σ^*
2	0% etching	2.823×10^0	4.487×10^0
	3.5% etching	3.687×10^0	5.570×10^0
	7% etching	3.685×10^0	5.542×10^0
	7% etching with noise	3.633×10^0	5.472×10^0
	7%, no filling in upper watershed	3.641×10^0	5.479×10^0
	14% etching	3.039×10^0	4.621×10^0

Table B.27: Initial Condition Sensitivity for Model 018, BasicDdHy
South East Watershed Domain

Initial Condition (Reference: 7% etch)	Lowering History	μ^*	σ^*
0% etching	1	1.197×10^2	3.552×10^1
	2	1.205×10^2	3.672×10^1
3.5% etching	1	4.771×10^1	6.790×10^0
	2	4.774×10^1	7.121×10^0
7% etching with noise	1	2.214×10^0	3.840×10^0
	2	2.297×10^0	3.993×10^0
7%, no filling in upper watershed	1	1.521×10^1	3.150×10^1
	2	1.527×10^1	3.162×10^1
14% etching	1	7.904×10^1	1.795×10^1
	2	7.840×10^1	1.867×10^1

Table B.28: Parameter Sensitivity for Model 030, BasicHyFi
South East Watershed Domain

Input	Lowering History	Initial Condition	μ^*	σ^*
D	1	0% etching	7.362×10^2	9.734×10^2
		3.5% etching	6.208×10^2	1.004×10^3
		7% etching	6.266×10^2	1.016×10^3
		7% etching with noise	8.713×10^2	9.782×10^2
		7%, no filling in upper watershed	6.270×10^2	1.010×10^3
		14% etching	6.544×10^2	1.056×10^3
	2	0% etching	7.506×10^2	9.954×10^2
		3.5% etching	6.401×10^2	1.032×10^3
		7% etching	6.429×10^2	1.044×10^3
		7% etching with noise	7.627×10^2	1.027×10^3
		7%, no filling in upper watershed	6.447×10^2	1.038×10^3
		14% etching	6.703×10^2	1.082×10^3
F_f	1	0% etching	1.190×10^4	3.742×10^4
		3.5% etching	1.191×10^4	3.742×10^4
		7% etching	1.191×10^4	3.742×10^4
		7% etching with noise	3.188×10^2	5.243×10^2
		7%, no filling in upper watershed	2.292×10^2	4.868×10^2
		14% etching	1.192×10^4	3.744×10^4
	2	0% etching	6.062×10^1	1.740×10^2
		3.5% etching	1.196×10^4	3.758×10^4
		7% etching	1.196×10^4	3.758×10^4
		7% etching with noise	7.066×10^1	1.943×10^2
		7%, no filling in upper watershed	9.347×10^1	2.826×10^2
		14% etching	1.197×10^4	3.758×10^4
$\log_{10} K$	1	0% etching	4.965×10^4	4.777×10^4
		3.5% etching	5.028×10^4	4.803×10^4
		7% etching	5.073×10^4	4.812×10^4
		7% etching with noise	5.053×10^4	4.812×10^4
		7%, no filling in upper watershed	5.163×10^4	4.769×10^4
		14% etching	5.169×10^4	4.832×10^4
	2	0% etching	5.047×10^4	4.835×10^4
		3.5% etching	5.109×10^4	4.859×10^4
		7% etching	5.152×10^4	4.866×10^4
		7% etching with noise	5.131×10^4	4.866×10^4
		7%, no filling in upper watershed	5.242×10^4	4.823×10^4
		14% etching	5.243×10^4	4.883×10^4

Table B.28: (continued)

Input	Lowering History	Initial Condition	μ^*	σ^*
$\log_{10} V_c$	1	0% etching	3.637×10^4	5.678×10^4
		3.5% etching	3.621×10^4	5.690×10^4
		7% etching	3.620×10^4	5.690×10^4
		7% etching with noise	2.462×10^4	4.965×10^4
		7%, no filling in upper watershed	2.446×10^4	4.973×10^4
		14% etching	3.621×10^4	5.692×10^4
	2	0% etching	2.459×10^4	4.976×10^4
		3.5% etching	3.632×10^4	5.703×10^4
		7% etching	3.631×10^4	5.704×10^4
		7% etching with noise	2.455×10^4	4.977×10^4
		7%, no filling in upper watershed	2.438×10^4	4.986×10^4
		14% etching	2.442×10^4	4.985×10^4
ϕ	1	0% etching	0.000×10^0	0.000×10^0
		3.5% etching	0.000×10^0	0.000×10^0
		7% etching	0.000×10^0	0.000×10^0
		7% etching with noise	0.000×10^0	0.000×10^0
		7%, no filling in upper watershed	0.000×10^0	0.000×10^0
		14% etching	0.000×10^0	0.000×10^0
	2	0% etching	0.000×10^0	0.000×10^0
		3.5% etching	0.000×10^0	0.000×10^0
		7% etching	0.000×10^0	0.000×10^0
		7% etching with noise	0.000×10^0	0.000×10^0
		7%, no filling in upper watershed	0.000×10^0	0.000×10^0
		14% etching	1.189×10^4	3.761×10^4

Table B.29: Lowering History Sensitivity for Model 030, BasicHyFi
South East Watershed Domain

Lowering History (Reference: History 1)	Initial Condition	μ^*	σ^*
2	0% etching	1.126×10^3	7.794×10^3
	3.5% etching	1.176×10^2	2.941×10^2
	7% etching	1.134×10^2	2.818×10^2
	7% etching with noise	1.376×10^2	3.021×10^2
	7%, no filling in upper watershed	1.291×10^2	3.013×10^2
	14% etching	2.103×10^3	1.088×10^4

Table B.30: Initial Condition Sensitivity for Model 030, BasicHyFi
South East Watershed Domain

Initial Condition (Reference: 7% etch)	Lowering History	μ^*	σ^*
0% etching	1	2.030×10^2	3.276×10^2
	2	1.206×10^3	7.785×10^3
3.5% etching	1	8.028×10^1	1.359×10^2
	2	7.613×10^1	1.290×10^2
7% etching with noise	1	1.040×10^3	7.685×10^3
	2	1.045×10^3	7.800×10^3
7%, no filling in upper watershed	1	1.114×10^3	7.675×10^3
	2	1.129×10^3	7.796×10^3
14% etching	1	1.484×10^2	2.805×10^2
	2	2.156×10^3	1.092×10^4

Table B.31: Parameter Sensitivity for Model 040, BasicCh
South East Watershed Domain

Input	Lowering History	Initial Condition	μ^*	σ^*
D	1	0% etching	1.520×10^3	4.780×10^3
		3.5% etching	1.577×10^3	4.970×10^3
		7% etching	1.622×10^3	5.091×10^3
		7% etching with noise	1.584×10^3	4.975×10^3
		7%, no filling in upper watershed	1.783×10^3	5.596×10^3
		14% etching	1.697×10^3	5.294×10^3
	2	0% etching	1.552×10^3	4.887×10^3
		3.5% etching	1.610×10^3	5.081×10^3
		7% etching	1.654×10^3	5.202×10^3
		7% etching with noise	1.616×10^3	5.083×10^3
		7%, no filling in upper watershed	1.816×10^3	5.710×10^3
		14% etching	1.727×10^3	5.400×10^3
S_c	1	0% etching	1.025×10^3	3.224×10^3
		3.5% etching	1.050×10^3	3.306×10^3
		7% etching	1.056×10^3	3.329×10^3
		7% etching with noise	1.042×10^3	3.286×10^3
		7%, no filling in upper watershed	1.128×10^3	3.556×10^3
		14% etching	1.120×10^3	3.533×10^3
	2	0% etching	1.050×10^3	3.307×10^3
		3.5% etching	1.075×10^3	3.388×10^3
		7% etching	1.081×10^3	3.408×10^3
		7% etching with noise	1.066×10^3	3.361×10^3
		7%, no filling in upper watershed	1.154×10^3	3.639×10^3
		14% etching	1.143×10^3	3.607×10^3
$\log_{10} K$	1	0% etching	7.272×10^4	4.436×10^4
		3.5% etching	7.316×10^4	4.408×10^4
		7% etching	7.351×10^4	4.383×10^4
		7% etching with noise	7.335×10^4	4.405×10^4
		7%, no filling in upper watershed	7.430×10^4	4.240×10^4
		14% etching	7.416×10^4	4.326×10^4
	2	0% etching	7.332×10^4	4.439×10^4
		3.5% etching	7.375×10^4	4.410×10^4
		7% etching	7.408×10^4	4.384×10^4
		7% etching with noise	7.392×10^4	4.407×10^4
		7%, no filling in upper watershed	7.489×10^4	4.243×10^4
		14% etching	7.470×10^4	4.328×10^4

Table B.32: Lowering History Sensitivity for Model 040, BasicCh
South East Watershed Domain

Lowering History (Reference: History 1)	Initial Condition	μ^*	σ^*
2	0% etching	1.491×10^2	2.358×10^2
	3.5% etching	1.496×10^2	2.354×10^2
	7% etching	1.439×10^2	2.244×10^2
	7% etching with noise	1.431×10^2	2.244×10^2
	7%, no filling in upper watershed	1.478×10^2	2.334×10^2
	14% etching	1.365×10^2	2.126×10^2

Table B.33: Initial Condition Sensitivity for Model 040, BasicCh
South East Watershed Domain

Initial Condition (Reference: 7% etch)	Lowering History	μ^*	σ^*
0% etching	1	2.049×10^2	3.480×10^2
	2	1.993×10^2	3.488×10^2
3.5% etching	1	9.061×10^1	1.478×10^2
	2	8.487×10^1	1.451×10^2
7% etching with noise	1	5.382×10^1	1.034×10^2
	2	5.406×10^1	1.064×10^2
7%, no filling in upper watershed	1	3.182×10^2	6.001×10^2
	2	3.196×10^2	6.074×10^2
14% etching	1	1.914×10^2	3.170×10^2
	2	1.840×10^2	3.116×10^2

Table B.34: Parameter Sensitivity for Model 100, BasicSt
South East Watershed Domain

Input	Lowering History	Initial Condition	μ^*	σ^*
D	1	0% etching	2.841×10^3	7.060×10^3
		3.5% etching	2.840×10^3	7.364×10^3
		7% etching	2.912×10^3	7.613×10^3
		7% etching with noise	2.989×10^3	7.558×10^3
		7%, no filling in upper watershed	3.008×10^3	7.962×10^3
		14% etching	3.026×10^3	7.931×10^3
	2	0% etching	2.799×10^3	7.242×10^3
		3.5% etching	2.895×10^3	7.514×10^3
		7% etching	2.969×10^3	7.757×10^3
		7% etching with noise	2.970×10^3	7.730×10^3
		7%, no filling in upper watershed	3.044×10^3	8.118×10^3
		14% etching	3.079×10^3	8.067×10^3
F	1	0% etching	9.745×10^3	1.178×10^4
		3.5% etching	9.809×10^3	1.201×10^4
		7% etching	9.884×10^3	1.222×10^4
		7% etching with noise	9.875×10^3	1.216×10^4
		7%, no filling in upper watershed	1.003×10^4	1.260×10^4
		14% etching	9.944×10^3	1.254×10^4
	2	0% etching	9.804×10^3	1.245×10^4
		3.5% etching	9.872×10^3	1.265×10^4
		7% etching	9.942×10^3	1.283×10^4
		7% etching with noise	9.929×10^3	1.278×10^4
		7%, no filling in upper watershed	1.008×10^4	1.320×10^4
		14% etching	9.994×10^3	1.309×10^4
I_m	1	0% etching	1.524×10^4	2.437×10^4
		3.5% etching	1.535×10^4	2.474×10^4
		7% etching	1.539×10^4	2.501×10^4
		7% etching with noise	1.537×10^4	2.493×10^4
		7%, no filling in upper watershed	1.560×10^4	2.509×10^4
		14% etching	1.547×10^4	2.562×10^4
	2	0% etching	1.559×10^4	2.533×10^4
		3.5% etching	1.567×10^4	2.567×10^4
		7% etching	1.573×10^4	2.589×10^4
		7% etching with noise	1.572×10^4	2.580×10^4
		7%, no filling in upper watershed	1.592×10^4	2.597×10^4
		14% etching	1.577×10^4	2.643×10^4

Table B.34: (continued)

Input	Lowering History	Initial Condition	μ^*	σ^*
S_r	1	0% etching	3.850×10^2	5.954×10^2
		3.5% etching	3.778×10^2	5.952×10^2
		7% etching	3.785×10^2	5.942×10^2
		7% etching with noise	3.825×10^2	6.051×10^2
		7%, no filling in upper watershed	3.704×10^2	5.764×10^2
		14% etching	3.821×10^2	6.091×10^2
	2	0% etching	4.002×10^2	6.127×10^2
		3.5% etching	3.913×10^2	6.115×10^2
		7% etching	3.930×10^2	6.109×10^2
		7% etching with noise	3.974×10^2	6.221×10^2
		7%, no filling in upper watershed	3.847×10^2	5.934×10^2
		14% etching	3.941×10^2	6.241×10^2
$\log_{10} K_q$	1	0% etching	4.190×10^4	5.209×10^4
		3.5% etching	4.233×10^4	5.241×10^4
		7% etching	4.256×10^4	5.260×10^4
		7% etching with noise	4.243×10^4	5.254×10^4
		7%, no filling in upper watershed	4.281×10^4	5.246×10^4
		14% etching	4.316×10^4	5.307×10^4
	2	0% etching	4.355×10^4	5.423×10^4
		3.5% etching	4.393×10^4	5.446×10^4
		7% etching	4.410×10^4	5.458×10^4
		7% etching with noise	4.396×10^4	5.452×10^4
		7%, no filling in upper watershed	4.438×10^4	5.448×10^4
		14% etching	4.460×10^4	5.492×10^4
c	1	0% etching	1.432×10^2	3.780×10^2
		3.5% etching	1.418×10^2	3.740×10^2
		7% etching	1.372×10^2	3.553×10^2
		7% etching with noise	1.348×10^2	3.589×10^2
		7%, no filling in upper watershed	1.314×10^2	3.503×10^2
		14% etching	1.271×10^2	3.393×10^2
	2	0% etching	1.496×10^2	4.011×10^2
		3.5% etching	1.393×10^2	3.917×10^2
		7% etching	1.406×10^2	3.739×10^2
		7% etching with noise	1.373×10^2	3.782×10^2
		7%, no filling in upper watershed	1.337×10^2	3.690×10^2
		14% etching	1.291×10^2	3.558×10^2

Table B.34: (continued)

Input	Lowering History	Initial Condition	μ^*	σ^*
n_{ts}	1	0% etching	2.465×10^2	4.262×10^2
		3.5% etching	2.253×10^2	3.799×10^2
		7% etching	2.278×10^2	3.932×10^2
		7% etching with noise	2.387×10^2	4.185×10^2
		7%, no filling in upper watershed	1.988×10^2	3.204×10^2
		14% etching	1.664×10^2	2.621×10^2
	2	0% etching	1.965×10^2	3.338×10^2
		3.5% etching	1.708×10^2	2.865×10^2
		7% etching	1.828×10^2	3.089×10^2
		7% etching with noise	1.910×10^2	3.281×10^2
		7%, no filling in upper watershed	1.693×10^2	2.814×10^2
		14% etching	1.674×10^2	2.821×10^2
p_d	1	0% etching	4.847×10^3	7.966×10^3
		3.5% etching	4.865×10^3	8.102×10^3
		7% etching	4.880×10^3	8.214×10^3
		7% etching with noise	4.888×10^3	8.209×10^3
		7%, no filling in upper watershed	4.818×10^3	8.184×10^3
		14% etching	4.910×10^3	8.419×10^3
	2	0% etching	4.904×10^3	8.256×10^3
		3.5% etching	4.915×10^3	8.380×10^3
		7% etching	4.932×10^3	8.480×10^3
		7% etching with noise	4.945×10^3	8.477×10^3
		7%, no filling in upper watershed	4.859×10^3	8.448×10^3
		14% etching	4.957×10^3	8.666×10^3

Table B.35: Lowering History Sensitivity for Model 100, BasicSt
South East Watershed Domain

Lowering History (Reference: History 1)	Initial Condition	μ^*	σ^*
2	0% etching	5.939×10^2	8.539×10^2
	3.5% etching	5.693×10^2	8.116×10^2
	7% etching	5.532×10^2	7.898×10^2
	7% etching with noise	5.594×10^2	7.993×10^2
	7%, no filling in upper watershed	5.597×10^2	7.989×10^2
	14% etching	5.131×10^2	7.292×10^2

Table B.36: Initial Condition Sensitivity for Model 100, BasicSt
South East Watershed Domain

Initial Condition (Reference: 7% etch)	Lowering History	μ^*	σ^*
0% etching	1	3.334×10^2	4.285×10^2
	2	2.925×10^2	4.283×10^2
3.5% etching	1	1.388×10^2	1.823×10^2
	2	1.200×10^2	1.790×10^2
7% etching with noise	1	5.522×10^1	8.433×10^1
	2	4.912×10^1	7.939×10^1
7%, no filling in upper watershed	1	1.711×10^2	3.608×10^2
	2	1.701×10^2	3.647×10^2
14% etching	1	2.922×10^2	3.830×10^2
	2	2.540×10^2	3.722×10^2

Table B.37: Parameter Sensitivity for Model 102, BasicThSt
South East Watershed Domain

Input	Lowering History	Initial Condition	μ^*	σ^*
D	1	0% etching	8.296×10^2	1.860×10^3
		3.5% etching	8.208×10^2	1.795×10^3
		7% etching	8.209×10^2	1.795×10^3
		7% etching with noise	8.829×10^2	1.975×10^3
		7%, no filling in upper watershed	8.691×10^2	1.925×10^3
		14% etching	8.065×10^2	1.708×10^3
	2	0% etching	9.085×10^2	2.073×10^3
		3.5% etching	8.895×10^2	1.977×10^3
		7% etching	8.966×10^2	2.002×10^3
		7% etching with noise	9.729×10^2	2.227×10^3
		7%, no filling in upper watershed	9.516×10^2	2.150×10^3
		14% etching	8.823×10^2	1.905×10^3
F	1	0% etching	5.041×10^3	7.053×10^3
		3.5% etching	4.976×10^3	6.957×10^3
		7% etching	4.916×10^3	6.883×10^3
		7% etching with noise	4.929×10^3	6.896×10^3
		7%, no filling in upper watershed	5.062×10^3	7.097×10^3
		14% etching	4.783×10^3	6.720×10^3
	2	0% etching	5.250×10^3	7.647×10^3
		3.5% etching	5.169×10^3	7.510×10^3
		7% etching	5.109×10^3	7.414×10^3
		7% etching with noise	5.120×10^3	7.430×10^3
		7%, no filling in upper watershed	5.259×10^3	7.629×10^3
		14% etching	4.954×10^3	7.190×10^3
I_m	1	0% etching	8.099×10^3	2.069×10^4
		3.5% etching	8.226×10^3	2.116×10^4
		7% etching	8.338×10^3	2.155×10^4
		7% etching with noise	8.304×10^3	2.147×10^4
		7%, no filling in upper watershed	8.395×10^3	2.154×10^4
		14% etching	8.545×10^3	2.222×10^4
	2	0% etching	8.409×10^3	2.126×10^4
		3.5% etching	8.524×10^3	2.171×10^4
		7% etching	8.632×10^3	2.209×10^4
		7% etching with noise	8.601×10^3	2.202×10^4
		7%, no filling in upper watershed	8.688×10^3	2.209×10^4
		14% etching	8.820×10^3	2.273×10^4

Table B.37: (continued)

Input	Lowering History	Initial Condition	μ^*	σ^*
S_r	1	0% etching	9.709×10^2	1.460×10^3
		3.5% etching	9.372×10^2	1.399×10^3
		7% etching	9.023×10^2	1.362×10^3
		7% etching with noise	9.168×10^2	1.378×10^3
		7%, no filling in upper watershed	8.953×10^2	1.355×10^3
		14% etching	8.539×10^2	1.276×10^3
	2	0% etching	1.060×10^3	1.622×10^3
		3.5% etching	1.005×10^3	1.557×10^3
		7% etching	9.967×10^2	1.526×10^3
		7% etching with noise	1.008×10^3	1.540×10^3
		7%, no filling in upper watershed	9.906×10^2	1.525×10^3
		14% etching	9.364×10^2	1.423×10^3
$\log_{10} K_q$	1	0% etching	1.179×10^4	3.428×10^4
		3.5% etching	1.189×10^4	3.445×10^4
		7% etching	1.194×10^4	3.455×10^4
		7% etching with noise	1.190×10^4	3.453×10^4
		7%, no filling in upper watershed	1.214×10^4	3.453×10^4
		14% etching	1.213×10^4	3.478×10^4
	2	0% etching	1.226×10^4	3.571×10^4
		3.5% etching	1.234×10^4	3.582×10^4
		7% etching	1.238×10^4	3.587×10^4
		7% etching with noise	1.234×10^4	3.586×10^4
		7%, no filling in upper watershed	1.259×10^4	3.586×10^4
		14% etching	1.254×10^4	3.600×10^4
$\log_{10} \omega_c$	1	0% etching	3.034×10^4	4.894×10^4
		3.5% etching	3.058×10^4	4.932×10^4
		7% etching	3.067×10^4	4.947×10^4
		7% etching with noise	3.059×10^4	4.934×10^4
		7%, no filling in upper watershed	3.060×10^4	4.935×10^4
		14% etching	3.094×10^4	4.989×10^4
	2	0% etching	3.162×10^4	5.101×10^4
		3.5% etching	3.181×10^4	5.131×10^4
		7% etching	3.185×10^4	5.138×10^4
		7% etching with noise	3.176×10^4	5.123×10^4
		7%, no filling in upper watershed	3.179×10^4	5.126×10^4
		14% etching	3.203×10^4	5.165×10^4

Table B.37: (continued)

Input	Lowering History	Initial Condition	μ^*	σ^*
c	1	0% etching	8.691×10^1	1.702×10^2
		3.5% etching	7.973×10^1	1.725×10^2
		7% etching	8.523×10^1	1.746×10^2
		7% etching with noise	7.071×10^1	1.391×10^2
		7%, no filling in upper watershed	7.039×10^1	1.482×10^2
		14% etching	7.652×10^1	1.523×10^2
	2	0% etching	8.537×10^1	1.587×10^2
		3.5% etching	8.045×10^1	1.656×10^2
		7% etching	9.340×10^1	1.924×10^2
		7% etching with noise	7.036×10^1	1.313×10^2
		7%, no filling in upper watershed	7.142×10^1	1.438×10^2
		14% etching	7.310×10^1	1.368×10^2
n_{ts}	1	0% etching	3.439×10^2	5.581×10^2
		3.5% etching	3.353×10^2	5.321×10^2
		7% etching	3.094×10^2	4.681×10^2
		7% etching with noise	3.172×10^2	4.903×10^2
		7%, no filling in upper watershed	2.951×10^2	4.304×10^2
		14% etching	2.940×10^2	4.483×10^2
	2	0% etching	3.631×10^2	5.826×10^2
		3.5% etching	3.347×10^2	5.086×10^2
		7% etching	3.331×10^2	5.065×10^2
		7% etching with noise	3.418×10^2	5.304×10^2
		7%, no filling in upper watershed	3.135×10^2	4.577×10^2
		14% etching	3.091×10^2	4.688×10^2
p_d	1	0% etching	4.613×10^3	7.493×10^3
		3.5% etching	4.484×10^3	7.272×10^3
		7% etching	4.360×10^3	7.065×10^3
		7% etching with noise	4.411×10^3	7.156×10^3
		7%, no filling in upper watershed	4.247×10^3	6.904×10^3
		14% etching	4.136×10^3	6.707×10^3
	2	0% etching	4.965×10^3	8.070×10^3
		3.5% etching	4.823×10^3	7.826×10^3
		7% etching	4.677×10^3	7.579×10^3
		7% etching with noise	4.736×10^3	7.684×10^3
		7%, no filling in upper watershed	4.566×10^3	7.428×10^3
		14% etching	4.425×10^3	7.172×10^3

Table B.38: Lowering History Sensitivity for Model 102, BasicThSt
South East Watershed Domain

Lowering History (Reference: History 1)	Initial Condition	μ^*	σ^*
2	0% etching	4.664×10^2	8.437×10^2
	3.5% etching	4.515×10^2	8.120×10^2
	7% etching	4.358×10^2	7.833×10^2
	7% etching with noise	4.352×10^2	7.835×10^2
	7%, no filling in upper watershed	4.394×10^2	7.894×10^2
	14% etching	4.035×10^2	7.237×10^2

Table B.39: Initial Condition Sensitivity for Model 102, BasicThSt
South East Watershed Domain

Initial Condition (Reference: 7% etch)	Lowering History	μ^*	σ^*
0% etching	1	2.544×10^2	3.284×10^2
	2	2.236×10^2	3.114×10^2
3.5% etching	1	9.848×10^1	1.343×10^2
	2	8.328×10^1	1.273×10^2
7% etching with noise	1	4.094×10^1	7.409×10^1
	2	4.160×10^1	7.901×10^1
7%, no filling in upper watershed	1	9.422×10^1	1.991×10^2
	2	9.817×10^1	2.012×10^2
14% etching	1	2.316×10^2	3.063×10^2
	2	1.992×10^2	2.798×10^2

Table B.40: Parameter Sensitivity for Model 104, BasicSsSt
South East Watershed Domain

Input	Lowering History	Initial Condition	μ^*	σ^*
D	1	0% etching	3.941×10^2	9.529×10^2
		3.5% etching	4.099×10^2	9.308×10^2
		7% etching	4.117×10^2	8.800×10^2
		7% etching with noise	3.975×10^2	8.384×10^2
		7%, no filling in upper watershed	4.287×10^2	8.664×10^2
		14% etching	3.822×10^2	8.240×10^2
	2	0% etching	7.267×10^1	2.148×10^2
		3.5% etching	8.304×10^1	2.247×10^2
		7% etching	8.960×10^1	2.350×10^2
		7% etching with noise	8.753×10^1	2.304×10^2
		7%, no filling in upper watershed	9.409×10^1	2.492×10^2
		14% etching	1.064×10^2	2.724×10^2
F	1	0% etching	7.474×10^2	2.176×10^3
		3.5% etching	7.922×10^2	2.266×10^3
		7% etching	8.286×10^2	2.308×10^3
		7% etching with noise	8.134×10^2	2.268×10^3
		7%, no filling in upper watershed	8.909×10^2	2.545×10^3
		14% etching	8.348×10^2	2.409×10^3
	2	0% etching	7.512×10^2	2.225×10^3
		3.5% etching	8.011×10^2	2.318×10^3
		7% etching	8.125×10^2	2.370×10^3
		7% etching with noise	7.992×10^2	2.327×10^3
		7%, no filling in upper watershed	8.695×10^2	2.609×10^3
		14% etching	8.255×10^2	2.467×10^3
I_m	1	0% etching	1.890×10^2	2.788×10^2
		3.5% etching	1.719×10^2	2.903×10^2
		7% etching	1.865×10^2	3.056×10^2
		7% etching with noise	1.807×10^2	2.937×10^2
		7%, no filling in upper watershed	1.718×10^2	3.420×10^2
		14% etching	1.901×10^2	3.357×10^2
	2	0% etching	1.096×10^2	2.657×10^2
		3.5% etching	1.294×10^2	2.942×10^2
		7% etching	1.359×10^2	3.112×10^2
		7% etching with noise	1.324×10^2	3.022×10^2
		7%, no filling in upper watershed	1.444×10^2	3.504×10^2
		14% etching	1.443×10^2	3.440×10^2

Table B.40: (continued)

Input	Lowering History	Initial Condition	μ^*	σ^*
S_r	1	0% etching	2.667×10^1	3.585×10^1
		3.5% etching	2.542×10^1	3.362×10^1
		7% etching	2.821×10^1	4.208×10^1
		7% etching with noise	2.199×10^1	2.450×10^1
		7%, no filling in upper watershed	2.870×10^1	3.429×10^1
		14% etching	3.180×10^1	5.326×10^1
	2	0% etching	5.544×10^0	1.738×10^1
		3.5% etching	6.023×10^0	1.888×10^1
		7% etching	6.349×10^0	1.993×10^1
		7% etching with noise	6.210×10^0	1.950×10^1
		7%, no filling in upper watershed	7.208×10^0	2.265×10^1
		14% etching	7.044×10^0	2.214×10^1
$\log_{10} K_{q,ss}$	1	0% etching	6.755×10^4	5.666×10^4
		3.5% etching	6.787×10^4	5.676×10^4
		7% etching	6.811×10^4	5.686×10^4
		7% etching with noise	6.806×10^4	5.687×10^4
		7%, no filling in upper watershed	6.826×10^4	5.673×10^4
		14% etching	6.859×10^4	5.706×10^4
	2	0% etching	6.922×10^4	5.804×10^4
		3.5% etching	6.947×10^4	5.808×10^4
		7% etching	6.964×10^4	5.813×10^4
		7% etching with noise	6.960×10^4	5.814×10^4
		7%, no filling in upper watershed	6.980×10^4	5.801×10^4
		14% etching	6.999×10^4	5.822×10^4
c	1	0% etching	2.270×10^2	5.706×10^2
		3.5% etching	2.545×10^2	7.239×10^2
		7% etching	3.019×10^2	8.152×10^2
		7% etching with noise	2.199×10^2	6.197×10^2
		7%, no filling in upper watershed	2.112×10^2	5.725×10^2
		14% etching	2.748×10^2	7.070×10^2
	2	0% etching	2.619×10^2	7.716×10^2
		3.5% etching	2.564×10^2	7.469×10^2
		7% etching	2.577×10^2	7.475×10^2
		7% etching with noise	2.488×10^2	7.206×10^2
		7%, no filling in upper watershed	2.060×10^2	5.779×10^2
		14% etching	2.257×10^2	6.408×10^2

Table B.40: (continued)

Input	Lowering History	Initial Condition	μ^*	σ^*
n_{ts}	1	0% etching	4.233×10^{2}	1.049×10^{3}
		3.5% etching	4.052×10^{2}	1.028×10^{3}
		7% etching	4.015×10^{2}	9.974×10^{2}
		7% etching with noise	4.023×10^{2}	1.002×10^{3}
		7%, no filling in upper watershed	3.957×10^{2}	9.920×10^{2}
		14% etching	3.594×10^{2}	9.013×10^{2}
	2	0% etching	3.939×10^{-2}	1.163×10^{-1}
		3.5% etching	7.080×10^{-2}	2.148×10^{-1}
		7% etching	8.538×10^{-2}	2.598×10^{-1}
		7% etching with noise	6.991×10^{-2}	2.114×10^{-1}
		7%, no filling in upper watershed	5.321×10^{-2}	1.590×10^{-1}
		14% etching	8.756×10^{-2}	2.655×10^{-1}
p_d	1	0% etching	2.743×10^{1}	4.020×10^{1}
		3.5% etching	2.424×10^{1}	3.618×10^{1}
		7% etching	4.528×10^{1}	7.757×10^{1}
		7% etching with noise	5.099×10^{1}	8.535×10^{1}
		7%, no filling in upper watershed	3.486×10^{1}	5.434×10^{1}
		14% etching	3.608×10^{1}	5.889×10^{1}
	2	0% etching	5.836×10^{0}	1.778×10^{1}
		3.5% etching	8.301×10^{0}	2.550×10^{1}
		7% etching	8.243×10^{0}	2.523×10^{1}
		7% etching with noise	8.180×10^{0}	2.507×10^{1}
		7%, no filling in upper watershed	6.853×10^{0}	2.091×10^{1}
		14% etching	6.961×10^{0}	2.108×10^{1}

Table B.41: Lowering History Sensitivity for Model 104, BasicSsSt
South East Watershed Domain

Lowering History (Reference: History 1)	Initial Condition	μ^*	σ^*
2	0% etching	4.727×10^2	7.449×10^2
	3.5% etching	4.613×10^2	7.239×10^2
	7% etching	4.410×10^2	6.937×10^2
	7% etching with noise	4.396×10^2	6.931×10^2
	7%, no filling in upper watershed	4.412×10^2	6.941×10^2
	14% etching	4.085×10^2	6.416×10^2

Table B.42: Initial Condition Sensitivity for Model 104, BasicSsSt
South East Watershed Domain

Initial Condition (Reference: 7% etch)	Lowering History	μ^*	σ^*
0% etching	1	1.274×10^2	1.561×10^2
	2	9.550×10^1	1.532×10^2
3.5% etching	1	6.117×10^1	8.314×10^1
	2	4.045×10^1	6.776×10^1
7% etching with noise	1	1.404×10^1	2.934×10^1
	2	5.273×10^0	1.820×10^1
7%, no filling in upper watershed	1	5.099×10^1	1.335×10^2
	2	4.202×10^1	1.343×10^2
14% etching	1	1.153×10^2	1.900×10^2
	2	8.279×10^1	1.820×10^2

Table B.43: Parameter Sensitivity for Model 108, BasicDdSt
South East Watershed Domain

Input	Lowering History	Initial Condition	μ^*	σ^*
D	1	0% etching	5.993×10^0	9.468×10^0
		3.5% etching	6.415×10^0	1.075×10^1
		7% etching	1.347×10^2	4.013×10^2
		7% etching with noise	7.078×10^0	1.624×10^1
		7%, no filling in upper watershed	7.534×10^0	1.659×10^1
		14% etching	1.302×10^1	2.587×10^1
	2	0% etching	6.188×10^0	9.831×10^0
		3.5% etching	6.452×10^0	1.067×10^1
		7% etching	8.150×10^0	1.562×10^1
		7% etching with noise	8.038×10^0	1.582×10^1
		7%, no filling in upper watershed	7.507×10^0	1.637×10^1
		14% etching	1.306×10^1	2.568×10^1
F	1	0% etching	1.107×10^1	3.236×10^1
		3.5% etching	1.369×10^1	3.953×10^1
		7% etching	1.374×10^1	3.986×10^1
		7% etching with noise	1.288×10^2	4.038×10^2
		7%, no filling in upper watershed	1.217×10^1	3.501×10^1
		14% etching	1.249×10^1	3.623×10^1
	2	0% etching	1.580×10^2	4.607×10^2
		3.5% etching	1.508×10^2	4.293×10^2
		7% etching	1.422×10^1	4.125×10^1
		7% etching with noise	1.391×10^1	4.027×10^1
		7%, no filling in upper watershed	1.265×10^1	3.640×10^1
		14% etching	1.288×10^1	3.735×10^1
I_m	1	0% etching	4.076×10^1	9.287×10^1
		3.5% etching	5.192×10^1	1.166×10^2
		7% etching	5.152×10^1	1.167×10^2
		7% etching with noise	1.434×10^2	4.000×10^2
		7%, no filling in upper watershed	4.589×10^1	1.023×10^2
		14% etching	4.647×10^1	1.050×10^2
	2	0% etching	1.886×10^2	4.581×10^2
		3.5% etching	1.903×10^2	4.304×10^2
		7% etching	5.332×10^1	1.207×10^2
		7% etching with noise	5.230×10^1	1.182×10^2
		7%, no filling in upper watershed	4.768×10^1	1.063×10^2
		14% etching	1.569×10^2	3.456×10^2

Table B.43: (continued)

Input	Lowering History	Initial Condition	μ^*	σ^*
S_r	1	0% etching	1.400×10^{0}	4.194×10^{0}
		3.5% etching	1.802×10^{0}	5.399×10^{0}
		7% etching	1.607×10^{0}	4.993×10^{0}
		7% etching with noise	1.249×10^{2}	3.950×10^{2}
		7%, no filling in upper watershed	1.391×10^{0}	4.092×10^{0}
		14% etching	7.945×10^{-1}	2.164×10^{0}
	2	0% etching	1.310×10^{0}	3.901×10^{0}
		3.5% etching	1.726×10^{0}	5.138×10^{0}
		7% etching	1.582×10^{0}	4.646×10^{0}
		7% etching with noise	1.508×10^{0}	4.441×10^{0}
		7%, no filling in upper watershed	1.319×10^{0}	3.846×10^{0}
		14% etching	7.138×10^{-1}	1.897×10^{0}
$\log_{10} K_q$	1	0% etching	8.348×10^{1}	1.552×10^{2}
		3.5% etching	1.158×10^{2}	2.086×10^{2}
		7% etching	3.710×10^{2}	5.172×10^{2}
		7% etching with noise	3.055×10^{2}	5.195×10^{2}
		7%, no filling in upper watershed	9.980×10^{1}	1.629×10^{2}
		14% etching	1.130×10^{2}	1.806×10^{2}
	2	0% etching	8.639×10^{1}	1.615×10^{2}
		3.5% etching	1.195×10^{2}	2.158×10^{2}
		7% etching	1.226×10^{2}	2.159×10^{2}
		7% etching with noise	1.216×10^{2}	2.144×10^{2}
		7%, no filling in upper watershed	1.033×10^{2}	1.696×10^{2}
		14% etching	1.157×10^{2}	1.857×10^{2}
$\log_{10} \omega_c$	1	0% etching	3.600×10^{0}	7.659×10^{0}
		3.5% etching	5.409×10^{0}	1.176×10^{1}
		7% etching	1.345×10^{2}	4.014×10^{2}
		7% etching with noise	1.350×10^{2}	4.013×10^{2}
		7%, no filling in upper watershed	6.749×10^{0}	1.526×10^{1}
		14% etching	1.070×10^{1}	2.516×10^{1}
	2	0% etching	3.592×10^{0}	7.656×10^{0}
		3.5% etching	5.424×10^{0}	1.175×10^{1}
		7% etching	7.246×10^{0}	1.632×10^{1}
		7% etching with noise	7.434×10^{0}	1.672×10^{1}
		7%, no filling in upper watershed	6.748×10^{0}	1.526×10^{1}
		14% etching	1.069×10^{1}	2.515×10^{1}

Table B.43: (continued)

Input	Lowering History	Initial Condition	μ^*	σ^*
b	1	0% etching	1.763×10^{1}	4.832×10^{1}
		3.5% etching	2.257×10^{1}	6.021×10^{1}
		7% etching	1.507×10^{2}	4.022×10^{2}
		7% etching with noise	1.314×10^{2}	4.047×10^{2}
		7%, no filling in upper watershed	2.012×10^{1}	5.375×10^{1}
		14% etching	2.030×10^{1}	5.538×10^{1}
	2	0% etching	1.840×10^{1}	5.054×10^{1}
		3.5% etching	2.339×10^{1}	6.241×10^{1}
		7% etching	2.324×10^{1}	6.258×10^{1}
		7% etching with noise	2.263×10^{1}	6.088×10^{1}
		7%, no filling in upper watershed	2.091×10^{1}	5.585×10^{1}
		14% etching	2.094×10^{1}	5.712×10^{1}
c	1	0% etching	3.239×10^{0}	9.892×10^{0}
		3.5% etching	4.177×10^{0}	1.280×10^{1}
		7% etching	1.324×10^{2}	4.043×10^{2}
		7% etching with noise	1.277×10^{2}	4.035×10^{2}
		7%, no filling in upper watershed	3.830×10^{0}	1.166×10^{1}
		14% etching	3.950×10^{0}	1.193×10^{1}
	2	0% etching	3.364×10^{0}	1.028×10^{1}
		3.5% etching	4.319×10^{0}	1.324×10^{1}
		7% etching	4.288×10^{0}	1.308×10^{1}
		7% etching with noise	4.148×10^{0}	1.265×10^{1}
		7%, no filling in upper watershed	3.964×10^{0}	1.208×10^{1}
		14% etching	4.062×10^{0}	1.227×10^{1}
n_{ts}	1	0% etching	3.681×10^{-1}	1.086×10^{0}
		3.5% etching	4.670×10^{-1}	1.381×10^{0}
		7% etching	4.341×10^{-1}	1.281×10^{0}
		7% etching with noise	4.719×10^{2}	6.186×10^{2}
		7%, no filling in upper watershed	3.233×10^{-1}	9.302×10^{-1}
		14% etching	3.652×10^{-1}	1.047×10^{0}
	2	0% etching	2.406×10^{-1}	6.837×10^{-1}
		3.5% etching	1.369×10^{2}	4.316×10^{2}
		7% etching	3.307×10^{-1}	9.449×10^{-1}
		7% etching with noise	3.343×10^{-1}	9.586×10^{-1}
		7%, no filling in upper watershed	2.309×10^{-1}	6.372×10^{-1}
		14% etching	1.093×10^{2}	3.446×10^{2}

Table B.43: (continued)

Input	Lowering History	Initial Condition	μ^*	σ^*
p_d	1	0% etching	4.613×10^0	9.089×10^0
		3.5% etching	6.756×10^0	1.293×10^1
		7% etching	5.629×10^0	1.270×10^1
		7% etching with noise	3.821×10^2	6.121×10^2
		7%, no filling in upper watershed	8.524×10^0	1.869×10^1
		14% etching	4.797×10^0	7.767×10^0
	2	0% etching	4.778×10^0	9.504×10^0
		3.5% etching	6.746×10^0	1.269×10^1
		7% etching	6.627×10^0	1.244×10^1
		7% etching with noise	7.231×10^0	1.424×10^1
		7%, no filling in upper watershed	8.668×10^0	1.890×10^1
		14% etching	5.091×10^0	8.397×10^0

Table B.44: Lowering History Sensitivity for Model 108, BasicDdSt
South East Watershed Domain

Lowering History (Reference: History 1)	Initial Condition	μ^*	σ^*
2	0% etching	7.483×10^{0}	7.045×10^{1}
	3.5% etching	1.352×10^{1}	9.245×10^{1}
	7% etching	1.062×10^{2}	2.388×10^{2}
	7% etching with noise	1.495×10^{2}	2.583×10^{2}
	7%, no filling in upper watershed	9.256×10^{-1}	2.426×10^{0}
	14% etching	5.765×10^{0}	5.242×10^{1}

Table B.45: Initial Condition Sensitivity for Model 108, BasicDdSt
South East Watershed Domain

Initial Condition (Reference: 7% etch)	Lowering History	μ^*	σ^*
0% etching	1	2.066×10^{2}	2.378×10^{2}
	2	1.064×10^{2}	5.598×10^{1}
3.5% etching	1	1.518×10^{2}	2.395×10^{2}
	2	5.719×10^{1}	7.994×10^{1}
7% etching with noise	1	1.146×10^{2}	2.310×10^{2}
	2	5.700×10^{-1}	1.344×10^{0}
7%, no filling in upper watershed	1	1.094×10^{2}	2.365×10^{2}
	2	4.965×10^{0}	1.091×10^{1}
14% etching	1	1.622×10^{2}	1.749×10^{2}
	2	9.069×10^{1}	5.382×10^{1}

Table B.46: Parameter Sensitivity for Model 110, BasicHySt
South East Watershed Domain

Input	Lowering History	Initial Condition	μ^*	σ^*
D	1	0% etching	1.502×10^3	3.901×10^3
		3.5% etching	1.570×10^3	4.022×10^3
		7% etching	1.536×10^3	3.896×10^3
		7% etching with noise	1.423×10^3	4.081×10^3
		7%, no filling in upper watershed	1.524×10^3	3.822×10^3
		14% etching	1.525×10^3	3.794×10^3
	2	0% etching	1.555×10^3	4.046×10^3
		3.5% etching	1.704×10^3	4.421×10^3
		7% etching	1.598×10^3	4.069×10^3
		7% etching with noise	1.627×10^3	4.161×10^3
		7%, no filling in upper watershed	1.625×10^3	4.118×10^3
		14% etching	1.568×10^3	3.907×10^3
F	1	0% etching	1.144×10^2	2.809×10^2
		3.5% etching	1.338×10^2	2.991×10^2
		7% etching	1.415×10^2	3.175×10^2
		7% etching with noise	1.173×10^2	3.144×10^2
		7%, no filling in upper watershed	1.553×10^2	3.417×10^2
		14% etching	1.517×10^2	3.370×10^2
	2	0% etching	1.197×10^2	2.889×10^2
		3.5% etching	1.399×10^2	3.122×10^2
		7% etching	1.480×10^2	3.307×10^2
		7% etching with noise	2.387×10^2	6.431×10^2
		7%, no filling in upper watershed	1.618×10^2	3.550×10^2
		14% etching	1.583×10^2	3.508×10^2
I_m	1	0% etching	5.248×10^3	9.849×10^3
		3.5% etching	1.670×10^4	3.607×10^4
		7% etching	1.670×10^4	3.641×10^4
		7% etching with noise	2.772×10^3	8.315×10^3
		7%, no filling in upper watershed	5.112×10^3	9.442×10^3
		14% etching	2.407×10^4	4.367×10^4
	2	0% etching	2.841×10^4	4.826×10^4
		3.5% etching	1.699×10^4	3.721×10^4
		7% etching	1.642×10^4	3.661×10^4
		7% etching with noise	5.123×10^3	9.996×10^3
		7%, no filling in upper watershed	1.688×10^4	3.717×10^4
		14% etching	2.828×10^4	4.838×10^4

Table B.46: (continued)

Input	Lowering History	Initial Condition	μ^*	σ^*
S_r	1	0% etching	2.355×10^4	4.901×10^4
		3.5% etching	2.844×10^2	5.248×10^2
		7% etching	2.316×10^2	4.161×10^2
		7% etching with noise	2.347×10^4	4.918×10^4
		7%, no filling in upper watershed	1.198×10^4	3.688×10^4
		14% etching	1.198×10^4	3.705×10^4
	2	0% etching	1.222×10^4	3.780×10^4
		3.5% etching	2.508×10^2	5.098×10^2
		7% etching	1.219×10^4	3.776×10^4
		7% etching with noise	1.230×10^4	3.774×10^4
		7%, no filling in upper watershed	2.671×10^2	5.403×10^2
		14% etching	1.221×10^4	3.778×10^4
$\log_{10} K_q$	1	0% etching	4.108×10^4	5.205×10^4
		3.5% etching	5.287×10^4	5.491×10^4
		7% etching	4.179×10^4	5.256×10^4
		7% etching with noise	1.872×10^4	3.870×10^4
		7%, no filling in upper watershed	5.356×10^4	5.474×10^4
		14% etching	3.079×10^4	4.716×10^4
	2	0% etching	4.230×10^4	5.362×10^4
		3.5% etching	4.262×10^4	5.375×10^4
		7% etching	1.939×10^4	3.756×10^4
		7% etching with noise	4.255×10^4	5.392×10^4
		7%, no filling in upper watershed	5.489×10^4	5.610×10^4
		14% etching	3.153×10^4	4.831×10^4
$\log_{10} V$	1	0% etching	1.636×10^4	3.692×10^4
		3.5% etching	5.886×10^3	1.266×10^4
		7% etching	5.840×10^3	1.258×10^4
		7% etching with noise	8.182×10^2	2.549×10^3
		7%, no filling in upper watershed	6.159×10^3	1.248×10^4
		14% etching	4.919×10^3	1.268×10^4
	2	0% etching	1.699×10^4	3.831×10^4
		3.5% etching	6.038×10^3	1.318×10^4
		7% etching	1.600×10^4	3.521×10^4
		7% etching with noise	1.686×10^4	3.815×10^4
		7%, no filling in upper watershed	6.114×10^3	1.281×10^4
		14% etching	1.604×10^4	3.544×10^4

Table B.46: (continued)

Input	Lowering History	Initial Condition	μ^*	σ^*
ϕ	1	0% etching	0.000×10^0	0.000×10^0
		3.5% etching	0.000×10^0	0.000×10^0
		7% etching	0.000×10^0	0.000×10^0
		7% etching with noise	4.155×10^3	1.314×10^4
		7%, no filling in upper watershed	0.000×10^0	0.000×10^0
		14% etching	0.000×10^0	0.000×10^0
	2	0% etching	0.000×10^0	0.000×10^0
		3.5% etching	0.000×10^0	0.000×10^0
		7% etching	0.000×10^0	0.000×10^0
		7% etching with noise	0.000×10^0	0.000×10^0
		7%, no filling in upper watershed	0.000×10^0	0.000×10^0
		14% etching	0.000×10^0	0.000×10^0
c	1	0% etching	1.244×10^4	3.659×10^4
		3.5% etching	1.254×10^4	3.667×10^4
		7% etching	1.239×10^4	3.678×10^4
		7% etching with noise	2.355×10^4	4.914×10^4
		7%, no filling in upper watershed	8.118×10^2	2.189×10^3
		14% etching	2.417×10^4	4.902×10^4
	2	0% etching	8.287×10^2	2.354×10^3
		3.5% etching	1.280×10^4	3.762×10^4
		7% etching	1.282×10^4	3.763×10^4
		7% etching with noise	1.272×10^4	3.764×10^4
		7%, no filling in upper watershed	1.281×10^4	3.763×10^4
		14% etching	2.468×10^4	5.015×10^4
n_{ts}	1	0% etching	1.969×10^2	4.414×10^2
		3.5% etching	1.785×10^2	4.001×10^2
		7% etching	1.194×10^4	3.683×10^4
		7% etching with noise	5.626×10^3	1.719×10^4
		7%, no filling in upper watershed	2.838×10^2	7.315×10^2
		14% etching	2.765×10^2	7.346×10^2
	2	0% etching	1.633×10^2	3.690×10^2
		3.5% etching	1.215×10^4	3.777×10^4
		7% etching	1.214×10^4	3.779×10^4
		7% etching with noise	1.857×10^2	4.397×10^2
		7%, no filling in upper watershed	2.270×10^2	5.690×10^2
		14% etching	1.225×10^4	3.775×10^4

Table B.46: (continued)

Input	Lowering History	Initial Condition	μ^*	σ^*
p_d	1	0% etching	4.292×10^3	8.388×10^3
		3.5% etching	4.138×10^3	8.352×10^3
		7% etching	4.167×10^3	8.324×10^3
		7% etching with noise	2.632×10^4	4.839×10^4
		7%, no filling in upper watershed	1.555×10^4	3.611×10^4
		14% etching	3.382×10^3	8.454×10^3
	2	0% etching	4.080×10^3	8.655×10^3
		3.5% etching	2.668×10^4	4.801×10^4
		7% etching	2.672×10^4	4.817×10^4
		7% etching with noise	1.562×10^4	3.734×10^4
		7%, no filling in upper watershed	3.863×10^3	8.349×10^3
		14% etching	2.588×10^4	4.754×10^4

Table B.47: Lowering History Sensitivity for Model 110, BasicHySt
South East Watershed Domain

Lowering History (Reference: History 1)	Initial Condition	μ^*	σ^*
2	0% etching	2.966×10^3	1.238×10^4
	3.5% etching	2.435×10^3	1.110×10^4
	7% etching	4.515×10^3	1.536×10^4
	7% etching with noise	6.206×10^3	1.674×10^4
	7%, no filling in upper watershed	1.935×10^3	9.681×10^3
	14% etching	3.920×10^3	1.436×10^4

Table B.48: Initial Condition Sensitivity for Model 110, BasicHySt
South East Watershed Domain

Initial Condition (Reference: 7% etch)	Lowering History	μ^*	σ^*
0% etching	1	2.828×10^3	1.202×10^4
	2	3.431×10^3	1.350×10^4
3.5% etching	1	1.154×10^3	7.853×10^3
	2	3.370×10^3	1.374×10^4
7% etching with noise	1	7.490×10^3	1.831×10^4
	2	4.968×10^3	1.642×10^4
7%, no filling in upper watershed	1	1.711×10^3	9.581×10^3
	2	4.483×10^3	1.570×10^4
14% etching	1	4.367×10^3	1.504×10^4
	2	4.000×10^3	1.476×10^4

Table B.49: Parameter Sensitivity for Model 200, BasicVs
South East Watershed Domain

Input	Lowering History	Initial Condition	μ^*	σ^*
D	1	0% etching	1.652×10^4	2.458×10^4
		3.5% etching	1.675×10^4	2.470×10^4
		7% etching	1.689×10^4	2.479×10^4
		7% etching with noise	1.694×10^4	2.505×10^4
		7%, no filling in upper watershed	1.675×10^4	2.469×10^4
		14% etching	1.733×10^4	2.520×10^4
	2	0% etching	1.725×10^4	2.563×10^4
		3.5% etching	1.746×10^4	2.575×10^4
		7% etching	1.762×10^4	2.582×10^4
		7% etching with noise	1.761×10^4	2.603×10^4
		7%, no filling in upper watershed	1.741×10^4	2.565×10^4
		14% etching	1.795×10^4	2.612×10^4
H_{init}	1	0% etching	1.362×10^3	1.978×10^3
		3.5% etching	1.401×10^3	2.025×10^3
		7% etching	1.431×10^3	2.027×10^3
		7% etching with noise	1.372×10^3	1.957×10^3
		7%, no filling in upper watershed	1.625×10^3	2.294×10^3
		14% etching	1.535×10^3	2.169×10^3
	2	0% etching	1.432×10^3	2.075×10^3
		3.5% etching	1.481×10^3	2.142×10^3
		7% etching	1.504×10^3	2.125×10^3
		7% etching with noise	1.440×10^3	2.049×10^3
		7%, no filling in upper watershed	1.705×10^3	2.404×10^3
		14% etching	1.617×10^3	2.297×10^3
K_{sat}	1	0% etching	8.091×10^3	1.090×10^4
		3.5% etching	8.283×10^3	1.126×10^4
		7% etching	8.410×10^3	1.143×10^4
		7% etching with noise	8.264×10^3	1.134×10^4
		7%, no filling in upper watershed	8.761×10^3	1.170×10^4
		14% etching	8.553×10^3	1.167×10^4
	2	0% etching	8.455×10^3	1.146×10^4
		3.5% etching	8.625×10^3	1.177×10^4
		7% etching	8.842×10^3	1.212×10^4
		7% etching with noise	8.598×10^3	1.184×10^4
		7%, no filling in upper watershed	9.115×10^3	1.222×10^4
		14% etching	8.893×10^3	1.218×10^4

Table B.49: (continued)

Input	Lowering History	Initial Condition	μ^*	σ^*
R_m	1	0% etching	8.372×10^3	1.175×10^4
		3.5% etching	8.359×10^3	1.171×10^4
		7% etching	8.365×10^3	1.173×10^4
		7% etching with noise	8.199×10^3	1.166×10^4
		7%, no filling in upper watershed	8.632×10^3	1.167×10^4
		14% etching	8.441×10^3	1.182×10^4
	2	0% etching	8.670×10^3	1.224×10^4
		3.5% etching	8.619×10^3	1.216×10^4
		7% etching	8.639×10^3	1.217×10^4
		7% etching with noise	8.473×10^3	1.211×10^4
		7%, no filling in upper watershed	8.919×10^3	1.213×10^4
		14% etching	8.732×10^3	1.224×10^4
$\log_{10} K$	1	0% etching	3.128×10^4	3.133×10^4
		3.5% etching	3.144×10^4	3.135×10^4
		7% etching	3.148×10^4	3.137×10^4
		7% etching with noise	3.093×10^4	3.155×10^4
		7%, no filling in upper watershed	3.083×10^4	3.148×10^4
		14% etching	3.179×10^4	3.138×10^4
	2	0% etching	3.281×10^4	3.278×10^4
		3.5% etching	3.295×10^4	3.281×10^4
		7% etching	3.288×10^4	3.270×10^4
		7% etching with noise	3.233×10^4	3.291×10^4
		7%, no filling in upper watershed	3.222×10^4	3.288×10^4
		14% etching	3.305×10^4	3.259×10^4

Table B.50: Lowering History Sensitivity for Model 200, BasicVs
South East Watershed Domain

Lowering History (Reference: History 1)	Initial Condition	μ^*	σ^*
2	0% etching	3.671×10^2	5.174×10^2
	3.5% etching	3.576×10^2	5.041×10^2
	7% etching	3.441×10^2	4.884×10^2
	7% etching with noise	3.334×10^2	4.725×10^2
	7%, no filling in upper watershed	3.307×10^2	4.753×10^2
	14% etching	3.092×10^2	4.321×10^2

Table B.51: Initial Condition Sensitivity for Model 200, BasicVs
South East Watershed Domain

Initial Condition (Reference: 7% etch)	Lowering History	μ^*	σ^*
0% etching	1	1.816×10^2	1.962×10^2
	2	1.945×10^2	2.100×10^2
3.5% etching	1	7.989×10^1	8.775×10^1
	2	8.929×10^1	1.009×10^2
7% etching with noise	1	1.706×10^2	1.911×10^2
	2	1.833×10^2	2.003×10^2
7%, no filling in upper watershed	1	2.740×10^2	3.937×10^2
	2	2.910×10^2	4.472×10^2
14% etching	1	1.473×10^2	1.575×10^2
	2	1.468×10^2	1.446×10^2

Table B.52: Parameter Sensitivity for Model 202, BasicThVs South East Watershed Domain

Input	Lowering History	Initial Condition	μ^*	σ^*
D	1	0% etching	9.296×10^2	1.829×10^3
		3.5% etching	9.446×10^2	1.874×10^3
		7% etching	9.510×10^2	1.866×10^3
		7% etching with noise	9.409×10^2	1.830×10^3
		7%, no filling in upper watershed	9.876×10^2	1.987×10^3
		14% etching	9.635×10^2	1.906×10^3
	2	0% etching	9.632×10^2	1.872×10^3
		3.5% etching	9.703×10^2	1.912×10^3
		7% etching	1.001×10^3	1.946×10^3
		7% etching with noise	9.743×10^2	1.880×10^3
		7%, no filling in upper watershed	1.004×10^3	2.035×10^3
		14% etching	9.993×10^2	1.981×10^3
H_{init}	1	0% etching	1.815×10^3	3.481×10^3
		3.5% etching	1.794×10^3	3.425×10^3
		7% etching	1.809×10^3	3.384×10^3
		7% etching with noise	1.745×10^3	3.257×10^3
		7%, no filling in upper watershed	1.907×10^3	3.573×10^3
		14% etching	1.805×10^3	3.309×10^3
	2	0% etching	1.859×10^3	3.502×10^3
		3.5% etching	1.833×10^3	3.447×10^3
		7% etching	1.853×10^3	3.411×10^3
		7% etching with noise	1.762×10^3	3.252×10^3
		7%, no filling in upper watershed	1.947×10^3	3.606×10^3
		14% etching	1.842×10^3	3.359×10^3
K_{sat}	1	0% etching	2.761×10^3	5.377×10^3
		3.5% etching	2.748×10^3	5.342×10^3
		7% etching	2.678×10^3	5.278×10^3
		7% etching with noise	2.617×10^3	5.280×10^3
		7%, no filling in upper watershed	2.840×10^3	5.645×10^3
		14% etching	2.659×10^3	5.150×10^3
	2	0% etching	2.881×10^3	5.690×10^3
		3.5% etching	2.836×10^3	5.576×10^3
		7% etching	2.781×10^3	5.471×10^3
		7% etching with noise	2.723×10^3	5.485×10^3
		7%, no filling in upper watershed	2.940×10^3	5.831×10^3
		14% etching	2.662×10^3	5.098×10^3

Table B.52: (continued)

Input	Lowering History	Initial Condition	μ^*	σ^*
R_m	1	0% etching	8.739×10^3	1.641×10^4
		3.5% etching	8.746×10^3	1.644×10^4
		7% etching	8.729×10^3	1.640×10^4
		7% etching with noise	8.581×10^3	1.648×10^4
		7%, no filling in upper watershed	8.781×10^3	1.618×10^4
		14% etching	8.687×10^3	1.630×10^4
	2	0% etching	8.948×10^3	1.684×10^4
		3.5% etching	8.951×10^3	1.682×10^4
		7% etching	8.958×10^3	1.679×10^4
		7% etching with noise	8.808×10^3	1.685×10^4
		7%, no filling in upper watershed	9.015×10^3	1.657×10^4
		14% etching	8.912×10^3	1.666×10^4
$\log_{10} K$	1	0% etching	3.353×10^4	4.184×10^4
		3.5% etching	3.349×10^4	4.175×10^4
		7% etching	3.343×10^4	4.165×10^4
		7% etching with noise	3.313×10^4	4.166×10^4
		7%, no filling in upper watershed	3.303×10^4	4.151×10^4
		14% etching	3.326×10^4	4.135×10^4
	2	0% etching	3.510×10^4	4.365×10^4
		3.5% etching	3.496×10^4	4.343×10^4
		7% etching	3.488×10^4	4.330×10^4
		7% etching with noise	3.453×10^4	4.329×10^4
		7%, no filling in upper watershed	3.441×10^4	4.314×10^4
		14% etching	3.455×10^4	4.285×10^4
$\log_{10} \omega_c$	1	0% etching	4.477×10^3	6.116×10^3
		3.5% etching	4.494×10^3	6.129×10^3
		7% etching	4.548×10^3	6.141×10^3
		7% etching with noise	4.433×10^3	5.998×10^3
		7%, no filling in upper watershed	4.835×10^3	6.267×10^3
		14% etching	4.659×10^3	6.213×10^3
	2	0% etching	4.733×10^3	6.416×10^3
		3.5% etching	4.770×10^3	6.433×10^3
		7% etching	4.826×10^3	6.451×10^3
		7% etching with noise	4.702×10^3	6.319×10^3
		7%, no filling in upper watershed	5.126×10^3	6.569×10^3
		14% etching	5.025×10^3	6.543×10^3

Table B.53: Lowering History Sensitivity for Model 202, BasicThVs
South East Watershed Domain

Lowering History (Reference: History 1)	Initial Condition	μ^*	σ^*
2	0% etching	4.389×10^2	7.676×10^2
	3.5% etching	4.132×10^2	7.265×10^2
	7% etching	3.995×10^2	7.020×10^2
	7% etching with noise	3.930×10^2	6.981×10^2
	7%, no filling in upper watershed	3.889×10^2	7.001×10^2
	14% etching	3.549×10^2	6.408×10^2

Table B.54: Initial Condition Sensitivity for Model 202, BasicThVs
South East Watershed Domain

Initial Condition (Reference: 7% etch)	Lowering History	μ^*	σ^*
0% etching	1	1.545×10^2	1.239×10^2
	2	1.886×10^2	1.555×10^2
3.5% etching	1	6.982×10^1	6.110×10^1
	2	8.075×10^1	7.019×10^1
7% etching with noise	1	1.096×10^2	1.720×10^2
	2	1.177×10^2	1.827×10^2
7%, no filling in upper watershed	1	1.690×10^2	2.443×10^2
	2	1.739×10^2	2.540×10^2
14% etching	1	1.241×10^2	9.364×10^1
	2	1.666×10^2	1.498×10^2

Table B.55: Parameter Sensitivity for Model 204, BasicSsVs
South East Watershed Domain

Input	Lowering History	Initial Condition	μ^*	σ^*
D	1	0% etching	1.465×10^4	3.018×10^4
		3.5% etching	1.472×10^4	3.024×10^4
		7% etching	1.475×10^4	3.039×10^4
		7% etching with noise	1.477×10^4	3.042×10^4
		7%, no filling in upper watershed	1.468×10^4	3.019×10^4
		14% etching	1.485×10^4	3.059×10^4
	2	0% etching	1.520×10^4	3.130×10^4
		3.5% etching	1.532×10^4	3.152×10^4
		7% etching	1.527×10^4	3.144×10^4
		7% etching with noise	1.558×10^4	3.204×10^4
		7%, no filling in upper watershed	1.539×10^4	3.162×10^4
		14% etching	1.530×10^4	3.153×10^4
H_{init}	1	0% etching	4.067×10^3	5.055×10^3
		3.5% etching	4.022×10^3	4.959×10^3
		7% etching	4.164×10^3	5.310×10^3
		7% etching with noise	4.169×10^3	5.348×10^3
		7%, no filling in upper watershed	4.365×10^3	5.462×10^3
		14% etching	4.270×10^3	5.372×10^3
	2	0% etching	4.278×10^3	5.267×10^3
		3.5% etching	4.269×10^3	5.282×10^3
		7% etching	4.295×10^3	5.433×10^3
		7% etching with noise	4.320×10^3	5.538×10^3
		7%, no filling in upper watershed	4.595×10^3	5.753×10^3
		14% etching	4.373×10^3	5.549×10^3
K_{sat}	1	0% etching	8.750×10^3	1.844×10^4
		3.5% etching	8.926×10^3	1.866×10^4
		7% etching	8.972×10^3	1.923×10^4
		7% etching with noise	9.075×10^3	1.929×10^4
		7%, no filling in upper watershed	9.401×10^3	1.999×10^4
		14% etching	9.248×10^3	1.988×10^4
	2	0% etching	9.227×10^3	1.933×10^4
		3.5% etching	9.239×10^3	1.964×10^4
		7% etching	9.518×10^3	2.006×10^4
		7% etching with noise	9.327×10^3	2.025×10^4
		7%, no filling in upper watershed	9.745×10^3	2.091×10^4
		14% etching	9.734×10^3	2.067×10^4

Table B.55: (continued)

Input	Lowering History	Initial Condition	μ^*	σ^*
R_m	1	0% etching	8.975×10^3	1.367×10^4
		3.5% etching	9.065×10^3	1.390×10^4
		7% etching	8.991×10^3	1.382×10^4
		7% etching with noise	8.831×10^3	1.370×10^4
		7%, no filling in upper watershed	9.537×10^3	1.481×10^4
		14% etching	9.128×10^3	1.391×10^4
	2	0% etching	9.396×10^3	1.445×10^4
		3.5% etching	9.362×10^3	1.457×10^4
		7% etching	9.402×10^3	1.465×10^4
		7% etching with noise	9.161×10^3	1.437×10^4
		7%, no filling in upper watershed	9.902×10^3	1.566×10^4
		14% etching	9.399×10^3	1.456×10^4
$\log_{10} K_{ss}$	1	0% etching	3.911×10^4	3.562×10^4
		3.5% etching	3.941×10^4	3.616×10^4
		7% etching	3.941×10^4	3.623×10^4
		7% etching with noise	3.907×10^4	3.613×10^4
		7%, no filling in upper watershed	3.890×10^4	3.651×10^4
		14% etching	3.971×10^4	3.659×10^4
	2	0% etching	4.107×10^4	3.732×10^4
		3.5% etching	4.119×10^4	3.772×10^4
		7% etching	4.124×10^4	3.789×10^4
		7% etching with noise	4.084×10^4	3.777×10^4
		7%, no filling in upper watershed	4.064×10^4	3.813×10^4
		14% etching	4.138×10^4	3.811×10^4

Table B.56: Lowering History Sensitivity for Model 204, BasicSsVs
South East Watershed Domain

Lowering History (Reference: History 1)	Initial Condition	μ^*	σ^*
2	0% etching	6.703×10^2	9.244×10^2
	3.5% etching	6.181×10^2	8.984×10^2
	7% etching	6.000×10^2	8.654×10^2
	7% etching with noise	6.069×10^2	9.054×10^2
	7%, no filling in upper watershed	6.094×10^2	8.960×10^2
	14% etching	5.533×10^2	7.914×10^2

Table B.57: Initial Condition Sensitivity for Model 204, BasicSsVs
South East Watershed Domain

Initial Condition (Reference: 7% etch)	Lowering History	μ^*	σ^*
0% etching	1	2.272×10^2	2.170×10^2
	2	2.545×10^2	2.708×10^2
3.5% etching	1	1.306×10^2	1.454×10^2
	2	1.124×10^2	1.276×10^2
7% etching with noise	1	1.888×10^2	2.251×10^2
	2	1.893×10^2	2.285×10^2
7%, no filling in upper watershed	1	2.505×10^2	4.366×10^2
	2	2.599×10^2	4.453×10^2
14% etching	1	1.593×10^2	1.598×10^2
	2	1.798×10^2	1.576×10^2

Table B.58: Parameter Sensitivity for Model 208, BasicDdVs
South East Watershed Domain

Input	Lowering History	Initial Condition	μ^*	σ^*
D	1	0% etching	5.841×10^1	1.647×10^2
		3.5% etching	6.840×10^1	1.819×10^2
		7% etching	6.767×10^1	1.729×10^2
		7% etching with noise	7.021×10^1	1.799×10^2
		7%, no filling in upper watershed	6.695×10^1	1.684×10^2
		14% etching	6.894×10^1	1.646×10^2
	2	0% etching	6.271×10^1	1.773×10^2
		3.5% etching	7.347×10^1	1.970×10^2
		7% etching	7.245×10^1	1.872×10^2
		7% etching with noise	7.488×10^1	1.940×10^2
		7%, no filling in upper watershed	7.175×10^1	1.827×10^2
		14% etching	7.319×10^1	1.772×10^2
H_{init}	1	0% etching	1.400×10^0	1.781×10^0
		3.5% etching	2.133×10^0	3.018×10^0
		7% etching	2.177×10^0	3.021×10^0
		7% etching with noise	1.631×10^0	2.229×10^0
		7%, no filling in upper watershed	3.528×10^0	6.233×10^0
		14% etching	2.252×10^0	2.918×10^0
	2	0% etching	1.477×10^0	1.903×10^0
		3.5% etching	2.440×10^0	3.353×10^0
		7% etching	2.274×10^0	3.254×10^0
		7% etching with noise	1.995×10^0	2.544×10^0
		7%, no filling in upper watershed	3.394×10^0	5.856×10^0
		14% etching	2.373×10^0	3.175×10^0
K_{sat}	1	0% etching	1.130×10^1	3.225×10^1
		3.5% etching	1.457×10^1	3.232×10^1
		7% etching	1.580×10^1	3.479×10^1
		7% etching with noise	1.385×10^1	3.277×10^1
		7%, no filling in upper watershed	1.184×10^1	2.821×10^1
		14% etching	1.452×10^1	3.184×10^1
	2	0% etching	1.225×10^1	3.444×10^1
		3.5% etching	1.555×10^1	3.408×10^1
		7% etching	1.682×10^1	3.650×10^1
		7% etching with noise	1.453×10^1	3.356×10^1
		7%, no filling in upper watershed	1.237×10^1	2.968×10^1
		14% etching	1.527×10^1	3.344×10^1

Table B.58: (continued)

Input	Lowering History	Initial Condition	μ^*	σ^*
R_m	1	0% etching	2.300×10^0	3.901×10^0
		3.5% etching	2.427×10^0	4.330×10^0
		7% etching	3.401×10^0	5.246×10^0
		7% etching with noise	3.407×10^0	4.960×10^0
		7%, no filling in upper watershed	7.968×10^0	1.710×10^1
		14% etching	4.015×10^0	5.518×10^0
	2	0% etching	2.489×10^0	3.922×10^0
		3.5% etching	2.784×10^0	4.740×10^0
		7% etching	3.630×10^0	5.499×10^0
		7% etching with noise	3.615×10^0	5.419×10^0
		7%, no filling in upper watershed	8.409×10^0	1.789×10^1
		14% etching	4.502×10^0	6.206×10^0
$\log_{10} K$	1	0% etching	2.307×10^2	2.514×10^2
		3.5% etching	2.710×10^2	2.641×10^2
		7% etching	2.731×10^2	2.692×10^2
		7% etching with noise	2.694×10^2	2.651×10^2
		7%, no filling in upper watershed	2.977×10^2	3.537×10^2
		14% etching	2.729×10^2	2.990×10^2
	2	0% etching	2.458×10^2	2.658×10^2
		3.5% etching	2.893×10^2	2.799×10^2
		7% etching	2.913×10^2	2.853×10^2
		7% etching with noise	2.867×10^2	2.809×10^2
		7%, no filling in upper watershed	3.157×10^2	3.712×10^2
		14% etching	2.896×10^2	3.183×10^2
$\log_{10} \omega_c$	1	0% etching	9.524×10^1	1.900×10^2
		3.5% etching	1.071×10^2	2.137×10^2
		7% etching	1.106×10^2	2.192×10^2
		7% etching with noise	1.083×10^2	2.174×10^2
		7%, no filling in upper watershed	1.179×10^2	2.445×10^2
		14% etching	1.171×10^2	2.331×10^2
	2	0% etching	9.784×10^1	1.942×10^2
		3.5% etching	1.097×10^2	2.185×10^2
		7% etching	1.133×10^2	2.246×10^2
		7% etching with noise	1.109×10^2	2.222×10^2
		7%, no filling in upper watershed	1.207×10^2	2.501×10^2
		14% etching	1.193×10^2	2.371×10^2

Table B.58: (continued)

Input	Lowering History	Initial Condition	μ^*	σ^*
b	1	0% etching	1.948×10^1	4.836×10^1
		3.5% etching	2.112×10^1	4.903×10^1
		7% etching	2.132×10^1	5.000×10^1
		7% etching with noise	2.016×10^1	4.635×10^1
		7%, no filling in upper watershed	3.049×10^1	7.887×10^1
		14% etching	2.613×10^1	6.708×10^1
	2	0% etching	2.051×10^1	5.009×10^1
		3.5% etching	2.307×10^1	5.335×10^1
		7% etching	2.329×10^1	5.444×10^1
		7% etching with noise	2.199×10^1	5.066×10^1
		7%, no filling in upper watershed	3.238×10^1	8.325×10^1
		14% etching	2.811×10^1	7.183×10^1

Table B.59: Lowering History Sensitivity for Model 208, BasicDdVs South East Watershed Domain

Lowering History (Reference: History 1)	Initial Condition	μ^*	σ^*
2	0% etching	4.084×10^0	6.816×10^0
	3.5% etching	4.956×10^0	7.993×10^0
	7% etching	4.746×10^0	7.817×10^0
	7% etching with noise	4.576×10^0	7.540×10^0
	7%, no filling in upper watershed	4.747×10^0	7.896×10^0
	14% etching	4.179×10^0	7.438×10^0

Table B.60: Initial Condition Sensitivity for Model 208, BasicDdVs South East Watershed Domain

Initial Condition (Reference: 7% etch)	Lowering History	μ^*	σ^*
0% etching	1	1.125×10^2	2.646×10^1
	2	1.126×10^2	2.701×10^1
3.5% etching	1	4.637×10^1	5.995×10^0
	2	4.612×10^1	6.407×10^0
7% etching with noise	1	1.670×10^0	3.282×10^0
	2	1.762×10^0	3.544×10^0
7%, no filling in upper watershed	1	1.506×10^1	4.035×10^1
	2	1.508×10^1	4.048×10^1
14% etching	1	8.015×10^1	1.619×10^1
	2	7.954×10^1	1.711×10^1

Table B.61: Parameter Sensitivity for Model 210, BasicHyVs
South East Watershed Domain

Input	Lowering History	Initial Condition	μ^*	σ^*
D	1	0% etching	7.800×10^3	1.732×10^4
		3.5% etching	7.956×10^3	1.765×10^4
		7% etching	7.908×10^3	1.762×10^4
		7% etching with noise	8.042×10^3	1.792×10^4
		7%, no filling in upper watershed	7.819×10^3	1.772×10^4
		14% etching	8.111×10^3	1.808×10^4
	2	0% etching	8.002×10^3	1.774×10^4
		3.5% etching	8.154×10^3	1.806×10^4
		7% etching	8.063×10^3	1.795×10^4
		7% etching with noise	8.208×10^3	1.828×10^4
		7%, no filling in upper watershed	7.972×10^3	1.803×10^4
		14% etching	8.253×10^3	1.838×10^4
H_{init}	1	0% etching	4.420×10^3	5.250×10^3
		3.5% etching	4.559×10^3	5.279×10^3
		7% etching	4.603×10^3	5.333×10^3
		7% etching with noise	4.670×10^3	5.466×10^3
		7%, no filling in upper watershed	4.782×10^3	5.646×10^3
		14% etching	4.794×10^3	5.663×10^3
	2	0% etching	4.569×10^3	5.410×10^3
		3.5% etching	4.655×10^3	5.381×10^3
		7% etching	4.792×10^3	5.572×10^3
		7% etching with noise	4.758×10^3	5.558×10^3
		7%, no filling in upper watershed	4.881×10^3	5.762×10^3
		14% etching	4.948×10^3	5.826×10^3
K_{sat}	1	0% etching	1.169×10^4	1.866×10^4
		3.5% etching	5.758×10^3	7.944×10^3
		7% etching	5.896×10^3	8.124×10^3
		7% etching with noise	1.180×10^4	1.855×10^4
		7%, no filling in upper watershed	6.215×10^3	8.611×10^3
		14% etching	6.099×10^3	8.357×10^3
	2	0% etching	1.212×10^4	1.937×10^4
		3.5% etching	1.223×10^4	1.947×10^4
		7% etching	6.055×10^3	8.330×10^3
		7% etching with noise	1.216×10^4	1.906×10^4
		7%, no filling in upper watershed	6.390×10^3	8.860×10^3
		14% etching	1.264×10^4	1.979×10^4

Table B.61: (continued)

Input	Lowering History	Initial Condition	μ^*	σ^*
R_m	1	0% etching	1.377×10^4	2.230×10^4
		3.5% etching	7.860×10^3	1.559×10^4
		7% etching	7.999×10^3	1.584×10^4
		7% etching with noise	1.397×10^4	2.234×10^4
		7%, no filling in upper watershed	8.532×10^3	1.679×10^4
		14% etching	8.130×10^3	1.602×10^4
	2	0% etching	1.711×10^4	2.814×10^4
		3.5% etching	1.421×10^4	2.302×10^4
		7% etching	8.135×10^3	1.611×10^4
		7% etching with noise	1.422×10^4	2.278×10^4
		7%, no filling in upper watershed	1.083×10^4	2.257×10^4
		14% etching	1.463×10^4	2.354×10^4
$\log_{10} K$	1	0% etching	2.768×10^4	3.226×10^4
		3.5% etching	2.777×10^4	3.243×10^4
		7% etching	2.773×10^4	3.256×10^4
		7% etching with noise	2.736×10^4	3.237×10^4
		7%, no filling in upper watershed	2.690×10^4	3.204×10^4
		14% etching	2.796×10^4	3.275×10^4
	2	0% etching	1.756×10^4	1.727×10^4
		3.5% etching	2.850×10^4	3.311×10^4
		7% etching	2.843×10^4	3.322×10^4
		7% etching with noise	2.807×10^4	3.304×10^4
		7%, no filling in upper watershed	1.674×10^4	1.656×10^4
		14% etching	2.860×10^4	3.335×10^4
$\log_{10} V_c$	1	0% etching	3.378×10^2	4.611×10^2
		3.5% etching	3.483×10^2	4.815×10^2
		7% etching	4.031×10^2	5.130×10^2
		7% etching with noise	3.675×10^2	4.833×10^2
		7%, no filling in upper watershed	3.703×10^2	5.128×10^2
		14% etching	3.558×10^2	4.909×10^2
	2	0% etching	3.564×10^2	4.542×10^2
		3.5% etching	3.575×10^2	4.820×10^2
		7% etching	3.950×10^2	5.046×10^2
		7% etching with noise	3.979×10^2	5.061×10^2
		7%, no filling in upper watershed	4.081×10^2	5.224×10^2
		14% etching	3.471×10^2	4.994×10^2

Table B.61: (continued)

Input	Lowering History	Initial Condition	μ^*	σ^*
ϕ	1	0% etching	0.000×10^0	0.000×10^0
		3.5% etching	0.000×10^0	0.000×10^0
		7% etching	0.000×10^0	0.000×10^0
		7% etching with noise	0.000×10^0	0.000×10^0
		7%, no filling in upper watershed	0.000×10^0	0.000×10^0
		14% etching	0.000×10^0	0.000×10^0
	2	0% etching	0.000×10^0	0.000×10^0
		3.5% etching	0.000×10^0	0.000×10^0
		7% etching	0.000×10^0	0.000×10^0
		7% etching with noise	0.000×10^0	0.000×10^0
		7%, no filling in upper watershed	0.000×10^0	0.000×10^0
		14% etching	0.000×10^0	0.000×10^0

Table B.62: Lowering History Sensitivity for Model 210, BasicHyVs
South East Watershed Domain

Lowering History (Reference: History 1)	Initial Condition	μ^*	σ^*
2	0% etching	8.817×10^2	6.150×10^3
	3.5% etching	5.830×10^2	3.543×10^3
	7% etching	1.726×10^2	2.650×10^2
	7% etching with noise	1.880×10^2	2.881×10^2
	7%, no filling in upper watershed	8.394×10^2	6.109×10^3
	14% etching	5.654×10^2	3.601×10^3

Table B.63: Initial Condition Sensitivity for Model 210, BasicHyVs
South East Watershed Domain

Initial Condition (Reference: 7% etch)	Lowering History	μ^*	σ^*
0% etching	1	5.719×10^2	3.401×10^3
	2	1.301×10^3	7.178×10^3
3.5% etching	1	9.779×10^1	1.285×10^2
	2	5.065×10^2	3.544×10^3
7% etching with noise	1	4.803×10^2	3.371×10^3
	2	5.038×10^2	3.461×10^3
7%, no filling in upper watershed	1	2.987×10^2	5.671×10^2
	2	1.000×10^3	6.308×10^3
14% etching	1	1.260×10^2	1.145×10^2
	2	5.249×10^2	3.599×10^3

Table B.64: Parameter Sensitivity for Model 300, BasicStVs
South East Watershed Domain

Input	Lowering History	Initial Condition	μ^*	σ^*
D	1	0% etching	9.538×10^2	1.803×10^3
		3.5% etching	9.923×10^2	1.881×10^3
		7% etching	9.376×10^2	1.912×10^3
		7% etching with noise	9.872×10^2	1.922×10^3
		7%, no filling in upper watershed	8.633×10^2	1.901×10^3
		14% etching	9.897×10^2	1.993×10^3
	2	0% etching	7.178×10^2	1.911×10^3
		3.5% etching	7.393×10^2	1.980×10^3
		7% etching	7.511×10^2	2.014×10^3
		7% etching with noise	7.566×10^2	2.026×10^3
		7%, no filling in upper watershed	7.325×10^2	1.991×10^3
		14% etching	7.806×10^2	2.088×10^3
F	1	0% etching	1.105×10^2	1.438×10^2
		3.5% etching	1.245×10^2	1.826×10^2
		7% etching	3.037×10^2	6.065×10^2
		7% etching with noise	1.103×10^2	1.422×10^2
		7%, no filling in upper watershed	1.564×10^2	2.450×10^2
		14% etching	1.662×10^2	2.515×10^2
	2	0% etching	8.876×10^0	1.347×10^1
		3.5% etching	1.473×10^1	2.259×10^1
		7% etching	1.547×10^1	2.349×10^1
		7% etching with noise	1.493×10^1	2.283×10^1
		7%, no filling in upper watershed	1.435×10^1	2.176×10^1
		14% etching	1.578×10^1	2.373×10^1
H_{init}	1	0% etching	1.597×10^2	4.275×10^2
		3.5% etching	1.855×10^2	4.417×10^2
		7% etching	1.664×10^2	4.572×10^2
		7% etching with noise	1.567×10^2	4.370×10^2
		7%, no filling in upper watershed	1.802×10^2	5.164×10^2
		14% etching	1.809×10^2	4.814×10^2
	2	0% etching	1.440×10^2	4.427×10^2
		3.5% etching	1.490×10^2	4.592×10^2
		7% etching	1.520×10^2	4.713×10^2
		7% etching with noise	1.454×10^2	4.494×10^2
		7%, no filling in upper watershed	1.712×10^2	5.299×10^2
		14% etching	1.599×10^2	4.968×10^2

Table B.64: (continued)

Input	Lowering History	Initial Condition	μ^*	σ^*
K_{sat}	1	0% etching	3.307×10^3	5.756×10^3
		3.5% etching	3.309×10^3	5.916×10^3
		7% etching	3.354×10^3	6.011×10^3
		7% etching with noise	3.307×10^3	6.006×10^3
		7%, no filling in upper watershed	3.430×10^3	6.270×10^3
		14% etching	3.400×10^3	6.219×10^3
	2	0% etching	3.363×10^3	5.965×10^3
		3.5% etching	3.417×10^3	6.092×10^3
		7% etching	3.436×10^3	6.186×10^3
		7% etching with noise	3.415×10^3	6.168×10^3
		7%, no filling in upper watershed	3.522×10^3	6.446×10^3
		14% etching	3.485×10^3	6.374×10^3
S_r	1	0% etching	6.384×10^1	9.854×10^1
		3.5% etching	6.080×10^1	9.646×10^1
		7% etching	8.717×10^1	1.185×10^2
		7% etching with noise	6.898×10^1	8.759×10^1
		7%, no filling in upper watershed	6.769×10^1	1.002×10^2
		14% etching	9.192×10^1	1.175×10^2
	2	0% etching	4.441×10^1	9.417×10^1
		3.5% etching	4.446×10^1	9.213×10^1
		7% etching	4.462×10^1	9.248×10^1
		7% etching with noise	4.221×10^1	8.961×10^1
		7%, no filling in upper watershed	4.707×10^1	9.788×10^1
		14% etching	4.193×10^1	8.780×10^1
$\log_{10} K_q$	1	0% etching	9.007×10^4	4.075×10^4
		3.5% etching	9.047×10^4	4.054×10^4
		7% etching	9.076×10^4	4.031×10^4
		7% etching with noise	9.070×10^4	4.052×10^4
		7%, no filling in upper watershed	9.104×10^4	3.943×10^4
		14% etching	9.135×10^4	3.983×10^4
	2	0% etching	9.181×10^4	4.147×10^4
		3.5% etching	9.215×10^4	4.121×10^4
		7% etching	9.240×10^4	4.097×10^4
		7% etching with noise	9.233×10^4	4.117×10^4
		7%, no filling in upper watershed	9.268×10^4	4.009×10^4
		14% etching	9.288×10^4	4.044×10^4

Table B.64: (continued)

Input	Lowering History	Initial Condition	μ^*	σ^*
c	1	0% etching	1.628×10^2	2.970×10^2
		3.5% etching	1.692×10^2	2.983×10^2
		7% etching	3.245×10^2	5.779×10^2
		7% etching with noise	1.609×10^2	3.013×10^2
		7%, no filling in upper watershed	1.682×10^2	2.982×10^2
		14% etching	2.030×10^2	3.201×10^2
	2	0% etching	1.457×10^2	3.072×10^2
		3.5% etching	1.451×10^2	3.071×10^2
		7% etching	1.461×10^2	3.104×10^2
		7% etching with noise	1.456×10^2	3.100×10^2
		7%, no filling in upper watershed	1.454×10^2	3.121×10^2
		14% etching	1.456×10^2	3.145×10^2
n_{ts}	1	0% etching	3.305×10^2	8.110×10^2
		3.5% etching	4.079×10^2	8.699×10^2
		7% etching	3.228×10^2	8.488×10^2
		7% etching with noise	4.151×10^2	8.901×10^2
		7%, no filling in upper watershed	2.880×10^2	8.304×10^2
		14% etching	3.033×10^2	8.426×10^2
	2	0% etching	2.767×10^2	8.367×10^2
		3.5% etching	2.912×10^2	8.769×10^2
		7% etching	2.909×10^2	8.740×10^2
		7% etching with noise	2.903×10^2	8.741×10^2
		7%, no filling in upper watershed	2.872×10^2	8.574×10^2
		14% etching	2.888×10^2	8.629×10^2
p_d	1	0% etching	4.489×10^3	7.493×10^3
		3.5% etching	4.526×10^3	7.615×10^3
		7% etching	4.561×10^3	7.712×10^3
		7% etching with noise	4.505×10^3	7.693×10^3
		7%, no filling in upper watershed	4.504×10^3	7.664×10^3
		14% etching	4.606×10^3	7.901×10^3
	2	0% etching	4.562×10^3	7.749×10^3
		3.5% etching	4.598×10^3	7.860×10^3
		7% etching	4.635×10^3	7.942×10^3
		7% etching with noise	4.619×10^3	7.902×10^3
		7%, no filling in upper watershed	4.620×10^3	7.873×10^3
		14% etching	4.696×10^3	8.100×10^3

Table B.65: Lowering History Sensitivity for Model 300, BasicStVs
South East Watershed Domain

Lowering History (Reference: History 1)	Initial Condition	μ^*	σ^*
2	0% etching	4.894×10^2	6.000×10^2
	3.5% etching	4.660×10^2	5.714×10^2
	7% etching	4.408×10^2	5.501×10^2
	7% etching with noise	4.527×10^2	5.548×10^2
	7%, no filling in upper watershed	4.494×10^2	5.517×10^2
	14% etching	4.157×10^2	5.107×10^2

Table B.66: Initial Condition Sensitivity for Model 300, BasicStVs
South East Watershed Domain

Initial Condition (Reference: 7% etch)	Lowering History	μ^*	σ^*
0% etching	1	2.002×10^2	2.576×10^2
	2	1.435×10^2	2.488×10^2
3.5% etching	1	1.001×10^2	1.405×10^2
	2	6.272×10^1	1.109×10^2
7% etching with noise	1	6.580×10^1	1.254×10^2
	2	3.685×10^1	8.631×10^1
7%, no filling in upper watershed	1	1.640×10^2	3.564×10^2
	2	1.480×10^2	3.586×10^2
14% etching	1	1.811×10^2	2.365×10^2
	2	1.332×10^2	2.307×10^2

Table B.67: Parameter Sensitivity for Model 400, BasicSa
South East Watershed Domain

Input	Lowering History	Initial Condition	μ^*	σ^*
D	1	0% etching	2.379×10^{4}	5.014×10^{4}
		3.5% etching	3.570×10^{4}	5.746×10^{4}
		7% etching	2.381×10^{4}	5.016×10^{4}
		7% etching with noise	9.759×10^{0}	9.987×10^{0}
		7%, no filling in upper watershed	1.191×10^{4}	3.762×10^{4}
		14% etching	1.528×10^{1}	1.689×10^{1}
	2	0% etching	1.192×10^{4}	3.769×10^{4}
		3.5% etching	1.193×10^{4}	3.769×10^{4}
		7% etching	8.283×10^{0}	1.121×10^{1}
		7% etching with noise	1.193×10^{4}	3.769×10^{4}
		7%, no filling in upper watershed	1.193×10^{4}	3.769×10^{4}
		14% etching	1.193×10^{4}	3.769×10^{4}
H_0	1	0% etching	8.999×10^{0}	1.624×10^{1}
		3.5% etching	8.781×10^{0}	1.292×10^{1}
		7% etching	6.661×10^{0}	1.140×10^{1}
		7% etching with noise	6.336×10^{0}	9.487×10^{0}
		7%, no filling in upper watershed	8.847×10^{0}	1.982×10^{1}
		14% etching	6.501×10^{0}	9.842×10^{0}
	2	0% etching	6.844×10^{0}	1.652×10^{1}
		3.5% etching	8.374×10^{0}	1.350×10^{1}
		7% etching	5.014×10^{0}	1.208×10^{1}
		7% etching with noise	4.153×10^{0}	9.919×10^{0}
		7%, no filling in upper watershed	7.519×10^{0}	2.087×10^{1}
		14% etching	4.999×10^{0}	1.085×10^{1}
H_s	1	0% etching	1.190×10^{4}	3.761×10^{4}
		3.5% etching	2.782×10^{0}	5.664×10^{0}
		7% etching	2.795×10^{0}	4.513×10^{0}
		7% etching with noise	2.504×10^{0}	3.305×10^{0}
		7%, no filling in upper watershed	3.129×10^{0}	5.543×10^{0}
		14% etching	1.265×10^{0}	1.666×10^{0}
	2	0% etching	1.170×10^{0}	2.382×10^{0}
		3.5% etching	2.048×10^{0}	5.801×10^{0}
		7% etching	1.192×10^{4}	3.769×10^{4}
		7% etching with noise	1.213×10^{0}	2.471×10^{0}
		7%, no filling in upper watershed	3.839×10^{-1}	7.893×10^{-1}
		14% etching	2.314×10^{-1}	3.805×10^{-1}

Table B.67: (continued)

Input	Lowering History	Initial Condition	μ^*	σ^*
H_{init}	1	0% etching	1.245×10^1	2.841×10^1
		3.5% etching	2.381×10^4	5.014×10^4
		7% etching	1.382×10^1	3.269×10^1
		7% etching with noise	1.843×10^1	3.253×10^1
		7%, no filling in upper watershed	1.678×10^1	2.804×10^1
		14% etching	1.584×10^1	3.398×10^1
	2	0% etching	1.193×10^4	3.769×10^4
		3.5% etching	2.295×10^1	5.429×10^1
		7% etching	1.298×10^1	3.335×10^1
		7% etching with noise	1.632×10^1	3.334×10^1
		7%, no filling in upper watershed	1.567×10^1	2.826×10^1
		14% etching	1.193×10^4	3.769×10^4
P_0	1	0% etching	1.191×10^4	3.764×10^4
		3.5% etching	1.191×10^4	3.764×10^4
		7% etching	1.192×10^4	3.763×10^4
		7% etching with noise	7.808×10^0	8.597×10^0
		7%, no filling in upper watershed	3.746×10^0	4.945×10^0
		14% etching	5.937×10^0	7.403×10^0
	2	0% etching	1.469×10^0	3.311×10^0
		3.5% etching	1.193×10^4	3.769×10^4
		7% etching	1.226×10^1	2.961×10^1
		7% etching with noise	6.720×10^0	1.181×10^1
		7%, no filling in upper watershed	1.192×10^4	3.769×10^4
		14% etching	1.192×10^4	3.769×10^4
$\log_{10} K$	1	0% etching	6.328×10^4	4.371×10^4
		3.5% etching	7.503×10^4	4.070×10^4
		7% etching	7.508×10^4	4.064×10^4
		7% etching with noise	8.600×10^4	3.386×10^4
		7%, no filling in upper watershed	7.645×10^4	3.926×10^4
		14% etching	8.714×10^4	3.260×10^4
	2	0% etching	6.623×10^4	4.381×10^4
		3.5% etching	6.754×10^4	4.356×10^4
		7% etching	8.706×10^4	3.352×10^4
		7% etching with noise	7.635×10^4	4.070×10^4
		7%, no filling in upper watershed	8.771×10^4	3.205×10^4
		14% etching	7.753×10^4	3.993×10^4

Table B.68: Lowering History Sensitivity for Model 400, BasicSa
South East Watershed Domain

Lowering History (Reference: History 1)	Initial Condition	μ^*	σ^*
2	0% etching	3.663×10^3	1.408×10^4
	3.5% etching	2.805×10^3	1.229×10^4
	7% etching	4.520×10^3	1.562×10^4
	7% etching with noise	1.074×10^3	7.195×10^3
	7%, no filling in upper watershed	1.942×10^3	1.011×10^4
	14% etching	2.783×10^3	1.227×10^4

Table B.69: Initial Condition Sensitivity for Model 400, BasicSa
South East Watershed Domain

Initial Condition (Reference: 7% etch)	Lowering History	μ^*	σ^*
0% etching	1	4.597×10^3	1.558×10^4
	2	5.459×10^3	1.697×10^4
3.5% etching	1	2.714×10^3	1.228×10^4
	2	4.438×10^3	1.565×10^4
7% etching with noise	1	2.633×10^3	1.230×10^4
	2	2.638×10^3	1.232×10^4
7%, no filling in upper watershed	1	3.711×10^3	1.405×10^4
	2	2.858×10^3	1.228×10^4
14% etching	1	2.837×10^3	1.226×10^4
	2	2.829×10^3	1.229×10^4

Table B.70: Parameter Sensitivity for Model 410, BasicHySa
South East Watershed Domain

Input	Lowering History	Initial Condition	μ^*	σ^*
D	1	0% etching	1.051×10^{0}	2.176×10^{0}
		3.5% etching	2.839×10^{0}	8.845×10^{0}
		7% etching	1.544×10^{2}	4.615×10^{2}
		7% etching with noise	5.956×10^{0}	1.825×10^{1}
		7%, no filling in upper watershed	3.820×10^{1}	1.048×10^{2}
		14% etching	8.652×10^{1}	2.736×10^{2}
	2	0% etching	1.056×10^{1}	3.153×10^{1}
		3.5% etching	3.838×10^{0}	1.200×10^{1}
		7% etching	9.482×10^{3}	2.996×10^{4}
		7% etching with noise	3.954×10^{3}	1.218×10^{4}
		7%, no filling in upper watershed	1.251×10^{2}	3.782×10^{2}
		14% etching	6.475×10^{1}	1.926×10^{2}
H_*	1	0% etching	3.164×10^{2}	6.505×10^{2}
		3.5% etching	1.032×10^{2}	3.118×10^{2}
		7% etching	2.899×10^{2}	5.999×10^{2}
		7% etching with noise	7.071×10^{0}	1.516×10^{1}
		7%, no filling in upper watershed	2.931×10^{2}	6.146×10^{2}
		14% etching	2.610×10^{2}	5.610×10^{2}
	2	0% etching	3.116×10^{2}	6.529×10^{2}
		3.5% etching	3.996×10^{2}	6.565×10^{2}
		7% etching	1.286×10^{2}	3.651×10^{2}
		7% etching with noise	1.257×10^{2}	3.658×10^{2}
		7%, no filling in upper watershed	2.914×10^{2}	6.154×10^{2}
		14% etching	2.639×10^{2}	5.595×10^{2}
H_0	1	0% etching	7.727×10^{-1}	2.381×10^{0}
		3.5% etching	1.722×10^{2}	5.439×10^{2}
		7% etching	9.446×10^{-2}	2.228×10^{-1}
		7% etching with noise	9.656×10^{-2}	2.974×10^{-1}
		7%, no filling in upper watershed	2.942×10^{-1}	8.753×10^{-1}
		14% etching	3.921×10^{-1}	1.234×10^{0}
	2	0% etching	5.886×10^{-1}	1.797×10^{0}
		3.5% etching	1.870×10^{-1}	5.302×10^{-1}
		7% etching	4.671×10^{-1}	1.409×10^{0}
		7% etching with noise	9.811×10^{-2}	2.441×10^{-1}
		7%, no filling in upper watershed	2.922×10^{-1}	8.793×10^{-1}
		14% etching	4.260×10^{-1}	1.324×10^{0}

Table B.70: (continued)

Input	Lowering History	Initial Condition	μ^*	σ^*
H_s	1	0% etching	6.091×10^1	1.426×10^2
		3.5% etching	2.416×10^1	5.706×10^1
		7% etching	2.122×10^1	4.771×10^1
		7% etching with noise	1.665×10^1	4.465×10^1
		7%, no filling in upper watershed	1.056×10^1	1.796×10^1
		14% etching	2.691×10^1	6.669×10^1
	2	0% etching	2.374×10^1	5.468×10^1
		3.5% etching	1.073×10^2	3.204×10^2
		7% etching	2.363×10^1	5.486×10^1
		7% etching with noise	3.299×10^1	8.566×10^1
		7%, no filling in upper watershed	2.388×10^1	5.780×10^1
		14% etching	1.745×10^1	3.710×10^1
H_{init}	1	0% etching	1.712×10^1	2.526×10^1
		3.5% etching	9.540×10^0	2.193×10^1
		7% etching	1.191×10^1	2.217×10^1
		7% etching with noise	2.353×10^1	5.456×10^1
		7%, no filling in upper watershed	1.487×10^1	2.297×10^1
		14% etching	1.184×10^1	2.290×10^1
	2	0% etching	1.725×10^1	2.613×10^1
		3.5% etching	1.151×10^2	3.217×10^2
		7% etching	1.217×10^1	2.325×10^1
		7% etching with noise	3.851×10^3	1.215×10^4
		7%, no filling in upper watershed	1.370×10^1	2.241×10^1
		14% etching	1.369×10^1	2.259×10^1
P_0	1	0% etching	1.169×10^3	1.872×10^3
		3.5% etching	8.904×10^3	2.731×10^4
		7% etching	6.480×10^2	1.156×10^3
		7% etching with noise	5.468×10^2	1.199×10^3
		7%, no filling in upper watershed	6.548×10^2	1.147×10^3
		14% etching	5.851×10^2	1.236×10^3
	2	0% etching	6.080×10^2	1.106×10^3
		3.5% etching	2.592×10^2	3.498×10^2
		7% etching	9.241×10^3	2.828×10^4
		7% etching with noise	9.417×10^2	1.258×10^3
		7%, no filling in upper watershed	6.634×10^2	1.172×10^3
		14% etching	6.804×10^2	1.193×10^3

Table B.70: (continued)

Input	Lowering History	Initial Condition	μ^*	σ^*
$\log_{10} K_2$	1	0% etching	1.642×10^4	2.879×10^4
		3.5% etching	7.965×10^3	1.621×10^4
		7% etching	1.713×10^4	2.982×10^4
		7% etching with noise	1.268×10^4	2.874×10^4
		7%, no filling in upper watershed	1.781×10^4	3.042×10^4
		14% etching	9.395×10^3	2.846×10^4
	2	0% etching	1.679×10^4	2.952×10^4
		3.5% etching	4.051×10^3	1.155×10^4
		7% etching	8.464×10^3	1.695×10^4
		7% etching with noise	1.749×10^4	3.049×10^4
		7%, no filling in upper watershed	1.817×10^4	3.112×10^4
		14% etching	1.809×10^4	3.140×10^4
$\log_{10} K_s$	1	0% etching	4.797×10^3	1.242×10^4
		3.5% etching	1.332×10^4	2.873×10^4
		7% etching	4.811×10^3	1.323×10^4
		7% etching with noise	5.214×10^2	1.261×10^3
		7%, no filling in upper watershed	5.155×10^3	1.420×10^4
		14% etching	4.410×10^2	6.098×10^2
	2	0% etching	4.841×10^3	1.260×10^4
		3.5% etching	5.666×10^2	7.134×10^2
		7% etching	1.374×10^4	2.984×10^4
		7% etching with noise	5.061×10^3	1.330×10^4
		7%, no filling in upper watershed	5.342×10^3	1.438×10^4
		14% etching	5.099×10^3	1.396×10^4
$\log_{10} V_c$	1	0% etching	4.765×10^3	1.373×10^4
		3.5% etching	9.277×10^3	2.847×10^4
		7% etching	4.224×10^2	8.953×10^2
		7% etching with noise	3.031×10^2	8.002×10^2
		7%, no filling in upper watershed	3.223×10^2	8.519×10^2
		14% etching	1.229×10^2	3.698×10^2
	2	0% etching	2.519×10^2	6.874×10^2
		3.5% etching	2.544×10^2	7.881×10^2
		7% etching	4.160×10^2	8.903×10^2
		7% etching with noise	1.538×10^2	4.675×10^2
		7%, no filling in upper watershed	4.376×10^2	9.516×10^2
		14% etching	3.835×10^2	8.763×10^2

Table B.70: (continued)

Input	Lowering History	Initial Condition	μ^*	σ^*
ϕ	1	0% etching	0.000×10^0	0.000×10^0
		3.5% etching	0.000×10^0	0.000×10^0
		7% etching	0.000×10^0	0.000×10^0
		7% etching with noise	0.000×10^0	0.000×10^0
		7%, no filling in upper watershed	0.000×10^0	0.000×10^0
		14% etching	0.000×10^0	0.000×10^0
	2	0% etching	0.000×10^0	0.000×10^0
		3.5% etching	0.000×10^0	0.000×10^0
		7% etching	0.000×10^0	0.000×10^0
		7% etching with noise	1.312×10^4	3.046×10^4
		7%, no filling in upper watershed	0.000×10^0	0.000×10^0
		14% etching	0.000×10^0	0.000×10^0

Table B.71: Lowering History Sensitivity for Model 410, BasicHySa
South East Watershed Domain

Lowering History (Reference: History 1)	Initial Condition	μ^*	σ^*
2	0% etching	7.008×10^2	3.482×10^3
	3.5% etching	1.907×10^3	8.647×10^3
	7% etching	9.219×10^2	6.063×10^3
	7% etching with noise	1.286×10^3	5.620×10^3
	7%, no filling in upper watershed	1.036×10^2	2.991×10^2
	14% etching	1.436×10^3	5.057×10^3

Table B.72: Initial Condition Sensitivity for Model 410, BasicHySa
South East Watershed Domain

Initial Condition (Reference: 7% etch)	Lowering History	μ^*	σ^*
0% etching	1	7.883×10^2	3.479×10^3
	2	9.952×10^2	6.048×10^3
3.5% etching	1	1.350×10^3	7.473×10^3
	2	2.401×10^3	9.948×10^3
7% etching with noise	1	3.545×10^2	2.053×10^3
	2	1.862×10^3	8.142×10^3
7%, no filling in upper watershed	1	1.302×10^2	3.770×10^2
	2	9.925×10^2	6.230×10^3
14% etching	1	1.393×10^3	4.739×10^3
	2	1.017×10^3	6.365×10^3

Table B.73: Parameter Sensitivity for Model 440, BasicChSa
South East Watershed Domain

Input	Lowering History	Initial Condition	μ^*	σ^*
D	1	0% etching	5.298×10^1	1.032×10^2
		3.5% etching	6.039×10^1	1.119×10^2
		7% etching	5.306×10^1	9.882×10^1
		7% etching with noise	5.356×10^1	1.024×10^2
		7%, no filling in upper watershed	5.282×10^1	9.162×10^1
		14% etching	6.671×10^1	1.178×10^2
	2	0% etching	4.971×10^1	1.020×10^2
		3.5% etching	5.880×10^1	1.170×10^2
		7% etching	4.826×10^1	9.633×10^1
		7% etching with noise	5.451×10^1	1.048×10^2
		7%, no filling in upper watershed	4.864×10^1	9.578×10^1
		14% etching	6.427×10^1	1.237×10^2
H_0	1	0% etching	1.122×10^1	2.086×10^1
		3.5% etching	1.121×10^1	1.972×10^1
		7% etching	1.241×10^1	1.931×10^1
		7% etching with noise	1.113×10^1	2.132×10^1
		7%, no filling in upper watershed	1.170×10^1	2.013×10^1
		14% etching	1.259×10^1	2.281×10^1
	2	0% etching	8.992×10^0	2.077×10^1
		3.5% etching	9.088×10^0	2.016×10^1
		7% etching	9.726×10^0	2.016×10^1
		7% etching with noise	1.000×10^1	2.167×10^1
		7%, no filling in upper watershed	9.916×10^0	2.068×10^1
		14% etching	1.166×10^1	2.390×10^1
H_s	1	0% etching	9.275×10^0	1.283×10^1
		3.5% etching	1.157×10^1	1.424×10^1
		7% etching	6.930×10^0	1.202×10^1
		7% etching with noise	7.114×10^0	1.156×10^1
		7%, no filling in upper watershed	5.386×10^0	9.525×10^0
		14% etching	7.062×10^0	1.091×10^1
	2	0% etching	4.085×10^0	1.177×10^1
		3.5% etching	8.226×10^0	1.548×10^1
		7% etching	5.894×10^0	1.237×10^1
		7% etching with noise	3.821×10^0	1.036×10^1
		7%, no filling in upper watershed	3.288×10^0	9.876×10^0
		14% etching	4.920×10^0	1.140×10^1

Table B.73: (continued)

Input	Lowering History	Initial Condition	μ^*	σ^*
H_{init}	1	0% etching	4.767×10^0	5.777×10^0
		3.5% etching	5.445×10^0	6.940×10^0
		7% etching	8.055×10^0	1.125×10^1
		7% etching with noise	4.744×10^0	6.246×10^0
		7%, no filling in upper watershed	1.193×10^4	3.769×10^4
		14% etching	4.461×10^0	5.158×10^0
	2	0% etching	1.994×10^0	5.127×10^0
		3.5% etching	1.194×10^4	3.776×10^4
		7% etching	4.094×10^0	9.570×10^0
		7% etching with noise	1.541×10^0	3.255×10^0
		7%, no filling in upper watershed	1.194×10^4	3.776×10^4
		14% etching	2.695×10^0	5.392×10^0
P_0	1	0% etching	5.941×10^0	7.393×10^0
		3.5% etching	6.481×10^0	8.653×10^0
		7% etching	6.171×10^0	8.414×10^0
		7% etching with noise	7.049×10^0	9.334×10^0
		7%, no filling in upper watershed	6.193×10^0	9.878×10^0
		14% etching	5.632×10^0	8.098×10^0
	2	0% etching	5.522×10^0	1.036×10^1
		3.5% etching	3.077×10^0	7.734×10^0
		7% etching	3.413×10^0	7.965×10^0
		7% etching with noise	3.124×10^0	7.568×10^0
		7%, no filling in upper watershed	5.231×10^0	9.931×10^0
		14% etching	3.671×10^0	6.539×10^0
S_c	1	0% etching	2.011×10^1	4.471×10^1
		3.5% etching	1.193×10^4	3.768×10^4
		7% etching	1.194×10^4	3.769×10^4
		7% etching with noise	1.195×10^4	3.768×10^4
		7%, no filling in upper watershed	7.129×10^0	8.964×10^0
		14% etching	2.775×10^1	7.151×10^1
	2	0% etching	1.512×10^1	4.519×10^1
		3.5% etching	9.600×10^0	2.731×10^1
		7% etching	1.349×10^1	3.881×10^1
		7% etching with noise	2.449×10^1	7.530×10^1
		7%, no filling in upper watershed	3.803×10^0	8.078×10^0
		14% etching	2.470×10^1	7.601×10^1

Table B.73: (continued)

Input	Lowering History	Initial Condition	μ^*	σ^*
$\log_{10} K$	1	0% etching	8.985×10^4	3.533×10^4
		3.5% etching	9.065×10^4	3.518×10^4
		7% etching	9.120×10^4	3.501×10^4
		7% etching with noise	9.102×10^4	3.512×10^4
		7%, no filling in upper watershed	9.160×10^4	3.445×10^4
		14% etching	9.236×10^4	3.461×10^4
	2	0% etching	9.150×10^4	3.561×10^4
		3.5% etching	1.026×10^5	1.973×10^4
		7% etching	9.276×10^4	3.527×10^4
		7% etching with noise	1.029×10^5	1.939×10^4
		7%, no filling in upper watershed	1.033×10^5	1.847×10^4
		14% etching	1.040×10^5	1.799×10^4

Table B.74: Lowering History Sensitivity for Model 440, BasicChSa
South East Watershed Domain

Lowering History (Reference: History 1)	Initial Condition	μ^*	σ^*
2	0% etching	3.693×10^2	5.857×10^2
	3.5% etching	1.869×10^3	9.447×10^3
	7% etching	1.101×10^3	6.729×10^3
	7% etching with noise	1.858×10^3	9.457×10^3
	7%, no filling in upper watershed	2.614×10^3	1.149×10^4
	14% etching	2.589×10^3	1.150×10^4

Table B.75: Initial Condition Sensitivity for Model 440, BasicChSa
South East Watershed Domain

Initial Condition (Reference: 7% etch)	Lowering History	μ^*	σ^*
0% etching	1	9.970×10^2	6.731×10^3
	2	2.203×10^2	3.973×10^2
3.5% etching	1	9.972×10^1	1.758×10^2
	2	8.430×10^2	6.751×10^3
7% etching with noise	1	3.299×10^1	6.285×10^1
	2	2.299×10^3	1.155×10^4
7%, no filling in upper watershed	1	8.586×10^2	6.738×10^3
	2	8.615×10^2	6.751×10^3
14% etching	1	9.732×10^2	6.732×10^3
	2	2.461×10^3	1.152×10^4

Table B.76: Parameter Sensitivity for Model 600, BasicVsSa
South East Watershed Domain

Input	Lowering History	Initial Condition	μ^*	σ^*
D	1	0% etching	2.434×10^4	5.001×10^4
		3.5% etching	1.279×10^4	3.741×10^4
		7% etching	1.266×10^4	3.745×10^4
		7% etching with noise	1.275×10^4	3.742×10^4
		7%, no filling in upper watershed	1.263×10^4	3.746×10^4
		14% etching	3.491×10^3	8.478×10^3
	2	0% etching	2.442×10^4	5.016×10^4
		3.5% etching	1.281×10^4	3.754×10^4
		7% etching	1.277×10^4	3.755×10^4
		7% etching with noise	1.277×10^4	3.755×10^4
		7%, no filling in upper watershed	1.277×10^4	3.755×10^4
		14% etching	2.452×10^4	5.011×10^4
H_0	1	0% etching	2.386×10^4	5.028×10^4
		3.5% etching	9.580×10^0	2.086×10^1
		7% etching	1.193×10^4	3.769×10^4
		7% etching with noise	6.501×10^3	2.048×10^4
		7%, no filling in upper watershed	3.913×10^3	1.230×10^4
		14% etching	2.268×10^1	6.089×10^1
	2	0% etching	1.197×10^4	3.781×10^4
		3.5% etching	2.393×10^4	5.041×10^4
		7% etching	1.196×10^4	3.781×10^4
		7% etching with noise	5.433×10^3	1.703×10^4
		7%, no filling in upper watershed	1.198×10^4	3.780×10^4
		14% etching	1.196×10^4	3.781×10^4
H_s	1	0% etching	6.571×10^3	1.897×10^4
		3.5% etching	5.879×10^2	9.894×10^2
		7% etching	1.889×10^4	4.056×10^4
		7% etching with noise	1.033×10^3	1.597×10^3
		7%, no filling in upper watershed	1.017×10^3	1.711×10^3
		14% etching	9.603×10^2	1.486×10^3
	2	0% etching	1.897×10^4	4.070×10^4
		3.5% etching	6.774×10^3	1.937×10^4
		7% etching	9.935×10^2	1.554×10^3
		7% etching with noise	1.025×10^3	1.560×10^3
		7%, no filling in upper watershed	1.023×10^3	1.454×10^3
		14% etching	1.284×10^4	3.741×10^4

Table B.76: (continued)

Input	Lowering History	Initial Condition	μ^*	σ^*
H_{init}	1	0% etching	1.787×10^4	3.800×10^4
		3.5% etching	1.797×10^4	3.809×10^4
		7% etching	1.805×10^4	3.808×10^4
		7% etching with noise	1.842×10^4	3.855×10^4
		7%, no filling in upper watershed	1.749×10^4	3.772×10^4
		14% etching	1.821×10^4	3.816×10^4
	2	0% etching	1.811×10^4	3.824×10^4
		3.5% etching	6.245×10^3	1.417×10^4
		7% etching	1.829×10^4	3.831×10^4
		7% etching with noise	6.744×10^3	1.605×10^4
		7%, no filling in upper watershed	1.772×10^4	3.792×10^4
		14% etching	1.845×10^4	3.839×10^4
K_{sat}	1	0% etching	2.901×10^4	4.850×10^4
		3.5% etching	1.726×10^4	3.723×10^4
		7% etching	1.739×10^4	3.720×10^4
		7% etching with noise	1.758×10^4	3.730×10^4
		7%, no filling in upper watershed	1.736×10^4	3.707×10^4
		14% etching	1.759×10^4	3.722×10^4
	2	0% etching	2.919×10^4	4.862×10^4
		3.5% etching	1.739×10^4	3.732×10^4
		7% etching	1.753×10^4	3.734×10^4
		7% etching with noise	5.773×10^3	1.121×10^4
		7%, no filling in upper watershed	1.750×10^4	3.721×10^4
		14% etching	1.773×10^4	3.735×10^4
P_0	1	0% etching	1.303×10^4	3.712×10^4
		3.5% etching	1.490×10^3	2.606×10^3
		7% etching	1.407×10^3	2.673×10^3
		7% etching with noise	2.321×10^3	3.358×10^3
		7%, no filling in upper watershed	1.078×10^4	2.914×10^4
		14% etching	1.775×10^4	3.408×10^4
	2	0% etching	2.505×10^4	4.970×10^4
		3.5% etching	1.501×10^3	2.644×10^3
		7% etching	1.505×10^3	2.718×10^3
		7% etching with noise	2.259×10^3	3.349×10^3
		7%, no filling in upper watershed	1.099×10^4	2.924×10^4
		14% etching	1.329×10^4	3.732×10^4

Table B.76: (continued)

Input	Lowering History	Initial Condition	μ^*	σ^*
R_m	1	0% etching	6.646×10^3	1.864×10^4
		3.5% etching	1.861×10^4	3.990×10^4
		7% etching	1.323×10^4	2.599×10^4
		7% etching with noise	2.013×10^4	3.912×10^4
		7%, no filling in upper watershed	1.262×10^4	2.448×10^4
		14% etching	2.408×10^4	4.071×10^4
	2	0% etching	1.331×10^4	2.629×10^4
		3.5% etching	6.747×10^3	1.880×10^4
		7% etching	1.214×10^4	2.366×10^4
		7% etching with noise	8.206×10^3	1.800×10^4
		7%, no filling in upper watershed	1.267×10^4	2.456×10^4
		14% etching	2.412×10^4	4.078×10^4
$\log_{10} K$	1	0% etching	5.829×10^4	3.691×10^4
		3.5% etching	5.332×10^4	4.088×10^4
		7% etching	5.370×10^4	4.085×10^4
		7% etching with noise	5.680×10^4	3.732×10^4
		7%, no filling in upper watershed	7.018×10^4	2.970×10^4
		14% etching	5.994×10^4	3.646×10^4
	2	0% etching	5.362×10^4	4.122×10^4
		3.5% etching	5.973×10^4	3.710×10^4
		7% etching	6.007×10^4	3.699×10^4
		7% etching with noise	5.763×10^4	3.761×10^4
		7%, no filling in upper watershed	7.115×10^4	2.975×10^4
		14% etching	6.075×10^4	3.672×10^4

Table B.77: Lowering History Sensitivity for Model 600, BasicVsSa
South East Watershed Domain

Lowering History (Reference: History 1)	Initial Condition	μ^*	σ^*
2	0% etching	2.834×10^3	1.170×10^4
	3.5% etching	3.161×10^3	1.284×10^4
	7% etching	4.494×10^3	1.537×10^4
	7% etching with noise	1.482×10^3	8.943×10^3
	7%, no filling in upper watershed	5.999×10^2	4.269×10^3
	14% etching	5.045×10^3	1.603×10^4

Table B.78: Initial Condition Sensitivity for Model 600, BasicVsSa
South East Watershed Domain

Initial Condition (Reference: 7% etch)	Lowering History	μ^*	σ^*
0% etching	1	2.888×10^3	1.161×10^4
	2	4.548×10^3	1.530×10^4
3.5% etching	1	3.800×10^3	1.416×10^4
	2	3.820×10^3	1.425×10^4
7% etching with noise	1	6.418×10^3	1.707×10^4
	2	2.111×10^3	8.683×10^3
7%, no filling in upper watershed	1	5.723×10^3	1.634×10^4
	2	9.221×10^2	5.014×10^3
14% etching	1	6.123×10^3	1.724×10^4
	2	4.852×10^3	1.617×10^4

Table B.79: Parameter Sensitivity for Model 800, BasicRt
South East Watershed Domain

Input	Lowering History	Initial Condition	μ^*	σ^*
D	1	0% etching	4.525×10^2	4.836×10^2
		3.5% etching	4.614×10^2	5.024×10^2
		7% etching	4.788×10^2	5.166×10^2
		7% etching with noise	4.784×10^2	5.275×10^2
		7%, no filling in upper watershed	5.173×10^2	6.297×10^2
		14% etching	4.959×10^2	5.516×10^2
	2	0% etching	4.610×10^2	4.790×10^2
		3.5% etching	4.617×10^2	5.025×10^2
		7% etching	4.701×10^2	5.210×10^2
		7% etching with noise	4.771×10^2	5.287×10^2
		7%, no filling in upper watershed	5.255×10^2	6.256×10^2
		14% etching	4.908×10^2	5.542×10^2
W_c	1	0% etching	7.427×10^2	7.497×10^2
		3.5% etching	7.534×10^2	7.500×10^2
		7% etching	7.473×10^2	7.499×10^2
		7% etching with noise	7.429×10^2	7.505×10^2
		7%, no filling in upper watershed	7.277×10^2	7.491×10^2
		14% etching	7.470×10^2	7.516×10^2
	2	0% etching	7.732×10^2	7.772×10^2
		3.5% etching	7.789×10^2	7.741×10^2
		7% etching	7.738×10^2	7.752×10^2
		7% etching with noise	7.658×10^2	7.742×10^2
		7%, no filling in upper watershed	7.481×10^2	7.723×10^2
		14% etching	7.704×10^2	7.744×10^2
$\log_{10} K_1$	1	0% etching	1.199×10^4	8.216×10^3
		3.5% etching	1.225×10^4	8.439×10^3
		7% etching	1.232×10^4	8.322×10^3
		7% etching with noise	1.225×10^4	8.264×10^3
		7%, no filling in upper watershed	1.216×10^4	8.378×10^3
		14% etching	1.257×10^4	8.507×10^3
	2	0% etching	1.343×10^4	9.070×10^3
		3.5% etching	1.366×10^4	9.284×10^3
		7% etching	1.368×10^4	9.142×10^3
		7% etching with noise	1.360×10^4	9.080×10^3
		7%, no filling in upper watershed	1.352×10^4	9.200×10^3
		14% etching	1.383×10^4	9.290×10^3

Table B.79: (continued)

Input	Lowering History	Initial Condition	μ^*	σ^*
$\log_{10} K_2$	1	0% etching	5.990×10^3	1.303×10^4
		3.5% etching	6.147×10^3	1.325×10^4
		7% etching	6.316×10^3	1.352×10^4
		7% etching with noise	6.281×10^3	1.348×10^4
		7%, no filling in upper watershed	6.859×10^3	1.377×10^4
		14% etching	6.619×10^3	1.401×10^4
	2	0% etching	5.991×10^3	1.303×10^4
		3.5% etching	6.149×10^3	1.325×10^4
		7% etching	6.321×10^3	1.351×10^4
		7% etching with noise	6.279×10^3	1.348×10^4
		7%, no filling in upper watershed	6.867×10^3	1.377×10^4
		14% etching	6.614×10^3	1.401×10^4

Table B.80: Lowering History Sensitivity for Model 800, BasicRt
South East Watershed Domain

Lowering History (Reference: History 1)	Initial Condition	μ^*	σ^*
2	0% etching	3.624×10^2	3.959×10^2
	3.5% etching	3.562×10^2	3.880×10^2
	7% etching	3.468×10^2	3.760×10^2
	7% etching with noise	3.451×10^2	3.746×10^2
	7%, no filling in upper watershed	3.434×10^2	3.739×10^2
	14% etching	3.193×10^2	3.480×10^2

Table B.81: Initial Condition Sensitivity for Model 800, BasicRt
South East Watershed Domain

Initial Condition (Reference: 7% etch)	Lowering History	μ^*	σ^*
0% etching	1	1.552×10^2	2.232×10^2
	2	1.610×10^2	2.103×10^2
3.5% etching	1	7.326×10^1	9.479×10^1
	2	7.485×10^1	8.807×10^1
7% etching with noise	1	2.870×10^1	4.729×10^1
	2	2.857×10^1	4.999×10^1
7%, no filling in upper watershed	1	1.771×10^2	3.843×10^2
	2	1.785×10^2	3.853×10^2
14% etching	1	1.416×10^2	2.264×10^2
	2	1.467×10^2	2.085×10^2

Table B.82: Parameter Sensitivity for Model 802, BasicThRt
South East Watershed Domain

Input	Lowering History	Initial Condition	μ^*	σ^*
D	1	0% etching	1.064×10^2	2.947×10^2
		3.5% etching	1.209×10^2	3.120×10^2
		7% etching	1.229×10^2	3.108×10^2
		7% etching with noise	1.290×10^2	3.287×10^2
		7%, no filling in upper watershed	3.787×10^2	8.306×10^2
		14% etching	1.291×10^2	3.400×10^2
	2	0% etching	1.060×10^2	3.022×10^2
		3.5% etching	1.209×10^2	3.240×10^2
		7% etching	1.215×10^2	3.197×10^2
		7% etching with noise	1.279×10^2	3.382×10^2
		7%, no filling in upper watershed	3.776×10^2	8.348×10^2
		14% etching	1.292×10^2	3.506×10^2
W_c	1	0% etching	1.231×10^2	1.420×10^2
		3.5% etching	1.262×10^2	1.440×10^2
		7% etching	1.230×10^2	1.427×10^2
		7% etching with noise	1.193×10^2	1.394×10^2
		7%, no filling in upper watershed	1.187×10^2	1.382×10^2
		14% etching	1.224×10^2	1.427×10^2
	2	0% etching	1.299×10^2	1.506×10^2
		3.5% etching	1.336×10^2	1.525×10^2
		7% etching	1.297×10^2	1.506×10^2
		7% etching with noise	1.251×10^2	1.482×10^2
		7%, no filling in upper watershed	1.255×10^2	1.461×10^2
		14% etching	1.302×10^2	1.513×10^2
$\log_{10} K_1$	1	0% etching	6.195×10^3	6.833×10^3
		3.5% etching	6.292×10^3	6.737×10^3
		7% etching	6.404×10^3	6.904×10^3
		7% etching with noise	6.434×10^3	7.012×10^3
		7%, no filling in upper watershed	6.938×10^3	6.173×10^3
		14% etching	6.454×10^3	6.877×10^3
	2	0% etching	6.974×10^3	7.546×10^3
		3.5% etching	7.033×10^3	7.405×10^3
		7% etching	7.126×10^3	7.570×10^3
		7% etching with noise	7.160×10^3	7.687×10^3
		7%, no filling in upper watershed	7.653×10^3	6.790×10^3
		14% etching	7.107×10^3	7.487×10^3

Table B.82: (continued)

Input	Lowering History	Initial Condition	μ^*	σ^*
$\log_{10} K_2$	1	0% etching	9.984×10^3	2.141×10^4
		3.5% etching	1.024×10^4	2.187×10^4
		7% etching	1.048×10^4	2.233×10^4
		7% etching with noise	1.040×10^4	2.218×10^4
		7%, no filling in upper watershed	1.098×10^4	2.279×10^4
		14% etching	1.091×10^4	2.307×10^4
	2	0% etching	1.047×10^4	2.244×10^4
		3.5% etching	1.073×10^4	2.290×10^4
		7% etching	1.095×10^4	2.333×10^4
		7% etching with noise	1.087×10^4	2.318×10^4
		7%, no filling in upper watershed	1.147×10^4	2.382×10^4
		14% etching	1.136×10^4	2.402×10^4
$\log_{10} \omega_{c1}$	1	0% etching	1.059×10^4	2.737×10^4
		3.5% etching	1.066×10^4	2.775×10^4
		7% etching	1.076×10^4	2.809×10^4
		7% etching with noise	1.077×10^4	2.800×10^4
		7%, no filling in upper watershed	1.033×10^4	2.627×10^4
		14% etching	1.100×10^4	2.871×10^4
	2	0% etching	1.114×10^4	2.886×10^4
		3.5% etching	1.119×10^4	2.921×10^4
		7% etching	1.127×10^4	2.949×10^4
		7% etching with noise	1.129×10^4	2.940×10^4
		7%, no filling in upper watershed	1.084×10^4	2.768×10^4
		14% etching	1.147×10^4	3.002×10^4
$\log_{10} \omega_{c2}$	1	0% etching	8.660×10^3	1.808×10^4
		3.5% etching	8.735×10^3	1.823×10^4
		7% etching	8.738×10^3	1.823×10^4
		7% etching with noise	8.748×10^3	1.825×10^4
		7%, no filling in upper watershed	8.697×10^3	1.814×10^4
		14% etching	8.862×10^3	1.848×10^4
	2	0% etching	8.970×10^3	1.871×10^4
		3.5% etching	9.029×10^3	1.883×10^4
		7% etching	9.023×10^3	1.881×10^4
		7% etching with noise	9.033×10^3	1.884×10^4
		7%, no filling in upper watershed	8.984×10^3	1.872×10^4
		14% etching	9.124×10^3	1.902×10^4

Table B.83: Lowering History Sensitivity for Model 802, BasicThRt
South East Watershed Domain

Lowering History (Reference: History 1)	Initial Condition	μ^*	σ^*
2	0% etching	3.565×10^2	5.720×10^2
	3.5% etching	3.499×10^2	5.581×10^2
	7% etching	3.372×10^2	5.397×10^2
	7% etching with noise	3.371×10^2	5.398×10^2
	7%, no filling in upper watershed	3.410×10^2	5.455×10^2
	14% etching	3.145×10^2	5.033×10^2

Table B.84: Initial Condition Sensitivity for Model 802, BasicThRt
South East Watershed Domain

Initial Condition (Reference: 7% etch)	Lowering History	μ^*	σ^*
0% etching	1	1.848×10^2	2.957×10^2
	2	1.726×10^2	2.704×10^2
3.5% etching	1	8.098×10^1	1.408×10^2
	2	7.234×10^1	1.237×10^2
7% etching with noise	1	2.366×10^1	5.574×10^1
	2	2.409×10^1	5.818×10^1
7%, no filling in upper watershed	1	1.973×10^2	6.635×10^2
	2	2.007×10^2	6.651×10^2
14% etching	1	1.587×10^2	2.792×10^2
	2	1.471×10^2	2.500×10^2

Table B.85: Parameter Sensitivity for Model 804, BasicSsRt
South East Watershed Domain

Input	Lowering History	Initial Condition	μ^*	σ^*
D	1	0% etching	6.143×10^2	1.880×10^3
		3.5% etching	6.316×10^2	1.897×10^3
		7% etching	6.059×10^2	1.802×10^3
		7% etching with noise	6.008×10^2	1.789×10^3
		7%, no filling in upper watershed	5.926×10^2	1.763×10^3
		14% etching	6.227×10^2	1.821×10^3
	2	0% etching	6.193×10^2	1.878×10^3
		3.5% etching	6.313×10^2	1.897×10^3
		7% etching	6.052×10^2	1.802×10^3
		7% etching with noise	6.039×10^2	1.788×10^3
		7%, no filling in upper watershed	5.939×10^2	1.762×10^3
		14% etching	6.230×10^2	1.821×10^3
W_c	1	0% etching	1.403×10^2	2.755×10^2
		3.5% etching	1.409×10^2	2.831×10^2
		7% etching	1.418×10^2	2.845×10^2
		7% etching with noise	1.352×10^2	2.780×10^2
		7%, no filling in upper watershed	2.664×10^2	6.398×10^2
		14% etching	1.546×10^2	3.092×10^2
	2	0% etching	1.486×10^2	2.982×10^2
		3.5% etching	1.520×10^2	3.048×10^2
		7% etching	1.516×10^2	3.054×10^2
		7% etching with noise	1.480×10^2	2.962×10^2
		7%, no filling in upper watershed	2.791×10^2	6.607×10^2
		14% etching	1.585×10^2	3.284×10^2
$\log_{10} K_{ss1}$	1	0% etching	1.245×10^4	1.882×10^4
		3.5% etching	1.232×10^4	1.875×10^4
		7% etching	1.227×10^4	1.861×10^4
		7% etching with noise	1.231×10^4	1.858×10^4
		7%, no filling in upper watershed	1.203×10^4	1.869×10^4
		14% etching	1.212×10^4	1.836×10^4
	2	0% etching	1.358×10^4	2.040×10^4
		3.5% etching	1.338×10^4	2.025×10^4
		7% etching	1.329×10^4	2.004×10^4
		7% etching with noise	1.333×10^4	2.000×10^4
		7%, no filling in upper watershed	1.306×10^4	2.015×10^4
		14% etching	1.307×10^4	1.971×10^4

Table B.85: (continued)

Input	Lowering History	Initial Condition	μ^*	σ^*
$\log_{10} K_{ss2}$	1	0% etching	6.228×10^4	5.362×10^4
		3.5% etching	6.240×10^4	5.372×10^4
		7% etching	6.243×10^4	5.375×10^4
		7% etching with noise	6.240×10^4	5.372×10^4
		7%, no filling in upper watershed	6.302×10^4	5.422×10^4
		14% etching	6.259×10^4	5.388×10^4
	2	0% etching	6.486×10^4	5.584×10^4
		3.5% etching	6.486×10^4	5.584×10^4
		7% etching	6.480×10^4	5.579×10^4
		7% etching with noise	6.477×10^4	5.576×10^4
		7%, no filling in upper watershed	6.540×10^4	5.627×10^4
		14% etching	6.478×10^4	5.576×10^4

Table B.86: Lowering History Sensitivity for Model 804, BasicSsRt
South East Watershed Domain

Lowering History (Reference: History 1)	Initial Condition	μ^*	σ^*
2	0% etching	1.170×10^3	1.254×10^3
	3.5% etching	1.128×10^3	1.207×10^3
	7% etching	1.086×10^3	1.160×10^3
	7% etching with noise	1.087×10^3	1.161×10^3
	7%, no filling in upper watershed	1.090×10^3	1.165×10^3
	14% etching	1.003×10^3	1.070×10^3

Table B.87: Initial Condition Sensitivity for Model 804, BasicSsRt
South East Watershed Domain

Initial Condition (Reference: 7% etch)	Lowering History	μ^*	σ^*
0% etching	1	1.337×10^2	1.425×10^2
	2	1.293×10^2	1.320×10^2
3.5% etching	1	5.404×10^1	6.041×10^1
	2	5.954×10^1	5.866×10^1
7% etching with noise	1	1.572×10^1	2.118×10^1
	2	1.613×10^1	2.093×10^1
7%, no filling in upper watershed	1	8.739×10^1	3.193×10^2
	2	8.670×10^1	3.188×10^2
14% etching	1	1.164×10^2	1.374×10^2
	2	1.199×10^2	1.348×10^2

Table B.88: Parameter Sensitivity for Model 808, BasicDdRt
South East Watershed Domain

Input	Lowering History	Initial Condition	μ^*	σ^*
D	1	0% etching	4.209×10^{0}	4.910×10^{0}
		3.5% etching	7.939×10^{0}	6.567×10^{0}
		7% etching	1.202×10^{1}	1.154×10^{1}
		7% etching with noise	1.269×10^{1}	1.112×10^{1}
		7%, no filling in upper watershed	1.187×10^{1}	1.277×10^{1}
		14% etching	1.932×10^{1}	2.150×10^{1}
	2	0% etching	4.505×10^{0}	5.493×10^{0}
		3.5% etching	8.182×10^{0}	6.001×10^{0}
		7% etching	1.224×10^{1}	1.086×10^{1}
		7% etching with noise	1.289×10^{1}	1.046×10^{1}
		7%, no filling in upper watershed	1.201×10^{1}	1.208×10^{1}
		14% etching	1.951×10^{1}	2.089×10^{1}
W_c	1	0% etching	4.601×10^{-1}	5.944×10^{-1}
		3.5% etching	4.864×10^{-1}	5.244×10^{-1}
		7% etching	4.630×10^{-1}	4.562×10^{-1}
		7% etching with noise	4.395×10^{-1}	4.490×10^{-1}
		7%, no filling in upper watershed	5.549×10^{-1}	7.729×10^{-1}
		14% etching	3.753×10^{-1}	5.914×10^{-1}
	2	0% etching	4.577×10^{-1}	5.958×10^{-1}
		3.5% etching	4.896×10^{-1}	5.245×10^{-1}
		7% etching	4.547×10^{-1}	4.475×10^{-1}
		7% etching with noise	4.429×10^{-1}	4.593×10^{-1}
		7%, no filling in upper watershed	5.305×10^{-1}	7.386×10^{-1}
		14% etching	3.750×10^{-1}	6.139×10^{-1}
$\log_{10} K_1$	1	0% etching	2.691×10^{2}	3.073×10^{2}
		3.5% etching	3.381×10^{2}	3.672×10^{2}
		7% etching	3.356×10^{2}	3.584×10^{2}
		7% etching with noise	3.320×10^{2}	3.553×10^{2}
		7%, no filling in upper watershed	3.265×10^{2}	3.483×10^{2}
		14% etching	2.996×10^{2}	3.060×10^{2}
	2	0% etching	2.802×10^{2}	3.173×10^{2}
		3.5% etching	3.503×10^{2}	3.766×10^{2}
		7% etching	3.462×10^{2}	3.664×10^{2}
		7% etching with noise	3.433×10^{2}	3.641×10^{2}
		7%, no filling in upper watershed	3.369×10^{2}	3.561×10^{2}
		14% etching	3.065×10^{2}	3.106×10^{2}

Table B.88: (continued)

Input	Lowering History	Initial Condition	μ^*	σ^*
$\log_{10} K_2$	1	0% etching	7.327×10^1	2.312×10^2
		3.5% etching	7.665×10^1	2.418×10^2
		7% etching	7.758×10^1	2.446×10^2
		7% etching with noise	7.368×10^1	2.323×10^2
		7%, no filling in upper watershed	1.450×10^2	4.582×10^2
		14% etching	8.363×10^1	2.634×10^2
	2	0% etching	7.327×10^1	2.312×10^2
		3.5% etching	7.665×10^1	2.418×10^2
		7% etching	7.758×10^1	2.446×10^2
		7% etching with noise	7.368×10^1	2.323×10^2
		7%, no filling in upper watershed	1.450×10^2	4.582×10^2
		14% etching	8.363×10^1	2.634×10^2
$\log_{10} \omega_c$	1	0% etching	8.776×10^1	2.239×10^2
		3.5% etching	9.475×10^1	2.338×10^2
		7% etching	9.814×10^1	2.362×10^2
		7% etching with noise	9.548×10^1	2.237×10^2
		7%, no filling in upper watershed	1.646×10^2	4.496×10^2
		14% etching	1.091×10^2	2.547×10^2
	2	0% etching	8.884×10^1	2.233×10^2
		3.5% etching	9.421×10^1	2.338×10^2
		7% etching	9.791×10^1	2.362×10^2
		7% etching with noise	9.511×10^1	2.237×10^2
		7%, no filling in upper watershed	1.644×10^2	4.495×10^2
		14% etching	1.090×10^2	2.547×10^2
b	1	0% etching	6.342×10^1	7.738×10^1
		3.5% etching	7.875×10^1	9.257×10^1
		7% etching	8.692×10^1	9.431×10^1
		7% etching with noise	8.383×10^1	9.243×10^1
		7%, no filling in upper watershed	8.503×10^1	9.260×10^1
		14% etching	9.201×10^1	1.035×10^2
	2	0% etching	6.634×10^1	8.215×10^1
		3.5% etching	9.286×10^1	1.009×10^2
		7% etching	1.008×10^2	1.091×10^2
		7% etching with noise	9.748×10^1	1.048×10^2
		7%, no filling in upper watershed	9.870×10^1	1.074×10^2
		14% etching	1.051×10^2	1.256×10^2

Table B.89: Lowering History Sensitivity for Model 808, BasicDdRt
South East Watershed Domain

Lowering History (Reference: History 1)	Initial Condition	μ^*	σ^*
2	0% etching	4.429×10^0	6.548×10^0
	3.5% etching	5.477×10^0	8.429×10^0
	7% etching	5.449×10^0	9.044×10^0
	7% etching with noise	5.330×10^0	8.620×10^0
	7%, no filling in upper watershed	5.363×10^0	8.885×10^0
	14% etching	5.061×10^0	9.457×10^0

Table B.90: Initial Condition Sensitivity for Model 808, BasicDdRt
South East Watershed Domain

Initial Condition (Reference: 7% etch)	Lowering History	μ^*	σ^*
0% etching	1	1.102×10^2	3.343×10^1
	2	1.093×10^2	3.489×10^1
3.5% etching	1	4.269×10^1	1.111×10^1
	2	4.226×10^1	1.123×10^1
7% etching with noise	1	2.135×10^0	3.675×10^0
	2	2.274×10^0	4.044×10^0
7%, no filling in upper watershed	1	8.764×10^0	4.031×10^1
	2	8.828×10^0	4.031×10^1
14% etching	1	7.181×10^1	2.576×10^1
	2	7.108×10^1	2.627×10^1

Table B.91: Parameter Sensitivity for Model 810, BasicHyRt
South East Watershed Domain

Input	Lowering History	Initial Condition	μ^*	σ^*
D	1	0% etching	1.216×10^4	2.655×10^4
		3.5% etching	2.490×10^3	5.518×10^3
		7% etching	1.237×10^4	2.718×10^4
		7% etching with noise	1.237×10^4	2.713×10^4
		7%, no filling in upper watershed	1.230×10^4	2.728×10^4
		14% etching	1.260×10^4	2.782×10^4
	2	0% etching	7.824×10^2	2.085×10^3
		3.5% etching	7.842×10^2	2.068×10^3
		7% etching	7.868×10^2	2.054×10^3
		7% etching with noise	8.129×10^2	2.123×10^3
		7%, no filling in upper watershed	1.776×10^3	3.614×10^3
		14% etching	2.528×10^3	5.561×10^3
W_c	1	0% etching	3.356×10^2	5.815×10^2
		3.5% etching	1.752×10^2	3.751×10^2
		7% etching	4.598×10^2	6.267×10^2
		7% etching with noise	1.759×10^2	3.762×10^2
		7%, no filling in upper watershed	1.616×10^3	4.541×10^3
		14% etching	1.479×10^3	4.066×10^3
	2	0% etching	1.318×10^3	3.383×10^3
		3.5% etching	7.603×10^1	2.403×10^2
		7% etching	8.046×10^1	2.544×10^2
		7% etching with noise	7.835×10^1	2.477×10^2
		7%, no filling in upper watershed	6.675×10^1	2.110×10^2
		14% etching	1.564×10^3	4.677×10^3
$\log_{10} K_1$	1	0% etching	9.177×10^3	1.075×10^4
		3.5% etching	8.485×10^3	1.124×10^4
		7% etching	9.587×10^3	1.094×10^4
		7% etching with noise	9.450×10^3	1.077×10^4
		7%, no filling in upper watershed	8.753×10^3	1.175×10^4
		14% etching	9.982×10^3	1.121×10^4
	2	0% etching	6.230×10^3	1.120×10^4
		3.5% etching	6.360×10^3	1.142×10^4
		7% etching	6.513×10^3	1.147×10^4
		7% etching with noise	6.365×10^3	1.126×10^4
		7%, no filling in upper watershed	6.704×10^3	1.197×10^4
		14% etching	8.219×10^3	1.197×10^4

Table B.91: (continued)

Input	Lowering History	Initial Condition	μ^*	σ^*
$\log_{10} K_2$	1	0% etching	1.319×10^4	2.783×10^4
		3.5% etching	4.557×10^3	1.144×10^4
		7% etching	1.361×10^4	2.855×10^4
		7% etching with noise	1.341×10^4	2.855×10^4
		7%, no filling in upper watershed	1.498×10^4	2.840×10^4
		14% etching	1.519×10^4	2.895×10^4
	2	0% etching	6.871×10^3	1.135×10^4
		3.5% etching	4.555×10^3	1.144×10^4
		7% etching	4.685×10^3	1.175×10^4
		7% etching with noise	4.631×10^3	1.163×10^4
		7%, no filling in upper watershed	6.158×10^3	1.228×10^4
		14% etching	4.885×10^3	1.220×10^4
$\log_{10} V_c$	1	0% etching	3.742×10^3	5.382×10^3
		3.5% etching	2.297×10^3	3.904×10^3
		7% etching	5.141×10^3	6.016×10^3
		7% etching with noise	2.307×10^3	3.917×10^3
		7%, no filling in upper watershed	3.809×10^3	5.403×10^3
		14% etching	2.359×10^3	3.976×10^3
	2	0% etching	2.715×10^3	4.971×10^3
		3.5% etching	1.242×10^3	2.622×10^3
		7% etching	1.273×10^3	2.687×10^3
		7% etching with noise	1.249×10^3	2.638×10^3
		7%, no filling in upper watershed	1.302×10^3	2.744×10^3
		14% etching	2.785×10^3	5.031×10^3
ϕ	1	0% etching	2.406×10^3	5.077×10^3
		3.5% etching	0.000×10^0	0.000×10^0
		7% etching	0.000×10^0	0.000×10^0
		7% etching with noise	0.000×10^0	0.000×10^0
		7%, no filling in upper watershed	0.000×10^0	0.000×10^0
		14% etching	0.000×10^0	0.000×10^0
	2	0% etching	0.000×10^0	0.000×10^0
		3.5% etching	0.000×10^0	0.000×10^0
		7% etching	0.000×10^0	0.000×10^0
		7% etching with noise	0.000×10^0	0.000×10^0
		7%, no filling in upper watershed	0.000×10^0	0.000×10^0
		14% etching	0.000×10^0	0.000×10^0

Table B.92: Lowering History Sensitivity for Model 810, BasicHyRt
South East Watershed Domain

Lowering History (Reference: History 1)	Initial Condition	μ^*	σ^*
2	0% etching	1.374×10^3	5.477×10^3
	3.5% etching	4.930×10^2	1.630×10^3
	7% etching	1.932×10^3	5.749×10^3
	7% etching with noise	1.285×10^3	5.552×10^3
	7%, no filling in upper watershed	1.237×10^3	5.576×10^3
	14% etching	1.380×10^3	5.694×10^3

Table B.93: Initial Condition Sensitivity for Model 810, BasicHyRt
South East Watershed Domain

Initial Condition (Reference: 7% etch)	Lowering History	μ^*	σ^*
0% etching	1	4.157×10^2	1.284×10^3
	2	4.078×10^2	1.336×10^3
3.5% etching	1	1.507×10^3	5.626×10^3
	2	6.400×10^1	9.553×10^1
7% etching with noise	1	6.788×10^2	1.947×10^3
	2	3.208×10^1	6.952×10^1
7%, no filling in upper watershed	1	7.500×10^2	1.856×10^3
	2	2.065×10^2	7.066×10^2
14% etching	1	6.798×10^2	1.794×10^3
	2	3.411×10^2	1.360×10^3

Table B.94: Parameter Sensitivity for Model 840, BasicChRt
South East Watershed Domain

Input	Lowering History	Initial Condition	μ^*	σ^*
D	1	0% etching	5.309×10^2	1.408×10^3
		3.5% etching	5.412×10^2	1.425×10^3
		7% etching	5.032×10^2	1.349×10^3
		7% etching with noise	5.397×10^2	1.428×10^3
		7%, no filling in upper watershed	4.418×10^2	1.131×10^3
		14% etching	4.948×10^2	1.300×10^3
	2	0% etching	5.207×10^2	1.515×10^3
		3.5% etching	5.345×10^2	1.542×10^3
		7% etching	5.080×10^2	1.451×10^3
		7% etching with noise	5.336×10^2	1.536×10^3
		7%, no filling in upper watershed	4.317×10^2	1.229×10^3
		14% etching	4.904×10^2	1.393×10^3
S_c	1	0% etching	3.119×10^2	9.620×10^2
		3.5% etching	3.164×10^2	9.826×10^2
		7% etching	3.260×10^2	1.013×10^3
		7% etching with noise	3.279×10^2	9.947×10^2
		7%, no filling in upper watershed	3.849×10^2	1.192×10^3
		14% etching	3.572×10^2	1.085×10^3
	2	0% etching	3.087×10^2	9.627×10^2
		3.5% etching	3.146×10^2	9.824×10^2
		7% etching	3.241×10^2	1.013×10^3
		7% etching with noise	3.198×10^2	9.964×10^2
		7%, no filling in upper watershed	3.821×10^2	1.193×10^3
		14% etching	3.475×10^2	1.088×10^3
W_c	1	0% etching	5.897×10^2	7.590×10^2
		3.5% etching	5.859×10^2	7.691×10^2
		7% etching	5.789×10^2	7.717×10^2
		7% etching with noise	5.869×10^2	7.756×10^2
		7%, no filling in upper watershed	6.459×10^2	8.915×10^2
		14% etching	5.998×10^2	7.860×10^2
	2	0% etching	5.972×10^2	7.681×10^2
		3.5% etching	5.921×10^2	7.782×10^2
		7% etching	5.946×10^2	7.866×10^2
		7% etching with noise	5.903×10^2	7.814×10^2
		7%, no filling in upper watershed	6.493×10^2	8.967×10^2
		14% etching	6.039×10^2	7.922×10^2

Table B.94: (continued)

Input	Lowering History	Initial Condition	μ^*	σ^*
$\log_{10} K_1$	1	0% etching	1.174×10^4	1.050×10^4
		3.5% etching	1.210×10^4	1.067×10^4
		7% etching	1.225×10^4	1.054×10^4
		7% etching with noise	1.219×10^4	1.048×10^4
		7%, no filling in upper watershed	1.183×10^4	1.040×10^4
		14% etching	1.257×10^4	1.063×10^4
	2	0% etching	1.230×10^4	1.091×10^4
		3.5% etching	1.265×10^4	1.107×10^4
		7% etching	1.278×10^4	1.092×10^4
		7% etching with noise	1.271×10^4	1.086×10^4
		7%, no filling in upper watershed	1.236×10^4	1.080×10^4
		14% etching	1.306×10^4	1.099×10^4
$\log_{10} K_2$	1	0% etching	7.054×10^3	1.347×10^4
		3.5% etching	7.167×10^3	1.367×10^4
		7% etching	7.258×10^3	1.390×10^4
		7% etching with noise	7.202×10^3	1.388×10^4
		7%, no filling in upper watershed	7.375×10^3	1.390×10^4
		14% etching	7.467×10^3	1.437×10^4
	2	0% etching	7.102×10^3	1.349×10^4
		3.5% etching	7.209×10^3	1.369×10^4
		7% etching	7.299×10^3	1.391×10^4
		7% etching with noise	7.245×10^3	1.389×10^4
		7%, no filling in upper watershed	7.413×10^3	1.392×10^4
		14% etching	7.504×10^3	1.438×10^4

Table B.95: Lowering History Sensitivity for Model 840, BasicChRt
South East Watershed Domain

Lowering History (Reference: History 1)	Initial Condition	μ^*	σ^*
2	0% etching	1.006×10^2	1.801×10^2
	3.5% etching	1.008×10^2	1.793×10^2
	7% etching	9.691×10^1	1.735×10^2
	7% etching with noise	9.532×10^1	1.716×10^2
	7%, no filling in upper watershed	9.781×10^1	1.743×10^2
	14% etching	8.993×10^1	1.636×10^2

Table B.96: Initial Condition Sensitivity for Model 840, BasicChRt
South East Watershed Domain

Initial Condition (Reference: 7% etch)	Lowering History	μ^*	σ^*
0% etching	1	1.500×10^2	2.372×10^2
	2	1.464×10^2	2.343×10^2
3.5% etching	1	6.535×10^1	9.013×10^1
	2	6.157×10^1	8.806×10^1
7% etching with noise	1	2.818×10^1	5.028×10^1
	2	2.612×10^1	5.225×10^1
7%, no filling in upper watershed	1	1.061×10^2	2.757×10^2
	2	1.051×10^2	2.766×10^2
14% etching	1	1.342×10^2	2.437×10^2
	2	1.272×10^2	2.377×10^2

Table B.97: Parameter Sensitivity for Model 00C, BasicSsDd
South East Watershed Domain

Input	Lowering History	Initial Condition	μ^*	σ^*
D	1	0% etching	1.012×10^1	1.884×10^1
		3.5% etching	1.877×10^1	3.541×10^1
		7% etching	2.197×10^1	3.837×10^1
		7% etching with noise	2.144×10^1	3.581×10^1
		7%, no filling in upper watershed	2.092×10^1	3.737×10^1
		14% etching	2.816×10^1	4.495×10^1
	2	0% etching	1.129×10^1	2.103×10^1
		3.5% etching	2.025×10^1	3.877×10^1
		7% etching	2.331×10^1	4.088×10^1
		7% etching with noise	2.279×10^1	3.806×10^1
		7%, no filling in upper watershed	2.144×10^1	4.008×10^1
		14% etching	2.924×10^1	4.649×10^1
$\log_{10} K_{ss}$	1	0% etching	2.662×10^3	7.485×10^3
		3.5% etching	2.815×10^3	7.798×10^3
		7% etching	2.838×10^3	7.844×10^3
		7% etching with noise	2.793×10^3	7.732×10^3
		7%, no filling in upper watershed	2.968×10^3	8.004×10^3
		14% etching	3.007×10^3	8.275×10^3
	2	0% etching	2.763×10^3	7.761×10^3
		3.5% etching	2.940×10^3	8.136×10^3
		7% etching	2.934×10^3	8.095×10^3
		7% etching with noise	2.883×10^3	7.967×10^3
		7%, no filling in upper watershed	3.064×10^3	8.256×10^3
		14% etching	3.099×10^3	8.513×10^3
$\log_{10} \omega_c$	1	0% etching	1.812×10^1	2.640×10^1
		3.5% etching	2.336×10^1	2.983×10^1
		7% etching	2.663×10^1	3.201×10^1
		7% etching with noise	2.642×10^1	3.216×10^1
		7%, no filling in upper watershed	2.311×10^1	2.664×10^1
		14% etching	3.065×10^1	3.431×10^1
	2	0% etching	1.887×10^1	2.798×10^1
		3.5% etching	2.408×10^1	3.034×10^1
		7% etching	2.731×10^1	3.237×10^1
		7% etching with noise	2.710×10^1	3.261×10^1
		7%, no filling in upper watershed	2.378×10^1	2.702×10^1
		14% etching	3.120×10^1	3.447×10^1

Table B.97: (continued)

Input	Lowering History	Initial Condition	μ^*	σ^*
b	1	0% etching	2.957×10^3	7.550×10^3
		3.5% etching	3.110×10^3	7.877×10^3
		7% etching	3.125×10^3	7.927×10^3
		7% etching with noise	3.078×10^3	7.813×10^3
		7%, no filling in upper watershed	3.217×10^3	8.103×10^3
		14% etching	3.288×10^3	8.366×10^3
	2	0% etching	3.073×10^3	7.829×10^3
		3.5% etching	3.248×10^3	8.216×10^3
		7% etching	3.233×10^3	8.181×10^3
		7% etching with noise	3.180×10^3	8.051×10^3
		7%, no filling in upper watershed	3.326×10^3	8.359×10^3
		14% etching	3.390×10^3	8.608×10^3

Table B.98: Lowering History Sensitivity for Model 00C, BasicSsDd
South East Watershed Domain

Lowering History (Reference: History 1)	Initial Condition	μ^*	σ^*
2	0% etching	1.403×10^1	6.577×10^1
	3.5% etching	1.735×10^1	7.989×10^1
	7% etching	1.385×10^1	6.031×10^1
	7% etching with noise	1.313×10^1	5.657×10^1
	7%, no filling in upper watershed	1.396×10^1	6.068×10^1
	14% etching	1.314×10^1	5.754×10^1

Table B.99: Initial Condition Sensitivity for Model 00C, BasicSsDd
South East Watershed Domain

Initial Condition (Reference: 7% etch)	Lowering History	μ^*	σ^*
0% etching	1	1.105×10^2	6.374×10^1
	2	1.101×10^2	5.908×10^1
3.5% etching	1	4.384×10^1	8.122×10^0
	2	4.482×10^1	1.347×10^1
7% etching with noise	1	7.025×10^0	2.824×10^1
	2	7.745×10^0	3.192×10^1
7%, no filling in upper watershed	1	3.622×10^1	1.345×10^2
	2	3.635×10^1	1.350×10^2
14% etching	1	9.971×10^1	7.762×10^1
	2	9.901×10^1	7.502×10^1

Table B.100: Parameter Sensitivity for Model A00, BasicVsRt
South East Watershed Domain

Input	Lowering History	Initial Condition	μ^*	σ^*
D	1	0% etching	1.471×10^3	2.565×10^3
		3.5% etching	1.543×10^3	2.653×10^3
		7% etching	1.538×10^3	2.616×10^3
		7% etching with noise	1.531×10^3	2.550×10^3
		7%, no filling in upper watershed	1.527×10^3	2.341×10^3
		14% etching	1.610×10^3	2.673×10^3
	2	0% etching	1.538×10^3	2.694×10^3
		3.5% etching	1.607×10^3	2.775×10^3
		7% etching	1.598×10^3	2.730×10^3
		7% etching with noise	1.589×10^3	2.662×10^3
		7%, no filling in upper watershed	1.601×10^3	2.458×10^3
		14% etching	1.667×10^3	2.784×10^3
H_{init}	1	0% etching	2.049×10^3	3.110×10^3
		3.5% etching	2.213×10^3	3.167×10^3
		7% etching	2.341×10^3	3.297×10^3
		7% etching with noise	2.352×10^3	3.330×10^3
		7%, no filling in upper watershed	2.357×10^3	3.310×10^3
		14% etching	2.527×10^3	3.528×10^3
	2	0% etching	2.049×10^3	3.129×10^3
		3.5% etching	2.280×10^3	3.276×10^3
		7% etching	2.374×10^3	3.366×10^3
		7% etching with noise	2.371×10^3	3.368×10^3
		7%, no filling in upper watershed	2.388×10^3	3.391×10^3
		14% etching	2.551×10^3	3.597×10^3
K_{sat}	1	0% etching	4.320×10^3	9.955×10^3
		3.5% etching	4.343×10^3	1.007×10^4
		7% etching	4.388×10^3	1.016×10^4
		7% etching with noise	4.404×10^3	1.012×10^4
		7%, no filling in upper watershed	4.508×10^3	1.044×10^4
		14% etching	4.501×10^3	1.040×10^4
	2	0% etching	4.350×10^3	1.003×10^4
		3.5% etching	4.369×10^3	1.013×10^4
		7% etching	4.423×10^3	1.024×10^4
		7% etching with noise	4.425×10^3	1.018×10^4
		7%, no filling in upper watershed	4.532×10^3	1.051×10^4
		14% etching	4.528×10^3	1.047×10^4

Table B.100: (continued)

Input	Lowering History	Initial Condition	μ^*	σ^*
R_m	1	0% etching	1.269×10^3	2.189×10^3
		3.5% etching	1.136×10^3	1.854×10^3
		7% etching	1.031×10^3	1.676×10^3
		7% etching with noise	1.017×10^3	1.646×10^3
		7%, no filling in upper watershed	1.039×10^3	1.690×10^3
		14% etching	9.043×10^2	1.492×10^3
	2	0% etching	1.240×10^3	2.170×10^3
		3.5% etching	1.063×10^3	1.751×10^3
		7% etching	9.903×10^2	1.631×10^3
		7% etching with noise	9.821×10^2	1.614×10^3
		7%, no filling in upper watershed	9.956×10^2	1.644×10^3
		14% etching	8.755×10^2	1.472×10^3
W_c	1	0% etching	4.133×10^2	5.420×10^2
		3.5% etching	4.178×10^2	5.446×10^2
		7% etching	4.050×10^2	5.310×10^2
		7% etching with noise	4.087×10^2	5.462×10^2
		7%, no filling in upper watershed	4.672×10^2	6.093×10^2
		14% etching	4.551×10^2	6.053×10^2
	2	0% etching	4.146×10^2	5.418×10^2
		3.5% etching	4.272×10^2	5.607×10^2
		7% etching	4.115×10^2	5.418×10^2
		7% etching with noise	4.109×10^2	5.441×10^2
		7%, no filling in upper watershed	4.768×10^2	6.221×10^2
		14% etching	4.500×10^2	5.918×10^2
$\log_{10} K_1$	1	0% etching	5.363×10^3	5.713×10^3
		3.5% etching	5.503×10^3	5.828×10^3
		7% etching	5.565×10^3	5.860×10^3
		7% etching with noise	5.520×10^3	5.821×10^3
		7%, no filling in upper watershed	5.501×10^3	5.720×10^3
		14% etching	5.663×10^3	5.923×10^3
	2	0% etching	5.518×10^3	5.856×10^3
		3.5% etching	5.672×10^3	5.982×10^3
		7% etching	5.720×10^3	5.987×10^3
		7% etching with noise	5.680×10^3	5.959×10^3
		7%, no filling in upper watershed	5.651×10^3	5.844×10^3
		14% etching	5.818×10^3	6.023×10^3

Table B.100: (continued)

Input	Lowering History	Initial Condition	μ^*	σ^*
$\log_{10} K_2$	1	0% etching	7.637×10^3	1.603×10^4
		3.5% etching	7.749×10^3	1.623×10^4
		7% etching	7.841×10^3	1.646×10^4
		7% etching with noise	7.745×10^3	1.630×10^4
		7%, no filling in upper watershed	7.971×10^3	1.657×10^4
		14% etching	8.058×10^3	1.688×10^4
	2	0% etching	7.762×10^3	1.629×10^4
		3.5% etching	7.881×10^3	1.653×10^4
		7% etching	7.973×10^3	1.673×10^4
		7% etching with noise	7.863×10^3	1.653×10^4
		7%, no filling in upper watershed	8.113×10^3	1.686×10^4
		14% etching	8.176×10^3	1.713×10^4

Table B.101: Lowering History Sensitivity for Model A00, BasicVsRt
South East Watershed Domain

Lowering History (Reference: History 1)	Initial Condition	μ^*	σ^*
2	0% etching	7.852×10^1	1.181×10^2
	3.5% etching	7.848×10^1	1.166×10^2
	7% etching	7.464×10^1	1.102×10^2
	7% etching with noise	7.334×10^1	1.074×10^2
	7%, no filling in upper watershed	7.529×10^1	1.133×10^2
	14% etching	6.879×10^1	1.028×10^2

Table B.102: Initial Condition Sensitivity for Model A00, BasicVsRt
South East Watershed Domain

Initial Condition (Reference: 7% etch)	Lowering History	μ^*	σ^*
0% etching	1	1.196×10^2	1.648×10^2
	2	1.161×10^2	1.701×10^2
3.5% etching	1	5.046×10^1	6.946×10^1
	2	4.840×10^1	5.756×10^1
7% etching with noise	1	3.928×10^1	6.613×10^1
	2	3.994×10^1	6.898×10^1
7%, no filling in upper watershed	1	5.740×10^1	1.277×10^2
	2	5.517×10^1	1.265×10^2
14% etching	1	9.979×10^1	1.200×10^2
	2	9.445×10^1	1.140×10^2

Table B.103: Parameter Sensitivity for Model C00, BasicSaRt
South East Watershed Domain

Input	Lowering History	Initial Condition	μ^*	σ^*
D	1	0% etching	1.502×10^3	4.004×10^3
		3.5% etching	2.640×10^2	6.291×10^2
		7% etching	2.410×10^2	6.004×10^2
		7% etching with noise	2.367×10^2	5.573×10^2
		7%, no filling in upper watershed	2.385×10^2	6.075×10^2
		14% etching	2.321×10^2	5.573×10^2
	2	0% etching	2.484×10^2	6.132×10^2
		3.5% etching	2.547×10^2	6.328×10^2
		7% etching	2.459×10^2	5.992×10^2
		7% etching with noise	2.353×10^2	5.581×10^2
		7%, no filling in upper watershed	2.403×10^2	6.075×10^2
		14% etching	2.286×10^2	5.595×10^2
H_0	1	0% etching	5.017×10^1	1.150×10^2
		3.5% etching	4.249×10^1	1.188×10^2
		7% etching	3.912×10^1	9.312×10^1
		7% etching with noise	3.082×10^1	8.404×10^1
		7%, no filling in upper watershed	4.507×10^1	1.141×10^2
		14% etching	4.182×10^1	1.075×10^2
	2	0% etching	4.645×10^1	1.130×10^2
		3.5% etching	4.687×10^1	1.186×10^2
		7% etching	4.405×10^1	9.504×10^1
		7% etching with noise	3.574×10^1	8.347×10^1
		7%, no filling in upper watershed	5.526×10^1	1.194×10^2
		14% etching	4.624×10^1	1.082×10^2
H_s	1	0% etching	2.889×10^1	6.690×10^1
		3.5% etching	2.991×10^1	7.324×10^1
		7% etching	2.804×10^1	7.602×10^1
		7% etching with noise	2.984×10^1	6.925×10^1
		7%, no filling in upper watershed	3.175×10^1	8.674×10^1
		14% etching	2.867×10^1	7.483×10^1
	2	0% etching	3.175×10^1	6.957×10^1
		3.5% etching	3.486×10^1	7.678×10^1
		7% etching	3.134×10^1	7.698×10^1
		7% etching with noise	2.356×10^1	6.793×10^1
		7%, no filling in upper watershed	4.166×10^1	9.241×10^1
		14% etching	3.018×10^1	7.516×10^1

Table B.103: (continued)

Input	Lowering History	Initial Condition	μ^*	σ^*
H_{init}	1	0% etching	2.810×10^1	6.942×10^1
H_{init}	1	3.5% etching	2.861×10^1	7.068×10^1
H_{init}	1	7% etching	3.444×10^1	8.270×10^1
H_{init}	1	7% etching with noise	3.031×10^1	7.081×10^1
H_{init}	1	7%, no filling in upper watershed	2.091×10^1	6.390×10^1
H_{init}	1	14% etching	1.509×10^1	4.293×10^1
H_{init}	2	0% etching	2.918×10^1	6.978×10^1
H_{init}	2	3.5% etching	2.850×10^1	7.079×10^1
H_{init}	2	7% etching	2.939×10^1	8.176×10^1
H_{init}	2	7% etching with noise	2.577×10^1	6.958×10^1
H_{init}	2	7%, no filling in upper watershed	2.117×10^1	6.382×10^1
H_{init}	2	14% etching	1.764×10^1	4.310×10^1
P_0	1	0% etching	1.318×10^3	4.097×10^3
P_0	1	3.5% etching	1.867×10^1	3.149×10^1
P_0	1	7% etching	2.501×10^1	3.617×10^1
P_0	1	7% etching with noise	2.424×10^1	4.595×10^1
P_0	1	7%, no filling in upper watershed	1.314×10^1	2.532×10^1
P_0	1	14% etching	1.437×10^1	2.865×10^1
P_0	2	0% etching	2.832×10^1	5.199×10^1
P_0	2	3.5% etching	2.378×10^1	3.884×10^1
P_0	2	7% etching	1.952×10^1	3.300×10^1
P_0	2	7% etching with noise	2.006×10^1	3.585×10^1
P_0	2	7%, no filling in upper watershed	1.780×10^1	3.035×10^1
P_0	2	14% etching	1.566×10^1	3.159×10^1
W_c	1	0% etching	6.197×10^2	5.535×10^2
W_c	1	3.5% etching	6.357×10^2	5.515×10^2
W_c	1	7% etching	6.476×10^2	5.583×10^2
W_c	1	7% etching with noise	6.024×10^2	5.571×10^2
W_c	1	7%, no filling in upper watershed	5.830×10^2	5.459×10^2
W_c	1	14% etching	6.391×10^2	5.619×10^2
W_c	2	0% etching	6.370×10^2	5.501×10^2
W_c	2	3.5% etching	6.419×10^2	5.683×10^2
W_c	2	7% etching	6.527×10^2	5.693×10^2
W_c	2	7% etching with noise	6.062×10^2	5.701×10^2
W_c	2	7%, no filling in upper watershed	5.939×10^2	5.468×10^2
W_c	2	14% etching	6.425×10^2	5.761×10^2

Table B.103: (continued)

Input	Lowering History	Initial Condition	μ^*	σ^*
$\log_{10} K_1$	1	0% etching	1.201×10^4	7.874×10^3
		3.5% etching	1.221×10^4	7.935×10^3
		7% etching	1.236×10^4	8.032×10^3
		7% etching with noise	1.231×10^4	7.981×10^3
		7%, no filling in upper watershed	1.225×10^4	7.860×10^3
		14% etching	1.255×10^4	8.108×10^3
	2	0% etching	1.257×10^4	8.260×10^3
		3.5% etching	1.274×10^4	8.311×10^3
		7% etching	1.287×10^4	8.397×10^3
		7% etching with noise	1.282×10^4	8.337×10^3
		7%, no filling in upper watershed	1.277×10^4	8.244×10^3
		14% etching	1.302×10^4	8.456×10^3
$\log_{10} K_2$	1	0% etching	1.338×10^4	2.594×10^4
		3.5% etching	1.361×10^4	2.628×10^4
		7% etching	1.391×10^4	2.670×10^4
		7% etching with noise	1.385×10^4	2.663×10^4
		7%, no filling in upper watershed	1.451×10^4	2.710×10^4
		14% etching	1.436×10^4	2.736×10^4
	2	0% etching	1.356×10^4	2.645×10^4
		3.5% etching	1.380×10^4	2.682×10^4
		7% etching	1.409×10^4	2.719×10^4
		7% etching with noise	1.402×10^4	2.709×10^4
		7%, no filling in upper watershed	1.468×10^4	2.757×10^4
		14% etching	1.453×10^4	2.782×10^4

Table B.104: Lowering History Sensitivity for Model C00, BasicSaRt
South East Watershed Domain

Lowering History (Reference: History 1)	Initial Condition	μ^*	σ^*
2	0% etching	2.639×10^2	7.362×10^2
	3.5% etching	1.877×10^2	2.863×10^2
	7% etching	1.789×10^2	2.696×10^2
	7% etching with noise	1.799×10^2	2.727×10^2
	7%, no filling in upper watershed	1.815×10^2	2.750×10^2
	14% etching	1.691×10^2	2.566×10^2

Table B.105: Initial Condition Sensitivity for Model C00, BasicSaRt
South East Watershed Domain

Initial Condition (Reference: 7% etch)	Lowering History	μ^*	σ^*
0% etching	1	3.336×10^2	7.562×10^2
	2	2.491×10^2	3.515×10^2
3.5% etching	1	1.383×10^2	2.052×10^2
	2	1.298×10^2	1.946×10^2
7% etching with noise	1	3.595×10^1	6.133×10^1
	2	3.489×10^1	6.226×10^1
7%, no filling in upper watershed	1	1.896×10^2	4.367×10^2
	2	1.918×10^2	4.394×10^2
14% etching	1	2.171×10^2	3.042×10^2
	2	2.074×10^2	2.966×10^2

Table B.106: Parameter Sensitivity for Model CCC, BasicCv
South East Watershed Domain

Input	Lowering History	Initial Condition	μ^*	σ^*
D	1	0% etching	9.803×10^1	2.899×10^2
		3.5% etching	9.719×10^1	2.559×10^2
		7% etching	9.384×10^1	2.368×10^2
		7% etching with noise	1.089×10^2	2.841×10^2
		7%, no filling in upper watershed	9.367×10^1	2.334×10^2
		14% etching	1.054×10^2	2.484×10^2
	2	0% etching	9.656×10^1	2.806×10^2
		3.5% etching	8.030×10^1	2.029×10^2
		7% etching	9.153×10^1	2.248×10^2
		7% etching with noise	9.538×10^1	2.391×10^2
		7%, no filling in upper watershed	1.079×10^2	2.791×10^2
		14% etching	1.045×10^2	2.451×10^2
$\log_{10} K$	1	0% etching	8.080×10^4	4.256×10^4
		3.5% etching	8.135×10^4	4.221×10^4
		7% etching	8.181×10^4	4.188×10^4
		7% etching with noise	8.160×10^4	4.209×10^4
		7%, no filling in upper watershed	8.246×10^4	4.042×10^4
		14% etching	8.260×10^4	4.121×10^4
	2	0% etching	8.479×10^4	4.458×10^4
		3.5% etching	8.519×10^4	4.410×10^4
		7% etching	8.550×10^4	4.368×10^4
		7% etching with noise	8.533×10^4	4.394×10^4
		7%, no filling in upper watershed	8.618×10^4	4.221×10^4
		14% etching	8.601×10^4	4.283×10^4
f	1	0% etching	3.963×10^2	1.191×10^3
		3.5% etching	3.862×10^2	1.207×10^3
		7% etching	3.947×10^2	1.185×10^3
		7% etching with noise	4.379×10^2	1.225×10^3
		7%, no filling in upper watershed	3.402×10^2	1.019×10^3
		14% etching	4.081×10^2	1.195×10^3
	2	0% etching	4.134×10^2	1.268×10^3
		3.5% etching	4.447×10^2	1.274×10^3
		7% etching	4.188×10^2	1.258×10^3
		7% etching with noise	4.326×10^2	1.306×10^3
		7%, no filling in upper watershed	3.687×10^2	1.084×10^3
		14% etching	4.079×10^2	1.268×10^3

Table B.107: Lowering History Sensitivity for Model CCC, BasicCv
South East Watershed Domain

Lowering History (Reference: History 1)	Initial Condition	μ^*	σ^*
2	0% etching	1.216×10^3	1.346×10^3
	3.5% etching	1.173×10^3	1.291×10^3
	7% etching	1.129×10^3	1.240×10^3
	7% etching with noise	1.133×10^3	1.248×10^3
	7%, no filling in upper watershed	1.134×10^3	1.243×10^3
	14% etching	1.044×10^3	1.142×10^3

Table B.108: Initial Condition Sensitivity for Model CCC, BasicCv
South East Watershed Domain

Initial Condition (Reference: 7% etch)	Lowering History	μ^*	σ^*
0% etching	1	2.077×10^2	3.358×10^2
	2	2.520×10^2	2.958×10^2
3.5% etching	1	9.668×10^1	1.564×10^2
	2	1.118×10^2	1.367×10^2
7% etching with noise	1	4.616×10^1	9.188×10^1
	2	4.688×10^1	9.543×10^1
7%, no filling in upper watershed	1	1.759×10^2	3.880×10^2
	2	1.793×10^2	3.941×10^2
14% etching	1	1.775×10^2	3.057×10^2
	2	2.216×10^2	2.599×10^2

Appendix C

Calibration Calculations and Plots

C.1 Introduction

This appendix contains summary results from the calibration procedure. The first section below contains tables that list, for each calibrated model, the parameters and their best-fit (calibrated) values. (Note that in these tables, parameter D should be read as $\log_{10} D$). The next section contains a series of four-panel images. For each calibrated model, the corresponding images show maps of simulated modern topography, differences between observed and simulated topography, cumulative postglacial erosion, and residuals from calculation of the objective function (weighted differences between observed and simulated elevations; see Chapter 6). The final section presents a series of tables listing, for each of eight selected models, the first four statistical moments (mean, standard deviation, skewness, and kurtosis) of the posterior distribution obtained from Bayesian calibration (see Chapter 8).

C.2 Hybrid EGO-NL2SOL Results

C.2.1 Calibrated Parameter Tables

Table C.1: Calibrated parameters from hybrid calibration method (EGO and NL2SOL) for model 000 in Upper Franks Creek Watershed (SEW domain)

Parameter Name	Optimal Value	Standard Deviation
$\log_{10} K$	-3.991	0.207
D	-1.969	1.865

Table C.2: Calibrated parameters from hybrid calibration method (EGO and NL2SOL) for model 001 in Upper Franks Creek Watershed (SEW domain)

Parameter Name	Optimal Value	Standard Deviation
$\log_{10} K$	-6.000	1.666
D	-1.300	0.572
m	0.855	0.268

Table C.3: Calibrated parameters from hybrid calibration method (EGO and NL2SOL) for model 002 in Upper Franks Creek Watershed (SEW domain)

Parameter Name	Optimal Value	Standard Deviation
$\log_{10} K$	-2.555	0.124
$\log_{10} \omega_c$	-0.120	0.174
D	-1.300	0.806

Table C.4: Calibrated parameters from hybrid calibration method (EGO and NL2SOL) for model 004 in Upper Franks Creek Watershed (SEW domain)

Parameter Name	Optimal Value	Standard Deviation
$\log_{10} K_{ss}$	-3.657	0.269
D	-2.446	3.461

Table C.5: Calibrated parameters from hybrid calibration method (EGO and NL2SOL) for model 008 in Upper Franks Creek Watershed (SEW domain)

Parameter Name	Optimal Value	Standard Deviation
$\log_{10} K$	-1.987	0.974
$\log_{10} \omega_c$	0.209	3.960
D	-1.530	2.273
b	0.895	3.216

Table C.6: Calibrated parameters from hybrid calibration method (EGO and NL2SOL) for model 00C in Upper Franks Creek Watershed (SEW domain)

Parameter Name	Optimal Value	Standard Deviation
$\log_{10} K_{ss}$	-1.099	2.122
$\log_{10} \omega_c$	-0.349	3.104
D	-2.570	8.008
b	4.412	43.656

Table C.7: Calibrated parameters from hybrid calibration method (EGO and NL2SOL) for model 010 in Upper Franks Creek Watershed (SEW domain)

Parameter Name	Optimal Value	Standard Deviation
$\log_{10} K$	-3.584	0.114
D	-1.340	0.557
$\log_{10} V_c$	0.965	0.302

Table C.8: Calibrated parameters from hybrid calibration method (EGO and NL2SOL) for model 012 in Upper Franks Creek Watershed (SEW domain)

Parameter Name	Optimal Value	Standard Deviation
$\log_{10} K$	-3.263	0.656
$\log_{10} \omega_c$	-1.703	1.602
D	-1.388	0.573
$\log_{10} V_c$	0.642	0.500

Table C.9: Calibrated parameters from hybrid calibration method (EGO and NL2SOL) for model 014 in Upper Franks Creek Watershed (SEW domain)

Parameter Name	Optimal Value	Standard Deviation
$\log_{10} K_{ss}$	-3.222	0.250
D	-1.937	1.255
$\log_{10} V_c$	0.941	0.549

Table C.10: Calibrated parameters from hybrid calibration method (EGO and NL2SOL) for model 018 in Upper Franks Creek Watershed (SEW domain)

Parameter Name	Optimal Value	Standard Deviation
$\log_{10} K$	-1.810	0.093
$\log_{10} \omega_c$	0.257	0.135
D	-1.301	0.262
b	1.311	0.394
$\log_{10} V_c$	0.973	0.461

Table C.11: Calibrated parameters from hybrid calibration method (EGO and NL2SOL) for model 030 in Upper Franks Creek Watershed (SEW domain)

Parameter Name	Optimal Value	Standard Deviation
F_f	0.135	0.414
$\log_{10} K$	-3.605	0.416
D	-1.353	1.209
$\log_{10} V_c$	0.943	0.932

Table C.12: Calibrated parameters from hybrid calibration method (EGO and NL2SOL) for model 100 in Upper Franks Creek Watershed (SEW domain)

Parameter Name	Optimal Value	Standard Deviation
$\log_{10} K_q$	-2.264	4.707
I_m	6397.967	117478.666
F	0.565	38350.546
D	-1.962	2.332
p_d	2.083	141330.434

Table C.13: Calibrated parameters from hybrid calibration method (EGO and NL2SOL) for model 102 in Upper Franks Creek Watershed (SEW domain)

Parameter Name	Optimal Value	Standard Deviation
$\log_{10} K_q$	-1.984	1.250
$\log_{10} \omega_c$	-0.504	5.233
I_m	1405.721	25031.966
F	0.594	8.206
D	-1.301	0.511
p_d	4.380	8.745

Table C.14: Calibrated parameters from hybrid calibration method (EGO and NL2SOL) for model 104 in Upper Franks Creek Watershed (SEW domain)

Parameter Name	Optimal Value	Standard Deviation
$\log_{10} K_{q,ss}$	-2.702	9.454
I_m	2312.896	72345.580
F	0.475	1.094
D	-2.475	5.575
p_d	3.961	140.742

Table C.15: Calibrated parameters from hybrid calibration method (EGO and NL2SOL) for model 108 in Upper Franks Creek Watershed (SEW domain)

Parameter Name	Optimal Value	Standard Deviation
$\log_{10} K_q$	-0.641	3.960
$\log_{10} \omega_c$	-0.536	55.079
I_m	2150.387	83170.366
F	0.369	15.944
D	-1.624	2.670
p_d	3.340	21.836
b	4.606	29.327

Table C.16: Calibrated parameters from hybrid calibration method (EGO and NL2SOL) for model 110 in Upper Franks Creek Watershed (SEW domain)

Parameter Name	Optimal Value	Standard Deviation
$\log_{10} K_q$	-1.981	0.221
I_m	5096.191	1417.958
F	0.511	0.080
D	-1.591	0.210
p_d	2.142	0.653
$\log_{10} V$	-0.476	0.052

Table C.17: Calibrated parameters from hybrid calibration method (EGO and NL2SOL) for model 200 in Upper Franks Creek Watershed (SEW domain)

Parameter Name	Optimal Value	Standard Deviation
K_{sat}	300.000	208.937
$\log_{10} K$	-3.692	0.148
D	-1.526	0.363

Table C.18: Calibrated parameters from hybrid calibration method (EGO and NL2SOL) for model 202 in Upper Franks Creek Watershed (SEW domain)

Parameter Name	Optimal Value	Standard Deviation
K_{sat}	299.502	1948.820
$\log_{10} K$	-3.379	0.699
$\log_{10} \omega_c$	-2.273	1.288
D	-1.300	1.150

Table C.19: Calibrated parameters from hybrid calibration method (EGO and NL2SOL) for model 204 in Upper Franks Creek Watershed (SEW domain)

Parameter Name	Optimal Value	Standard Deviation
K_{sat}	231.349	810.285
$\log_{10} K_{ss}$	-3.401	0.457
D	-1.732	1.014

Table C.20: Calibrated parameters from hybrid calibration method (EGO and NL2SOL) for model 208 in Upper Franks Creek Watershed (SEW domain)

Parameter Name	Optimal Value	Standard Deviation
K_{sat}	0.352	541.793
$\log_{10} K$	-1.656	0.447
$\log_{10} \omega_c$	1.393	1.490
D	-1.411	1.702
b	1.861	17.478

Table C.21: Calibrated parameters from hybrid calibration method (EGO and NL2SOL) for model 210 in Upper Franks Creek Watershed (SEW domain)

Parameter Name	Optimal Value	Standard Deviation
K_{sat}	13.376	22.372
$\log_{10} K$	-3.636	0.245
D	-1.418	1.364
$\log_{10} V_c$	0.993	0.035

Table C.22: Calibrated parameters from hybrid calibration method (EGO and NL2SOL) for model 300 in Upper Franks Creek Watershed (SEW domain)

Parameter Name	Optimal Value	Standard Deviation
K_{sat}	300.000	1332.005
$\log_{10} K_q$	-3.879	2.504
F	0.533	2.897
D	-1.718	1.047
p_d	1.830	7.050

Table C.23: Calibrated parameters from hybrid calibration method (EGO and NL2SOL) for model 400 in Upper Franks Creek Watershed (SEW domain)

Parameter Name	Optimal Value	Standard Deviation
$\log_{10} K$	-4.095	0.223
D	-1.525	1.695
P_0	0.001	0.003
H_s	0.700	6.401

Table C.24: Calibrated parameters from hybrid calibration method (EGO and NL2SOL) for model 600 in Upper Franks Creek Watershed (SEW domain)

Parameter Name	Optimal Value	Standard Deviation
K_{sat}	0.030	517.045
$\log_{10} K$	-4.027	0.312
D	-1.300	1.167
P_0	0.001	0.004
H_s	0.697	19.263
H_0	0.101	2.756

Table C.25: Calibrated parameters from hybrid calibration method (EGO and NL2SOL) for model 800 in Upper Franks Creek Watershed (SEW domain)

Parameter Name	Optimal Value	Standard Deviation
$\log_{10} K_2$	-7.174	504.639
$\log_{10} K_1$	-3.624	0.131
D	-1.376	0.585

Table C.26: Calibrated parameters from hybrid calibration method (EGO and NL2SOL) for model 802 in Upper Franks Creek Watershed (SEW domain)

Parameter Name	Optimal Value	Standard Deviation
$\log_{10} K_2$	-3.000	5.171
$\log_{10} K_1$	-3.220	1.082
D	-1.300	0.260
$\log_{10} \omega_{c2}$	0.173	8.780
$\log_{10} \omega_{c1}$	-1.579	2.445

Table C.27: Calibrated parameters from hybrid calibration method (EGO and NL2SOL) for model 804 in Upper Franks Creek Watershed (SEW domain)

Parameter Name	Optimal Value	Standard Deviation
$\log_{10} K_{ss2}$	-7.670	1042.141
$\log_{10} K_{ss1}$	-3.801	0.082
D	-1.372	0.355

Table C.28: Calibrated parameters from hybrid calibration method (EGO and NL2SOL) for model 808 in Upper Franks Creek Watershed (SEW domain)

Parameter Name	Optimal Value	Standard Deviation
$\log_{10} K_2$	-3.000	11.841
$\log_{10} K_1$	-1.377	1.069
$\log_{10} \omega_c$	1.390	2.424
D	-1.300	0.417
b	2.775	18.158

Table C.29: Calibrated parameters from hybrid calibration method (EGO and NL2SOL) for model 810 in Upper Franks Creek Watershed (SEW domain)

Parameter Name	Optimal Value	Standard Deviation
$\log_{10} K_2$	-8.000	4291.350
$\log_{10} K_1$	-3.592	0.203
D	-1.324	0.667
$\log_{10} V_c$	-0.528	1.275

Table C.30: Calibrated parameters from hybrid calibration method (EGO and NL2SOL) for model 840 in Upper Franks Creek Watershed (SEW domain)

Parameter Name	Optimal Value	Standard Deviation
$\log_{10} K_2$	-8.000	3396.120
$\log_{10} K_1$	-3.620	0.207
D	-1.404	1.001
S_c	1.250	18.571

Table C.31: Calibrated parameters from hybrid calibration method (EGO and NL2SOL) for model 842 in Upper Franks Creek Watershed (SEW domain)

Parameter Name	Optimal Value	Standard Deviation
$\log_{10} K_2$	-3.000	0.191
$\log_{10} K_1$	-3.065	0.531
D	-2.298	0.282
$\log_{10} \omega_{c2}$	0.194	0.145
S_c	0.375	0.061
$\log_{10} \omega_{c1}$	-1.230	0.977

Table C.32: Calibrated parameters from hybrid calibration method (EGO and NL2SOL) for model A00 in Upper Franks Creek Watershed (SEW domain)

Parameter Name	Optimal Value	Standard Deviation
K_{sat}	0.030	37.350
$\log_{10} K_2$	-7.816	2178.203
$\log_{10} K_1$	-3.628	0.162
D	-1.382	0.772

Table C.33: Calibrated parameters from hybrid calibration method (EGO and NL2SOL) for model C00 in Upper Franks Creek Watershed (SEW domain)

Parameter Name	Optimal Value	Standard Deviation
$\log_{10} K_2$	-4.926	3.365
$\log_{10} K_1$	-3.855	0.257
D	-1.321	0.673
P_0	0.001	0.004
H_s	0.700	6.328

Table C.34: Calibrated parameters from hybrid calibration method (EGO and NL2SOL) for model CCC in Upper Franks Creek Watershed (SEW domain)

Parameter Name	Optimal Value	Standard Deviation
$\log_{10} K$	-3.939	0.277
f	0.500	1.744
D	-1.949	1.573

C.2.2 Modeled Modern Topography

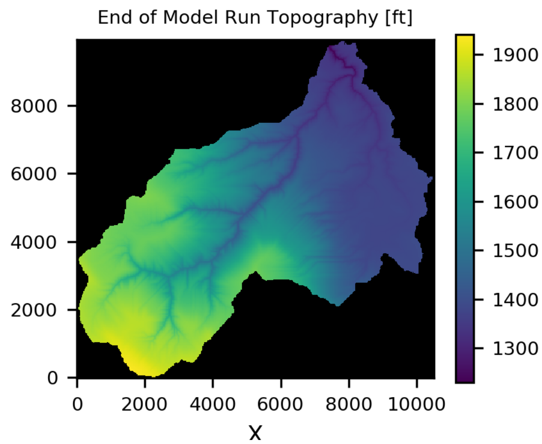

(a) Modeled modern topography.

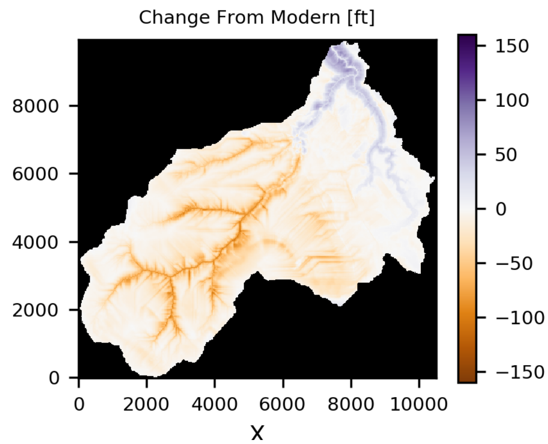

(b) Modeled modern topography minus actual modern topography. Purple indicates that modeled topography is above actual topography and orange indicates that modeled topography is below actual topography.

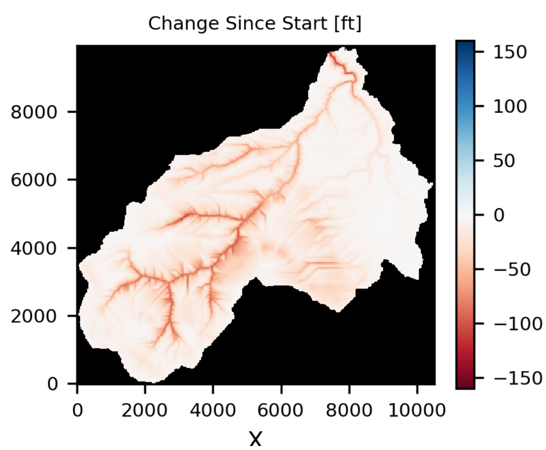

(c) Cumulative erosion from 13 ka to modern. Red indicates that erosion occurred, and blue indicates that deposition occurred.

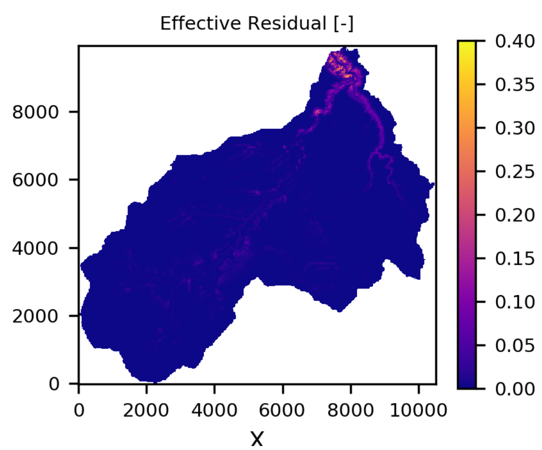

(d) Effective residual value at each grid node used in objective function calculation.

Figure C.1: Calibration results summary for Model 000 showing spatially distributed values at the end of the 13 ka to present model run with calibrated parameter values in Upper Franks Creek Watershed (SEW domain).

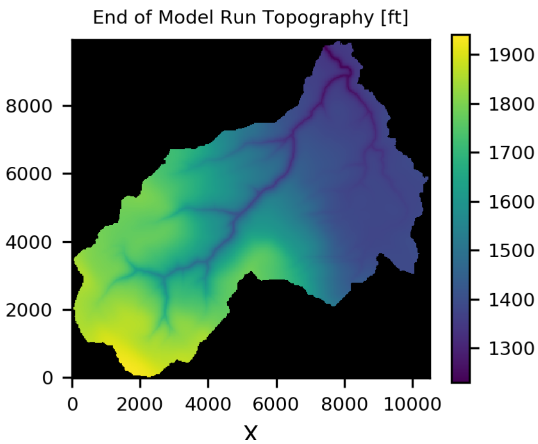

(a) Modeled modern topography.

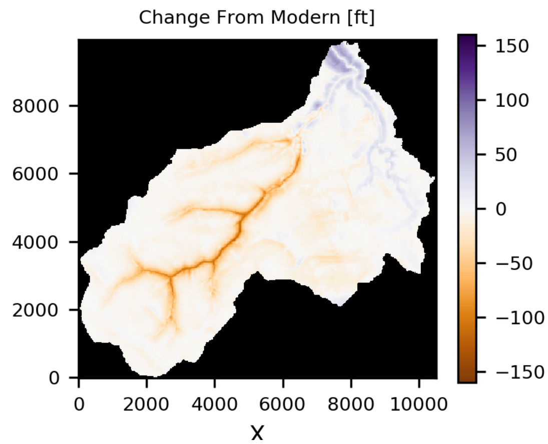

(b) Modeled modern topography minus actual modern topography. Purple indicates that modeled topography is above actual topography and orange indicates that modeled topography is below actual topography.

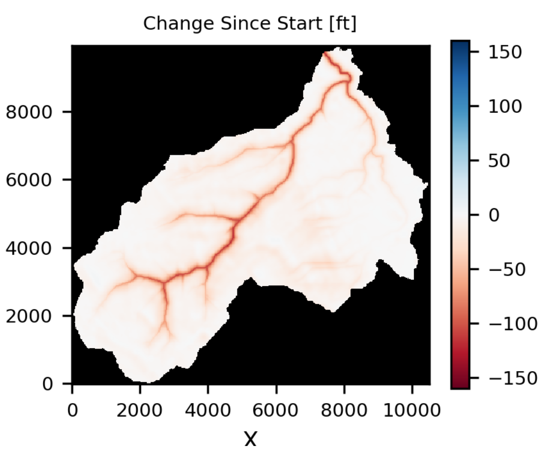

(c) Cumulative erosion from 13 ka to modern. Red indicates that erosion occurred, and blue indicates that deposition occurred.

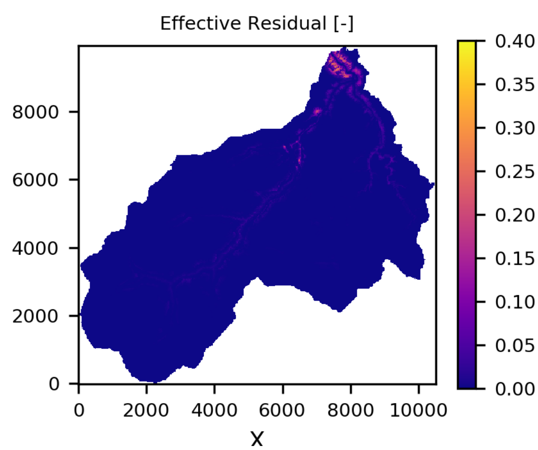

(d) Effective residual value at each grid node used in objective function calculation.

Figure C.2: Calibration results summary for Model 001 showing spatially distributed values at the end of the 13 ka to present model run with calibrated parameter values in Upper Franks Creek Watershed (SEW domain).

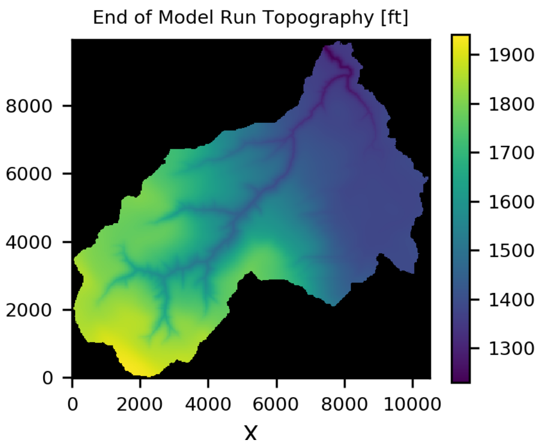

(a) Modeled modern topography.

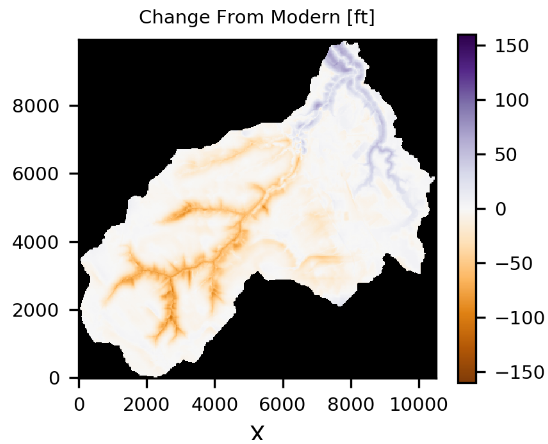

(b) Modeled modern topography minus actual modern topography. Purple indicates that modeled topography is above actual topography and orange indicates that modeled topography is below actual topography.

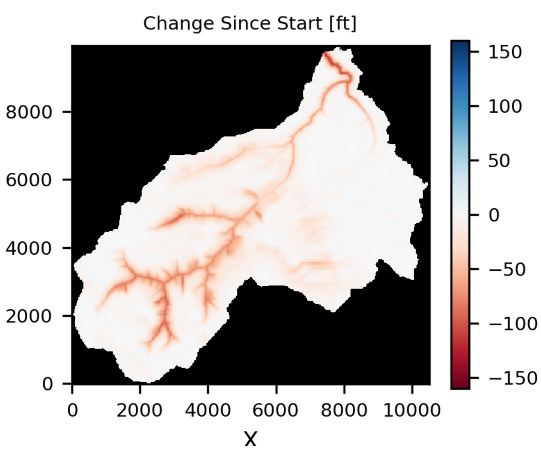

(c) Cumulative erosion from 13 ka to modern. Red indicates that erosion occurred, and blue indicates that deposition occurred.

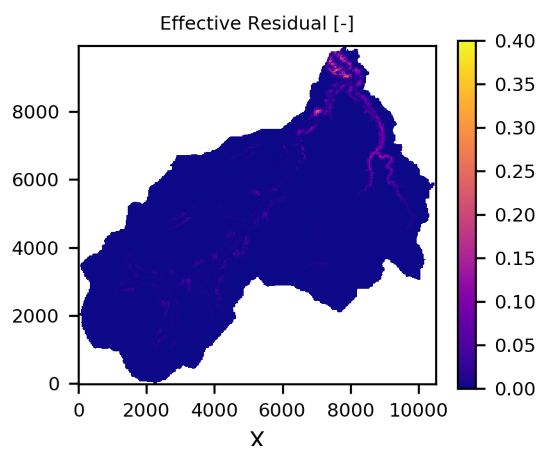

(d) Effective residual value at each grid node used in objective function calculation.

Figure C.3: Calibration results summary for Model 002 showing spatially distributed values at the end of the 13 ka to present model run with calibrated parameter values in Upper Franks Creek Watershed (SEW domain).

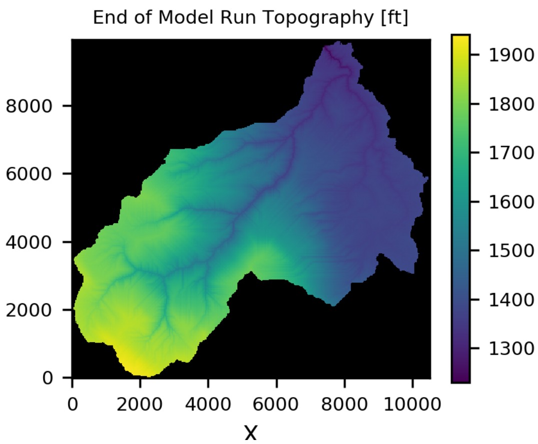

(a) Modeled modern topography.

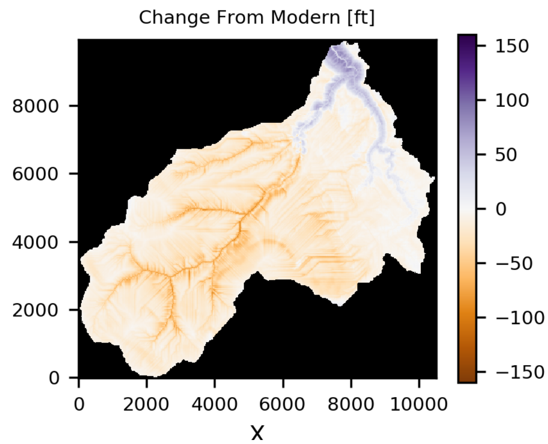

(b) Modeled modern topography minus actual modern topography. Purple indicates that modeled topography is above actual topography and orange indicates that modeled topography is below actual topography.

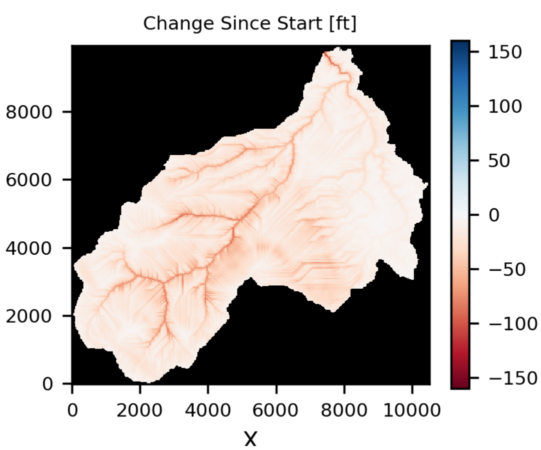

(c) Cumulative erosion from 13 ka to modern. Red indicates that erosion occurred, and blue indicates that deposition occurred.

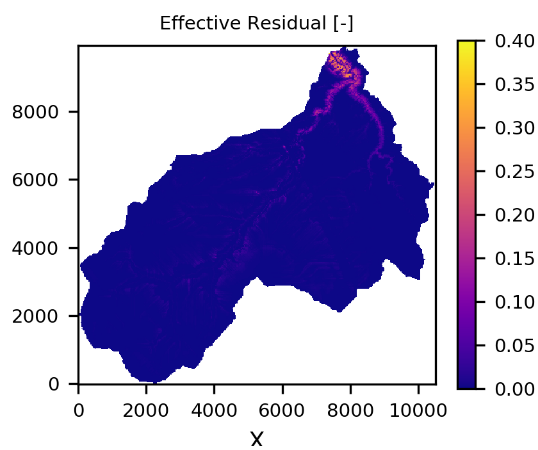

(d) Effective residual value at each grid node used in objective function calculation.

Figure C.4: Calibration results summary for Model 004 showing spatially distributed values at the end of the 13 ka to present model run with calibrated parameter values in Upper Franks Creek Watershed (SEW domain).

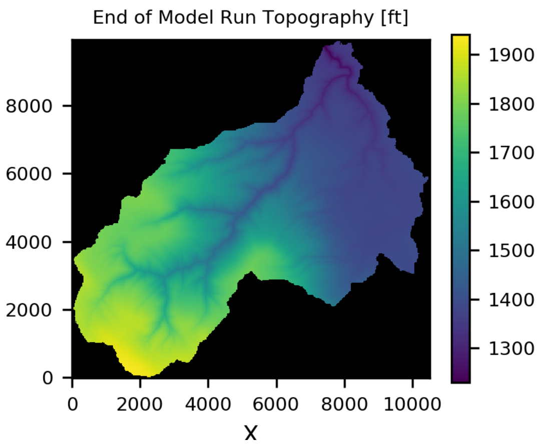

(a) Modeled modern topography.

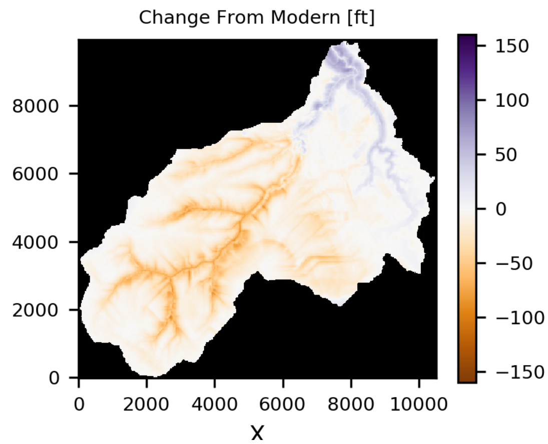

(b) Modeled modern topography minus actual modern topography. Purple indicates that modeled topography is above actual topography and orange indicates that modeled topography is below actual topography.

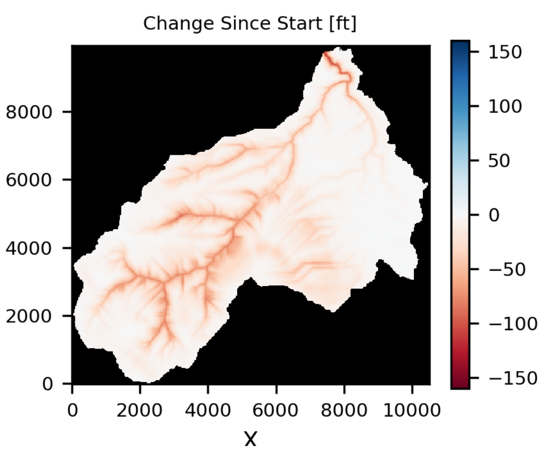

(c) Cumulative erosion from 13 ka to modern. Red indicates that erosion occurred, and blue indicates that deposition occurred.

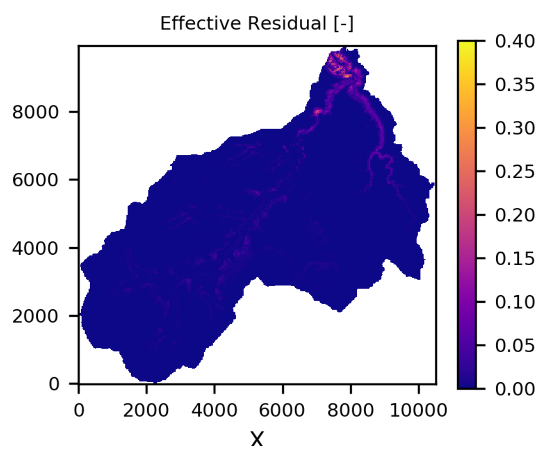

(d) Effective residual value at each grid node used in objective function calculation.

Figure C.5: Calibration results summary for Model 008 showing spatially distributed values at the end of the 13 ka to present model run with calibrated parameter values in Upper Franks Creek Watershed (SEW domain).

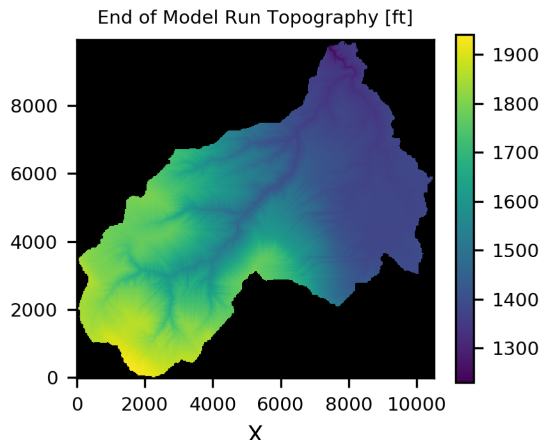

(a) Modeled modern topography.

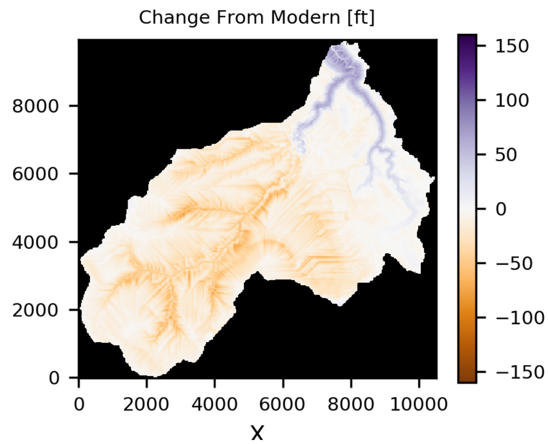

(b) Modeled modern topography minus actual modern topography. Purple indicates that modeled topography is above actual topography and orange indicates that modeled topography is below actual topography.

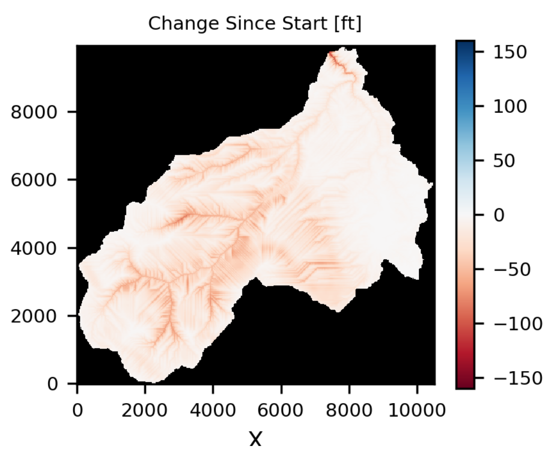

(c) Cumulative erosion from 13 ka to modern. Red indicates that erosion occurred, and blue indicates that deposition occurred.

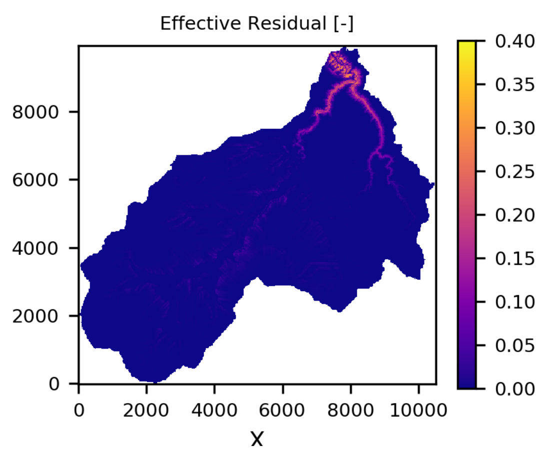

(d) Effective residual value at each grid node used in objective function calculation.

Figure C.6: Calibration results summary for Model 00C showing spatially distributed values at the end of the 13 ka to present model run with calibrated parameter values in Upper Franks Creek Watershed (SEW domain).

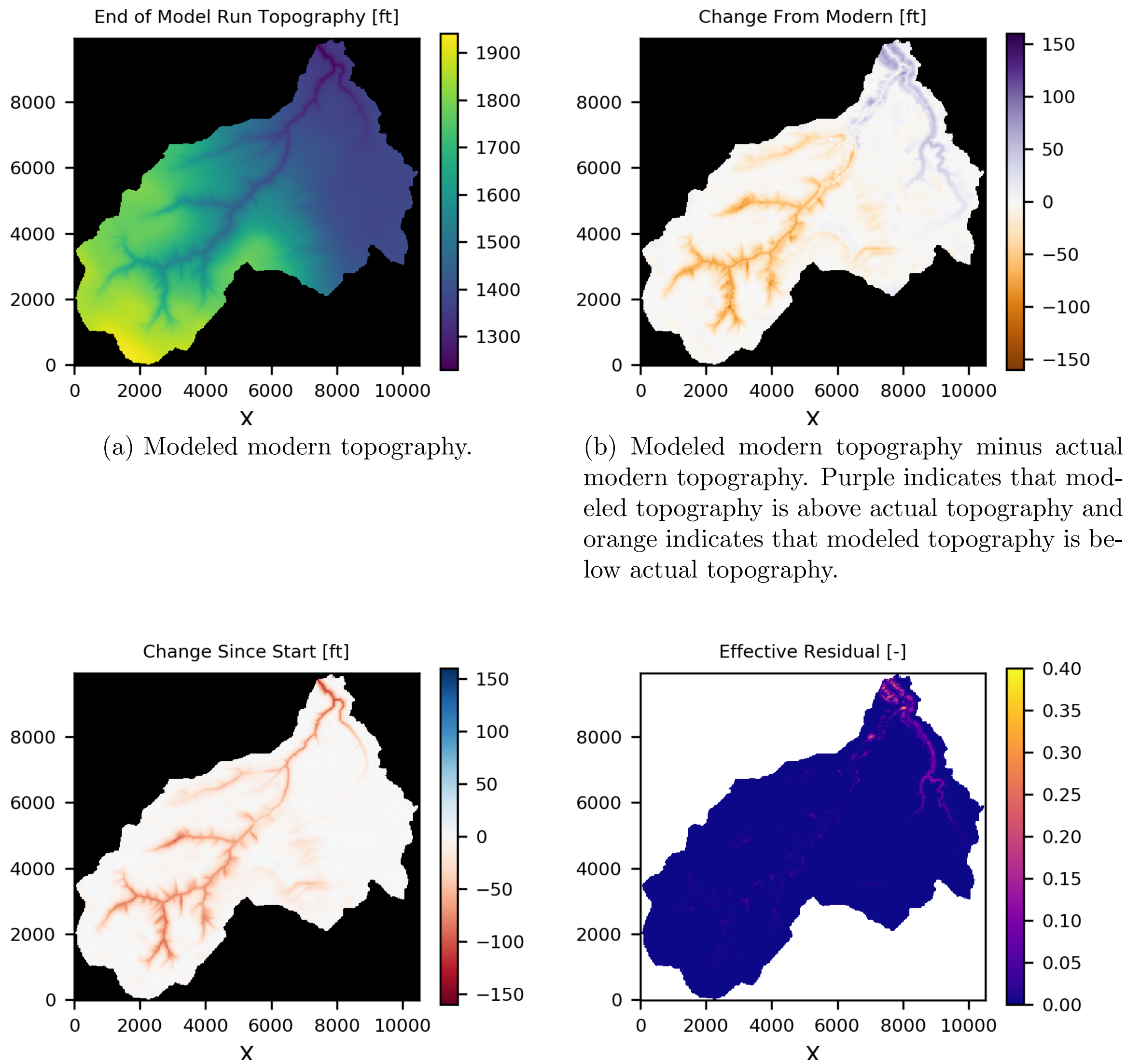

(a) Modeled modern topography.

(b) Modeled modern topography minus actual modern topography. Purple indicates that modeled topography is above actual topography and orange indicates that modeled topography is below actual topography.

(c) Cumulative erosion from 13 ka to modern. Red indicates that erosion occurred, and blue indicates that deposition occurred.

(d) Effective residual value at each grid node used in objective function calculation.

Figure C.7: Calibration results summary for Model 012 showing spatially distributed values at the end of the 13 ka to present model run with calibrated parameter values in Upper Franks Creek Watershed (SEW domain).

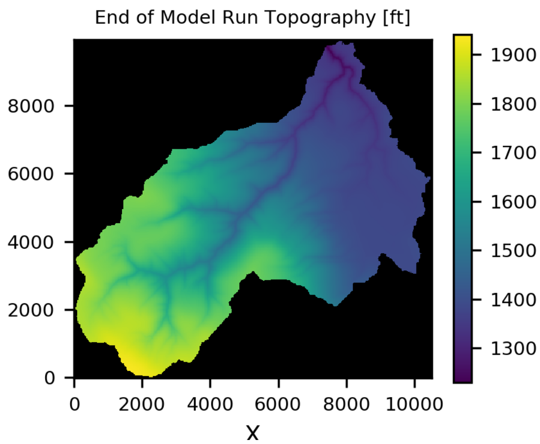

(a) Modeled modern topography.

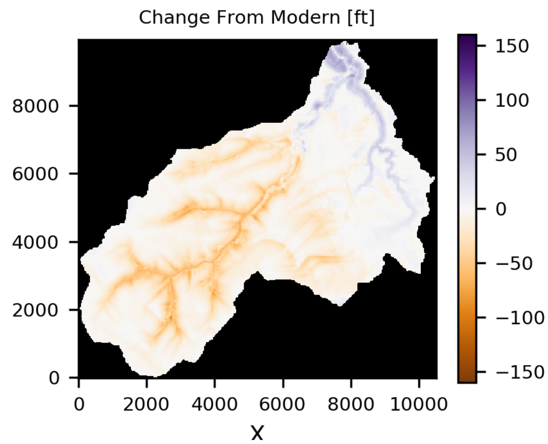

(b) Modeled modern topography minus actual modern topography. Purple indicates that modeled topography is above actual topography and orange indicates that modeled topography is below actual topography.

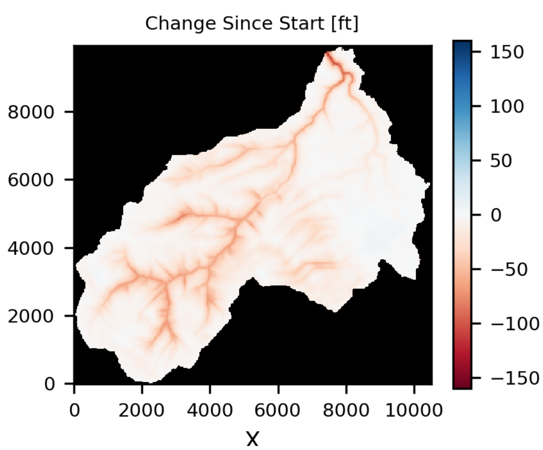

(c) Cumulative erosion from 13 ka to modern. Red indicates that erosion occurred, and blue indicates that deposition occurred.

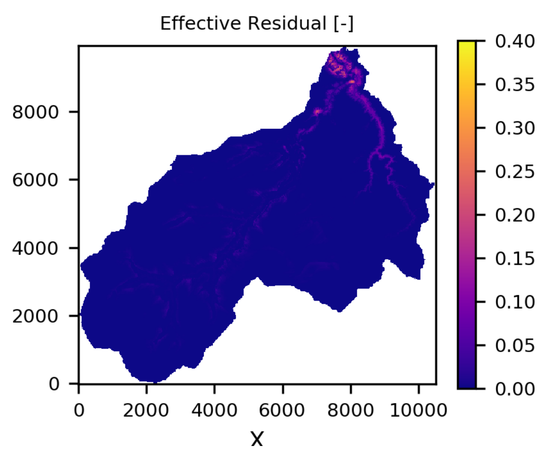

(d) Effective residual value at each grid node used in objective function calculation.

Figure C.8: Calibration results summary for Model 018 showing spatially distributed values at the end of the 13 ka to present model run with calibrated parameter values in Upper Franks Creek Watershed (SEW domain).

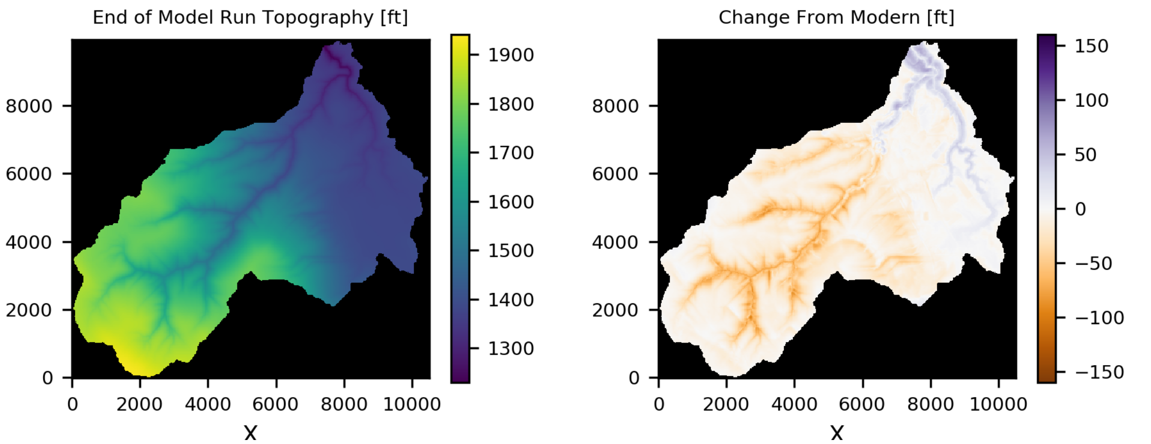

(a) Modeled modern topography.

(b) Modeled modern topography minus actual modern topography. Purple indicates that modeled topography is above actual topography and orange indicates that modeled topography is below actual topography.

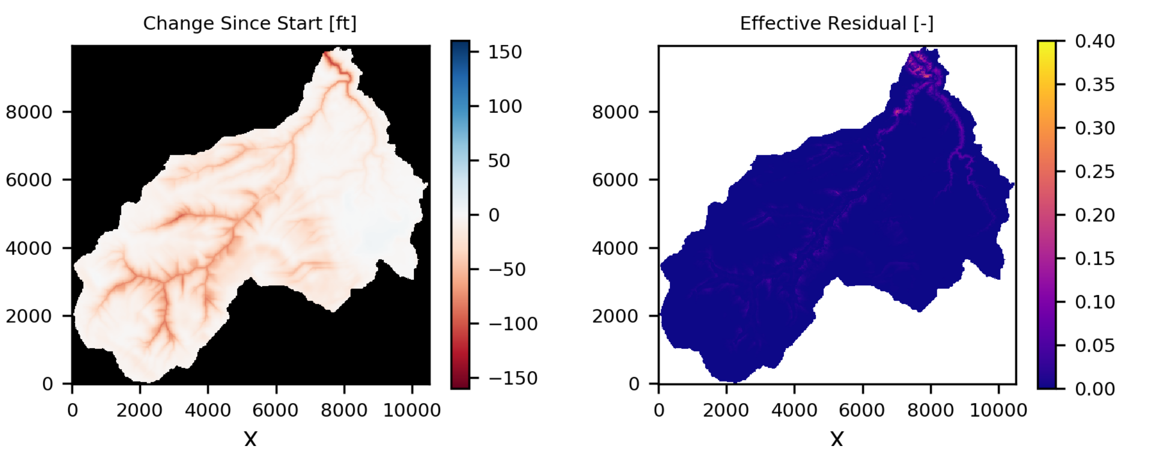

(c) Cumulative erosion from 13 ka to modern. Red indicates that erosion occurred, and blue indicates that deposition occurred.

(d) Effective residual value at each grid node used in objective function calculation.

Figure C.9: Calibration results summary for Model 030 showing spatially distributed values at the end of the 13 ka to present model run with calibrated parameter values in Upper Franks Creek Watershed (SEW domain).

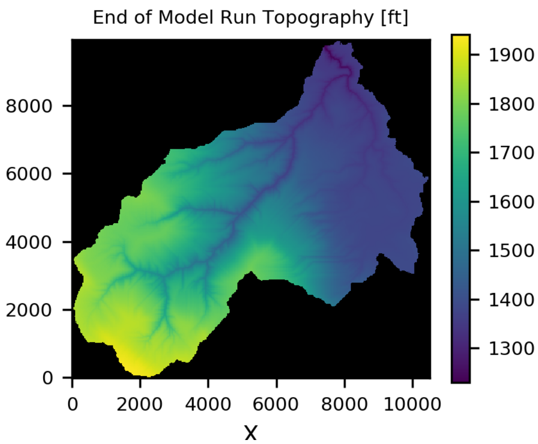

(a) Modeled modern topography.

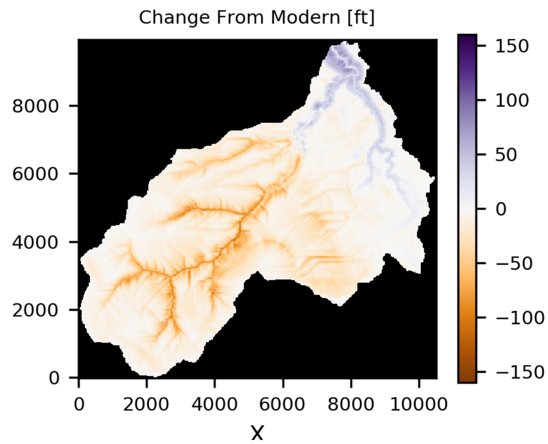

(b) Modeled modern topography minus actual modern topography. Purple indicates that modeled topography is above actual topography and orange indicates that modeled topography is below actual topography.

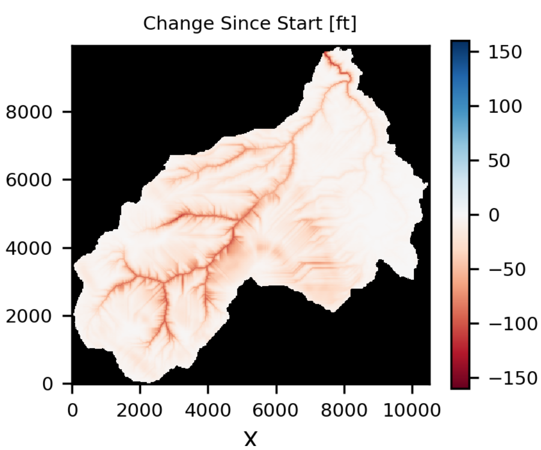

(c) Cumulative erosion from 13 ka to modern. Red indicates that erosion occurred, and blue indicates that deposition occurred.

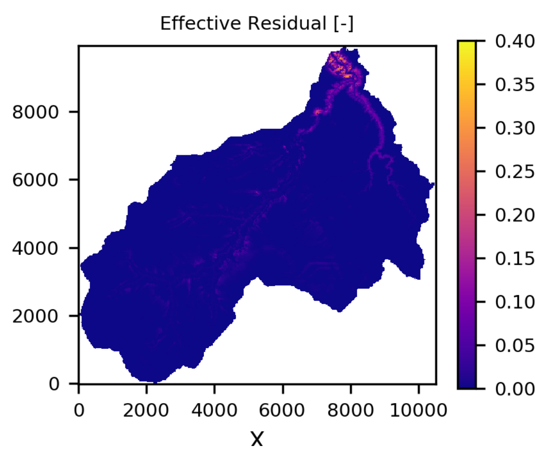

(d) Effective residual value at each grid node used in objective function calculation.

Figure C.10: Calibration results summary for Model 100 showing spatially distributed values at the end of the 13 ka to present model run with calibrated parameter values in Upper Franks Creek Watershed (SEW domain).

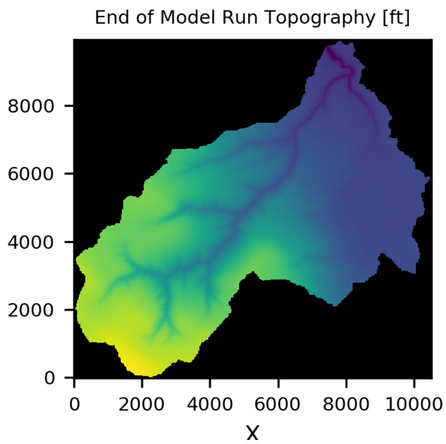

(a) Modeled modern topography.

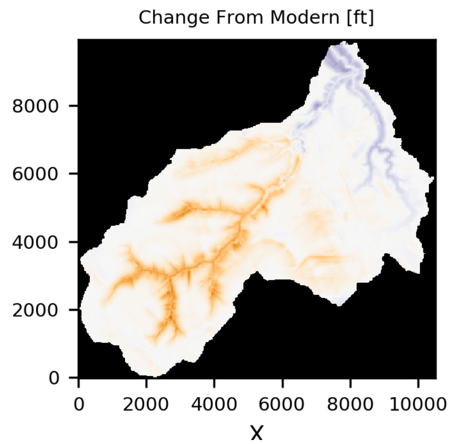

(b) Modeled modern topography minus actual modern topography. Purple indicates that modeled topography is above actual topography and orange indicates that modeled topography is below actual topography.

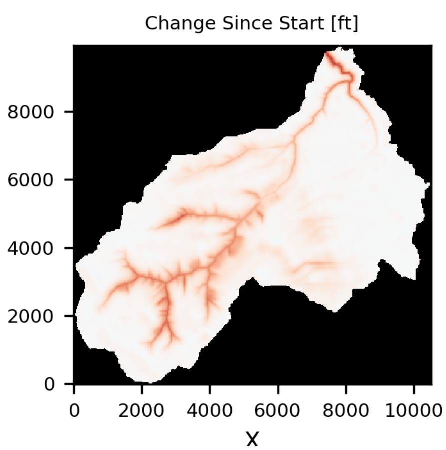

(c) Cumulative erosion from 13 ka to modern. Red indicates that erosion occurred, and blue indicates that deposition occurred.

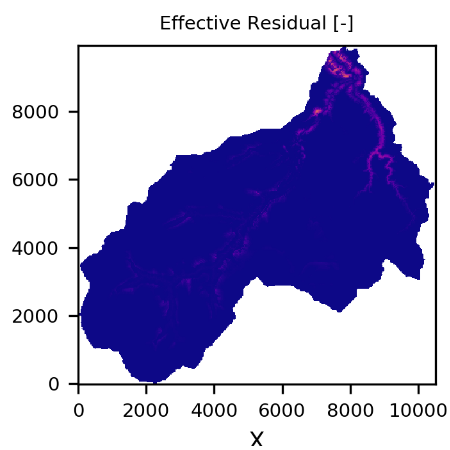

(d) Effective residual value at each grid node used in objective function calculation.

Figure C.11: Calibration results summary for Model 102 showing spatially distributed values at the end of the 13 ka to present model run with calibrated parameter values in Upper Franks Creek Watershed (SEW domain).

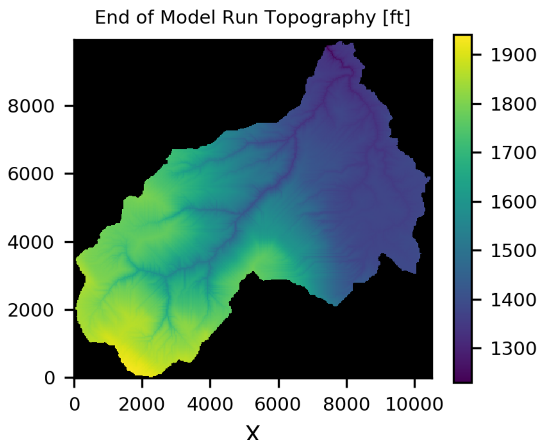

(a) Modeled modern topography.

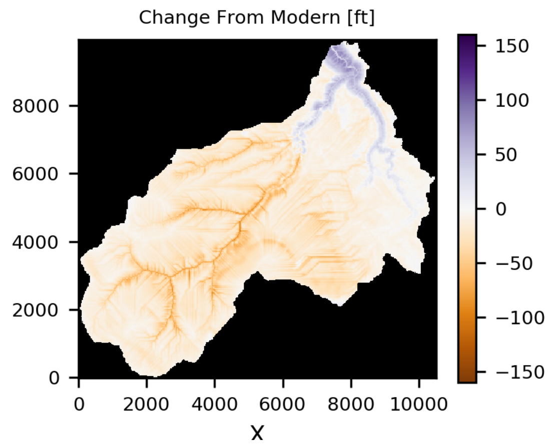

(b) Modeled modern topography minus actual modern topography. Purple indicates that modeled topography is above actual topography and orange indicates that modeled topography is below actual topography.

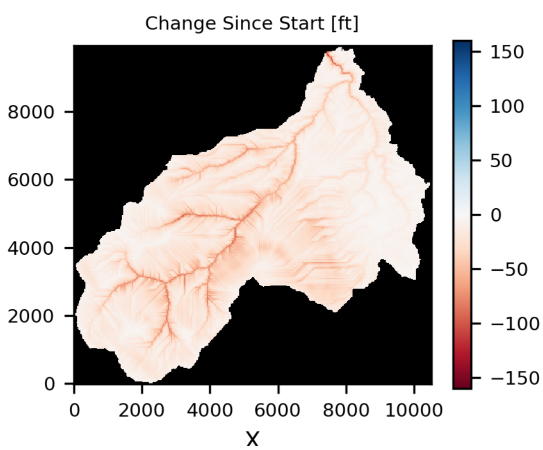

(c) Cumulative erosion from 13 ka to modern. Red indicates that erosion occurred, and blue indicates that deposition occurred.

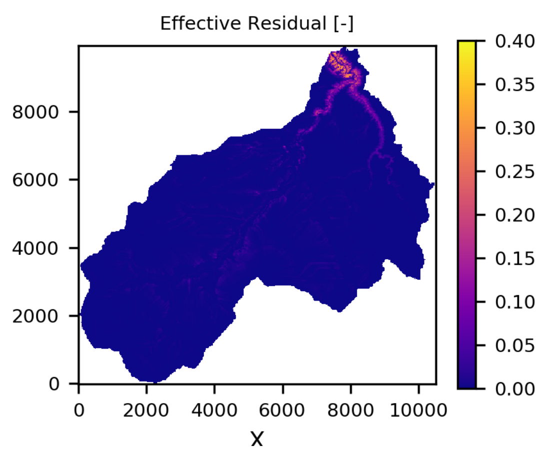

(d) Effective residual value at each grid node used in objective function calculation.

Figure C.12: Calibration results summary for Model 104 showing spatially distributed values at the end of the 13 ka to present model run with calibrated parameter values in Upper Franks Creek Watershed (SEW domain).

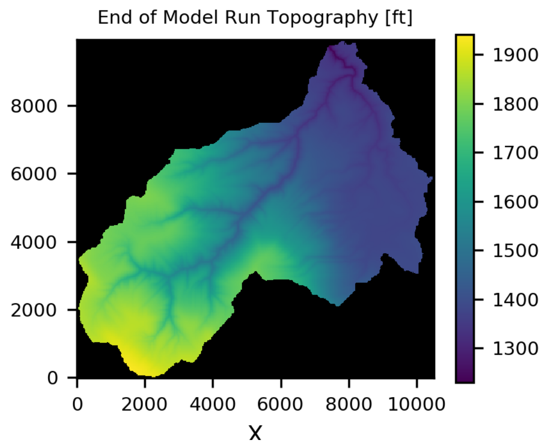

(a) Modeled modern topography.

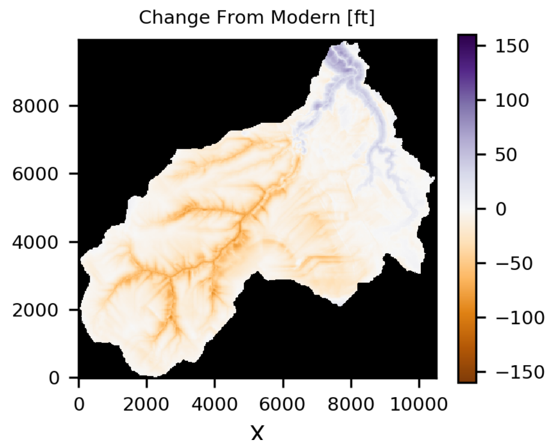

(b) Modeled modern topography minus actual modern topography. Purple indicates that modeled topography is above actual topography and orange indicates that modeled topography is below actual topography.

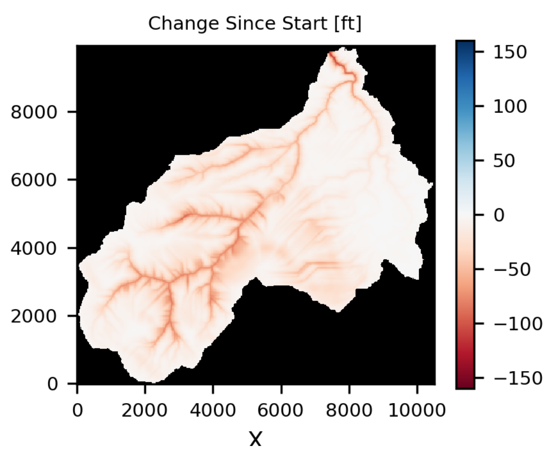

(c) Cumulative erosion from 13 ka to modern. Red indicates that erosion occurred, and blue indicates that deposition occurred.

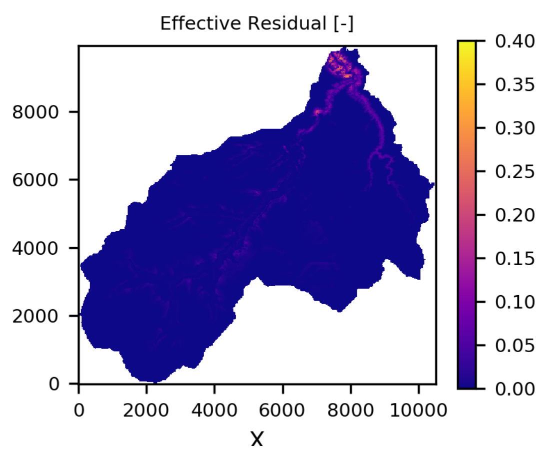

(d) Effective residual value at each grid node used in objective function calculation.

Figure C.13: Calibration results summary for Model 108 showing spatially distributed values at the end of the 13 ka to present model run with calibrated parameter values in Upper Franks Creek Watershed (SEW domain).

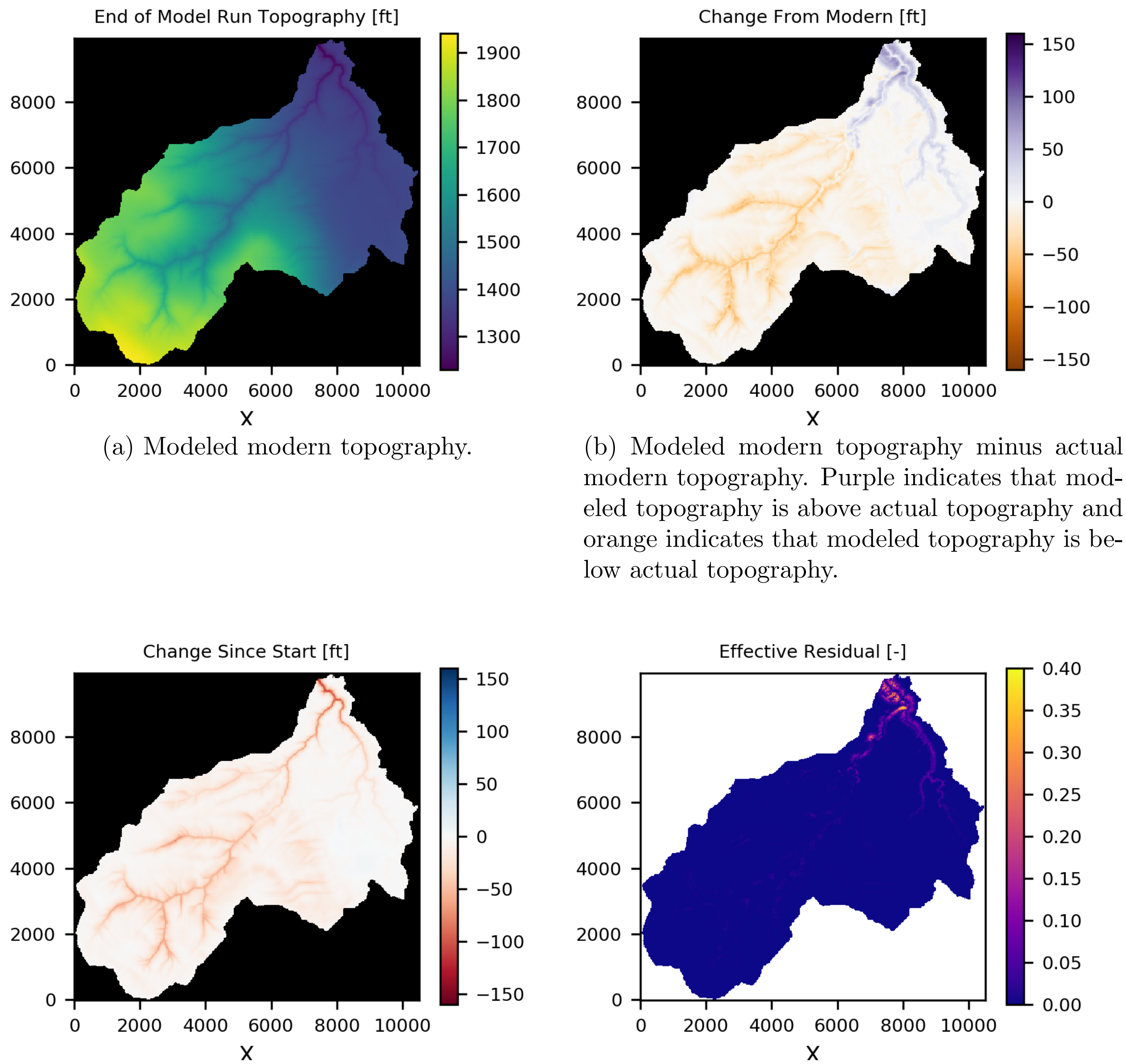

(a) Modeled modern topography.

(b) Modeled modern topography minus actual modern topography. Purple indicates that modeled topography is above actual topography and orange indicates that modeled topography is below actual topography.

(c) Cumulative erosion from 13 ka to modern. Red indicates that erosion occurred, and blue indicates that deposition occurred.

(d) Effective residual value at each grid node used in objective function calculation.

Figure C.14: Calibration results summary for Model 110 showing spatially distributed values at the end of the 13 ka to present model run with calibrated parameter values in Upper Franks Creek Watershed (SEW domain).

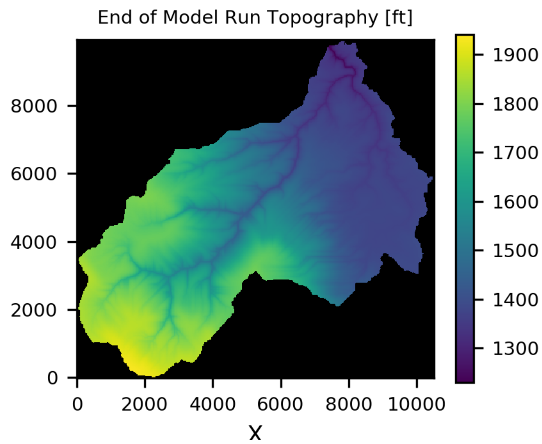

(a) Modeled modern topography.

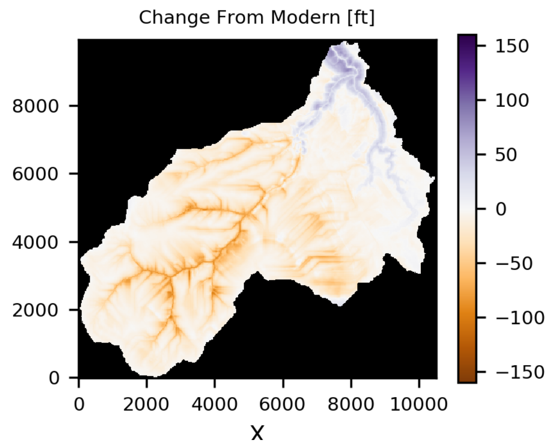

(b) Modeled modern topography minus actual modern topography. Purple indicates that modeled topography is above actual topography and orange indicates that modeled topography is below actual topography.

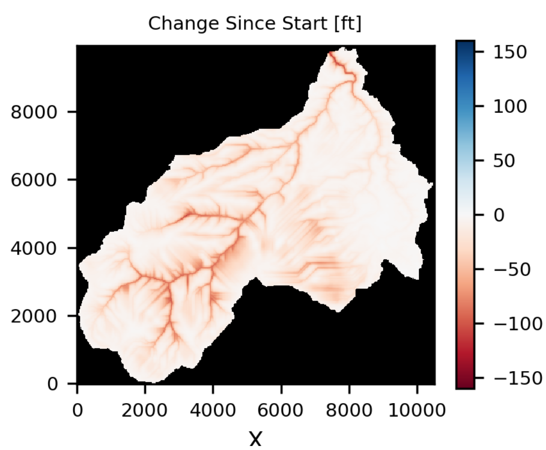

(c) Cumulative erosion from 13 ka to modern. Red indicates that erosion occurred, and blue indicates that deposition occurred.

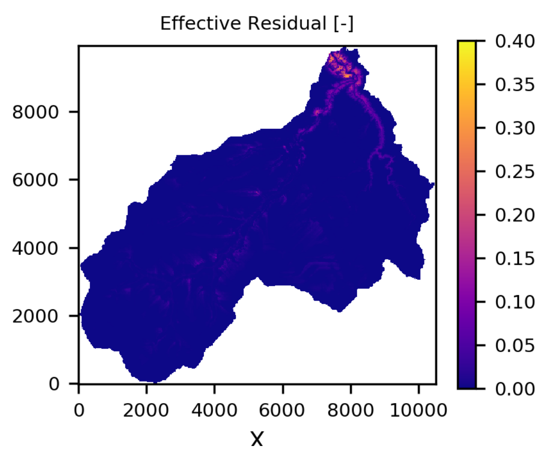

(d) Effective residual value at each grid node used in objective function calculation.

Figure C.15: Calibration results summary for Model 200 showing spatially distributed values at the end of the 13 ka to present model run with calibrated parameter values in Upper Franks Creek Watershed (SEW domain).

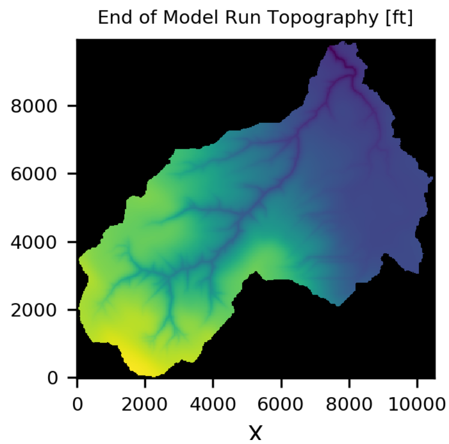

(a) Modeled modern topography.

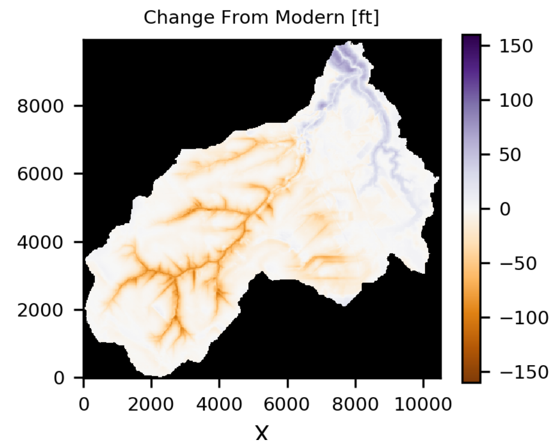

(b) Modeled modern topography minus actual modern topography. Purple indicates that modeled topography is above actual topography and orange indicates that modeled topography is below actual topography.

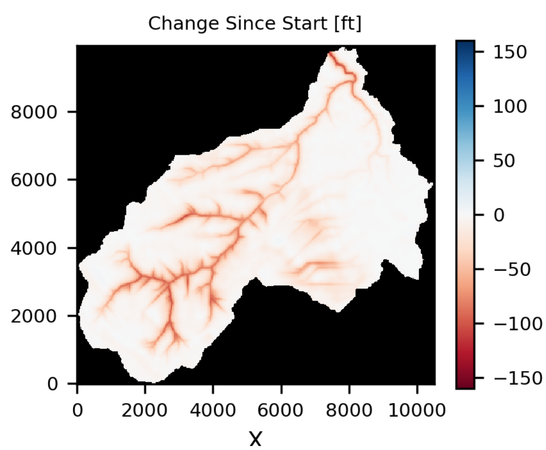

(c) Cumulative erosion from 13 ka to modern. Red indicates that erosion occurred, and blue indicates that deposition occurred.

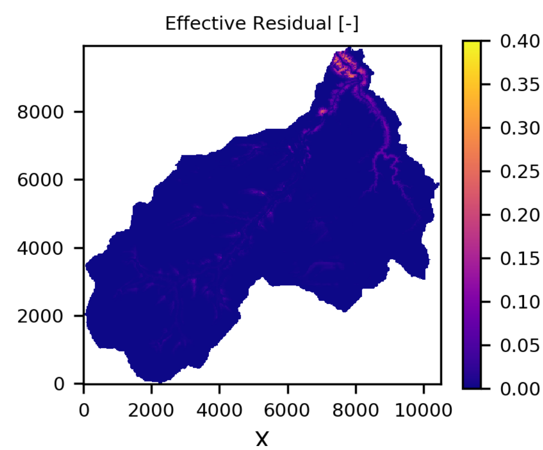

(d) Effective residual value at each grid node used in objective function calculation.

Figure C.16: Calibration results summary for Model 202 showing spatially distributed values at the end of the 13 ka to present model run with calibrated parameter values in Upper Franks Creek Watershed (SEW domain).

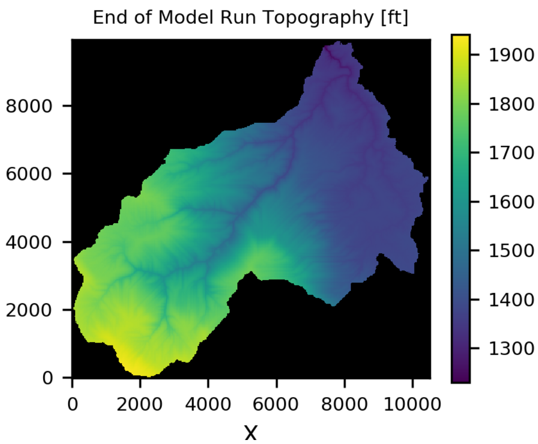

(a) Modeled modern topography.

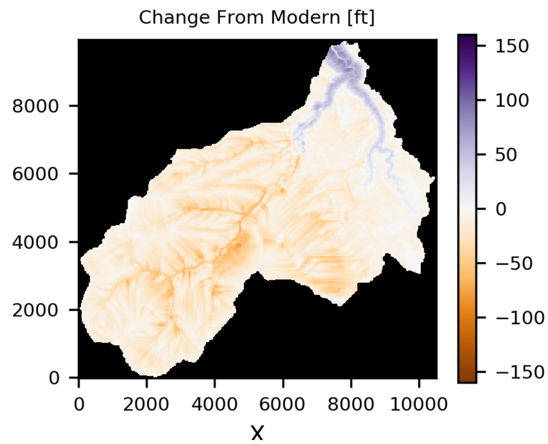

(b) Modeled modern topography minus actual modern topography. Purple indicates that modeled topography is above actual topography and orange indicates that modeled topography is below actual topography.

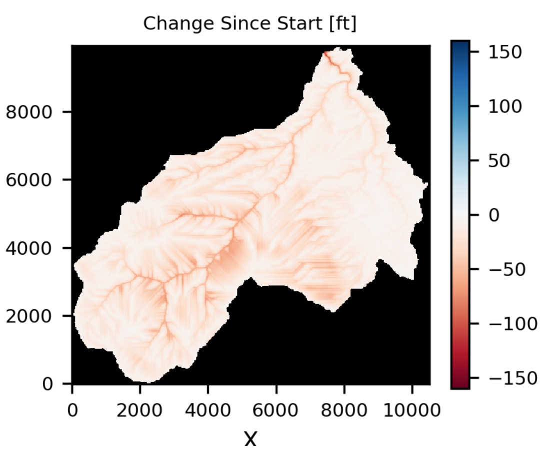

(c) Cumulative erosion from 13 ka to modern. Red indicates that erosion occurred, and blue indicates that deposition occurred.

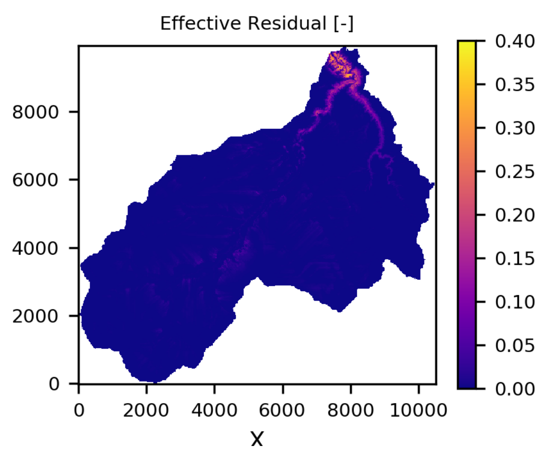

(d) Effective residual value at each grid node used in objective function calculation.

Figure C.17: Calibration results summary for Model 204 showing spatially distributed values at the end of the 13 ka to present model run with calibrated parameter values in Upper Franks Creek Watershed (SEW domain).

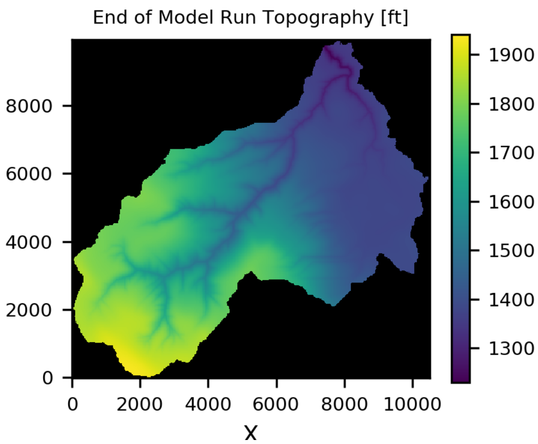

(a) Modeled modern topography.

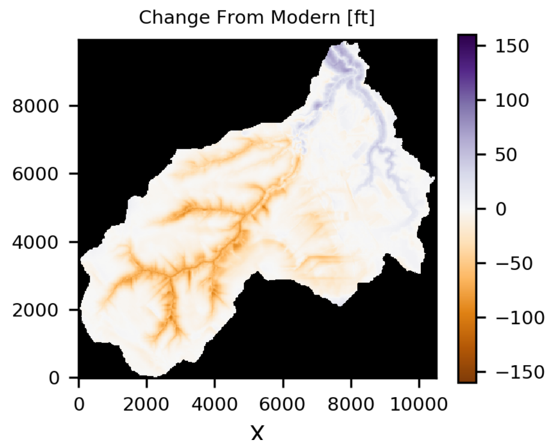

(b) Modeled modern topography minus actual modern topography. Purple indicates that modeled topography is above actual topography and orange indicates that modeled topography is below actual topography.

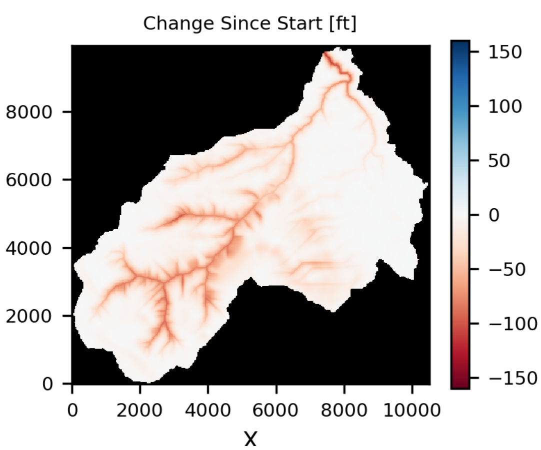

(c) Cumulative erosion from 13 ka to modern. Red indicates that erosion occurred, and blue indicates that deposition occurred.

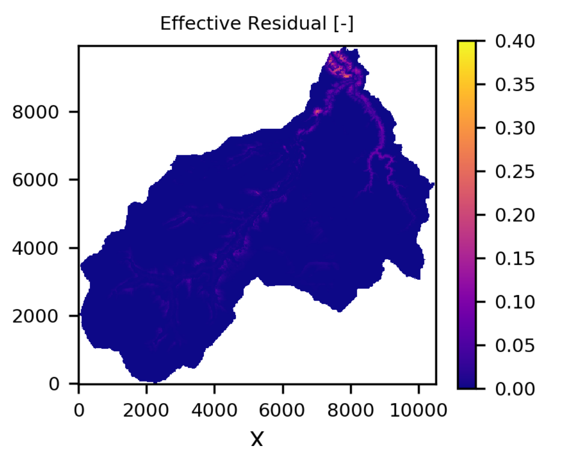

(d) Effective residual value at each grid node used in objective function calculation.

Figure C.18: Calibration results summary for Model 208 showing spatially distributed values at the end of the 13 ka to present model run with calibrated parameter values in Upper Franks Creek Watershed (SEW domain).

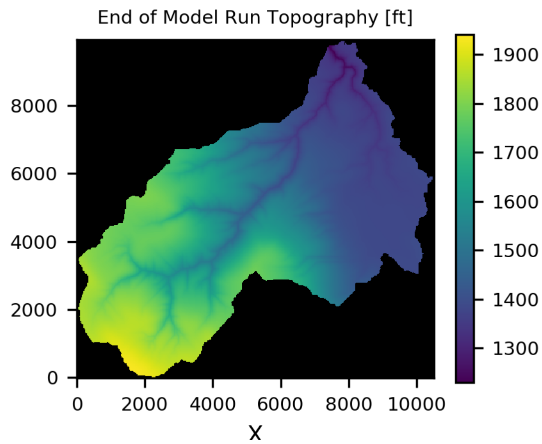

(a) Modeled modern topography.

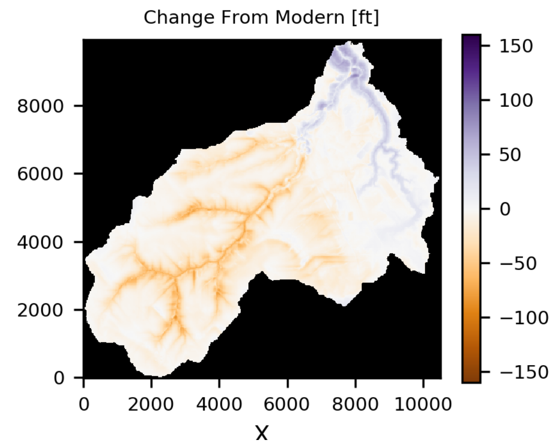

(b) Modeled modern topography minus actual modern topography. Purple indicates that modeled topography is above actual topography and orange indicates that modeled topography is below actual topography.

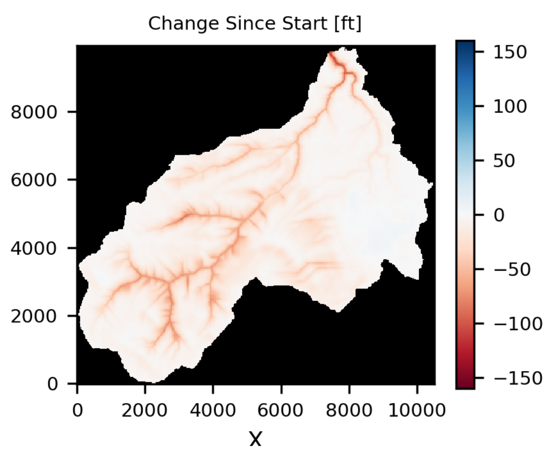

(c) Cumulative erosion from 13 ka to modern. Red indicates that erosion occurred, and blue indicates that deposition occurred.

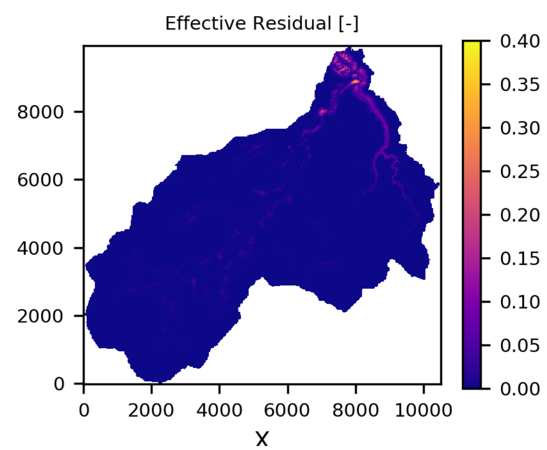

(d) Effective residual value at each grid node used in objective function calculation.

Figure C.19: Calibration results summary for Model 210 showing spatially distributed values at the end of the 13 ka to present model run with calibrated parameter values in Upper Franks Creek Watershed (SEW domain).

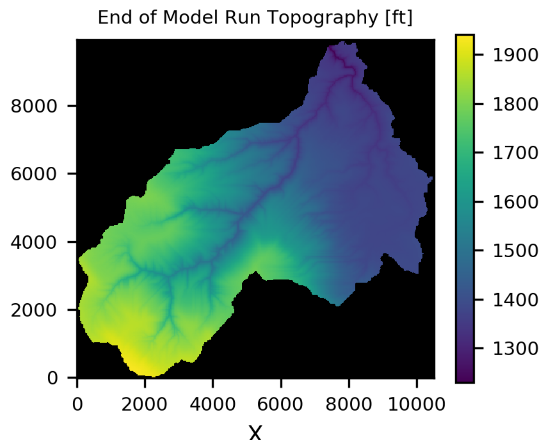

(a) Modeled modern topography.

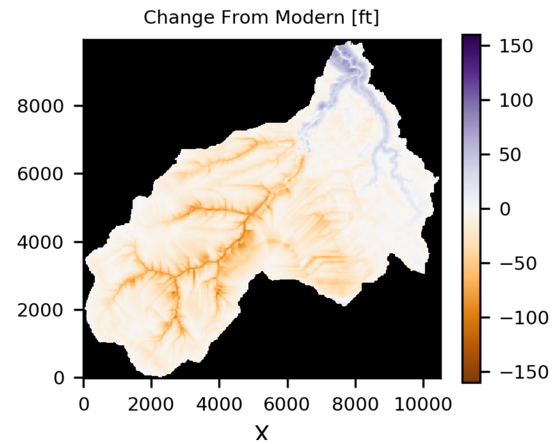

(b) Modeled modern topography minus actual modern topography. Purple indicates that modeled topography is above actual topography and orange indicates that modeled topography is below actual topography.

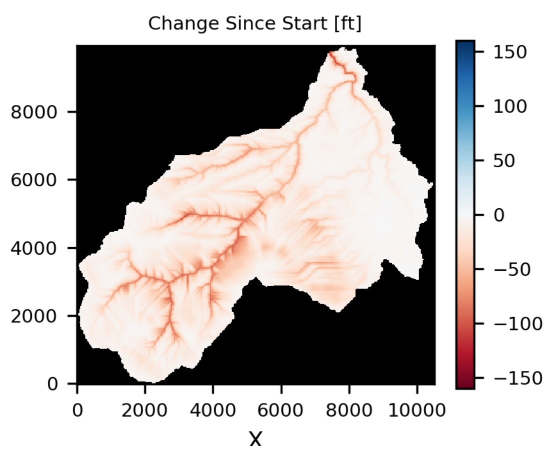

(c) Cumulative erosion from 13 ka to modern. Red indicates that erosion occurred, and blue indicates that deposition occurred.

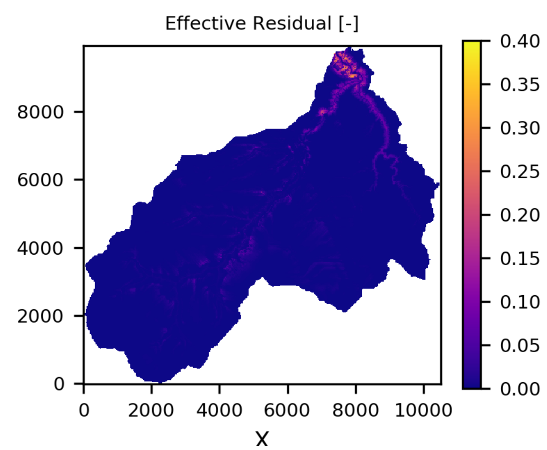

(d) Effective residual value at each grid node used in objective function calculation.

Figure C.20: Calibration results summary for Model 300 showing spatially distributed values at the end of the 13 ka to present model run with calibrated parameter values in Upper Franks Creek Watershed (SEW domain).

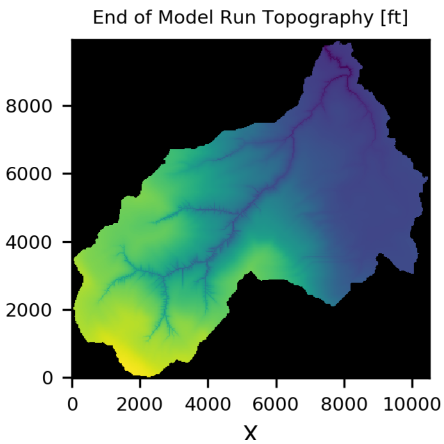

(a) Modeled modern topography.

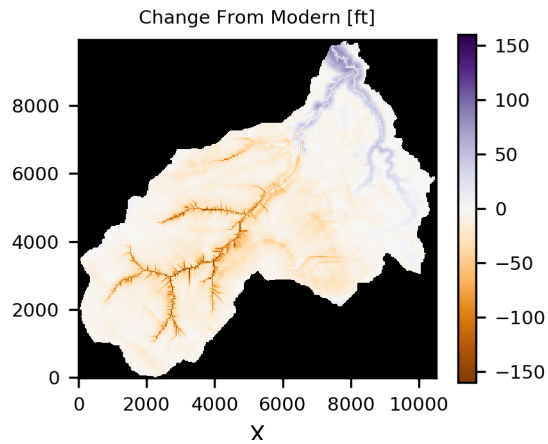

(b) Modeled modern topography minus actual modern topography. Purple indicates that modeled topography is above actual topography and orange indicates that modeled topography is below actual topography.

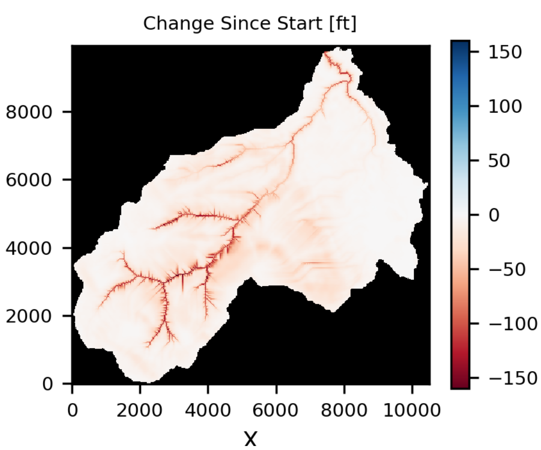

(c) Cumulative erosion from 13 ka to modern. Red indicates that erosion occurred, and blue indicates that deposition occurred.

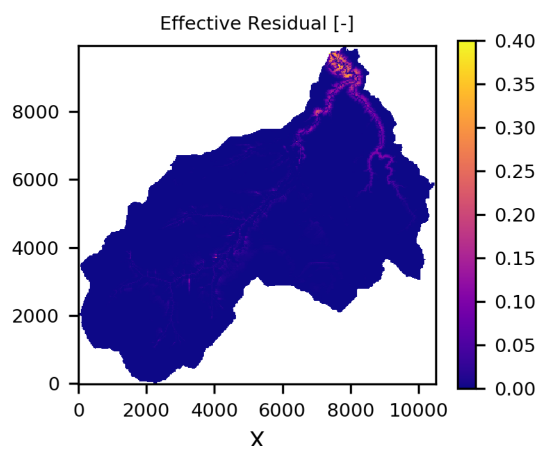

(d) Effective residual value at each grid node used in objective function calculation.

Figure C.21: Calibration results summary for Model 400 showing spatially distributed values at the end of the 13 ka to present model run with calibrated parameter values in Upper Franks Creek Watershed (SEW domain).

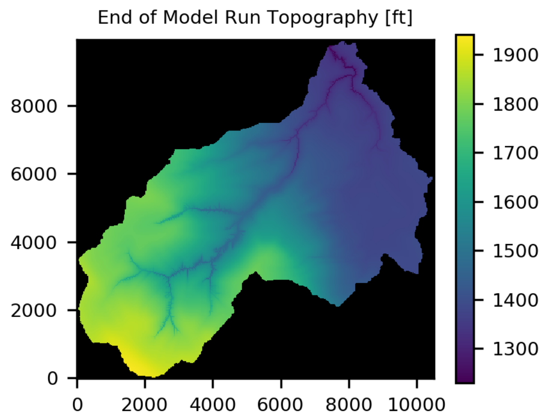

(a) Modeled modern topography.

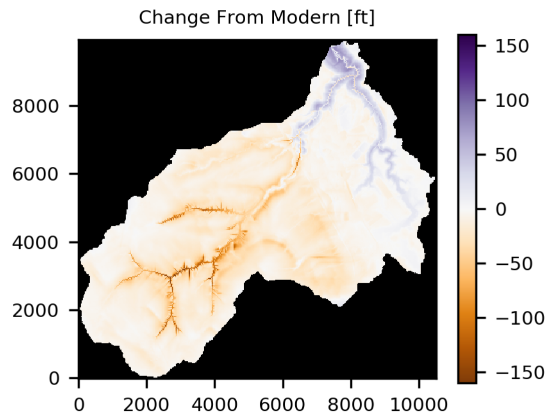

(b) Modeled modern topography minus actual modern topography. Purple indicates that modeled topography is above actual topography and orange indicates that modeled topography is below actual topography.

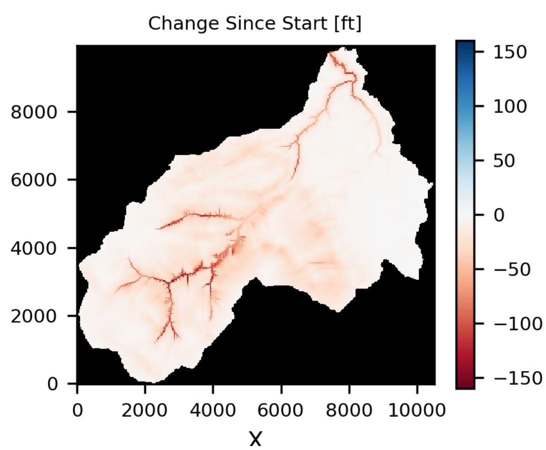

(c) Cumulative erosion from 13 ka to modern. Red indicates that erosion occurred, and blue indicates that deposition occurred.

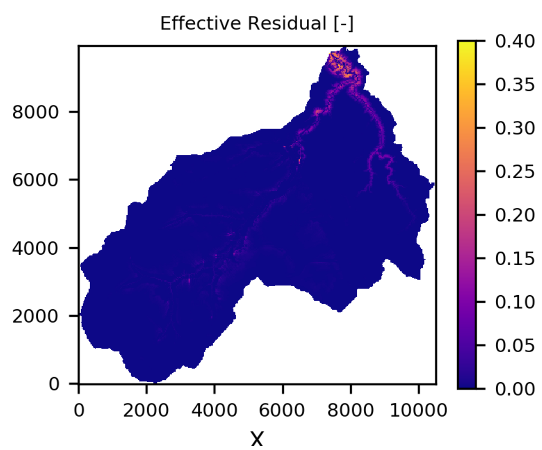

(d) Effective residual value at each grid node used in objective function calculation.

Figure C.22: Calibration results summary for Model 600 showing spatially distributed values at the end of the 13 ka to present model run with calibrated parameter values in Upper Franks Creek Watershed (SEW domain).

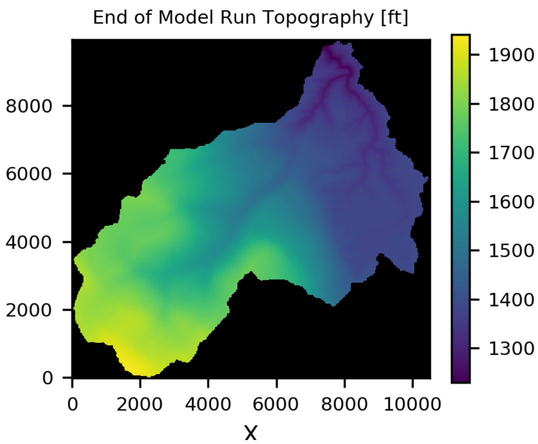

(a) Modeled modern topography.

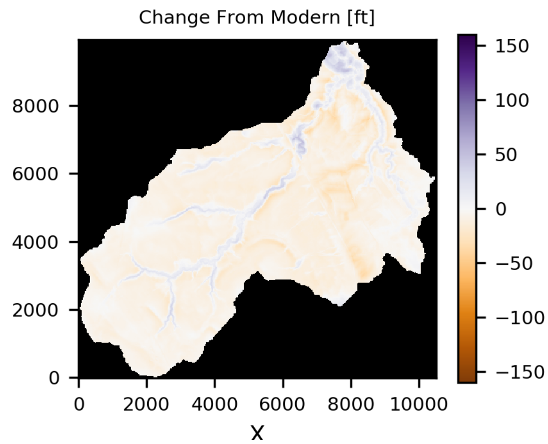

(b) Modeled modern topography minus actual modern topography. Purple indicates that modeled topography is above actual topography and orange indicates that modeled topography is below actual topography.

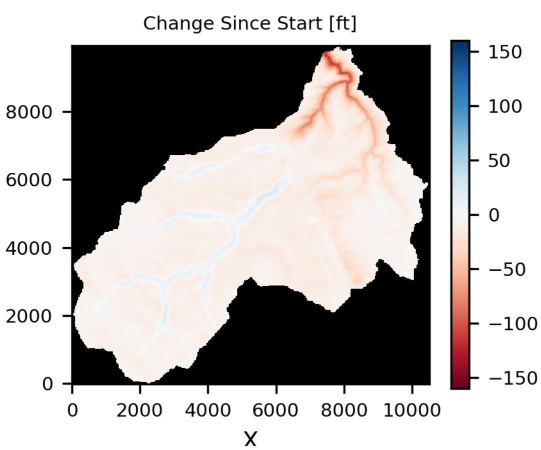

(c) Cumulative erosion from 13 ka to modern. Red indicates that erosion occurred, and blue indicates that deposition occurred.

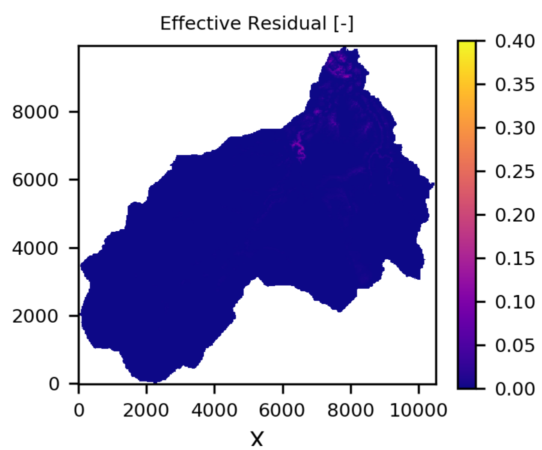

(d) Effective residual value at each grid node used in objective function calculation.

Figure C.23: Calibration results summary for Model 800 showing spatially distributed values at the end of the 13 ka to present model run with calibrated parameter values in Upper Franks Creek Watershed (SEW domain).

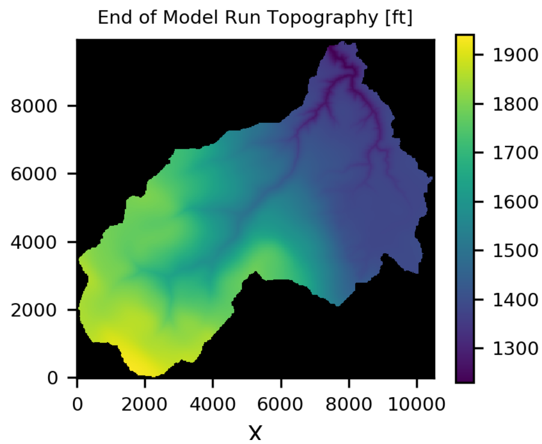

(a) Modeled modern topography.

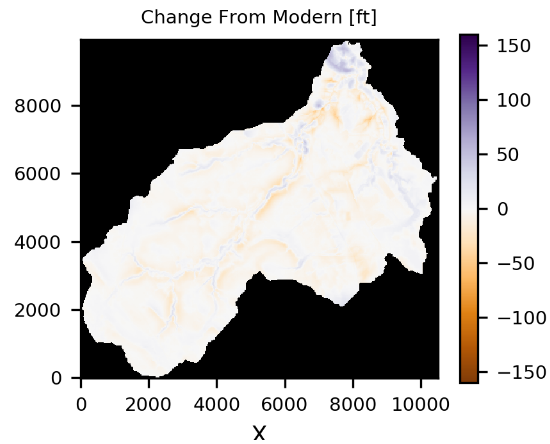

(b) Modeled modern topography minus actual modern topography. Purple indicates that modeled topography is above actual topography and orange indicates that modeled topography is below actual topography.

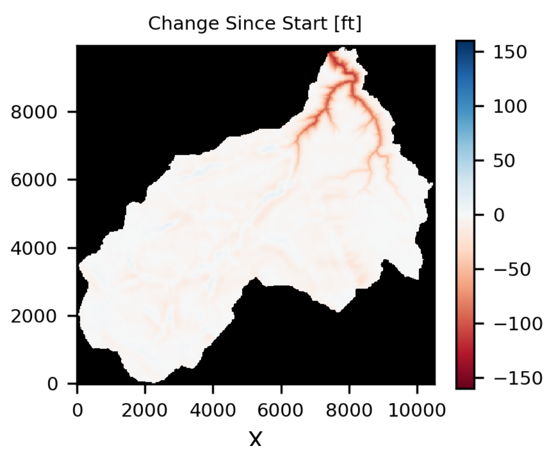

(c) Cumulative erosion from 13 ka to modern. Red indicates that erosion occurred, and blue indicates that deposition occurred.

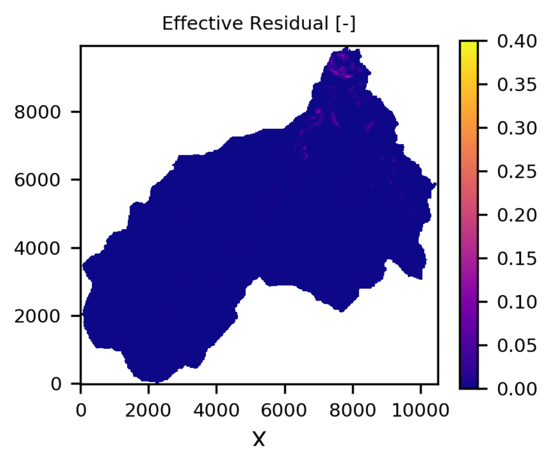

(d) Effective residual value at each grid node used in objective function calculation.

Figure C.24: Calibration results summary for Model 802 showing spatially distributed values at the end of the 13 ka to present model run with calibrated parameter values in Upper Franks Creek Watershed (SEW domain).

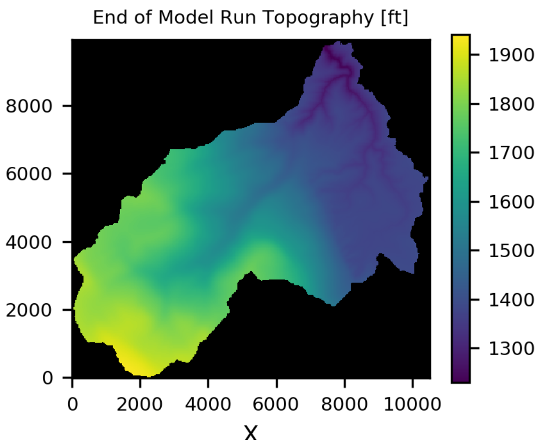

(a) Modeled modern topography.

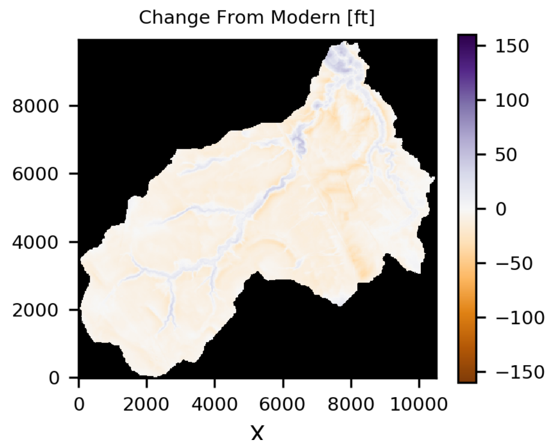

(b) Modeled modern topography minus actual modern topography. Purple indicates that modeled topography is above actual topography and orange indicates that modeled topography is below actual topography.

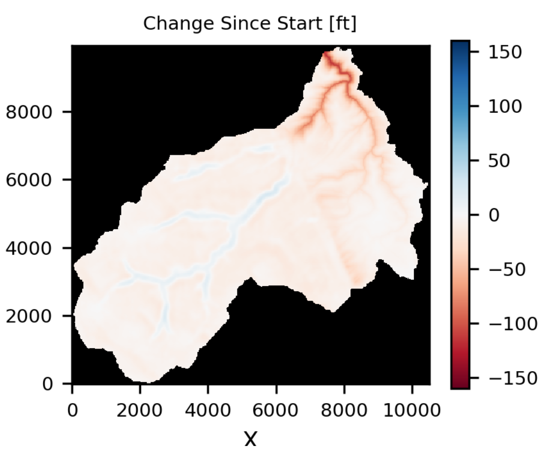

(c) Cumulative erosion from 13 ka to modern. Red indicates that erosion occurred, and blue indicates that deposition occurred.

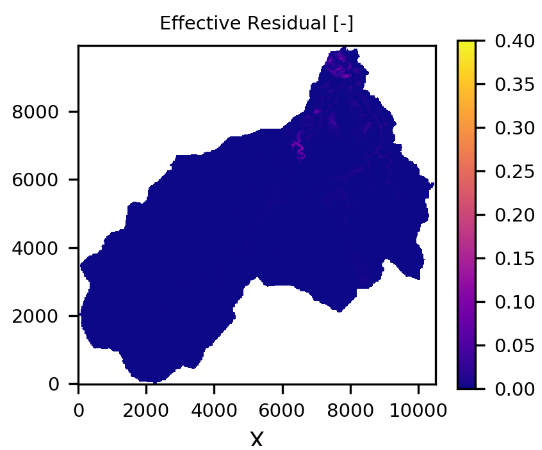

(d) Effective residual value at each grid node used in objective function calculation.

Figure C.25: Calibration results summary for Model 804 showing spatially distributed values at the end of the 13 ka to present model run with calibrated parameter values in Upper Franks Creek Watershed (SEW domain).

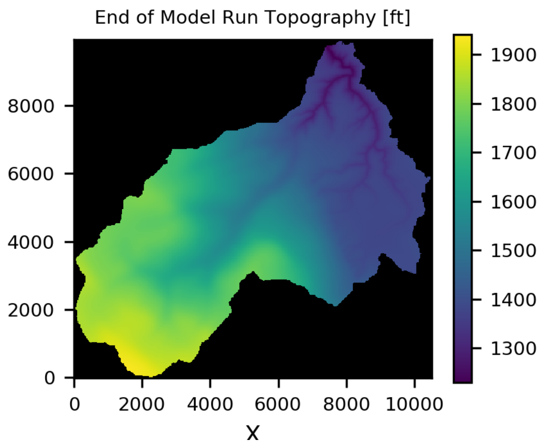

(a) Modeled modern topography.

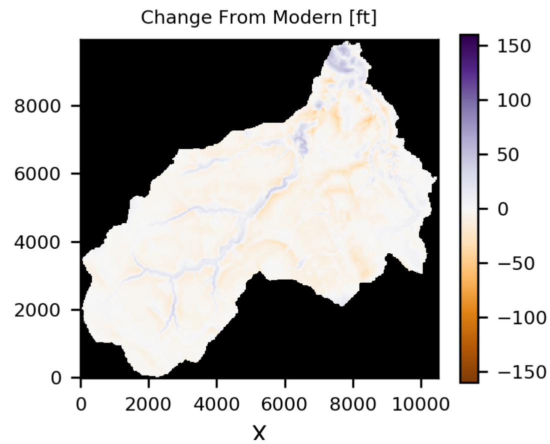

(b) Modeled modern topography minus actual modern topography. Purple indicates that modeled topography is above actual topography and orange indicates that modeled topography is below actual topography.

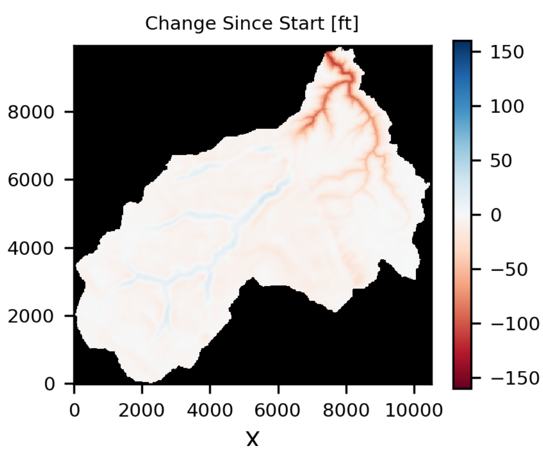

(c) Cumulative erosion from 13 ka to modern. Red indicates that erosion occurred, and blue indicates that deposition occurred.

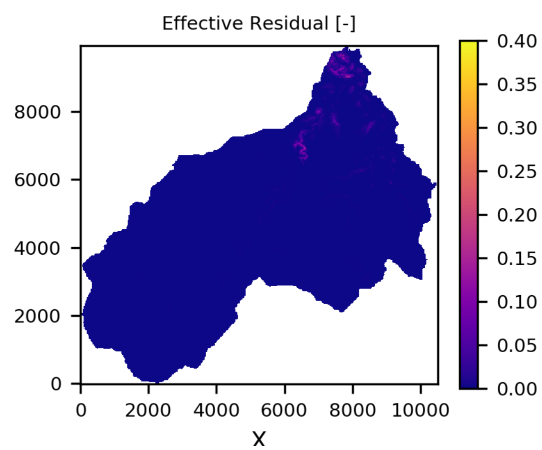

(d) Effective residual value at each grid node used in objective function calculation.

Figure C.26: Calibration results summary for Model 808 showing spatially distributed values at the end of the 13 ka to present model run with calibrated parameter values in Upper Franks Creek Watershed (SEW domain).

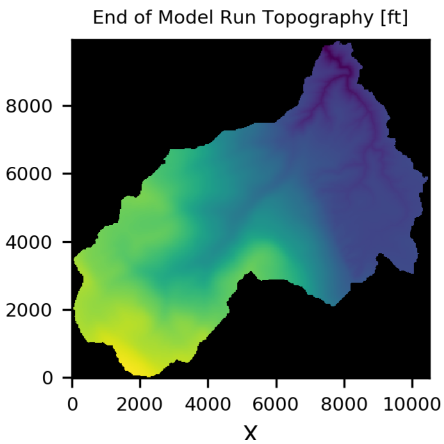

(a) Modeled modern topography.

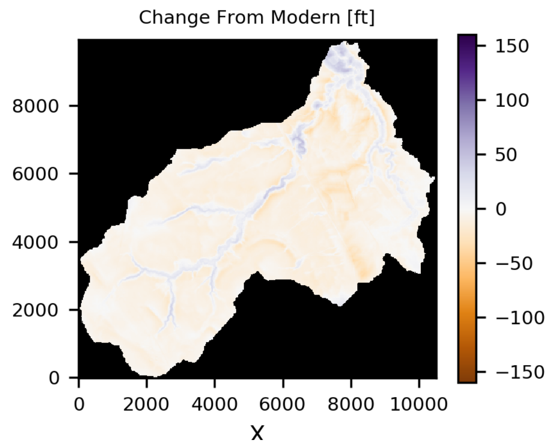

(b) Modeled modern topography minus actual modern topography. Purple indicates that modeled topography is above actual topography and orange indicates that modeled topography is below actual topography.

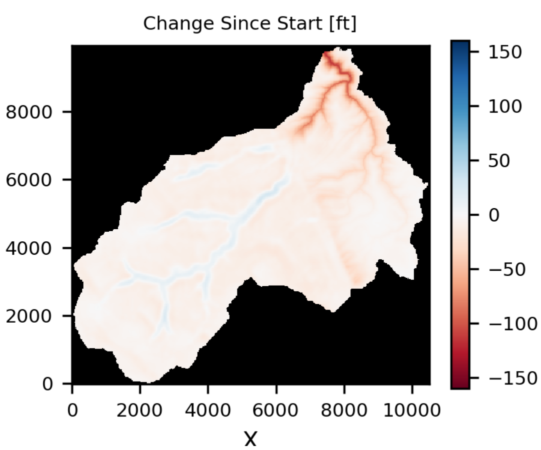

(c) Cumulative erosion from 13 ka to modern. Red indicates that erosion occurred, and blue indicates that deposition occurred.

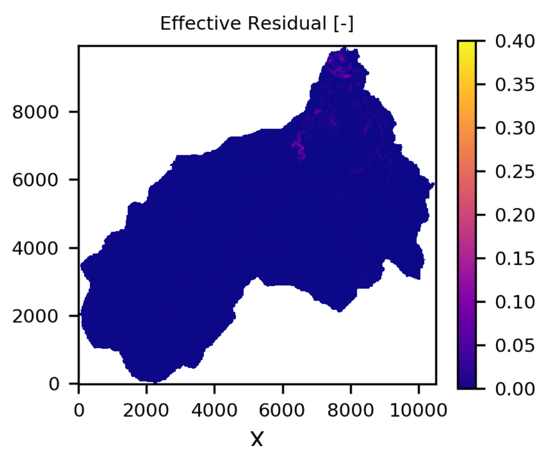

(d) Effective residual value at each grid node used in objective function calculation.

Figure C.27: Calibration results summary for Model 810 showing spatially distributed values at the end of the 13 ka to present model run with calibrated parameter values in Upper Franks Creek Watershed (SEW domain).

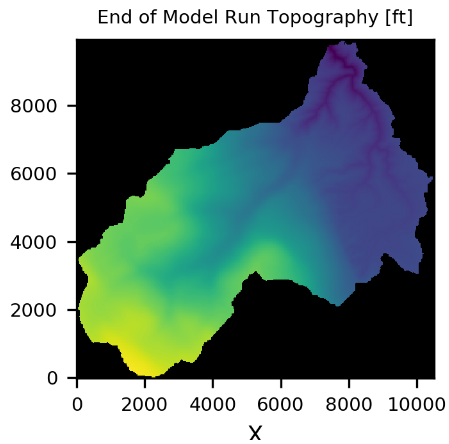

(a) Modeled modern topography.

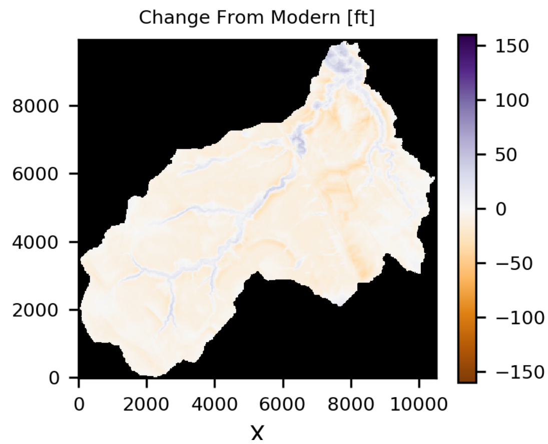

(b) Modeled modern topography minus actual modern topography. Purple indicates that modeled topography is above actual topography and orange indicates that modeled topography is below actual topography.

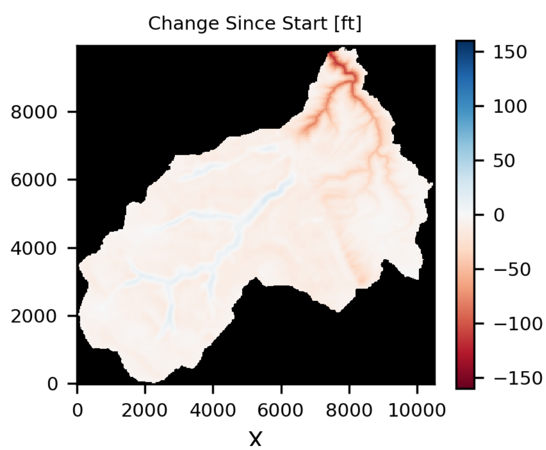

(c) Cumulative erosion from 13 ka to modern. Red indicates that erosion occurred, and blue indicates that deposition occurred.

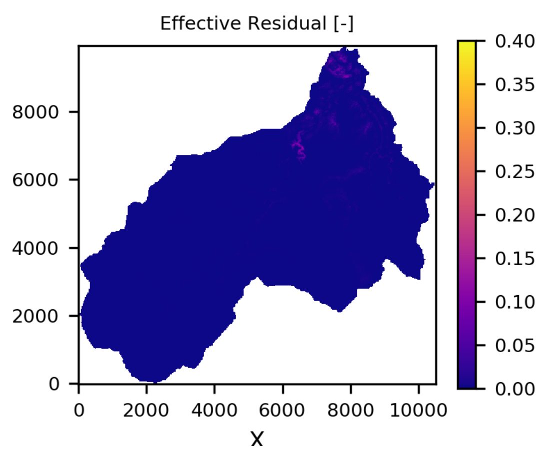

(d) Effective residual value at each grid node used in objective function calculation.

Figure C.28: Calibration results summary for Model 840 showing spatially distributed values at the end of the 13 ka to present model run with calibrated parameter values in Upper Franks Creek Watershed (SEW domain).

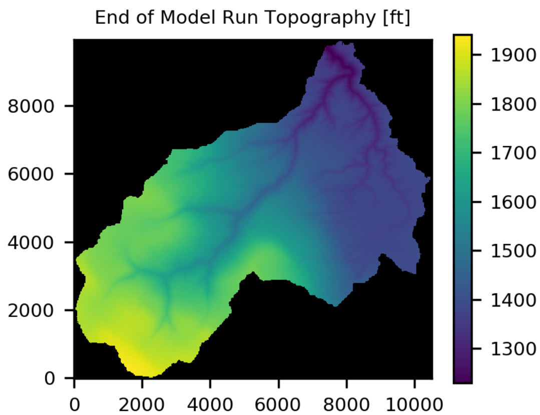

(a) Modeled modern topography.

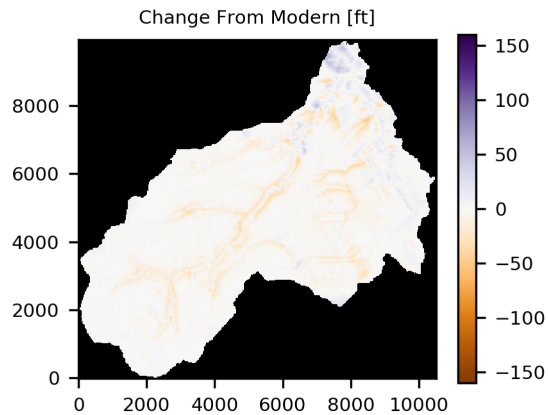

(b) Modeled modern topography minus actual modern topography. Purple indicates that modeled topography is above actual topography and orange indicates that modeled topography is below actual topography.

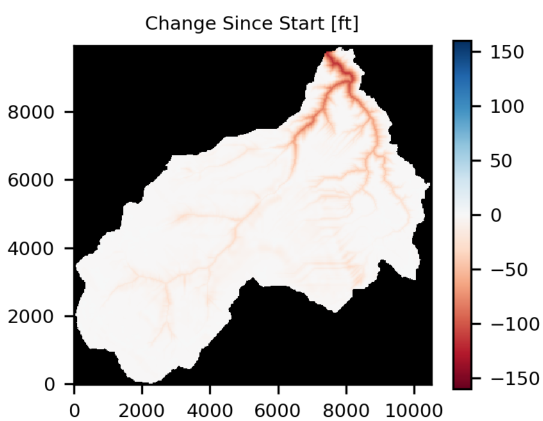

(c) Cumulative erosion from 13 ka to modern. Red indicates that erosion occurred, and blue indicates that deposition occurred.

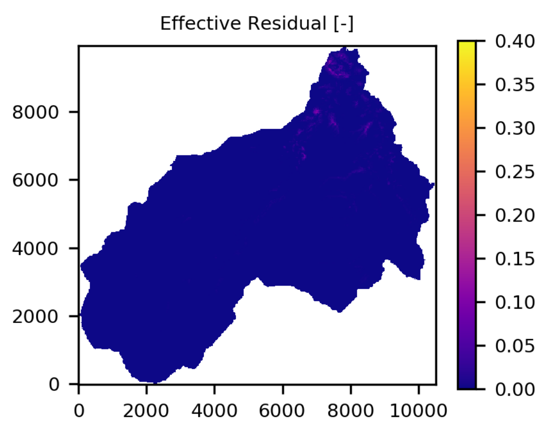

(d) Effective residual value at each grid node used in objective function calculation.

Figure C.29: Calibration results summary for Model 842 showing spatially distributed values at the end of the 13 ka to present model run with calibrated parameter values in Upper Franks Creek Watershed (SEW domain).

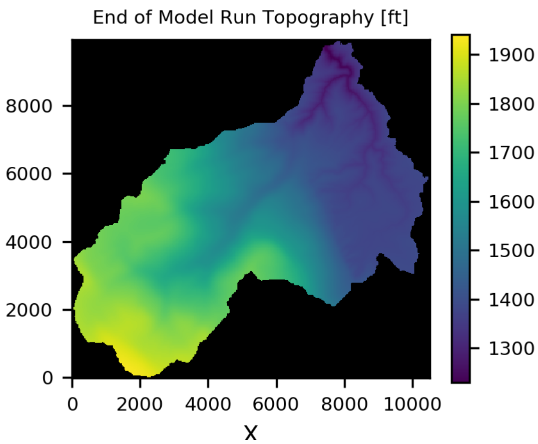

(a) Modeled modern topography.

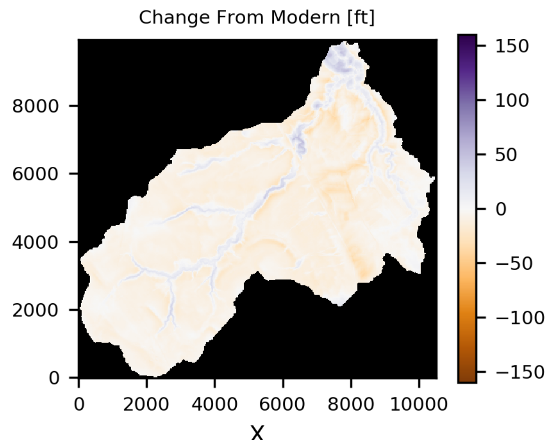

(b) Modeled modern topography minus actual modern topography. Purple indicates that modeled topography is above actual topography and orange indicates that modeled topography is below actual topography.

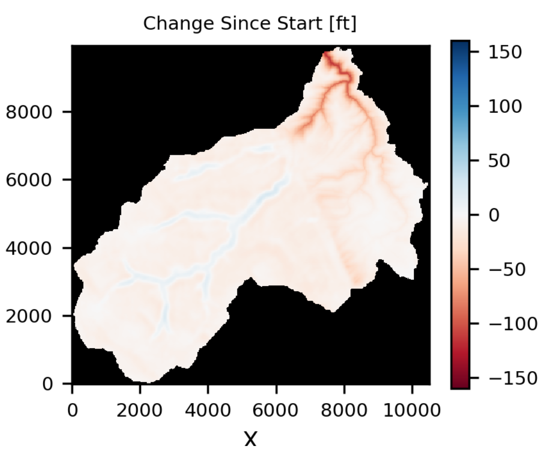

(c) Cumulative erosion from 13 ka to modern. Red indicates that erosion occurred, and blue indicates that deposition occurred.

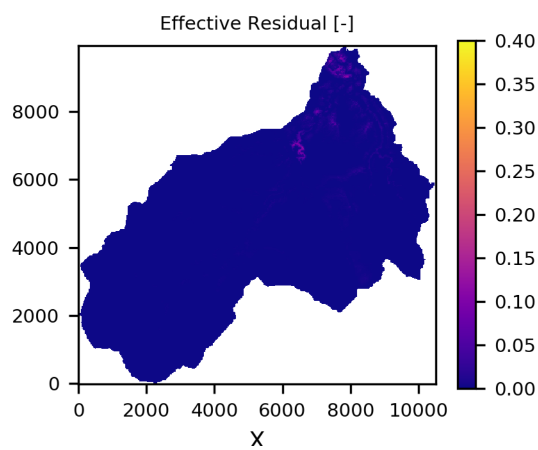

(d) Effective residual value at each grid node used in objective function calculation.

Figure C.30: Calibration results summary for Model A00 showing spatially distributed values at the end of the 13 ka to present model run with calibrated parameter values in Upper Franks Creek Watershed (SEW domain).

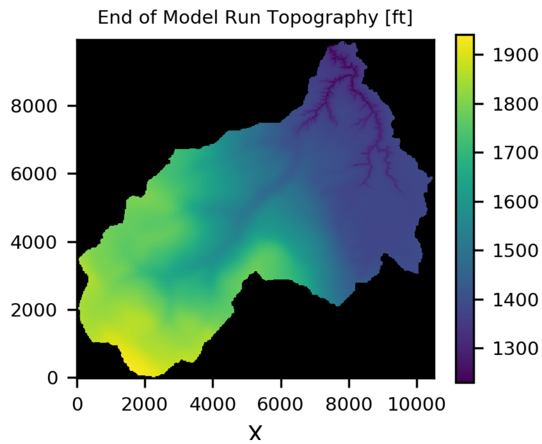

(a) Modeled modern topography.

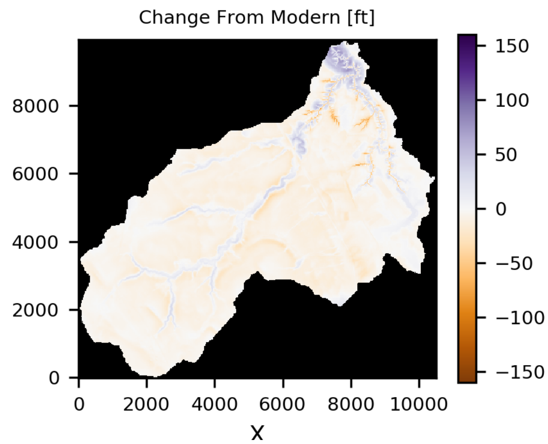

(b) Modeled modern topography minus actual modern topography. Purple indicates that modeled topography is above actual topography and orange indicates that modeled topography is below actual topography.

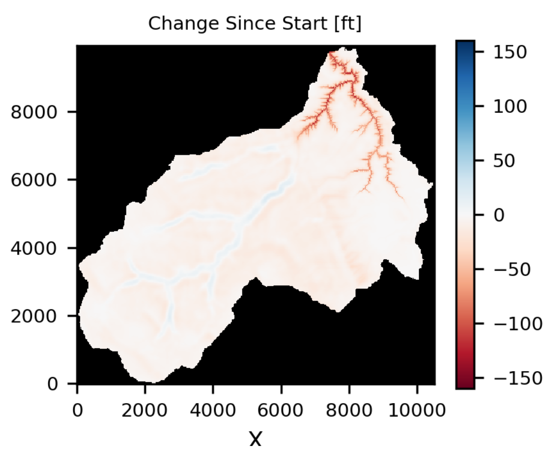

(c) Cumulative erosion from 13 ka to modern. Red indicates that erosion occurred, and blue indicates that deposition occurred.

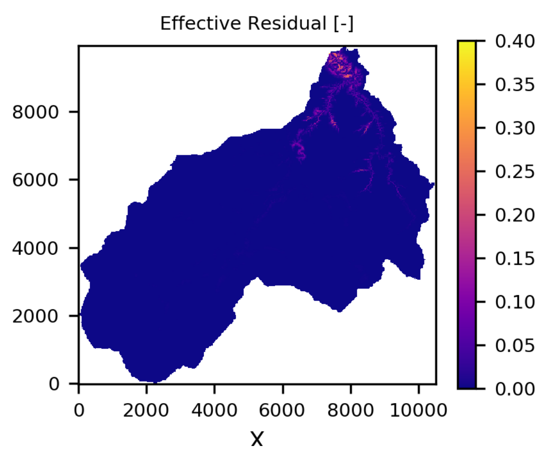

(d) Effective residual value at each grid node used in objective function calculation.

Figure C.31: Calibration results summary for Model C00 showing spatially distributed values at the end of the 13 ka to present model run with calibrated parameter values in Upper Franks Creek Watershed (SEW domain).

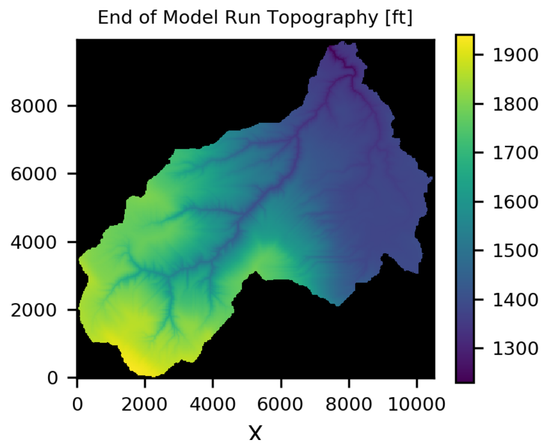

(a) Modeled modern topography.

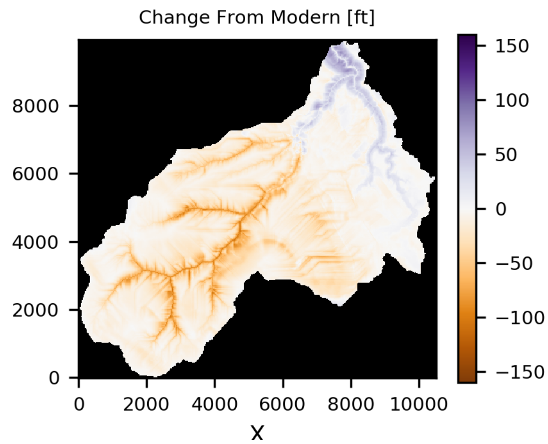

(b) Modeled modern topography minus actual modern topography. Purple indicates that modeled topography is above actual topography and orange indicates that modeled topography is below actual topography.

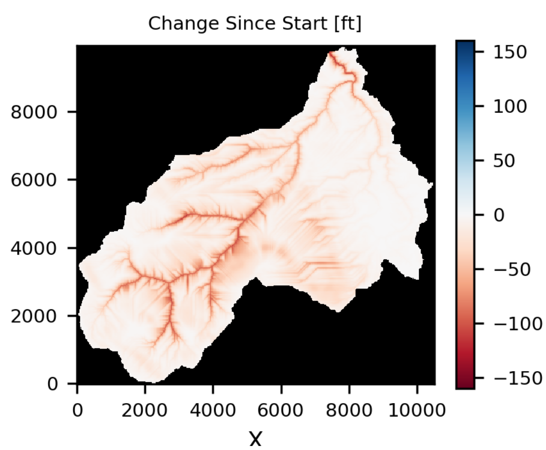

(c) Cumulative erosion from 13 ka to modern. Red indicates that erosion occurred, and blue indicates that deposition occurred.

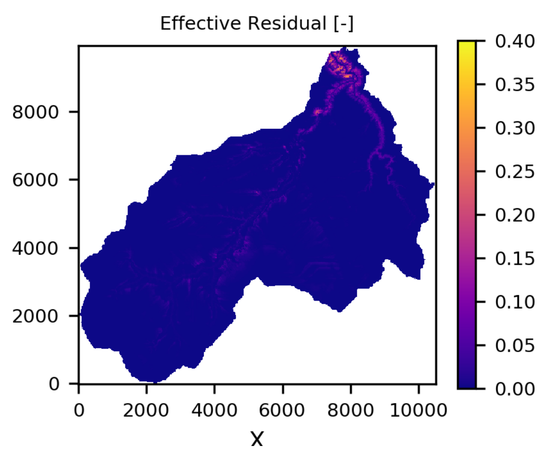

(d) Effective residual value at each grid node used in objective function calculation.

Figure C.32: Calibration results summary for Model CCC showing spatially distributed values at the end of the 13 ka to present model run with calibrated parameter values in Upper Franks Creek Watershed (SEW domain).

C.3 Bayesian Calibration

C.3.1 Parameter Posterior Distribution Tables

Table C.35: First for moments of the posterior distribution estimated with QUESO-DRAM for model 800 in Upper Franks Creek Watershed (SEW domain).

Parameter Name	Mean	Standard Deviation	Skewness	Kurtosis
$\log_{10} K_2$	-6.36ˆ+00	7.71ˆ-01	-4.72ˆ-03	-6.4ˆ-01
D	-1.43ˆ+00	8.5ˆ-02	-8.79ˆ-01	8.51ˆ-01
$\log_{10} K_1$	-3.64ˆ+00	2.44ˆ-02	-3.38ˆ-01	2.62ˆ-01

Table C.36: First for moments of the posterior distribution estimated with QUESO-DRAM for model 802 in Upper Franks Creek Watershed (SEW domain).

Parameter Name	Mean	Standard Deviation	Skewness	Kurtosis
D	-1.42^+00	6.43^-02	7.74^-03	-8.53^-01
$\log_{10}\omega_{c2}$	-6.37^-01	4.53^-01	-1.05^+00	4.99^-01
$\log_{10}\omega_{c1}$	-2.58^+00	3.26^-01	1.17^+00	1.23^+00
$\log_{10}K_2$	-4.47^+00	5.59^-01	-6.33^-01	-1.24^+00
$\log_{10}K_1$	-3.52^+00	9.06^-02	1.28^+00	1.81^+00

Table C.37: First for moments of the posterior distribution estimated with QUESO-DRAM for model 804 in Upper Franks Creek Watershed (SEW domain).

Parameter Name	Mean	Standard Deviation	Skewness	Kurtosis
D	-1.43^+00	7.33^-02	-6.19^-01	1.22^-01
$\log_{10}K_{ss1}$	-3.81^+00	2.19^-02	-8.25^-02	-1.19^-01
$\log_{10}K_{ss2}$	-6.16^+00	6.5^-01	-1.68^-01	-9.31^-01

Table C.38: First for moments of the posterior distribution estimated with QUESO-DRAM for model 808 in Upper Franks Creek Watershed (SEW domain).

Parameter Name	Mean	Standard Deviation	Skewness	Kurtosis
D	-1.72^+00	5.49^-03	-2.38^+00	3.68^+00
b	6.42^+00	4.79^-03	-1.66^+00	7.33^+00
$\log_{10}\omega_c$	1.02^+00	3.26^-02	2.38^+00	3.67^+00
$\log_{10}K_2$	-7.89^+00	1.58^-02	2.38^+00	3.69^+00
$\log_{10}K_1$	-1.29^+00	4.11^-03	-6.2^-01	2.56^+00

Table C.39: First for moments of the posterior distribution estimated with QUESO-DRAM for model 810 in Upper Franks Creek Watershed (SEW domain).

Parameter Name	Mean	Standard Deviation	Skewness	Kurtosis
$\log_{10}K_2$	-4.77^+00	2.1^-01	-3.69^+00	2.18^+01
$\log_{10}K_1$	-3.66^+00	3.3^-02	2.25^+00	1.03^+01
$\log_{10}V_c$	-1.41^+00	3.55^-01	2.51^+00	1.46^+01
D	-1.34^+00	3.94^-02	-2.08^+00	7.73^+00

Table C.40: First for moments of the posterior distribution estimated with QUESO-DRAM for model 842 in Upper Franks Creek Watershed (SEW domain).

Parameter Name	Mean	Standard Deviation	Skewness	Kurtosis
$\log_{10} K_2$	-3.06ˆ+00	5.72ˆ-02	-1.49ˆ+00	1.73ˆ+00
$\log_{10} K_1$	-3.24ˆ+00	9.17ˆ-02	-4.56ˆ-01	-1.1ˆ-01
$\log_{10} \omega_{c2}$	-2.46ˆ-02	9.92ˆ-02	-1.88ˆ-01	4.88ˆ-01
$\log_{10} \omega_{c1}$	-1.68ˆ+00	2.64ˆ-01	-7.72ˆ-01	1.82ˆ-01
D	-2.09ˆ+00	1.06ˆ-01	-3.21ˆ-01	5.39ˆ-01
S_c	3.68ˆ-01	1.96ˆ-02	-5.03ˆ-01	6.01ˆ-01

Table C.41: First for moments of the posterior distribution estimated with QUESO-DRAM for model A00 in Upper Franks Creek Watershed (SEW domain).

Parameter Name	Mean	Standard Deviation	Skewness	Kurtosis
$\log_{10} K_2$	-5.64ˆ+00	3.46ˆ-04	3.08ˆ-02	-1.78ˆ+00
$\log_{10} K_1$	-3.63ˆ+00	3.64ˆ-04	-2.1ˆ-01	-1.5ˆ+00
D	-1.73ˆ+00	1.23ˆ-03	1.09ˆ+00	-4.62ˆ-01
K_{sat}	1.88ˆ+01	7.9ˆ-02	6.69ˆ-01	-7.78ˆ-01

Table C.42: First for moments of the posterior distribution estimated with QUESO-DRAM for model C00 in Upper Franks Creek Watershed (SEW domain).

Parameter Name	Mean	Standard Deviation	Skewness	Kurtosis
D	-1.58ˆ+00	2.67ˆ-02	-5.46ˆ-01	-1.19ˆ+00
P_0	5.01ˆ-04	6.17ˆ-07	-9.97ˆ-01	-6.27ˆ-02
$\log_{10} K_2$	-4.96ˆ+00	7.54ˆ-02	-4.4ˆ-01	-1.48ˆ+00
$\log_{10} K_1$	-3.85ˆ+00	1.14ˆ-02	1.99ˆ-01	5.26ˆ-01
H_s	4.93ˆ-01	1.67ˆ-03	2.19ˆ-01	-1.41ˆ+00

Appendix D

Capture Scenario Construction

D.1 Introduction

In Section 11.3.3 we described the basis for considering stream capture of Upper Franks Creek by either Buttermilk Creek or a gully to the southeast of the SDA. In this Appendix we first outline the derivation of the capture boundary conditions and then describe the details of implementation.

D.2 Derivation of capture boundary condition

Stream capture within the modeled domain due to motion of a stream outside the study domain could be implemented within the EMS framework in any way that a user could choose to conceptualize modification of the modeled domain to reflect changes outside the modeled domain. Further, if a user wished, the entire domain comprising both the captured domain and the capturing stream could be modeled. For the purposes of the capture experiments introduced in Section 11 we have implemented capture as the lowering of a model domain boundary node, termed the *captured node*, to the elevation of the capturing stream or gully, over a specified period of time.

Consider a stream adjacent to the modeled domain. The stream is lowering at a rate of I_d, and moving laterally towards the edge of the modeled domain at a rate of w_b (dark blue square in Figure D.1). The incision and lateral cutting of the stream will influence the erosion of adjacent hillslopes between the adjacent stream and the modeled domain, resulting in the horizontal movement of the hill crest toward the edge of the modeled domain (yellow square in Figure D.1). If the model domain boundary is a watershed boundary, as is the case in this report, the node that will be captured (green square in Figure D.1) will not be impacted by the widening of the adjacent stream until the hill crest reaches the captured node. We define this time t_{cs} as the onset of a capture event. After a time interval t_{cs}, the captured node will lower towards the elevation of adjacent stream. In this framework, no explicit treatment of the drainage divide that was located at the capture node is made — that is, after time t_{cs} the drainage divide will migrate into the explicitly modeled domain at a rate determined by the model physics.

With W as the width of the drainage divide outside of the explicitly modeled domain we

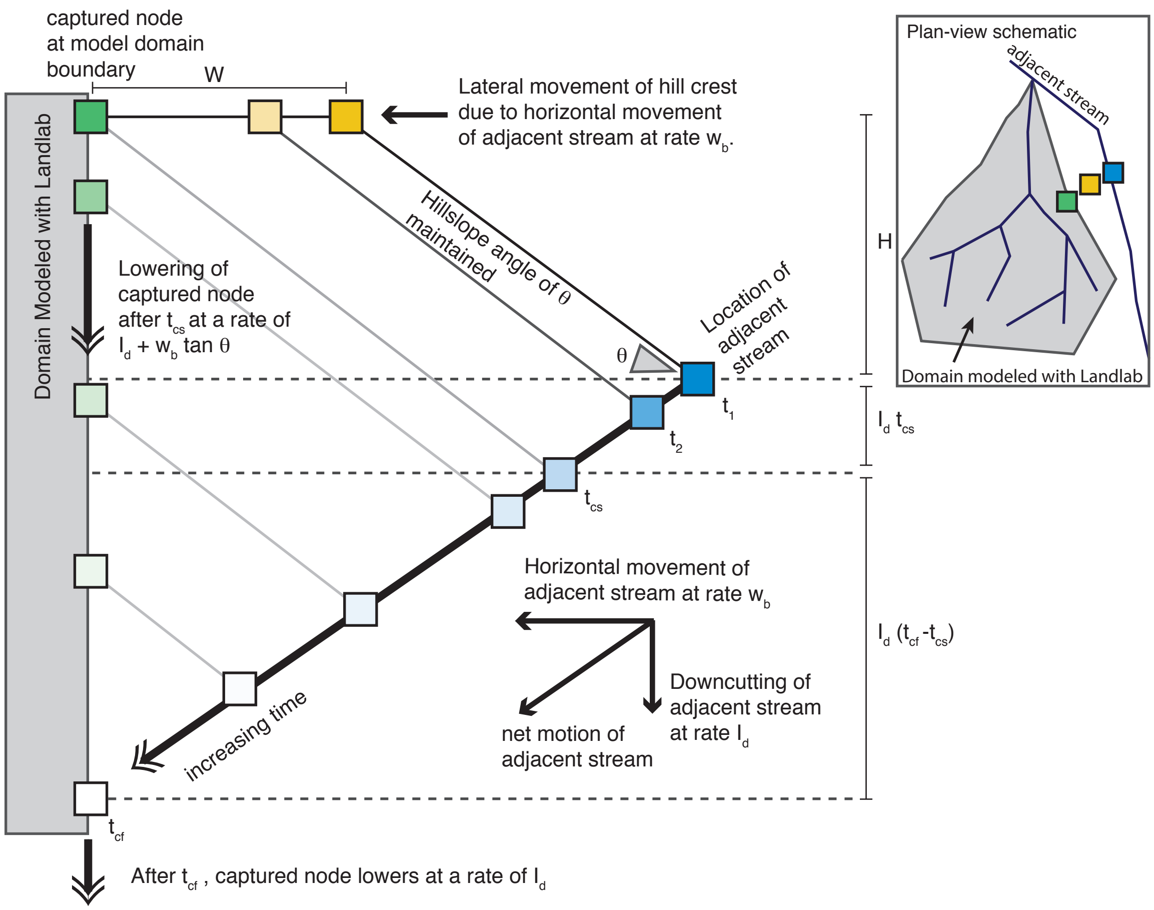

Figure D.1: Cartoon describing the geometry used for construction of downcutting scenarios. See the text for definition of all symbols used.

Table D.1: Geometric parameters for capture scenarios used in numerical experiments.

Scenario Name	Captured Node ID	W [ft]	H [ft]	θ [radians]
Buttermilk Capture	118237	400	160	0.453
Gully Capture	86269	260	143	0.155

can write an expression for t_{cs} if we assume that the angle of slopes between the hill crest and the stream location maintain a constant angle θ,

$$t_{cs} = \frac{W}{w_b} \ . \tag{D.1}$$

During capture, the captured node will lower at a rate of $I_c = I_d + w_b \tan\theta$ due to the combined effect of the the lateral and vertical motion of the adjacent captor stream. We define the end of capture t_{cf} as the time at which the captured note reaches the same elevation as the adjacent stream. Between t_{cs} and t_{cf} the captured node must lower an amount that combines the original height of the divide H, the additional height added before capture began $I_d t_{cs}$, and the additional height added while capture progresses $I_d \Delta_c$.

We can write an expression for the duration of the rapid downcutting of the captured node during the capture event $t_{cf} - t_{cs}$,

$$\Delta_c = \frac{H + I_d t_{cs} + I_d \Delta_c}{I_d + w_b \tan\theta} \ . \tag{D.2}$$

Rearranging to solve for Δ_c we get the following expression,

$$\Delta_c = \frac{H + I_b \frac{W}{w_b}}{w_b \tan\theta}. \tag{D.3}$$

Thus, the duration of capture-related downcutting, Δ_c, at a capture node can be determined from the original height of the drainage divide relative to the valley of the captor stream (in this case, the plateau and Buttermilk valley, respectively), the initial distance between the two streams, and the incision rate and lateral migration rate of the captor stream.

D.3 Implementation

We consider two capture scenarios, one for capture by Buttermilk Creek and one for capture by the gully in the southeastern part of the watershed. The topography of each of the captured locations prescribes the values for W, H, and θ (Table D.1).

For the purposes of the numerical experiments we elect to consider the following values for t_{cs}: 100, 2000, 4000, 6000, 8000 years in the future. Based on the results of EWG Study 1 (*Wilson and Young*, 2018), commencement of capture any earlier than about 4,000 years into the future appears highly unlikely, but we have included a wide range of onset times in order to address a worst-case scenario, and to examine the model's sensitivity to capture onset time.

Table D.2: Additional parameters implied by geometric parameters and capture start time t_{cs} for each of two capture locations

Scenario	t_{cs}	Climate	Lowering	w_b [ft/yr]	Δ_c [yr]	t_{cf} [yr]	I_c [ft/yr]	I_d [ft/yr]
Buttermilk	100.0	constant	1	4	82.27	182.27	1.96	0.005
		RCP85	3	4	83.29	183.29	1.98	0.025
	2000.0	constant	1	0.2	1742.76	3742.76	0.1	0.005
		RCP85	3	0.2	2152.82	4152.82	0.12	0.025
	4000.0	constant	1	0.1	3690.55	7690.55	0.05	0.005
		RCP85	3	0.1	5330.79	9330.79	0.07	0.025
	6000.0	constant	1	0.07	5843.37	11843.4	0.04	0.005
		RCP85	3	0.07	9533.91	15533.9	0.06	0.025
	8000.0	constant	1	0.05	8201.22	16201.2	0.03	0.005
		RCP85	3	0.05	14762.2	22762.2	0.05	0.025
SE Gully	100.0	constant	1	2.6	352.61	452.61	0.41	0.005
		RCP85	3	2.6	357.52	457.52	0.43	0.025
	2000.0	constant	1	0.13	7519.03	9519.03	0.03	0.005
		RCP85	3	0.13	9484.79	11484.8	0.05	0.025
	4000.0	constant	1	0.06	16021	20021	0.02	0.005
		RCP85	3	0.06	23884	27884	0.04	0.025
	6000.0	constant	1	0.04	25505.7	31505.7	0.01	0.005
		RCP85	3	0.04	43197.6	49197.6	0.03	0.025
	8000.0	constant	1	0.03	35973.4	43973.4	0.01	0.005
		RCP85	3	0.03	67425.6	75425.6	0.03	0.025

Within the conceptual framework for stream capture, a value of t_{cs} and W will implie a value for w_b, and so on. For the two scenarios, Table D.2 lists the implied parameters for all twenty implemented capture scenarios. Rather than running all nine combinations of climate and lowering futures, we chose to run only the two end-member combinations.

Appendix E

Uncertainty Partitioning

E.1 Methodology

Our predictions are from $N_m = 9$ alternative landscape evolution models under $N_c = 3$ alternative climate scenarios and $N_l = 3$ alternative lowering scenarios. We consider $N_i = 100$ alternative initial topographies for all nine models and the two end-member lowering and climate scenario combinations. The model, lowering, and climate scenarios are all factorial treatment levels.

Following *Yip et al.* (2011) we partition the uncertainty of future elevation with an ANOVA model. An ANOVA is a method originally developed by Roland Fischer to assess difference among group means and partition variation to different sources. It is appropriate for assessing the effect of one or more categorical input variables on a continuous output variables. For a complete review and discussion see *Box et al.* (2005); for a less complete treatment focused more closely on applications to projections in climatology see *Storch and Zwiers* (2001). Our application of ANOVA follows the methodological framework within climate science that seeks to partition uncertainty in climate projection into categorical sources such as model physics and emissions scenario (*Hawkins and Sutton*, 2009; *Madden*, 1976; *Yip et al.*, 2011). In our application, we consider three categorical variables: model physics, climate scenario and, lowering future scenario. This leads to the use of a three-way ANOVA.

Note here that the equations presented here assume that all models and scenarios have equal probability. In our application we either consider only one model (842) or nine models that are weighted equally. We also consider each climate and downcutting scenario as equally probably. For information regarding how this approach can be modified based on assigned model probabilities see *Burnham and Anderson* (2003).

E.1.1 ANOVA model

We consider the following model for elevation at a given location through time $z(m, l, c, i, t)$:

$$
\begin{aligned}
z(m,l,c,i,t) =&\mu(t)+ \\
&\alpha(m,t)+\beta(l,t)+\gamma(c,t) \\
&\delta(m,l,t)+\zeta(m,c,t)+\theta(l,c,t)+ \\
&\kappa(m,l,c,t)+ \\
&\epsilon(m,l,c,i,t)\ .
\end{aligned}
\tag{E.1}
$$

Here $\mu(t)$ is the grand ensemble mean of all simulations at a given time and represents the expected value of erosion overall. $\alpha(m,t)$, $\beta(l,t)$, and $\gamma(c,t)$ are main effects that represent the independent contributions of model selection, lowering scenario, and climate scenario, respectively. Note here that model selection refers both to uncertainty in model choice *and* uncertainty in model calibration (see Section E.1.4 for a detailed discussion of the separation of these two terms). The terms $\delta(m,l,t)$, $\zeta(m,c,t)$, and $\theta(l,c,t)$ are two-way interaction terms and $\kappa(m,l,c,t)$ is the three way interaction term. $\delta(m,l,t)$ represents the climate scenario and initial topography independent interaction between model and lowering scenario. $\zeta(m,c,t)$ represents the lowering scenario and initial topography independent interaction between model and climate scenario, and $\theta(l,c,t)$ represents the model and initial topography independent interaction between the lowering and climate scenarios. Finally, $\kappa(m,l,c,t)$ represents the initial topography independent interation between model and both type of scenarios. The interaction terms represent variance derived from non-additive behavior (*de González et al.*, 2007). Finally, $\epsilon(m,l,c,i,t)$ represents an independent and identically distributed error term.

E.1.2 ANOVA parameter estimation

The method of least squares is used for parameter estimation. Applying the following constraints:

$$\sum_{m=1}^{N_m} \hat{\alpha}(m,t) = 0 \ ; \tag{E.2}$$

$$\sum_{l=1}^{N_l} \hat{\beta}(l,t) = 0 \ ; \tag{E.3}$$

$$\sum_{c=1}^{N_c} \hat{\gamma}(c,t) = 0 \ ' \tag{E.4}$$

$$\sum_{m=1}^{N_m} \hat{\delta}(m,l,t) = 0 \text{ , for all lowering scenarios;} \tag{E.5}$$

$$\sum_{l=1}^{N_l} \hat{\delta}(m,l,t) = 0 \text{ , for all models;} \tag{E.6}$$

$$\sum_{m=1}^{N_m} \hat{\zeta}(m,c,t) = 0 \text{ , for all climate scenarios;} \tag{E.7}$$

$$\sum_{c=1}^{N_c} \hat{\zeta}(m,c,t) = 0 \text{ , for all models;} \tag{E.8}$$

$$\sum_{l=1}^{N_l} \hat{\theta}(l,c,t) = 0 \text{ , for all climate scenarios;} \tag{E.9}$$

$$\sum_{c=1}^{N_c} \hat{\theta}(l,c,t) = 0 \text{ , for all lowering scenarios} \tag{E.10}$$

$$\sum_{m=1}^{N_m} \hat{\kappa}(m,l,c,t) = 0 \text{ , for all models;} \tag{E.11}$$

$$\sum_{l=1}^{N_l} \hat{\kappa}(m,l,c,t) = 0 \text{ , for lowering scenarios;} \tag{E.12}$$

$$\sum_{c=1}^{N_c} \hat{\kappa}(m,l,c,t) = 0 \text{ , for climate scenarios.} \tag{E.13}$$

we obtain the following estimates:

$$\hat{\mu}(t) = z(\cdot,\cdot,\cdot,\cdot,t) - z(\cdot,\cdot,\cdot,\cdot,t) \tag{E.14}$$
$$\hat{\alpha}(m,t) = z(m,\cdot,\cdot,\cdot,t) - z(\cdot,\cdot,\cdot,\cdot,t) \tag{E.15}$$
$$\hat{\beta}(l,t) = z(\cdot,l,\cdot,\cdot,t) - z(\cdot,\cdot,\cdot,\cdot,t) \tag{E.16}$$
$$\hat{\gamma}(c,t) = (\cdot,\cdot,c,\cdot,t) - z(\cdot,\cdot,\cdot,\cdot,t) \tag{E.17}$$
$$\hat{\delta}(m,l,t) = z(m,l,\cdot,\cdot,t) + z(\cdot,\cdot,\cdot,\cdot,t) - z(m,\cdot,\cdot,\cdot,t) - z(\cdot,l,\cdot,\cdot,t) \tag{E.18}$$
$$\hat{\zeta}(m,c,t) = z(m,\cdot,c,\cdot,t) + z(\cdot,\cdot,\cdot,\cdot,t) - z(m,\cdot,\cdot,\cdot,t) - z(\cdot,\cdot,c,\cdot,t) \tag{E.19}$$
$$\hat{\theta}(l,c,t) = z(\cdot,l,c,\cdot,t) + z(\cdot,\cdot,\cdot,\cdot,t) - z(\cdot,l,\cdot,\cdot,t) - z(\cdot,\cdot,c,\cdot,t) \tag{E.20}$$
$$\hat{\kappa}(m,l,c,t) = z(m,l,c,\cdot,t) - z(\cdot,\cdot,\cdot,\cdot,t) - \tag{E.21}$$
$$z(m,l,\cdot,\cdot,t) - z(m,\cdot,c,\cdot,t) - z(\cdot,l,c,\cdot,t) + \tag{E.22}$$
$$z(m,\cdot,\cdot,\cdot,t) + z(\cdot,l,\cdot,\cdot,t) + z(\cdot,\cdot,c,\cdot,t)\ . \tag{E.23}$$

where $z(\cdot,\cdot,\cdot,\cdot,t)$ is the overall mean at time t; $z(m,\cdot,\cdot,\cdot,t)$ is the mean over all lowering scenarios, lowering scenarios and initial topographies; $z(m,\cdot,\cdot,\cdot,t)$ is the mean over all lowering scenarios, lowering scenarios and initial topographies; $z(\cdot,l,\cdot,\cdot,t))$ is the mean over all models, climate scenarios, and initial topographies; $z(\cdot,\cdot,c,\cdot,t))$ is the mean over all models, lowering scenarios, and initial topographies; $z(\cdot,\cdot,\cdot,i,t))$ is the mean over all models, lowering scenarios, and climate scenarios; $z(m,l,\cdot,\cdot,t))$ is the mean over all climate scenarios and initial topographies for each model and lowering scenario combination; $z(m,\cdot,c,\cdot,t))$ is the mean over all lowering scenarios and initial topographies for each model and climate scenario combination; $z(\cdot,l,c,\cdot,t))$ is the mean over all models and initial topographies for each lowering and climate scenario combination.

E.1.3 Variance components

We consider eight variance terms associated with the components of a full form three-way ANOVA statistical: model uncertainty $M(t)$, lowering scenario uncertainty $L(t)$, climate scenario uncertainty $C(t)$, initial topography uncertainty $T(t)$, model-lowering interaction uncertainty $I_{ml}(t)$, model-climate interaction uncertainty $I_{mc}(t)$, lowering-climate interaction uncertainty $I_{lc}(t)$, and model-lowering-climate interaction uncertainty $I_{mlc}(t)$. $V(t)$ represents the remaining variance, termed "the variance not explained by the statistical model".

Thus, the total variance as a function of time, $T(t)$ is given as:

$$\begin{aligned} T(t) =& M(t) + L(t) + C(t) + I_{ml}(t) + I_{mc}(t) + I_{lc}(t) + I_{mlc}(t) + V(t) \\ =& \mathrm{Var}_m\left[\hat{\alpha}(m,t)\right] + \mathrm{Var}_l\left[\hat{\beta}(l,t)\right] + \mathrm{Var}_c\left[\hat{\gamma}(c,t)\right] + \\ & \mathrm{Var}_{ml}\left[\hat{\delta}(m,l,t)\right] + \mathrm{Var}_{mc}\left[\hat{\zeta}(m,c,t)\right] + \mathrm{Var}_{lc}\left[\hat{\theta}(l,c,t)\right] + \\ & \mathrm{Var}_{mlt}\left[\hat{\delta}(m,l,c,t)\right] + V(t)\ . \end{aligned} \tag{E.24}$$

Note that $\mathrm{Var}\left[\hat{\mu}(t)\right] = 0$ and is thus not represented in Equation E.24.

The scenario and initial topography independent model uncertainty $M(t)$ is represented by the variance of the model means around the overall mean and is given as,

$$M(t) = \frac{1}{N_m} \sum_{m=1}^{N_m} \left[z(m,\cdot,\cdot,\cdot,t) - z(\cdot,\cdot,\cdot,\cdot,t)\right]^2 = \mathrm{Var}_m \left[\hat{\alpha}(m,t)\right] \ . \tag{E.25}$$

The model, climate scenario, and initial topography independent lowering scenario uncertainty $L(t)$ is represented by the variance of the lowering scenario means around the overall mean and is given as,

$$L(t) = \frac{1}{N_l} \sum_{l=1}^{N_l} \left[z(\cdot,l,\cdot,\cdot,t) - z(\cdot,\cdot,\cdot,\cdot,t)\right]^2 = \mathrm{Var}_l \left[\hat{\beta}(l,t)\right] \ . \tag{E.26}$$

The model, lowering scenario, and initial topography independent climate scenario uncertainty $C(t)$ is represented by the variance of the climate scenario means around the overall mean and is given as,

$$C(t) = \frac{1}{N_c} \sum_{c=1}^{N_c} \left[z(\cdot,\cdot,c,\cdot,t) - z(\cdot,\cdot,\cdot,\cdot,t)\right]^2 = \mathrm{Var}_c \left[\hat{\gamma}(c,t)\right] \ . \tag{E.27}$$

The uncertainty associated with the climate scenario and initial topography independent interaction between model and lowering scenario $I_{ml}(t)$ is represented by the variance of the model-lowering mean about the sum of the overall mean $\mu(t)$, and the model and lowering scenario main effects $\alpha(m,t)$ and $\beta(l,t)$. It is defined as,

$$\begin{aligned} I_{ml}(t) &= \frac{1}{N_m N_l} \sum_{m=1}^{N_m} \sum_{l=1}^{N_l} \left[z(m,l,\cdot,\cdot,t) - \left\{\hat{\mu}(t) + \hat{\alpha}(m,t) + \hat{\beta}(l,t)\right\}\right]^2 \\ &= \frac{1}{N_m N_l} \sum_{m=1}^{N_m} \sum_{l=1}^{N_l} \langle z(m,l,\cdot,\cdot,t) \\ &\qquad - \{z(\cdot,\cdot,\cdot,\cdot,t) + [z(m,\cdot,\cdot,\cdot,t) - z(\cdot,\cdot,\cdot,\cdot,t)] + [z(\cdot,l,\cdot,\cdot,t) - z(\cdot,\cdot,\cdot,\cdot,t)]\}\rangle^2 \\ &= \frac{1}{N_m N_l} \sum_{m=1}^{N_m} \sum_{l=1}^{N_l} \left[z(m,l,\cdot,\cdot,t) + z(\cdot,\cdot,\cdot,\cdot,t) - z(m,\cdot,\cdot,\cdot,t) + z(\cdot,l,\cdot,\cdot,t)\right]^2 \\ &= \mathrm{Var}_{ml} \left[\hat{\delta}(m,l,t)\right] \ . \end{aligned} \tag{E.28}$$

The uncertainty associated with the lowering scenario and initial topography independent interaction between model and climate scenario $I_{mc}(t)$ is represented by the variance of the model-climate mean about the sum of the overall mean $\mu(t)$, and the model and climate scenario main effects $\alpha(m,t)$, and $\gamma(c,t)$. It is defined as,

$$
\begin{aligned}
I_{ml}(t) &= \frac{1}{N_m N_c} \sum_{m=1}^{N_m} \sum_{c=1}^{N_c} \left[z(m,\cdot,c,\cdot,t) - \{ \hat{\mu}(t) + \hat{\alpha}(m,t) + \hat{\gamma}(c,t) \} \right]^2 \\
&= \frac{1}{N_m N_c} \sum_{m=1}^{N_m} \sum_{c=1}^{N_c} \langle z(m,\cdot,c,\cdot,t) \\
&\qquad - \{ z(\cdot,\cdot,\cdot,\cdot,t) + [z(m,\cdot,\cdot,\cdot,t) - z(\cdot,\cdot,\cdot,\cdot,t)] + [z(\cdot,\cdot,c,\cdot,t) - z(\cdot,\cdot,\cdot,\cdot,t)] \} \rangle^2 \\
&= \frac{1}{N_m N_c} \sum_{m=1}^{N_m} \sum_{c=1}^{N_c} \left[z(m,\cdot,c,\cdot,t) + z(\cdot,\cdot,\cdot,\cdot,t) - z(m,\cdot,\cdot,\cdot,t) + z(\cdot,\cdot,c,\cdot,t) \right]^2 \\
&= \mathrm{Var}_{mc} \left[\hat{\zeta}(m,c,t) \right] .
\end{aligned} \tag{E.29}
$$

The uncertainty associated with the model and initial topography independent interaction between lowering and climate scenarios $I_{lc}(t)$ is represented by the variance of the lowering-climate mean about the sum of the overall mean $\mu(t)$, and the lowering and climate scenario main effects $\beta(l,t)$ and $\gamma(c,t)$. It is defined as,

$$
\begin{aligned}
I_{lc}(t) &= \frac{1}{N_l N_c} \sum_{l=1}^{N_l} \sum_{c=1}^{N_c} \left[z(\cdot,l,c,\cdot,t) - \left\{ \hat{\mu}(t) + \hat{\beta}(l,t) + \hat{\gamma}(c,t) \right\} \right]^2 \\
&= \frac{1}{N_l N_c} \sum_{l=1}^{N_l} \sum_{c=1}^{N_c} \langle z(\cdot,l,c,\cdot,t) \\
&\qquad - \{ z(\cdot,\cdot,\cdot,\cdot,t) + [z(\cdot,l,\cdot,\cdot,t) - z(\cdot,\cdot,\cdot,\cdot,t)] + [z(\cdot,\cdot,c,\cdot,t) - z(\cdot,\cdot,\cdot,\cdot,t)] \} \rangle^2 \\
&= \frac{1}{N_l N_c} \sum_{l=1}^{N_l} \sum_{c=1}^{N_c} \left[z(\cdot,l,c,\cdot,t) + z(\cdot,\cdot,\cdot,\cdot,t) - z(\cdot,l,\cdot,\cdot,t) + z(\cdot,\cdot,c,\cdot,t) \right]^2 \\
&= \mathrm{Var}_{cl} \left[\hat{\theta}(l,c,t) \right] .
\end{aligned} \tag{E.30}
$$

This ANOVA has one three way interaction associated with the initial topography independent interaction between the model and the lowering and climate scenarios, $I_{mlc}(t)$. It is represented by the variance of the initial topography mean about the sum of the overall mean $\mu(t)$; the model, lowering scenario, and climate scenario main effects $\alpha(m,t)$, $\beta l,t$, and $\gamma c,t$; and the three two-way interaction terms $\delta(m,l,t)$, $\zeta m,c,t$, and $\theta(l,c,t)$. It is defined as:

(E.31)

$$
\begin{aligned}
I_{mlc}(t) = \frac{1}{N_m N_l N_c} \sum_{m=1}^{N_m} \sum_{l=1}^{N_l} \sum_{c=1}^{N_c} \Big[& z(m,l,c,\cdot,t) \\
& - \left\{ \hat{\mu}(t) + \hat{\beta}(l,t) + \hat{\gamma}(c,t) + \hat{\delta}(m,l,t) + \hat{\zeta}(m,c,t) + \hat{\theta}(l,c,t) \right\} \Big]^2
\end{aligned}
$$

$$
\begin{aligned}
&= \frac{1}{N_m N_l N_c} \sum_{m=1}^{N_m} \sum_{l=1}^{N_l} \sum_{c=1}^{N_c} \langle z(\cdot, l, c, \cdot, t) \\
&\qquad - \{ z(\cdot,\cdot,\cdot,\cdot,t) + [z(m,\cdot,\cdot,\cdot,t) - z(\cdot,\cdot,\cdot,\cdot,t)] + [z(\cdot,l,\cdot,\cdot,t) - z(\cdot,\cdot,\cdot,\cdot,t)] \\
&\qquad + [z(\cdot,\cdot,c,\cdot,t) - z(\cdot,\cdot,\cdot,\cdot,t)] + [z(m,l,\cdot,\cdot,t) + z(\cdot,\cdot,\cdot,\cdot,t) - z(m,\cdot,\cdot,\cdot,t) - z(\cdot,l,\cdot,\cdot,t)] \\
&\qquad + [z(m,\cdot,c,\cdot,t) + z(\cdot,\cdot,\cdot,\cdot,t) - z(m,\cdot,\cdot,\cdot,t) - z(\cdot,\cdot,c,\cdot,t)] \\
&\qquad + [z(\cdot,l,c,\cdot,t) + z(\cdot,\cdot,\cdot,\cdot,t) - z(\cdot,l,\cdot,\cdot,t) - z(\cdot,\cdot,c,\cdot,t)] \} \rangle^2 \\
&= \frac{1}{N_m N_l N_c} \sum_{m=1}^{N_m} \sum_{l=1}^{N_l} \sum_{c=1}^{N_c} [z(m,l,c,\cdot,t) - z(\cdot,\cdot,\cdot,\cdot,t) - z(m,l,\cdot,\cdot,t) - z(m,\cdot,c,\cdot,t) \\
&\qquad - z(\cdot,l,c,\cdot,t) + z(m,\cdot,\cdot,\cdot,t) + z(\cdot,l,\cdot,\cdot,t) + z(\cdot,\cdot,c,\cdot,t)]^2 \\
&= \mathrm{Var}_{mlc} [\hat{\kappa}(m,l,c,t)] \ .
\end{aligned}
$$

Finally, the remaining variance not explained by the statistical model is given as,

$$
V(t) = \frac{1}{N_m N_l N_c N_i} \sum_{m=1}^{N_m} \sum_{l=1}^{N_l} \sum_{c=1}^{N_c} \sum_{i=1}^{N_i} [z(m,l,c,i,t) - z(m,l,c,\cdot,t)]^2 \ . \tag{E.32}
$$

This term represents variance associated with initial condition about the model-climate-lowering means. Thus it is appropriate to consider $V(t)$ as the uncertainty associated with initial topography.

The total variance can be written as,

$$
\begin{aligned}
T(t) &= \frac{1}{N_m N_l N_c N_i} \sum_{m=1}^{N_m} \sum_{l=1}^{N_l} \sum_{c=1}^{N_c} \sum_{i=1}^{N_i} [z(m,l,c,i,t) - z(\cdot,\cdot,\cdot,\cdot,t)]^2 \\
&\quad + \frac{1}{N_m} \sum_{m=1}^{N_m} [z(m,\cdot,\cdot,\cdot,t) - z(\cdot,\cdot,\cdot,\cdot,t)]^2 \\
&\quad + \frac{1}{N_l} \sum_{l=1}^{N_l} [z(\cdot,l,\cdot,\cdot,t) - z(\cdot,\cdot,\cdot,\cdot,t)]^2 + \frac{1}{N_c} \sum_{c=1}^{N_c} [z(\cdot,\cdot,c,\cdot,t) - z(\cdot,\cdot,\cdot,\cdot,t)]^2 \\
&\quad + \frac{1}{N_m N_l} \sum_{m=1}^{N_m} \sum_{l=1}^{N_l} [z(m,l,\cdot,\cdot,t) + z(\cdot,\cdot,\cdot,\cdot,t) - z(m,\cdot,\cdot,\cdot,t) + z(\cdot,l,\cdot,\cdot,t)]^2 \\
&\quad + \frac{1}{N_m N_c} \sum_{m=1}^{N_m} \sum_{c=1}^{N_c} [z(m,\cdot,c,\cdot,t) + z(\cdot,\cdot,\cdot,\cdot,t) - z(m,\cdot,\cdot,\cdot,t) + z(\cdot,\cdot,c,\cdot,t)]^2 \\
&\quad + \frac{1}{N_l N_c} \sum_{l=1}^{N_l} \sum_{c=1}^{N_c} [z(\cdot,l,c,\cdot,t) + z(\cdot,\cdot,\cdot,\cdot,t) - z(\cdot,l,\cdot,\cdot,t) + z(\cdot,\cdot,c,\cdot,t)]^2 \\
&\quad + \frac{1}{N_m N_l N_c} \sum_{m=1}^{N_m} \sum_{l=1}^{N_l} \sum_{c=1}^{N_c} [z(m,l,c,\cdot,t) - z(\cdot,\cdot,\cdot,\cdot,t) - z(m,l,\cdot,\cdot,t) - z(m,\cdot,c,\cdot,t) \\
&\qquad - z(\cdot,l,c,\cdot,t) + z(m,\cdot,\cdot,\cdot,t) + z(\cdot,l,\cdot,\cdot,t) + z(\cdot,\cdot,c,\cdot,t)]^2 \\
&\quad + \frac{1}{N_m N_l N_c N_i} \sum_{m=1}^{N_m} \sum_{l=1}^{N_l} \sum_{c=1}^{N_c} \sum_{i=1}^{N_i} [z(m,l,c,i,t) - z(m,l,c,\cdot,t)]^2 \ .
\end{aligned} \tag{E.33}
$$

E.1.4 Separation of Model Structure and Model Calibration Uncertainties

In this work we consider both uncertainty associated with model structure $M(t)$ and the uncertainty associated with the calibration of model parameters $P(t)$. Due to computational considerations we are not able to consider $P(t)$ in the same experiment as all other components of uncertainty described here. In this Section we describe how we treat $P(t)$ and combine it with the other sources of uncertain. In this work we follow the theoretical basis and recommendations laid out in *Burnham and Anderson* (2003).

To begin let us consider only treating $M(t)$ and $P(t)$. If these two sources of uncertainty were independent we could add them together to construct $U_{MP,i}(t)$. This is given by

$$U_{MP,i}(t) = M(t) + P(t) = \sum_{m}^{N_m} w_m^2 \left\{ P_m(t) + \left[z(m,\cdot,\cdot,\cdot,t) - z(\cdot,\cdot,\cdot,\cdot,t) \right]^2 \right\} \tag{E.34}$$

where $P(t)_m$ is the calibration uncertainty associated with model m.

Note here that $M(t)$ and $P(t)$ are variances and thus can be combined in this way. However, *Buckland et al.* (1997) points out that each of the N_m considered models is likely to be calibrated with the same data. This may result in covariance between $M(t)$ and $P(t)$. *Buckland et al.* (1997) derive an expression for the combined model and parameter calibration uncertainty that represents a conservative estimate as it assumes perfect pairwise correlation. This expression is given as,

$$U_{MP,c}(t) = \left\{ \sum_{m}^{N_m} w_m \sqrt{P_m(t) + \left[z(m,\cdot,\cdot,\cdot,t) - z(\cdot,\cdot,\cdot,\cdot,t) \right]^2} \right\}^2 \tag{E.35}$$

where $U_{MP,c}$ is the combined uncertainty assuming covariance.

On our approach we consider both of these options. We combine this combination with that presented in the ANOVA framework to present to present the total uncertainty if independence is assumed $T_i(t)$ and the total uncertainty if covariance is assumed $T_c(t)$. These are defined as

$$T_i(t) = M(t) + P(t) + L(t) + C(t) + I_{ml}(t) + I_{mc}(t) + I_{lc}(t) + I_{mlc}(t) + V(t) \tag{E.36}$$

and

$$T_c(t) = U_{MP,c}(t) + L(t) + C(t) + I_{ml}(t) + I_{mc}(t) + I_{lc}(t) + I_{mlc}(t) + V(t)\ . \tag{E.37}$$

Appendix F

Projection Plots

F.1 Prediction Summaries at Analysis Points

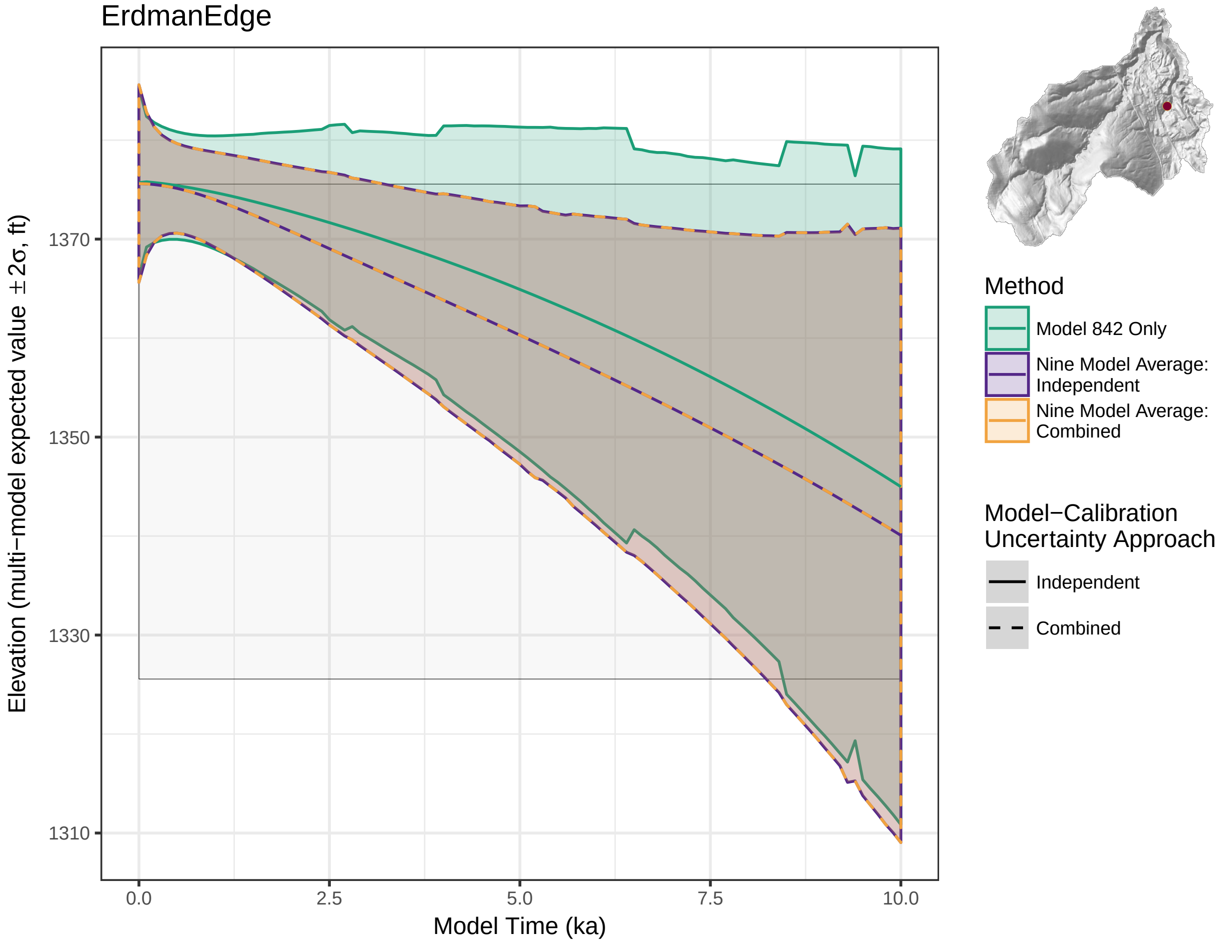

Figure F.1: Summary of prediction results at ErdmanEdge showing expected elevation and uncertainty through time. The gray box is a 50 foot deep reference box that extends below the modern surface. Three expected values and 95% confidence regions are shown that corresponds to the two approaches to model selection (only 842 and all nine 800 variants) and the two approaches to model structure and calibration uncertainty (independent or covarying).

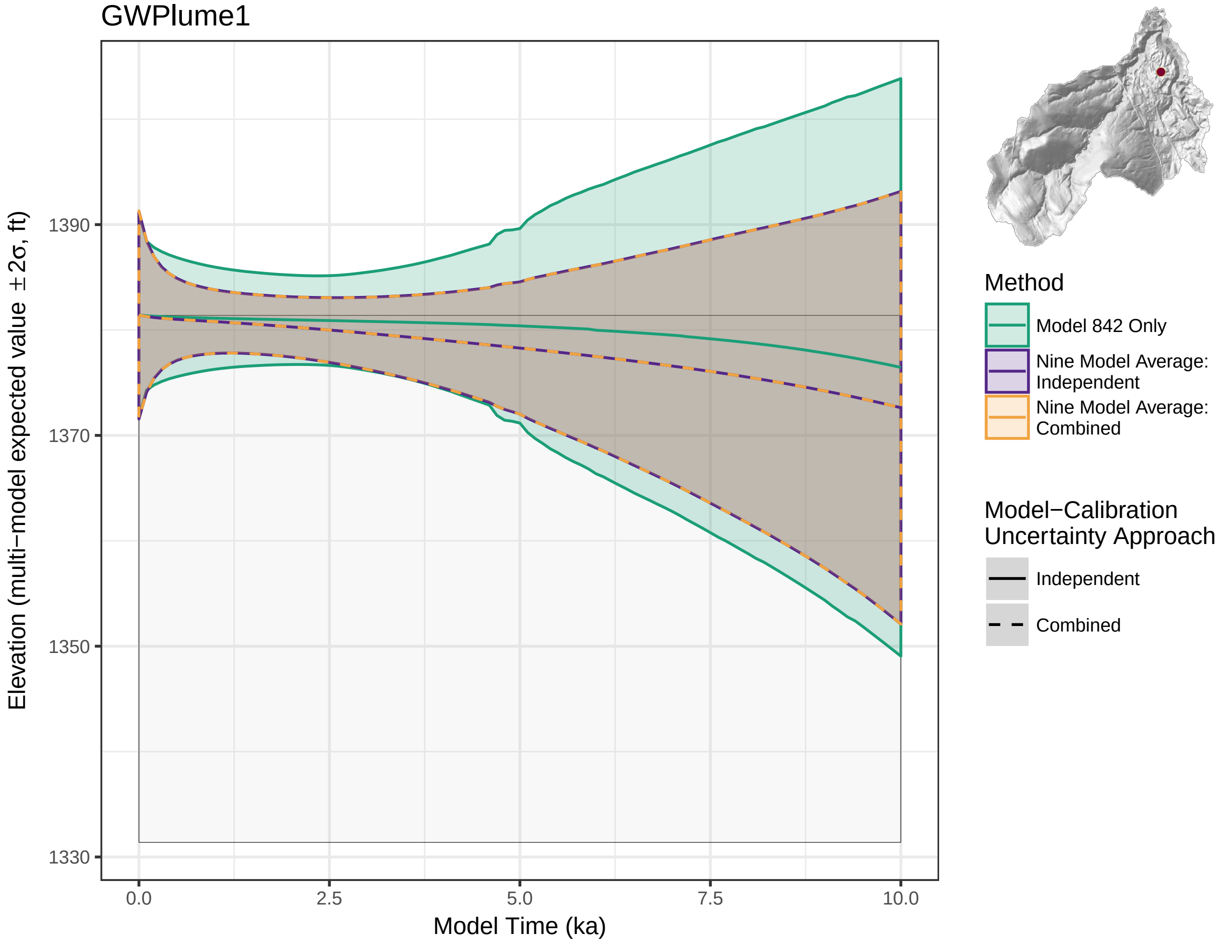

Figure F.2: Summary of prediction results at GWPlume1 showing expected elevation and uncertainty through time. The gray box is a 50 foot deep reference box that extends below the modern surface. Three expected values and 95% confidence regions are shown that corresponds to the two approaches to model selection (only 842 and all nine 800 variants) and the two approaches to model structure and calibration uncertainty (independent or covarying).

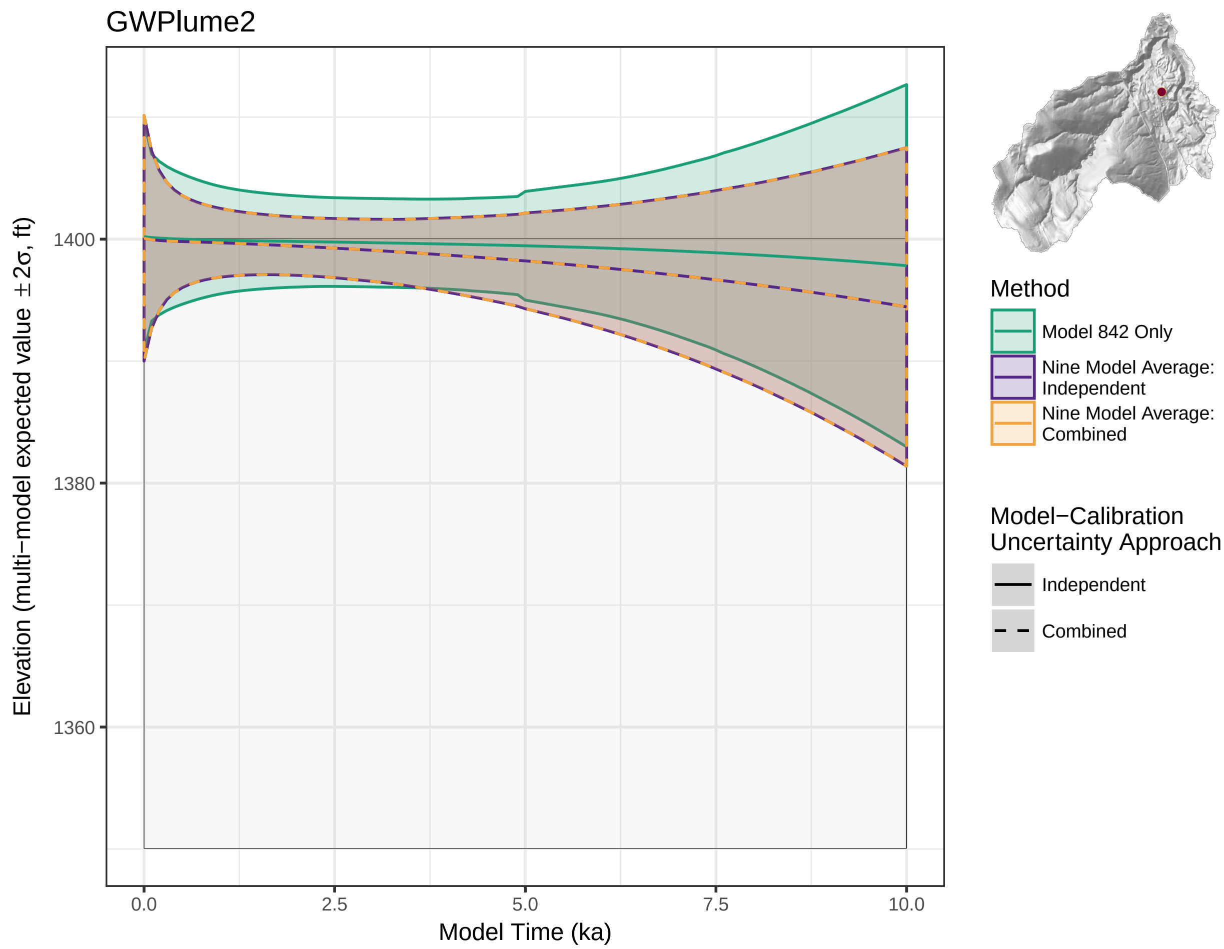

Figure F.3: Summary of prediction results at GWPlume2 showing expected elevation and uncertainty through time. The gray box is a 50 foot deep reference box that extends below the modern surface. Three expected values and 95% confidence regions are shown that corresponds to the two approaches to model selection (only 842 and all nine 800 variants) and the two approaches to model structure and calibration uncertainty (independent or covarying).

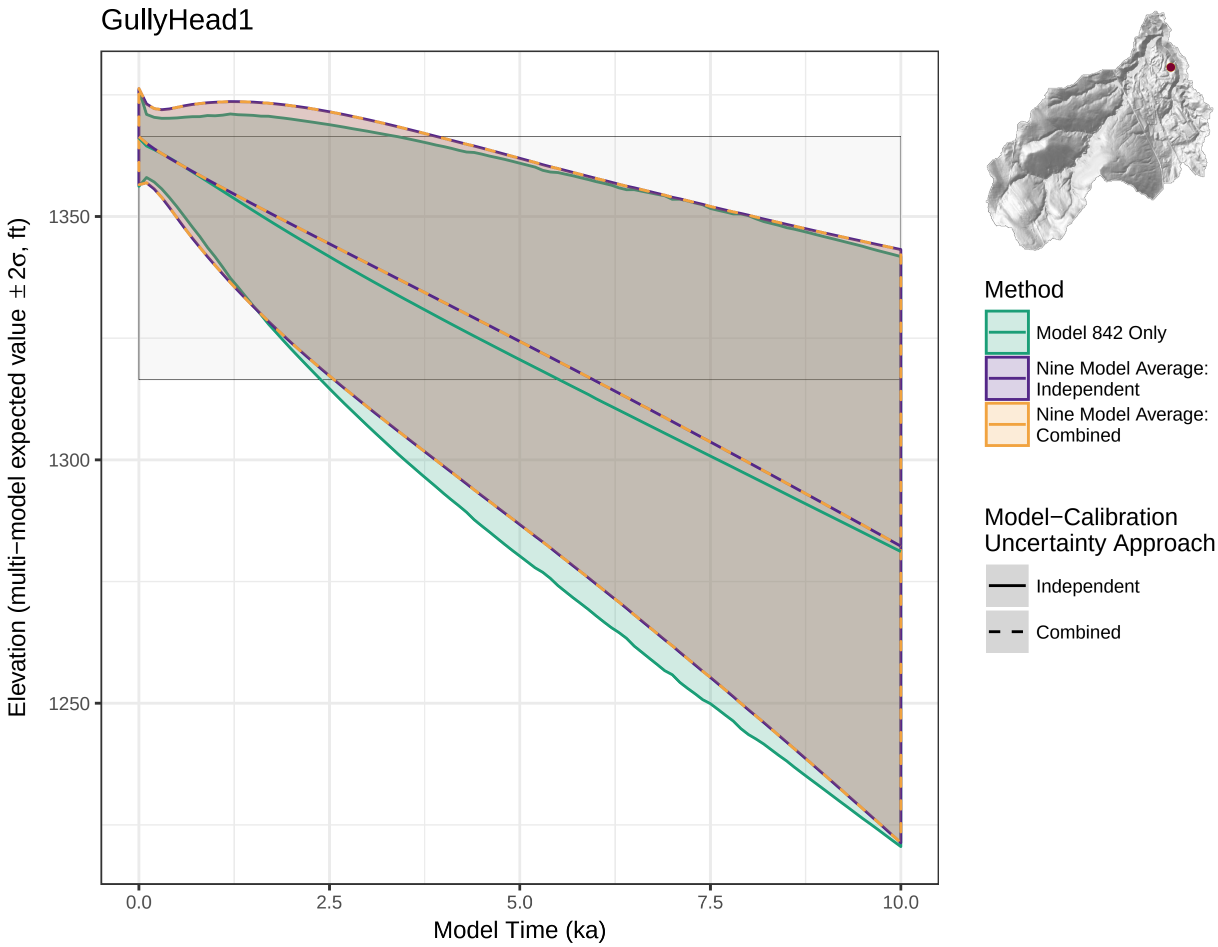

Figure F.4: Summary of prediction results at GullyHead1 showing expected elevation and uncertainty through time. The gray box is a 50 foot deep reference box that extends below the modern surface. Three expected values and 95% confidence regions are shown that corresponds to the two approaches to model selection (only 842 and all nine 800 variants) and the two approaches to model structure and calibration uncertainty (independent or covarying).

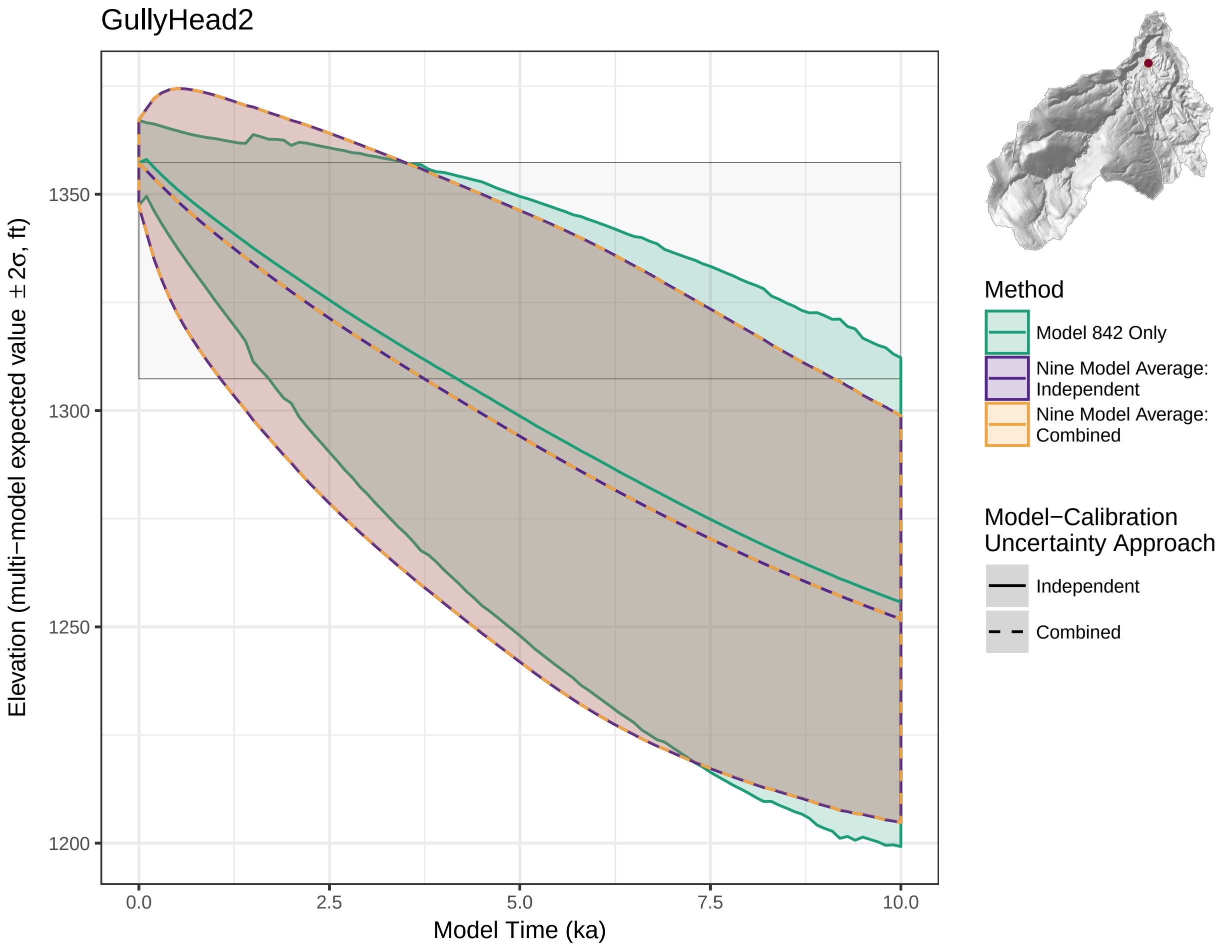

Figure F.5: Summary of prediction results at GullyHead2 showing expected elevation and uncertainty through time. The gray box is a 50 foot deep reference box that extends below the modern surface. Three expected values and 95% confidence regions are shown that corresponds to the two approaches to model selection (only 842 and all nine 800 variants) and the two approaches to model structure and calibration uncertainty (independent or covarying).

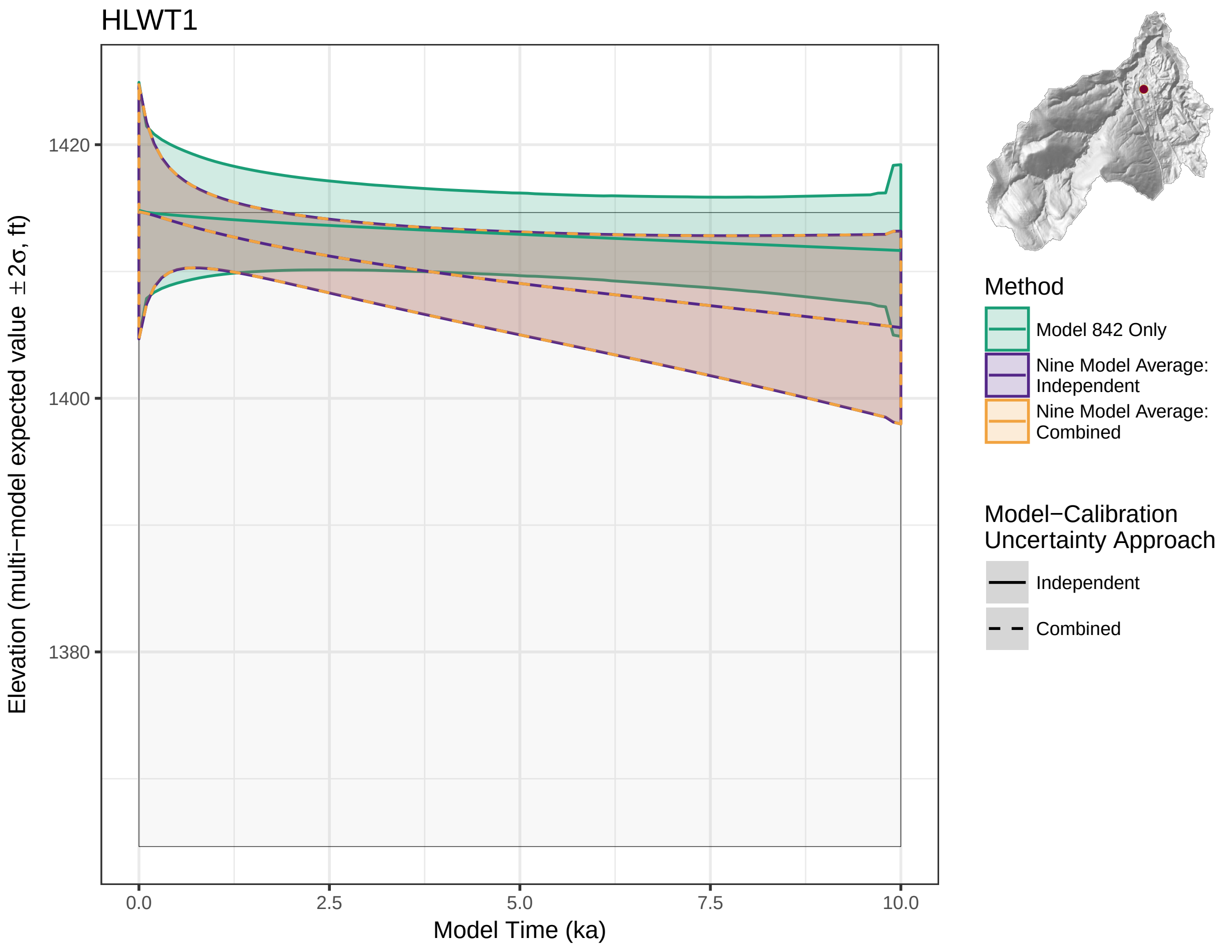

Figure F.6: Summary of prediction results at HLWT1 showing expected elevation and uncertainty through time. The gray box is a 50 foot deep reference box that extends below the modern surface. Three expected values and 95% confidence regions are shown that corresponds to the two approaches to model selection (only 842 and all nine 800 variants) and the two approaches to model structure and calibration uncertainty (independent or covarying).

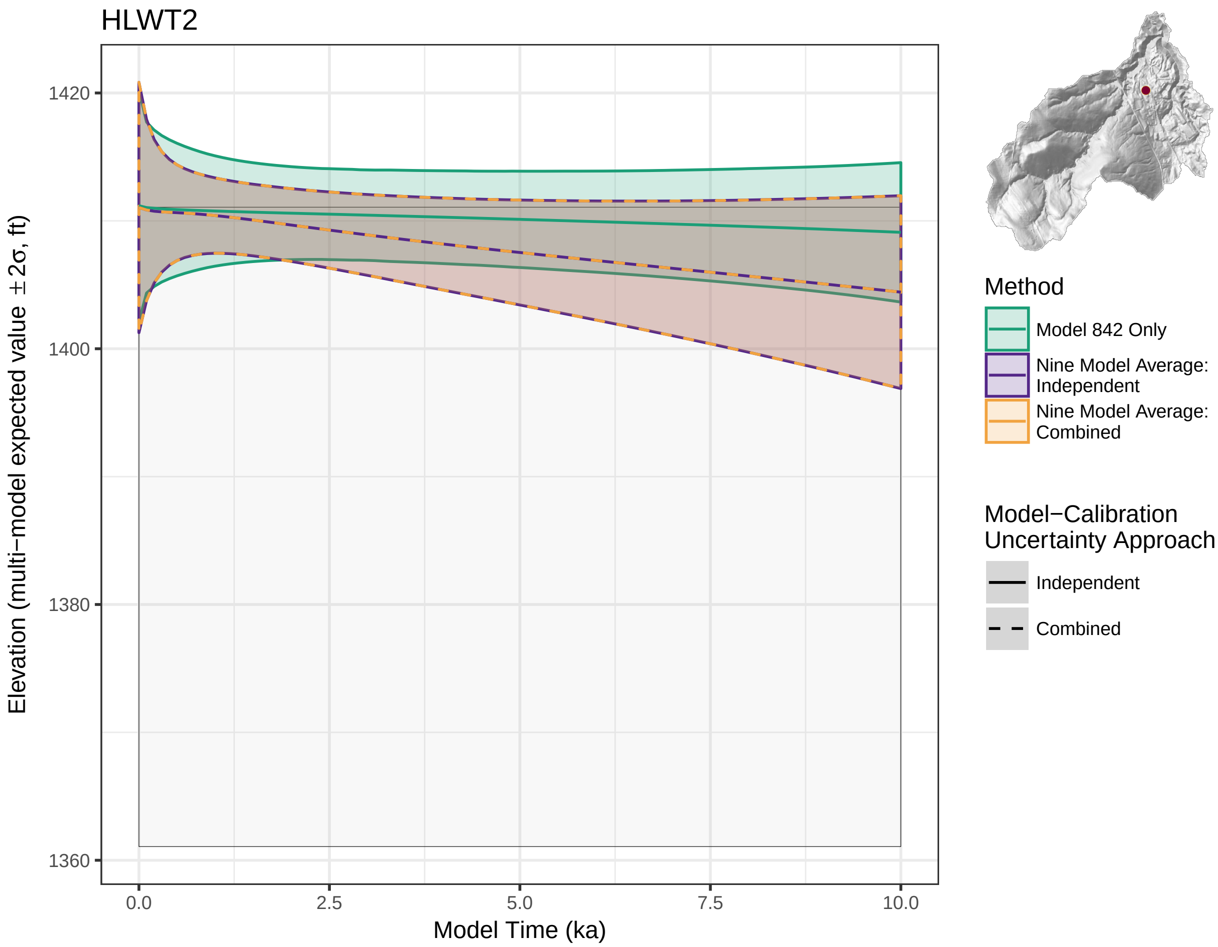

Figure F.7: Summary of prediction results at HLWT2 showing expected elevation and uncertainty through time. The gray box is a 50 foot deep reference box that extends below the modern surface. Three expected values and 95% confidence regions are shown that corresponds to the two approaches to model selection (only 842 and all nine 800 variants) and the two approaches to model structure and calibration uncertainty (independent or covarying).

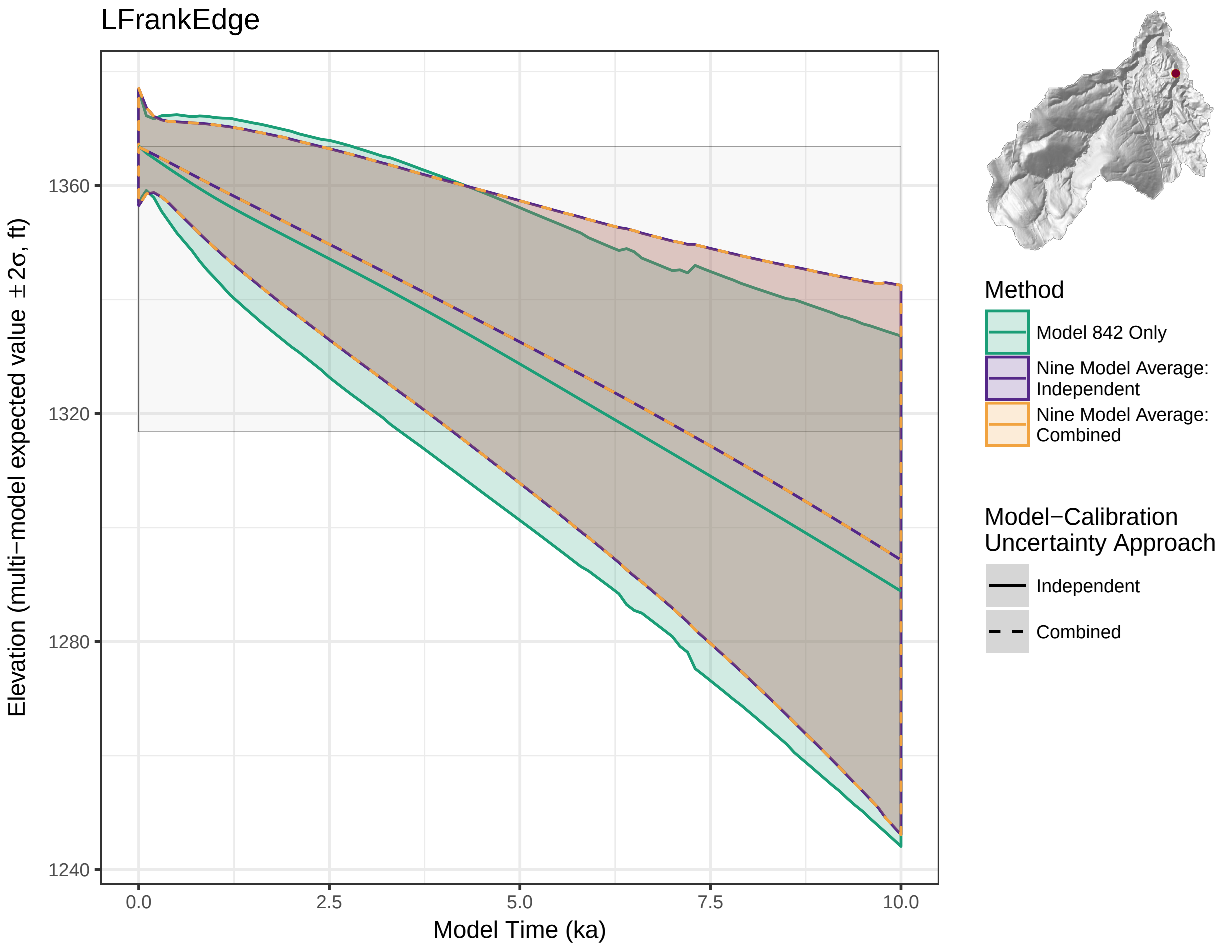

Figure F.8: Summary of prediction results at LFrankEdge showing expected elevation and uncertainty through time. The gray box is a 50 foot deep reference box that extends below the modern surface. Three expected values and 95% confidence regions are shown that corresponds to the two approaches to model selection (only 842 and all nine 800 variants) and the two approaches to model structure and calibration uncertainty (independent or covarying).

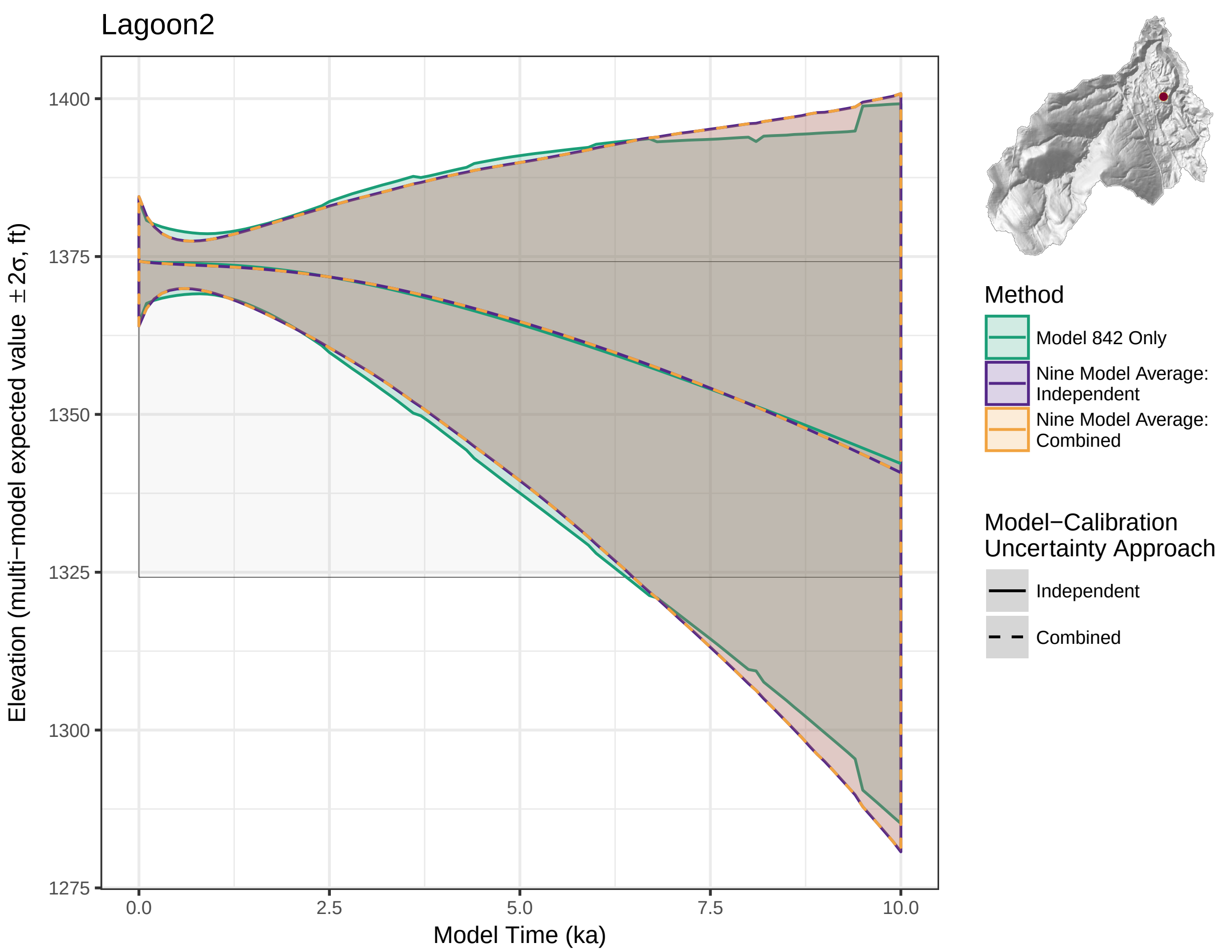

Figure F.9: Summary of prediction results at Lagoon2 showing expected elevation and uncertainty through time. The gray box is a 50 foot deep reference box that extends below the modern surface. Three expected values and 95% confidence regions are shown that corresponds to the two approaches to model selection (only 842 and all nine 800 variants) and the two approaches to model structure and calibration uncertainty (independent or covarying).

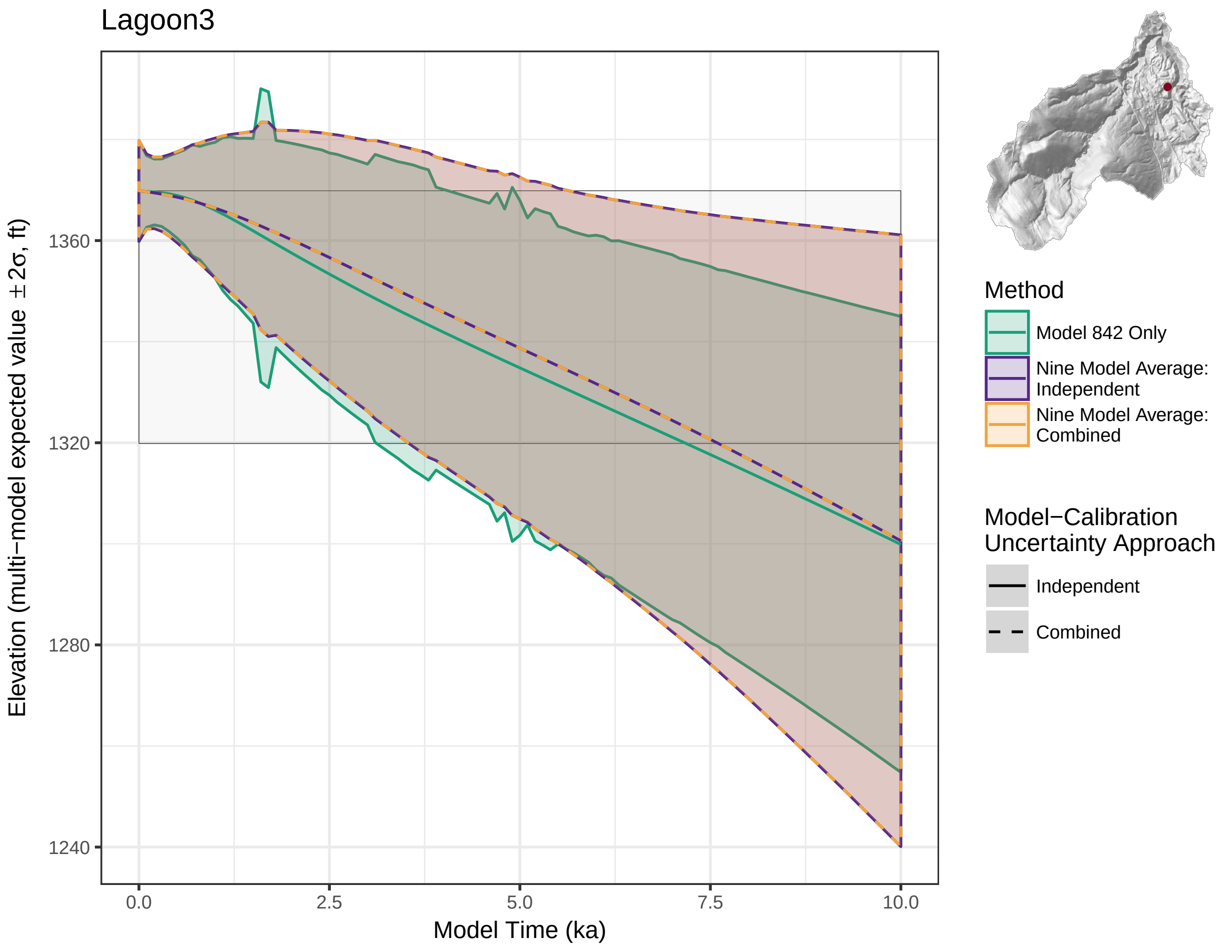

Figure F.10: Summary of prediction results at Lagoon3 showing expected elevation and uncertainty through time. The gray box is a 50 foot deep reference box that extends below the modern surface. Three expected values and 95% confidence regions are shown that corresponds to the two approaches to model selection (only 842 and all nine 800 variants) and the two approaches to model structure and calibration uncertainty (independent or covarying).

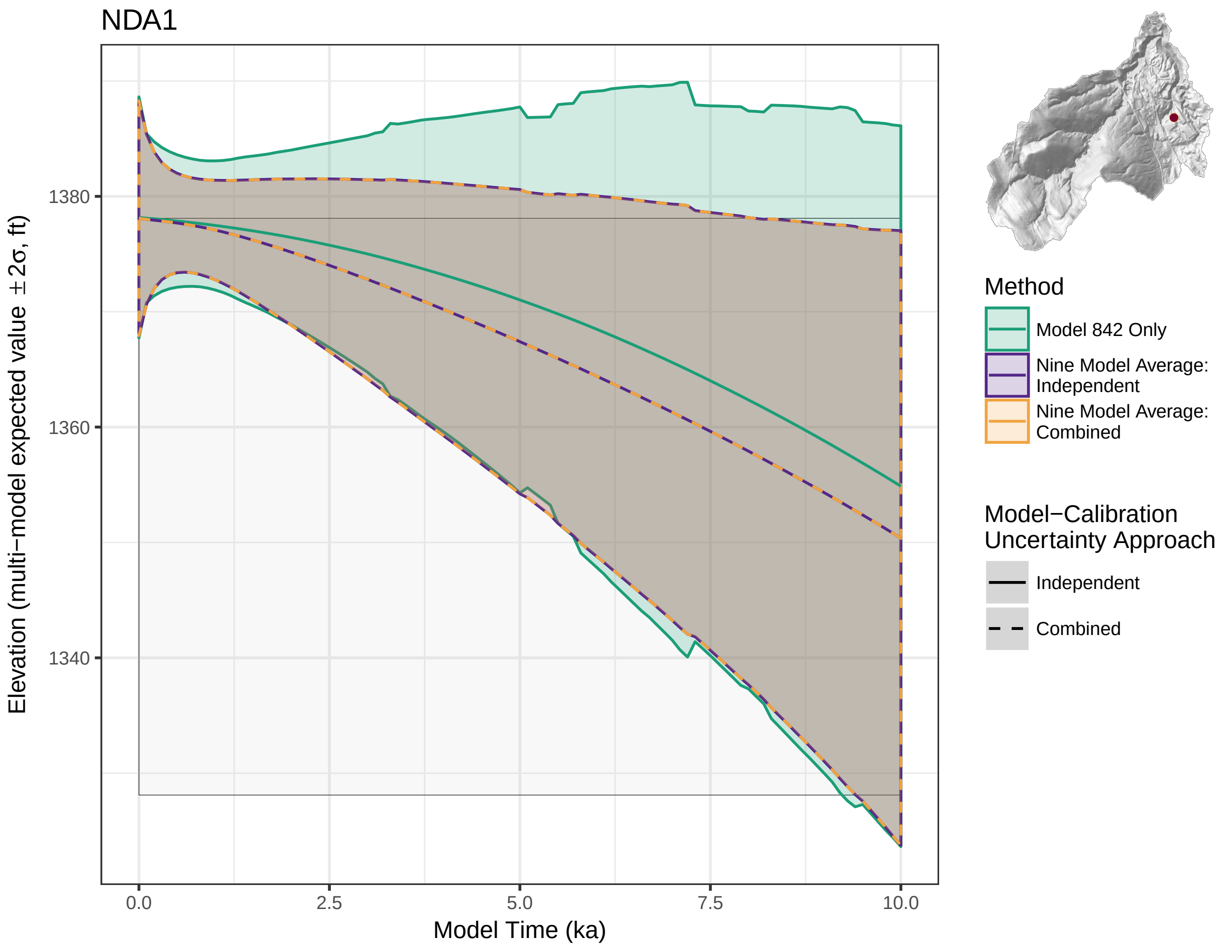

Figure F.11: Summary of prediction results at NDA1 showing expected elevation and uncertainty through time. The gray box is a 50 foot deep reference box that extends below the modern surface. Three expected values and 95% confidence regions are shown that corresponds to the two approaches to model selection (only 842 and all nine 800 variants) and the two approaches to model structure and calibration uncertainty (independent or covarying).

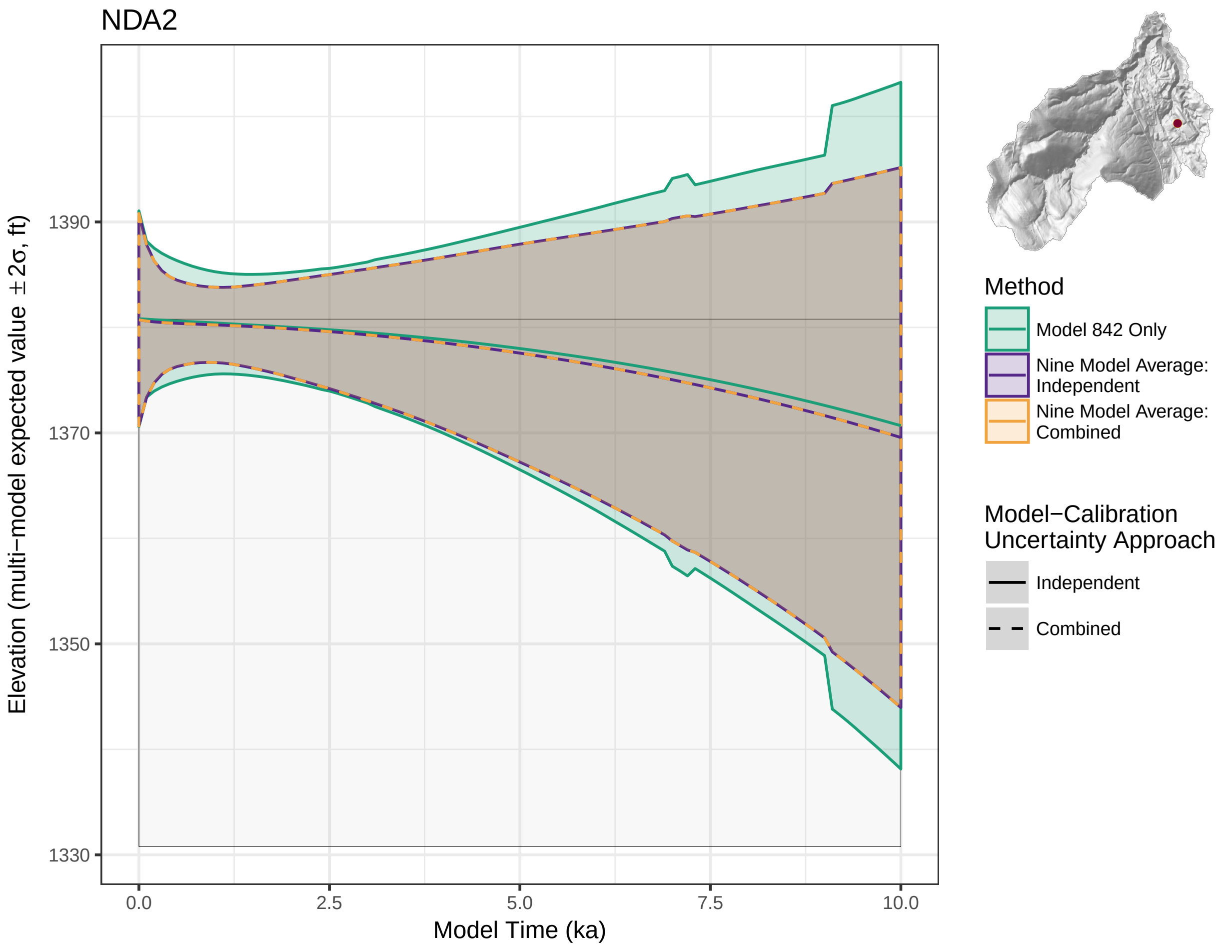

Figure F.12: Summary of prediction results at NDA2 showing expected elevation and uncertainty through time. The gray box is a 50 foot deep reference box that extends below the modern surface. Three expected values and 95% confidence regions are shown that corresponds to the two approaches to model selection (only 842 and all nine 800 variants) and the two approaches to model structure and calibration uncertainty (independent or covarying).

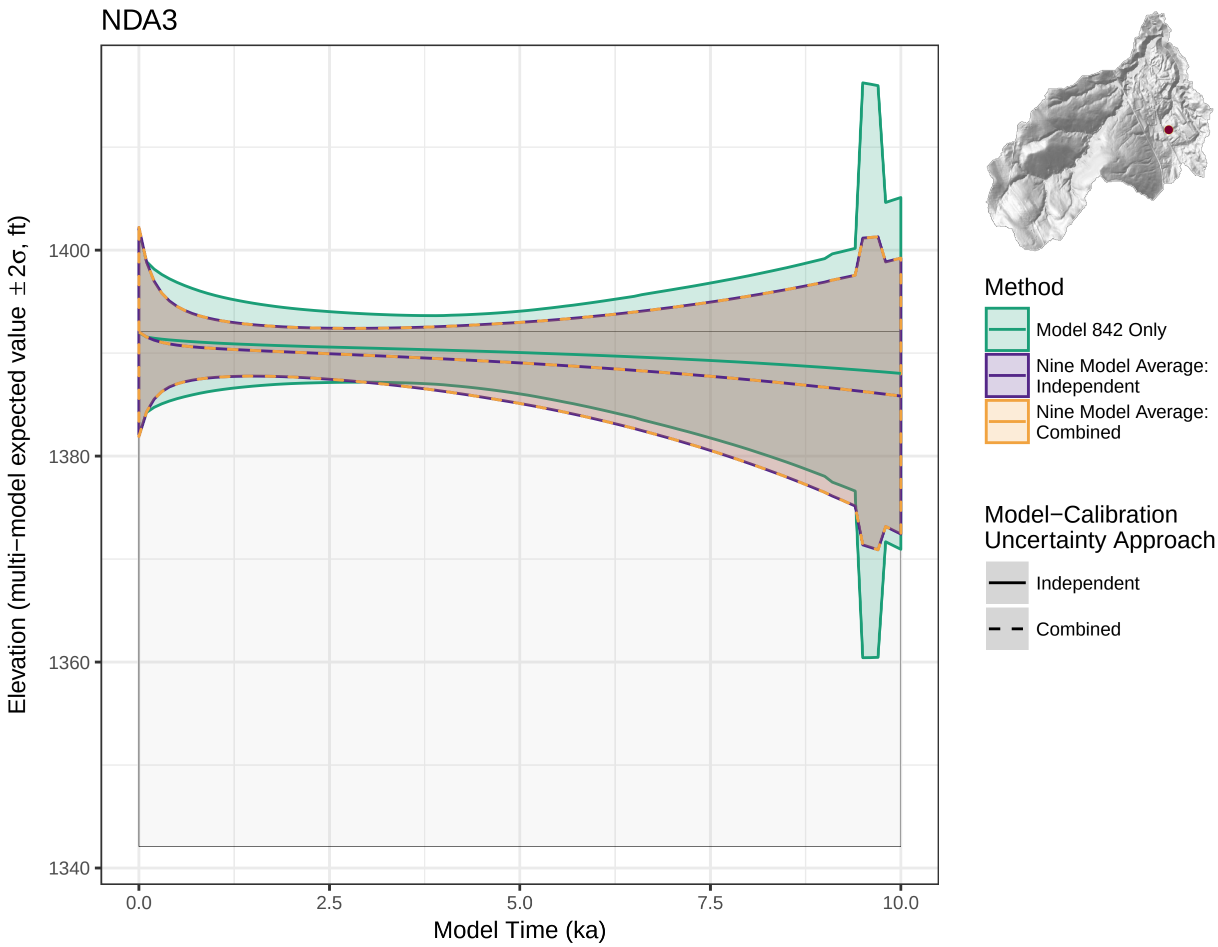

Figure F.13: Summary of prediction results at NDA3 showing expected elevation and uncertainty through time. The gray box is a 50 foot deep reference box that extends below the modern surface. Three expected values and 95% confidence regions are shown that corresponds to the two approaches to model selection (only 842 and all nine 800 variants) and the two approaches to model structure and calibration uncertainty (independent or covarying).

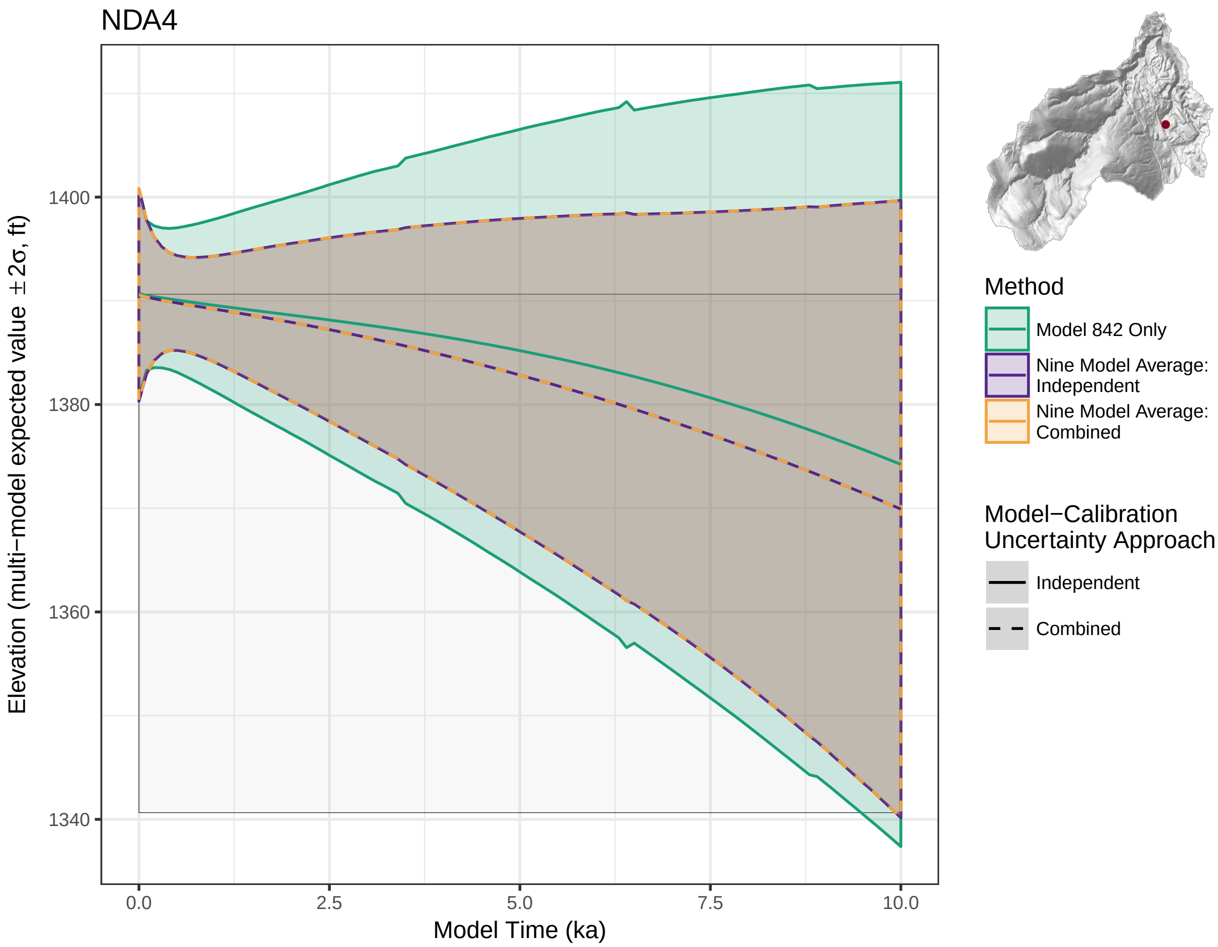

Figure F.14: Summary of prediction results at NDA4 showing expected elevation and uncertainty through time. The gray box is a 50 foot deep reference box that extends below the modern surface. Three expected values and 95% confidence regions are shown that corresponds to the two approaches to model selection (only 842 and all nine 800 variants) and the two approaches to model structure and calibration uncertainty (independent or covarying).

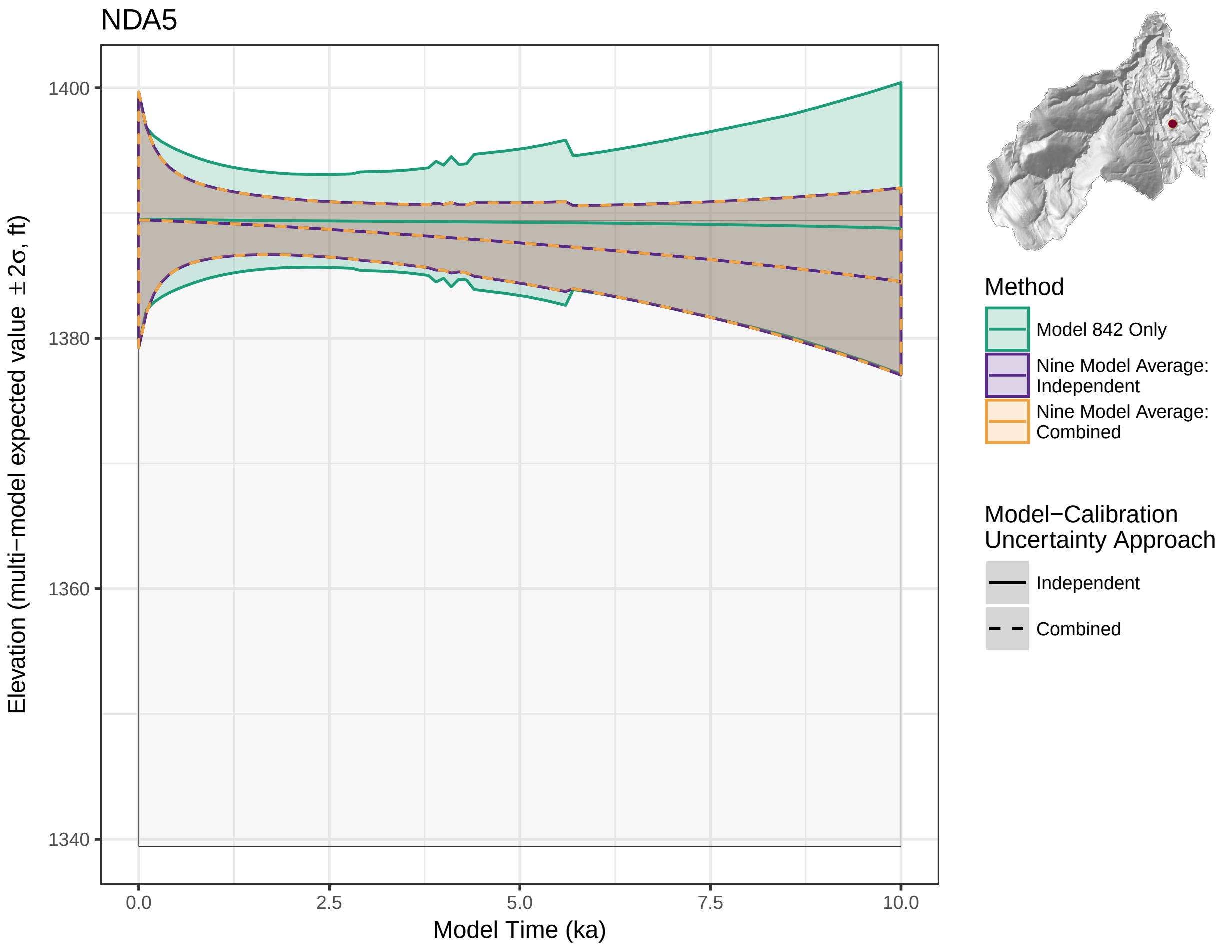

Figure F.15: Summary of prediction results at NDA5 showing expected elevation and uncertainty through time. The gray box is a 50 foot deep reference box that extends below the modern surface. Three expected values and 95% confidence regions are shown that corresponds to the two approaches to model selection (only 842 and all nine 800 variants) and the two approaches to model structure and calibration uncertainty (independent or covarying).

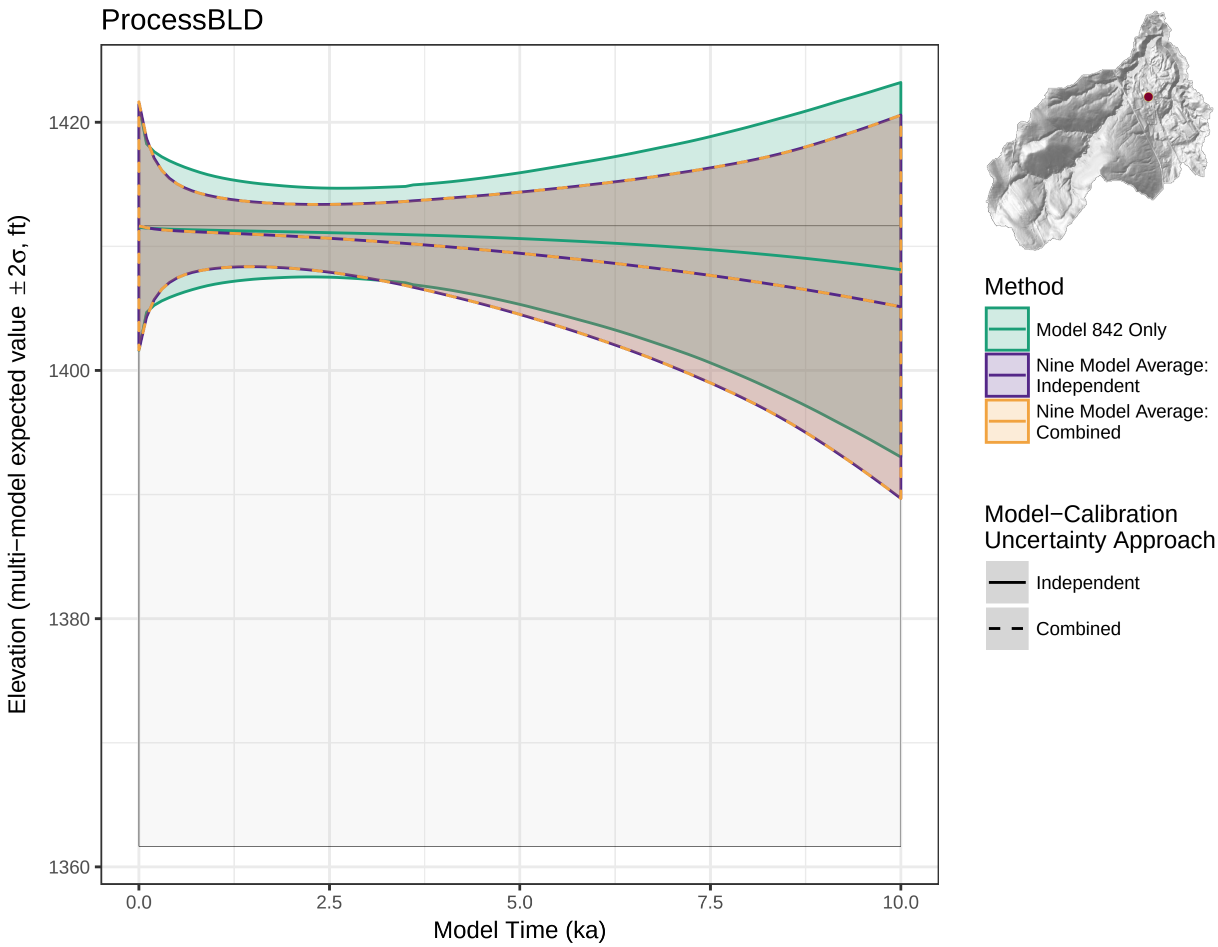

Figure F.16: Summary of prediction results at ProcessBLD showing expected elevation and uncertainty through time. The gray box is a 50 foot deep reference box that extends below the modern surface. Three expected values and 95% confidence regions are shown that corresponds to the two approaches to model selection (only 842 and all nine 800 variants) and the two approaches to model structure and calibration uncertainty (independent or covarying).

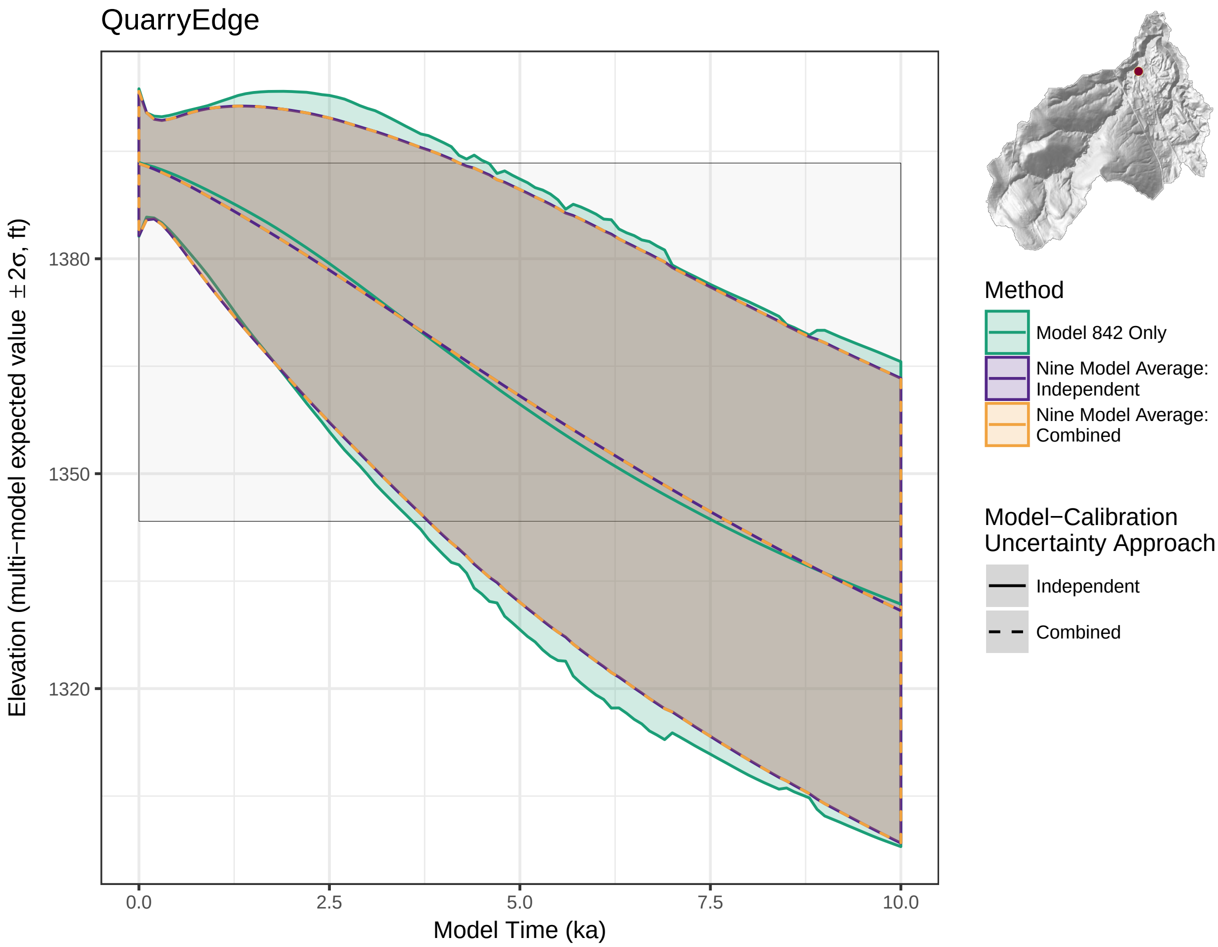

Figure F.17: Summary of prediction results at QuarryEdge showing expected elevation and uncertainty through time. The gray box is a 50 foot deep reference box that extends below the modern surface. Three expected values and 95% confidence regions are shown that corresponds to the two approaches to model selection (only 842 and all nine 800 variants) and the two approaches to model structure and calibration uncertainty (independent or covarying).

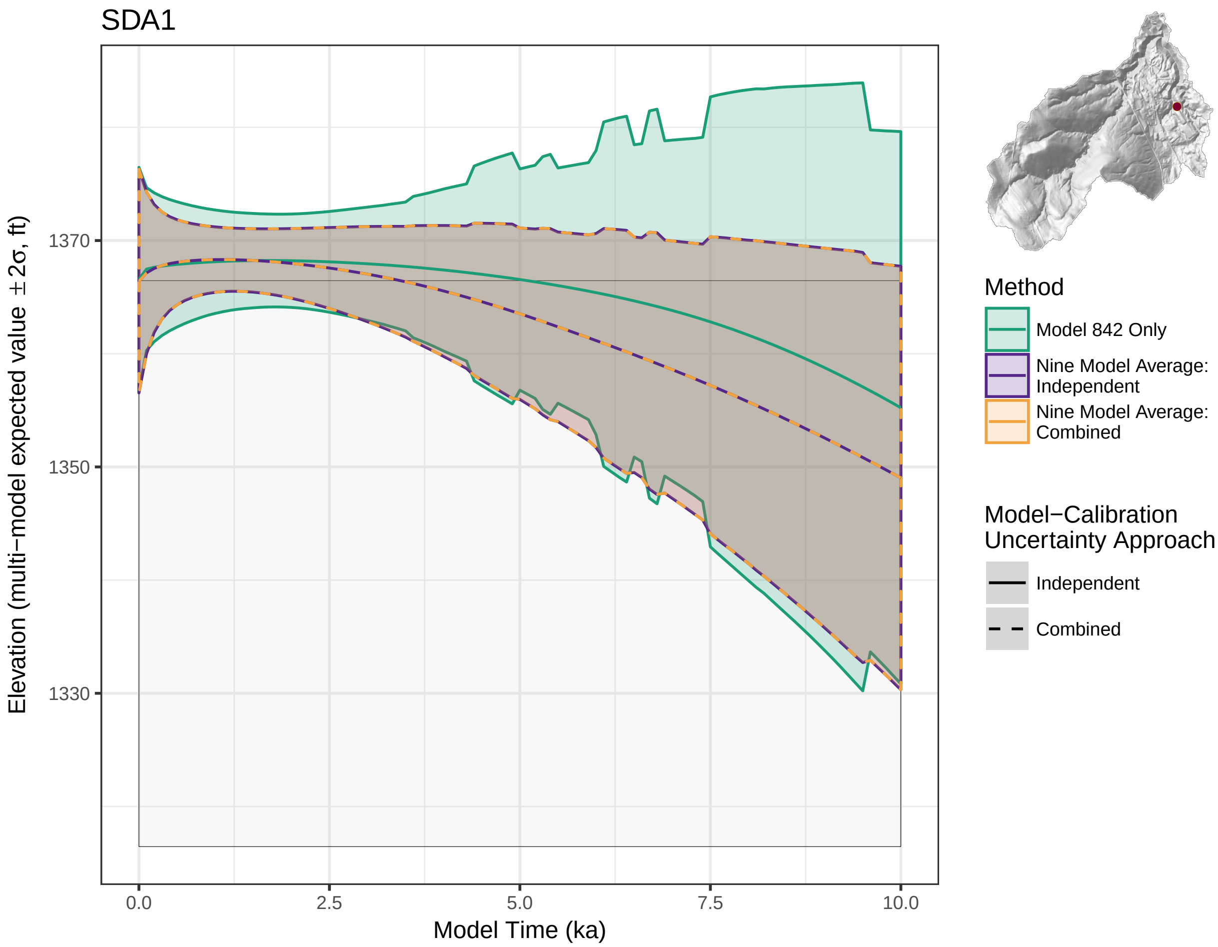

Figure F.18: Summary of prediction results at SDA1 showing expected elevation and uncertainty through time. The gray box is a 50 foot deep reference box that extends below the modern surface. Three expected values and 95% confidence regions are shown that corresponds to the two approaches to model selection (only 842 and all nine 800 variants) and the two approaches to model structure and calibration uncertainty (independent or covarying).

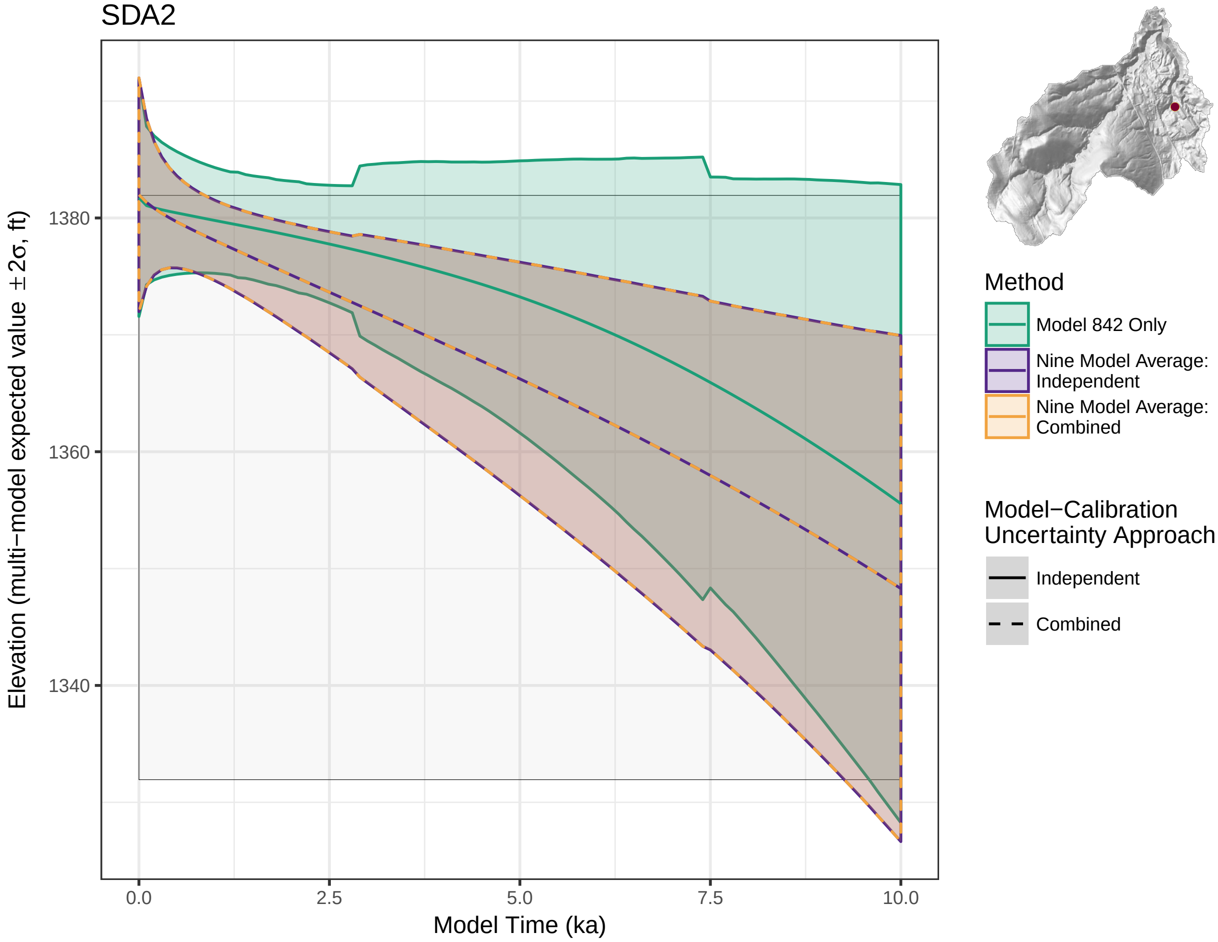

Figure F.19: Summary of prediction results at SDA2 showing expected elevation and uncertainty through time. The gray box is a 50 foot deep reference box that extends below the modern surface. Three expected values and 95% confidence regions are shown that corresponds to the two approaches to model selection (only 842 and all nine 800 variants) and the two approaches to model structure and calibration uncertainty (independent or covarying).

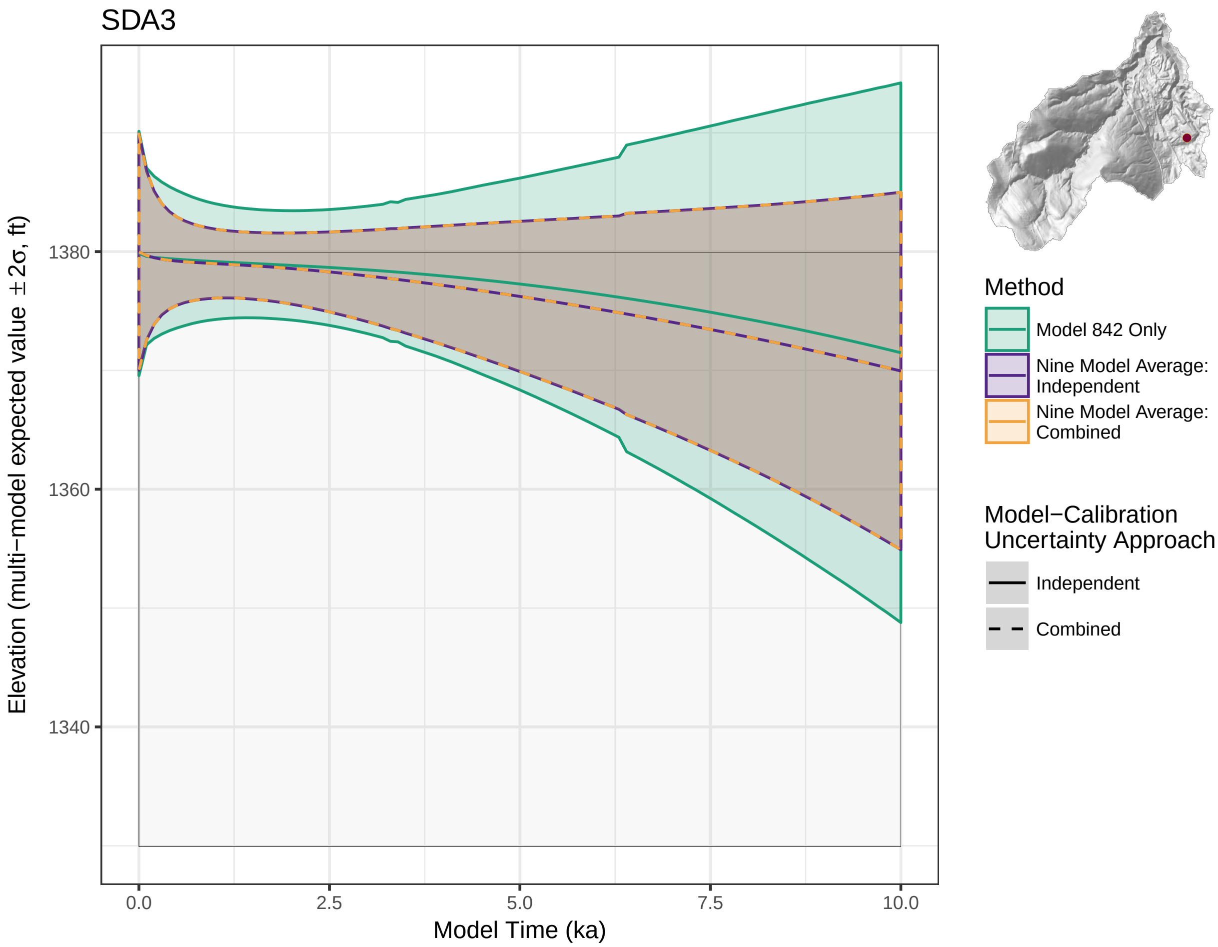

Figure F.20: Summary of prediction results at SDA3 showing expected elevation and uncertainty through time. The gray box is a 50 foot deep reference box that extends below the modern surface. Three expected values and 95% confidence regions are shown that corresponds to the two approaches to model selection (only 842 and all nine 800 variants) and the two approaches to model structure and calibration uncertainty (independent or covarying).

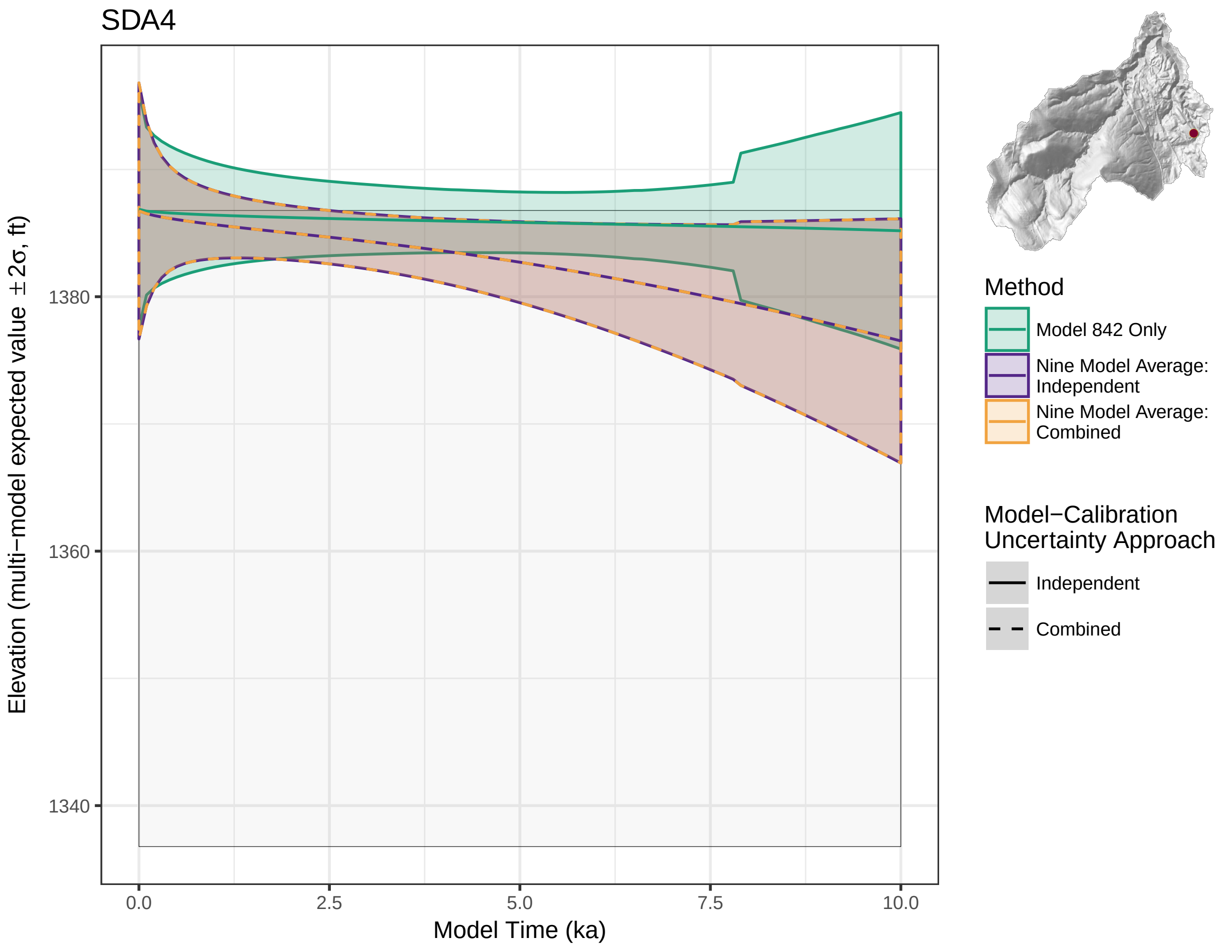

Figure F.21: Summary of prediction results at SDA4 showing expected elevation and uncertainty through time. The gray box is a 50 foot deep reference box that extends below the modern surface. Three expected values and 95% confidence regions are shown that corresponds to the two approaches to model selection (only 842 and all nine 800 variants) and the two approaches to model structure and calibration uncertainty (independent or covarying).

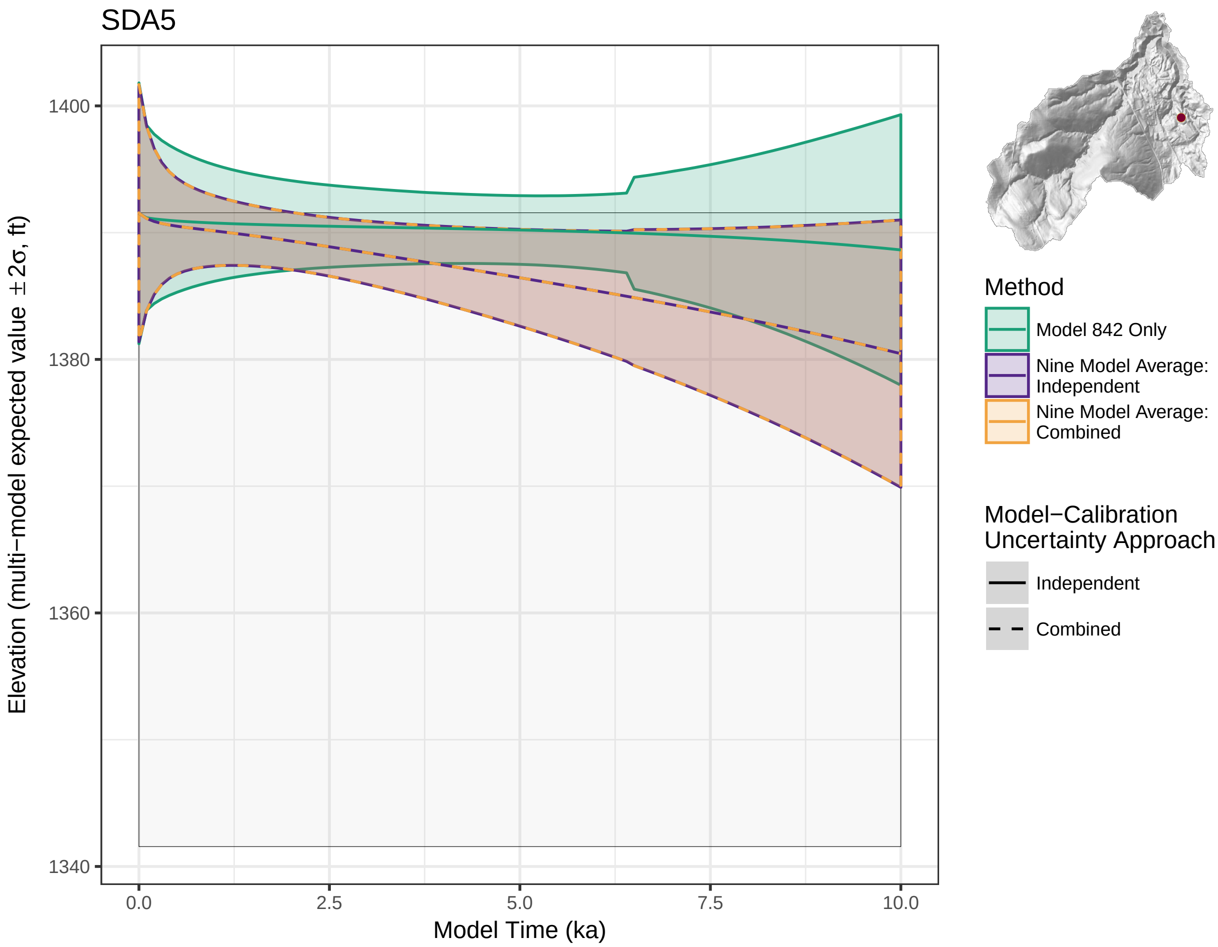

Figure F.22: Summary of prediction results at SDA5 showing expected elevation and uncertainty through time. The gray box is a 50 foot deep reference box that extends below the modern surface. Three expected values and 95% confidence regions are shown that corresponds to the two approaches to model selection (only 842 and all nine 800 variants) and the two approaches to model structure and calibration uncertainty (independent or covarying).

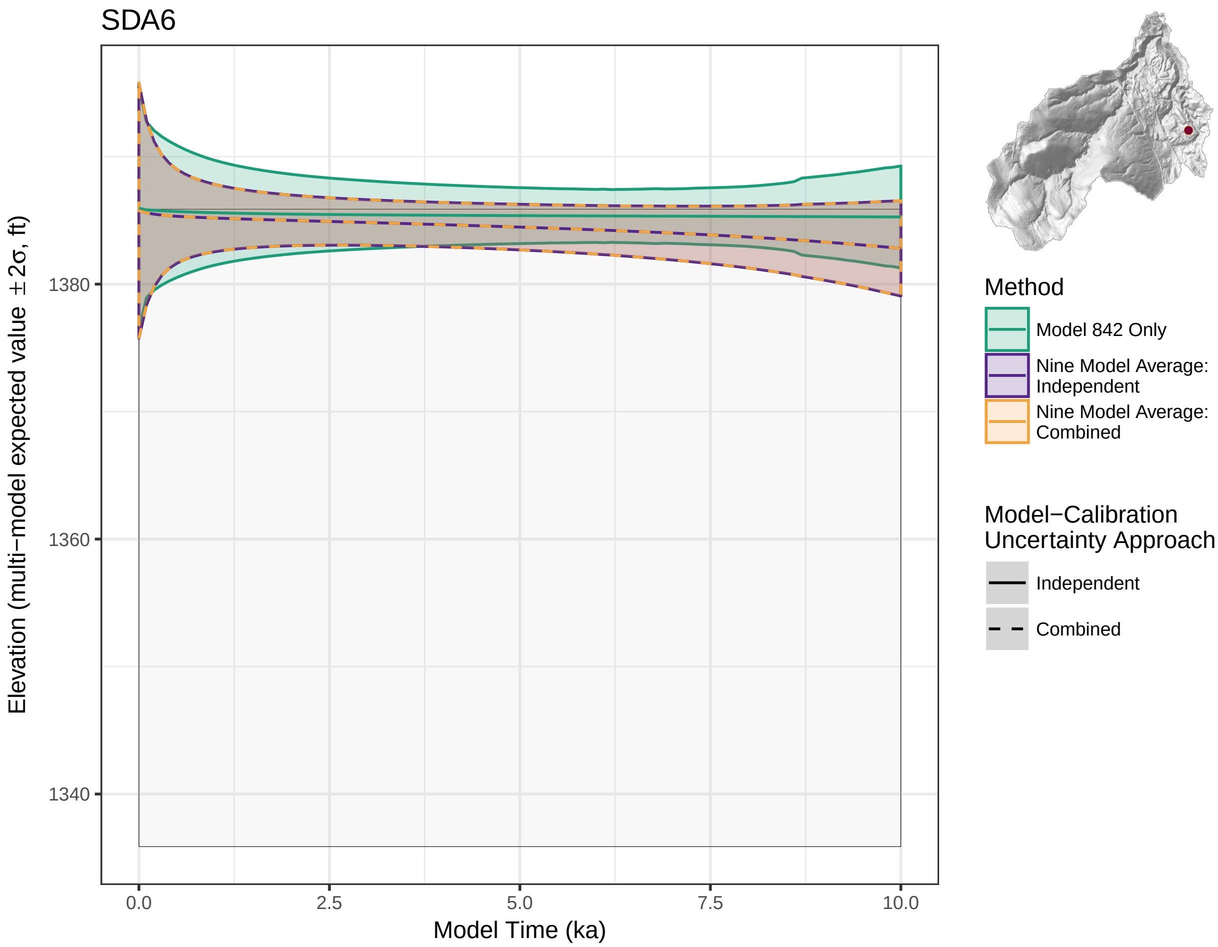

Figure F.23: Summary of prediction results at SDA6 showing expected elevation and uncertainty through time. The gray box is a 50 foot deep reference box that extends below the modern surface. Three expected values and 95% confidence regions are shown that corresponds to the two approaches to model selection (only 842 and all nine 800 variants) and the two approaches to model structure and calibration uncertainty (independent or covarying).

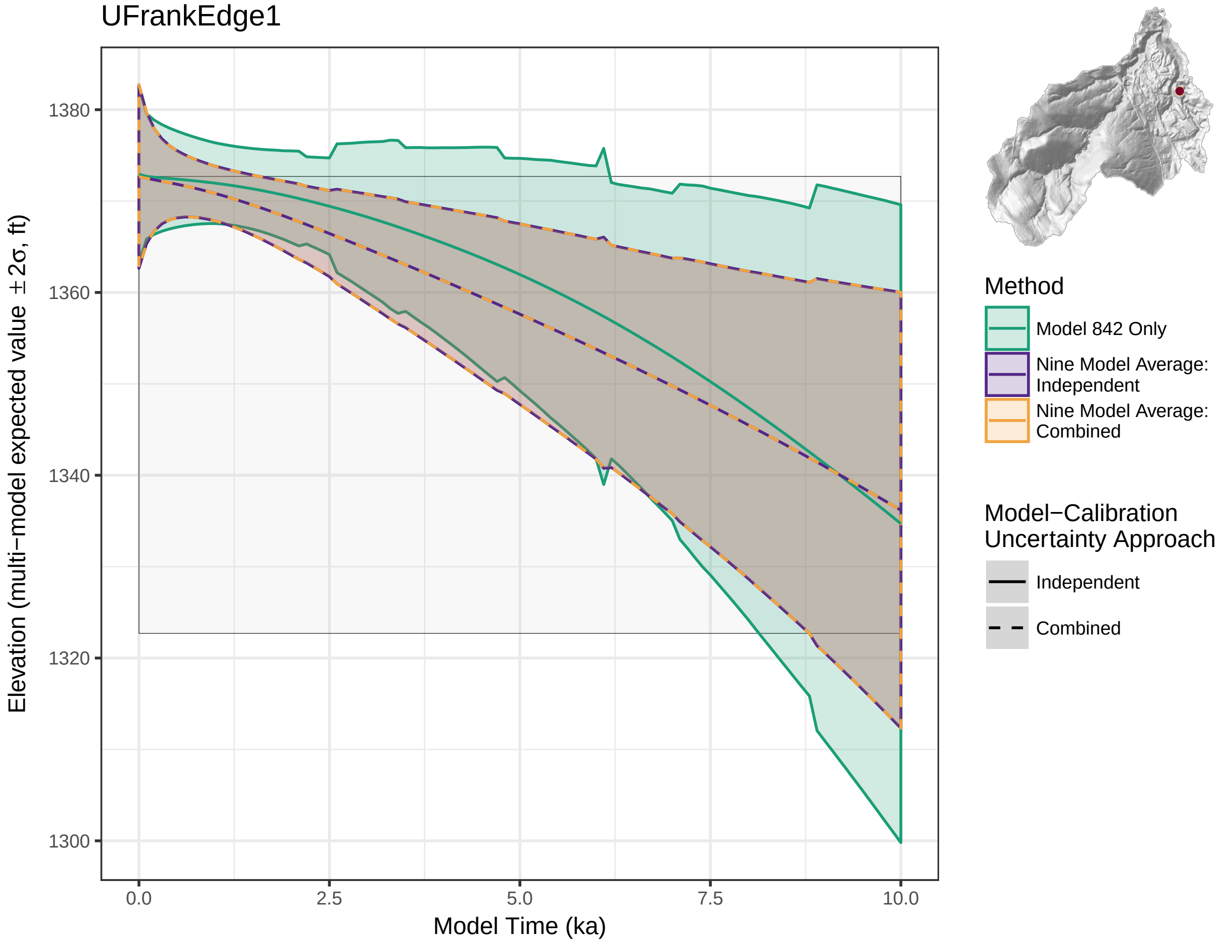

Figure F.24: Summary of prediction results at UFrankEdge1 showing expected elevation and uncertainty through time. The gray box is a 50 foot deep reference box that extends below the modern surface. Three expected values and 95% confidence regions are shown that corresponds to the two approaches to model selection (only 842 and all nine 800 variants) and the two approaches to model structure and calibration uncertainty (independent or covarying).

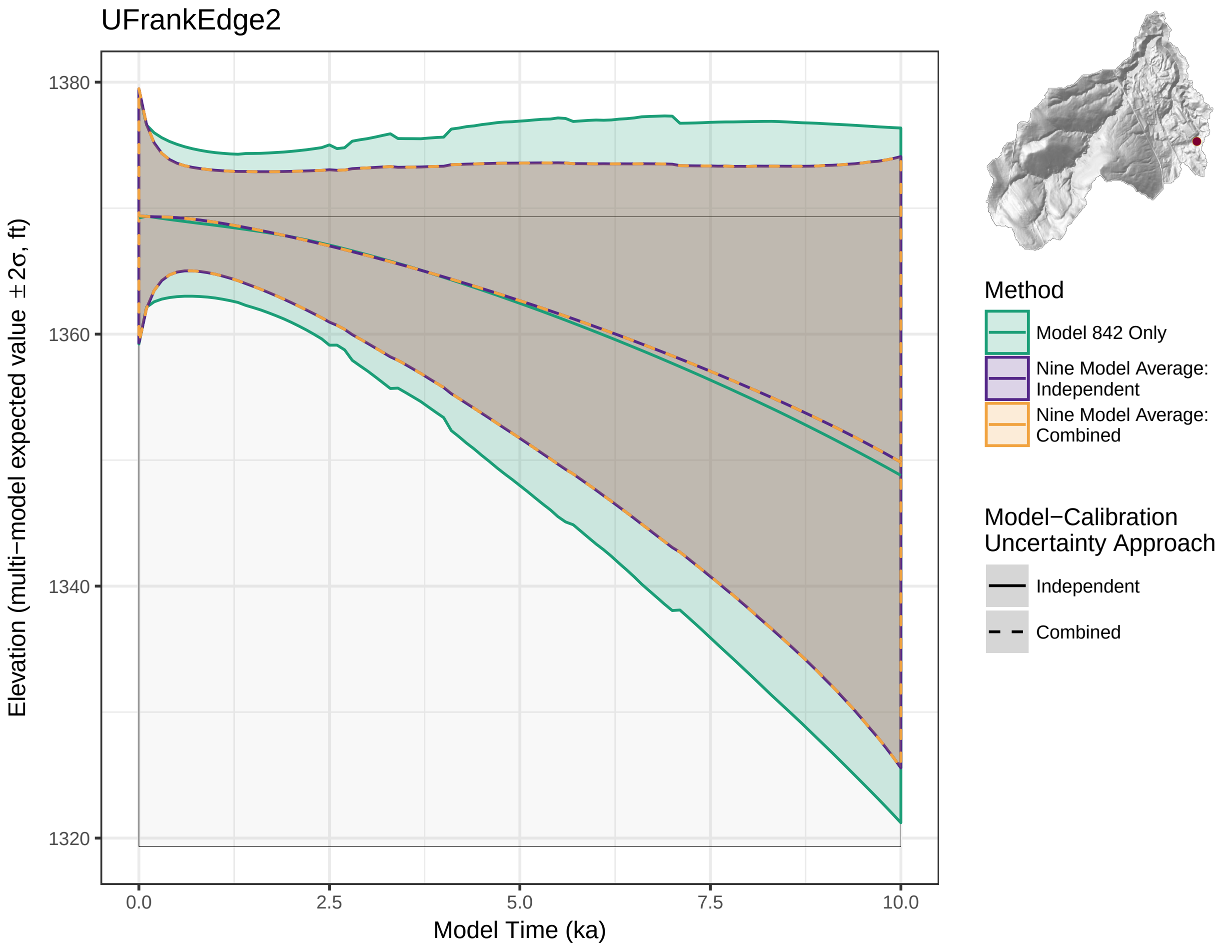

Figure F.25: Summary of prediction results at UFrankEdge2 showing expected elevation and uncertainty through time. The gray box is a 50 foot deep reference box that extends below the modern surface. Three expected values and 95% confidence regions are shown that corresponds to the two approaches to model selection (only 842 and all nine 800 variants) and the two approaches to model structure and calibration uncertainty (independent or covarying).

Bibliography

Abatzoglou, J. T. (2013), Development of gridded surface meteorological data for ecological applications and modelling, *International Journal of Climatology*, *33*(1), 121–131.

Abatzoglou, J. T., and T. J. Brown (2012), A comparison of statistical downscaling methods suited for wildfire applications, *International Journal of Climatology*, *32*(5), 772–780.

Adams, B., et al. (2017a), ”dakota, a multilevel parallel object-oriented framework for design optimization, parameter estimation, uncertainty quantification, and sensitivity analysis: Version 6.6 user manual,”, *Sandia Technical Report SAND2014-4253*.

Adams, B., et al. (2017b), ”dakota, a multilevel parallel object-oriented framework for design optimization, parameter estimation, uncertainty quantification, and sensitivity analysis: Version 6.6 theory manual,”, *Sandia Technical Report SAND2014-4253*.

Ahnert, F. (1976), Brief description of a comprehensive three-dimensional process-response model of landform development, *Zeitschrift für Geomorfologie, Supplementband*, *25*, 29–49.

Akaike, H. (1973), Information theory and an extension of the maximum likelihood principle, in *Second International Symposium on Information Theory*, edited by B. N. Petrov and F. Csaki, pp. 267–281, Akadémiai Kiado, Budapest.

Akaike, H. (1974), A new look at the statistical model identification, *IEEE transactions on automatic control*, *19*(6), 716–723.

Anderson, R. S. (1994), Evolution of the santa cruz mountains, california, through tectonic growth and geomorphic decay, *Journal of Geophysical Research*, *99*, 20,161–20,179.

Anderson, R. S., S. P. Anderson, and G. E. Tucker (2013), Rock damage and regolith transport by frost: An example of climate modulation of the geomorphology of the critical zone, *Earth Surface Processes and Landforms*, *38*(3), 299–316.

Andrews, D., and R. C. Bucknam (1987), Fitting degradation of shoreline scarps by a nonlinear diffusion model, *Journal of Geophysical Research*, *92*(B12), 12,857–12.

Attal, M., G. E. Tucker, A. C. Whittaker, P. A. Cowie, and G. P. Roberts (2008), Modeling fluvial incision and transient landscape evolution: Influence of dynamic channel adjustment, *Journal of Geophysical Research*, *113*, F03,013.

Attal, M., P. Cowie, A. Whittaker, D. Hobley, G. Tucker, and G. Roberts (2011), Testing fluvial erosion models using the transient response of bedrock rivers to tectonic forcing in the Apennines, Italy, *Journal of Geophysical Research*, *116*(F2), F02,005.

Bauer, H., and M. C. Mastin (1997), *Recharge from precipitation in three small glacial-till-mantled catchments in the Puget Sound Lowland, Washington*, US Department of the Interior, US Geological Survey.

Begin, Z. B. (1992), Application of quantitative morphologic dating to paleo-seismicity of the northwestern negev, israel, *Israel journal of earth-sciences*, *41*(2-4), 95–103.

Bennett, S. J. (2017), Report of the west valley erosion working group study 2: Recent erosion and deposition processes: Task 2.2: Infiltration and soil moisture determination; task 2.5: Erodibility of cohesive sediment; task 2.6: Erodibility of clastic sediment in selected gullies, stream channels, and streambanks, *Tech. rep.*, Phase 1 Studies Erosion Working Group.

Bergeron, M. (1985), Records of wells, test borings, and some measured geologic sections near the western new york nuclear service center, cattaraugus county, new york, open-file report 83-682, *Tech. rep.*, U.S. Geological Survey.

Beven, K., and M. Kirkby (1979), A physically based, variable contributing area model of basin hydrology, *Hydrological Sciences Journal*, *24*(1), 43–69.

Bishop, P. (2007), Long-term landscape evolution: linking tectonics and surface processes, *Earth Surface Processes and Landforms,*, *32*, 329–365.

Booth, A., and J. Roering (2011), A 1-d mechanistic model for the evolution of earthflow-prone hillslopes, *Journal of Geophysical Research*, *116*(F4), F04,021.

Booth, A. M., J. J. Roering, and A. W. Rempel (2013), Topographic signatures and a general transport law for deep-seated landslides in a landscape evolution model, *Journal of Geophysical Research: Earth Surface*, *118*(2), 603–624.

Borgonovo, E., X. Lu, E. Plischke, O. Rakovec, and M. C. Hill (2017), Making the most out of a hydrological model data set: Sensitivity analyses to open the model black-box, *Water Resources Research*, *53*(9), 7933–7950.

Box, G. E., J. S. Hunter, and W. G. Hunter (2005), *Statistics for experimenters: design, innovation, and discovery*, vol. 2, Wiley-Interscience New York.

Buckland, S. T., K. P. Burnham, and N. H. Augustin (1997), Model selection: an integral part of inference, *Biometrics*, pp. 603–618.

Buffington, J., and D. Montgomery (1997), A systematic analysis of eight decades of incipient motion studies, with special reference to gravel-bedded rivers, *Water Resources Research*, *33*(8), 1993–2029.

Burnham, K. P., and D. R. Anderson (2003), *Model selection and multimodel inference: a practical information-theoretic approach*, Springer Science & Business Media.

Carretier, S., and F. Lucazeau (2005), How does alluvial sedimentation at range fronts modify the erosional dynamics of mountain catchments?, *Basin Research*, *17*(3), 361–381.

Carretier, S., P. Martinod, M. Reich, and Y. Godderis (2016), Modelling sediment clasts transport during landscape evolution, *Earth Surface Dynamics*, *4*(1), 237–251.

Chatanantavet, P., and G. Parker (2009), Physically based modeling of bedrock incision by abrasion, plucking, and macroabrasion, *Journal of Geophysical Research: Earth Surface (2003–2012)*, *114*(F4).

Clark, M. P., and D. Kavetski (2010), Ancient numerical daemons of conceptual hydrological modeling: 1. fidelity and efficiency of time stepping schemes, *Water Resources Research*, *46*(10).

Codilean, A. T., P. Bishop, and T. B. Hoey (2006), Surface process models and the links between tectonics and topography, *Progress in Physical Geography*, *30*, 307–333.

Cortes, L. (2016), 2015 high resolution lidar & aerial orthoimagery, project western new york nuclear service, center and environs, *Tech. rep.*, The Sanborn Map Company, Inc.

Coulthard, T. J. (2001), Landscape evolution models: a software review, *Hydrological Processes*, *15*, 165–173.

Dai, A. (2013), Increasing drought under global warming in observations and models, *Nature Climate Change*, *3*(1), 52.

Daly, C., M. Halbleib, J. I. Smith, W. P. Gibson, M. K. Doggett, G. H. Taylor, J. Curtis, and P. P. Pasteris (2008), Physiographically sensitive mapping of climatological temperature and precipitation across the conterminous united states, *International journal of climatology*, *28*(15), 2031–2064.

Daniels, D. P., S. J. Fritz, and D. I. Leap (1991), Estimating recharge rates through unsaturated glacial till by tritium tracing, *Groundwater*, *29*(1), 26–34.

Davy, P., and D. Lague (2009), Fluvial erosion/transport equation of landscape evolution models revisited, *Journal of Geophysical Research-Earth Surface*, *114*(F3), F03,007.

de González, A. B., D. R. Cox, et al. (2007), Interpretation of interaction: A review, *The Annals of Applied Statistics*, *1*(2), 371–385.

Dennis, J. E., Jr., D. M. Gay, and R. E. Walsh (1981), An adaptive nonlinear least-squares algorithm, *ACM Trans. Math. Softw.*, *7*(3), 348–368, doi:10.1145/355958.355965.

DiBiase, R., and K. Whipple (2011), The influence of erosion thresholds and runoff variability on the relationships among topography, climate, and erosion rate, *Journal of Geophysical Research*, *116*(F4), F04,036.

DiBiase, R., K. Whipple, A. Heimsath, and W. Ouimet (2010), Landscape form and millennial erosion rates in the San Gabriel Mountains, CA, *Earth and Planetary Science Letters*, *289*(1-2), 134–144.

Dietrich, W., C. Wilson, D. Montgomery, and J. McKean (1993), Analysis of erosion thresholds, channel networks, and landscape morphology using a digital terrain model, *The Journal of Geology*, *101*(2), 259–278.

Dietrich, W. E., D. G. Bellugi, L. S. Sklar, J. D. Stock, A. M. Heimsath, and J. J. Roering (2003), Geomorphic transport laws for predicting landscape form and dynamics, in *Prediction in geomorphology*, edited by P. Wilcock and R. Iverson, Geophysical Monograph Series, AGU, Washington, D.C., doi:10.1029/135GM09.

DOE, and NYSERDA (2010), Final environmental impact statement for decommissioning and/or long-term stewardship at the west valley demonstration project and western new york nuclear service center (doe/eis-0226), *Tech. rep.*, United States Department of Energy and New York State Energy Research and Development Authority.

Dunne, T., and R. Black (1970), Partial area contributions to storm runoff in a small new england watershed, *Water Resources Research*, *6*(5), 1296–1311.

Duvall, A., E. Kirby, and D. Burbank (2004), Tectonic and lithologic controls on bedrock channel profiles and processes in coastal california, *Journal of Geophysical Research*, *109*(F3), F03,002.

Duvall, A. R., and G. E. Tucker (2015), Dynamic ridges and valleys in a strike-slip environment, *Journal of Geophysical Research: Earth Surface*, *120*(10), 2016–2026.

ESRI (2014), Arcgis desktop: Release 10.3.

Fakundiny, R. (1985), Practical applications of geological methods at the west valley low-level radioactive waste burial ground, western new york, *Northeastern Environmental Science*, *4*(3-4).

Foglia, L., S. Mehl, M. Hill, and P. Burlando (2013), Evaluating model structure adequacy: The case of the maggia valley groundwater system, southern switzerland, *Water Resources Research*, *49*(1), 260–282.

Ganti, V., P. Passalacqua, and E. Foufoula-Georgiou (2012), A sub-grid scale closure for nonlinear hillslope sediment transport models, *Journal of Geophysical Research: Earth Surface*, *117*(F2).

Giorgi, F., E.-S. Im, E. Coppola, N. Diffenbaugh, X. Gao, L. Mariotti, and Y. Shi (2011), Higher hydroclimatic intensity with global warming, *Journal of Climate*, *24*(20), 5309–5324.

Gran, K. B., N. Finnegan, A. L. Johnson, P. Belmont, C. Wittkop, and T. Rittenour (2013), Landscape evolution, valley excavation, and terrace development following abrupt postglacial base-level fall, *Geological Society of America Bulletin*, *125*(11-12), 1851–1864.

Haario, H., M. Laine, A. Mira, and E. Saksman (2006), Dram: efficient adaptive mcmc, *Statistics and Computing*, *16*(4), 339–354.

Hancock, G., and G. Willgoose (2001), Use of a landscape simulator in the validation of the siberia catchment evolution model: Declining equilibrium landforms, *Water Resources Research*, *37*(7), 1981–1992.

Hancock, G., J. Lowry, T. Coulthard, K. Evans, and D. Moliere (2010), A catchment scale evaluation of the siberia and caesar landscape evolution models, *Earth Surface Processes and Landforms*, *35*(8), 863–875.

Hanks, T. C., R. C. Bucknam, K. R. Lajoie, and R. E. Wallace (1984), Modification of wave-cut and faulting-controlled landforms, *Journal of Geophysical Research: Solid Earth*, *89*(B7), 5771–5790.

Hawkins, E., and R. Sutton (2009), The potential to narrow uncertainty in regional climate predictions, *Bulletin of the American Meteorological Society*, *90*(8), 1095–1107.

Heimsath, A., W. Dietrich, K. Nishiizumi, and R. Finkel (1997), The soil production function and landscape equilibrium, *Nature*, *388*(6640), 358–361.

Heimsath, A., R. DiBiase, and K. Whipple (2012), Soil production limits and the transition to bedrock-dominated landscapes, *Nature Geoscience*, *5*(3), 210–214.

Heimsath, A. M., W. E. Dietrich, K. Nishiizumi, and R. C. Finkel (1999), Cosmogenic nuclides, topography, and the spatial variation of soil depth, *Geomorphology*, *27*(1), 151–172.

Heimsath, A. M., W. E. Dietrich, K. Nishiizumi, and R. C. Finkel (2001a), Stochastic processes of soil production and transport: Erosion rates, topographic variation and cosmogenic nuclides in the oregon coast range, *Earth Surface Processes and Landforms*, *26*(5), 531–552.

Heimsath, A. M., J. Chappell, W. E. Dietrich, K. Nishiizumi, and R. C. Finkel (2001b), Late quaternary erosion in southeastern australia: a field example using cosmogenic nuclides, *Quaternary International*, *83*, 169–185.

Held, I. M., and B. J. Soden (2006), Robust responses of the hydrological cycle to global warming, *Journal of climate*, *19*(21), 5686–5699.

Hill, M. C., and C. R. Tiedeman (2007), *Effective groundwater model calibration: with analysis of data, sensitivities, predictions, and uncertainty*, John Wiley & Sons.

Hill, M. C., D. Kavetski, M. Clark, M. Ye, M. Arabi, D. Lu, L. Foglia, and S. Mehl (2016), Practical use of computationally frugal model analysis methods, *Groundwater*, *54*(2), 159–170.

Hobley, D. E., H. D. Sinclair, S. M. Mudd, and P. A. Cowie (2011), Field calibration of sediment flux dependent river incision, *Journal of Geophysical Research: Earth Surface (2003–2012)*, *116*(F4).

Hobley, D. E., J. M. Adams, S. S. Nudurupati, E. W. Hutton, N. M. Gasparini, E. Istanbulluoglu, and G. E. Tucker (2017), Creative computing with landlab: an open-source toolkit for building, coupling, and exploring two-dimensional numerical models of earth-surface dynamics, *Earth Surface Dynamics*, *5*(1), 21.

Howard, A. D. (1994), A detachment-limited model of drainage basin evolution, *Water Resources Research*, *30*(7), 2261–2285.

Howard, A. D. (1998), Long profile development of bedrock channels: Interaction of weathering, mass wasting, bed erosion, and sediment transport, in *Rivers over Rock: Fluvial Processes in Bedrock Channels*, edited by K. J. Tinkler and E. E. Wohl, Geophysical Monograph Series, pp. 297–320, American Geoph. Union.

Howard, A. D., and G. Kerby (1983), Channel changes in badlands, *Geological Society of America Bulletin*, *94*, 739–752.

Howard, A. D., and H. E. Tierney (2012), Taking the measure of a landscape: Comparing a simulated and natural landscape in the virginia coastal plain, *Geomorphology*, *137*(1), 27–40.

Howard, A. D., W. E. Dietrich, and M. A. Seidl (1994), Modeling fluvial erosion on regional to continental scales, *Journal of Geophysical Research*, *99*(B7), 13,971–13,986.

Huang, D., T. T. Allen, W. I. Notz, and N. Zeng (2006), Global optimization of stochastic black-box systems via sequential kriging meta-models, *Journal of global optimization*, *34*(3), 441–466.

Huang, X., and J. Niemann (2006), An evaluation of the geomorphically effective event for fluvial processes over long periods, *Journal of Geophysical Research*, *111*(F3), F03,015.

Ijjász-Vásquez, E. J., R. L. Bras, and G. E. Moglen (1992), Sensitivity of a basin evolution model to the nature of runoff production and to initial conditions, *Water Resources Research*, *28*(10), 2733–2741.

Ijjasz-Vasquez, E. J., R. L. Bras, and I. Rodriguez-Iturbe (1993), Hack's relation and optimal channel networks: The elongation of river basins as a consequence of energy minimization, *Water Resources Research*, *20*, 1583–1586.

Jaynes, E., and G. Bretthorst (2003), *Probability Theory: The Logic of Science*, Cambridge University Press.

Johnstone, S. A., and G. E. Hilley (2015), Lithologic control on the form of soil-mantled hillslopes, *Geology*, *43*(1), 83–86.

Jones, D. R., M. Schonlau, and W. J. Welch (1998), Efficient global optimization of expensive black-box functions, *Journal of Global optimization*, *13*(4), 455–492.

Julien, P. (1998), *Erosion and sedimentation*, Cambridge Univ Pr.

Kavetski, D., and M. P. Clark (2010), Ancient numerical daemons of conceptual hydrological modeling: 2. impact of time stepping schemes on model analysis and prediction, *Water Resources Research*, *46*(10).

Kavetski, D., and G. Kuczera (2007), Model smoothing strategies to remove microscale discontinuities and spurious secondary optima in objective functions in hydrological calibration, *Water Resources Research*, *43*(3).

Kirby, E., and K. Whipple (2001), Quantifying differential rock-uplift rates via stream profile analysis, *Geology*, *29*(5), 415–418.

Kirkby, M., and L. Bull (2000), Some factors controlling gully growth in fine-grained sediments: a model applied in southeast spain, *Catena*, *40*(2), 127–146.

Kooi, H., and C. Beaumont (1994), Escarpment evolution on high-elevation rifted margins: Insights derived from a surface processes model that combines diffusion, advection, and reaction, *Journal of Geophysical Research*, *99*, 12,191–12,209.

LaFleur, R. G. (1979), Glacial geology and stratigraphy of western new york nuclear service center and vicinity, cattaraugus and erie counties, new york, *Tech. rep.*, US Geological Survey,.

Lague, D. (2010), Reduction of long-term bedrock incision efficiency by short-term alluvial cover intermittency, *Journal of Geophysical Research: Earth Surface*, *115*(F2).

Lague, D., N. Hovius, and P. Davy (2005), Discharge, discharge variability, and the bedrock channel profile, *J. Geophys. Res*, *110*(F04006), doi:10.1029/2004JF000259.

Laherrere, J., and D. Sornette (1998), Stretched exponential distributions in nature and economy: fat tails with characteristic scales, *The European Physical Journal B-Condensed Matter and Complex Systems*, *2*(4), 525–539.

Langston, A. L., and G. E. Tucker (2018), Developing and exploring a theory for the lateral erosion of bedrock channels for use in landscape evolution models, *Earth Surface Dynamics*, *6*(1), 1–27.

Lau, W. K.-M., H.-T. Wu, and K.-M. Kim (2013), A canonical response of precipitation characteristics to global warming from cmip5 models, *Geophysical Research Letters*, *40*(12), 3163–3169.

Lavé, J., and J. Avouac (2001), Fluvial incision and tectonic uplift across the Himalayas of central Nepal, *Journal of Geophysical Research*, *106*(B11), 26,561.

Liu, Z., et al. (2009), Transient simulation of last deglaciation with a new mechanism for bølling-allerød warming, *Science*, *325*(5938), 310–314.

Loget, N., P. Davy, and J. Van Den Driessche (2006), Mesoscale fluvial erosion parameters deduced from modeling the mediterranean sea level drop during the messinian (late miocene), *Journal of Geophysical Research: Earth Surface (2003–2012)*, *111*(F3).

Madden, R. A. (1976), Estimates of the natural variability of time-averaged sea-level pressure, *Monthly Weather Review*, *104*(7), 942–952.

Martin, Y., and M. Church (2004), Numerical modelling of landscape evolution: Geomorphological perspectives, *Progress in Physical Geography*, *28*, 317–339.

Matthews, H. D., and K. Caldeira (2008), Stabilizing climate requires near-zero emissions, *Geophysical research letters*, *35*(4).

McKean, J., W. Dietrich, R. Finkel, J. Southon, and M. Caffee (1993), Quantification of soil production and downslope creep rates from cosmogenic 10be accumulations on a hillslope profile, *Geology*, *21*(4), 343–346.

Menne, M. J., I. Durre, R. S. Vose, B. E. Gleason, and T. G. Houston (2012), An overview of the global historical climatology network-daily database, *Journal of Atmospheric and Oceanic Technology*, *29*(7), 897–910.

Meza, J. C., R. A. Oliva, P. Hough, and P. Williams (2007), Opt++: An object-oriented toolkit for nonlinear optimization, *ACM Transactions on Mathematical Software (TOMS)*, *33*(2), 12.

Miller, S. R., and R. L. Slingerland (2006), Topographic advection on fault-bend folds: Inheritance of valley positions and the formation of wind gaps, *Geology*, *34*(9), 769–772.

Miller, S. R., R. L. Slingerland, and E. Kirby (2007), Characteristics of steady state fluvial topography above fault-bend folds, *Journal of Geophysical Research*, *112*, F04,004.

Mohanty, B., R. S. Kanwar, and C. Everts (1994), Comparison of saturated hydraulic conductivity measurement methods for a glacial-till soil, *Soil Science Society of America Journal*, *58*(3), 672–677.

Morris, M. D. (1991), Factorial sampling plans for preliminary computational experiments, *Technometrics*, *33*(2), 161–174.

Nash, D. B. (1980), Morphologic dating of degraded normal fault scarps, *The Journal of Geology*, *88*(3), 353–360.

O'Gorman, P. A., and T. Schneider (2009), The physical basis for increases in precipitation extremes in simulations of 21st-century climate change, *Proceedings of the National Academy of Sciences*, *106*(35), 14,773–14,777.

O'Loughlin, E. (1986), Prediction of surface saturation zones in natural catchments by topographic analysis, *Water Resources Research*, *22*(5), 794–804.

Pazzaglia, F. J. (2003), Landscape evolution models, *Developments in Quaternary Sciences*, *1*, 247–274.

Peckham, S. D., E. W. Hutton, and B. Norris (2013), A component-based approach to integrated modeling in the geosciences: The design of csdms, *Computers & Geosciences*, *53*, 3–12.

Pelletier, J. (2013), Fundamental principles and techniques of landscape evolution modeling, in *Treatise on Geomorphology*, Elsevier Inc.

Pelletier, J. D. (2010), How do pediments form?: A numerical modeling investigation with comparison to pediments in southern arizona, usa, *Geological Society of America Bulletin*, *122*(11-12), 1815–1829.

Pelletier, J. D., and C. Rasmussen (2009), Geomorphically based predictive mapping of soil thickness in upland watersheds, *Water Resources Research*, *45*(9).

Perron, J. T., and L. Royden (2013), An integral approach to bedrock river profile analysis, *Earth Surface Processes and Landforms*, *38*(6), 570–576.

Perron, J. T., J. W. Kirchner, and W. E. Dietrich (2009), Formation of evenly spaced ridges and valleys, *Nature*, *460*(7254), 502–505.

Poeter, E. P., and M. C. Hill (2007), Mma, a computer code for multi-model analysis, *Tech. rep.*, United States Geological Survey-Nevada, Henderson, Nevada.

Prudencio, E. E., and K. W. Schulz (2012), The parallel C++ statistical library 'QUESO': Quantification of Uncertainty for Estimation, Simulation and Optimization, in *Euro-Par 2011: Parallel Processing Workshops*, pp. 398–407, Springer.

Randall, A. (1980), Glacial stratigraphy in part of buttermilk creek valley: in lafleur, r.g., guidebook for 43rd annual reunion for northeast friends of pleistocene, *Tech. rep.*, Northeast Friends of Pleistocene.

Rengers, F. K., and G. Tucker (2014), Analysis and modeling of gully headcut dynamics, north american high plains, *Journal of Geophysical Research: Earth Surface*, *119*(5), 983–1003.

Rickard, L. (1975), Correlation of the silurian and devonian rocks in new york state, map and chart series no. 24, *Tech. rep.*, New York State Museum and Science Service.

Roering, J. (2008), How well can hillslope evolution models "explain" topography? Simulating soil transport and production with high-resolution topographic data, *Geological Society of America Bulletin*, *120*(9-10), 1248–1262.

Roering, J., J. Perron, and J. Kirchner (2007), Functional relationships between denudation and hillslope form and relief, *Earth and Planetary Science Letters*, *264*(1), 245–258.

Roering, J., J. Kirchner, and W. Dietrich (1999), Evidence for nonlinear, diffusive sediment transport on hillslopes and implications for landscape morphology, *WATER RESOURCES RESEARCH*, *35*(3), 853–870.

Roering, J., J. Kirchner, L. Sklar, and W. Dietrich (2001), Hillslope evolution by nonlinear creep and landsliding: An experimental study, *GEOLOGY*, *29*(2), 143–146.

Ronayne, M. J., T. B. Houghton, and J. D. Stednick (2012), Field characterization of hydraulic conductivity in a heterogeneous alpine glacial till, *Journal of hydrology*, *458*, 103–109.

Rosenbloom, N. A., and R. S. Anderson (1994), Hillslope and channel evolution in a marine terraced landscape, santa cruz, california, *Journal of Geophysical Research*, *99*, 14,013–14,029.

Rossi, M. W., K. X. Whipple, and E. R. Vivoni (2016), Precipitation and evapotranspiration controls on daily runoff variability in the contiguous united states and puerto rico, *Journal of Geophysical Research: Earth Surface*, *121*(1), 128–145.

Saltelli, A., S. Tarantola, F. Campolongo, and M. Ratto (2004), *Sensitivity analysis in practice: a guide to assessing scientific models*, John Wiley & Sons.

Saltelli, A., M. Ratto, T. Andres, F. Campolongo, J. Cariboni, D. Gatelli, M. Saisana, and S. Tarantola (2008), *Global sensitivity analysis: the primer*, John Wiley & Sons.

Shobe, C. M., G. E. Tucker, and K. R. Barnhart (2017), The space 1.0 model: a landlab component for 2-d calculation of sediment transport, bedrock erosion, and landscape evolution, *Geoscientific Model Development*, *10*(12), 4577–4604.

Sidorchuk, A. (1999), Dynamic and static models of gully erosion, *Catena*, *37*(3), 401–414.

Sklar, L., and W. Dietrich (2004), A mechanistic model for river incision into bedrock by saltating bed load, *Water Resources Research*, *40*(6), W06,301.

Small, E., R. Anderson, and G. Hancock (1999), Estimates of the rate of regolith production using 10be and 26al from an alpine hillslope, *Geomorphology*, *27*(1), 131–150.

Small, E. E., R. S. Anderson, J. L. Repka, and R. Finkel (1997), Erosion rates of alpine bedrock summit surfaces deduced from in situ 10be and 26al, *Earth and Planetary Science Letters*, *150*(3-4), 413–425.

Smith, G., and R. Jacobi (2001), Tectonic and eustatic signals in the sequence stratigraphy of the upper devonian canadaway group, new york state, *AAPG Bulletin*, *85*(2), 325–357.

Snyder, N., K. Whipple, G. Tucker, and D. Merritts (2000), Landscape response to tectonic forcing: Digital elevation model analysis of stream profiles in the mendocino triple junction region, northern california, *Bulletin of the Geological Society of America*, *112*(8), 1250.

Snyder, N., K. Whipple, G. Tucker, and D. Merritts (2003), Importance of a stochastic distribution of floods and erosion thresholds in the bedrock river incision problem, *Journal of Geophysical Research*, *108*(B2), 2117.

Soil Survey Staff (2017), Soil survey geographic (ssurgo) database.

Solomon, S., G.-K. Plattner, R. Knutti, and P. Friedlingstein (2009), Irreversible climate change due to carbon dioxide emissions, *Proceedings of the national academy of sciences*, *106*(6), 1704–1709.

Stock, J. D., and D. R. Montgomery (1999), Geologic constraints on bedrock river incision using the stream power law, *Journal of Geophysical Research: Solid Earth (1978–2012)*, *104*(B3), 4983–4993.

Storch, H. v., and F. W. Zwiers (2001), Statistical analysis in climate research.

Strobel, M. L. (1993), Hydraulic properties of three types of glacial deposits in ohio, *Tech. rep.*, US Geological Survey; Books and Open-File Reports Section [distributor],.

Sugiura, N. (1978), Further analysts of the data by akaike's information criterion and the finite corrections: Further analysts of the data by akaike's, *Communications in Statistics-Theory and Methods*, *7*(1), 13–26.

Taylor, K. E., R. J. Stouffer, and G. A. Meehl (2012), An overview of cmip5 and the experiment design, *Bulletin of the American Meteorological Society*, *93*(4), 485–498.

Temme, A., J. Schoorl, L. Claessens, A. Veldkamp, and F. Shroder (2013), Quantitative modeling of landscape evolution, treatise on geomorphology, in *Quantitative Modeling of Geomorphology*, 2.13, pp. 180–200, Academic Press.

Tesmer, I. (1963), Geology of chautauqua county, new york, part 1 stratigraphy and paleontology (upper devonian), (391).

Tomkin, J. H., M. T. Brandon, F. J. Pazzaglia, J. R. Barbour, and S. D. Willett (2003), Quantitative testing of bedrock incision models for the clearwater river, nw washington state, *Journal of Geophysical Research*, *108*, 2308.

Trenberth, K. E. (2011), Changes in precipitation with climate change, *Climate Research*, *47*(1/2), 123–138.

Tucker, G. (2004), Drainage basin sensitivity to tectonic and climatic forcing: Implications of a stochastic model for the role of entrainment and erosion thresholds, *Earth Surface Processes and Landforms*, *29*(2), 185–205, doi:{10.1002/esp.1020}.

Tucker, G., and K. Whipple (2002), Topographic outcomes predicted by stream erosion models: Sensitivity analysis and intermodel comparison, *Journal of Geophysical Research*, *107*(B9), 2179.

Tucker, G. E. (2015), Landscape evolution, in *Treatise in Geophysics*, edited by G. Shubert, Elsevier.

Tucker, G. E., and R. L. Bras (1998), Hillslope processes, drainage density, and landscape morphology, *Water Resources Research*, *36*, 1953–1964.

Tucker, G. E., and R. L. Bras (2000), A stochastic approach to modeling the role of rainfall variability in drainage basin evolution, *Water Resources Research*, *36*(7), 1953–1964.

Tucker, G. E., and G. R. Hancock (2010), Modelling landscape evolution, *Earth Surface Processes and Landforms*, *46*, 28–50.

Tucker, G. E., and R. L. Slingerland (1997), Drainage basin response to climate change, *Water Resources Research*, *33*, 2031–2047.

Tucker, G. E., S. T. Lancaster, N. M. Gasparini, R. L. Bras, and S. M. Rybarczyk (2001), An object-oriented framework for hydrologic and geomorphic modeling using triangular irregular networks, *Computers and Geosciences*, *27*, 959–973.

Valla, P., P. van der Beek, and D. Lague (2010), Fluvial incision into bedrock: Insights from morphometric analysis and numerical modeling of gorges incising glacial hanging valleys (Western Alps, France), *Journal of Geophysical Research*, *115*(F2), F02,010.

Valters, D. (2016), Modelling geomorphic systems: Landscape evolution, *Geomorphological Techniques*, *12*, 1–24.

van der Beek, P., and P. Bishhop (2003), Cenozoic river profile development in the upper lachlan catchment (se australia) as a test quantitative fluvial incision models, *Journal of Geophysical Research*, *108*, 10.1029/2002JB002125.

Van Griensven, A., T. Meixner, S. Grunwald, T. Bishop, M. Diluzio, and R. Srinivasan (2006), A global sensitivity analysis tool for the parameters of multi-variable catchment models, *Journal of hydrology*, *324*(1), 10–23.

Whipple, K. X. (2004), Bedrock rivers and the geomorphology of active orogens, *Annual Review of Earth and Planetary Sciences*, *32*, 151–185.

Whipple, K. X., and G. E. Tucker (1999), Dynamics of the stream-power river incision model: Implications for height limits of mountain ranges, landscape response timescales, and research needs, *Journal of Geophysical Research*, *104*, 17,661–17,674.

Whipple, K. X., and G. E. Tucker (2002), Implications of sediment-flux-dependent river incision models for landscape evolution, *Journal of Geophysical Research*, *107*, doi 10.1029/2000JB000044.

Whipple, K. X., G. S. Hancock, and R. S. Anderson (2000a), River incision into bedrock: Mechanics and relative efficacy of plucking, abrasion, and cavitation, *Geological Society of America Bulletin*, *112*, 490–503.

Whipple, K. X., N. P. Snyder, and K. Dollenmayer (2000b), Rates and processes of bedrock incision by the upper ukak river since the 1912 novarupta ash flow in the valley of ten thousand smokes, alaska, *Geology*, *28*(9), 835–838.

Whittaker, A., P. Cowie, M. Attal, G. Tucker, and G. Roberts (2007), Contrasting transient and steady-state rivers crossing active normal faults: new field observations from the Central Apennines, Italy, *Basin Research*, *19*(4), 529–556.

Wilcock, P. R., and R. M. Iverson (2003), *Prediction in geomorphology*, AGU, Washington, D.C., geophysical Monograph Series 135 doi:10.1029/135GM01.

Willgoose, G. (2005), Mathematical modeling of whole landscape evolution, *Annual Review of Earth and Planetary Sciences*, *33*, 14.1–14.17.

Willgoose, G., R. L. Bras, and I. Rodriguez-Iturbe (1991a), A coupled channel network growth and hillslope evolution model, 1, theory, *Water Resources Research*, *27*(7), 1671–1684.

Willgoose, G., R. L. Bras, and I. Rodriguez-Iturbe (1991b), A physical explanation of an observed link area-slope relationship, *Water Resources Research*, *27*(7), 1697–1702.

Willgoose, G. R., and G. R. Hancock (2011), Applications of long-term erosion and landscape evolution models, in *Handbook of Erosion Modelling*, John Wiley & Sons.

Wilson, M., and R. A. Young (2018), Phase 1 erosion studies: Study 1 – terrain analysis, *Tech. rep.*, West Valley Erosion Working Group.

Wilson, P., and R. Toumi (2005), A fundamental probability distribution for heavy rainfall, *Geophysical Research Letters*, *32*(14).

Yanites, B., G. Tucker, K. Mueller, Y. Chen, T. Wilcox, S. Huang, and K. Shi (2010), Incision and channel morphology across active structures along the Peikang River, central Taiwan: Implications for the importance of channel width, *Geological Society of America Bulletin*, *122*(7-8), 1192.

Yip, S., C. A. Ferro, D. B. Stephenson, and E. Hawkins (2011), A simple, coherent framework for partitioning uncertainty in climate predictions, *Journal of Climate*, *24*(17), 4634–4643.

Zadins, Z. (1997), A Hydrogeologic Evaluation of “Geologic and Hydrologic Implication of the Buried Bedrock Valley that Extends from the Western New York Nuclear Service Center into Erie County, NY”, *Tech. rep.*, Dames and Moore.

Zhang, L., G. Parker, C. Stark, T. Inoue, E. Viparelli, X. Fu, and N. Izumi (2015), Macro-roughness model of bedrock-alluvial river morphodynamics, *Earth Surface Dynamics*, *3*(1), 113.